Fused Porphyrin Oligomers as Molecular Wires and Approaches to Related Nanobelts



Jieren Deng

Keble College

University of Oxford

A thesis submitted for the degree of

Doctor of Philosophy

Hilary 2022

Acknowledgement

First of all, I would like to express my deepest thanks of gratitude to my supervisor, Prof. Harry L. Anderson for his patient supervision and support of my study in the past four years. When I look back on the plans that we wrote on a paper on the first day we met, several ambitious targets have finally come true. These can not be achieved without his daily supervision and encouragement in these years.

I would also like to thank Dr. Pernille S. Bols, Dr. Henrik Gotfredsen, Dr. Jeff M. Van Raden and Sebastian M. Kopp, who I have been closely working with in the lab from dawn to dusk, sometimes in the weekend. I also want to present my appreciation to my collaborators, especially to Dr. James O. Thomas, Dr. Zhixin Chen and Dr. Edmund Leary for insightful discussions on the projects. I would also like to express my gratitude to Dr. Keith G. Andrews, Dr. Zhixin Chen, Dr. Yueze Gao, Dr. Henrik Gotfredsen, Dr. Connor W. Patrick, Dr. James O. Thomas, Dr. Wenjun Xu, Joshua L. Field, Janko Hergenhahn and Sebastian M. Kopp for proofreading parts of my thesis.

I would like to extend my deep gratitude to the current and past members in the Anderson group. They are Andrew, Bart, Bobby, Boom, Connor, Dennis, He, Henrik, Iago, Igor, Isa, Isaac, Jake, James, Janko, Jeff, Jibin, Joe, Josh, Julia, Kate, Keith, Lara, Lorel, Marcin, Martin, Michael, Michel, Paramveer, Pernille, Prakhar, Przemek, Qiang, Sebastian, Steffen, Stephen, Stuart, Théa, Tom, Virginia, Wenjun, Will, Wojtek and Yueze.

Finally, I want to express my deepest appreciation to my family, especially to my mother. Thank you for your love and support, which have helped me overcome the hardships in the COVID-19 pandemic, and finish this DPhil.

Abstract

Triply-linked (edge-fused) porphyrin oligomers with strongly coupled π orbitals can be used for studying long range charge transport, and are expected to be promising candidates for fabrication of electronic devices. This thesis details the synthesis, characterization and properties of a range of linear fused porphyrin oligomers with different metals (zinc and nickel), and attempts toward the cyclic fused porphyrin oligomers (nanobelts).

Chapter 1 reviews the synthesis, electronic properties and charge transport studies of three classes of conjugated porphyrin oligomers which have been intensively investigated — butadiyne-linked, ethyne-linked and fused porphyrin oligomers. The single-molecule conductance studies on the linear oligomers, the template-directed synthesis of cyclic oligomers, and the global (anti)aromaticity of porphyrin nanorings are detailed.

Chapter 2 details the attempts toward the *meso–meso* singly-linked porphyrin nanorings and the related fused porphyrin nanobelts. Guided by computational modeling, we show that oligopyridyl templates can be used to bend the rod-like *meso–meso* singly-linked porphyrin oligomers into covalent nanorings. These nanorings consist of 24 porphyrin units, with a single butadiyne link. Their elliptical conformations have been probed by scanning tunneling microscopy. Upon photoexcitation, the template-free nanorings exhibit ultrafast excited state energy transfer (~8.5 ps) from the exciton-coupled *meso–meso* linked porphyrin array to the π-conjugated butadiyne-linked porphyrin dimer segment, which mimics the B850 ring in the natural light harvesting system. The successful synthesis of these rings also provides insight into the future works on making the singly-linked porphyrin nanorings and fused porphyrin nanobelts.

Chapter 3 presents new advances in synthesis and charge transport studies on a family of linear fused nickel(II) porphyrin oligomers up to an octamer. The molecular conductance is measured by STM break junction technique, in which the molecules are connected to gold electrodes via covalent C–Au contacts. The fused porphyrin octamer junctions (~8 nm in length) express low-bias molecular conductance ranging from 10^{-3} to 10^{-5} G_0 that has been rarely observed in single-molecule junctions beyond 5 nm. This reflects the weakly distance-dependent attenuation feature for the fused porphyrin oligomers and the low effective contact resistance for the covalent C–Au contacts.

Chapter 4 studies the charge transport in a fused nickel(II) porphyrin octamer-graphene single-molecule transistor. We demonstrate how molecular and graphene transport pathways influence the overall device conductance and demonstrate that transport remains phase-coherent through a porphyrin octamer junction that is about 8 nm in length. We also investigate the relationship between the charge state of the molecule and its conductance — a three-fold increase of the conductance and the appearance of the Kondo resonance were observed upon oxidation of the porphyrin octamer to a radical cation.

Chapter 5 investigates the extent of polaron delocalization in the radical cations of fused zinc(II) porphyrin oligomers. The radical cations were generated in solution by chemical and electrochemical oxidation, and probed by UV–vis–NIR–IR and EPR spectroscopies. We demonstrate that the polaron states in the fused porphyrin oligomers are coherently delocalized over 10 porphyrin units ($\geq$ 8.5 nm in length). This is unprecedented for the extent of intrachain polaron delocalization in a π-conjugated organic material in solution. In addition to the polaron delocalization length, we also show that the fused zinc(II) porphyrin hexamer and longer oligomers are partially oxidized to form stable radical cations in air.

Supplement to Statement of Authorship

The works presented in this thesis involve collaborations with scientists from various fields, ranging from synthetic organic chemists, physical chemists to physicists and materials scientists.

In Chapter 1, the calculations of the ^{1}H NMR chemical shifts, Nucleus Independent Chemical Shift (NICS) plots and ring current susceptibilities for butadiyne-linked six-porphyrin nanoring were conducted by David Bradley, Dr. Martin D. Peeks (School of Chemistry, University of New South Wales, Australia) and Dr. Michael Jirásek (Laboratory of Organic Chemistry, ETH Zurich, Switzerland).

In Chapter 2, the design, synthesis and characterization of all the porphyrin oligomers as well as the oligopyridine templates were carried out by the author in close collaboration with Dr. Henrik Gotfredsen and Dr. Jeff M. Van Raden (Department of Chemistry, University of Oxford, UK). The molecular mechanics and molecular dynamics calculations were performed by Janko Hergenhahn, under the supervision of Prof. Fernanda Duarte (Department of Chemistry, University of Oxford, UK). The scanning probe microscopy experiments and analysis were carried out by Michael Clarke, Abigail Bellamy-Carter, Jack Hart, Dr. James O'Shea and Dr. Alex Saywell (School of Physics & Astronomy, University of Nottingham, UK). Dr. Marcello Righetto and Prof. Laura M. Herz (Department of Physics, University of Oxford, UK) investigated the time-resolved photophysics.

In Chapter 3, all STM break-junction measurements and data analysis were carried out by Dr. Edmund Leary (IMDEA Nanoscience Institute, Spain).

In Chapter 4, the device fabrication, conductance measurement, as well as data analysis were performed by Dr. Zhixin Chen, Dr. James O. Thomas, in collaboration with Prof. G. Andrew D. Briggs and Prof. Lapo Bogani (Department of Materials, University of Oxford, UK). The theoretical calculations were carried out by Dr. Songjun Hou and Dr. Qingqing Wu, under the supervision of Prof. Colin J. Lambert (Department of Physics, Lancaster University, UK).

In Chapter 5, the spectroelectrochemistry measurements and data analysis were performed by the author in close collaboration with Sebastian M. Kopp, assisted by Dr. Robert M. J. Jacobs (Department of Chemistry, University of Oxford, UK). The EPR experiments and data analysis were performed by Sebastian M. Kopp, working with Ashley J. Redman, under the supervision of Prof. Christiane R. Timmel (Department of Chemistry, University of Oxford, UK).

Contents

List of Publications ..... **ix**

1 Introduction **1**

1.1 Porphyrins **2**

1.2 Conjugated Porphyrin Oligomers as Molecular Wires **5**

1.3 Conjugated Porphyrin Oligomers as Nanorings **18**

1.4 Prospectus **31**

2 Toward *meso–meso* Singly-Linked Porphyrin Nanorings and Fused Porphyrin Nanobelts **33**

2.1 Introduction **35**

2.2 Molecular Design and Computational Modeling **42**

2.3 Synthesis of *ls*-P*N* **48**

2.4 Binding of T2 to *ls*-P2 ..... **50**

2.5 Attempted Syntheses of *cs*-P12 and *cs*[b_1]-P12 ..... **54**

2.6 Synthesis and Characterization of *cs*[b_1]-P24 ..... **62**

2.7 Binding of T12e to *cs*[b_1]-P24 and *ls*-P24 ..... **69**

2.8 Photophysics and Excitation Energy Transfer in *cs*[b_1]-P24 ..... **78**

2.9 Conclusion and Outlook **81**

3 Charge Transport Through Fused Porphyrin Oligomers Linked to Gold Electrodes via Covalent C–Au Bond **85**

3.1 Introduction **86**

3.2 Effect of End Capping Group on Formation of Au–C Contact **91**

3.3 Synthesis and Characterization of *lf*-NiP*N*-TMS$_2$ **95**

3.4 Single-Molecule Conductance for *lf*-NiP*N*-TMS$_2$ **101**

3.5 Conclusion 105

4 Phase-Coherent Transport and Quantum Interference in a Fused Porphyrin Octamer-Graphene Junction 106

4.1 Introduction 108

4.2 Molecular Design, Synthesis and Chemical Characterization 114

4.3 Charge Transport Measurements 117

4.4 Conclusion 125

5 Polaron Delocalization in the Radical Cations of Fused Porphyrin Oligomers 126

5.1 Introduction 127

5.2 Molecular Design, Synthesis and Chemical Characterization 132

5.3 Spectroelectrochemistry Measurements 136

5.4 EPR Measurements 141

5.5 Conclusion and Future Works 146

Appendix A — Overview of Compound Descriptors 149

Appendix B — Experimental Procedures and Supplementary Details for Chapter 2 ..151

Appendix C — Experimental Procedures and Supplementary Details for Chapter 3 ..285

Appendix D — Experimental Procedures and Supplementary Details for Chapter 4 ..341

Appendix E — Experimental Procedures and Supplementary Details for Chapter 5 ..354

Reference 388

List of Publications

1. **Global Aromaticity in a Partially Fused 8-Porphyrin Nanoring.** Kopp, S. M.;† Gotfredsen, H.;† **Deng, J.-R.**; Claridge, T. D. W.; Anderson, H. L. *J. Am. Chem. Soc.* **2020**, *142*, 19393.

2. **Correspondence on "How Aromatic Are Molecular Nanorings? The Case of a Six-Porphyrin Nanoring". Deng, J.-R.**;† Bradley, D.;† Jirásek, M.; Anderson, H. L.; Peeks, M. D. *Angew. Chem. Int. Ed.* **2022**, *61*, e202201231. (also in *ChemRxiv* **2021**, DOI: 10.26434/chemrxiv-2021-hm34v).

3. **Bending a Photonic Wire into a Ring.** Gotfredsen, H.;† **Deng, J.-R.;†** Van Raden, J. M.; Righetto, M.; Hergenhahn, J.; Clarke, M.; Bellamy-Carter, A.; Hart, J.; O'Shea, J.; Claridge, T. D. W.; Duarte, F.; Saywell, A.; Herz, L. M.; Anderson, H. L. *Nat. Chem.* **2022**, *14*, 1436–1442. (also in *ChemRxiv* **2022**, DOI: 10.26434/ chemrxiv-2022-6b0pc).

4. **Phase-Coherent Charge Transport through a Porphyrin Nanoribbon-Graphene Junction.** Chen, Z.;† **Deng, J.-R.**;† Hou, S.; Bian, X.; Swett, J. L.; Wu, Q.; Baugh, J.; Briggs, G. A. D.; Mol, J. A.; Lambert, C. J.; Anderson, H. L.; Thomas, J. O. *arXiv* **2022**, DOI: 10.48550/arXiv.2205.08499.

5. **Conjugated Porphyrin Tapes as Quantum Mediators for Vanadyl Qubits.** Pozo, I.; Lombardi, F.; Alexandropoulos, D. I.; Kong, F.; **Deng, J.-R.**; Horton, P. N.; Coles, S. J.; Myers, W. K.; Bogani, L.; Anderson, H. L. *arXiv* **2022**, DOI: 10.26434/chemrxiv-2022-1v5b4.

1

Introduction

1.1 Porphyrins 2

1.2 Conjugated Porphyrin Oligomers as Molecular Wires 5

1.2.1 Molecular Wires 5

1.2.2 Conjugated Porphyrin Oligomers 7

1.2.3 Butadiyne-Linked Porphyrin Oligomers 8

1.2.4 Ethyne-Linked Porphyrin Oligomers 11

1.2.5 Fused Porphyrin Oligomers 13

1.3 Conjugated Porphyrin Oligomers as Nanorings 18

1.3.1 Aromaticity and Ring Currents 18

1.3.2 Template-Directed Syntheses of Porphyrin Nanorings 20

1.3.3 Global Aromaticity of Porphyrin Nanorings 24

1.4 Prospectus 31

Parts of the works in this chapter were published in:

Deng, J.-R.;† Bradley, D.;† Jirásek, M.; Anderson, H. L.; Peeks, M. D. Correspondence on "How Aromatic Are Molecular Nanorings? The Case of a Six-Porphyrin Nanoring" *Angew. Chem. Int. Ed.* **2022**, *61*, e202201231; (also in *ChemRxiv* **2021**, DOI: 10.33774/chemrxiv-2021-hm34v).

1.1 Porphyrins

Porphyrins constitute one of the most intriguing class of pigments found in nature.[1,2] The parent compound of the family is porphine (Figure 1.1a), of which the chemical structure comprises four modified pyrroles connected by four methine bridges.[3] The derivatives of porphine with different substituents are called porphyrins. The atomic positions of porphyrins can be named using the common nomenclature (i.e., using *α*, *β* and *meso* to label different carbon positions) or systematically numbered by IUPAC nomenclature rules (Figure 1.1a). In this thesis, the common nomenclature is followed.

There are 26 delocalized π-electrons in a porphyrin, of which 18 π-electrons form a circuit (Figure 1.1b). Satisfying the Hückel's rule, porphyrins are aromatic. The aromatic ring current of a free-base porphyrin is clearly evidenced by ^{1}H NMR spectroscopy, which shows shielded N–H protons inside the ring (δ_H = –2 to –4 ppm) and deshielded C–H protons outside the ring (δ_H = 11 to 8 ppm).[4]

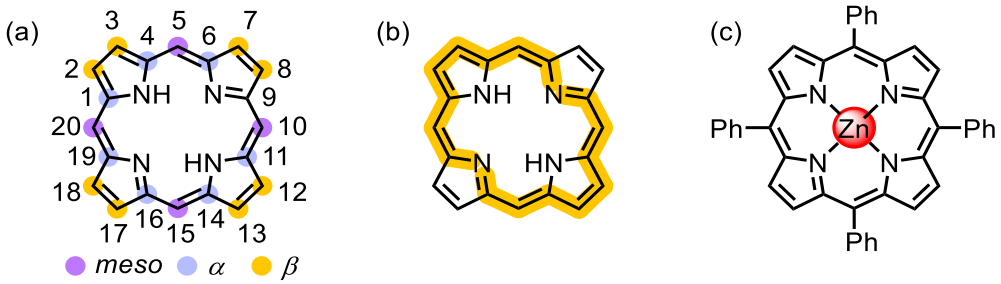

Figure 1.1: (a) General structure of a free-base porphyrin (porphine) numbered by common and IUPAC nomenclature. (b) The orange marks indicate the 18 π-electron aromatic circuit in a porphyrin. (c) Structure of ZnTPP (TPP = tetraphenylporphyrin).

The absorption spectrum of a simple porphyrin can be interpreted using the Gouterman four-orbital model.[5–7] Gouterman et al. stated that the absorption bands of a porphyrin arise from transitions among the four frontier orbitals, including two occupied π orbitals (a_{1u} and a_{2u}) and two unoccupied π* orbitals (e_g) (see Figure 1.2 for the calculated frontier orbitals of a zinc(II) tetraphenylporphyrin (TPP) as an example).[6–7] The four π–π* transitions ($a_{1u} \rightarrow e_g$, $a_{2u} \rightarrow e_g$) are mixed together by configuration interaction, resulting in the intense short-wavelength B band (or Soret band) at ~400 nm ($S_0 \rightarrow S_2$) and the weak long-wavelength Q band at ~550 nm ($S_0 \rightarrow S_1$). After the excitation ($S_0 \rightarrow S_2$), a rapid internal conversion ($S_2 \rightarrow S_1$) occurs and the emission detected (fluorescence) is only from S_1 (see Figure 1.2 for a schematic illustration).

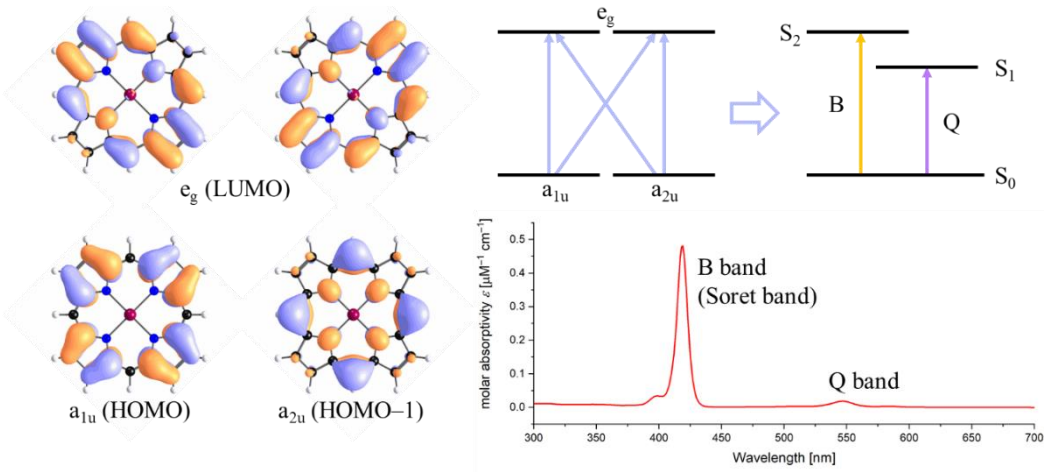

Figure 1.2: The Gouterman four-orbital model explains the absorption spectra of simple porphyrins.[5–7] Frontier orbitals of ZnTPP were calculated at B3LYP/6-31G* level of theory and plotted at a density isovalue of 0.03 au. The phenyl groups were replaced with hydrogen atoms to simplify the calculation. The UV–vis absorption spectrum of ZnTPP was measured in $CDCl_3$ at 298 K.

Free-base porphyrins can coordinate to various metal ions to form metalloporphyrins with fascinating properties. Zinc(II) porphyrins, such as ZnTPP, can bind axial ligands, such as pyridine, to form five-coordinate structures with association constants (formation constants) in the range $K_f \approx 10^3$–10^4 M^{-1} (Figure 1.3a).[8–10] The axial coordination of pyridine ligands to Zn(II) porphyrins is useful for designing oligopyridines as templates for synthesis of porphyrin supramolecular nanostructures, which will be discussed later in this chapter.[11,12] For nickel(II) porphyrins, axial coordination to ligands (e.g., pyridine or imidazole) induces spin crossover of the metal center from a low spin diamagnetic state (S = 0) to a high spin paramagnetic state (S = 1). Inspired by this property, Herges and coworkers reported a light-driven molecular switch by connecting a pyridine ligand to the Ni(II) porphyrin backbone with a tailor-made azobenzene tether (Figure 1.3b).[13] Light-induced isomerization of the tether causes an axial coordination (or decoordination) to the metal center, resulting in a concomitant spin state switch. A modified structure using an imidazole ligand, of which the back isomerization (*cis* → *trans*) occurs thermally, was demonstrated as a magnetic resonance imaging (MRI) contrast agent for temperature imaging.[14] Iron(III) porphyrins have attracted attention on their diverse roles in O_2 transport (myoglobin and hemoglobin), reduction of O_2 to water (cytochrome c oxidases), degradation of reactive oxygen species (catalases and peroxidases), and their dramatic catalytic activities (heme-containing oxygenase cytochrome P450).[15] Breslow and coworkers demonstrated that Fe(III) tetraphenylporphyrin chloride (FeTPPCl), working as a

biomimic molecular catalyst, could mediate intramolecular nitrene C–H insertions.[16] Arnold and coworkers conducted the reaction using an engineered cytochrome P450 enzyme (P411$_{BM3}$-CIS-T438S) as catalyst, which contains an iron(III) porphyrin center, resulting in a significant improvement of the total turnover number (TTN) and high stereoselectivity (Figure 1.3c).[17,18] In addition to C–H functionalization, Fe(III) porphyrins are also active catalysts for carbon dioxide reductions and oxygen reductions.[19–21] Copper(II) porphyrins with d^9 electron configuration are paramagnetic. Introduction of two Cu(II) porphyrins in a supramolecular complex allows investigation of molecular conformation and electronic communication by measuring through-space dipolar interactions and through-bond exchange couplings between two electron spins using electron paramagnetic resonance (EPR) spectroscopy.[22,23] Gold(III) porphyrins have been shown as potential anticancer drugs with high cytotoxicity toward cisplatin-resistant cancer cells and multidrug-resistant cells.[24,25]

To summarize, porphyrins with coplanar geometry, robust structure, strong aromaticity, interesting photophysical and electrochemical properties, as well as rich metal coordination chemistry, are not only playing important roles in natural biological systems, but also attracting attention in all areas of chemistry.

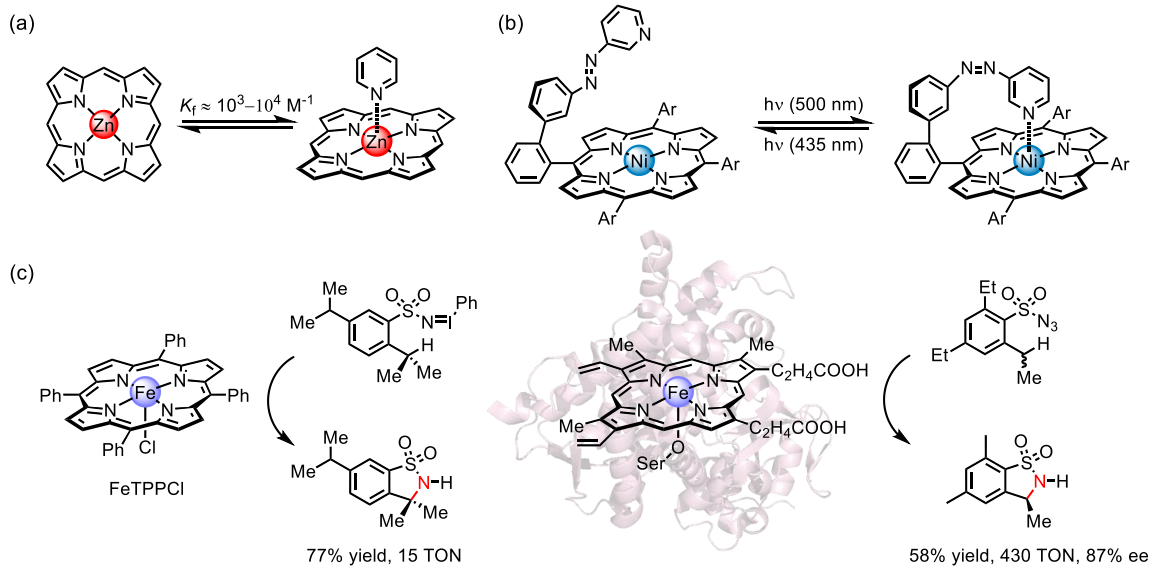

Figure 1.3: (a) Zinc(II) porphyrin coordinates to an axial pyridine ligand with association constant $K_f \approx 10^3$–10^4 M^{-1}.[8–10] (b) Light-induced reversibly magnetic switching of azopyridine functionalized Ni(II) porphyrin; Ar = pentafluorophenyl.[13] (c) Iron(III) tetraphenylporphyrin chloride (FeTPPCl) and engineered cytochrome P450 enzyme (P411$_{BM3}$-CIS-T438S) catalyze intramolecular nitrene C–H insertions; TTN = total turnover number, ee = enantiomeric excess (the protein crystal structure was reported by Arnold et al. in ref. 18).[16,17]

1.2 Conjugated Porphyrin Oligomers as Molecular Wires

1.2.1 Molecular Wires

Molecular wires are molecular structures that function as conduits for charge transport.[26] Their design and synthesis were initially motivated by the goal of miniaturizing devices, such as transistors, using molecular components as elementary building blocks.[27–35] Recent advancements in this field have also demonstrated that single-molecule devices can serve as an excellent platform for monitoring physical and chemical processes,[36,37] and for harnessing and exploiting a wide range of quantum phenomena at the molecular level (see Chapter 4 for more details).[38]

Charge transport through molecular wires can be probed by photo-induced electron transfer or direct electrical measurement. In the former, the "wirelike" molecule, serving as a bridge, is connected to an electron donor and an electron acceptor, giving a donor–bridge–acceptor system. The charge transfer rate constant (k_{ET}) in the system is measured by photophysical methods.[39,40] In the latter, the molecule is placed between two electrodes, giving an electrode–molecule–electrode junction and the rate of the charge transport is studied by conductance (G) measurement.[28–35,38,43,44]

The charge transport processes can be described by either or a combination of the two mechanisms: coherent tunneling and/or incoherent hopping.[39,44,45] Over short distances, charge transport is dominated by coherent tunneling, where electrons transport through a molecular bridge without charge localization (i.e., the bridge is not either oxidized or reduced). The simplest model is an electron tunnels through a rectangular potential energy barrier with a height of ΔE and a width of d. The transmission probability (T) decreases exponentially with the barrier width,

$$T \propto e^{-\beta_T d} \tag{1.1}$$

$$\beta_T = \frac{4\pi}{h}\sqrt{2m_e\Delta E} \tag{1.2}$$

where β is the transmission attenuation factor, h is the Planck constant, and m_e is the mass of an electron.[46] This exponentially distance-dependent attenuation has been found in both photo-induced electron transfer and conductance measurement mediated by coherent tunneling, where charge transfer rate constant and conductance decrease exponentially with transport distance.

$$k_{ET} = k_0 e^{-\beta_{ET} L} \tag{1.3}$$

$$G = G_0 e^{-\beta_C L} \tag{1.4}$$

Here, k_0 and G_0 are prefactors, and L is the donor–acceptor center-to-center distance for photo-induced electron transfer or molecular length for conductance measurement.[47] McConnell described the influence of the bridge with N identical repeating units on the electron transfer in a donor-bridge-acceptor system by the superexchange model:

$$\beta_{ET} = \frac{2}{R_0} \ln\left(\frac{\Delta E}{H_{BB}}\right) \tag{1.5}$$

where R_0 is the length of a repeating unit, ΔE is the tunneling energy gap, and H_{BB} is the electronic coupling between two repeating units.[48] A similar model to describe molecular conductance was derived by Frisbie and coworkers as follows:[49]

$$\beta_C = \frac{2}{R_0} \ln\left(\frac{E_B - E_F}{H_{BB}}\right) \tag{1.6}$$

If the energy difference between the site energy (E_B, energy of the repeating unit) and the Fermi energy (E_F) is regarded as the tunneling energy gap (ΔE), eqn. 1.6 can be reduced to eqn. 1.5.

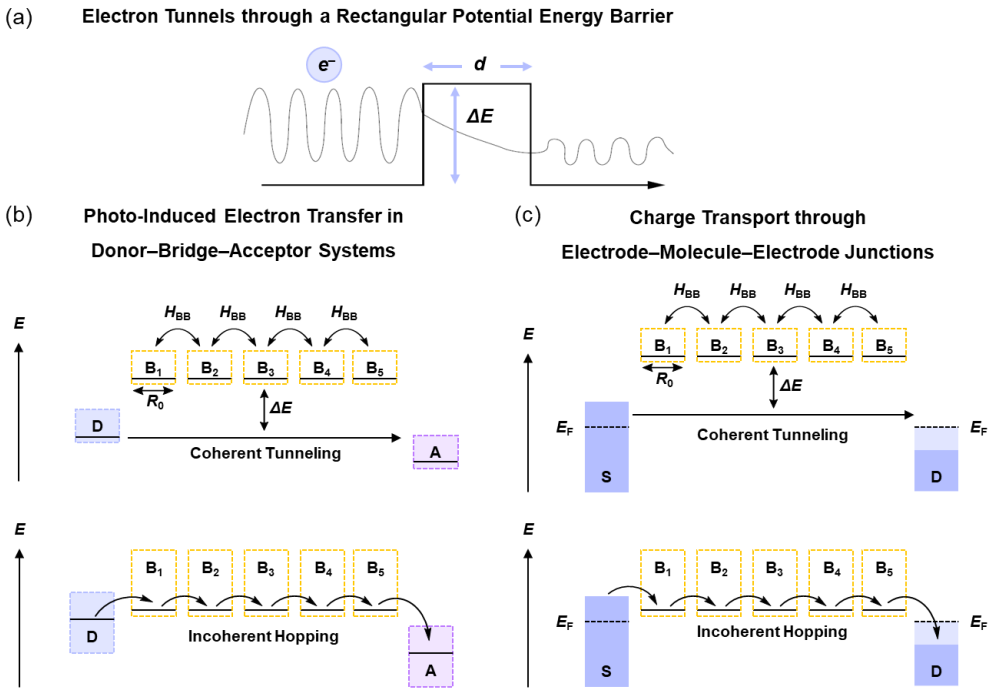

Figure 1.4: (a) An electron tunnels through a rectangular potential energy barrier with a height of ΔE and a width of d. (b) Comparison of coherent tunneling and incoherent hopping mechanisms in a photo-induced electron transfer process, where D is donor, B_i is bridge unit, A is acceptor and H_{BB} is the electronic coupling between two bridge units. (c) Comparison of two charge transport mechanisms in conductance measurement, where S and D are source and drain electrodes respectively.[39]

When the molecular wires become longer, the rate of tunneling is strongly suppressed, and charge can be injected into the molecule, leading to polaron formation, and transported along the system via an incoherent hopping mechanism. For incoherent hopping, the distance dependence of the electron transfer rate (or the molecular conductance) was interpreted by Segal, Ratner and coworkers as follows:

$$k_{\mathrm{ET}} = (\alpha_1 + \alpha_2 L)^{-1} e^{-\Delta E / k_{\mathrm{B}} T} \tag{1.7}$$

where k_{B} is the Boltzmann constant, factors α_1 and α_2 depend on the molecular properties and the coupling strength to the thermal environment.[50,51]

To compare these two mechanisms, as shown in eqn. 1.3, 1.4 and 1.7, the distance-dependent attenuation of the electron transfer rate (or molecular conductance) is more pronounced in a coherent tunneling process, while charge transport via incoherent hopping is strongly temperature-dependent. In general, for molecular wires made of π-conjugated oligomers, the coherent tunneling mechanism dominates charge transport over short distances, and crossover from tunneling to hopping transport occurs beyond the typical tunneling regime (i.e., $L \geq 4$–5 nm).[45]

1.2.2 Conjugated Porphyrin Oligomers

Connecting porphyrin rings together via organic synthesis to merge and enlarge the porphyrin π-systems creates conjugated porphyrin oligomers.[5,46] Bridging porphyrin units with unsaturated linkers (e.g., ethylene, ethyne, and 1,3-butadiyne) gives π-bridged porphyrin oligomers with moderate inter-porphyrin electronic coupling (π-overlap). Linking porphyrins with multiple covalent bonds results in fused porphyrin oligomers with strong π-conjugation (comparison of the experimental optical gaps and calculated band gaps among different porphyrin oligomers will be presented later in this chapter). *Meso–meso* singly-linked and phenylene-linked porphyrin oligomers with strongly twisted geometries and weak inter-porphyrin interactions are not considered as conjugated porphyrin oligomers, although the exciton coupling between the porphyrin units makes them promising as photonic wires for excited state energy transfer.[47] Among the reported conjugated porphyrin oligomers, *meso–meso* 1,3-butadiyne-linked, *meso–meso* ethyne-linked and *meso–meso*, *β–β*, *β–β* triply-linked porphyrin oligomers with moderate to strong electronic coupling between individual porphyrins have been intensively studied in the past three decades, and they are considered as promising molecular wires for charge transport investigation.[46] In the following, the syntheses and charge transport properties of these three classes of oligomers are briefly discussed.

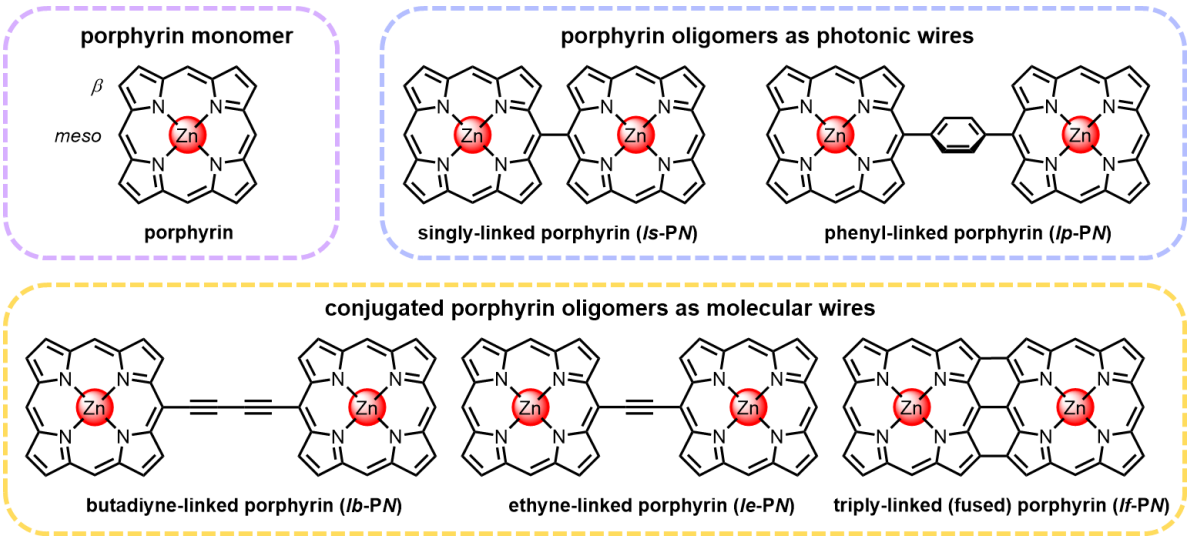

Figure 1.5: Structures of porphyrin monomer and intensively studied porphyrin oligomers, where *N* denotes the number of porphyrin units; *l*, *s*, *p*, *b*, *e* and *f* indicate linear, singly-linked, phenyl-linked, butadiyne-linked, ethynyl-linked and fused respectively.

1.2.3 Butadiyne-Linked Porphyrin Oligomers

The synthesis of *meso–meso* 1,3-butadiyne-linked (butadiyne-linked in the following) porphyrin oligomers ***lb*-P*N*** was initiated by Arnold, Johnson and coworkers in 1978,[52] in which a butadiyne-linked nickel(II) octaethylporphyrin dimer ***lb*-NiP2** was obtained by $Cu(OAc)_2$-mediated oxidative homocoupling of two ethynyl porphyrin monomers, which were afforded by dehydrobromination of the bromovinyl porphyrin monomers (Figure 1.6a). Arnold and coworkers continued to investigate the optical and electrochemical properties of the butadiyne-linked porphyrin dimers in 1990s,[53,54] and concomitantly, Anderson and coworkers reported the syntheses and properties of a series of zinc(II) butadiyne-linked porphyrin oligomers ***lb*-ZnP*N***.[55,56] With a combination of the optimized synthetic routes and introduction of the solubilizing side chains, pure monodisperse oligomers with up to 50 porphyrin units (***lb*-ZnP50**) have been isolated (Figure 1.6b).[57]

The butadiyne-linked porphyrin dimer has an extended π-conjugation compared to the corresponding monomer, which can be easily observed from a bathochromic shift of the Q band ($S_0 \rightarrow S_1$) in the UV–vis absorption spectrum (e.g., ~80 nm shift for Zn(II) porphyrins measured in CH_2Cl_2 + 1% pyridine).[55] As the oligomer gets longer, the bathochromic shift continues until the Q band absorption peak reaches a saturation at ~820 nm (~1.51 eV) in toluene + 1% pyridine, which indicates the effective conjugative length N_{ecl} is about 15–20 porphyrin units.[57] In addition to the experimental results, DFT calculations suggest the one-dimensional infinite butadiyne-linked porphyrin structures exhibit a band gap of 1.1 eV.[58]

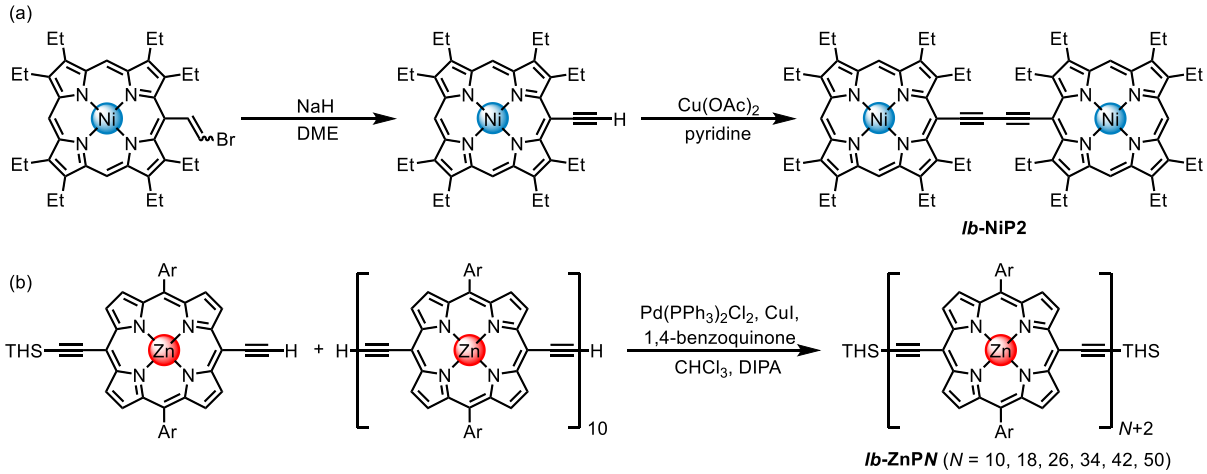

Figure 1.6: (a) Synthesis of butadiyne-linked porphyrin dimer ***lb*-NiP2** reported by Arnold and coworkers.[52] (b) Synthesis of butadiyne-linked porphyrin oligomers ***lb*-ZnP*n*** reported by Anderson and coworkers, THS = trihexylsilyl group, Ar = 3,5-bis(octyloxy)phenyl solubilizing group.[57]

The well-established synthetic methodology and remarkable inter-porphyrin interaction for butadiyne-linked porphyrin oligomers make them attractive candidates as molecular wires. Albinsson, Anderson and coworkers have designed and synthesized a series of D–B–A systems (**Fc–*lb*-ZnP*N*–C$_{60}$**, N = 1–4, Figure 1.7a) to investigate the ability of butadiyne-linked porphyrin oligomers to mediate long-range charge transport using photophysical methods.[59–61] After photoexcitation, the charge separation (**Fc–*lb*-ZnP*N**–C$_{60}$** → **Fc–*lb*-ZnP*N*$^{\bullet+}$–C$_{60}^{\bullet-}$**) and charge recombination (**Fc$^{\bullet+}$–*lb*-ZnP*N*–C$_{60}^{\bullet-}$** → **Fc–*lb*-ZnP*N*–C$_{60}$**) processes (Figure 1.7b) over a temperature range (180–300 K) were probed by time-resolved fluorescence and femtosecond transient absorption. The charge recombination at high temperatures (≥280 K) is dominated by coherent tunneling mechanism (attenuation factor β_{CR} = 0.28 nm^{-1} at 300 K), and crossover from coherent tunneling to incoherent hopping occurs for long oligomers ($N \geq 2$) at low temperatures (<280 K).[61] The low β_{CR} value indicates the electron transfer through butadiyne-linked porphyrin oligomers is weakly distance-dependent.

The low β values were also observed in single-molecule conductance measurements by Anderson, Nichols, Leary, Lambert and coworkers.[62,63] These measurements were carried out using the scanning tunneling microscope break-junction (STM-BJ) technique. Butadiyne-linked porphyrin oligomers with thiol or pyridyl anchor groups were used to connect to the gold electrodes. In each cycle, the current at a given bias voltage (or over a range of bias voltage) was recorded while the tip was retracting from the surface until the junction ruptured, and thousands of cycles were carried out for each compound to give a reliable measure of

single-molecule conductance. Experimental results and theoretical calculations indicate the charge transport through these junctions (as shown in Figure 1.7c) are mediated by coherent tunneling, and the length dependence of their conductance depends on the applied bias voltage V_{sd} (Figure 1.7d). The value of the attenuation factor β_C decreases from 2.0 (± 0.04) nm^{-1} at V_{sd} = 0 V to 1.4 (± 0.3) nm^{-1} at V_{sd} = 0.7 V, and it reaches 0.9 (± 0.3) nm^{-1} at V_{sd} = 0.9 V.[63] The bias voltage dependence of β_C can be extrapolated using a tight binding model (the same as Frisbie's model described in equation 1.6). If electronic coupling between the repeating unit in a molecular bridge H_{BB} is fixed, a smaller energy gap ΔE between the Fermi energy E_F and the energy of the repeating unit E_B, which can be tuned by the applied bias voltage V_{sd}, leads to a smaller β_C. Using H_{BB} = 0.17 eV and E_B = –0.8 eV, the simulated β_C values closely follow the experimental data.

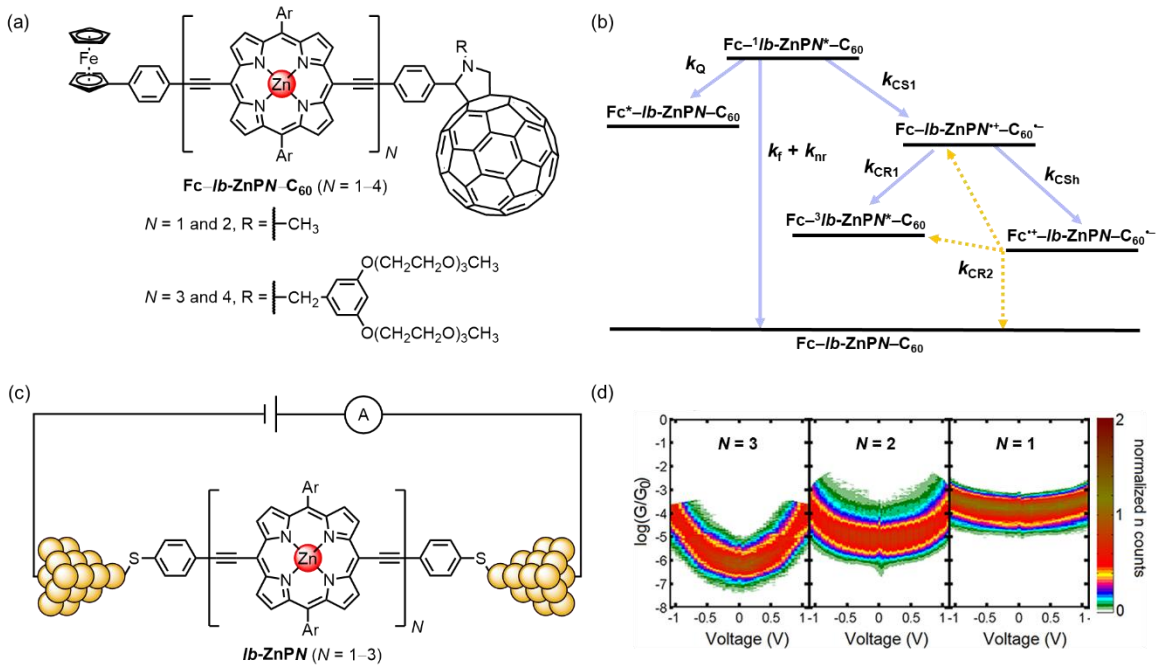

Figure 1.7: (a) Structures of **Fc–*lb*-ZnP*N*–C$_{60}$** (N = 1–4) as donor–bridge–acceptor systems for photoinduced electron transfer study. (b) Schematic energy level diagram showing the ferrocene quenching (Q), radiative and non-radiative decay (r and nr), charge separation (CS1), charge shift (CSh) and charge recombination (CR1 and CR2) pathways and the corresponding rate constants after photoexcitation. The orange dashed arrows indicate the possible competing recombination pathways (CR2) for the fully charge–separated state **Fc$^{\bullet+}$–*lb*-ZnP*N*–C$_{60}^{\bullet-}$**.[61] (c) Schematic diagram showing a connection of butadiyne-linked porphyrin oligomers ***lb*-ZnP*N*** (N = 1–3) to two gold electrodes. (d) $\log(G/G_0)$−V_{sd} 2D histograms generated from all I−V traces recorded for each junction as shown in (c), reproduced with permission from ref. 63.

1.2.4 Ethyne-Linked Porphyrin Oligomers

The synthesis of *meso–meso* ethyne-linked (ethyne-linked in the following) porphyrin oligomers was pioneered by Therien and coworkers in 1994,[64] in which ethyne-linked porphyrin dimer ***le*-ZnP2** and trimer ***le*-ZnP3** were constructed by palladium-catalyzed cross-coupling of ethynylated and brominated porphyrin monomers (Figure 1.8). Later, using $Pd_2(dba)_3$ and $AsPh_3$ as a copper-free condition, syntheses of long oligomers (e.g., ***le*-ZnP7**) were reported by Therien and coworkers.[65] Recently, Anderson and coworkers reported the synthesis of ***le*-ZnP13** with 13 porphyrin units, which is the longest ethyne-linked porphyrin chain yet achieved.[66] Similar to the butadiyne-linked porphyrin oligomers, the ethyne bridge leads to moderate inter-porphyrin electronic coupling, resulting in a smaller HOMO–LUMO gap, as indicated by a bathochromic shift of the Q band in the UV–vis absorption spectrum (e.g., λ_{abs} = 683 nm for ***le*-ZnP2**, λ_{abs} = 802 nm for ***le*-ZnP3**, compared to λ_{abs} = 540 nm for the parent monomer ZnDPP in $CHCl_3$ + 10% pyridine, DPP is 5,15-diphenylporphyrin). DFT studies indicate a band gap of 1.0 eV for 1D infinite ethyne-linked porphyrin structures.

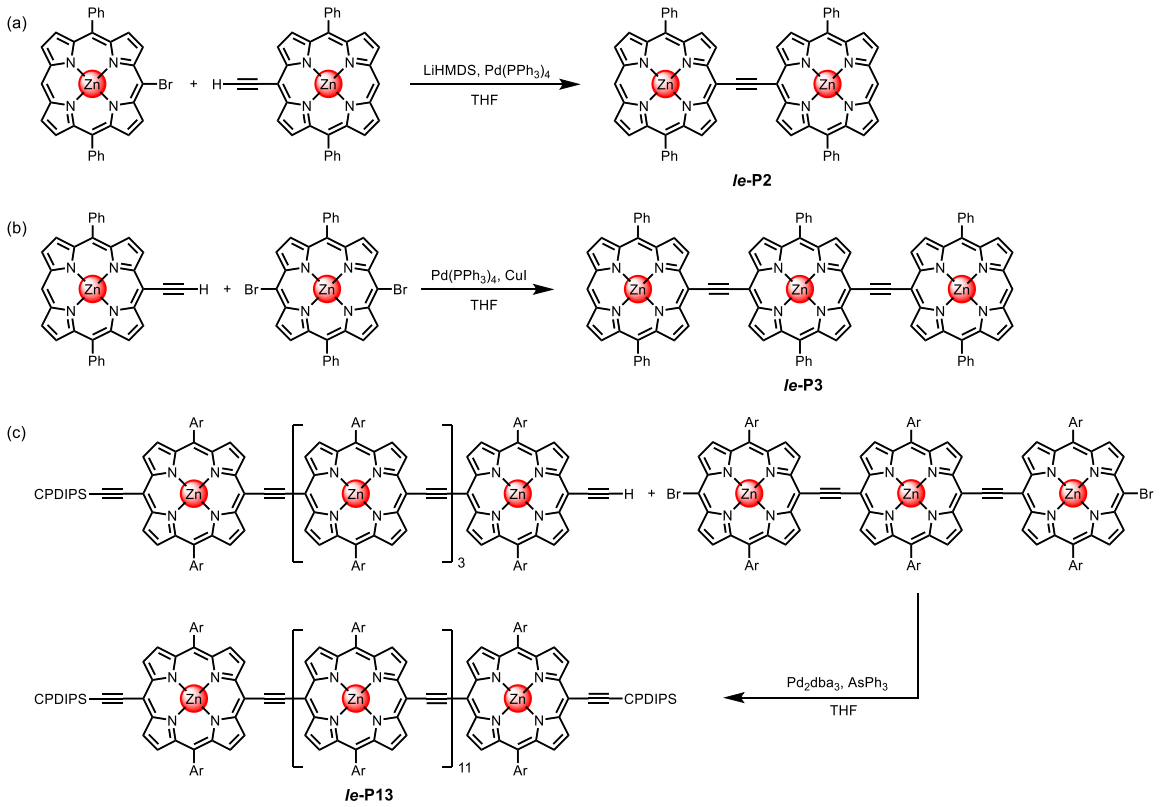

Figure 1.8: Syntheses of ethyne-linked porphyrin dimer ***le*-ZnP2** (a) and trimer ***le*-ZnP3** (b) reported by Therien and coworkers,[64] and tridecamer ***le*-ZnP13** (c) reported by Anderson and coworkers,[66] HMDS = bis(trimethylsilyl)amide, dba = dibenzylideneacetone, CPDIPS = (3-cyanopropyl)diisopropylsilyl group, Ar = 3,5-bis(trihexylsilyl)phenyl solubilizing group.

Charge transport through ethyne-linked porphyrin oligomers has been investigated in both single-molecule junctions and bulk molecular electronic devices by Therien, Borguet, You and coworkers.[67,68] In the former, it was investigated by STM-BJs technique using molecules ***le*-ZnP*N*** (N = 1–3) with thiol anchors. The resistance values (R = 1/G) show weekly distance-dependent, with attenuation factor β_C = 0.34 (± 0.06) nm^{-1} for high-conductance peaks and β_C = 0.34 (± 0.07) nm^{-1} for low-conductance peaks.[67] In the latter, self-assembled monolayers (SAMs) of ***le*-MP*N*** (M = Zn(II), Cu(II) or Ni(II); N = 1–3) were prepared on gold surfaces and the top gold electrodes were printed onto the SAMs via nanotransfer printing (nTP, see ref. 68 for the technical details). After that, a gold coated AFM tip was attached to the top gold electrodes for electrical characterization of the nTP devices as shown in Figure 1.9.[68] Fitting an exponential function to resistances determined in these devices as a function of molecular length gave β_C = 0.75 (± 0.13) nm^{-1} for ***le*-ZnP*N***, β_C = 1.32 (± 0.18) nm^{-1} for ***le*-CuP*N*** and β_C = 1.76 (± 0.15) nm^{-1} for ***le*-NiP*N***. The impact of the central metal ions on the values of β_C can be related to the HOMO energy levels E_H of these oligomers ($E_{H,Zn} > E_{H,Cu} > E_{H,Ni}$, with the same number of porphyrin units), because charge transport through these junctions is hole mediated, and a higher E_H leads to a smaller tunnelling energy barrier (i.e., $\Delta E = E_F - E_H$, assuming the Fermi level E_F sits between the HOMO–LUMO gap), resulting in a smaller β_C ($\beta_{C,Zn} < \beta_{C,Cu} < \beta_{C,Ni}$).

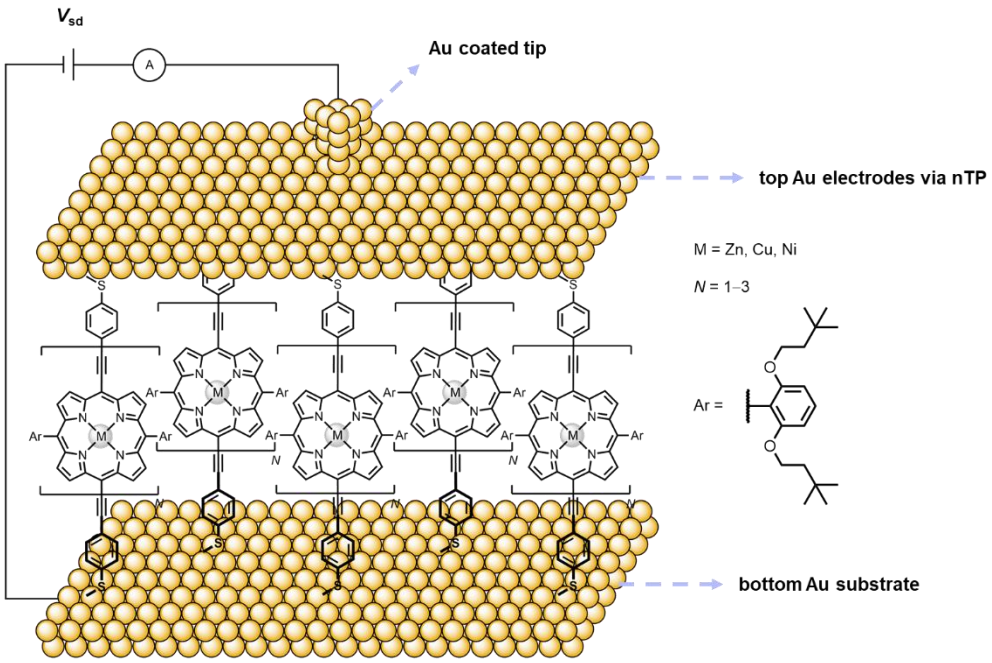

Figure 1.9: Schematic diagram showing electrical characterization of nanotransfer printed (nTP) molecular junctions with ethyne-linked porphyrin oligomers ***le*-MP*N*** (M = Zn(II), Cu(II) or Ni(II); N = 1–3) as molecular bridges.[68]

1.2.5 Fused Porphyrin Oligomers

The investigation of *meso–meso*, *β–β*, *β–β* triply-linked (triply-linked or fused in the following) porphyrin oligomers ***lf*-P*N*** was initiated by Osuka and coworkers in 2000.[69] In the beginning, fused porphyrin dimers ***lf*-MP2** (M = Cu(II) and Ni(II)) were afforded by oxidative fusion of the corresponding *meso–meso* singly-linked porphyrin dimers ***ls*-MP2** (M = Cu(II) and Ni(II)) using tris(4-bromophenyl)ammoniumyl hexachloroantimonate (BAHA, commonly known as magic blue) as oxidant.[69,70] However, chlorinated side products observed under this condition hampered its application. Soon after this, 2,3-dichloro-5,6-dicyano-1,4-benzoquinone (DDQ)/$Sc(OTf)_3$ promoted oxidation was reported as an efficient approach to construct a series of fused porphyrin oligomers ***lf*-ZnP*N*** (*N* = 2–4, 6, 8, 12) from the parent singly-linked oligomers ***ls*-ZnP*N*** (*N* = 2–4, 6, 8, 12).[71] In the past two decades, other oxidants, such as $AuCl_3$/AgOTf,[72] [bis(trifluoroacetoxy)iodo]benzene (PIFA),[73] $Cu(BF_4)_2$,[74] and $Fe(OTf)_3$,[63,75] were also reported as efficient oxidants for preparation of fused porphyrin oligomers.[76]

In general, synthesis of fused porphyrin oligomers requires a three-step approach: (*i*) synthesis of *meso–meso* singly-linked porphyrin oligomers ***ls*-P*N***; (*ii*) capping of the terminal *meso* positions; (*iii*) oxidative fusion of ***ls*-P*N*** using the aforementioned conditions. The *meso–meso* singly-linked porphyrin oligomers ***ls*-P*N*** can be afforded by stepwise oligomerizations using oxidative homocoupling ($AgPF_6$ or PIFA as oxidant), or Suzuki–Miyaura cross-coupling reactions.[76] The Ag(I)-mediated oxidative homocoupling of porphyrins was intensively studied by Osuka and coworkers, where *meso–meso* coupled oligomers with up to 1024 porphyrin units were achieved by stepwise elongation.[77–79] Capping the terminal *meso* positions with phenyl groups protects the oligomers from intermolecular coupling under oxidative fusion conditions. Bromination of the terminal *meso* positions allows post-functionalization of the oligomers after the oxidative fusion reaction for charge transport investigation.[63,75] To build up long oligomers, the solubilizing groups attached to the peripheral *meso* positions of the porphyrin rings should be carefully chosen to prevent severe intermolecular aggregation. To date, the longest fused porphyrin oligomer that has been reported is the triply-linked porphyrin tetracosamer, which contains 24 porphyin units.[80]

The successful synthesis of fused porphyrin oligomers is a ground-breaking development as the covalently triply-linked structures force the porphyrin rings into a coplanar geometry, which leads to extremely strong inter-porphyrin electronic coupling, and these oligomers are also commonly called “porphyrin tapes”.[76] The strong electronic coupling between the neighboring porphyrin units renders the HOMO–LUMO gaps falling steeply by increasing the

length of the oligomers. This trend can be evidenced by the remarkably bathochromic shift of the lowest absorption band (Q band), which corresponds to the π–π* transition, with an increase of the number of porphyrin units (e.g., $\lambda_{abs} \approx 2800$ nm for dodecamer, indicating an optical gap of 0.4 eV). DFT calculations indicate hypothetical one-dimensional infinite porphyrin tapes are metallic, with no band gap.[58] In contrast, Osuka and coworkers observed saturation of the bathochromic shift at $N = 16$ in $CHCl_3$, suggesting the effective conjugative length N_{ecl} is about 14–16 porphyrin units.[80] This estimation still remains arguable as they reported that long oligomers ($N > 8$) aggregated effectively in $CHCl_3$. Even though the debate on the effective conjugative length of these oligomers continues, the small HOMO–LUMO gaps of this family of oligomers, which have been rarely observed for soluble organic oligomers, make them attractive candidates as molecular wires for charge transport investigation.

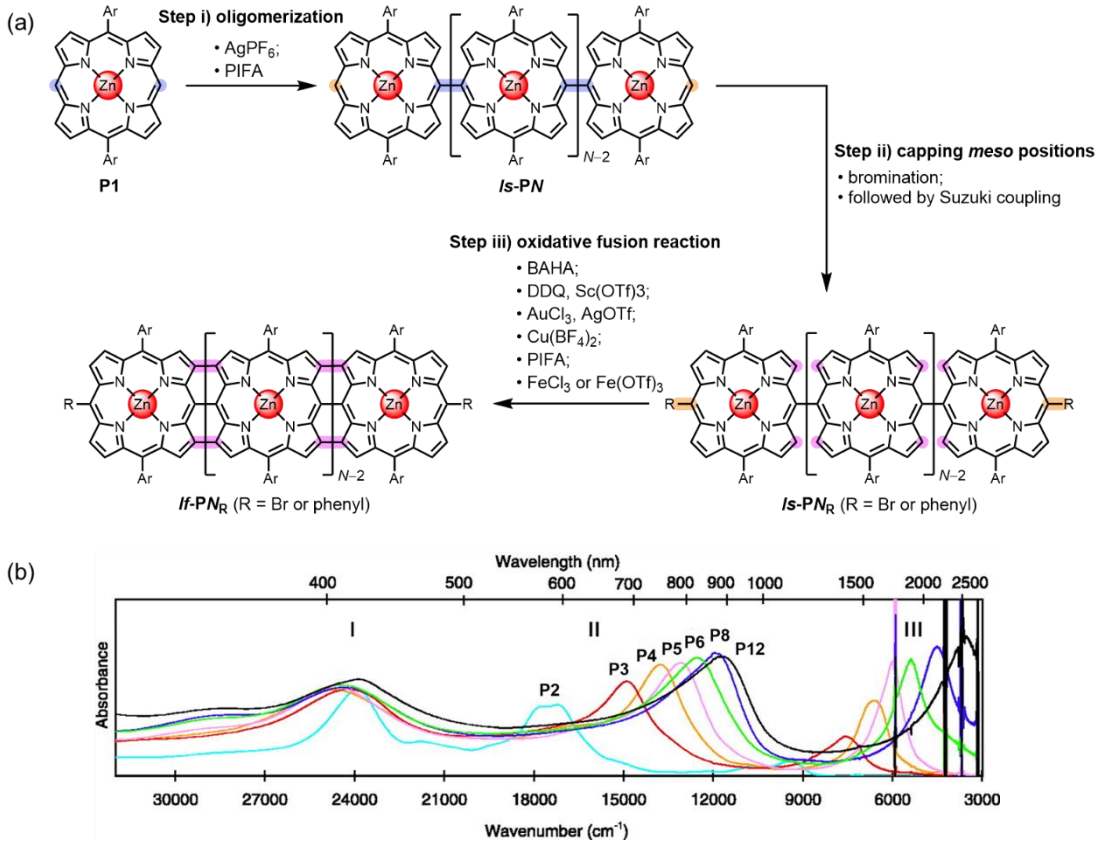

Figure 1.10: (a) General synthetic routes toward fused porphyrin oligomers. Ar is peripheral aryl group with solubilizing side chains. Reaction conditions may vary when different central metal ions, capping groups or solubilizing aryl groups are used.[76] (b) Normalized absorption spectra of fused porphyrin oligomers ***lf*-ZnP*N*$_{Ph}$** (N = 2–6, 8, 12; Ph = phenyl) reported by Osuka and coworkers. Peaks I, II and III are assigned to B_y, B_x and Q bands respectively.[71,81]

Early charge transport studies on fused porphyrin oligomers were carried out by Osuka, Kim, Yoo and coworkers in the 2000s,[81–84] which indicated the fused porphyrin oligomers were highly conductive compared to the *meso–meso* singly-linked porphyrin oligomers. Anderson, Nichols, Leary, Lambert and coworkers performed a systematic investigation of their distance-dependent charge transport behaviors by measuring the single-molecule conductance of Zn(II) porphyrin monomer, fused dimer and trimer using STM-BJ technique (Figure 1.11a).[63,75] In these experiments, porphyrins with pyridyl or thiol anchors were connected to two gold electrodes with strong molecule-electrode coupling. Within a low bias window, charge transport is meditated by coherent tunneling. Fused porphyrin oligomers with pyridyl anchors ***lf*-ZnP*N*$_{\mathbf{Py}}$** exhibit extremely weak distance-dependent attenuation of conductance (β_C = 0.19 ± 0.01 nm^{-1}), compared to the corresponding *meso–meso* singly-linked porphyrin oligomers ***ls*-ZnP*N*$_{\mathbf{Py}}$** (β_C = 1.1 ± 0.1 nm^{-1}) and the butadiyne-linked family ***lb*-ZnP*N*$_{\mathbf{Py}}$** (β_C = 0.42 ± 0.05 nm^{-1}).[75] Fused porphyrin oligomers with thiolacetate groups ***lf*-ZnP*N*$_{\mathbf{SAc}}$**, which cleaved to form S–Au bonds between the molecules and the gold electrodes in the measurements, were employed to study the effect of the applied bias voltage on the length dependence of conductance.[63] The values of β_C determined are voltage-dependent, decreasing from β_C = 0 nm^{-1} at V_{sd} = 0 V to β_C = –1.5 ± 0.4 nm^{-1} at V_{sd} = 0.7 V, which indicates the conductance increases with length. Theoretical studies reveal that the negative β_C observed results from the rapid decrease of the HOMO–LUMO gaps of the fused porphyrin oligomers with length, which significantly lowers the effective energy barrier (i.e., $\Delta E = E_F - E_H$, E_H is the HOMO energy) for coherent tunneling and overcome the distance-dependent conductance attenuation.[63,85]

When the applied bias voltage becomes higher, molecular charging was observed for fused dimer ($|V_{sd}| \geq 1.0$ V) and trimer ($|V_{sd}| \geq 0.8$ V), causing a significant change of the conductance.[86] The charging behavior is hysteretic, which means after the molecule is charged at a given high bias and switched to a high conductance state, this state survives and maintains its high conductance when the bias is swept back to the low bias region. In a number of junctions, the charging states were stable for a few seconds. Theoretical investigation indicates this behavior arises from the voltage-induced charging of localized molecular orbitals which are weakly coupled to the gold electrodes (i.e., HOMO–1 of the fused oligomers), which creates a slow charge-hopping channel in parallel to the fast coherent tunneling path. Modeling these two-channel systems requires a combination of Marcus theory to describe the electron transfer rates in the slow channel and Landauer–Büttiker theory to describe the coherent tunneling in the fast channel.

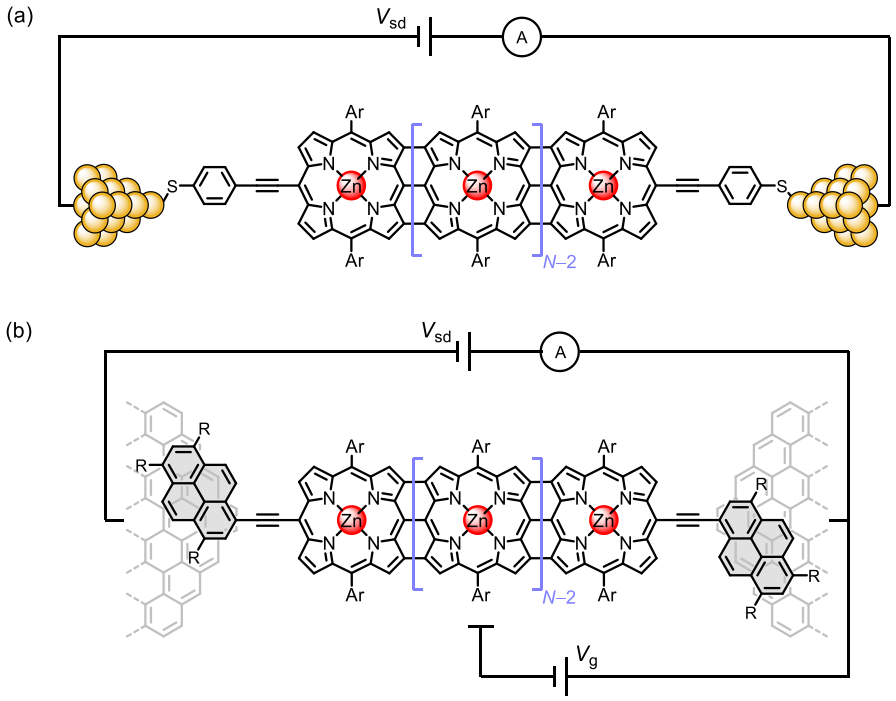

Figure 11. Schematic diagram showing single-molecule conductance measurements of fused porphyrin oligomers ***lf*-ZnP*N*** (*N* = 1–3) in two-terminal junctions, in which the molecules are connected to gold electrodes via S–Au interactions (a); and in three-terminal graphene-based junctions, where the molecules are connected to graphene electrodes via π-stacking (b). Ar = 3,5-bis(trihexylsilyl)phenyl group, R = dodecyloxy solubilizing chain.[63,86,87]

Besides the aforementioned measurements in two-terminal junctions with gold electrodes, the charge transport behaviors of fused porphyrin oligomers have also been studied in three-terminal graphene-based junctions.[87] In these experiments, porphyrin oligomers with pyrene anchors were connected to graphene-based electrodes via π-stacking (Figure 11b). The weak molecule–electrode coupling allows electrons to sequentially tunnel through the single-molecule junctions (i.e., electrons stepwise hop on the molecule from the source electrode and hop off molecule to the drain electrode). The gate electrode in the device can be used to shift the orbitals of the molecule to control the conductance. In a single-molecule junction with fused porphyrin trimer, the large, conjugated molecular structure and weak molecule–electrode coupling enabled observation of multiple sequential tunneling regions, which was related to the many-body electronic structure of the system in various charge states and could be described by the Hubbard dimer model.

To briefly summarize, in the past three decades, organic chemists have developed efficient methods to build up conjugative porphyrin oligomers with moderate and strong inter-porphyrin electronic coupling. Serving as molecular wires, their charge transport behaviors have been

studied by photophysical methods or direct electrical measurements. Over a short distance, in most cases, coherent tunneling is the dominant mechanism. Weak distance-dependent attenuation behaviors were determined for all three classes of aforementioned porphyrin oligomers, particularly the fused porphyrin oligomers, of which the distance-dependent attenuation factor β vanished or showed negative values over a range of applied bias. These β are extremely small compared to other organic molecules, such as oligo(phenylene-ethynylenes) (OPEs, β = 3–4 nm^{-1}),[88] oligo(arylene-ethynylenes) (OAEs, β = 3.3 nm^{-1}),[89] oligo(phenylene-vinylenes) (OPVs, β = 1.7–1.8 nm^{-1}),[90] acenes (β = 4.9 nm^{-1}),[91] oligoynes (β = 1.7–3.1 nm^{-1}),[90,92] and alkanes (β = 8.4 nm^{-1})[93]. The small (or negative) β values have also recently been observed from molecular wires with small bond-length alternation along the π-conjugated backbone, such as cumulenes ($\beta \approx 0$ nm^{-1})[94,95] and cyanines (β = –1.6 nm^{-1} within 3 nm in length)[96,97], and radical cations with open-shell character[98,99].The small β values for conjugated porphyrin oligomers might arise from the strong electronic coupling between the neighboring porphyrin units in these oligomers, which limits the charge localization when the electrons transport through the molecular bridge. The strong inter-ring electronic coupling and communication in conjugated porphyrin oligomers has also been implicated by other studies.[65,100–102] For example, electron paramagnetic resonance (EPR) spectroscopy studies indicated the spin density of a polaron state created by oxidation or reduction could span over 7.5 nm in ethyne-linked porphyrin oligomers.[65,100,101] The amazing properties render these porphyrin oligomers as promising candidates for the fabrication of future electronic devices.

Despite these advances, there have been few detailed investigations of charge transport in conjugated porphyrin oligomers longer than a trimer (about 4–5 nm in length), especially on the fused porphyrin family, because the synthesis and characterization of long porphyrin tapes ($N \geq 6$) with anchor groups still remain challenging (details are discussed in Chapter 3–5). Besides, it would also be challenging to conduct singe-molecule conductance measurement for a molecule junction approaching 10 nm in length. Therefore, it is of interest to explore new methodology to build up fused porphyrin oligomers over 5 nm, reaching a length as a "nanoribbon-like" structure as graphene nanoribbons,[103] and to investigate their long-range charge transport behaviors by single-molecule conductance measurement. Moreover, in most cases discussed, zinc(II) ions with d^{10} electron configuration were inserted as the central metal ions, and it would be intriguing to explore their charge transport behaviors using other central metal ions, such as metal ions with unpaired electrons, as they might become promising candidates for spintronic materials engineering.[104]

1.3 Conjugated Porphyrin Oligomers as Nanorings

1.3.1 Aromaticity and Ring Currents

Bending linear conjugated porphyrin oligomers into molecular nanorings enables investigation of charge transport in molecular ring wires. In classical physics, when a metal ring is placed in an external magnetic field, the changing magnetic flux through the ring forces the electrons to flow around its circumference.[105] Faraday's law indicates the induced current around the ring concomitantly induces a magnetic field in the opposite direction to the external field. When the diameter of the metal ring is limited to around 200–1000 nm, a mesoscopic system, at low temperature, an external magnetic field can induce a persistent current I in the ring, of which the direction oscillates as a function of the field strength B with a period of a flux quantum $\Phi_0 = h/e$, where h is Planck constant and e is elementary charge.[106] These Aharonov–Bohm oscillations of the induced current direction also change the direction of the induced magnetic field.

In chemistry, the magnetic behaviors in molecules are strongly related to a fundamental but important concept: (anti)aromaticity, although various other criteria have been developed to define whether a molecule is aromatic.[107–114] The magnetic criteria state that when an external magnetic field is applied on cyclic molecules with delocalized π electrons, molecules exhibiting diatropic ring currents, which create magnetic fields in an opposite direction to the external field inside the rings, are aromatic. Antiaromatic molecules sustain paratropic ring currents, strengthening the external magnetic field penetrating the ring. These magnetic behaviors can be studied by probing the shielding/deshielding effects using NMR spectroscopy, and modeled theoretically.[115]

Hückel's rule is commonly used to predict whether a molecule is (anti)aromatic. It suggests that conjugated cyclic structures with $4n + 2$ (or $4n$) π electrons are aromatic (or antiaromatic) molecules.[116–118] Hückel's rule is delineated by the Hückel molecular orbital theory (HMO theory or Hückel method in the following), which applies the linear combinations of atomic orbitals (LCMO) approach to construct the π orbital diagrams of conjugated molecules with a set of approximations.[119] The Hückel Hamiltonian matrix for cyclic π-conjugated molecules has the form as

$$H = \begin{vmatrix} \alpha & \beta & 0 & \cdots & \beta \\ \beta & \alpha & \beta & \cdots & 0 \\ 0 & \beta & \alpha & \cdots & 0 \\ \vdots & \vdots & \vdots & \ddots & \beta \\ \beta & 0 & 0 & \beta & \alpha \end{vmatrix} \quad (1.8)$$

where α is the Coulomb integral and β is the resonance integral. Diagonalization of the Hamiltonian matrix gives the molecular orbital energies as

$$E_l = \alpha + 2\beta \cos\left(\frac{2\pi l}{N}\right) \quad (1.9)$$

where N is the number of the atomic orbitals and the resulting molecular orbitals, and l = 0, ±1, ±2, …, N/2 is a quantum number. Implicated by the eqn. 1.9, all the molecular orbital levels are doubly degenerated except l = 0 or N/2. For molecules with $4n$ + 2 π electrons, such as benzene, two degenerate HOMOs ($l = \pm n$) are filled. For molecules with $4n$ π electrons, for example, cyclobutadiene, one might imagine the two degenerate MOs ($l = \pm n$) are each singly occupied with one electron, giving a triplet ground state electronic configuration. However, the HOMO degeneracy is commonly lifted by the pseudo-Jahn-Teller distortion, resulting in a closed-shell configuration and a small HOMO–LUMO gap.[111]

Applying an external magnetic field on the cyclic structures is expected to perturb the system, resulting in a change of the energies E_l from eqn. 1.9 to the following:

$$E_{l,\phi} = \alpha + 2\beta \cos\left[\frac{2\pi}{N}\left(l - \frac{\phi}{\phi_0}\right)\right] \quad (1.10)$$

where Φ is the magnetic flux passes through the rings, as expressed by

$$\Phi = B\pi r^2 \quad (1.11)$$

Here, B is the field strength of the applied external magnetic field and r is the radius.[114] The eqn. 1.10 suggests that, for an aromatic molecule, a flux of Φ/Φ_0 = 0.5 will cause a change of the ground state electronic configuration from two doubly occupied degenerate HOMOs to two half-filled HOMOs, resulting in an inverse of the ring current direction (i.e., the module becomes antiaromatic). A simulation showing a variation of the electronic configuration of benzene with respect to magnetic field is depicted in Figure 1.12. These variations estimated for molecules have a resemblance to the field-dependent oscillatory ring currents observed in mesoscopic rings. However, the oscillation has not yet been observed in molecules because it requires stronger magnetic fields for molecules, compared with the mesoscopic rings due to their large areas. Therefore, to probe the magnetically induced ring current oscillations in molecules, it is of importance to synthesize large (anti)aromatic macrocycles.

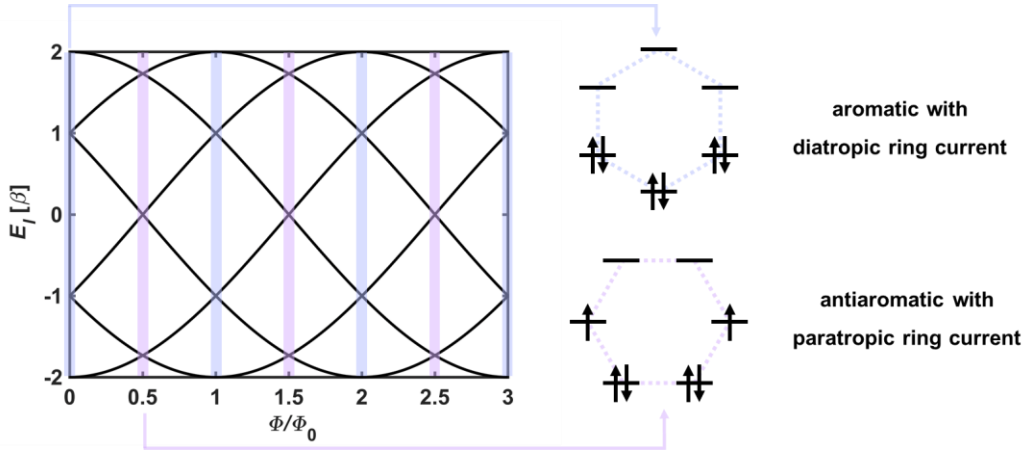

Figure 1.12: Simulation of electronic structure of benzene at high magnetic field as a function of the flux Φ/Φ_0 using a simple Hückel–London model (see eqn. 1.10).[114]

Anslyn and Dougherty suggested in their textbook "*Modern Physical Organic Chemistry*" that the Hückel's [4n + 2] rule is applicable to molecules with up to about 22 π electrons (n = 5), and beyond this point, larger molecules would no longer exhibit aromaticity.[120] However, some large molecules, such as conjugated porphyrin nanorings ***c*-P*N*** reported by Anderson and co-workers, exhibit global ring currents in their oxidized, reduced or excited states, which contradicts the size limitation indicated by the text book.[121–126] To date, the largest macrocycle showing global ring current has been evidenced is the charged butadiyne-linked porphyrin nanoring ***c*-P12^{6+}** with up to 162 π electrons (n = 40).[124] In the following, template-directed syntheses of conjugated porphyrin nanorings and studies on their global (anti)aromatic behaviors are briefly discussed.

1.3.2 Template-Directed Syntheses of Porphyrin Nanorings

The conjugated porphyrin nanorings ***c*-P*N*** reported by Anderson and coworkers are efficiently constructed by template-directed synthesis.[12] In this approach, a molecular (or an ion) as a template is employed to organize the reactants to orient formation of a specific product. In principle, the template is removable after the reaction. The formal definition of a chemical template was provided by Busch,[127] and refined by Sanders: the template provides instructions for the formation of a single product from a substrate or substrates which otherwise have the potential to assemble and react in a variety of ways.[128] To date, template-directed synthesis has become an important strategy to build up supramolecular structures, such as rotaxanes, catenanes, knots, cages and porphyrin nanostructures.[12,129–131]

Oligopyridines are mostly used as templates for synthesis of porphyrin nanorings, because the pyridyl legs in a template can readily coordinate to the porphyrin central metal ions

(typically Zn(II) or Mg(II)), which allows the template to wrap the linear porphyrin oligomers as a ring-shaped complex. Although the binding of a pyridine to Zn(II) porphyrin monomer is weak ($K_f \approx 10^3$–10^4 M^{-1}), the chelate cooperativity results in a strong binding of the oligopyridine template to the porphyrin oligomer to overcome the energy required to form the ring-shaped complex (e.g., template **T6** binds to linear butadiyne-linked porphyrin hexamer ***lb*-P6** with $K_f = 10^{20}$ M^{-1}, and cyclic hexamer ***cb*-P6** with $K_f = 10^{36}$ M^{-1}).[132] The following macrocylization reaction closes the ring to form covalent architecture. The macrocyclization is irreversible, and after the reaction, the template can be displaced by adding a large excess of a competing ligand (e.g., quinuclidine) or treating with an acid to remove the central metal ions from porphyrins together. Template-directed syntheses of porphyrin nanorings are under kinetic control, because the macrocyclization reactions afford covalent architectures and these reactions are irreversible.

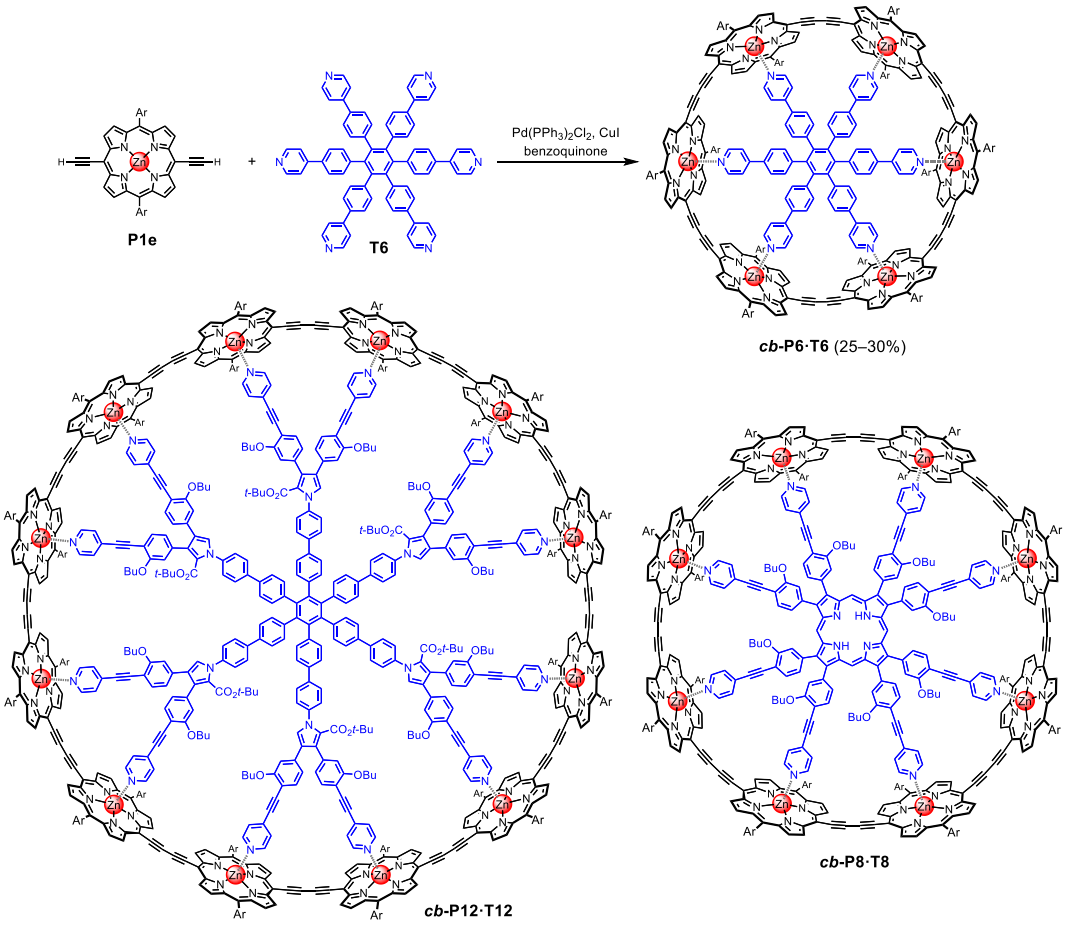

Figure 1.13: Template-directed synthesis of butadiyne-linked porphyrin nanoring ***cb*-P6**, and nanoring-template complexes ***cb*-P8·T8** and ***cb*-P12·T12** prepared using classical templates.[12] *c*, *b* and e indicate cyclic, butadiyne-linked and ethynyl respectively; Ar is aryl groups with solubilizing side chains.

Cyclic butadiyne-linked octamer ***cb*-P8** was reported in 2008 as the first success in template-directed syntheses of π-conjugated porphyrin nanorings (see Figure 1.13 for its nanoring-template complex structure ***cb*-P8·T8**).[133] Soon after that, a cyclic hexamer ***cb*-P6** was synthesized using a readily accessed **T6** template.[134] ***cb*-P6** was efficiently formed via palladium-catalyzed homocoupling of two linear trimers, three linear dimers or six monomers. This makes ***cb*-P6** an archetype for a family of nanorings. The aforementioned template-directed syntheses are mediated by classical templates, in which a single template, which has the same number of binding sites to the product, is used to orient the synthesis. A limitation of this approach is that it requires preparation of giant polydentate ligands as templates to build up large porphyrin nanorings. The largest single template reported for nanoring synthesis is **T12** as shown in Figure 1.12.[135]

One solution to overcome this obstacle is to use the Vernier templates, in which a template has a mismatched number of binding sites to the porphyrin oligomer and the Vernier complex formed comprises the lowest common multiple of binding sites.[135] Vernier template-directed synthesis can be classified into two types. (*i*) One is the twisted Vernier template approach, in which templates coordinate to porphyrin oligomers forming Vernier complexes in figure-of-eight geometries.[135,136] A typical example is template **T6** binds to linear tetramer ***lb*-P4$_{t\text{-Bu}}$** with 3,5-bis(*tert*-butyl)phenyl solubilizing groups to form Vernier assembles **(*lb*-P4$_{t\text{-Bu}}$)$_3$·(T6)$_2$** (Figure 1.14). It is followed by palladium-catalyzed coupling reaction to give ***cb*-P12$_{t\text{-Bu}}$·(T6)$_2$** in 39% yield. This approach enables efficient syntheses of large porphyrin macrocycles, such as ***cb*-P30** from ***lb*-P10** with **T6**, and ***cb*-P40** from ***lb*-P10** with **T8**. In the reaction toward ***cb*-P40**, ***cb*-P50** was isolated as the largest monodisperse covalent synthetic macrocycle yet.[136] The macrocycles ***cb*-P30**, ***cb*-P40** and ***cb*-P50** mentioned above are composed of porphyrins with comparatively flexible 3,5-bis(octyloxy)phenyl solubilizing groups, which minimizes the steric repulsion in forming the twisted Vernier complexes. The steric repulsion hinders the twisted complex formation when bulky 3,5-bis(trihexylsilyl)phenyl solubilizing groups are introduced to the porphyrins.[137] For example, treatment of **T6** with ***lb*-P4$_{THS}$** bearing bis(trihexylsilyl)phenyl solubilizing groups gave ***cb*-P12$_{THS}$·(T6)$_2$** in 18% yield. (*ii*) To overcome this limitation, an expanded hexadentate template **T6e** was made. Two **T6e** stacked closely to bind to three ***lb*-P4$_{THS}$**, forming **(*lb*-P4$_{THS}$)$_3$·(T6e)$_2$** Vernier complex in an open circular conformation. The coupling reaction gave ***cb*-P12$_{THS}$·(T6e)$_2$** in 30% yield. ***cb*-P12$_{t\text{-BuTHS}}$·(T6e)$_2$** in 21% yield was obtained using the same reaction conditions. This strategy involving two stacking templates to direct the macrocyclization is called stacked Vernier

template approach. It is useful for constructing large macrocycles while holding their conformations in an open circular shape.

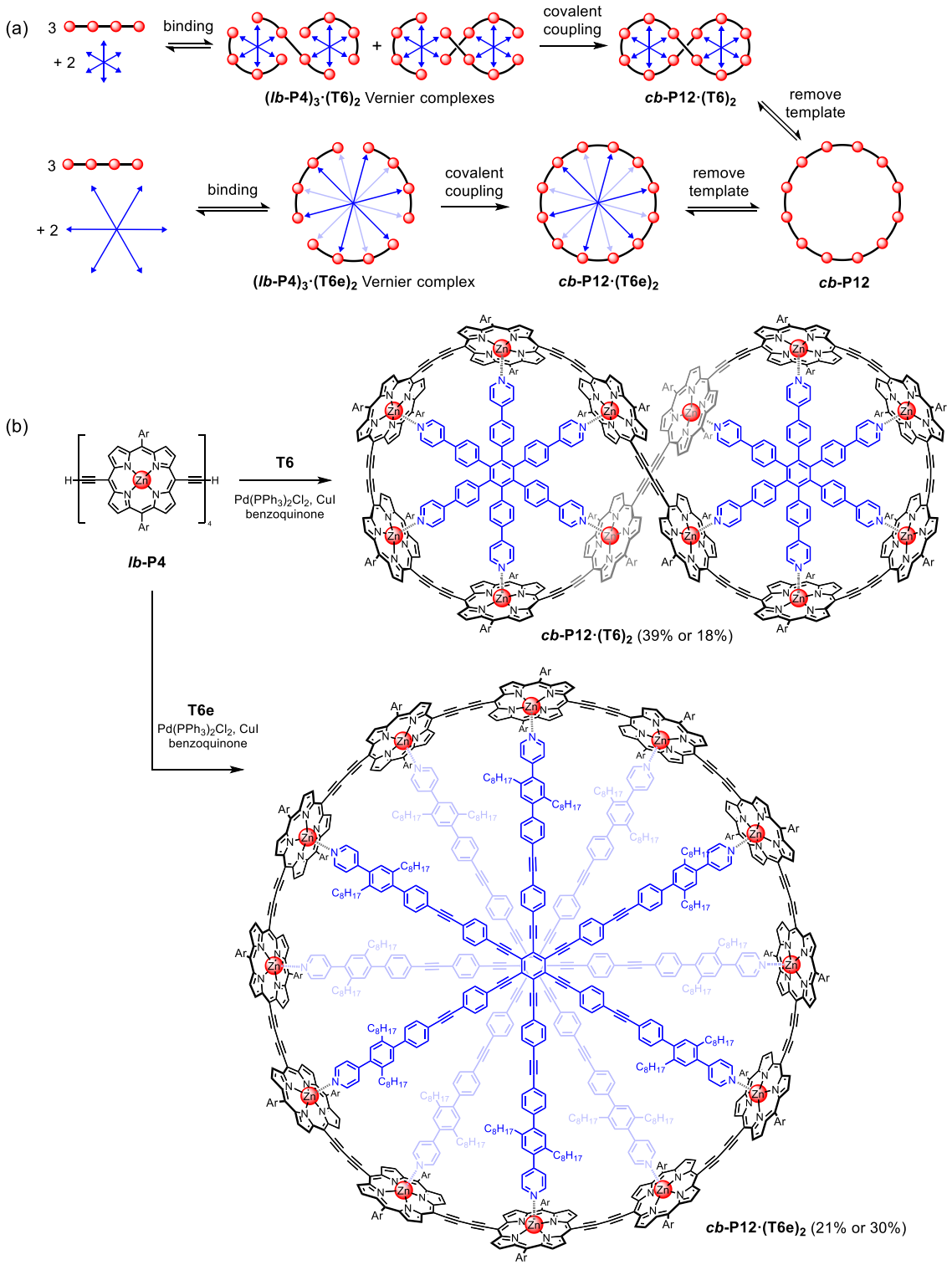

Figure 1.14: Cartoons (a) and chemical structures (b) showing Vernier template-directed synthesis of porphyrin nanoring ***cb*-P12**. The reaction yields depend on the size of the solubilizing aryl groups on the porphyrins.

In addition to the Vernier approach, other "nonclassical" strategies, such as caterpillar-track templating,[138] Russian-doll templating,[139] and shadow-mask templating,[140] were also invented for syntheses or functionalization of porphyrin nanorings. Apart from creating topologically flat cyclic porphyrin oligomers, these strategies have also been extended to build up three-dimensional supramolecular nanostructures, such as porphyrin nanotubes and nanoballs.[141–146] In brief, template-directed synthesis provides access to giant π-conjugated porphyrin nanostructures which were previously unimaginable and these giant macrocycles allows exploration of global (anti)aromaticity at the nanoscale.

1.3.3 Global Aromaticity of Porphyrin Nanorings

The first example of porphyrin nanorings exhibiting global (anti)aromatic behaviors is the π-conjugated butadiyne-linked porphyrin cyclic hexamer ***cb*-P6^{Q}** (or ***c*[*b*$_6$]-P6^{Q}**) in its 2+, 4+ and 6+ oxidation states (Q = +2, +4 and +6), which was evidenced by a detailed analysis of their ^{1}H NMR spectra.[121,124] In contrast, the ^{1}H NMR spectrum of the neutral nanoring (Q = 0) showed no sign of global (anti)aromaticity, suggesting the π electrons only delocalize within each porphyrin unit, showing local aromatic ring currents (i.e., a single porphyrin unit with 18 delocalized π electrons is aromatic).

The chemical structure of ***cb*-P6·T6^{Q}** is shown in Figure 1.15, where α, β, γ, δ, o_{in}, o_{out}, THS_{in} and THS_{out} label the protons in the system, of which the chemical shifts can indicate the presence of aromatic or antiaromatic ring currents. The ^{1}H NMR spectra of ***cb*-P6·T6^{Q}** (Q = 0, +2, +4, +6) are depicted in Figure 1.16. Four types of experimental chemical shift differences are summarized in Table 1.1, together with the DFT calculated values. The experimental data shown in Table 1.1 are summarized from two reported works.[121,124] $\delta(o_{in}) - \delta(o_{out})$ is the chemical shift difference between inner and outer *ortho*-aryl protons; $\delta(THS_{in}) - \delta(THS_{out})$ is the chemical shift difference between inner and outer Si-CH_2 protons; $\Delta\delta(\alpha)$ is the chemical shift difference between the α-proton of the template complex and that of the free unbound template, and similarly $\Delta\delta(\beta) = \delta(\beta) - \delta(\beta_{free})$. An aromatic ring current results in shielding within the ring, and deshielding outside. These effects are opposite for an antiaromatic ring. Negative values of $\Delta\delta(\alpha)$ and $\Delta\delta(\beta)$ indicate either a local aromatic ring current in each porphyrin unit, or a global ring current around the whole nanoring. On the contrary, the differences $\delta(o_{in}) - \delta(o_{out})$ and $\delta(THS_{in}) - \delta(THS_{out})$ are less affected by local ring currents and large negative (or positive) values of these parameters indicate the presence of global (anti)aromatic ring currents. The pattern of shielding in Figure 1.16 and Table 1.1 indicate that Q = 0 has locally aromatic porphyrin units, but no global ring current; Q = +2 has a global

aromatic ring current, Q = +4 has a global antiaromatic ring current, Q = +6 is globally aromatic and Q = +12 is locally antiaromatic. The spectrum of the 2+ oxidation state (Figure 1.16b) is relatively broad, suggesting ***cb*-P6·T6**$^{2+}$ has an open-shell character.[124]

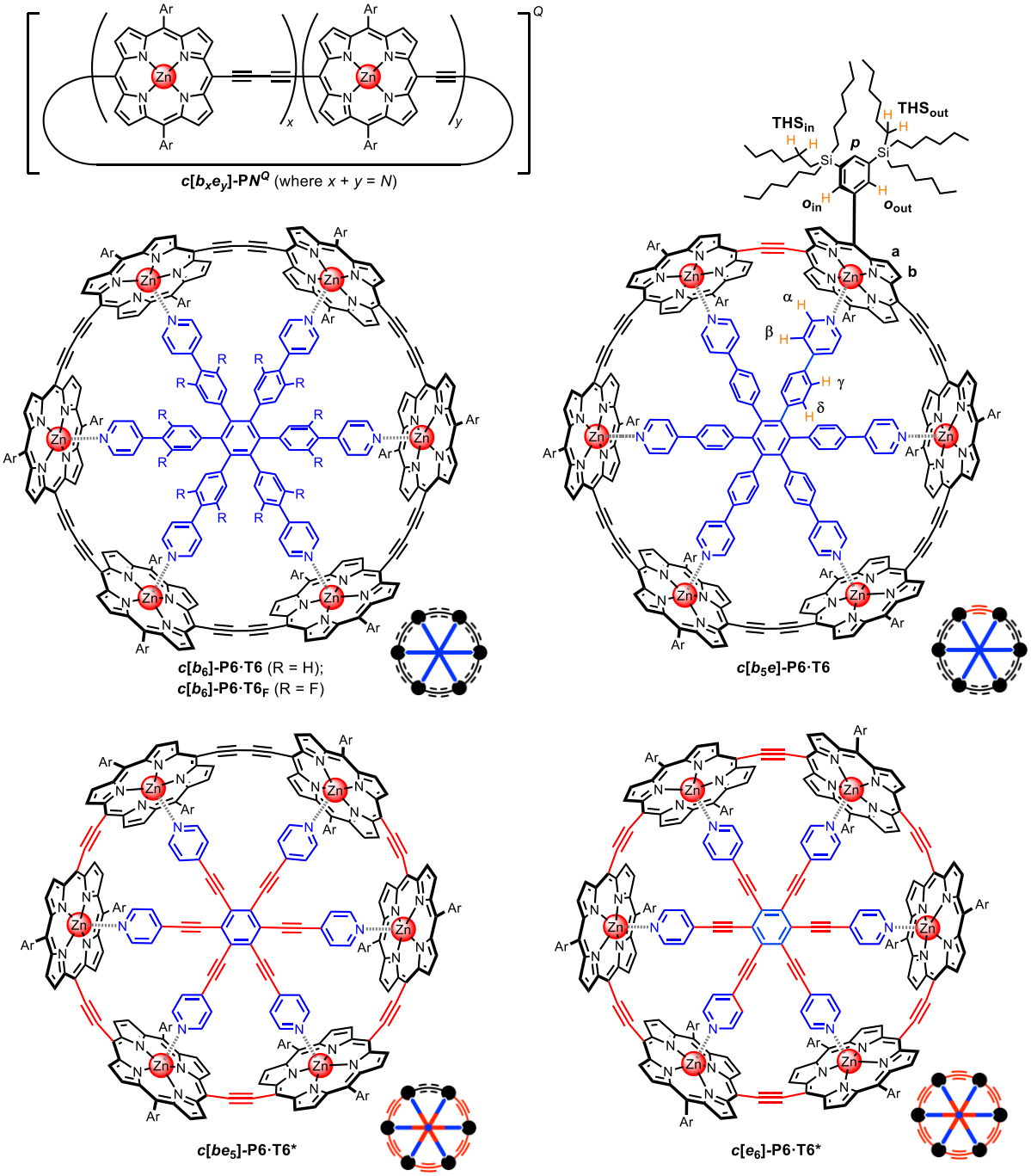

Figure 1.15: General structure, chemical structures and cartoon structures of porphyrin nanorings ***c*[*b*$_x$*e*$_y$]-P*N*^{Q}**. Here, *c*, *b* and *c* are cyclic, butadiyne and ethyne links; Q is the charge (oxidation state); *N*, *x* and *y* are the number of porphyrins, butadiyne and ethyne links; a, b, o_{in}, o_{out}, *p*, THS_{in}, THS_{out}, α, β, γ, δ are protons on the porphyrin nanorings and **T6** template, which were clearly assigned by ^{1}H–^{13}C HSQC and NOESY spectra.

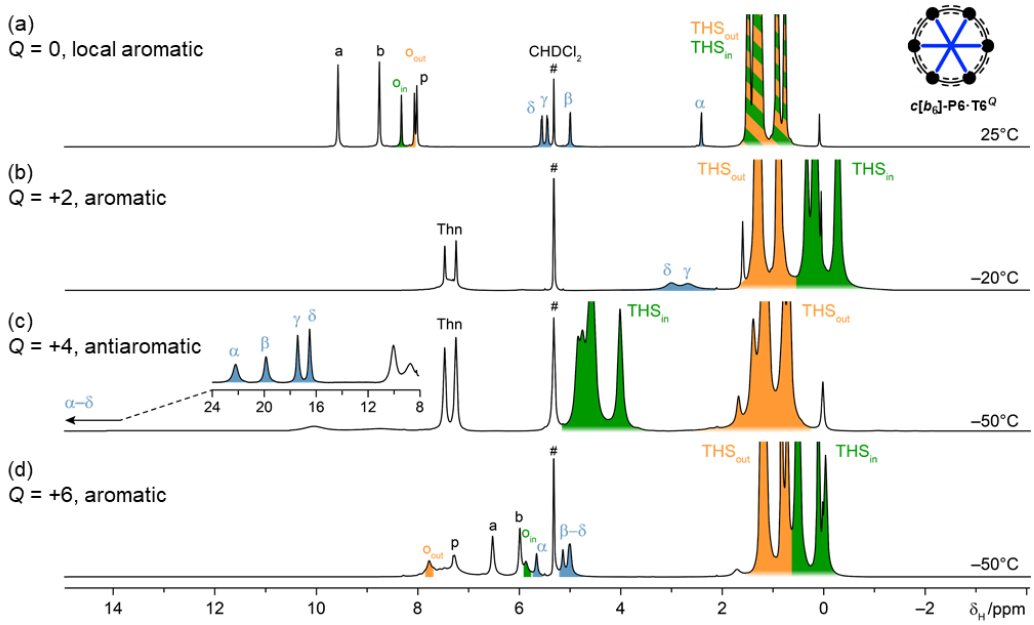

Figure 1.16: ^{1}H NMR (500 MHz, CD_2Cl_2) spectra of ***c*[*b*$_6$]-P6·T6^{Q}** at neutral, 2+, 4+ and 6+ oxidation states. Thn is neutral thianthrene. Reproduced with permission from ref. 124.

Table 1.1: Selected ^{1}H NMR chemical shift differences for ***c*[*b*$_6$]-P6·T6^{Q}** (in ppm).[143]

Q	method	$\delta(o_{in}) - \delta(o_{out})$	$\delta(THS_{in}) - \delta(THS_{out})$	$\Delta\delta(\alpha)$	$\Delta\delta(\beta)$	RMSE[a]
0	experimental	0.26	0.00	–6.31	–2.34	—
	CAM-B3LYP	0.09	—	–6.34	–2.54	0.15
	B3LYP	0.31	—	–5.34	–1.97	0.60
	LC-ωhPBE	0.39	—	–5.24	–2.00	0.65
	BLYP35	0.44	—	–5.79	–2.31	0.32
+2	experimental	—	–1.13	—	—	—
	LC-ωhPBE	–0.62	—	3.02	4.32	—
	BLYP35	–0.56	—	2.95	4.30	—
+4	experimental	—	3.93	14.2	12.6	—
	CAM-B3LYP	0.41	—	–1.92	–0.44	14.6
	B3LYP	36.36	—	60.4	49.1	41.7
	LC-ωhPBE	4.27	—	4.80	4.96	8.53
	BLYP35	8.56	—	12.1	10.8	1.93
+6	experimental	–1.87	–0.73	–2.83	–2.06	—
	CAM-B3LYP	–0.19	—	–0.97	–0.36	1.74
	B3LYP	–7.23	—	–12.3	–9.85	7.71
	LC-ωhPBE	–1.03	—	–2.53	–1.54	0.60
	BLYP35	–1.17	—	–1.99	–1.37	0.75
+12	experimental	–0.74	–0.16	2.77	1.50	—
	CAM-B3LYP	–0.91	—	1.88	1.13	0.57
	B3LYP	–2.67	—	5.63	2.68	2.10
	LC-ωhPBE	–2.76	—	5.33	2.67	2.00
	BLYP35	–1.53	—	3.09	1.64	0.50

[a] Root-mean square error (RMSE) values are calculated from the Δδ with respect to the experiment values. [b] A symmetry-broken singlet state was assumed. [c] ω = 0.1.

The chemical shifts can be simulated by DFT calculations using the Gauge-Independent Atomic Orbital (GIAO) method.[144] There are numbers of exchange–correlation functionals developed for DFT calculations, and choice of the functionals significantly affect the calculated chemical shifts. The popular used B3LYP functional exaggerates delocalization of electrons and overestimates the shielding/deshielding effects, owing to the self-interaction error. Matito and coworkers used CAM-B3LYP functional to calculate the chemical shifts and the results are closer to the experimental values than the ones predicted by the B3LYP functional.[145] However, CAM-B3LYP underestimates the global (anti)aromatic behaviors.

We have recently screened a number of range-separated density functional approximations (DFAs) and discovered that the ^{1}H NMR chemical shifts predicted by two DFAs, namely BLYP35 and LC-ωhPBE (ω = 0.1) well match the experimental data (see Table 1.1 for the details).[143†] In the 4+ and 6+ oxidation states (Q = +4 and +6), the CAM-B3LYP functional failed to reproduce the sign or magnitude of the chemical shifts, while BLYP35 and LC-ωhPBE (ω = 0.1) functionals provided great estimations. The calculations for Q = 0, +4, +6 and +12 restricted the systems in a singlet state, while it failed to reproduce the chemical shifts for Q = +2, and thus a broken-symmetry singlet guess is employed to predict the chemical shifts. The $\Delta\delta(\gamma) = \delta(\gamma) - \delta(\gamma_{free})$ and $\Delta\delta(\delta) = \delta(\delta) - \delta(\delta_{free})$ are used for comparison because the experimental ^{1}H signals for α and β protons were too broad to be observed in the 2+ oxidation state (Figure 1.16). The $\Delta\delta(\gamma)$ (−2.37 and −2.31 ppm) and $\Delta\delta(\delta)$ (−2.06 and −2.01) estimated by BLYP35 and LC-ωhPBE functionals qualitatively match the experimental data, where $\Delta\delta(\gamma)$ = −4.55 ppm and $\Delta\delta(\delta)$ = −4.02 ppm.

The simulated global (anti)aromatic behaviors can be clearly visualized by the Nucleus Independent Chemical Shift (NICS) plots.[146] In these calculations, a grid of so-called Banquo atoms or ghost atoms is placed across the zinc centers of the porphyrin nanoring, of which the chemical shifts are calculated by the GIAO method. The calculated NICS values are plotted as a map with contours showing the shielding/deshielding effects with blue/red colors. The $NICS_{iso}$ values average the effects from all three orthogonal orientations of the external magnetic field (i.e., x, y and z directions). The $NICS_{ZZ}$ values only account the effect from the z direction, which is more reflective of global (anti)aromaticity effects. NICS plots for

† The calculations were performed by the author, in collaboration with David Bradley, Dr. Martin D. Peeks (School of Chemistry, University of New South Wales, Australia) and Dr. Michael Jirásek (Laboratory of Organic Chemistry, ETH Zurich, Switzerland).

***c*[*b*$_6$]-P6^Q** (Q = 0, +2, +4, +6 and +12) calculated using the BLYP35 functional are shown in Figure 1.17a as examples.[143] The neutral ***c*[*b*$_6$]-P6** and its 12+ oxidation state only show local aromatic/antiaromatic characters as reflected by $NICS_{iso}$ plots. The $NICS_{ZZ}$ plots indicate no global ring current is present for these two states when an external magnetic field is applied across the ring. In contrast, for ***c*[*b*$_6$]-P6^Q** (Q = +2, +4 and +6), significant global (anti)aromatic behaviors are present. These can be clearly evidenced by the $NICS_{ZZ}$ plots. For 2+ and 6+ oxidations states, the blue color (shielding) inside the ring and red color (deshielding) outside reveals the presence of diatropic ring currents around their circumferences (i.e., they are global aromatic). The shielding pattern reverses in the 4+ oxidation states, suggesting it is global antiaromatic.

To quantify the ring currents from NMR data, one approach is to estimate the ring current susceptibility (in nA/T), i.e., the magnitude of the ring current (in nA) induced by an external magnetic field of 1 T. The magnitude of the ring current induced can be quantified by plotting the observed or calculated chemical shift differences $\Delta\delta$ against the ring current geometric factors RCGFs using the following equation:

$$\Delta\delta = (I/B)\mathrm{RCGF} \tag{12}$$

where I is the current, B is the external magnetic field, I/B is the ring current susceptibility.[114] The RCGF is calculated from the molecular geometry using the Biot–Savart law, which indicates the sensitivity of a given point in space to the induced magnetic field of the ring current. The ring current susceptibility values for ***c*[*b*$_6$]-P6·T6^Q** (Q = +2, +4 and +6) are summarized in Table 1.2, which again show a change of two π electrons reverses the direction of the induced ring current. The experimental values are consistent with the DFT predicted values.

The alternation of the ring current direction in its different oxidation states can be elucidated by the Hückel's [4n + 2] rule. In a porphyrin nanoring, each porphyrin contributes ten electrons to the Hückel π electron count N_e and each ethyne link contributes two electrons (i.e., four electrons are counted for each butadiyne link). The ***c*[*b*$_6$]-P6·T6^{2+}** (N_e = 82) and ***c*[*b*$_6$]-P6·T6^{6+}** (N_e = 78) having 4n + 2 delocalized π electrons are thus global aromatic while ***c*[*b*$_6$]-P6·T6^{4+}** (N_e = 80) with 4n delocalized π electrons is global antiaromatic. This alternation was also clearly evidenced by experimental and theoretical investigations of a family of six-porphyrin nanorings ***c*[*b*$_x$*e*$_y$]-P6^Q**, of which the chemical structures, ^{1}H NMR chemical shift differences and ring current susceptibilities are shown in Figure 1.15, Table 1.1 and 1.2, respectively.[124,143]

The N_e of these nanorings vary by changing the number of ethyne units (i.e., a butadiyne link accounts for two ethyne units). Adding or removing an ethyne unit in the charged ring changes a number of two π electrons in the Hückel electron count ($\Delta N_e = 2$), resulting in a reverse of global ring current direction (diatropic vs. paratropic). The periodicity of the shielding with respect to the Hückel electron count N_e provides the strongest evidence for global ring currents.

In addition to the six-porphyrin nanorings, the global (anti)aromatic effects have also been probed in a series of porphyrin nanoring template complexes.[124–125] A plot summarizing the experimental ring current susceptibilities of these rings against their Hückel π electron counts N_e is shown in Figure 1.18a.[114] Fluorinated templates, such as **T6$_F$** in Figure 1.15, allow evaluation of the aromaticity of the nanorings using ^{19}F NMR titrations. The results support the conclusions from ^{1}H NMR data. The conformation of the porphyrin nanoring template complexes also affects their magnetic responses. If a ring is folded into a figure-of-eight shape, such as ***cb*-P12$_{THS}$·(T6)$_2$** in Figure 1.14, the magnetic field induced ring currents in two loops have equal strengths and opposite directions, resulting in a vanished global ring current.[124] This behavior strengthens the importance of the stacked template approach, where the nanoring is held in an open circular conformation, enabling evaluation of its the global (anti)aromaticity. Apart from the oxidized porphyrin nanorings, the global (anti)aromatic behaviors have also been evaluated for porphyrin nanoring anions and their excited states.[121–123]

Table 1.2: Experimental (and BLYP35-calculated) changes in chemical shift, in ppm, and ring current susceptibilities *I*/*B* in six-porphyrin nanorings.[143]

species	*Q*	N_e[a]	$\delta(o_{in}) - \delta(o_{out})$	$\Delta\delta(\alpha)$	$\Delta\delta(\beta)$	*I*/*B* (nA/T)
***c*[*b*$_6$]-P6·T6^Q**	+2	82	— (–0.56)	— (–5.69)	— (–2.87)	–26 (–16)[b]
	+4	80	— (8.56)	14.2 (12.1)	12.6 (10.8)	62 (54)
	+6	78	–1.87 (–1.17)	–2.83 (–1.99)	–2.06 (–1.37)	–12 (–7.8)
***c*[*b*$_5$*e*]-P6·T6^Q**	+4	78	— (–6.36)	–14.0 (–14.0)	–10.2 (–10.4)	–57 (–54)
	+6	76	— (0.61)	2.17 (1.16)	1.92 (1.20)	9.5 (5.3)
***c*[*be*$_5$]-P6·T6^Q**	+4	70	— (–4.57)	–15.2 (–11.3)	–11.1 (–8.72)	–59 (–43)
	+6	68	— (1.06)	2.80 (1.93)	2.68 (1.50)	12 (7.8)
***c*[*e*$_6$]-P6·T6^Q**	+2	70	–5.92 (–8.30)	–16.0 (–21.3)	–11.0 (–15.8)	–55 (–76)
	+4	68	— (5.67)	27.3 (8.13)	22.7 (7.02)	111 (35)
	+6	66	–2.43 (–1.03)	–4.40 (–2.13)	–3.13 (–1.89)	–17 (–8.9)

[a] N_e is the number of π electrons in the Hückel circuit around the macrocycle. [b] The experimental *I*/*B* for ***c*[*b*$_6$]-P6·T6^{2+}** comes from the measured $\Delta\delta(\gamma)$ and $\Delta\delta(\delta)$ values.

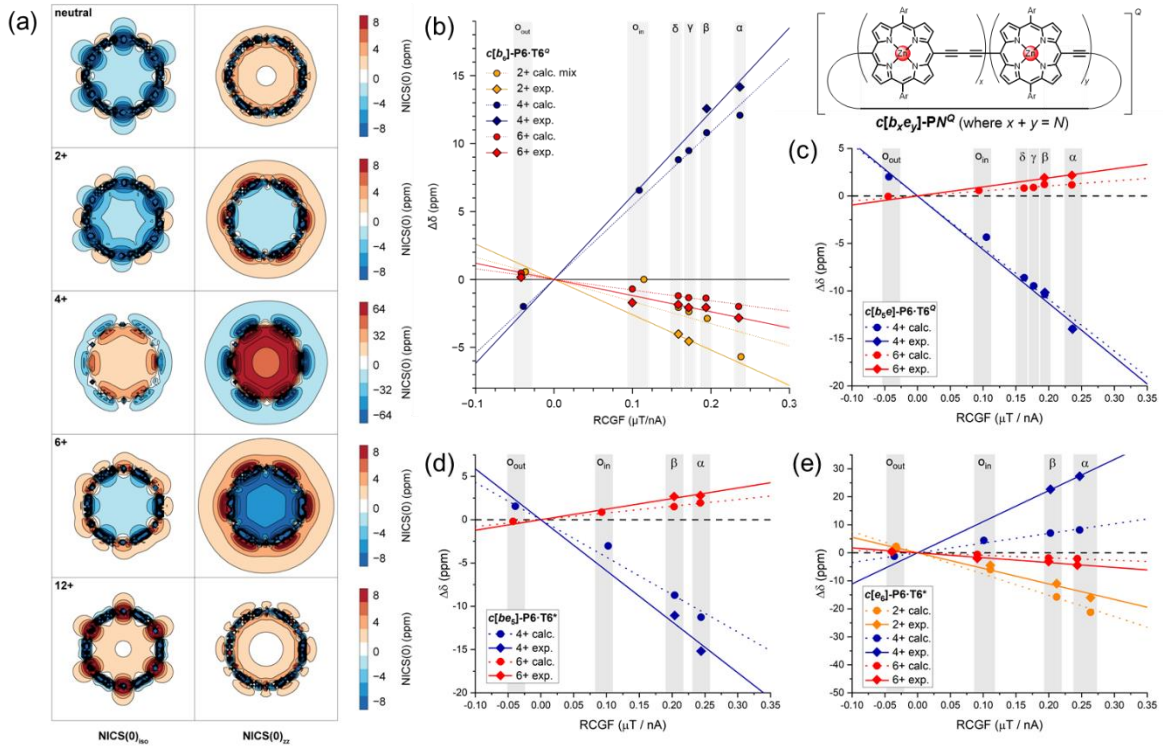

Figure 1.17: (a) Plots of NICS(0)iso and NICS(0)*zz* for ***c*[b_6]-P6^Q** (Q = 0, +2, +4, +6 and +12) calculated using the BLYP35 functional. The calculation for Q = +2 assumes a symmetry-broken unrestricted singlet state. (b)–(e) Plots of Δδ vs. RCGF for ***c*[b_6]-P6·T6^Q** (Q = +2, +4 and +6), ***c*[b_5e]-P6·T6^Q** (Q = +4 and +6), ***c*[be_5]-P6·T6^Q** (Q = +4 and +6) and ***c*[e_6]-P6·T6^Q** (Q = +2, +4 and +6), showing experimental points and BLYP35 calculated points. The ring current susceptibility values estimated from the slopes of the plots are summarized in Table 1.2.[143]

The discovery of the global (anti)aromatic behaviors of these large macrocycles implicates that these rings can behave as circular molecular wires, enabling electrons to flow around the circumferences of such molecules, and more importantly, the charge transport is phase-coherent. Studies on larger π-conjugated porphyrin nanorings could provide insight into the similarity between aromatic ring currents and persistent currents in non-molecular quantum rings. These studies could also shed light on the possibility to fabricate molecular interferometers by integration of these rings into metal|molecule|metal junctions.[114]

Despite these advances, there has been no report on global (anti)aromaticity for porphyrin nanorings in the neutral ground state, which is different from the small π-conjugated cyclic molecules, such as benzene and porphyrin monomer, which exhibit induced diatropic (or paratropic) ring currents without oxidation, reduction or photoexcitation. This probably indicates the inter-porphyrin electronic coupling in these butadiyne-linked or ethyne-linked porphyrin nanorings is still not strong enough to permit electrons to delocalize around the

whole macrocycle instead of delocalization only within a single porphyrin unit. Porphyrin nanorings comprising of fused porphyrin oligomers may overcome this limitation, because as discussed above, the fused oligomers exhibit extremely strong electronic coupling between neighboring porphyrin rings. Building up a belt-shaped porphyrin nanoring ***cf*-P*N*** (Figure 1.19), in which the porphyrins are triply-linked to the neighboring units is an ambitious target, because it requires to overcome a high strain energy barrier to form the ring.

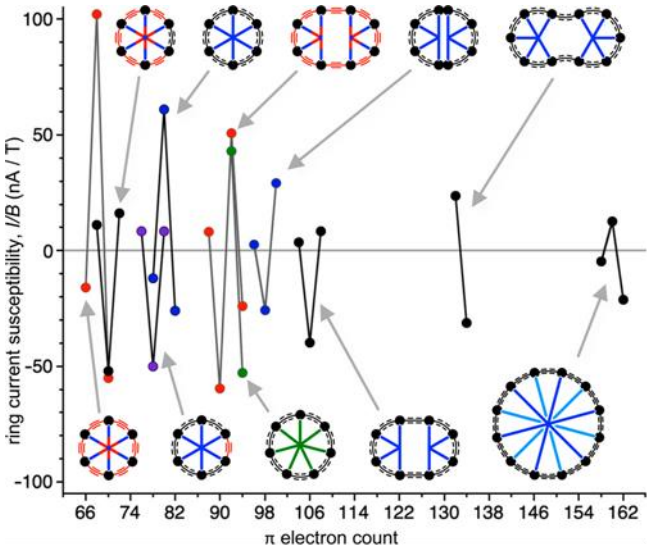

Figure 1.18: Plot of ring current susceptibility, *I*/*B*, from experimental NMR data against the Hückel electron count for various porphyrin nanoring template complexes, each in several oxidation states.[114]

1.4 Prospectus

This thesis aims to develop new strategies for syntheses of linear and cyclic fused porphyrin oligomers and to explore their charge transport behaviors using multiple approaches. We focus on molecular design, template-directed synthesis and characterizations of a strained *meso*–*meso* singly-linked 24-porphyrin nanoring ***cs*[*b*]-ZnP24** with a butadiyne-linked segment in Chapter 2, together with attempts toward smaller nanorings, such as ***cs*[*b*]-ZnP12**. These attempts could provide insights into the future works toward the ultimate goals of the project, to make the closely spaced exciton-coupled fully *meso*–*meso* singly-linked porphyrin nanorings ***cs*-P*N***, and strongly π-conjugated *meso*–*meso*, *β*–*β*, *β*–*β* triply-linked (fused) porphyrin nanobelts ***cf*-P*N***, and to investigate excitation energy transfer and charge transport in these systems.

In Chapters 3–5, we turn to study the linear fused porphyrin oligomers. New advances for preparing monodisperse fused porphyrin oligomers ***lf*-MP*N*** (M = Ni(II) and Zn(II)) are described. In addition to the syntheses, in Chapter 3, we investigate the single-molecule conductance of ***lf*-NiP*N*** using STM-BJs technique, in which molecules are connected to two gold electrodes via strong C–Au interactions. In Chapter 4, observation of strong evidences for coherent transport through a fused porphyrin octamer ***lf*-NiP8** graphene-based three-terminal junction is described. In the last chapter, radical cations of porphyrin oligomers ***lf*-ZnP*N*** are created by chemical or electrochemical oxidation, and probed by EPR and UV–vis–NIR–IR spectroscopies. All these studies would help to understand the long-range charge transport behaviors of fused porphyrin oligomers as molecular wires, which might open up a possibility for fabrication of future electronic devices using these molecules.

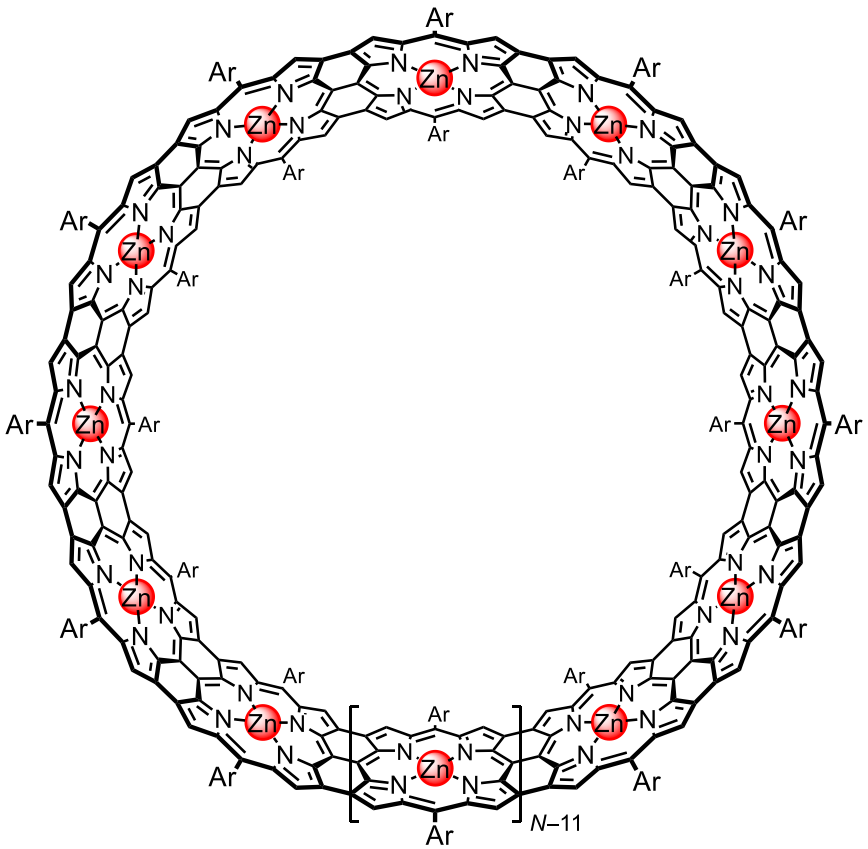

Figure 1.19: A general structure of fused porphyrin nanobelts ***cf*-P*N***. Ar = solubilizing group.

2

Toward *meso–meso* Singly-Linked Porphyrin Nanorings and Fused Porphyrin Nanobelts

2.1 Introduction 35

2.1.1 Natural Light-Harvesting Complexes and Synthetic Porphyrin Nanorings ... 35

2.1.2 *meso–meso* Singly-Linked Porphyrin Oligomers 37

2.1.3 Carbon Nanobelts and Fused Porphyrin Nanobelts 39

2.1.4 Project Aim 41

2.2 Molecular Design and Computational Modeling 42

2.2.1 Strain Energies of *cs*-P*N*, *cs*[b_1]-P*N* and *cf*-P*N* 42

2.2.2 Aromaticity and Antiaromaticity in *cf*-P*N* 44

2.2.3 Molecular Design and Synthetic Plan 46

2.3 Synthesis of *ls*-P*N* 48

2.4 Binding of T2 to *ls*-P2 50

2.5 Attempted Syntheses of *cs*-P12 and *cs*[b_1]-P12 54

2.5.1 Syntheses of T12a and T12b 54

2.5.2 Binding of T12a and T12b to *ls*-P12 55

2.5.3 Attempted Synthesis of *cs*-P12 57

2.5.4 Attempted Synthesis of *cs*[b_1]-P12 61

2.6 Synthesis and Characterization of *cs*[b_1]-P24 62

2.6.1 Computational Modeling and Design of the Template T12e 62

2.6.2 Synthesis of T12e 64

2.6.3 Synthesis and Chemical Characterization of *cs*[b_1]-P24 65

2.6.4 Scanning Probe Microscopy 67

2.7 Binding of T12e to *cs*[b_1]-P24 and *ls*-P24 69

2.7.1 Binding of T12e to *cs*[b_1]-P24 69

2.7.2 Binding of T12e to *ls*-P24 76

2.8 Photophysics and Excitation Energy Transfer in *cs*[b_1]-P24 78

2.9 Conclusion and Outlook 81

Parts of the works in this chapter were published in:

Gotfredsen, H.;† Deng, J.-R.;† Van Raden, J.; Righetto, M.; Hergenhahn, J.; Clarke, M.; Bellamy-Carter, A.; Hart, J.; O'Shea, J.; Claridge, T. D. W.; Duarte, F.; Saywell, A.; Herz, L. M.; Anderson, H. L. Bending a Photonic Wire into a Ring. *Nat. Chem.* **2022**, *14*, 1436–1442. (also in *ChemRxiv* **2022**, DOI: 10.26434/ chemrxiv-2022-6b0pc).

2.1 Introduction

2.1.1 Natural Light-Harvesting Complexes and Synthetic Porphyrin Nanorings

Green plants and other photosynthetic organisms power most life on earth by photosynthesis, in which energy from sunlight is captured and converted into a chemical form. Photosynthesis begins with light harvesting. Light-harvesting antenna complexes, which consist of large arrays of chlorophyll molecules, are responsible for light absorption. The initial light absorption is followed by a cascade of excitation energy transfer (EET) steps before the energy is funneled into a photochemical reaction center (RC). Light-harvesting systems have evolved so that the EET processes are remarkably rapid and efficient.[147,148] Among a variety of light-harvesting systems in different organisms, two of them, light-harvesting system 1 and 2 (LH1 and LH2) from purple bacteria, have been intensively investigated.[147]

In purple bacteria, LH2 serves as principal light harvester. LH2 comprises of two concentric rings of bacteriochlorophyll *a* (BChl*a*) units: the B800 ring of 9 BChl*a*s and the B850 ring of 18 BChl*a*s (both with diameters of ~6 nm).[149] In the B800 ring, BChl*a*s, separated by a center-to-center distance of 21 Å, are weakly coupled. The excitation of the B800 ring is found to be delocalized over 2–3 BChl*a* units, which rapidly decays to give a localized exciton (0.3–0.5 ps). The localized exciton further migrates around the B800 ring over a time of 1–3 ps.[148,150] The excitation energy can also transfer to the B850 ring (B800 → B850) on a time scale of 600–800 fs.[147] In the B850 ring, BChl*a*s are closely spaced with a center-to-center distance of ~9 Å, and thus the BChl*a*s are strongly coupled to the neighboring units (i.e., they are coupled via exciton coupling because there is no π-overlap between two BChl*a*s). After the excitation has reached the B850 ring, the strong inter-BChl*a* exciton coupling allows creation of a delocalized excited state over many BChl*a*s. The presence of various types of disorder makes the delocalized state lose its coherence (~50 fs), forming a more localized state (4–6 BChl*a*s) which migrates on an ultrafast time scale around the ring (<200 fs).[147,151,152] Since the LH2 complexes are closely positioned to each other and to the LH1 complexes, the excitation energy from a B850 ring can transfer to another B850 ring in the neighboring LH2 or to the B875 ring in LH1 (2–5 ps).[147] LH1 has a similar structure as LH2 but a larger diameter, where 32 BChl*a*s are closely spaced forming the B875 ring.[153] The reaction center (RC) is accommodated in the central cavity of LH1 and the excitation energy can be funneled into the reaction center from the surrounding B875 ring on a time scale of 20–50 ps.[147] The structures of Bchl*a* unit, LH2 and LH1–RC complexes, the energy paths, and the transfer time are summarized in Figure 2.1.[147,148,154]

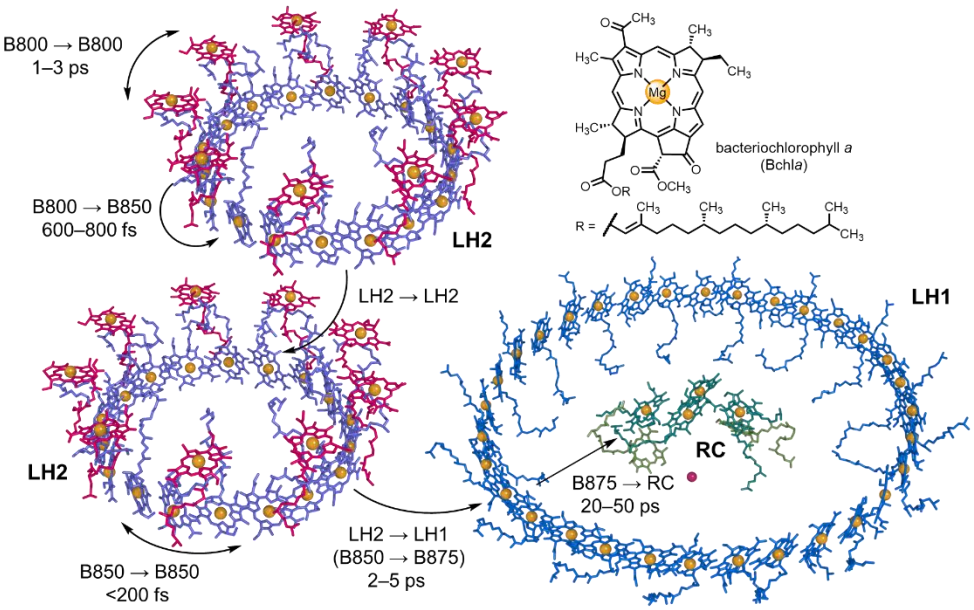

Figure 2.1: Schematic diagram showing the structures of Bchl*a* unit, LH2 and LH1–RC complexes, and the EET time of individual energy transfer process.[154–156] Protein crystal structures were acquired with permission from ref. 155 and 156.

The ultrafast EET dynamics and the cyclic architecture of natural light-harvesting complexes, where BChl*a*s are densely packed, have inspired chemists to design and build up porphyrin nanostructures as artificial models, especially for the B850 ring in LH2, and to investigate their intra-ring EET dynamics. Over the past two decades, a number of porphyrin arrays, including covalently bonded nanorings, self-assembled nanorings, and dendritic arrays, have been successfully synthesized.[154,157–160] However, the only synthetic cyclic porphyrin arrays that mimic intra-ring EET on the same time scale (<200 fs) and length scale (~6 nm diameter) as the B850 ring are the butadiyne-linked porphyrin nanorings ***cb*-P*N*** developed by Anderson, Herz and co-workers (Figure 2.2a).[57,159] Photophysical measurements reveal that, for ***cb*-P*N***, the absorbing state is delocalized over 20 porphyrin units (i.e., the exciton is delocalized over the entire ring when $N \leq 20$).[57,161] The following relaxation causes the emission to occur from more localized states (up to 6 porphyrin units).[57] However, these rings achieve strong inter-porphyrin coupling through π-conjugation (i.e., direct orbital overlap), which makes them fundamentally different from the exciton-coupled rings of BChl*a*s in LH2. Another class of porphyrin nanorings showing ultrafast intra-ring EET (300–700 fs) is the 5,10-linked porphyrin nanorings ***cs**-P*N*** reported by Osuka, Kim and co-workers (Figure 2.2b).[154,162] Although the reported ***cs**-P*N*** rings are much smaller than the B850 ring, the

ultrafast EET dynamics in these rings suggest that synthetic nanorings with closely spaced porphyrin units might be able to mimic the natural light-harvesting complexes.

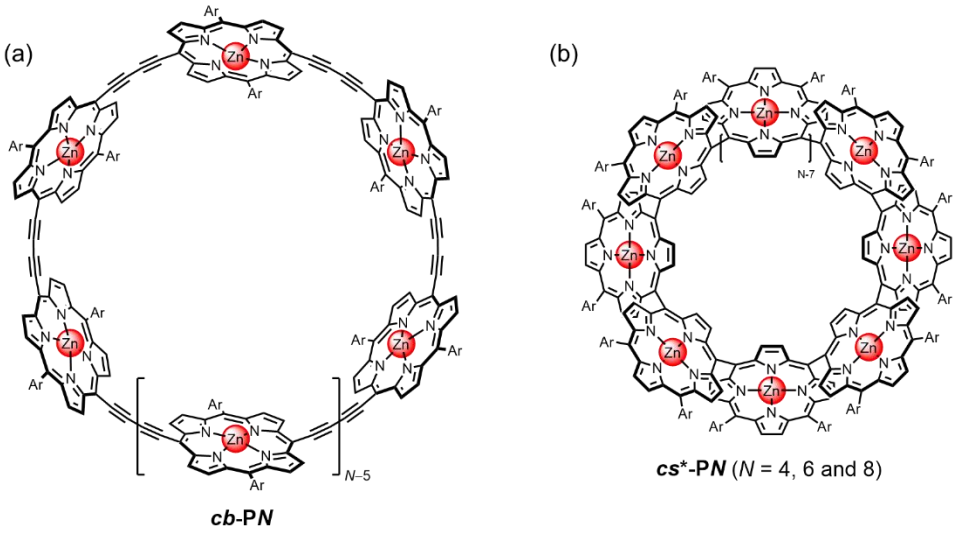

Figure 2.2: Chemical structures of (a) butadiyne-linked porphyrin nanorings ***cb*-P*N*** reported by Anderson, Herz and co-workers,[57,159] and (b) 5,10-linked porphyrin nanorings ***cs**-P*N*** reported by Osuka, Kim and co-workers.[162]

2.1.2 *meso–meso* Singly-Linked Porphyrin Oligomers

Directly *meso–meso* singly-linked (i.e., 5,15-linked) linear porphyrin oligomers ***ls*-P*N***, which can mediate ultrafast EET, have been described as "photonic wires" by Kim, Osuka and coworkers.[163,164] These oligomers have twisted conformations, in which the dihedral angle between neighboring porphyrin rings is typically 70–90°. The twisted conformations prevent direct inter-porphyrin π-overlap, and thus the porphyrin rings are weakly π-conjugated to their neighboring units. The center-to-center distance between two neighboring porphyrin units is 8.35 Å, which is similar to the center-to-center distance between two Bchl*a* units in the B850 ring (~9 Å), resulting in strong inter-porphyrin exciton coupling.[165]

The exciton coupling in ***ls*-P*N*** can be clearly evidenced from their steady-state absorption spectra and interpreted by the exciton coupling theory developed by Kasha and co-workers.[166] The simplest example is a porphyrin dimer ***ls*-P2**, which exhibits split B bands and a red-shifted Q band, compared with the corresponding monomer **P1** (Figure 2.3a and 2.3b). The parallel B_x transitions of two porphyrin rings in ***ls*-P2** are coupled, resulting in a lower energy absorption peak (at ~450 nm), while the B_y and B_z transitions are orthogonal, expressing a resemblance to the monomeric absorption peak (at ~410 nm). For long oligomers ***ls*-P*N***, the exciton coupling

theory indicates the splitting energy ΔE_{ex} (or the energy shifted compared to a monomer) is related to the coupling strength V_{ex} and number of the porphyrin units N as

$$\Delta E_{ex} = 2V_{ex}\cos(\pi/N + 1) \quad (2.1)$$

Eqn. 2.1 provides an excellent description of the split B bands and red-shifted Q band observed from ***ls*-P*N*** up to N = 16, suggesting the absorbing state for ***ls*-P*N*** can span over many porphyrin units.[165] The fluorescence measurements suggest the emission state of ***ls*-P*N*** has a coherence length of about 4–6 porphyrin units, which again resembles that of the B850 ring.[165,167] Connecting ***ls*-P*N*** to an ethynyl monomer affords ***ls*-P*N*-A** as donor–acceptor systems, which allows investigation of the EET from ***ls*-P*N*** to the monomer acceptor (Figure 2.3c).[168,169] The observed rate constants ($k_{EET} = \tau_{EET}^{-1}$) are much faster than the simulated Förster energy transfer rate constants, and instead, they match the simulated rate constants using quantum mechanical treatments that assume the lowest exciton state of the ***ls*-P*N*** is delocalized over 4 porphyrin units. These remarkable photophysical properties suggest the *meso–meso* singly-linked porphyrin oligomers could be promising candidates as mimics of natural light harvesting chlorophyll arrays. However, they have long been considered as "rod-like" arrays, and it has not been possible to bend them into rings.

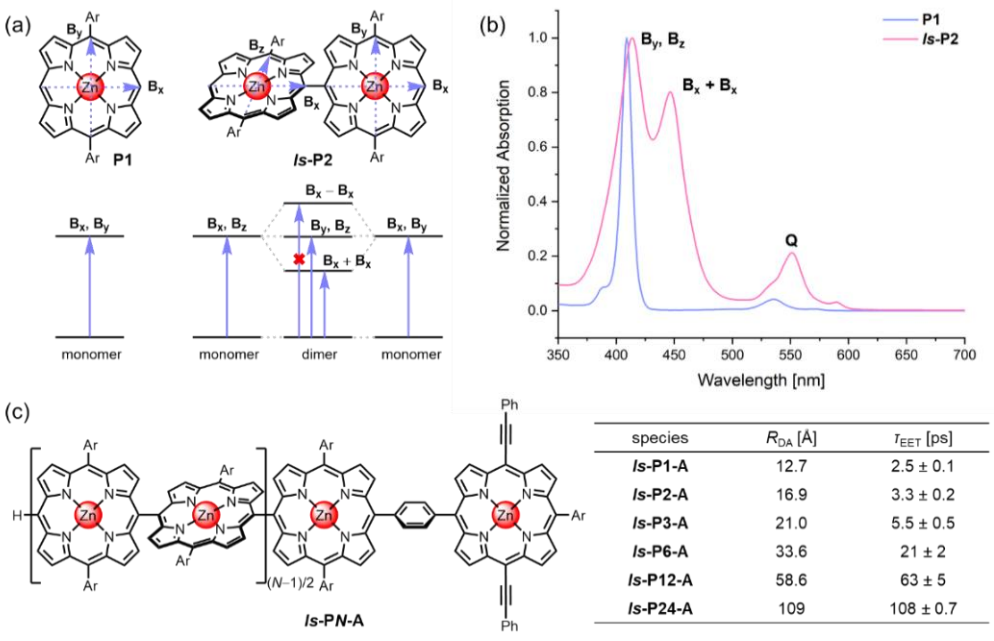

species	R_{DA} [Å]	τ_{EET} [ps]
***ls*-P1-A**	12.7	2.5 ± 0.1
***ls*-P2-A**	16.9	3.3 ± 0.2
***ls*-P3-A**	21.0	5.5 ± 0.5
***ls*-P6-A**	33.6	21 ± 2
***ls*-P12-A**	58.6	63 ± 5
***ls*-P24-A**	109	108 ± 0.7

Figure 2.3: (a) The spectral change (split B bands) of a *meso–meso* singly-linked porphyrin dimer ***ls*-P2** compared to a monomer **P1** as a result from the exciton coupling.[163] (b) Normalized UV–vis absorption spectra of ***ls*-P2** and **P1** measured in $CDCl_3$ at 298 K. (c) Chemical structures of donor–acceptor systems ***ls*-P*N*-A**, their center-to-center distances R_{DA}, and the measured EET time constants t_{EET}.[168,169] Ar is 3,5-bis(octyloxy)phenyl solubilizing group.

2.1.3 Carbon Nanobelts and Fused Porphyrin Nanobelts

Aromatic hydrocarbon nanobelts (carbon nanobelts or CNBs in the following), which are defined as double-stranded and belt-shaped structures comprising of unsaturated and fused benzenoid rings, have fascinated chemists for more than 50 years (Figure 2.3a), since cyclacenes were first proposed for theoretical investigation by Heilbronner in 1954.[170,171] They have attracted more attentions since the discovery of multi-walled carbon nanotubes (MWNTs) in 1991 and single-walled carbon nanotubes (SWNTs) in 1993.[172,173] Carbon nanotubes (CNTs) exhibit remarkable physical and chemical properties (e.g., SWNTs can be either metallic or semiconducting depending on their structures), which make them fascinating materials for diverse applications.[174,175] CNBs can be considered as segments of CNTs (Figure 2.3b). Chemical synthesis of CNBs is envisioned as a bottom-up approach to build up structurally uniform CNTs and to study their single-molecule characteristics.[171,176] Compared to cycloparaphenylenes (CPPs), the single-stranded segments of CNTs which have been readily prepared,[177–179] there have been only a few reports on successful syntheses of CNBs,[180–185] presumably due to their highly strained structures.

In 2017, a breakthrough in successful synthesis of armchair (6,6)CNB was achieved by Itami and co-workers.[180] The synthesis involves two steps: (*i*) a less strained single-stranded macrocycle was first formed by *Z*-selective Wittig reactions; (*ii*) this was followed by intramolecular Yamamoto coupling reactions as a strain-inducing step to construct the CNB. This two-step strategy (i.e., close two strands stepwise) was also employed by Miao and co-workers in construction of armchair (12,12)CNB, zigzag (16,0)CNB and (24,0)CNB.[182,185]

Similar to carbon nanorings (e.g., CPPs) and CNBs, porphyrin nanorings ***cb*-P*N*** and ***ce*-P*N***, and nanobelts ***cf*-P*N*** can also be regarded as segments of porphyrin nanotubes ***tb*-P*N***, ***te*-P*N*** and ***tf*-P*N***, respectively (i.e., here, all the porphyrin nanotubes are formed by stacking of porphyrin nanorings or nanobelts with six porphyrin units, Figure 2.3c). Butadiyne-linked porphyrin nanotubes ***tb*-P12** and ***tb*-P18** have been achieved by template-directed synthesis.[141,186] For infinite porphyrin nanotubes, DFT calculations suggest that ***tb*-P*N*** and ***te*-P*N*** exhibit band gaps of 0.50 and 0.59 eV, respectively, while fused porphyrin nanotubes ***tf*-P*N*** with extremely strong inter-porphyrin electronic coupling are metallic (i.e., they have a zero-gap band structure).[58] To unveil the properties of fused porphyrin nanobelts ***cf*-P*N*** or nanotubes ***tf*-P*N***, the first step is to develop bottom-up approaches to construct these structures. The calculated strain energy (per porphyrin) for ***tf*-P*N*** (56 kJ mol^{-1}) is much higher than the energies for ***tb*-P*N*** (11 kJ mol^{-1}) and ***te*-P*N*** (28 kJ mol^{-1}),[58] which makes the synthesis of fused

porphyrin nanobelts or nanotubes more challenging than that of the analogous nanostructures connected by butadiyne or ethyne links.

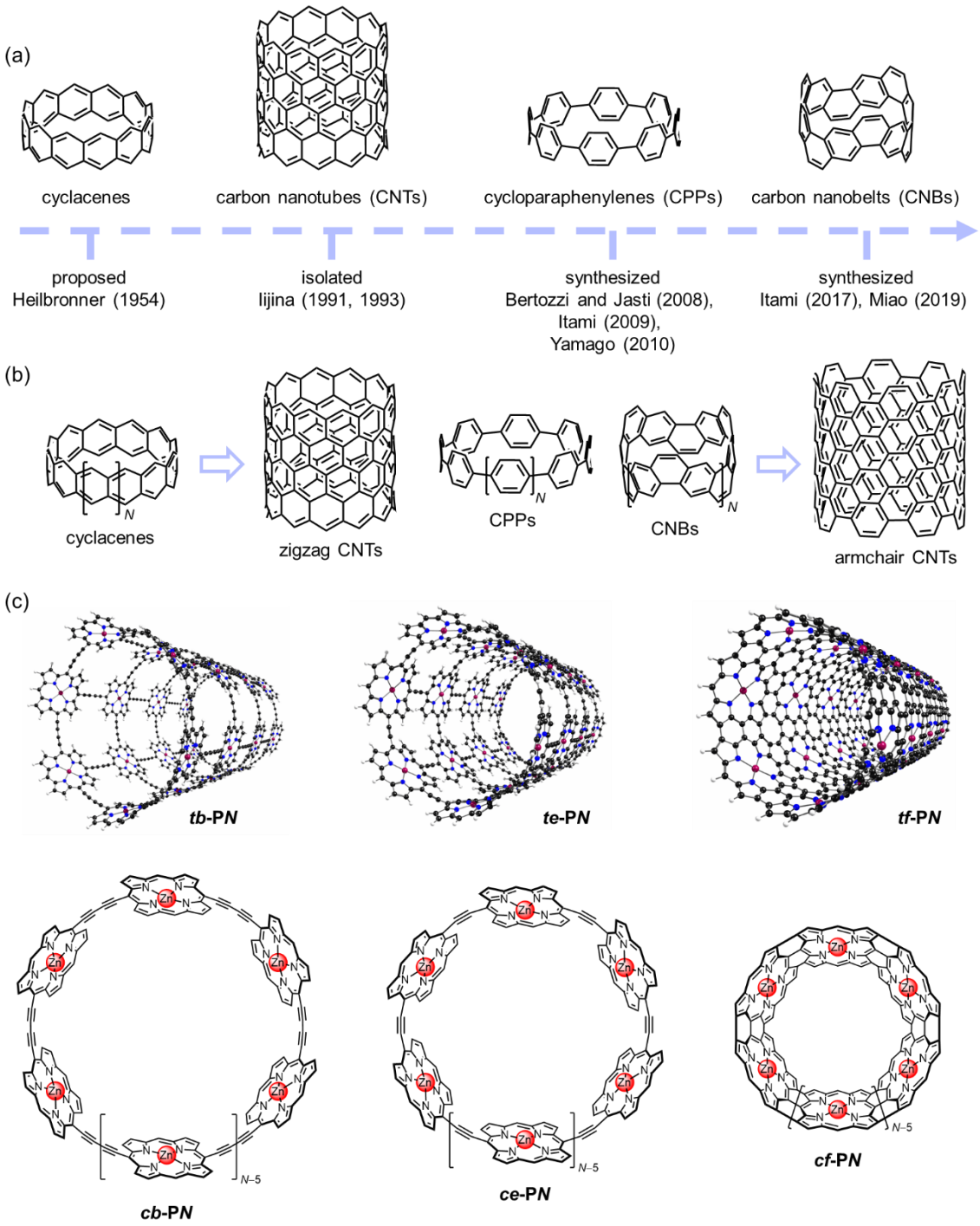

Figure 2.3: (a) Timeline of selected events in the development of carbon nanotubes (CNTs) and nanobelts (CNBs).[171] (b) Schematic diagram illustrating carbon nanorings and nanobelts as fragments of CNTs. (c) Structures of butadiyne-linked, ethyne-linked and fused porphyrin nanorings and nanobelts.

2.1.4 Project Aim

This project aims to develop a bottom-up approach to modular synthesis of *meso–meso* singly-linked porphyrin nanorings ***cs*-P*N*** and fused porphyrin nanobelts ***cf*-P*N*** (see Figure 2.4 for their chemical structures), and to explore the excitation energy transfer (EET) and electron flow (aromaticity) in these unprecedented systems.

The presence of the Zn(II) porphyrin units should make it possible to develop template-directed strategies to prepare these nanostructures. We plan to design and synthesize multidentate oligopyridine templates to bend the linear *meso–meso* singly-linked porphyrin oligomers ***ls*-P*N*** into circular geometries, and then to couple the ends to form porphyrin nanorings ***cs*-P*N***. These synthetic porphyrin nanorings with closely spaced exciton-coupled porphyrin units are envisioned to be photonic wire rings, acting as fascinating models for the B850 ring in natural light-harvesting complexes, to mediate rapid and efficient intra-ring EET.[154]

Removal of the template and connection of the appropriate β positions by oxidative fusion reactions may allow us to convert the singly-linked porphyrin nanorings ***cs*-P*N*** into fused porphyrin nanobelts ***cf*-P*N***. This will be the first example of a highly-strained porphyrin tape belt. It will also be intriguing to investigate whether these strongly π-conjugated systems could exhibit global ring currents in their neutral ground states, which are unprecedented for molecular rings at the nanoscale.[187]

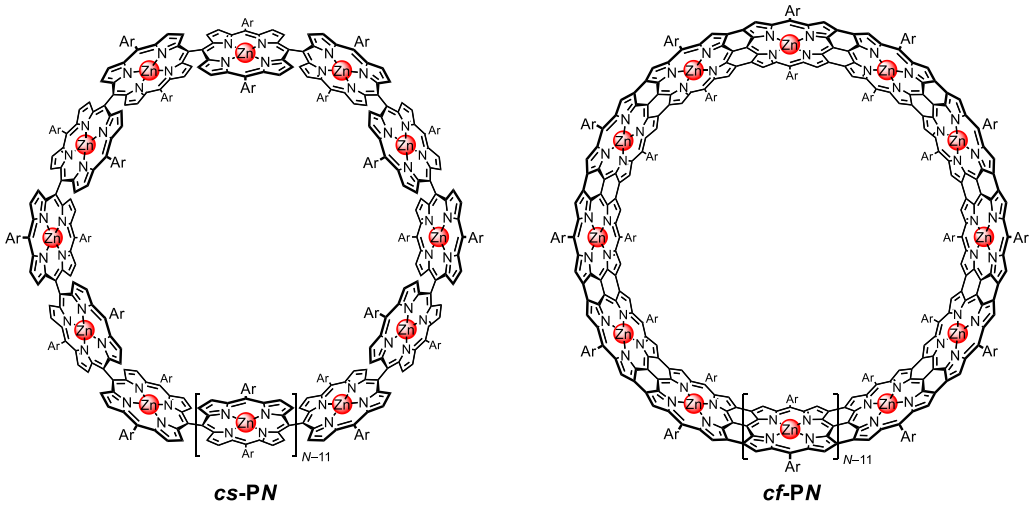

Figure 2.4: Chemical structures of *meso–meso* singly-linked porphyrin nanorings ***cs*-P*N*** (left) and fused porphyrin nanobelts ***cf*-P*N*** (right). Ar is solubilizing aryl group. In the rest of this chapter, all the metalloporphyrins mentioned are Zn(II) porphyrins.

2.2 Molecular Design and Computational Modeling†

2.2.1 Strain Energies of *cs*-P*N*, *cs*[b_1]-P*N* and *cf*-P*N*

The *meso–meso* singly-linked porphyrin nanorings ***cs*-P*N*** and fused porphyrin nanobelts ***cf*-P*N***, in which the porphyrin units are directly connected, are anticipated to be highly strained.[58] We started the project by calculating the ring strain energies of ***cs*-P*N***, ***cf*-P*N***, and ***cs*[b_1]-P*N***, which are *meso–meso* singly-linked porphyrin nanorings with a single butadiyne link. ***cs*[b_1]-P*N*** are designed as prototypes of ***cs*-P*N*** to examine whether the *meso–meso* singly-linked porphyrin oligomers can be bent into rings, because the macrocyclization reaction (i.e., Pd-catalyzed homocoupling of two terminal alkyne units) has been widely explored in template-directed syntheses of butadiyne-linked porphyrin nanorings.[57] It would also be easier to probe the intra-ring EET in ***cs*[b_1]-P*N***, because the excitation would migrate to the site of the π-conjugated butadiyne-linked porphyrin dimer unit, which has a lower S_1 excited state than a *meso–meso* singly-linked porphyrin oligomer.

The strain in these macrocycles was estimated by calculating the free energy change for the gas-phase homodesmotic reactions (eqn. 2.2–2.4).[188]

$$\boldsymbol{cs}\text{-}\mathbf{P}\boldsymbol{N} + N \cdot \boldsymbol{ls}\text{-}\mathbf{P4} \rightarrow N \cdot \boldsymbol{ls}\text{-}\mathbf{P5} \tag{2.2}$$

$$\boldsymbol{cf}\text{-}\mathbf{P}\boldsymbol{N} + N \cdot \boldsymbol{lf}\text{-}\mathbf{P4} \rightarrow N \cdot \boldsymbol{lf}\text{-}\mathbf{P5} \tag{2.3}$$

$$\boldsymbol{cs}[\boldsymbol{b_1}]\text{-}\mathbf{P}\boldsymbol{N} + (N-1) \cdot \boldsymbol{ls}\text{-}\mathbf{P4} + \boldsymbol{ls}\text{-}\mathbf{P4}\text{-}\boldsymbol{e_2} \rightarrow (N-1) \cdot \boldsymbol{ls}\text{-}\mathbf{P5} + \boldsymbol{ls}\text{-}\mathbf{P5}\text{-}\boldsymbol{e_2} \tag{2.4}$$

Here, ***ls*-P*N***, ***lf*-P*N*** and ***lb*-P*N*-e_2** are linear *meso–meso* singly-linked, fused and butadiyne-linked porphyrin oligomers, respectively. We began our studies with structures comprising of 12 porphyrin units, because the largest porphyrin nanoring yet to be held in an open circular shape by a single or two stacked oligopyridine templates, was butadiyne-linked porphyrin nanoring ***cb*-P12**. The strain energies of porphyrin nanorings ***cs*-P12** (156.4 kJ mol^{-1}), ***cs*[b_1]-P12** (139.8 kJ mol^{-1}) and nanobelt ***cf*-P12** (180.2 kJ mol^{-1}) were calculated using DFT (PBE0+GD3BJ/Def2SVP). The strain in these rings are larger than in the alkyne-linked porphyrin nanorings (100–130 kJ mol^{-1}) that Anderson and coworkers have reported previously,[189] implying that it is challenging to bend these "rod-like" structures, especially the fused porphyrin dodecamer, into rings. We next calculated the strain in porphyrin

† All molecular mechanics (MM) and molecular dynamics (MD) calculations were performed by Janko Hergenhahn, under the supervision of Prof. Fernanda Duarte (Department of Chemistry, University of Oxford, UK).

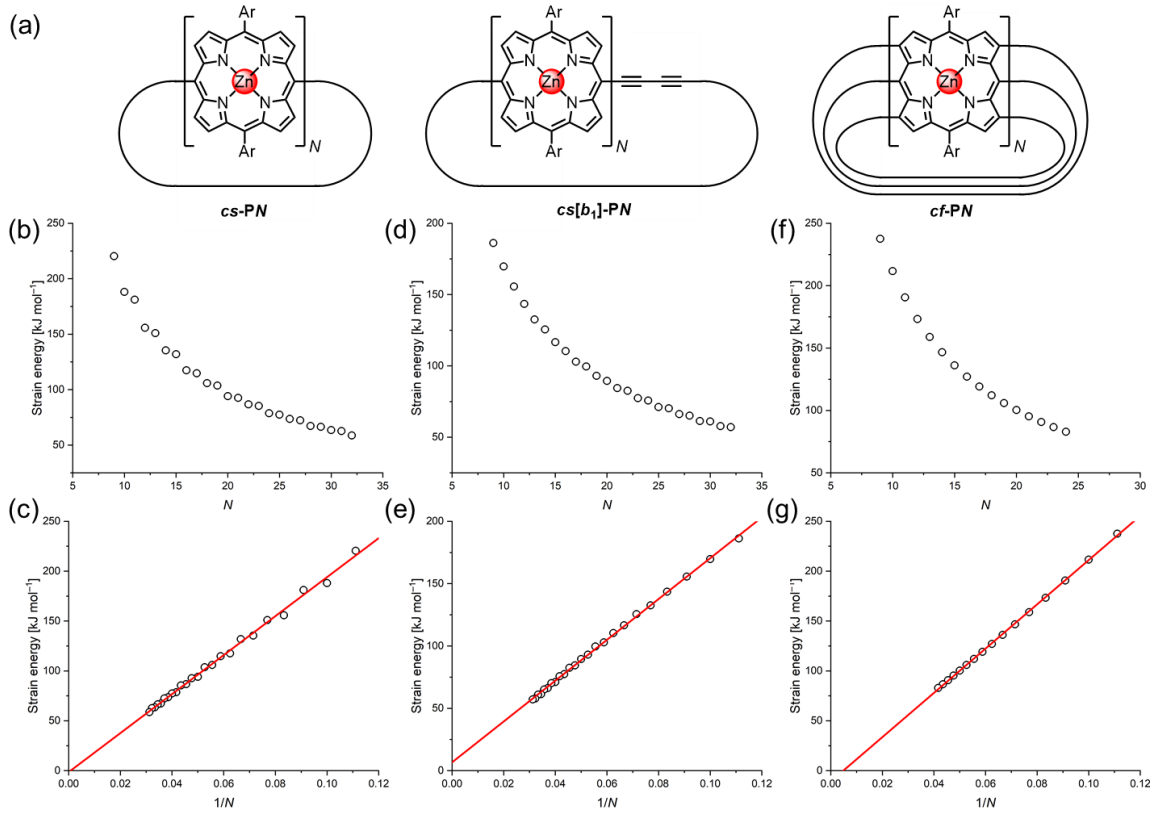

Figure 2.5: (a) Structures of porphyrin nanorings ***cs*-P*N***, ***cs*[b_1]-P*N*** and nanobelts ***cf*-P*N***. Plots of the strain in ***cs*-P*N*** as a function of *N* (b), and 1/*N* (c). Plots of the strain in ***cs*[b_1]-P*N*** as a function of *N* (d), and 1/*N* (e). Plots of the strain in ***cf*-P*N*** as a function of *N* (f), and 1/*N* (g). The energies for strain calculations were obtained from MM calculations (AMBER force field) by considering the gas-phase homodesmotic reactions (eqn. 2.2–2.4). The Ar solubilizing groups were replaced with H to accelerate the calculations. Data were collected and analyzed by Janko Hergenhahn.

nanorings and nanobelt with 24 porphyrin units. These larger rings have almost half the strain energies of the smaller rings (80.5 kJ mol^{-1} for ***cs*-P24**, 75.8 kJ mol^{-1} for ***cs*[b_1]-P24**, 78.4 kJ mol^{-1} for ***cf*-P24**), less than in the alkyne-linked porphyrin nanorings.

To explore the strain in the whole family of these structures, we employed molecular mechanics (MM) calculations using modified AMBER force field parameters (see Section 2.10.12 for more details). The estimated strain energies of the smaller rings ***cs*-P12** (155.8 kJ mol^{-1}), ***cs*[b_1]-P12** (143.5 kJ mol^{-1}) and ***cf*-P12** (173.3 kJ mol^{-1}), and larger rings ***cs*-P24** (78.7 kJ mol^{-1}), ***cs*[b_1]-P24** (75.7 kJ mol^{-1}) and ***cf*-P24** (82.9 kJ mol^{-1}) are similar to the DFT calculated energies. The strain energies of these families of structures are plotted as a function of *N* (Figure 2.5b, d and f) or 1/*N* (Figure 2.5c, e and g), showing a decrease of the strain energy by increasing the number of the porphyrin units (*N*, or the radius of the rings). A

steeper decrease is found for the triple-stranded ***cf*-P*N***, in comparison to the single-stranded ***cs*-P*N***. For small rings ($N \leq 12$), the strain in ***cf*-P*N*** are much larger than in ***cs*-P*N***. The difference becomes subtle (< 5 kJ mol^{-1}) in large rings ($N \geq 17$). ***cs*[*b*$_1$]-P*N*** with a butadiyne link exhibit smaller strain, implying they might be slightly easier to make by template-directed synthesis.

2.2.2 Aromaticity and Antiaromaticity in *cf*-P*N*

We carried out Nucleus Independent Chemical Shift (NICS) calculations to investigate whether the fused porphyrin nanobelts ***cf*-P*N*** with strong electronic coupling between the neighboring porphyrin units might exhibit global (anti)aromaticity in the neutral ground state.[190] In a typical NICS plot, a grid of Banquo (Bq) atoms with 1 Å resolution is placed across the plane of zinc centers of the porphyrin units. The chemical shifts of these Bq atoms were estimated by DFT calculations using the GIAO method with the BLYP35/6-31G* functional/basis set. The BLYP35 functional was chosen because as discussed in Chapter 1, it reproduced the experimental NMR chemical shift changes in the butadiyne-linked porphyrin nanorings.[143] The positive NICS values (red color) indicate a deshielding effect and the negative NICS values (blue color) suggest a shielding effect.

For porphyrin nanobelt ***cf*-P12** in its neutral ground state, the NICS(0)$_{ZZ}$ plot, as shown in Figure 2.6a, shows a positive NICS value inside the ring and a negative NICS value outside the ring, suggesting ***cf*-P12** has a global paratropic ring current (i.e., it is globally antiaromatic). Similar to the butadiyne-linked porphyrin nanorings, if we assume each porphyrin contributes ten electrons to the Hückel π electron count N_e of the porphyrin nanobelts, ***cf*-P12** (N_e = 120) is predicted to be antiaromatic according to the Hückel's [4n + 2] rule. Addition of one more porphyrin unit is expected to add ten π electrons in the Hückel electron count (ΔN_e = 10), leading to a reverse of the global ring current direction (diatropic vs. paratropic). In agreement with the estimation by Hückel's rule (i.e., ***cf*-P13** with N_e = 130 is aromatic), the NICS(0)$_{ZZ}$ plot, which exhibits a negative NICS value inside the ring and a positive NICS value in the outside, also predicts ***cf*-P13** to be globally aromatic (Figure 2.6b). Since ***cf*-P12** and ***cf*-P13** are expected to be highly strained, we also carried out NICS calculations on the larger structures, ***cf*-P24** and ***cf*-P25** (Figure 2.6c and d). However, the NICS grids indicate that these structures only display local porphyrin aromaticity, implying the global (anti)aromatic behaviors of fused porphyrin nanobelts in the neutral ground state may vanish in large rings.

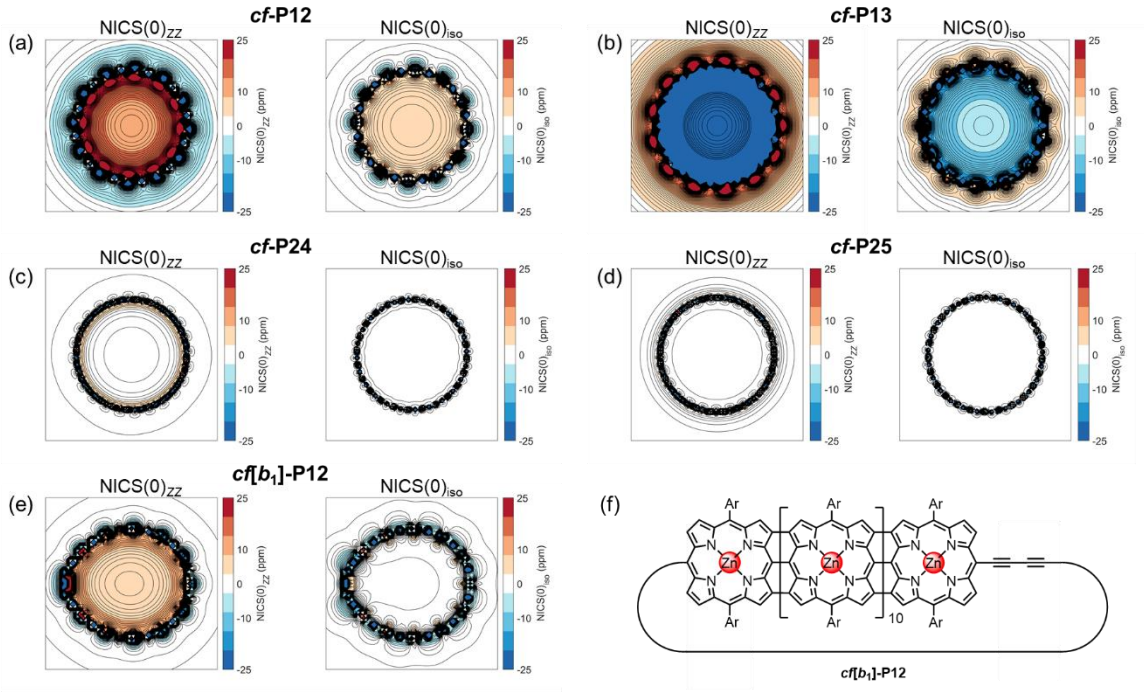

Figure 2.6: (a) Plots of NICS(0)$_{ZZ}$ and NICS(0)$_{iso}$ for ***cf*-P12**. (b) Plots of NICS(0)$_{ZZ}$ and NICS(0)$_{iso}$ for ***cf*-P13**. (c) Plots of NICS(0)$_{ZZ}$ and NICS(0)$_{iso}$ for ***cf*-P24**. (d) Plots of NICS(0)$_{ZZ}$ and NICS(0)$_{iso}$ for ***cf*-P25**. (e) Plots of NICS(0)$_{ZZ}$ and NICS(0)$_{iso}$ for ***cf*[*b*$_1$]-P12**. (f) chemical structure of ***cf*[*b*$_1$]-P12**. All the NICS calculations were carried out by DFT calculations using the BLYP35/6-31G* functional/basis set. The Ar solubilizing groups were omitted to accelerate the calculations.

Introduction of a butadiyne link into the fused porphyrin nanobelt ***cf*-P12** gives a nanobelt ***cf*[*b*$_1$]-P12** with four more π electrons in the Hückel electron count (ΔN_e = 4) and a weaker inter-porphyrin electronic coupling due to the presence of a butadiyne link (see Figure 2.6f for its chemical structure). Hückel's rule predicts ***cf*[*b*$_1$]-P12** (N_e = 124) to be antiaromatic. The NICS(0)$_{ZZ}$ grid shows a global paratropic ring current in ***cf*[*b*$_1$]-P12** (Figure 2.6e), but it is much weaker than in ***cf*-P12**. The global antiaromatic behavior is unclear from the NICS(0)$_{iso}$ plot, and the presence of the local aromatic ring currents in the porphyrin units may affect the observation of the global ring current.

To summarize, the predicted global (anti)aromatic behaviors of ***cf*-P12** and ***cf*-P13** in the neutral ground state are unprecedented, and behavior of this type has not yet been observed in other conjugated porphyrin nanorings, such as the butadiyne-linked porphyrin nanorings, which exhibit local aromatic ring currents in the neutral ground state.[114] The predicted global (anti)aromaticity may arise from the extremely strong electronic coupling between the neighboring porphyrin rings in the fused porphyrin nanobelts, and thus the π electrons can

delocalize around the circumference in the presence of an external magnetic field. However, this effect is estimated to be weaker in large rings (e.g., ***cf*-P24** and ***cf*-P25**) and rings incorporated with a butadiyne link (e.g., ***cf*[*b*$_1$]-P12**). These theoretical calculations imply that it will be interesting to synthesize the fused porphyrin nanobelts in different sizes, and to experimentally probe the global (anti)aromaticity in these fascinating structures.

2.2.3 Molecular Design and Synthetic Plan

Given the prospective global antiaromatic behavior of the fused porphyrin nanobelt ***cf*-P12**, and a smaller strain in the *meso–meso* singly-linked porphyrin nanoring ***cs*-P12** compared with ***cf*-P12**, we planned to employ a "ring-to-belt" strategy to build up ***cf*-P12** as the first target of this project (see Figure 2.7 for the proposed synthetic scheme for ***cs*-P12** and ***cf*-P12**).

The proposed synthetic route includes four main steps: (*i*) synthesis of a linear *meso–meso* singly-linked porphyrin dodecamer ***ls*-P12** with appropriate solubilizing groups; (*ii*) design and synthesis of a 12-leg template to bend the ***ls*-P12** into a circular geometry; (*iii*) coupling the ends of the bent dodecamer to form nanoring ***cs*-P12**; (*iv*) removal of the template and fusion of all the porphyrin units to afford nanobelt ***cf*-P12**.

The difficulty in preparing the linear *meso–meso* singly-linked porphyrin oligomers depends on the size of the solubilizing side chains on the porphyrin units. Oligomers with 3,5-bis(octyloxy)phenyl solubilizing groups can be readily made by Ag(I) or PIFA-mediated oxidative coupling reaction.[79,191] Introduction of bulky side chains (e.g., 3,5-bis(trihexylsilyl)-phenyl solubilizing group), which in principle make the oligomers more soluble, hampers the efficiency of the previously developed oxidative coupling reactions,[192] and thus it requires a new method to prepare these oligomers.

The bending of porphyrin dodecamer was expected to be challenging because the *meso–meso* singly-linked porphyrin oligomers have twisted conformations, with a dihedral angle about 70–90° between two neighboring porphyrin units. The twisted conformations make the axial vectors of the porphyrin units unable to point toward the center of the nanoring all at the same time, and thereby it is difficult to use a template, in which the legs are connected to the central core by rigid links, to bind strongly to the oligomers. Inspired by the work of Osuka and coworkers on the binding of α,ω-diaminoalkanes to dimers ***ls*-P2**,[193] we designed a binding unit **T2**, which has two 4-pyridyl binding sites connected to a benzene core via flexible *meta*-linked -O(CH_2)$_3$- chains, and planned to connect six **T2** units to a benzene core to build up a

template **T12a**. **T12a** with flexible links that was expected to bind strongly to ***ls*-P12** to enforce a circular geometry.

After the bending, we planned to use Ag(I) or PIFA-mediated oxidative coupling reaction to couple the ends of the oligomer to form ***cs*-P12**. The oligomer-template complex ***ls*-P12·T12** was envisioned to be stable under these conditions, because the $CHCl_3$ used as the solvent for these reactions would not weaken the binding of the pyridine to the Zn(II) porphyrin. Ni-mediated Yamamoto coupling reaction (i.e., homocoupling of two bromine-terminated porphyrins) was also considered as a promising approach for the macrocyclization. However, the Yamamoto coupling reaction is mostly carried out in polar solvents like *N*,*N*-dimethylformamide (DMF) and tetrahydrofuran (THF), which might displace the **T12** from the complex ***ls*-P12·T12** in the reaction,[194] and thus optimization of the reaction conditions would be needed.

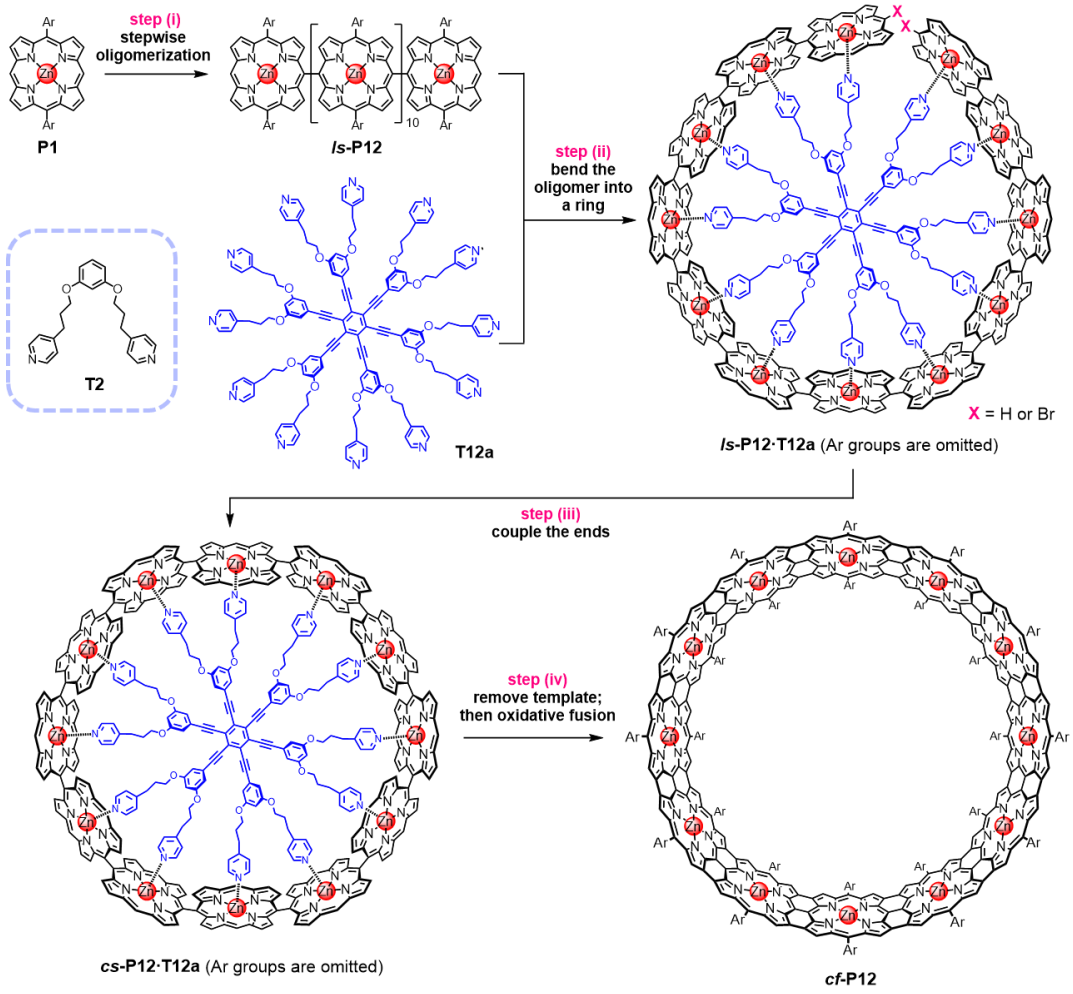

Figure 2.7: Proposed strategy for syntheses of *meso–meso* singly-linked porphyrin nanoring ***cs*-P12** and fused porphyrin nanobelt ***cf*-P12**. Ar is solubilizing aryl group.

In the final step, it would be necessary to remove the template before the fusion reaction, because the pyridine units might react with the oxidized porphyrins in the reaction, giving undesired side products. The template can be displaced by treatment of the nanoring-template complex ***cs*-P12·T12** with trifluoacetic acid (TFA) or competing ligands (e.g., quinuclidine). The DDQ/$Sc(OTf)_3$ or PIFA oxidative fusion reaction, which has been used to construct the linear fused porphyrin tapes,[71,73] would be employed to construct the nanobelt ***cf*-P12** from nanoring ***cs*-P12**.

2.3 Synthesis of *ls*-P*N*[†]

We began the synthesis by stepwise oligomerization of porphyrin monomer to build up linear *meso–meso* singly-linked porphyrin oligomers ***ls*-P*N*** with appropriate solubilizing groups. ***ls*-P$N_{t\text{-Bu}}$** ($N \geq 8$) equipped with 3,5-bis(*tert*-butyl)phenyl solubilizing groups were found to be less soluble in $CHCl_3$ in previous work.[78] The binding of a dimer ***ls*-P2$_{THS}$** with 3,5-bis(trihexylsilyl)phenyl solubilizing groups to **T2**, which will be discussed later in this chapter, was found to be weak. Therefore, in this project, we chose 3,5-bis(octyloxy)phenyl solubilizing group for the porphyrin units because it provides a balance between the solubility and the steric bulkiness. In the rest of this chapter, unless specified, ***ls*-P*N*** indicates Zn(II) porphyrin oligomers bearing 3,5-bis(octyloxy)phenyl solubilizing groups.

We used PIFA-mediated oxidative coupling for the oligomerization instead of the Ag(I)-mediated coupling. This is because the former reaction can be conducted under ambient condition (i.e., in air, at 25 °C) and harsher reaction conditions are needed for the latter reaction (i.e., it must be conducted in dry solvents, under inert atmosphere, at 50 °C).[79,191] The PIFA-mediated coupling completes within a few hours, which is more efficient than the Ag(I)-mediated coupling that needs a day to give satisfactory yields. For multistep oligomerizations, the comparatively short reaction time for the PIFA-mediated reaction strongly accelerates the synthesis.

We started the oligomerizations by treatment of porphyrin monomer **P1** (2.0 g, 1.8 mmol, 1.0 equiv.) with PIFA (0.39 g, 0.91 mmol, 0.5 equiv.) in dry CH_2Cl_2 (250 mL) at 25 °C for 2 h, followed by addition of a suspension of $NaBH_4$ (0.69 g, 18 mmol, 10 equiv.) in CH_3OH (50

[†] The synthesis and characterization of all the porphyrin oligomers as well as the oligopyridine templates in this chapter were carried out by the author in close collaboration with Dr. Henrik Gotfredsen and Dr. Jeff M. Van Raden (Department of Chemistry, University of Oxford, UK).

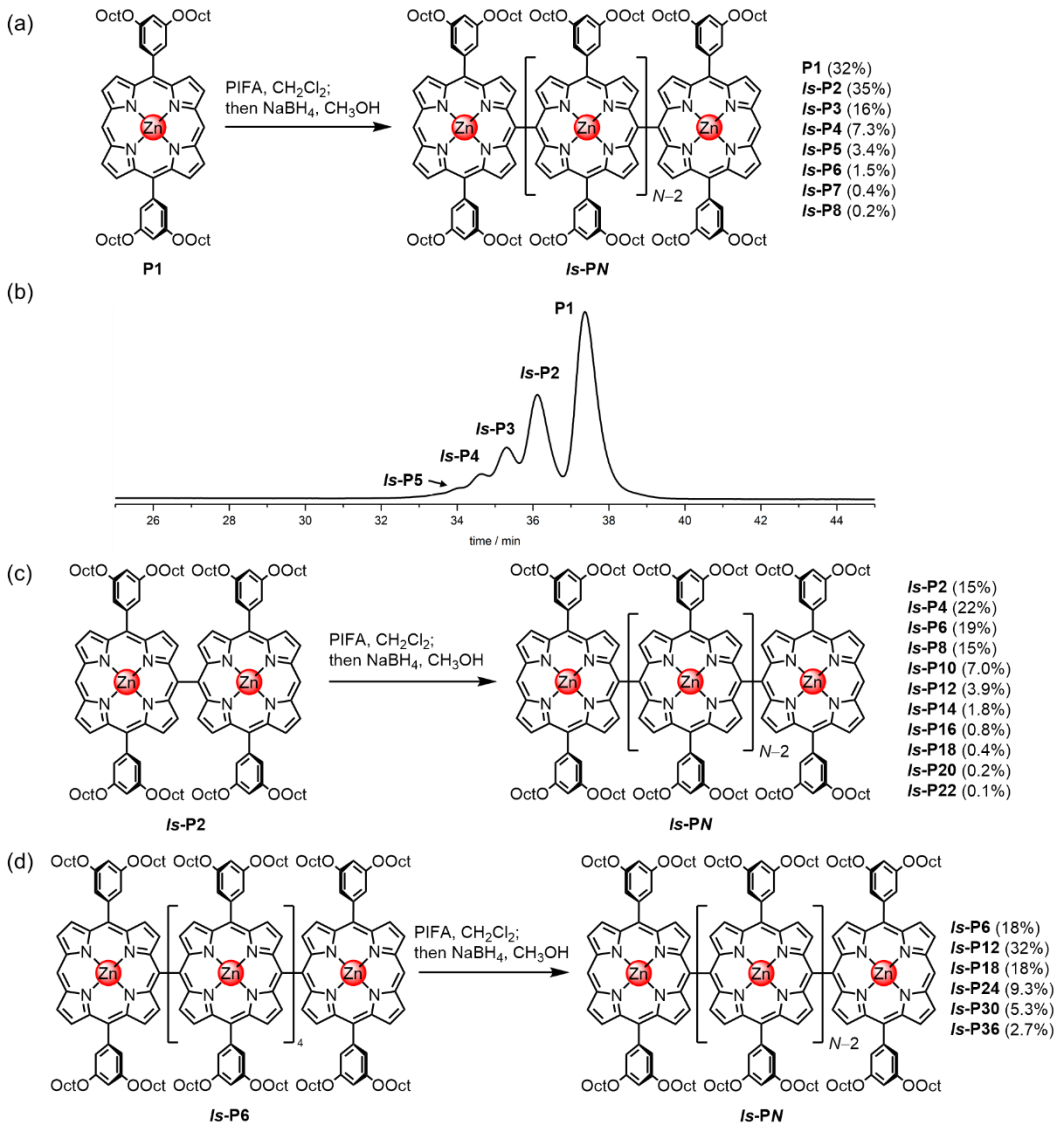

Figure 2.8 (a) Oligomerization of porphyrin monomer **P1**. (b) Analytical GPC trace of the crude reaction from PIFA-mediated oligomerization of **P1** (THF + 1% pyridine, λ = 420 nm). (c) Oligomerization of *meso–meso* singly-linked porphyrin dimer ***ls*-P2**. (d) Oligomerization of *meso–meso* singly-linked porphyrin hexamer ***ls*-P6**. PIFA is (bis(trifluoroacetoxy)iodo)-benzene. Characterization data of these oligomers, including the ^{1}H NMR spectra, mass spectra and optical absorption bands are summarized in Appendix B.3.

mL) (Figure 2.8a). After reaction, the oligomers as a crude mixture were separated by recycling gel permeation chromatography (GPC) to give the monodisperse oligomers ***ls*-P2** (696 mg, 35%), ***ls*-P3** (321 mg, 16%), ***ls*-P4** (145 mg, 7.3%), ***ls*-P5** (67 mg, 3.4%), ***ls*-P6** (29 mg, 1.5%) and the recovered **P1** (630 mg, 32%). During the reaction, the progress of the oligomerization was monitored by analytical GPC and an example of the GPC trace for the crude mixture before the separation was shown in Figure 2.8b. It is important to control the amount of the PIFA

added (≤ 0.5 equiv.), because the excess oxidant may cause oxidative fusion of the oligomers, forming undesired side products. Since pyridine would react with oxidized porphyrin on its free *meso* position to form undesired adduct, removal of the pyridine that is introduced to improve the solubility during the separation is necessary before carrying out the oxidation step.

The dimer ***ls*-P2** was oligomerized using the similar reaction conditions, resulting in ***ls*-P2** (242 mg, 15%), ***ls*-P4** (356 mg, 22%), ***ls*-P6** (311 mg, 19%), ***ls*-P8** (246 mg, 15%), ***ls*-P10** (115 mg, 7.0%), ***ls*-P12** (64 mg, 3.9%), ***ls*-P14** (30 mg, 1.8%), ***ls*-P16** (14 mg, 0.8%), ***ls*-P18** (6.8 mg, 0.4%), ***ls*-P20** (3.9 mg, 0.2%) and ***ls*-P22** (1.6 mg, 0.1%). Then, ***ls*-P6** was employed to build up longer oligomers ***ls*-P12** (95 mg, 32%), ***ls*-P18** (53 mg, 18%), ***ls*-P24** (28 mg, 9.3%), ***ls*-P30** (16 mg, 5.3%) and ***ls*-P36** (7.7 mg, 2.7%), with ***ls*-P6** (54 mg, 18%) recovered.

2.4 Binding of T2 to *ls*-P2

With the oligomers ***ls*-P*N*** in hand, we next moved to study the binding of the porphyrin dimer ***ls*-P2** to the designed binding unit **T2**, which would provide insight into the possible application of **T2** as legs to build up templates for syntheses of nanorings ***cs*-P*N***. Template (or ligand) **T2** was synthesized by a nucleophilic substitution reaction of resorcinol and 4-(3-bromopropyl)-pyridine in 51% yield (see Appendix B.4 for the details).

The binding was studied by UV–vis absorption titrations. In a typical titration experiment, a solution of ligand **T2** (guest) was added to a ***ls*-P2** (host) solution. The porphyrin concentration was kept constant by adding ***ls*-P2** to the **T2** solution before the start of the titration. The formation (association) constant (K_f) was determined by fitting the binding curve to the 1:1 binding isotherm using the following equation:[195]

$$\frac{A-A_0}{A_f-A_0} = \frac{(K_f([P]_0+[L])+1)-\sqrt{(K_f([P]_0+[L])+1)^2-4K_f{}^2[P]_0[L]}}{2K_f[P]_0} \tag{2.5}$$

where A is the difference of absorbance between two wavelengths; A_0 is the starting absorption difference; A_f is the final absorption difference; $[L]$ is the concentration of ligand (or template); $[P]_0$ is the concentration of porphyrin host.

UV–vis titrations indicate ***ls*-P2** binds to ligand **T2** to form complex ***ls*-P2·T2** with K_f = (7.81 ± 0.21) × 10^5 M^{-1} (Figure 2.10a), which was compared to the binding of a monomer **P1** to 4-ethylpyidine (K_f = (1.19 ± 0.09) × 10^4 M^{-1}), to give the effective molarity of this system to be *EM* = 2.7 mM (see Figure 2.9 for a schematic illustration of the bindings of the system). The effective molarity *EM* in this system is defined by eqn. 2.6,

$$\frac{1}{2}K_{\text{chem}}\,EM = \frac{[\textit{c}\text{-}\textit{ls}\text{-}\mathbf{P2}\cdot\mathbf{T2}]}{[\textit{o}\text{-}\textit{ls}\text{-}\mathbf{P2}\cdot\mathbf{T2}]} \tag{2.6}$$

where *c* (or *o*) indicates the ***ls*-P2·T2** complex is closed (or opened). K_{chem}, the microscopic formation constant that is approximated to K_{f}(**P1·EtPy**), the association constant of the binding of **P1** to 4-ethylpyridine.[196] It is difficult to directly measure the concentrations of closed and opened ***ls*-P2·T2** complexes from experiments. Therefore, in practice, the value of *EM* is calculated using the following relationship:

$$EM = \frac{K_{\text{f}}(\textit{ls}\text{-}\mathbf{P2}\cdot\mathbf{T2})}{2K_{\text{f}}(\mathbf{P1}\cdot\mathbf{EtPy})^2} \tag{2.7}$$

in which K_{f}(***ls*-P2·T2**) is the association constant of the binding of ***ls*-P2** to **T2**.

Although the effective molarity of this system is quite low (*EM* = 2.7 mM), it is sufficiently high enough for the ***ls*-P2·T2** complex to be 94% closed (i.e., coordinated at both sites).

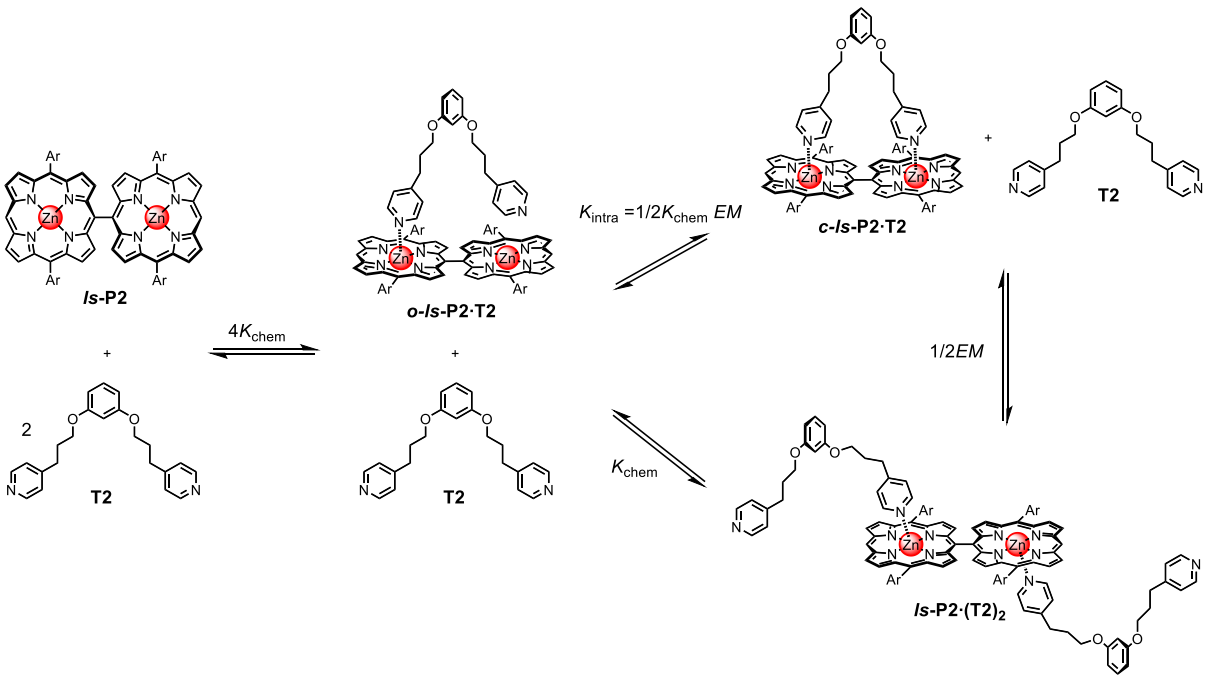

Figure 2.9: Binding of ***ls*-P2** (host) to **T2** (guest), where [***ls*-P2**] is assumed to be much smaller than [**T2**]. K_{chem} is the microscopic formation constant of binding a single porphyrin unit to a pyridine leg, which was approximated to the binding of **P1** to 4-ethylpyridine in this study. *EM*, *o* and *c* indicate effective molarity, opened and closed species, respectively.[196] Ar = 3,5-bis(octyloxy)phenyl solubilizing group.

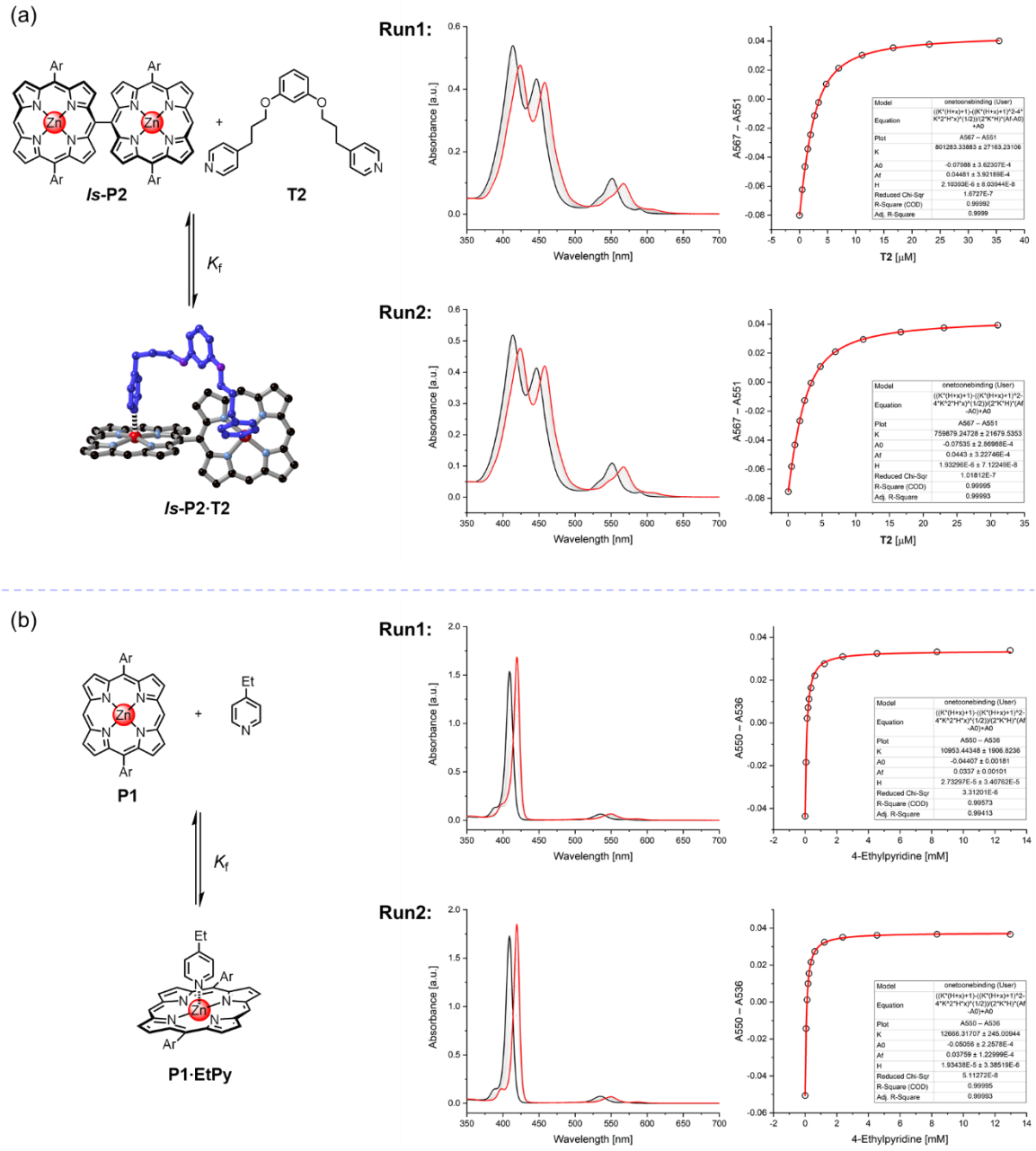

Figure 2.10: (a) UV–vis titration of ***ls*-P2** and **T2**. The binding curves were fitted to eqn. 2.5 to give K_f = (7.81 ± 0.21) × 10^5 M^{-1}. Run 1: R^2 = 0.99990 ($CDCl_3$, 298 K, [***ls*-P2**] = 2.00 × 10^{-6} M, K_f = 8.01 × 10^5 M^{-1}). Run 2: R^2 = 0.99993 ($CDCl_3$, 298 K, [***ls*-P2**] = 2.00 × 10^{-6} M, K_f = 7.60 × 10^5 M^{-1}). ***ls*-P2·T2** was optimized by DFT calculation at PBE0+GD3BJ/ Def2SVP level of theory. (b) UV–vis titration of **P1** and **EtPy** (4-ethylpyridine). The binding curves were fitted to eqn. 2.5 to give K_f = (1.19 ± 0.09) × 10^4 M^{-1}. Run 1: R^2 = 0.99413 ($CDCl_3$, 298 K, [***ls*-P2**] = 3.00 × 10^{-6} M, K_f = 1.10 × 10^4 M^{-1}). Run 2: R^2 = 0.99993 ($CDCl_3$, 298 K, [***ls*-P2**] = 3.00 × 10^{-6} M, K_f = 1.27 × 10^4 M^{-1}). Ar = 3,5-bis(octyloxy)phenyl solubilizing group.

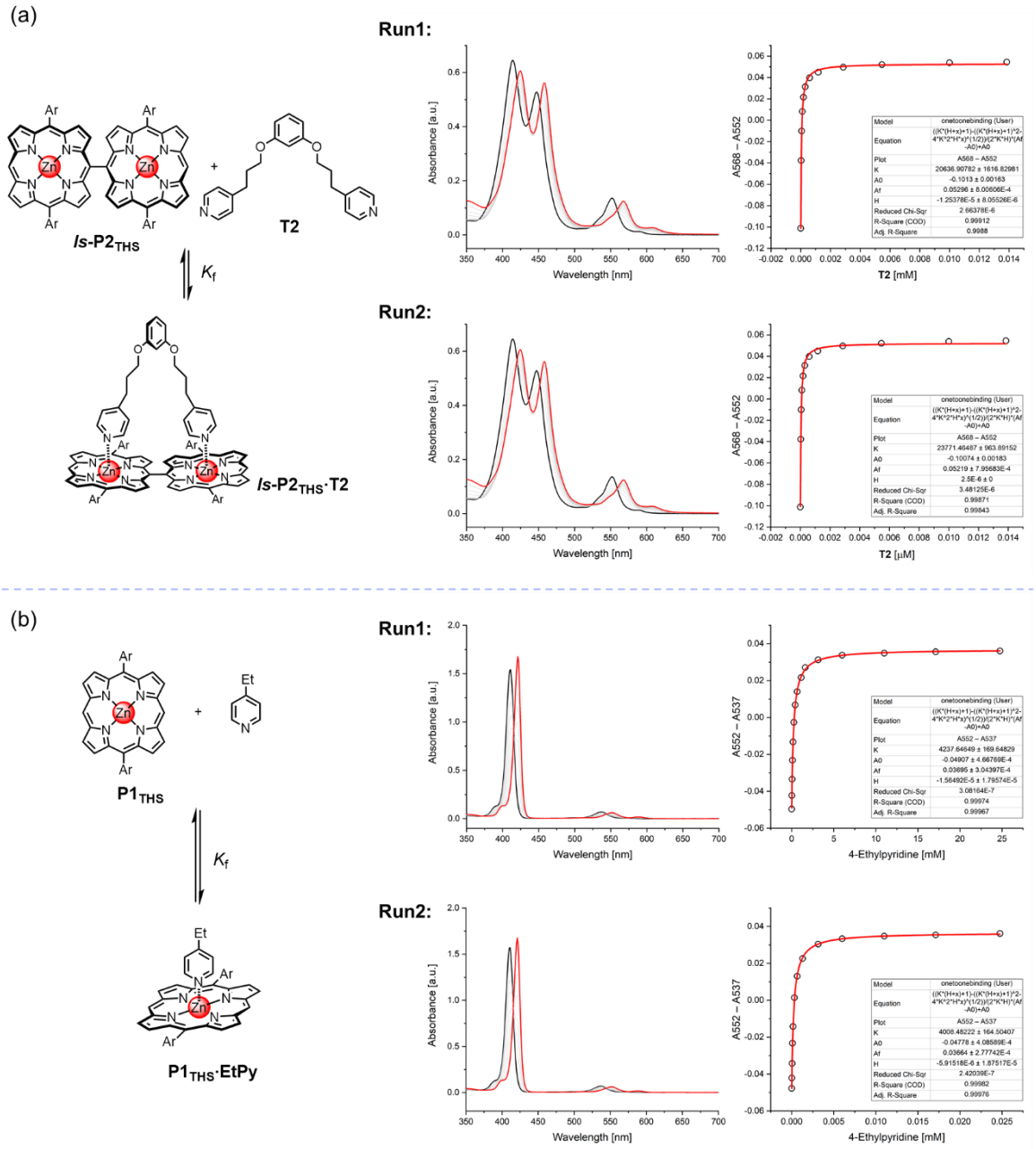

Figure 2.11: (a) UV–vis titration of ***ls*-P2$_{THS}$** and **T2**. The binding curves were fitted to eqn. 2.5 to give $K_f = (2.23 \pm 0.16) \times 10^4$ M^{-1}. Run 1: $R^2 = 0.99880$ ($CDCl_3$, 298 K, [***ls*-P2$_{THS}$**] = 2.50×10^{-6} M, $K_f = 2.07 \times 10^4$ M^{-1}). Run 2: $R^2 = 0.99843$ ($CDCl_3$, 298 K, [***ls*-P2$_{THS}$**] = 2.50×10^{-6} M, $K_f = 2.38 \times 10^4$ M^{-1}). (b) UV–vis titration of **P1$_{THS}$** and **EtPy** (4-ethylpyridine). The binding curves were fitted to eqn. 2.5 to give $K_f = (4.13 \pm 0.12) \times 10^3$ M^{-1}. Run 1: $R^2 = 0.99967$ ($CDCl_3$, 298 K, [**P1$_{THS}$**] = 3.00×10^{-6} M, $K_f = 4.01 \times 10^3$ M^{-1}). Run 2: $R^2 = 0.99976$ ($CDCl_3$, 298 K, [**P1$_{THS}$**] = 3.00×10^{-6} M, $K_f = 4.24 \times 10^3$ M^{-1}). Ar = 3,5-bis(trihexylsilyl)phenyl solubilizing group.

We next compared the association constant to that of the binding of a porphyrin dimer ***ls*-P2$_{THS}$** to **T2**, because the bis(trihexylsilyl)phenyl solubilizing groups would strongly improve the solubility of the porphyrin oligomers. ***ls*-P2$_{THS}$** was synthesized by Ag(I)-mediated oxidative coupling reaction using the $AgPF_6$ salt in 19% yield, or the $Ag[Al(pftb)_4]$ (pftb = perfluoro-*tert*-butoxy) salt in 82% yield (the experimental procedures, characterization data and the reasons for using the $Ag[Al(pftb)_4]$ salt are discussed in Chapter 3).

The association constant of complex ***ls*-P2$_{THS}$·T2** formation was estimated to be K_f = (2.23 ± 0.16) × 10^4 M^{-1} by fitting the binding curve to eqn. 2.5, and a value of K_f = (4.13 ± 0.12) × 10^3 M^{-1} was determined for the coordination of 4-ethylpyridine to **P1$_{THS}$** monomer (Figure 2.11). The effective molarity of this system is calculated to be 0.65 mM, an order of magnitude smaller than that of the ***ls*-P2·T2** (*EM* = 2.7 mM). This value of *EM* also implies that the complex ***ls*-P2$_{THS}$·T2** is only about 58% closed, and the 2:1 complex ***ls*-P2$_{THS}$·(T2)$_2$** is about 42%. This estimation might be inaccurate because eqn. 2.5 assumes the system follows a "all-or-nothing" model with no significant population of intermediate ***o*-*ls*-P2·T2** or 2:1 complex ***ls*-P2$_{THS}$·(T2)$_2$**. Besides, we could not differentiate the absorption spectrum of ***o*-*ls*-P2$_{THS}$·T2** or ***ls*-P2$_{THS}$·(T2)$_2$** from that of ***c*-*ls*-P2$_{THS}$·T2** in the titrations, and we are not able to accurately calculate the formation constants for all the equilibriums in this system.

Despite that, the UV–vis titrations show that the binding of ***ls*-P2$_{THS}$** to **T2** is much weaker than of ***ls*-P2** to **T2**. We attribute this to the size difference between octyloxy and trihexylsilyl side chains, and the steric bulkiness of trihexylsilyl group in ***ls*-P2$_{THS}$** which has a twisted conformation hinders the coordination of the second leg of **T2** to the porphyrin. Therefore, we used porphyrins with 3,5-bis(octyloxy)phenyl solubilizing groups in this project.

2.5 Attempted Syntheses of *cs*-P12 and *cs*[b_1]-P12

2.5.1 Syntheses of T12a and T12b

We planned to connect six binding units **T2** to a core to give template **T12a** to direct the synthesis of porphyrin nanoring ***cs*-P12**. A key step in synthesis of template **T12a** was to conduct a six-fold Sonogashira reaction to couple six **T2$_I$** units to a hexaethynylbenzene core using $Pd(PPh_3)_4$ and CuI as catalysts, which gave **T12a** in 48% yield (details are given in Figure 2.12 and Appendix B, Section B.4). The synthesis of iodinated **T2** (**T2$_I$**) was similar to that of **T2**. The hexaethynylbenzene core was afforded by deprotection of hexakis[(trimethylsilyl)ethynyl]benzene, which was prepared by another six-fold Sonogashira coupling reaction of trimethylsilylacetylene and hexabromobenzene.[197]

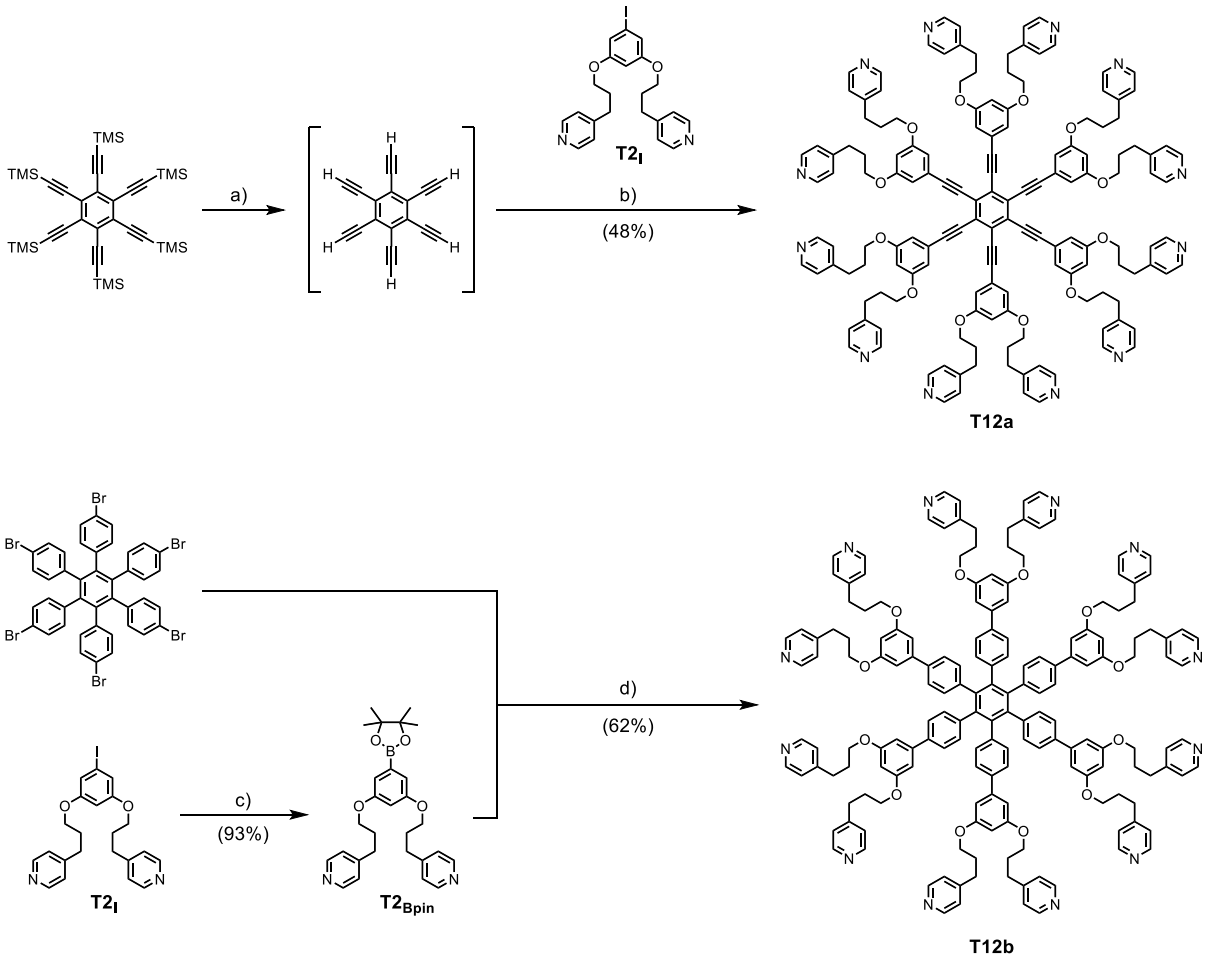

Figure 2.12: Syntheses of templates **T12a** and **T12b**. Reagents and conditions: (a) K_2CO_3, THF/CH_3OH 9:1; (b) **T2I** (8 equiv.), $Pd(PPh_3)_4$, CuI, Et_3N, THF, 25 °C, 24 h; (c) B_2pin_2, KOAc, $Pd(dppf)Cl_2 \cdot CH_2Cl_2$, 1,4-dioxane, 90 °C, 5 d; (d) **T2Bpin** (20 equiv.), XPhos Pd G2, K_3PO_4 (aq, 1.0 M), 1,4-dioxane, 90 °C, 3 d.

T12b, a slightly larger version of **T12a**, was also prepared using a six-fold Suzuki coupling reaction of **T2Bpin** and hexakis(4-bromophenyl)benzenebenzene. We expected that **T12b** is a promising template to direct the synthesis of nanoring ***cs*[*b*$_1$]-P12** with a butadiyne link, because ***cs*[*b*$_1$]-P12** has a larger circumference compared with ***cs*-P12**.

2.5.2 Binding of T12a and T12b to *ls*-P12

Before testing the macrocyclization conditions, we conducted UV–vis titrations to test whether the templates **T12a** and **T12b** could bind strongly to the porphyrin oligomers ***ls*-P12**. Both titrations gave sharp end points (Figure 2.13) and preliminary analyses by fitting the binding curves to the 1:1 binding isotherm (eqn. 2.5) gave formation constants K_f = 2.26 × 10^8 M^{-1} for complex ***ls*-P12·T12a**, and K_f = 2.22 × 10^8 M^{-1} for ***ls*-P12·T12b**. These results

suggest that stable 1:1 complexes are formed in $CDCl_3$, although they are too stable ($K_f > 10^8$ M^{-1}) to be determined accurately by these direct formation titrations.

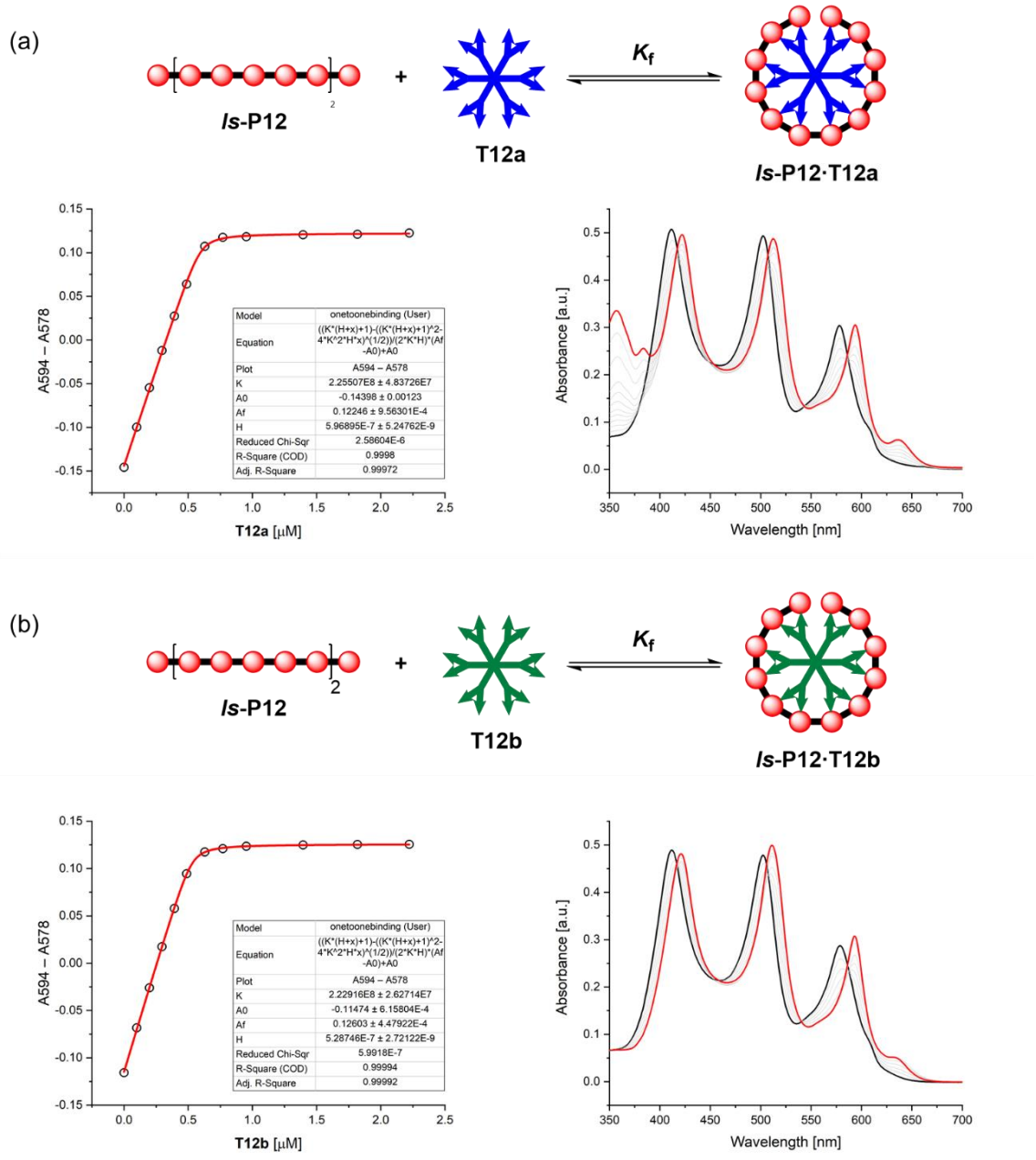

Figure 2.13: (a) UV–vis titration of ***ls*-P12** and **T12a**. The binding curve was fitted to eqn. 2.5 to give $K_f = 2.26 \times 10^8$ M^{-1} ($CDCl_3$, 298 K, [***ls*-P12**] = 6.00×10^{-7} M, $R^2 = 0.99972$). (b) UV–vis titration of ***ls*-P12** and **T12b**. The binding curve was fitted to eqn. 2.5 to give $K_f = 2.22 \times 10^8$ M^{-1} ($CDCl_3$, 298 K, [***ls*-P12**] = 6.00×10^{-7} M, $R^2 = 0.99992$).

2.5.3 Attempted Synthesis of *cs*-P12

Given that **T12a** binds to ***ls*-P12** to form stable 1:1 complex in $CDCl_3$ ($K_f > 10^8$ M^{-1}), we next explored the macrocyclization conditions to couple the ends of the bent ***ls*-P12** to construct nanoring ***cs*-P12**.

We started the macrocyclization trials by using the Ag(I)-mediated oxidative coupling reaction (Condition 1 in Figure 2.14a), because it is highly selective for *meso–meso* coupling. Ag[Al(pftb)$_4$] (pftb = perfluoro-*tert*-butoxy) was used instead of $AgPF_6$, because $AgPF_6$ was found to be less reactive compared to Ag[Al(pftb)$_4$] in the *meso–meso* coupling reaction. Additionally, $AgPF_6$ is barely soluble in $CHCl_3$, and it needs to be dissolved in CH_3CN before being added to the porphyrin solution.[79] However, the presence of CH_3CN could weaken the binding of the oligopyridine template to the porphyrins. In comparison, Ag[Al(pftb)$_4$] is highly soluble in $CHCl_3$ and thus was considered to be promising for the macrocyclization.[198] In the trial, we first mixed equal amounts of ***ls*-P12** and **T12a** in $CHCl_3$ to form a ***ls*-P12·T12a** (1.0 mM) solution. Then, a solution of Ag[Al(pftb)$_4$] (1.0 equiv.) in $CHCl_3$ was added and the mixture was stirred at 25 °C. The progress of the reaction was monitored by analytical GPC (Figure 2.14b), which suggested ***ls*-P12** was poorly converted and no expected cyclized product formed after 6 h (i.e., a cyclized product is expected to have a longer retention time compared to the corresponding linear oligomer). Addition of more Ag[Al(pftb)$_4$] (10–100 equiv.) or heating the reaction mixture at 50 °C for > 24 h barely improved the conversion of ***ls*-P12**.

We next explored the PIFA-mediated oxidative coupling reaction for the macrocyclization (Condition 2 in Figure 2.14a). In the trial, ***ls*-P12** and **T12a** was premixed to give a solution of ***ls*-P12·T12a** (1.3 mM) in CH_2Cl_2. After that, a solution of PIFA (0.5 equiv.) in CH_2Cl_2 was added to the complex solution and the mixture was stirred at 25 °C and the reaction progress was monitored by analytical GPC. We observed conversion of ***ls*-P12** to longer oligomers, such as ***ls*-P24** and ***ls*-P36**, after 1 h. A prolonged stirring (~40 h) slightly increased the conversion to long oligomers (Figure 2.14c). However, again, no desired ring product was detected. We also tried to increase the loading of the PIFA to 2 equiv. and then to 4 equiv., which caused severe precipitation of the oligomers without formation of ***cs*-P12**. The precipitation presumably resulted from the oxidative fusion of the porphyrin oligomers in the presence of excess PIFA, which gave less soluble fused porphyrin oligomers.

These two oxidative coupling reactions have proven to be efficient methods for synthesis of *meso–meso* singly-linked linear porphyrin oligomers ***ls*-P*N***. However, poor conversions of

***ls*-P12** to longer oligomers or nanorings were found in these trials, especially the Ag(I)-mediated reaction. The mechanism for these coupling reactions remains largely unexplored. A plausible mechanism proposed by Osuka and coworkers suggests a porphyrin unit **P** is first oxidized to form a charged porphyrin $\mathbf{P}^{+\cdot}$, followed by a nucleophilic attack of another **P** to $\mathbf{P}^{+\cdot}$ to give coupled species $\mathbf{P}\text{–}\mathbf{P}^{+\cdot}$.[77] A further oxidation ($-1e^-$) and proton eliminations ($-2H^+$) result in formation of *meso–meso* singly-linked product **P–P**. Considering the nucleophilic attack requires an overlap of the frontier orbitals (i.e., π orbitals of the porphyrins), we suspect that, in these syntheses, the preorganized geometry formed by coordination of all the porphyrin units on ***ls*-P12** to the pyridine legs in **T12** probably hamper the frontier orbital overlapping between two terminal porphyrin units, leading to poor conversions.

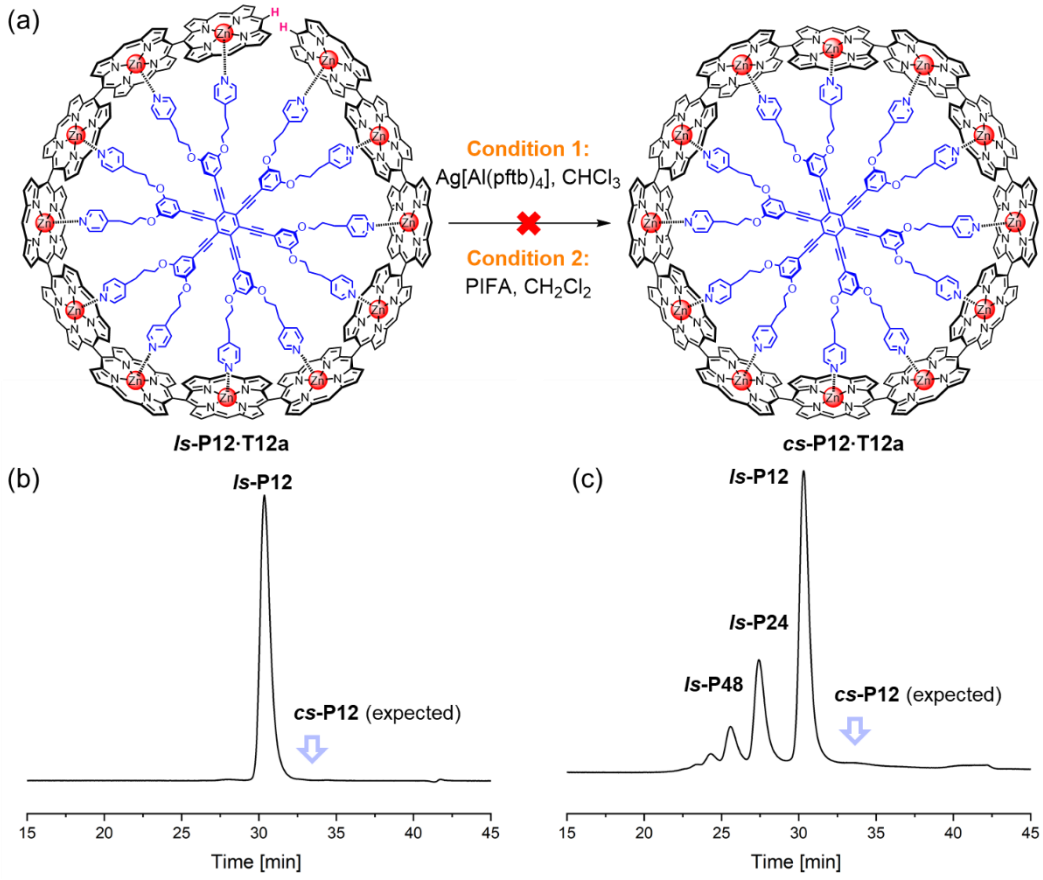

Figure 2.14: (a) Macrocyclization of ***ls*-P12·T12a** using Ag(I) or PIFA-mediated oxidative coupling reaction. (b) Analytical GPC trace of the crude reaction from Ag(I)-mediated macrocyclization of ***ls*-P12·T12a** after 6 h (THF + 1% pyridine, λ = 420 nm). (c) Analytical GPC trace of the crude reaction from PIFA-mediated macrocyclization of ***ls*-P12·T12a** after 40 h (THF + 1% pyridine, λ = 420 nm). The 3,5-bis(octyloxy)phenyl solubilizing groups are omitted.

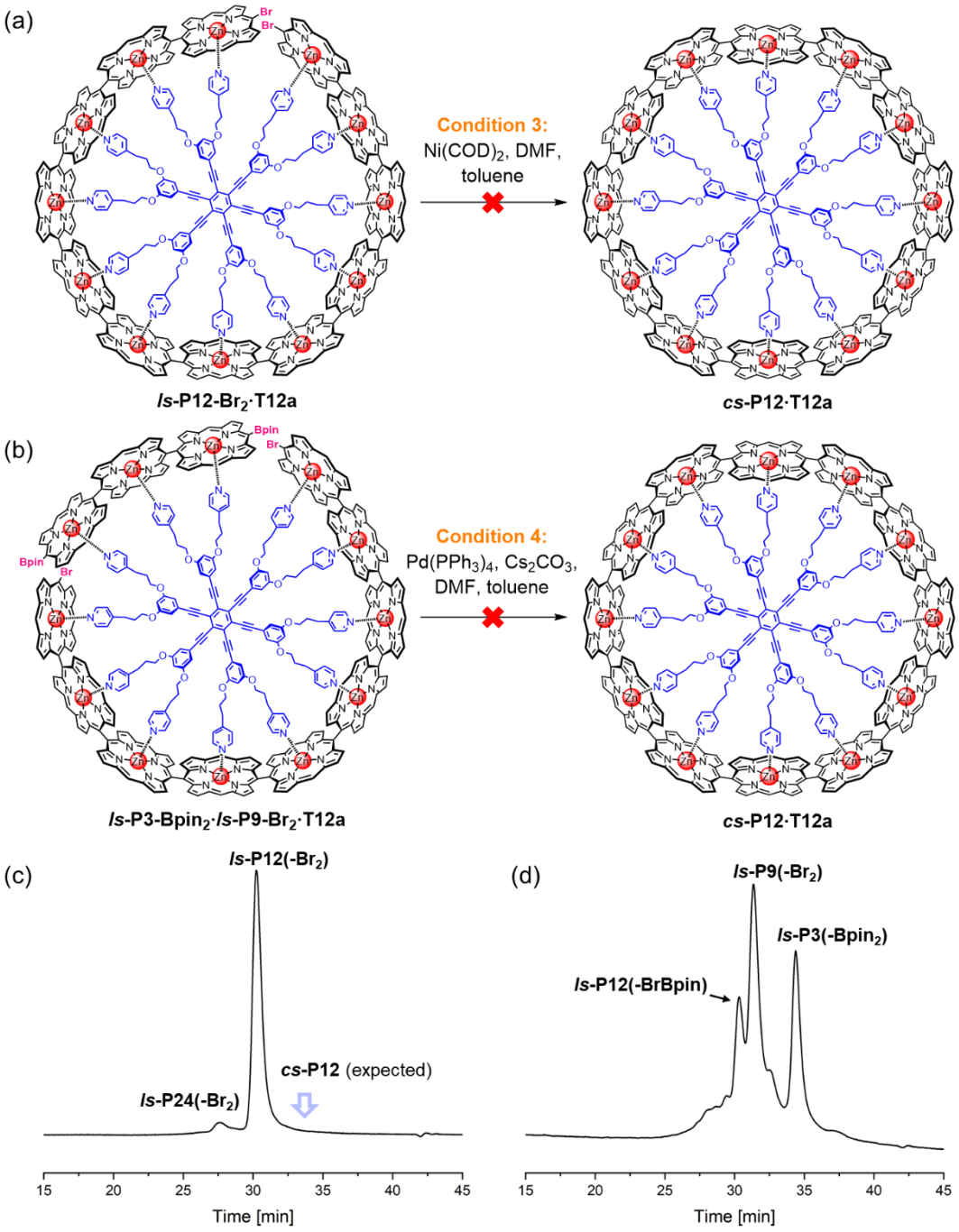

Figure 2.15: (a) Macrocyclization of ***ls*-P12-Br$_2$·T12a** using Yamamoto coupling reaction. (b) Macrocyclization of ***ls*-P3-Bpin$_2$·*ls*-P9-Br$_2$·T12a** using Suzuki coupling reaction. (c) Analytical GPC trace of the crude reaction from macrocyclization of ***ls*-P12-Br$_2$·T12a** after 5 h (THF + 1% pyridine, λ = 420 nm). (d) Analytical GPC trace of the crude reaction from macrocyclization of ***ls*-P3-Bpin$_2$·*ls*-P9-Br$_2$·T12a** after 20 h (THF + 1% pyridine, λ = 420 nm). The 3,5-bis(octyloxy)phenyl solubilizing groups are omitted.

Since the aforementioned oxidative coupling conditions failed to give ***cs*-P12**, Ni-promoted homocoupling of dibrominated porphyrin dodecamer ***ls*-P12-Br$_2$** in the presence of **T12a** was examined as the third macrocyclization condition. As both ***ls*-P12-Br$_2$** and **T12a** are less soluble in DMF at 25 °C, we premixed the oligomer with the template to form ***ls*-P12-Br$_2$·T12a** in $CHCl_3$ and removed the solvent before starting the reaction. $Ni(COD)_2$ (COD = 1,5-cyclooctadiene) was used as the nickel(0) source. In the reaction, ***ls*-P12-Br$_2$·T12a** was still poorly soluble in DMF despite the mixture had been heated to 80 °C, resulting in poor conversion of ***ls*-P12-Br$_2$**. We next moved to use toluene/DMF (1:1) as solvent, which improved the solubility of ***ls*-P12-Br$_2$** in the reaction. However, the starting materials still barely converted or they formed ***ls*-P12** by debromination (Figure 2.15c).

Macrocyclization using Suzuki coupling reaction was also explored. It is difficult to synthesize a porphyrin dodecamer with pinacolborane (Bpin) and Br groups at two ends separately, and thus ***ls*-P3-Bpin$_2$** and ***ls*-P9-Br$_2$** (see Figure 2.15b for their chemical structures) were prepared for a "[9 + 3]" two-fold Suzuki coupling. We employed $Pd(PPh_3)_4$ as catalyst, Cs_2CO_3 as base and toluene/DMF (4:1) as solvent for this reaction, similar to the conditions reported by Osuka for making ***ls*-P*N***.[199] After 20 h, we observed a small portion of ***ls*-P3-Bpin$_2$** and ***ls*-P9-Br$_2$** reacted to give singly coupled ***ls*-P12** (< 20% yield estimated from the GPC trace in Figure 2.15d), of which the terminal *meso* positions could be deborylated or debrominated. Although we might not be able to determine the formation of ***cs*-P12** from the GPC trace as the ***cs*-P12** peak might overlap with the ***ls*-P9** peak, the low yield (< 20%) of the singly coupled ***ls*-P12** implies the doubly coupled product ***cs*-P12** was barely afforded in this reaction. Zn(II) porphyrins bearing Bpin or Br groups easily undergo deborylation or debromination in Suzuki reaction, which might lead to poor conversion to longer oligomers.

To briefly summarize, we tried four macrocyclization conditions to synthesize *meso–meso* singly-linked porphyrin nanoring ***cs*-P12** but they failed to yield any cyclized product. These results, together with the calculated high strain energy of ***cs*-P12**, raise the following questions: is the binding of ***ls*-P12** to **T12a** too weak to overcome the strain to bend the porphyrin dodecamer into a ring? Are these conditions incompatible with the oligopyridine template-directed macrocyclization? To shed light on their answers, in the following section, we explored the synthesis of porphyrin nanoring ***cs*[b_1]-P12** with a butadiyne link, because the synthesis also involved the binding of ***ls*-P12** to a 12-leg oligopyridine template (**T12a** or **T12b**), and the macrocyclization condition (Pd-mediated Glaser coupling) has been intensively used for syntheses of butadiyne-linked porphyrin nanorings.[12]

2.5.4 Attempted Synthesis of *cs*[*b*$_1$]-P12

To test the templated-directed synthesis of ***cs*[*b*$_1$]-P12**, we first prepared ***ls*-P12-THS$_2$** via bromination of ***ls*-P12**, followed by a Sonogashira coupling reaction (see Figure 2.16 for the synthetic route and Appendix B for further information). Treatment of ***ls*-P12-THS$_2$** with tetra-*n*-butylammonium fluoride (TBAF) afforded deprotected ***ls*-P12-*e*$_2$** in 98% yield, which was directly subjected to the macrocyclization. The macrocyclization was conducted by addition of a catalyst solution (i.e., a solution of $Pd(PPh_3)_4$, CuI, diisopropylamine (DIPA) in $CHCl_3$) to a solution of ***ls*-P12-*e*$_2$** and template **T12a** in $CHCl_3$. The progress was monitored by analytical GPC analysis, which suggests no desired cyclized product ***cs*[*b*$_1$]-P12** formed after 16 h. Considering the circumference of ***cs*[*b*$_1$]-P12** would be slightly larger than ***cs*-P12**, we also tested the macrocyclization employing template **T12b**, which still binds to ***ls*-P12** (K_f > 10^8 M^{-1}). However, as inferred by the analytical GPC trace, no ***cs*[*b*$_1$]-P12** was observed from the macrocyclization.

These failed attempts imply that the strain energy needed to overcome for synthesis of the 12-porphyrin nanoring (***cs*-P12** or ***cs*[*b*$_1$]-P12**) may be so large that the template **T12a** (or **T12b**) is not able to bend the linear oligomer into an appropriate conformation for the macrocyclization, and thus we hypothesized that making a larger ring (e.g., 24-porphyrin nanoring ***cs*-P24** or ***cs*[*b*$_1$]-P24**) with a smaller curvature might be more accessible.

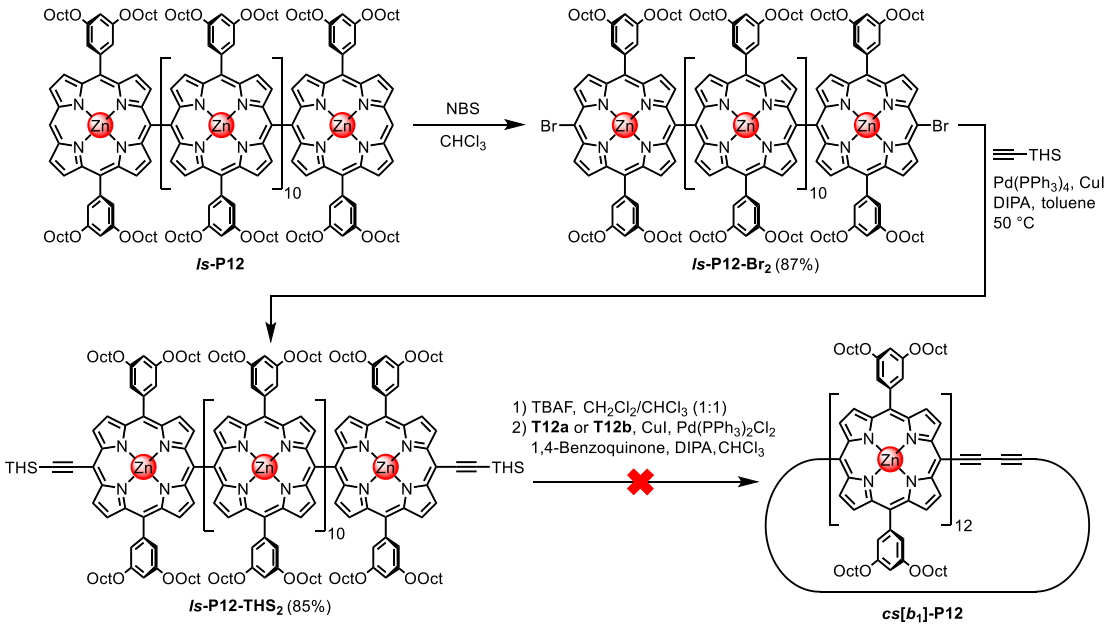

Figure 2.16: Termini functionalization of ***ls*-P12** and attempts to synthesize ***cs*[*b*$_1$]-P12** using **T12a** or **T12b**.

2.6 Synthesis and Characterization of *cs*[*b*$_1$]-P24

2.6.1 Computational Modeling and Design of the Template T12e

We began our attempts toward 24-porphyrin nanorings with ***cs*[*b*$_1$]-P24**, because the synthesis was expected to be easier compared with the fully symmetric ***cs*-P24**, and introduction of a butadiyne unit would help to probe the EET in this system. It would be difficult to design a single template capable of binding all 24 zinc sites in ***ls*-P24-e$_2$**, the precursor for making ***cs*[*b*$_1$]-P24**. Instead, we designed the **T12e** template, an expanded version of **T12a**, which has six **T2** binding units linked to a benzene core, and is shaped so that a cofacial stack of two molecules of **T12e** can bind inside the cavity of ***cs*[*b*$_1$]-P24** (see Figure 2.17 for its chemical structure).

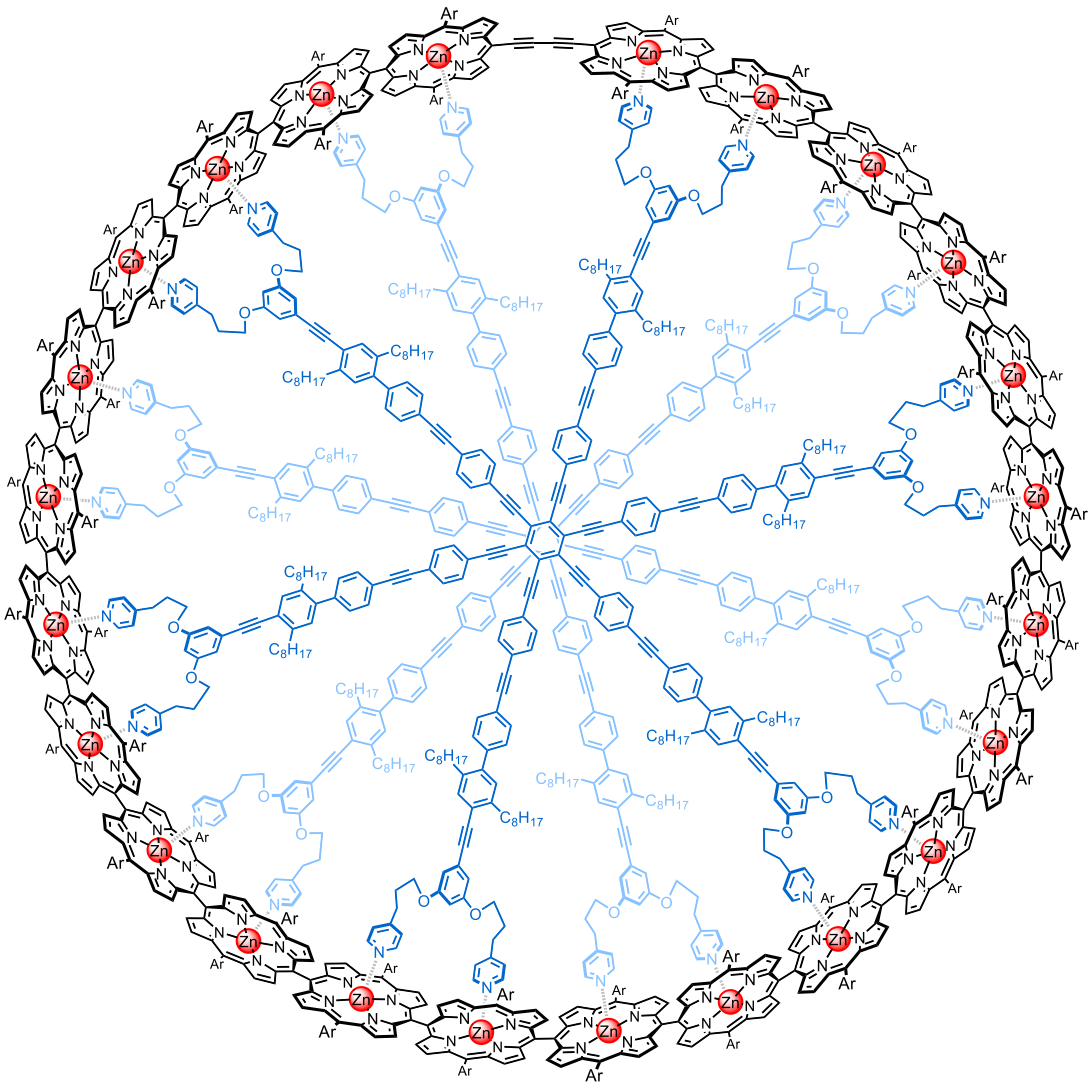

***cs*[*b*$_1$]-P24·(T12e)$_2$**

Figure 2.17: Chemical structure of nanoring-template complex ***cs*[*b*$_1$]-P24·(T12e)$_2$**. Ar = 3,5-bis(octyloxy)phenyl solubilizing group.

We performed molecular mechanics (MM) and molecular dynamics (MD) simulations to model the ***ls*-P24-e2·(T12e)2** complex. ***ls*-P24-e2·(T12e)2** was predicted to exist as two isomers with similar energies (binding modes A and B in Figure 2.18). MD simulations suggest that all 24 of the pyridyl binding sites of the templates remain coordinated to zinc atoms in the 1:2 complex. The angle θ and distance d between the terminal alkynes fluctuates across a distribution of values in these complexes (Figure 2.18b and 2.18c), including those in a range suitable for Glaser coupling.[200] There is no strong correlation between the two parameters, θ and d, because the alkynes tend to move apart by displacement away from the mean plane of the complex, rather than unwrapping from the templates.

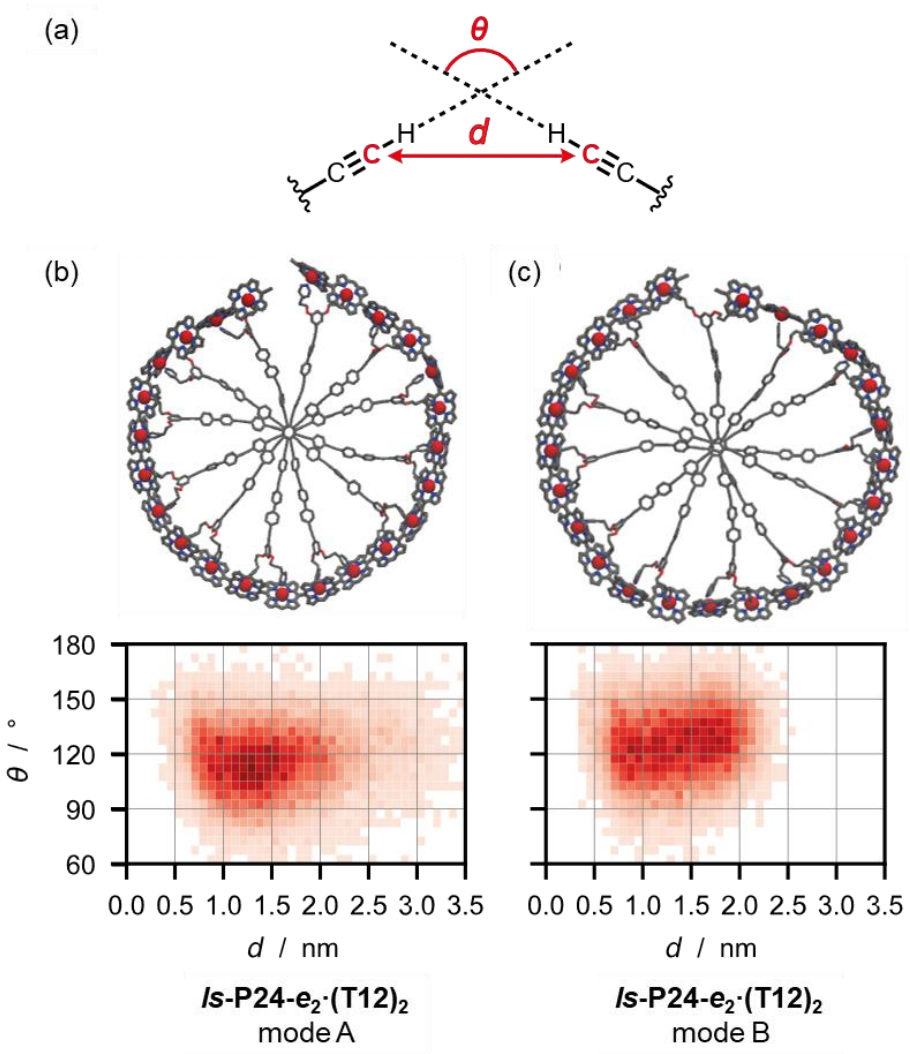

Figure 2.18: Molecular dynamics (MD) simulations of ***ls*-P24-e2·(T12e)2** complex. (a) Definition of parameters θ and d. (b) and (c) Geometry distributions for the two binding modes A and B with structures representative of the highest probabilities of θ and d. Data were collected and analyzed by Janko Hergenhahn.

2.6.2 Synthesis of T12e

Template **T12e** was constructed by multistep synthesis (see Figure **2.19** for the synthetic route and Section B.4 for the details). Compared with **T12a**, bridge units **2.4** with solubilizing alkyl chains (i.e., -C_8H_{17}) were incorporated to connect the binding units $\mathbf{T2_I}$ to the core **2.6** to elongate the backbone and improve the solubility of **T12e**.

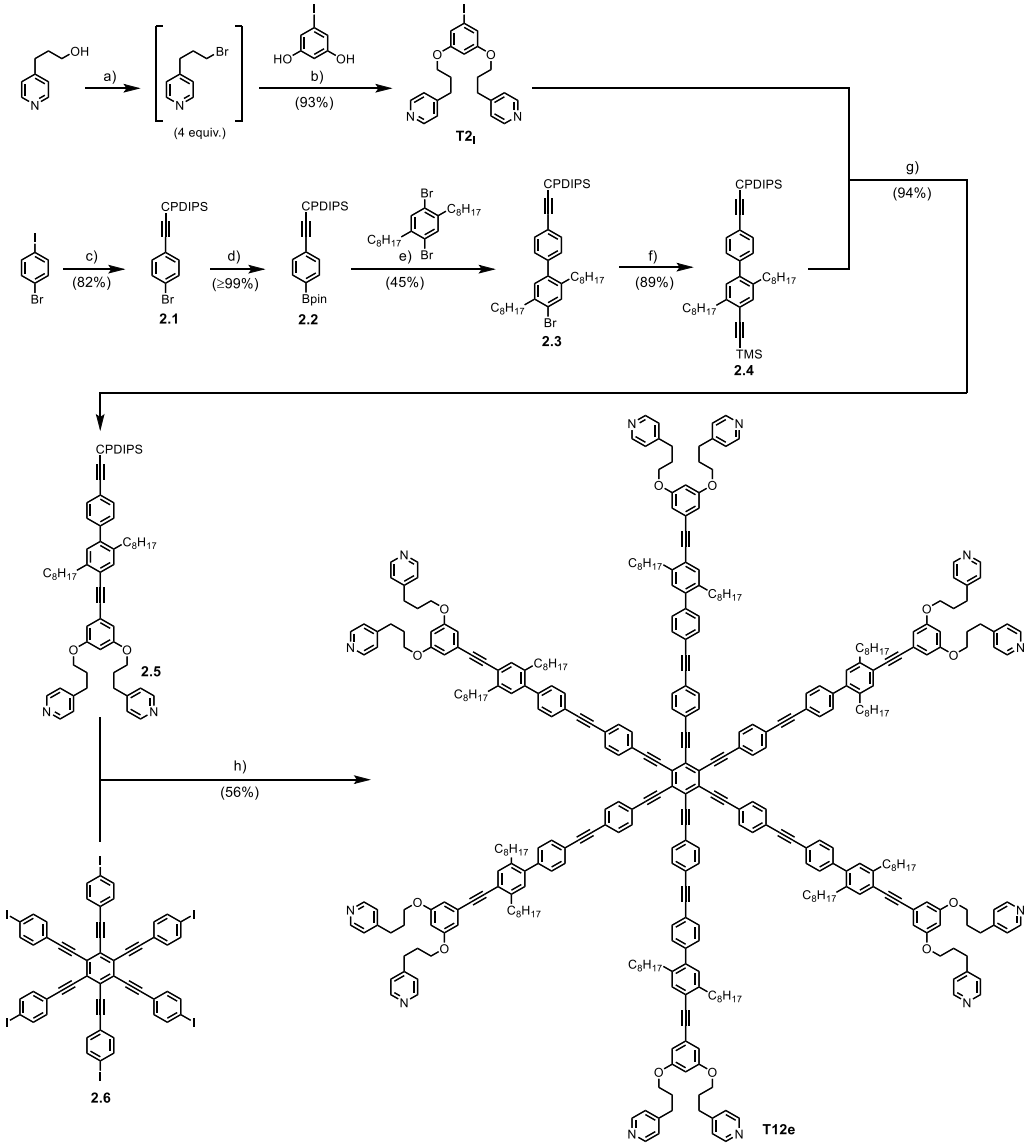

Figure 2.19: Synthesis of template **T12e**. Conditions: (a) 48% HBr (aq.) neat, reflux, 16 h; (b) K_2CO_3, DMF, 40–50 °C, 4–5 h; (c) CPDIPS-acetylene, $Pd(PPh_3)_2Cl_2$, CuI, DIPA/THF (1:5), 25 °C, 12 h; (d) B_2pin_2, KOAc, $Pd(dppf)Cl_2{\cdot}CH_2Cl_2$, 1,4-dioxane, 90 °C, 1.5 d; (e) 1,4-dibromo-2,5-dioctylbenzene (2.0 equiv.), $Pd(PPh_3)_2Cl_2$, K_2CO_3, 1,4-dioxane, 90 °C, 16 h; (f) TMS-acetylene, $Pd(PPh_3)_2Cl_2$, CuI, Et_3N, 50 °C, 3 d; (g) *i*. **2.4**, TBAF, THF, 25 °C, 2 h; *ii*. $\mathbf{T2_I}$, Pd_2dba_3, $AsPh_3$, CuI, Et_3N/THF (1:3), 25 °C, 16 h; (h) *i*. **2.5** (11.9 equiv), TBAF, THF, 25 °C, 1 h; *ii*. **2.6**, $Pd(PPh_3)_4$, CuI, DIPA/THF (1:6), 25 °C, 3 d.

2.6.3 Synthesis and Chemical Characterization of *cs*[b_1]-P24

Porphyrin oligomer ***ls*-P24-*e*$_2$** was prepared following the same synthetic route as ***ls*-P12-*e*$_2$** (Figure 2.20a). With ***ls*-P24-*e*$_2$** and **T12e** in hand, we next explored the synthesis of ***cs*[b_1]-P24** using Pd-catalyzed oxidative coupling reaction. The reaction conditions, which failed to cyclize ***ls*-P12-e$_2$** in previous trials, successfully coupled the terminal alkynes in ***ls*-P24-*e*$_2$** in the presence of **T12e** (2.1 equiv.) to give nanoring ***cs*[b_1]-P24**. The progress of the reaction was monitored by analytical GPC. The trace of the reaction mixture showing a peak (at ~30 min) appeared after the ***ls*-P24-*e*$_2$** peak (at ~28 min) indicated the formation of ***cs*[b_1]-P24·(T12e)$_2$** (Figure 2.20a). After removal of **T12e** with pyridine, nanoring ***cs*[b_1]-P24** was isolated by recycling GPC in 26% yield. Using a low concentration of ***ls*-P24-*e*$_2$** (1.7 μM) is important for the macrocyclization, to favor the intramolecular coupling rather than the intermolecular reactions.

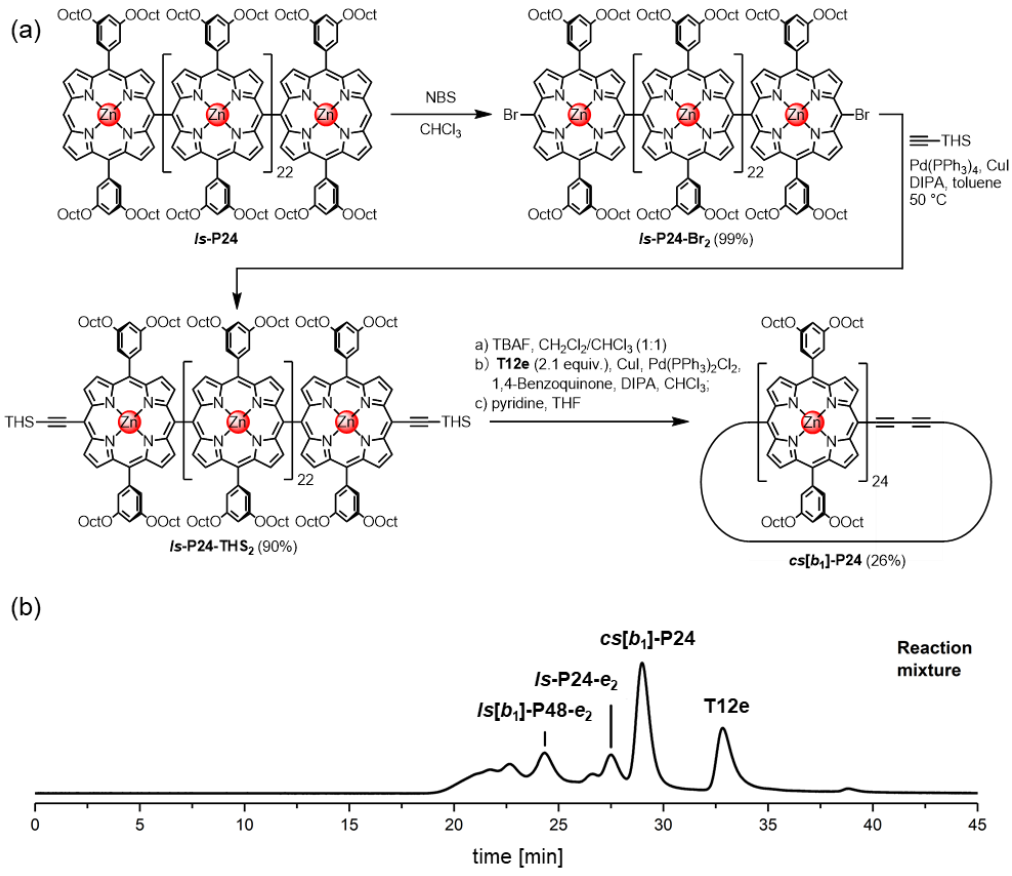

Figure 2.20: (a) Termini functionalization of ***ls*-P24-*e*$_2$** and template-directed synthesis of ***cs*[b_1]-P24** using **T12e**. (b) Analytical GPC traces (THF + 1% pyridine, λ = 420 nm) of the reaction mixture from cyclization of ***ls*-P24-*e*$_2$** in the presence of **T12e**. Here, **T12e** was assumed to be displaced from the complex in THF + 1% pyridine.

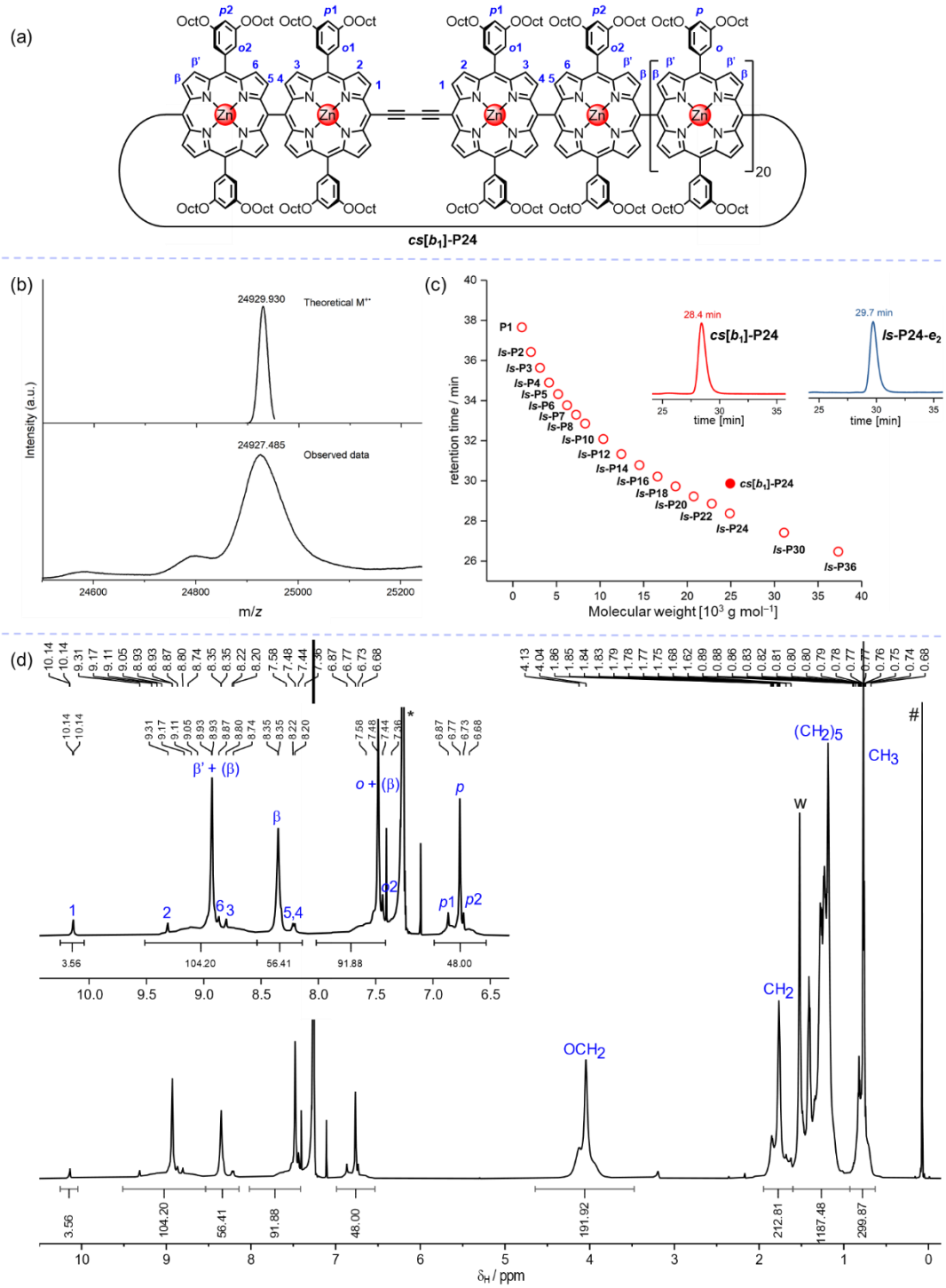

Figure 2.21: (a) Chemical structure of ***cs*[*b*$_1$]-P24**. (b) MALDI-ToF spectrum of ***cs*[*b*$_1$]-P24** with DCTB as matrix. (c) Plot of retention time versus molecular weight, including unsubstituted linear oligomers (open circles) and the cyclic 24-ring ***cs*[*b*$_1$]-P24** (solid circle). Retention times were obtained from analytical GPC traces using **P1** as reference (THF + 1% pyridine, λ = 420 nm). The inserts show the analytical GPC traces indicating the retention times of ***cs*[*b*$_1$]-P24** and ***ls*-P24-*e*$_2$**. (d) ^{1}H NMR spectrum of ***cs*[*b*$_1$]-P24** (700 MHz, $CDCl_3$, 298 K). * = $CHCl_3$, w = water, # = silicone grease.

After purification, nanoring ***cs*[*b*$_1$]-P24** was initially identified by observation of its molecular ion in mass spectrometry (found *m*/*z* 24927.5; cal. 24930.0; Figure 2.21b). The GPC retention time of ***cs*[*b*$_1$]-P24** was plotted in comparison to other linear oligomers in Figure 2.21b. The retention time of ***cs*[*b*$_1$]-P24** is a ~5% longer than that of the linear oligomer ***ls*-P24** (or ***ls*-P24-*e*$_2$**), as expected for the smaller hydrodynamic radius of the cyclic compound (Figure 2.21c). The same effect is also observed by diffusion-ordered NMR spectroscopy (DOSY), where ***cs*[*b*$_1$]-P24** and ***ls*-P24** have diffusion coefficients of 1.37×10^{-10} m^2 s^{-1} and 9.40×10^{-11} m^2 s^{-1}, respectively, in $CDCl_3$ at 298 K.

Compared to the fully symmetric systems, the ^{1}H NMR spectrum of ***cs*[*b*$_1$]-P24** is more complicated to analyze. As shown in Figure 2.21d, the ^{1}H NMR spectrum of ***cs*[*b*$_1$]-P24** is similar to that of ***ls*-P24-*e*$_2$**, except without the terminal alkyne peak at δ_H 4.28 ppm, as expected for the cyclized product. The ^{1}H NMR environments of ***cs*[*b*$_1$]-P24** also show a wider chemical shift dispersion than for ***ls*-P24-*e*$_2$**. We attempted to assign the peaks by analysis of its COSY and NOESY spectra and comparing to those of the linear chain (Figure 2.21a, d). The porphyrin rings in ***cs*[*b*$_1$]-P24** exhibit a wide range of angle of twist relative to the plane across all the zinc centers, leading to many similar unresolved ^{1}H NMR environments, which might explain the dispersion of the chemical shifts.

We also attempted to analyze the ^{1}H NMR spectrum of the nanoring-template 1:2 complex ***cs*[*b*$_1$]-P24·(T12e)$_2$**, which was formed by addition of an excess of **T12e** (2.25 equiv.) in small increments to the ***cs*[*b*$_1$]-P24** solution ($CDCl_3$), followed by removal of the unbound template using size-exclusion chromatography (Bio-Beads, S-X1, $CHCl_3$). However, the spectrum of ***cs*[*b*$_1$]-P24·(T12e)$_2$** is more complicated than that of the ***cs*[*b*$_1$]-P24**, plausibly owing to the presence of two binding modes, or restriction of the rotation across the butadiyne link after the complexation.

2.6.4 Scanning Probe Microscopy[†]

To provide direct evidence of forming a cyclic compound, we recorded the image of ***cs*[*b*$_1$]-P24** by scanning tunneling microscopy (STM). The ***cs*[*b*$_1$]-P24** nanoring was transferred from solution in toluene/CH_3OH onto a Au(111) substrate, held under vacuum conditions, by

[†] The scanning probe microscopy experiments and analysis were carried out by Michael Clarke, Abigail Bellamy-Carter, Jack Hart, Dr. James O'Shea and Dr. Alex Saywell (School of Physics & Astronomy, University of Nottingham, UK).

electrospray deposition using a previously reported procedure.[201] Images, as illustrated in Figure 2.22a and 2.22b (and Figure 2.36–2.39) were acquired at 293 K in constant current mode using electrochemically etched tungsten tips, coated in gold during tip optimization (further details are described in the Appendix B, Section B.8).

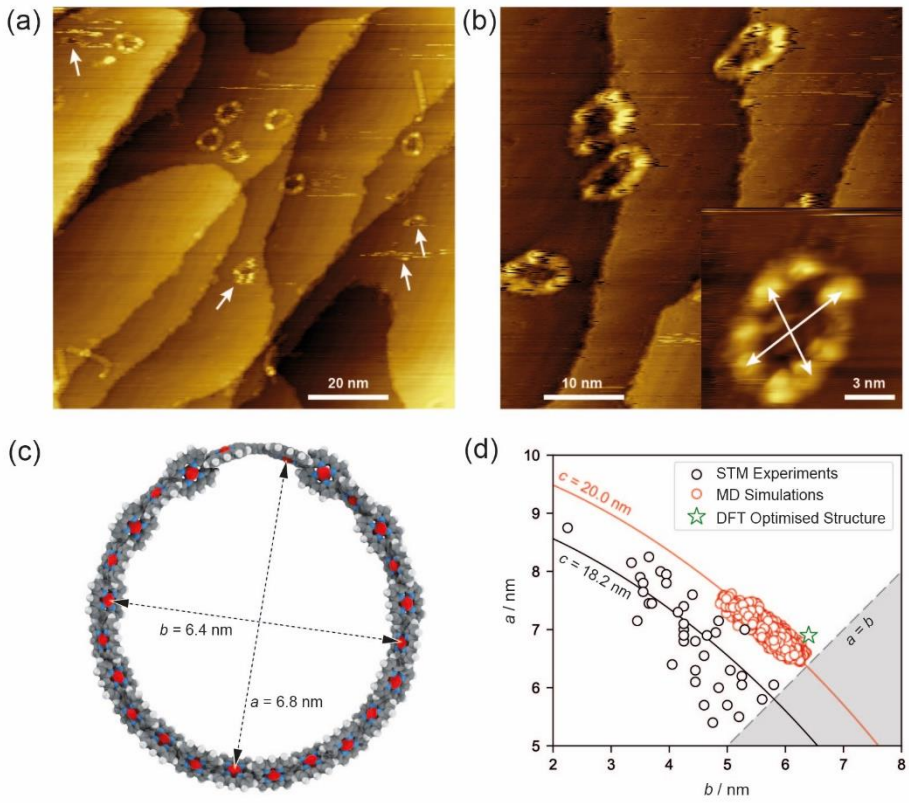

Figure 2.22: STM characterization of ***cs*[*b*$_1$]-P24** on Au(111). (a) and (b) STM-images of the ***cs*[*b*$_1$]-P24** nanoring deposited on a Au(111) surface under UHV (–1.8 V sample-bias, 20 pA set-point current, T = 293 K, image sizes: 100 × 100 nm, 50 × 50 nm, and 12 × 12 nm). In panel (a), arrows indicate ***cs*[*b*$_1$]-P24** nanorings which are mobile on the timescale of image acquisition. In panel (b), arrows show an example of the measured dimensions. (c) Optimized geometry of ***cs*[*b*$_1$]-P24** (PBE0+GD3BJ/Def2SVP). 3,5-Bis(octyloxy)phenyl solubilizing groups were replaced by hydrogen to simplify the calculation. (d) Plot of long (a) vs. short (b) axes values for 38 rings observed by STM (black circles) and points from the MD simulation (red circles). The black and red curves are the corresponding best fit lines for ellipses of fixed circumference (c = 18.2 nm and 20.0 nm, respectively, calculated using Ramanujan's approximation: $c \approx \pi \left[3\left(\frac{a}{2}+\frac{b}{2}\right) - \sqrt{\left(3\frac{a}{2}+\frac{b}{2}\right)\left(3\frac{b}{2}+\frac{a}{2}\right)}\right]$). The dashed line indicates circular geometries, $a = b$. Data were collected and analyzed by Dr. Alex Saywell et al.

The variation in contrast around the nanorings is attributed to the non-planar orientation of the porphyrin sub-units, with the brighter features assigned to porphyrins tilted upwards from the surface plane. The measured long and short axes of the rings indicate some structural flexibility. Average values of the long axis (a = 6.9 ± 0.9 nm) and short axis (b = 4.3 ± 0.7 nm) correspond to an ellipticity or flattening factor of $f = 1 - b/a$ = 0.4 ± 0.2 on the gold surface, which is significantly greater than for the optimized geometry from DFT (a = 6.8 nm; b = 6.4 nm; f = 0.07; Figure 2.22c). The distribution of conformations observed by STM is compared with that from molecular dynamics calculations (at 300 K with explicit $CHCl_3$ solvent; a = 6.9 ± 0.3 nm; b = 5.8 ± 0.3 nm; f = 0.16 ± 0.07) in Figure 2.22d. The mean circumference from the MD calculations (c = 20.0 nm) is slightly larger than the apparent average circumference from the STM images (18.2 nm, for the average of 38 images), but this probably reflects the fact that the molecules on the surface are not exactly elliptical. Interactions with substrate features, such as step-edges and the herringbone reconstruction of Au(111), may favor alternative conformations to those predicted by solution-phase calculations. The nanorings display significant mobility under these measurement conditions, with several lateral translation events observed (diffusion occurs at a faster rate than the acquisition time of an STM image – translation events highlighted with arrows in Figure 2.22a). This mobility indicates a decreased adsorption energy compared to the butadiyne-linked porphyrin nanorings,[201] which can be attributed to the nonplanarity of ***cs*[b_1]-P24**.

2.7 Binding of T12e to *cs*[b_1]-P24 and *ls*-P24

2.7.1 Binding of T12e to *cs*[b_1]-P24

The interaction of the nanoring ***cs*[b_1]-P24** with template **T12e** was studied by UV–vis and fluorescence titrations (in $CDCl_3$ at 298 K). The formation titration confirms that ***cs*[b_1]-P24** binds strongly with two equivalents of **T12e** to give a 1:2 complex ***cs*[b_1]-P24·(T12e)$_2$** (Figure 2.23). The formation constant (K_f) is too high to measure directly from the formation titration, and denaturation titrations, in which a competing ligand (quinuclidine) is added to displace the template, were used to determine the stability of the complex.[202]

Displacement of **T12e** from ***cs*[b_1]-P24·(T12e)$_2$** with increasing quinuclidine (**Q**) concentration can be monitored by the turn-on response of fluorescence at 472 nm, because the free **T12e** template is highly florescent, whereas its fluorescence is quenched in the complex (due to energy transfer to the porphyrin nanoring, as shown in the following section).

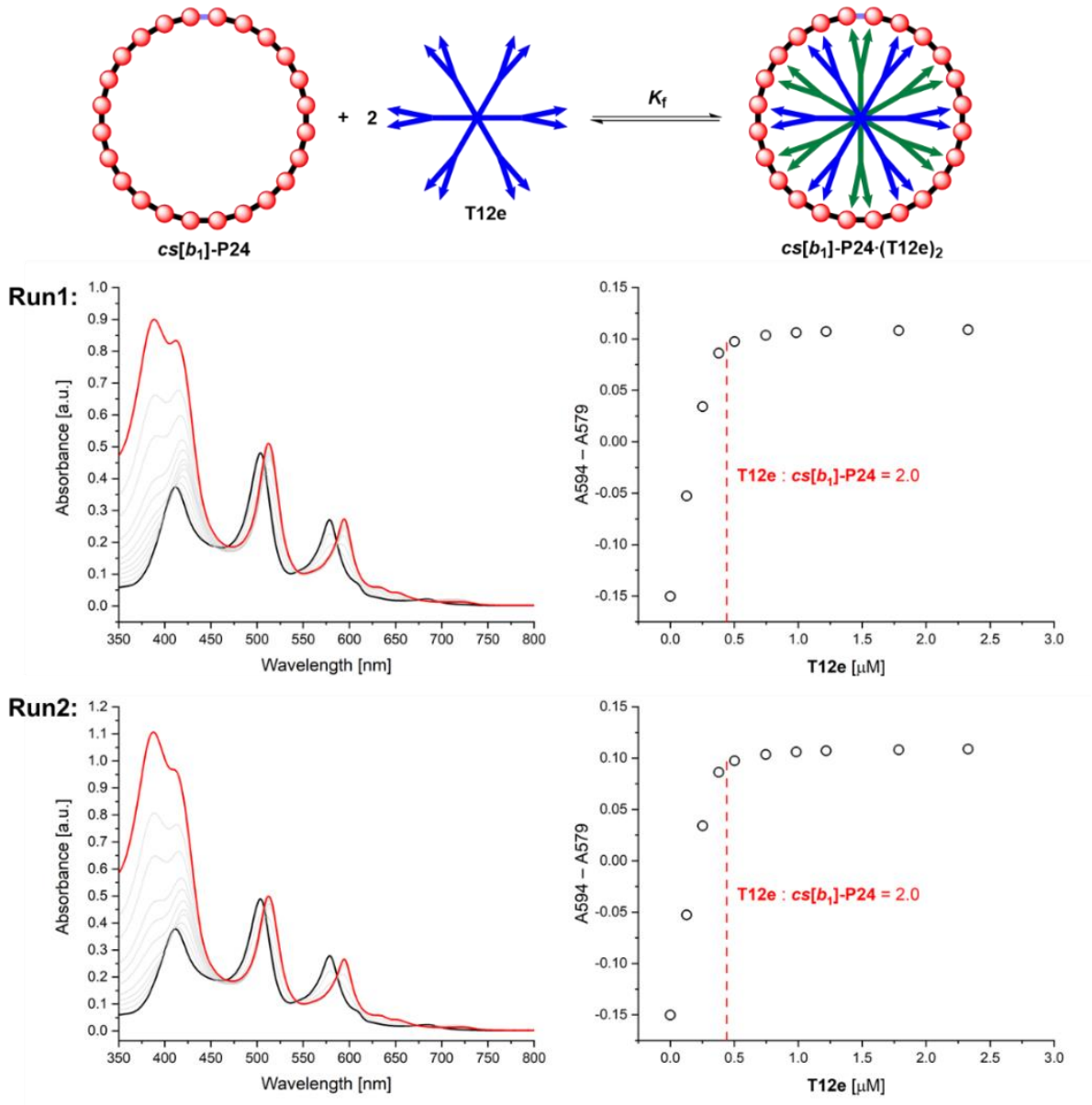

Figure 2.23: UV–vis–NIR formation titration of ***cs*[*b*1]-P24** with **T12e** ([***cs*[*b*1]-P24**] = 2.20 × 10^{-7} M, $CDCl_3$, 298 K).

The denaturation of ***cs*[*b*1]-P24·(T12e)2** was initially analyzed using a simple all-or-nothing model (eqn. 2.8 and 2.9) by fitting the experimental isotherm to eqn. 2.11 (see ref. 137 for the derivation of eqn. 2.10).

$$\textit{cs}[b_1]\text{-P24}\cdot(\text{T12e})_2 + 24\text{Q} \rightleftharpoons \textit{cs}[b_1]\text{-P24}\cdot\text{Q}_{24} + 2\text{T12e} \tag{2.8}$$

$$K_{\text{dn}} = \frac{[\textit{cs}[b_1]\text{-P24}\cdot\text{Q}_{24}][\text{T12e}]^2}{[\textit{cs}[b_1]\text{-P24}\cdot(\text{T12e})_2][\text{Q}]^{24}} \tag{2.9}$$

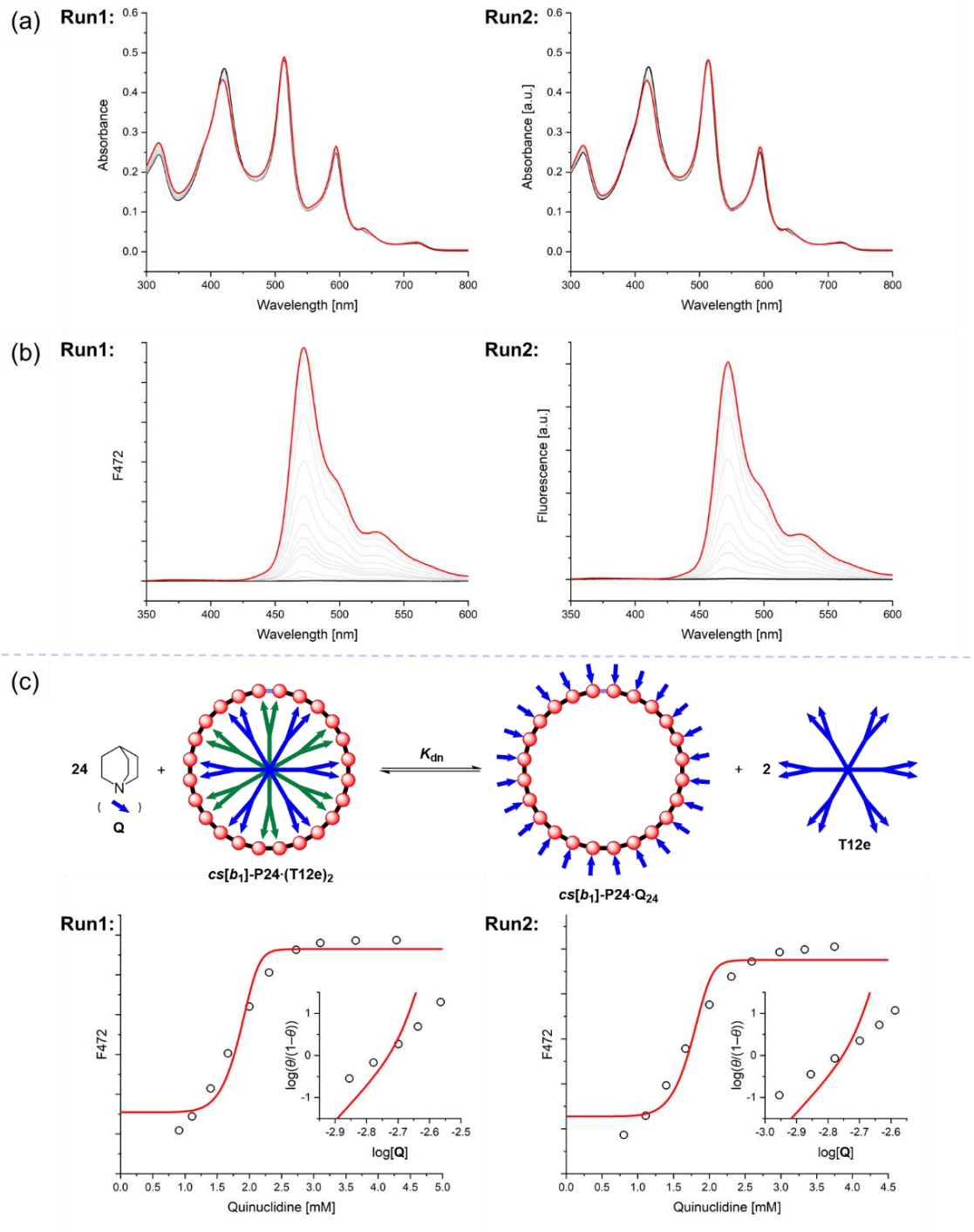

Figure 2.24: UV–vis–NIR absorption and fluorescence denaturation titration of ***cs*[*b*$_1$]-P24·(T12e)$_2$** with **Q** ([***cs*[*b*$_1$]-P24·(T12e)$_2$**] = 2.50 × 10^{-7} M, $CDCl_3$, 298 K). (a) and (b) show the experimental absorption and fluorescence spectra, respectively. (c) Fitting the experimental binding isotherm to all-or-nothing model described by eqn. 2.10. log K_{dn} = 52.31, R^2 = 0.96753 (Run 1); log K_{dn} = 52.87, R^2 = 0.95861 (Run 2). Insert: Hill plots of experimental (black circles) and simulated (red line) isotherms. θ is the extent of denaturation against [**Q**].

$$\frac{F-F_0}{F_f-F_0}=\frac{[\mathrm{T12}e]}{[\mathrm{T12}e]_f}=\frac{[\boldsymbol{cs[b_1]}\text{-}\mathbf{P24}\cdot\mathbf{Q_{24}}]}{[\boldsymbol{cs[b_1]}\text{-}\mathbf{P24}\cdot\mathbf{(T12e)_2}]_0}=$$

$$\frac{1}{2[\boldsymbol{cs[b_1]}\text{-}\mathbf{P24}\cdot\mathbf{(T12e)_2}]_0}\left(\frac{\sqrt[3]{\sqrt{3}\sqrt{{K_{dn}}^3{[\mathbf{Q}]_0}^{72}+27{K_{dn}}^2{[\boldsymbol{cs[b_1]}\text{-}\mathbf{P24}\cdot\mathbf{(T12e)_2}]_0}^2{[\mathbf{Q}]_0}^{48}}+9K_{dn}[\boldsymbol{cs[b_1]}\text{-}\mathbf{P24}\cdot\mathbf{(T12e)_2}]_0{[\mathbf{Q}]_0}^{24}}}{3^{\frac{2}{3}}}-\right.$$

$$\left.\frac{K_{dn}{[\mathbf{Q}]_0}^{24}}{\sqrt[3]{3}\sqrt[3]{\sqrt{3}\sqrt{{K_{dn}}^3{[\mathbf{Q}]_0}^{72}+27{K_{dn}}^2{[\boldsymbol{cs[b_1]}\text{-}\mathbf{P24}\cdot\mathbf{(T12e)_2}]_0}^2{[\mathbf{Q}]_0}^{48}}+9K_{dn}[\boldsymbol{cs[b_1]}\text{-}\mathbf{P24}\cdot\mathbf{(T12e)_2}]_0{[\mathbf{Q}]_0}^{24}}}}\right) \quad (2.10)$$

Here, F is fluorescence intensity, F_0 is the first point in the titration, F_f is the final asymptote of the titration curve, [**T12e**] (or [**T12e**]$_f$) is the concentration of unbound template **T12e** (or at the end point of the titration), [***cs*[*b*$_1$]-P24·Q$_{24}$**] is the concentration of ***cs*[*b*$_1$]-P24·Q$_{24}$**, [***cs*[*b*$_1$]-P24·(T12e)$_2$**]$_0$ is the total concentration of ***cs*[*b*$_1$]-P24**, [**Q**]$_0$ is the total concentration of quinuclidine, and K_{dn} is the denaturation constant.

As shown in Figure 2.24c, the fitted binding isotherms (red lines), which give log K_{dn} = 52.59 ± 0.09 and log K_f = 81.57 ± 0.7 (average of two independent runs), are sharper than the experimental isotherms (black circles), implying that the simple all-or-nothing model (i.e., two templates were displaced almost simultaneously with no significant population of the complex ***cs*[*b*$_1$]-P24·T12e·Q$_{12}$**) might oversimplify the denaturation process.

We next analyzed the denaturation by considering there are two equilibria in the denaturation process (i.e., a two-step denaturation model):

$$\boldsymbol{cs[b_1]}\text{-}\mathbf{P24}\cdot\mathbf{(T12e)_2}+12\mathbf{Q}\rightleftharpoons\boldsymbol{cs[b_1]}\text{-}\mathbf{P24}\cdot\mathbf{T12e}\cdot\mathbf{Q_{12}}+\mathbf{T12e} \quad (2.11)$$

$$\boldsymbol{cs[b_1]}\text{-}\mathbf{P24}\cdot\mathbf{T12e}\cdot\mathbf{Q_{12}}+12\mathbf{Q}\rightleftharpoons\boldsymbol{cs[b_1]}\text{-}\mathbf{P24}\cdot\mathbf{Q_{24}}+2\mathbf{T12e} \quad (2.12)$$

$$K_{dn,2}=\frac{[\boldsymbol{cs[b_1]}\text{-}\mathbf{P24}\cdot\mathbf{T12e}\cdot\mathbf{Q_{12}}][\mathbf{T12e}]}{[\boldsymbol{cs[b_1]}\text{-}\mathbf{P24}\cdot\mathbf{(T12e)_2}][\mathbf{Q}]^{12}} \quad (2.13)$$

$$K_{dn,1}=\frac{[\boldsymbol{cs[b_1]}\text{-}\mathbf{P24}\cdot\mathbf{Q_{24}}][\mathbf{T12e}]}{[\boldsymbol{cs[b_1]}\text{-}\mathbf{P24}\cdot\mathbf{T12e}\cdot\mathbf{Q_{12}}][\mathbf{Q}]^{12}} \quad (2.14)$$

Here, $K_{dn,2}$ and $K_{dn,1}$ are denaturation constants for two equilibria in the denaturation process. The experimental binding isotherm was fitted to the following equation:

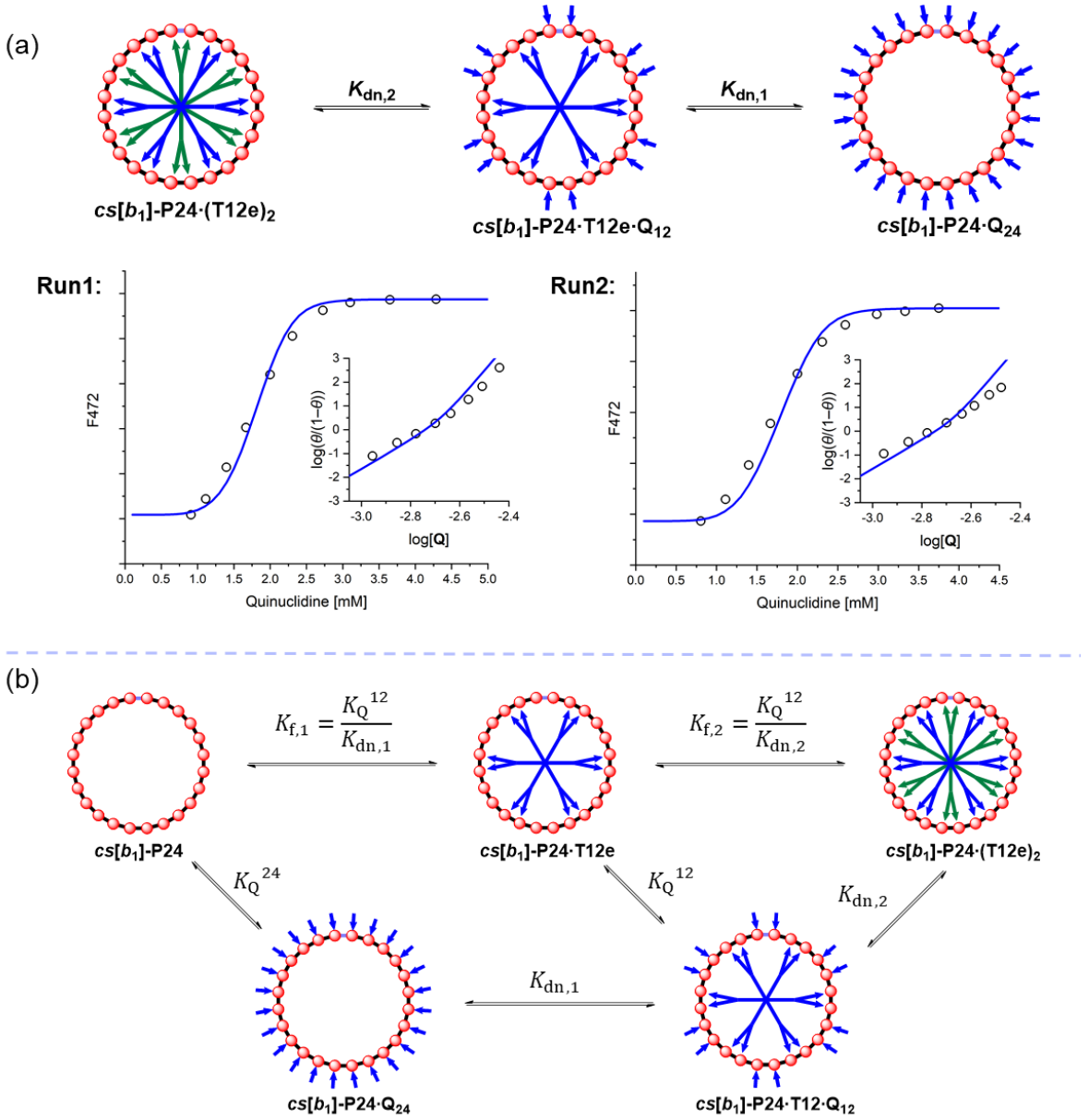

Figure 2.25: (a) Experimental and simulated binding isotherms of the denaturation titration of ***cs*[b_1]-P24·(T12e)$_2$** and **Q**. Fitting the experimental binding isotherm to the two-step model described by eqn. 2.11–2.18. Run1: binding curve (blue line) was obtained with estimated log $K_{dn,1}$ = 25.88, log $K_{dn,2}$ = 26.70, R^2 = 0.99833. Run 2: binding curve (blue line) was obtained with estimated log $K_{dn,1}$ = 25.86, log $K_{dn,2}$ = 26.83, R^2 = 0.99727. Insert: Hill plots of experimental (black circles) and simulated (blue line) isotherms. (b) Schematic showing the two-step formation and denaturation of ***cs*[b_1]-P24·(T12e)$_2$**.

$$\frac{F-F_0}{F_f-F_0} = \frac{[\mathbf{T12e}]}{[\mathbf{T12e}]_f} = \frac{[\mathbf{T12e}]}{2[\boldsymbol{cs}[\boldsymbol{b}_1]\text{-}\mathbf{P24}\cdot(\mathbf{T12e})_2]_0} \tag{2.15}$$

where [**T12e**] is the concentration of **T12e**, which is expressed by $K_{dn,2}$, $K_{dn,1}$ and [***cs*[*b*$_1$]-P24·(T12e)$_2$**]$_0$ by solving the following equation:

$$[\mathbf{T12e}]^3 + K_{dn,2}[\mathbf{Q}]_0{}^{12}[\mathbf{T12e}]^2 + \left(K_{dn,2}K_{dn,1}[\mathbf{Q}]_0{}^{24} - K_{dn,2}[\boldsymbol{cs}[\boldsymbol{b}_1]\text{-}\mathbf{P24}\cdot(\mathbf{T12e})_2]_0[\mathbf{Q}]_0{}^{12}\right)\cdot$$
$$[\mathbf{T12e}] - 2K_{dn,2}K_{dn,1}[\boldsymbol{cs}[\boldsymbol{b}_1]\text{-}\mathbf{P24}\cdot(\mathbf{T12e})_2]_0[\mathbf{Q}]_0{}^{24} = 0 \tag{2.16}$$

(see Appendix B, Section B.9 for the derivation).

Since it is difficult to directly solve eqn. 2.17 for data fitting, we simulated binding curves (blue lines) and compared to the experimental binding curves (orange lines) to estimate the denaturation constants (Figure 2.25a), giving log $K_{dn,1}$ = 25.87 ± 0.09, log $K_{dn,2}$ = 26.77 ± 0.09. The formation constants were calculated to be log $K_{f,1}$ = 41.20 ± 0.37, log $K_{f,2}$ = 40.30 ± 0.37 using the following relationships:

$$K_{f,2} = \frac{K_Q{}^{12}}{K_{dn,2}} \tag{2.17}$$

$$K_{f,1} = \frac{K_Q{}^{24}}{K_{dn,1}K_Q{}^{12}} \tag{2.18}$$

where K_Q is the association constant for the 1:1 **P1·Q** complex.

The formation constant for 1:2 complex ***cs*[*b*$_1$]-P24·(T12e)$_2$** was thus determined as log K_f = log ($K_{f,1}$ $K_{f,2}$) = 81.5 ± 0.7 with ΔG = 465 kJ mol^{-1}, which illustrates that there is ample binding energy to overcome the strain energy (75.7 kJ mol^{-1}) required to form the nanoring.

The binding of nanoring ***cs*[*b*$_1$]-P24** to two equivalents of **T12e** exhibits two types of cooperativity: chelate cooperativity and allosteric cooperativity.[196] The effective molarity (*EM*) for binding a **T12e** was estimated to be 0.1 M using the following equation:

$$K_f = K_{f,1}K_{f,2} = K_\sigma K_{chem}{}^{24}EM^{22} \tag{2.19}$$

where K_σ is the statistical factor of formation of the 1:2 complex (see Appendix B, Section B.9 for the calculation), K_{chem} is the association constant for binding an isolated zinc porphyrin to 4-ethylpyridine. The corresponding chelate cooperativity factor is K_{chem} EM ≈ 1000. The estimated *EM* (0.1 M) of the system is much greater than that of the model bidentate system described in Section 2.4 (*EM* = 2.8 mM), which reflects a strong chelate cooperativity resulting from the shape-complementarity between the template **T12e** and the nanoring.

The cooperativity factor α is a measure of allosteric cooperativity,[196] which can be calculated by the following equation:

$$\alpha = \frac{K_{\text{chem},2}}{K_{\text{chem},1}} = \frac{K_{\sigma,1}}{K_{\sigma,2}} \frac{K_{\text{f},2}}{K_{\text{f},1}} \tag{2.20}$$

where $K_{\sigma,1}$ and $K_{\sigma,2}$ are statistical factors for the two-step formation process, which are calculated to be 6144 and 576, respectively (see Appendix B for the details of calculation of the statistical factors). $K_{\text{chem},1}$ and $K_{\text{chem},2}$ are statistically corrected formation constants. log $K_{\text{chem},1}$ and log $K_{\text{chem},2}$ are calculated to be 37.4 ± 0.4 and 37.5 ± 0.4. The estimated $\alpha \approx 1.3 > 1$ for the system indicates a slightly positive allosteric cooperativity for binding the second equivalent of **T12e**.

At a macroscopic level, the cooperativity of the system was analyzed by the Hill plots of experimental data, together with simulated curves (Figure 2.26).[203,204] The estimated Hill coefficient $n_{\text{H}} = 5.7 \pm 0.3$ suggests a highly positive cooperativity ($n_{\text{H}} > 1$) for the system. The value is high compared to other natural and synthetic allosteric systems,[205–215] manifesting a combination of the chelate cooperativity and the allosteric cooperativity in forming the 1:2 nanoring-template complex.

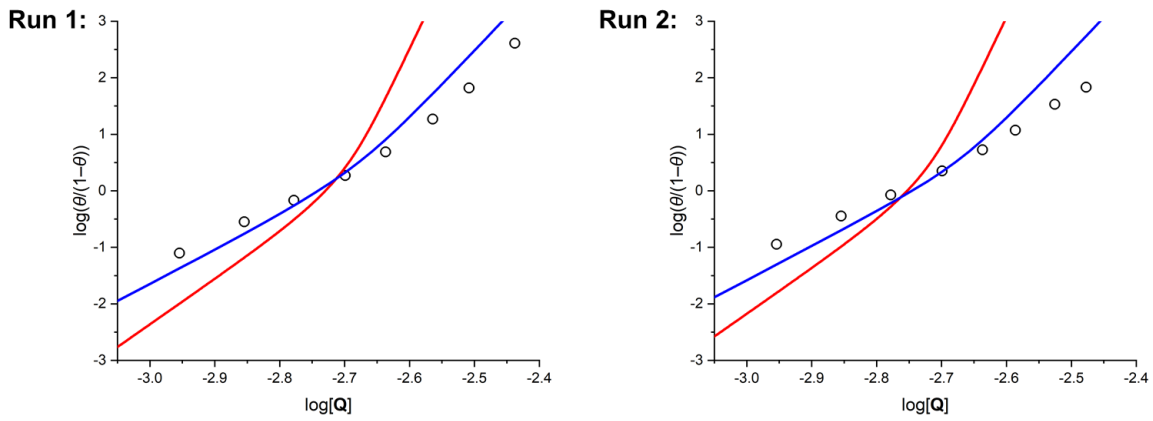

Figure 2.26: Hill plot of experimental data and simulated curves (i.e., red line for all-or-nothing model; blue line for two-step model) for the denaturation process. The Hill coefficients n_{H} are estimated: Run 1: 5.9 (experimental), 11.6 (all-or-nothing), 7.6 (two-step); Run 2: 5.4 (experimental), 11.7 (all-or-nothing), 7.1 (two-step). θ is the extent of denaturation against [**Q**].

2.7.2 Binding of T12e to *ls*-P24

We also attempted to determine the association constant K_f for the 1:2 complex formed via binding of a linear chain ***ls*-P24** to two **T12e** templates. By analogous with the ring system, the direct formation titrations gave sharp end points, suggesting formation of 1:2 ***ls*-P24·(T12e)$_2$** complexes (or complexes with a 1:2 ratio of ***ls*-P24** to **T12e**) in the solution (Figure 2.27). The experimental spectra and isotherms (Figure 2.28a–f) suggest the denaturation of ***ls*-P24·(T12e)$_2$** complex is typically under a stepwise process. We simulated the isotherms using the two-step model described in the previous section (eqn. 2.11–2.18). Comparison of the simulated isotherms to the experimental isotherms gave log $K_{dn,1}$ = 28.13 ± 0.09, log $K_{dn,2}$ = 36.53 ± 0.09, and log $K_{f,1}$ = 38.95 ± 0.37, log $K_{f,2}$ = 30.55 ± 0.37 (Figure 2.28e and 2.28f).

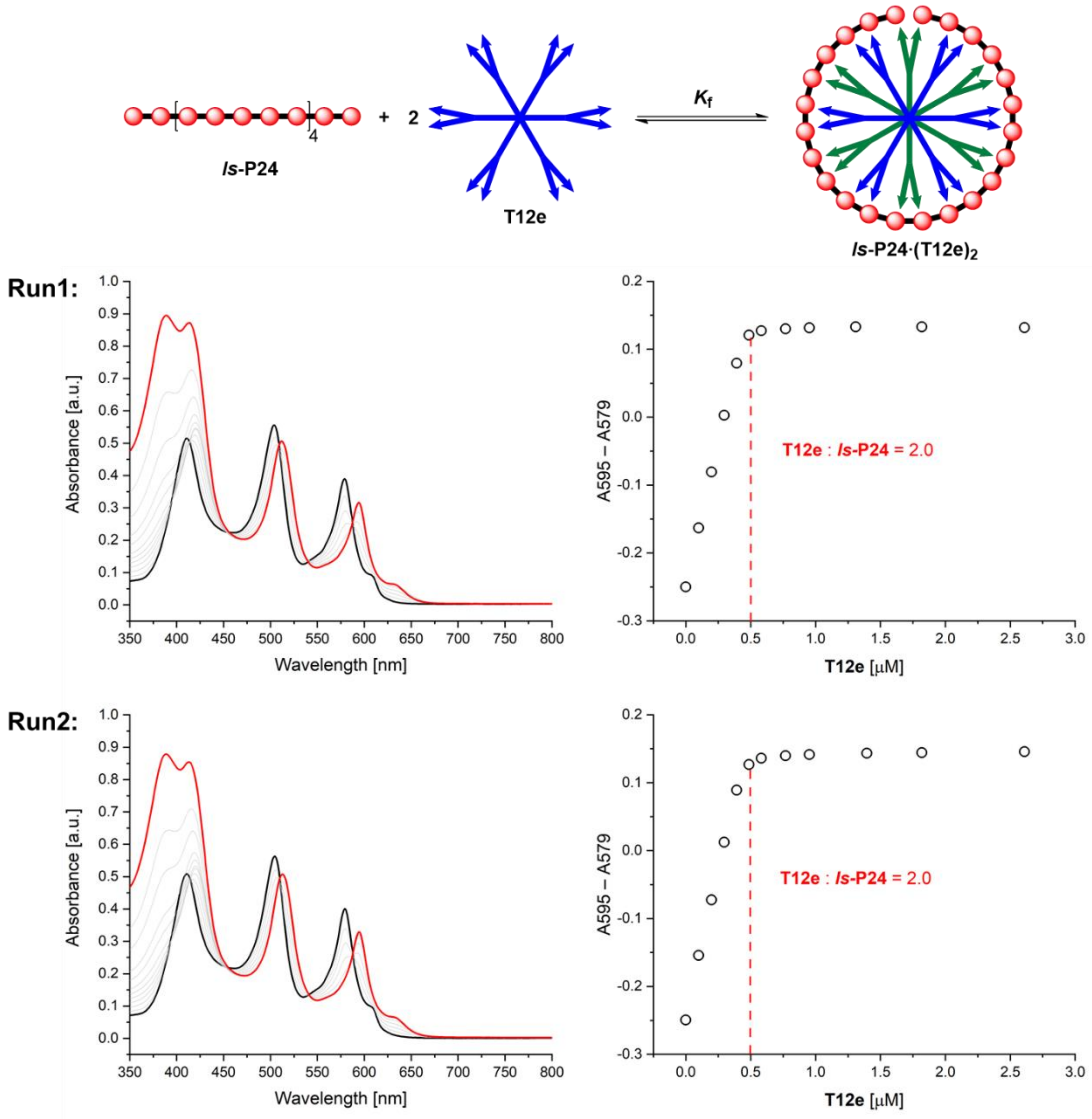

Figure 2.27: UV–vis–NIR formation titration of ***ls*-P24** and **T12e** ([***ls*-P24**] = 2.50 × 10^{-7} M, $CDCl_3$, 298 K).

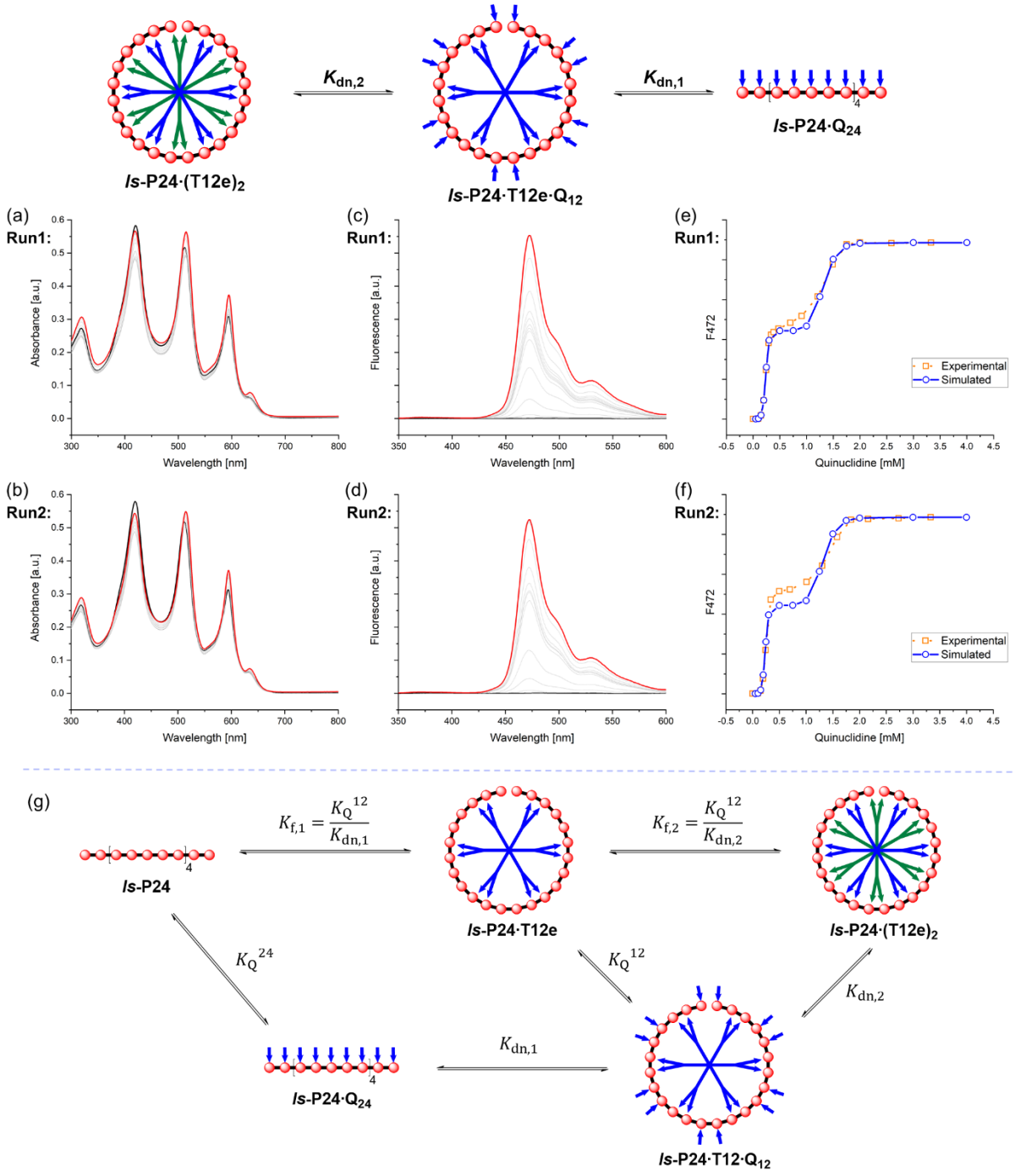

Figure 2.28: UV–vis–NIR absorption and fluorescence denaturation titration of ***ls*-P24·(T12e)$_2$** and **Q** ([***ls*-P24·(T12e)$_2$**] = 2.50 × 10^{-7} M, $CDCl_3$, 298 K). (a) and (b) show the experimental absorption spectra; (c) and (d) show the experimental fluorescence spectra. (e) and (f) Experimental and simulated binding isotherms of the denaturation titrations. Run1: binding curve (blue line) was obtained with estimated log $K_{dn,1}$ = 28.18, log $K_{dn,2}$ = 36.54. Run 2: binding curve (blue line) was obtained with estimated log $K_{dn,1}$ = 28.08, log $K_{dn,2}$ = 36.52. (g) Schematic showing the two-step formation and denaturation of ***ls*-P24·(T12e)$_2$**.

The estimated values showing $K_{f,1} \gg K_{f,2}$ suggests the model used must oversimplify the denaturation process. If a 1:1 complex ***ls*-P24·T12e** forms in the first step, we would expect $K_{f,2}$ to be much larger than $K_{f,1}$, because formation of ***ls*-P24·T12e** would overcome the strain energy of bending the linear chain (Figure 2.28g). The cooperativity factor calculated $\alpha = 1.3$ in the previous section also implies that coordination of a second template would not cause a strong repulsion between two templates embedded in the cavity. Therefore, one possible explanation for the denaturation process for ***ls*-P24·(T12e)$_2$** is that two templates are required to bend the linear chain into a circular shape. Displacement of one template changes the shape of the complex, leading to formation of less strained structures (e.g., 2:2 or high order *n*:*n* complexes).

2.8 Photophysics and Excitation Energy Transfer in *cs*[*b*$_1$]-P24[†]

The UV–visible-NIR absorption and fluorescence spectra of ***cs*[*b*$_1$]-P24** and ***ls*-P24** are compared with those of a porphyrin tetramer with a central butadiyne link, ***ls*[*b*$_1$]-P4b**, in Figure 2.29a and 2.29b. The absorption spectra of ***cs*[*b*$_1$]-P24** and ***ls*-P24** feature intense bands at 419, 515 and 594 nm which are assigned to the B_y, B_x and Q transition (see Figure 2.3a for an explanation), respectively.[165] The absorption spectra of ***cs*[*b*$_1$]-P24** and ***ls*[*b*$_1$]-P4b** also feature a weaker band at 650–700 nm, which is not present for ***ls*-P24**, and this is attributed to the π-conjugated butadiyne-linked porphyrin dimer unit (Figure 2.29a, insert). The fluorescence spectrum of ***cs*[*b*$_1$]-P24** has a similarity to ***ls*[*b*$_1$]-P4b**, showing peaks at 729 and 723 nm respectively (Figure 2.29b), and both compounds emit at a longer wavelength than ***ls*-P24** (λ_{em} = 651 nm), which indicates that EET to the butadiyne-linked porphyrin dimer unit occurs efficiently in ***cs*[*b*$_1$]-P24**. Comparison of the steady-state emission spectra of ***ls*-P24**, ***ls*[*b*$_1$]-P4b** and ***cs*[*b*$_1$]-P24** (at 651 and 729 nm, Figure 2.29b) implies that the EET efficiency is ≥ 93%.

The EET process in ***cs*[*b*$_1$]-P24** was investigated by monitoring the evolution of its fluorescence on a ps-timescale through fluorescence up-conversion spectroscopy (time resolution: ~350 fs, λ_{ex} = 410 nm). The fluorescence from ***cs*[*b*$_1$]-P24** displays a rapid decay at 650 nm and a concomitant rise at 720 nm (Figures 2.29c, 2.49 and 2.50). A stretched exponential decay, eqn. 2.21, provides an excellent description of the 650 nm emission kinetics for the ring (see Appendix B, Section B.11).

[†] The measurements and data analysis were conducted by Dr. Marcello Righetto under the supervision of Prof. Laura M. Herz (Department of Physics, University of Oxford, UK).

$$I(t) = I_0 e^{-(t/\tau_0)^{\beta}} \quad (2.21)$$

where $I(t)$ is the photoluminescence intensity, t is time, τ_0 is the time constant and β is the stretching exponent.[216]

The extracted parameters are τ_0 = 8.5 ± 0.6 ps and β = 0.54 ± 0.04. The value of β is significantly below unity (monoexponential decay), indicating that a range of excitation transfer times is present, as expected for random placement of excitation across the different porphyrin units comprising the ring. Accordingly, the characteristic transfer time τ_0 represents an average time taken for an excitation to migrate from the *meso–meso* linked porphyrin donor segments to the butadiyne-linked porphyrin dimer acceptor unit. The matching rise dynamics observed in the emission at 720 nm confirms that these coupled dynamics are associated with energy transfer. Modeling of the transient fluorescence at 650 and 720 nm (Figure 2.29c and Figure 2.50) with an exciton generation function (Appendix B, eqn. B.20) indicates that approximately 40% of the excitation arrives at the butadiyne-linked porphyrin unit within the time-resolution. We attribute 9% of the excitation to directly exciting the butadiyne-linked acceptor unit by comparing the absorption spectra of ***ls*[*b*$_1$]-P4** and ***cs*[*b*$_1$]-P24** (λ_{abs} = 410 nm, Figure 2.29a), and thus it is about 30% of the EET occurs within the time resolution (350 fs).

Further evidence of EET is provided by the pronounced redshift of the peak emission wavelength in ***cs*[*b*$_1$]-P24**, during 0–50 ps after excitation (Figure 2.29d and 2.29e). Again, it is clear that part of the EET occurs within the time resolution, because the emission maximum of ***cs*[*b*$_1$]-P24** is redshifted with respect to that of ***ls*-P24** even at the earliest times we can measure (Figure 2.29e). On a longer timescale (~500 ps), the emission spectrum of ***cs*[*b*$_1$]-P24** exhibits a slower redshift due to planarization of the excited state of the butadiyne-linked porphyrin dimer unit;[217,218] this slow process is also observed in ***ls*[*b*$_1$]-P4**. In contrast, ***ls*-P24** displays only weak shifts due to EET among segments of the chain with different porphyrin-porphyrin dihedral angles.[20] It is interesting that the average rate of EET in ***cs*[*b*$_1$]-P24** is significantly faster than in a similar linear 24-porphyrin chain terminated with an ethynyl-porphyrin energy acceptor (time constant 110 ps as discussed in Section 2.1.2).[23,24]

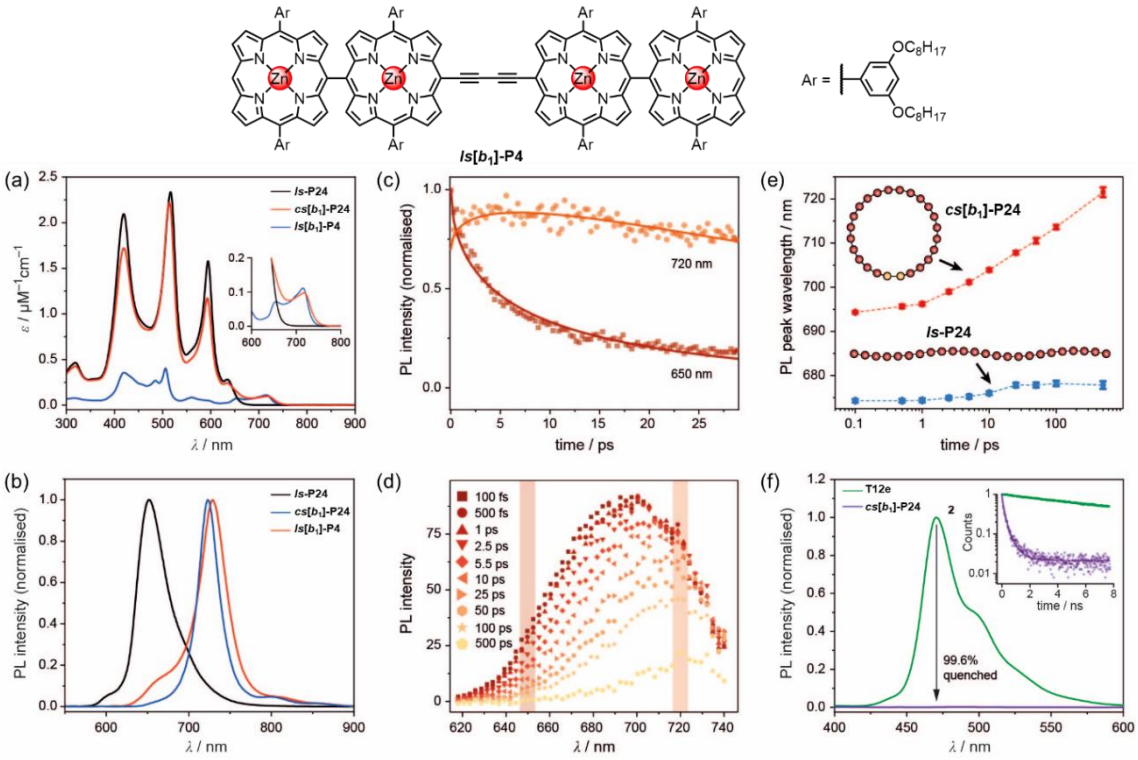

Figure 2.29: Absorption and fluorescence spectra. (a) UV–vis–NIR absorption spectra. (b), Steady-state fluorescence spectra. (c), Transient fluorescence of ***cs*[*b*$_1$]-P24**, detected at 650 nm (red squares) and 720 nm (orange circles) under 410 nm wavelength excitation at 2.5 μJ cm^{-2}. Solid lines represent fits to the model described in Appendix B, Section B.11. (d) Time-resolved fluorescence spectra for ***cs*[*b*$_1$]-P24** following 410 nm wavelength pulsed excitation at a fluence of 2.5 μJ cm^{-2}. Different symbols represent spectra taken at different times after the excitation, in the range 100 fs (dark red square) – 500 ps (yellow pentagon). (e), Comparison between the time evolution of the peak wavelength of the photoluminescence spectra for ***cs*[*b*$_1$]-P24** (red squares), and ***ls*-P24** (blue circles). Data points are extracted through Gaussian fitting of the time-resolved photoluminescence spectra measured under the same excitation as a function of time after excitation. Dashed lines are guides for the eye. (f), Emission spectra of **T12e** (1.6×10^{-7} M) and ***cs*[*b*$_1$]-P24·(T12e)$_2$** (0.8×10^{-8} M), i.e., at identical template concentration, with λ_{ex} = 318 nm. The **T12e** quenching efficiency in the complex is 99.6%. The insert shows the transient fluorescence decay from both solutions (λ_{ex}: 380 nm, power 6 mW). The free template exhibits a mono-exponential decay $\tau = 8 \pm 1$ ns. The template emission can be fitted with stretched exponential decay ($\tau_0 = 0.15 \pm 0.04$ ns; $\beta = 0.7$). All spectra were recorded in toluene containing 1% pyridine at 298 K, except for ***cs*[*b*$_1$]-P24·(T12e)$_2$** which was dissolved in toluene without pyridine. Data were collected and analyzed by Dr. Marcello Righetto and Prof. Laura M. Herz.

Energy transfer is also observed from the central template units in ***cs*[*b*$_1$]-P24·(T12e)$_2$** to the surrounding zinc porphyrins. The **T12e** template is highly fluorescent (λ_{em}: 472 nm; ϕ_f = 0.26, in toluene at 298 K) and its fluorescence is quenched (by a factor of 99.6%) in the ***cs*[*b*$_1$]-P24·(T12e)$_2$** complex, as shown in Figure 2.29f. The excitation spectrum of ***cs*[*b*$_1$]-P24·(T12e)$_2$**, based on emission at 760 nm, has a peak at 319 nm corresponding to the absorption spectrum of the template (Figure 2.44), which demonstrates that there is energy transfer from the **T12e** unit to the porphyrin manifold. Analysis of transient fluorescence decays (inset of Figure 2.29f) reveals an average energy transfer time of 0.15 ns. EET from *meso*-*meso*-linked porphyrins to the butadiyne-linked porphyrin dimer unit in ***cs*[*b*$_1$]-P24·(T12e)$_2$** is much less efficient than in ***cs*[*b*$_1$]-P24**, as indicated by the broad fluorescence spectrum of ***cs*[*b*$_1$]-P24·(T12e)$_2$**, which extends from around 650 nm to 750 nm (Figure 2.44). Molecular dynamics simulations provide an explanation for the reduced efficiency of EET in the nanoring-template complex: the **T12e** template tends to hold the butadiyne-linked porphyrins in a twisted conformation, with the two porphyrins orthogonal. This conformation is less π-conjugated and it has a higher energy S_1 excited state,[83] so that the butadiyne-linked porphyrins cease to constitute an effective energy acceptor when the nanoring is bound to two **T12e** units.

2.9 Conclusion and Outlook

In the beginning of this project, we had an ambitious plan to develop a modular strategy, using template-directed synthesis, to construct a family of fully symmetric *meso–meso* singly-linked porphyrin nanorings ***cs*-P*N*** and the corresponding fused porphyrin nanobelts ***cf*-P*N***. Until this moment, we have been able to isolate the nanoring ***cs*[*b*$_1$]-P24** with a butadiyne link, which demonstrates that oligopyridine templates (e.g., **T12e**) can be used to direct the synthesis of large zinc porphyrin nanorings, even from linear oligomers that are twisted and rod-like. The UV–vis–NIR titrations reveal that two equivalents of **T12e** can be embedded in the cavity of ***cs*[*b*$_1$]-P24**, forming self-assembled 1:2 nanoring-template complex showing high cooperativity. Excited state energy transfer from the 22 *meso–meso* linked porphyrin units to the butadiyne-linked segment of ***cs*[*b*$_1$]-P24** occurs over a range of time scales, as expected from the distribution of donor–acceptor distances. About 30% of the energy is transferred within the time resolution of our measurements (350 fs), while the EET process has an average time constant of 8.5 ps. The ***cs*[*b*$_1$]-P24** macrocycle mimics the photophysics of LH2, although the arrangement of transition dipoles in this nanoring, with neighboring

porphyrins almost orthogonal, results in slower EET than the arrangement in the natural system, in which neighboring chromophores are almost parallel.

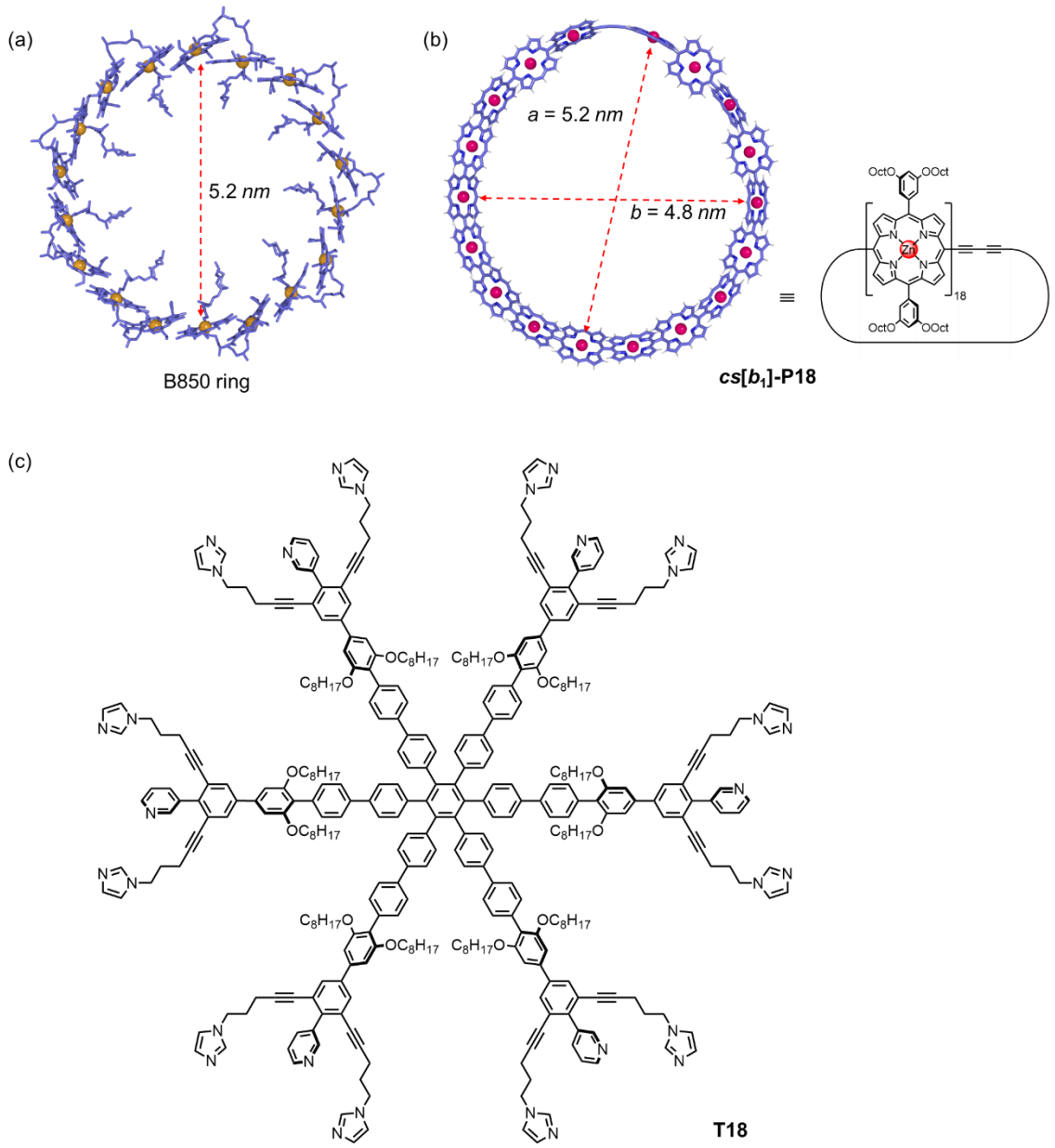

Figure 2.30: Structures of (a) the B850 rings in LH2,[155] (b) porphyrin nanoring ***cs*[*b*$_1$]-P18** (PBE0+GD3BJ/Def2SVP), and (c) template **T18**. *a* and *b* indicate the calculated length of the long and short axes in ***cs*[*b*$_1$]-P18**, respectively.

Although we were successful in the synthesis of ***cs*[*b*$_1$]-P24**, no cyclic product was obtained in attempted syntheses of ***cs*[*b*$_1$]-P12**, probably attributed to the relatively high strain in the small nanoring. Ongoing work is to explore the synthesis of an 18-porphyrin nanoring ***cs*[*b*$_1$]-P18**,[†] which is expected to serve as a better mimic to the B850 ring in LH2, because it has a similar diameter (~5 nm, Figure 2.30) and the same number of the subunits (i.e., zinc porphyrin for ***cs*[*b*$_1$]-P18** and Bchl*a* for the B850 ring) to the natural light-harvesting complex. The calculated strain energy of ***cs*[*b*$_1$]-P18** (99.6 kJ mol^{-1}) is comparable to that of the reported alkyne-linked porphyrin nanorings (100–130 kJ mol^{-1}). An 18-leg template **T18**, comprising of 18 coordination sites (i.e., six pyridines and twelve imidazoles), was designed and recently made to direct the synthesis of ***cs*[*b*$_1$]-P18** (Figure 2.30c). Preliminary results suggest the cyclized product formed by palladium-catalyzed coupling of ***ls*-P18-*e*$_2$** in the presence of **T18**. Optimization of conditions to improve the macrocyclization yield and isolate the targeted nanoring are in progress.

We have also not yet been able to make any fully symmetric *meso–meso* linked porphyrin nanoring (***cs*-P12** or ***cs*-P24**), suggesting that the linear oligomer-template complex might be incompatible with the final macrocyclization conditions. To overcome this obstacle, inspired by our previous success in synthesis of ***cs*[*b*$_1$]-P24**, we proposed a stepwise template-directed synthesis to construct ***cs*-P24** using a combination of noncovalent and covalent templates (Figure 2.31). Instead of using the oligopyridine templates (e.g., **T12e**) to direct the coupling of two terminal *meso* positions of ***ls*-P24**, we planned to employ this noncovalent template to direct the formation of a temporary tether, which could serve as a covalent template to enforce a close contact between two ends of ***ls*-P24** after removal of the oligopyridine templates. Here, we plan to incorporate two handles, each of which contains a terminal alkene, onto the peripheral aryl groups of two terminal porphyrins in ***ls*-P24** via ester linkages. Connecting the handles using template-directed ring-closing alkene metathesis, which has been used in syntheses of porphyrin-based nanostructures,[219–221] would allow formation of a covalent tether. The oxidative macrocyclization could be conducted under a coordination template-free condition, directed by the covalent tether. Once the cyclized product has formed, the tether can be removed by hydrolysis, followed by alkylation of the resulting phenol groups to give the fully symmetric *meso–meso* singly-linked nanoring ***cs*-P24**.

[†] The project was initiated by Dr. Jeff M. Van Raden (Department of Chemistry, University of Oxford, UK).

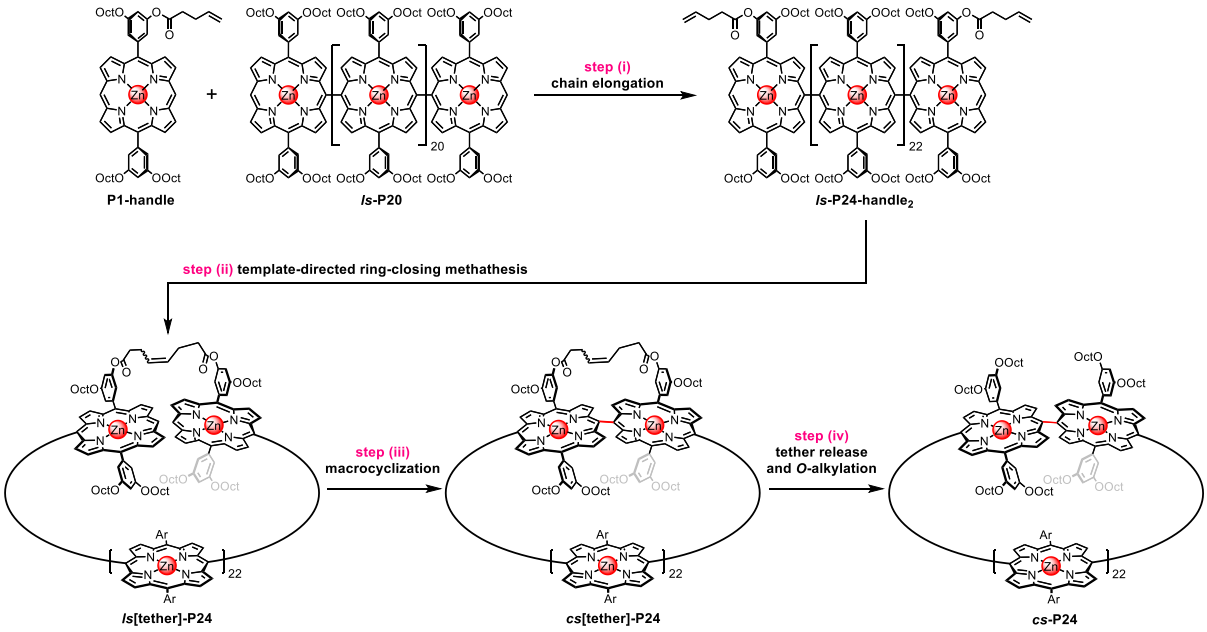

Figure 2.31: Proposed stepwise template-directed synthesis of ***cs*-P24**.

A more challenging target is to prepare the fully fused porphyrin nanobelts ***cf*-P*N***, because the 3,5-bis(octyloxy)-phenyl solubilizing groups chosen for synthesis of ***cs*-P*N*** might not provide enough solubility for ***cf*-P*N***, and thus it might require highly soluble side chains, such as the 3,5-bis(trihexylsilyl)-phenyl solubilizing groups. As discussed before, the bulky side chains could hinder the metal-ligand coordination in bending the *meso–meso* singly-linked porphyrin oligomers. Accordingly, a plausible solution is to bend the fused porphyrin oligomers ***lf*-P*N*** rather than the *meso–meso* linked oligomers ***ls*-P*N***, because for large systems, the estimated strain difference between ***cf*-P*N*** and ***cs*-P*N*** is subtle (~2 kJ mol^{-1} for systems that consist of 24 porphyrin units).

3

Charge Transport Through Fused Porphyrin Oligomers Linked to Gold Electrodes via Covalent C–Au Bond

3.1 Introduction 86

3.1.1 STM Break Junctions 86

3.1.2 Charge Transport 88

3.1.3 Anchor Group 89

3.1.4 Project Aim 90

3.2 Effect of End Capping Group on Formation of Au–C Contact 91

3.2.1 Syntheses of porphyrin monomers with different end capping groups 91

3.2.2 STM Break-Junction Study 93

3.3 Synthesis and Characterization of *lf*-NiP*N*-TMS$_2$ 95

3.3.1 Synthesis of *ls*-ZnP*N* 95

3.3.2 Synthesis of *lf*-NiP*N*-TMS$_2$ 96

3.3.3 ^{1}H NMR Spectroscopy and Mass Spectrometry 98

3.3.4 UV–vis–NIR Absorption Spectra 99

3.4 Single-Molecule Conductance for *lf*-NiP*N*-TMS$_2$ 101

3.5 Conclusion 105

3.1 Introduction

Single-molecule electronics is a field of science which attempts to use individual molecules as building blocks to fabricate electronic devices.[29,42,222] One of the enduring challenges in the field is to design and synthesize molecular wires that can mediate efficient charge transport over a distance of several nanometers.[223,224] As discussed in Chapter 1, previous studies demonstrate that fused porphyrin oligomers, up to a trimer, serving as molecular bridges in single-molecule junctions, can mediate coherent charge transport with low attenuation of conductance.[63,75] In this chapter, we explore the synthesis of long porphyrin tapes (up to an octamer with ~8 nm in length), and investigate the charge transport through these molecules using the scanning tunneling microscope break-junction (STM-BJ) technique by wiring the molecules to gold electrodes via C–Au linkage. The goal is to use fused porphyrin oligomers as molecular wires to achieve long and highly conducting single-molecule junctions by combining a molecule with a low attenuation factor with anchor groups that achieve a low contact resistance.

3.1.1 STM Break Junctions

Break-junction experiments have been intensively used to measure single-molecule conductance. There are two main break-junction techniques: mechanical break junctions, such as STM break junctions (STM-BJs)[225,226] and mechanically controlled break junctions (MCBJs),[227,228] and electrical break junctions created by electromigration or electroburning,[229] such as the graphene nanogaps that will be discussed in Chapter 4.[230] In this chapter, we focus on STM-BJs with gold electrodes, which were first used to study single-molecule conductance by Tao and Xu in 2003.[225] Gold is widely used as electrode material in STM-BJ experiments because of its inertness — it does not form a natural oxide layer on exposure to air.[231]

In a typical STM-BJ experiment,[231,232] molecules are deposited onto the substrate at submonolayer coverage prior to the stretching cycle. A STM-BJ cycle starts with moving the tip toward the substrate (Figure 3.1a) until a sufficient contact, typically, a metal–metal contact, between tip and surface is made (Figure 3.1b). Afterwards, the tip is withdrawn from the substrate at a constant speed and a molecule is possibly be trapped between the tip and the substrate, forming a single-molecule junction (Figure 3.1c and 3.1d). Upon further stretching, the molecular junction ruptures and the stretching cycle ends (Figure 3.1e). During this period, the measured current I or conductance $G = I/V_{bias}$ is plotted as a function of the distance z travelled by the tip. The measured conductance G is higher than the conductance quantum G_0 (77.5 μS) when the STM tip is connected to the substrate, and it approaches to G_0 once the

atomic contact is reached. The measured G becomes lower than G_0 by pulling the tip away from the substrate. When no molecule is trapped in the junction, the charge transport is mediated by tunnelling through the medium, resulting in an exponential decay of the measured G. Once a molecule is trapped between the tip and the substrate, the charge transport through the molecular junction results in a conductance plateau until the junction ruptures by further stretching. The conductance decreases sharply as soon as the junction breaks. Two individual conductance plateaus from a STM-BJ measurement of porphyrin monomer **ZnP1-SAc** are shown in Figure 3.1g.[63] The thioacetate groups in **ZnP1-SAc** cleave to produce Au–S contacts to gold electrodes during the measurement (Figure 3.1f). For a typical STM-BJ measurement, the aforementioned stretching cycle is repeated hundreds to thousands of times, which allows a statistical analysis of the data to provide a general conductance profile of a compound. Figure 3.1h shows a 2D histogram generated from 1928 individual plateau-containing conductance traces of **ZnP1-SAc** measured at a fixed bias V_{bias} = 0.2 V.[63]

In addition to the fixed bias measurement, in the break-junction cycle, the tip retraction can be paused at several regular intervals to record the current–voltage (I–V) traces by sweeping the bias at a given rate and range. These I–V measurements reveal the voltage-dependent transport behaviors of the single-molecule junctions. For example, as discussed in Chapter 1, the values of the conductance attenuation factor β_C for both butadiyne-linked and fused porphyrin oligomers vary with the bias voltage applied in the measurement.[63]

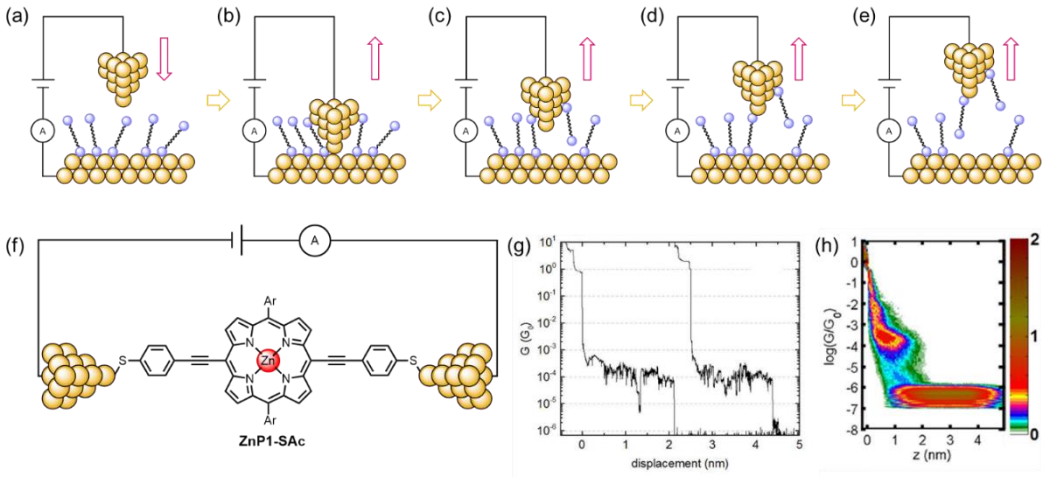

Figure 3.1: (a)–(e) Schematic of a break junction cycle in STM configuration.[232] (f) Schematic showing a zinc porphyrin monomer connected gold electrodes via S–Au linkage. Ar = 3,5-bis(octyloxy)phenyl solubilizing groups. (g) Two individual conductance plateaus, and (h) 2D histogram for the $G(z)$ measurements of **ZnP1-SAc**; V_{bias} = 0.2 V.[63] Figures (g) and (h) are reproduced with permission from ref. 63.

3.1.2 Charge Transport

In general, connecting molecules to gold electrodes via covalent bonds forms single-molecule junctions with intermediate molecule–electrode coupling (Figure 3.2a).[233,234] In this regime, at low-bias, charge transport through the junctions is mediated by off-resonant coherent tunneling (Figure 3.2b). When the charge transport is dominated by a single molecule level (e.g., the HOMO orbital as shown in Figure 3.2b), the conductance can be quantified using the Landauer–Büttiker model:[42,222,234,235]

$$G = G_0 \int_{-\infty}^{\infty} dE T(E)\big(f_S(E) - f_D(E)\big) \tag{3.1}$$

$$T(E) = \frac{4\Gamma_S\Gamma_D}{(E-\epsilon)^2+(\Gamma_S+\Gamma_d)^2} \tag{3.2}$$

in which $T(E)$ is the transmission function, $f_S(E)$ and $f_D(E)$ are the Fermi–Dirac functions, Γ_s and Γ_d describe the coupling to the source and drain electrodes, and ε is the energy of the molecular level, which may be shifted by coupling to the electrodes.

For off-resonant coherent charge transport, the measured conductance G decreases exponentially with transport distance, which can be described by the following empirical model:

$$G = A_0 e^{-\beta_c L} \tag{3.3}$$

where L represents the molecular length, A_0 in the case of direct molecule–electrode coupling can be denoted as a contact conductance, related to the effective contact resistance R_0 ($A_0 = 1/R_0$), and β is the conductance attenuation factor that describes the degree to which the conductance decays as the length of the wire is increased.[233,236]

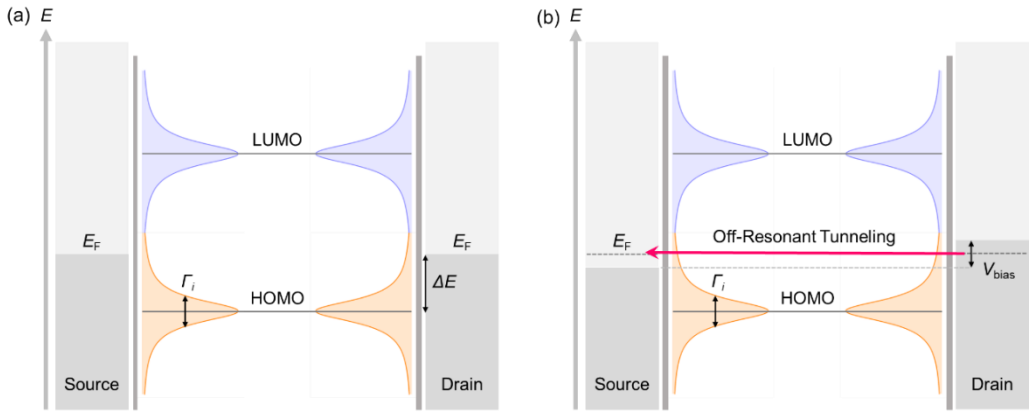

Figure 3.2: Chemical potential diagram showing a single-molecule junction in the intermediate molecule–electrode coupling regime in equilibrium (a) and at low bias (b). Upon application of bias, charge conducts through the junction via off-resonant coherent tunneling mechanism.

3.1.3 Anchor Group

In single-molecule junctions, anchor groups are handles that connect the molecular wires to the electrodes. As a linker between the electrode and the molecular backbone, the anchor group dictates the molecule–electrode coupling Γ and influences the energy alignment of the molecule ε in the junction.[34,231] In practice, the effect of anchor groups on the molecular conductance can be evaluated by comparing the measured conductance G or the estimated effective contact resistance A_0 of junctions using the same series of molecular bridge functionalized with a library of anchor groups.[237–240]

The contact between the anchor group and the electrode can be classified as non-covalent or covalent bonds. Anchor groups, such as pyridines,[241] amines,[242] thioethers,[240] and fullerenes,[243] connect to gold electrodes via donor–acceptor (non-covalent) interactions. Comparted with the non-covalent linkage, covalent contacts generally create relatively strong electronic coupling between the molecule and the electrode, leading to higher molecular conductance. Thiols readily form covalent Au–S contacts on gold surface through chemical adsorption, and thus they are extensively employed as anchors for break-junction measurements.[225] Connecting molecules to gold electrodes via covalent Au–C bond generally features higher single-molecule conductance than the analogous junctions with Au–S contacts.[244] Doerrer and coworkers first demonstrated the formation of Au–C contact in STM-BJ measurements, in which they found that the terminal end groups (H, TMS or $AuP(OMe)_3$) in 1,4-diethynylbenzenes cleave *in situ* to produce direct Au–acetylene linkages between the molecular bridge and the gold electrodes.[245] Later, Venkataraman, Breslow, Hybertsen and coworkers discovered that molecules equipped with $SnMe_3$ end groups can readily bond to gold electrodes after *in situ* cleavage of the organotin moieties.[239,246] Wandlowski and coworkers used tetrabutylammonium fluoride (TBAF) to deprotect the terminal TMS groups in oligo(phenylene ethynylene)s (OPEs) to yield single-molecule junctions with Au–C contacts.[244] They also discovered that these junctions exhibit extremely low effective contact resistance ($R_0 \sim 1/G_0$ = 12.9 kΩ), which is closed to a metallic Au–Au nanocontact. In comparison, OPEs connected to electrodes via Au–S bond results in estimated $R_0 \sim$ 40 kΩ. The high conductance of single-molecule junctions with Au–C contacts was also reported by Venkataraman and Akita.[246–248] Compared to Au–S bond and non-covalent linkages, the Au–C bond increases the molecule–electrode coupling Γ and shifts molecular energy level ε toward the electrode Fermi level E_F (i.e., $\Delta E = E_F - \varepsilon$ becomes smaller), and therefore increase the molecular conductance.[34]

3.1.4 Project Aim

In this chapter, we aim to create long and highly conducting single-molecule junctions using porphyrins as building blocks. In previous studies, porphyrins as molecular wires were attached to gold electrodes using pyridines or thiols as anchors, resulting in relatively low measured conductance for porphyrin monomer junctions (10^{-4} to 10^{-5} G_0). Given that the Au–C contact could minimize the contact resistance,[244–248] in this work, we plan to wire the molecular components into circuits by directly connect the alkyne handles on the porphyrins to the gold electrodes. Since the direct Au–C link has not yet been used in constructing porphyrin-based single molecule junction, we plan to use a family of porphyrin monomers with different capping groups at the termini of the alkyne handles to optimize the conditions for forming the single-molecule junctions (Figure 3.3a). After that, the optimal model system will be extended to create junctions with longer molecular bridges.

Fused porphyrin oligomers ***lf*-P*N*** that exhibit minimal (or reverse) length-dependent conductance decay are promising bridging units.[63,75] Despite their promising properties, there have been few previous reports of charge transport studies on fused porphyrin tapes longer than a trimer (about 4 nm in length).[63,75,86,87] Additionally, the reported structures that have been well-characterized (by NMR spectroscopy or mass spectrometry) are limited to $N = 4$, probably because the longer oligomers are less soluble or chemically unstable.[71,80,250] In this chapter, we aim to explore the synthesis of well-characterized fused porphyrin oligomers ***lf*-NiP*N*** up to an octamer (about 8 nm in length). Nickel was inserted as the metal center to facilitate the synthesis and to reduce the energy of the HOMO, thus enhancing the chemical stability of the long oligomers. After the synthesis, the molecular conductance of these oligomers will be measured by STM-BJ technique, where the molecules are connected to electrodes by Au–C bond (Figure 3.3b).

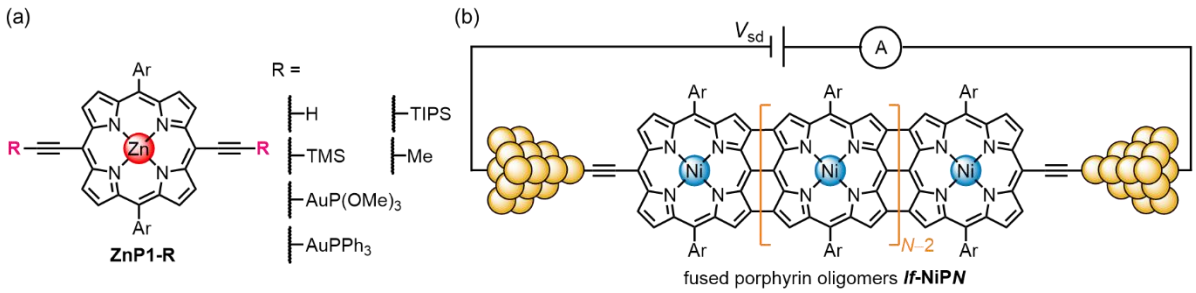

Figure 3.3: (a) Porphyrin monomer **ZnP1-R** with different end capping groups as model compounds for evaluation of forming the molecular junctions with direct Au–C contacts. (b) Single molecular junctions of fused porphyrin oligomers ***lf*-NiP*N*** bonded to gold electrodes.

3.2 Effect of End Capping Group on Formation of Au–C Contact

3.2.1 Syntheses of porphyrin monomers with different end capping groups

To achieve a direct Au–C link and evaluate the effectiveness of junction formation, we designed and prepared a family of six porphyrin monomers **ZnP1-R$_2$** with various end capping groups attached to the molecular backbones for comparison. Compounds **ZnP1-H$_2$**, **ZnP1-TMS$_2$** and **ZnP1-(AuP(OMe)$_3$)$_2$** were expected to form single-molecular junctions in the break-junction measurement, because these end capping groups (H, trimethyl silyl (TMS) and AuP(OMe)$_3$) have been examined by the other groups to produce molecular junctions with Au–C contacts.[244,245,247] **ZnP1-(AuPPh$_3$)$_2$** might give a low yield of the junction formation because the relatively steric bulkiness of the phosphorous ligand PPh$_3$ (compared to P(OMe)$_3$) may hinder the formation of a molecular junction. **ZnP1-TIPS$_2$** with bulky triisopropylsilyl (TIPS) group and **ZnP1-Me$_2$** are used as reference molecules because the end capping groups were expected to prevent the junction formation.

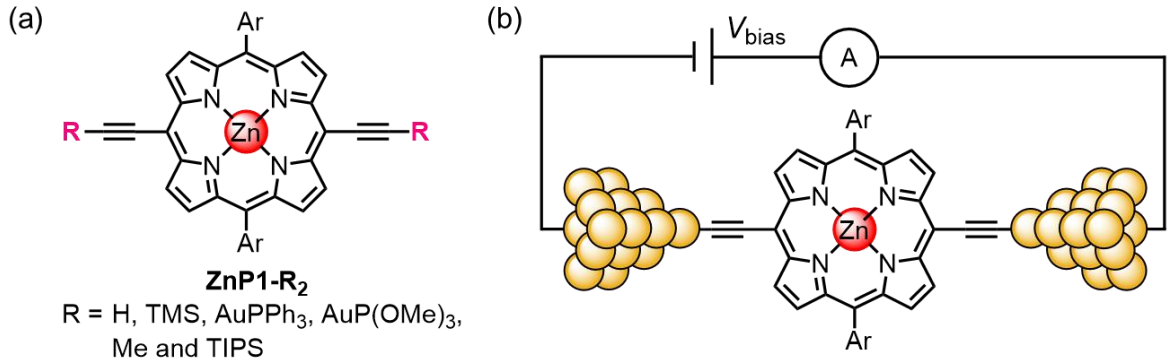

Figure 3.4: (a) Chemical structures of **ZnP1-R$_2$** (R = H, TMS, AuPPh$_3$, AuP(OMe)$_3$, Me and TIPS); Ar = 3,5-bis(tert-butyl)phenyl solubilizing group. (b) Schematic showing a porphyrin monomer bonded to gold electrodes via direct Au–C contacts.

The synthetic routes for **ZnP1-R$_2$** are summarized in Figure 3.5 (see Appendix C, Section C.2 for detailed synthetic procedures and characterization data). **ZnP1-TMS$_2$** (76%) and **ZnP1-TIPS$_2$** (96%) were readily prepared by Sonogashira coupling reactions using **ZnP1-Br$_2$** and different acetylenes. **ZnP1-H$_2$** (98%) was afforded by TBAF-mediated deprotection of trihexylsilyl (THS) groups on **ZnP1-THS$_2$**. Treatment of **ZnP1-H$_2$** with sodium methoxide and different gold complexes (Ph$_3$PAuCl and (MeO)$_3$PAuCl) in THF/CH$_3$OH (1:1) yielded **ZnP1-(AuPPh$_3$)$_2$** (83%) and **ZnP1-(AuP(OMe)$_3$)$_2$** (53%), respectively. For synthesis of **ZnP1-(AuP(OMe)$_3$)$_2$**, the progress was monitored by collecting and comparing the ^{1}H NMR spectrum of the reaction mixture at different time points of the reaction, which showed that it

required a prolonged reaction time (about 5 days) to achieve full conversion of **ZnP1-H$_2$**. **ZnP1-Me$_2$** (83%) was synthesized by treatment of **ZnP1-H$_2$** with lithium bis(trimethylsilyl)amide (LiHMDS), followed by addition of iodomethane.

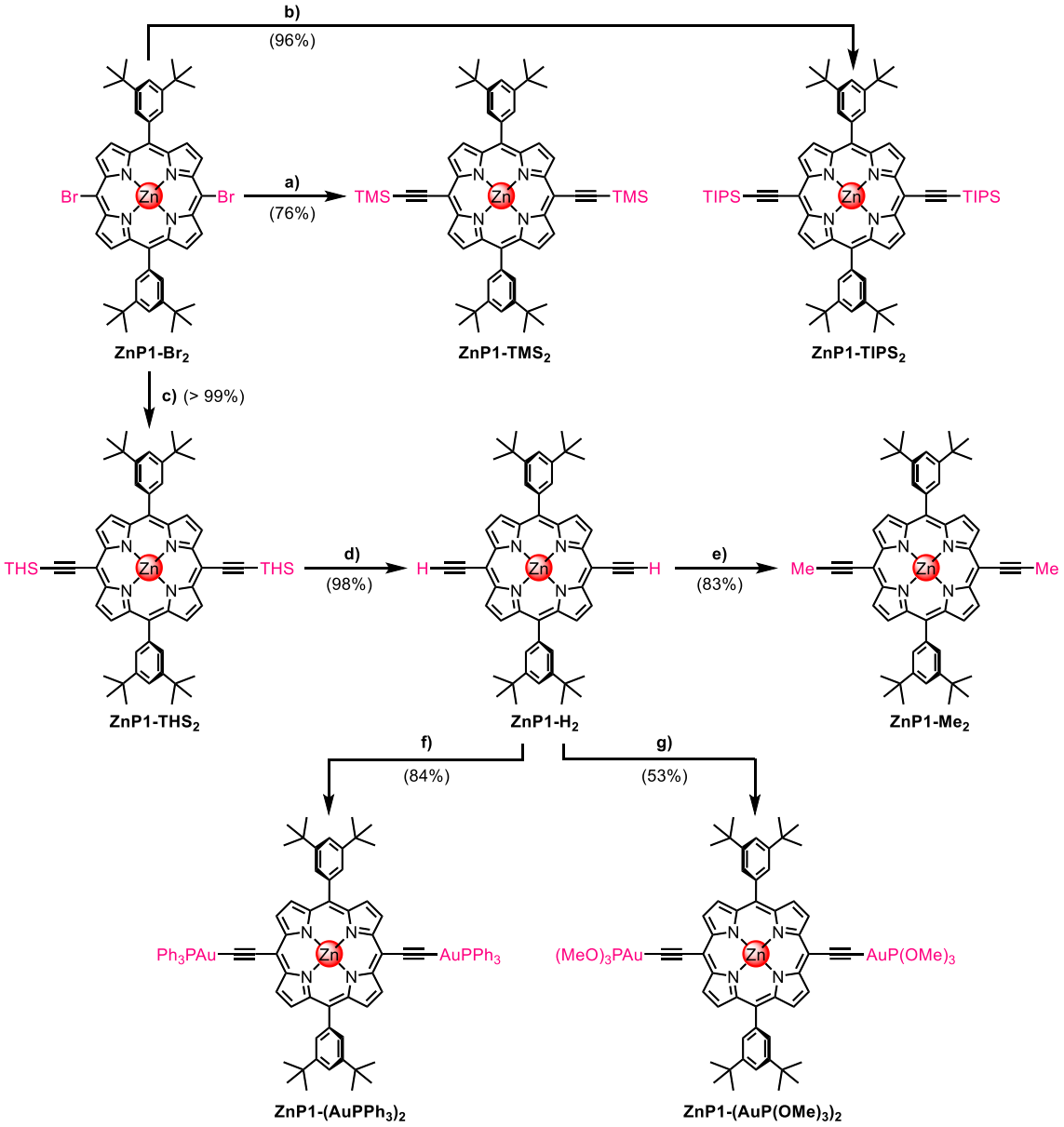

Figure 3.5: Syntheses of **ZnP1-R$_2$**. Conditions: (a) TMS-acetylene, Pd_2dba_3, CuI, PPh_3, DIPA/toluene (1:2), 50 ºC, 3h; (b) TIPS-acetylene, Pd_2dba_3, CuI, PPh_3, DIPA/toluene (1:2), 50 ºC, 3h; (c) THS-acetylene, Pd_2dba_3, CuI, PPh_3, DIPA/toluene (1:2), 50 ºC, 3h; (d) TBAF, CH_2Cl_2, 25 ºC, 15 min; (e) LiHMDS, THF, 25 ºC, 10 min; then CH_3I, 25 ºC, 1 h; (f) Ph_3PAuCl, CH_3ONa, THF/CH_3OH (1:1), 25 ºC, 24 h; (g) $(MeO)_3PAuCl$, CH_3ONa, THF/CH_3OH (1:1), 25 ºC, 5 d.

3.2.2 STM Break-Junction Study[†]

The single-molecule conductance for each porphyrin monomer, **ZnP1-R$_2$** (R = H, TMS, AuPPh$_3$, AuP(OMe)$_3$, Me and TIPS), was measured using the STM-BJ method.[63] In each experiment, the sample with molecules deposited on a gold surface was prepared by placing a gold substrate in a dichloromethane solution (2 mL) containing 0.5 mg of the relevant compound for 20 min. After that, the sample was briefly dried under N_2 before the measurement. All measurements were carried out under ambient condition, with a tip-sample bias of 0.2 V. The break-junction results are summarized in Figure 3.6.

Plateau-containing traces were clearly identified for four compounds (R = H, TMS, AuPPh$_3$ and AuP(OMe)$_3$; Figure 3.6a–f). The overall percentage of traces with plateaus ranges from 8.9% to 26.8%. All of these compounds exhibit a conductance peak at about 10^{-2} G_0, which is typically higher than the measured conductance for a porphyrin monomer connected to gold electrodes using pyridine ($10^{-4.7}$ G_0)[75] or thiol ($10^{-3.7}$ G_0)[63] anchor groups. The extracted "plateaus" for **ZnP1-Me$_2$** resembles the tunneling-only traces, indicating that typical molecular junctions are not formed in the measurement (Figure 3.6g). This observation is basically the same for **ZnP1-TIPS$_2$** (Figure 3.6h), where very few of plateaus at 10^{-2} G_0 were observed. These findings suggest that, for the compounds exhibiting plateau-containing traces, the terminal capping groups on the alkyne termini cleaved *in situ*, allowing the molecules to bond to the gold electrodes via direct Au–C link (Figure 3.6b). For reference compound **ZnP1-Me$_2$**, the methyl groups are strongly bonded to the terminal alkynes, which thus prevents the junction formation. For **ZnP1-TIPS$_2$**, the junction formation is probably hindered by steric bulky TIPS group, implying the *in situ* cleavage of the Au–Si bond might require a contact between the gold electrode and the alkyne moiety.

There is no significant difference of the junction formation probability between **ZnP1-(AuPPh$_3$)$_2$** and **ZnP1-(AuP(OMe)$_3$)$_2$** in our study. This contrasts with Doerrer's observation, where no molecular junction was achieved in conductance measurement of 1,4-diethynylbenzene with AuPPh$_3$ as end capping group.[246] A more interesting finding from our study is that the effectiveness of the junction formation using **ZnP1-TMS$_2$** is comparable to that using **ZnP1-H$_2$**, **ZnP1-(AuPPh$_3$)$_2$** or **ZnP1-(AuP(OMe)$_3$)$_2$**, implying deprotection or transmetalation step is not necessary for forming Au–C(sp) contact. This is an important

[†] All STM break-junction measurements in this chapter were performed and analyzed by Dr. Edmund Leary (IMDEA Nanoscience Institute, Spain).

discovery, because for porphyrin oligomers (e.g., butadiyne-linked or fused porphyrin oligomers), the silyl end capping groups strongly improve the stability of the molecules, and preparation of the organometallic gold species may be complicated. Given that highly conductive single-molecule junctions (~10^{-2} G_0) can be achieved by using **ZnP1-TMS$_2$**, in the rest of this chapter, we employ this compound as an archetype to build up long molecular wires that involve fused porphyrin oligomers as molecular bridges.

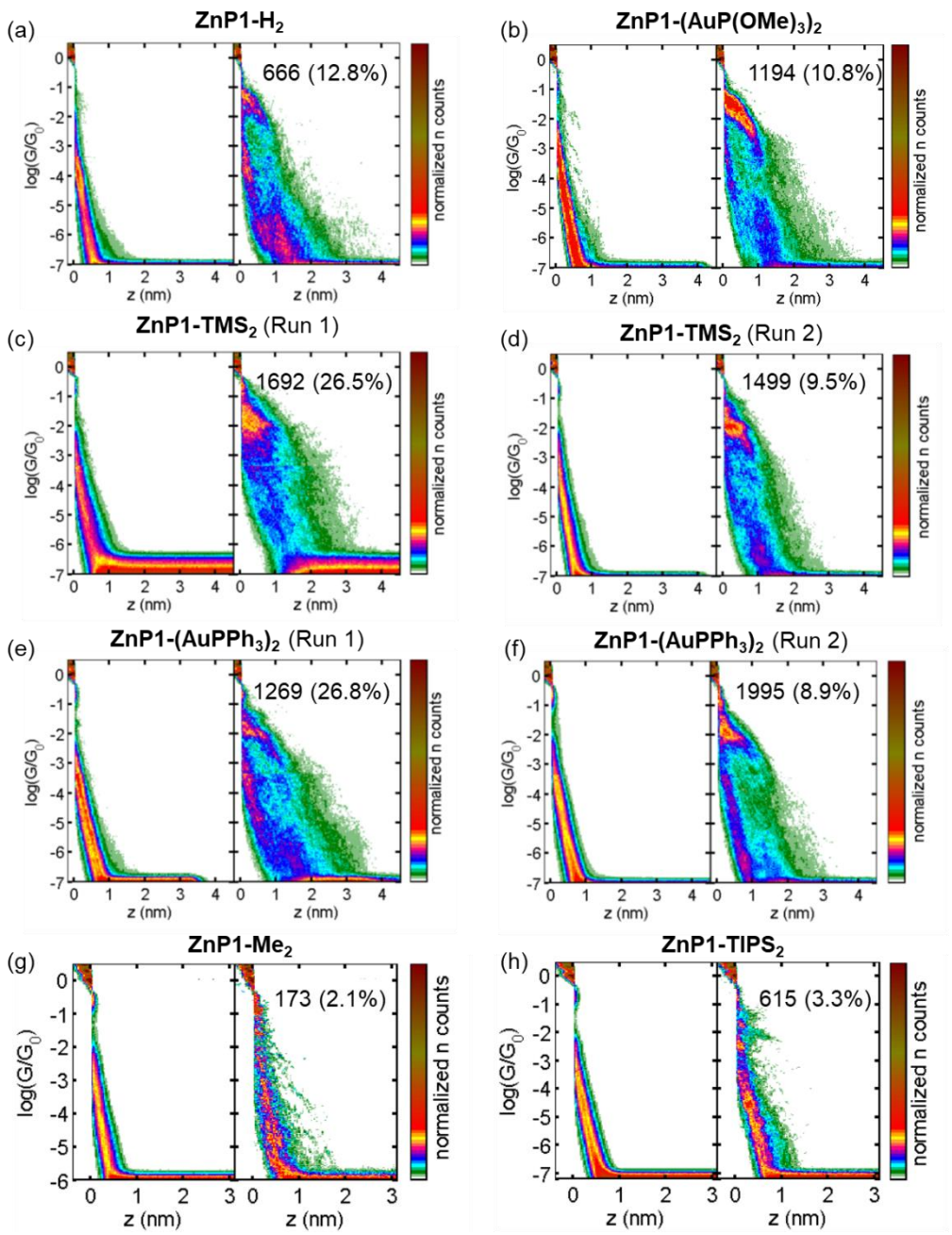

Figure 3.5: (a)–(h) 2D histograms for tunneling-only (left) and plateau-containing (right) traces for **ZnP1-R$_2$**. Inserts depict the number of junction (percentage of traces with plateaus) for each compound (or run). Data were recorded and analyzed by Dr. Edmund Leary.

3.3 Synthesis and Characterization of *lf*-NiP*N*-TMS$_2$

3.3.1 Synthesis of *ls*-ZnP*N*

To prepare fused porphyrin oligomers ***lf*-NiP*N*-TMS$_2$**, the first step is to oligomerize the porphyrin monomer **ZnP1** to make *meso–meso* singly-linked porphyrin oligomers ***ls*-ZnP*N***. Bulky 3,5-bis(trihexylsilyl)phenyl solubilizing groups were chosen to improve the solubility of the oligomers. In Chapter 2, we used PIFA-mediated oxidative coupling to oligomerize the porphyrin monomer bearing 3,5-bis(octyloxy)phenyl solubilizing groups. However, the same reaction conditions failed to yield singly-linked porphyrin oligomers ***ls*-ZnP*N*** with 3,5-bis(trihexylsilyl)phenyl solubilizing groups.

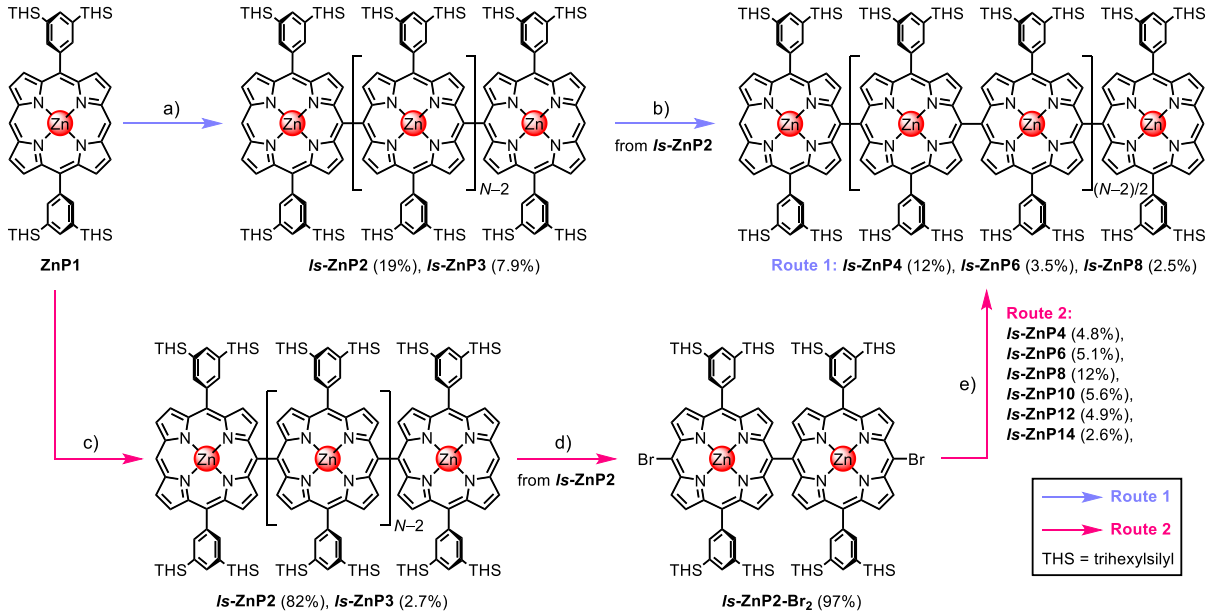

Figure 3.7: Synthesis of ***ls*-ZnP*N***. Route 1: (a) $AgPF_6$, $CHCl_3$, reflux, 2 d; (b) $AgPF_6$, $CHCl_3$, reflux, 6 d. Route 2: (c) Ag[Al(pftb)$_4$] (pftb = perfluoro-*tert*-butoxy), $CHCl_3$, 25 ºC, 30 min; (d) *N*-bromosuccinimide (NBS), $CHCl_3$, 0 ºC, 5 min; (e) Ni(COD)$_2$ (COD = 1,5-cyclooctadiene), DMF, 50 ºC, 24 h.

We tried to optimize the Ag(I)-mediated oligomerization conditions to build up ***ls*-ZnP*N*** (Route 1 in Figure 3.7; $AgPF_6$ was used as oxidant). The initial trials using conditions reported by Osuka and coworkers gave poor conversion of the monomer.[79] Keeping the reaction at reflux for a prolonged period (2 days) slowly improved the conversion, giving ***ls*-ZnP2** (19%) and ***ls*-ZnP3** (7.9%) in moderate yields. Oligomerization of ***ls*-ZnP2** to afford longer oligomers using the same method is more challenging. ***ls*-ZnP4** (12%), ***ls*-ZnP6** (3.5%) and ***ls*-ZnP8** (2.5%) were isolated after heating the mixture of ***ls*-ZnP2** and $AgPF_6$ (36 equiv.) at reflux for

6 days, and this reaction was difficult to reproduce. The poor conversion and yield found for this reaction arises from the steric bulkiness of the 3,5-bis(trihexylsilyl)phenyl solubilizing groups, which hinders the coupling between two monomers (or oligomers). We found that porphyrin monomer **ZnP1$_{Oct}$** with less bulky 3,5-bis(octyloxy)phenyl solubilizing groups oligomerized smoothly at 25 ºC — the analytical GPC trace of the crude reaction mixture (after 1 day) is similar to Figure 2.8b in Chapter 2. The influence of the steric bulkiness of the side chains on the coupling efficiency was also observed by Osuka and coworkers.[80,192]

We sought to explore other methods to prepare the oligomers (Route 2 in Figrue 3.7). It was found that using the Ag[Al(pftb)$_4$] salt[198] as oxidant significantly improved the coupling efficiency in preparation of ***ls*-ZnP2**. The oligomerization proceeded smoothly at 25 ºC, in gram scale, giving ***ls*-ZnP2** in > 80% yield within 30 min. Although this reaction failed to yield longer oligomers (N > 4), we found that long oligomers ***ls*-ZnP*N*** could be afforded by Ni-mediated Yamamoto coupling of ***ls*-ZnP2-Br$_2$** that was readily prepared by bromination of ***ls*-ZnP2**. Using Ni(COD)$_2$ (3 equiv.) as catalyst and sacrificial reductant, oligomers ***ls*-ZnP4** (4.8%), ***ls*-ZnP6** (5.1%), ***ls*-ZnP8** (12%), ***ls*-ZnP10** (5.6%), ***ls*-ZnP12** (4.9%) and ***ls*-ZnP14** (2.6%) were isolated by recycling GPC. Zinc porphyrins were chosen for the oligomerization because they gave higher yields in Yamamoto coupling reaction, comparted to the nickel complexes.

3.3.2 Synthesis of *lf*-NiP*N*-TMS$_2$

With the *meso–meso* singly-linked oligomers ***ls*-ZnP*N*** in hand, the next step is to prepare the fused porphyrin oligomers (Figure 3.8). Bromination of the terminal *meso* positions of ***ls*-ZnP*N*-Br$_2$** allows functionalization with TMS-acetylene in the last step of the synthesis. However, it is difficult directly convert ***ls*-ZnP*N*-Br$_2$** to ***lf*-ZnP*N*-Br$_2$** by oxidative fusion reactions.[75,251,252] It was reported that using $AuCl_3$ as oxidant, a dibrominated *meso–meso* singly-linked nickel porphyrin dimer was readily converted to become a fused dimer.[72] We thus employed this strategy to synthesize ***ls*-NiP*N*-Br$_2$**. Oligomers ***ls*-ZnP*N*** (N = 2, 4, 6 and 8) were converted to ***ls*-NiP*N*-Br$_2$** after bromination and demetalation, followed by insertion of the nickel ions. The nickel complexes ***ls*-NiP*N*-Br$_2$** were then treated with $AuCl_3$/AgOTf at ambient condition (25 ºC, under air) to give fused porphyrin oligomers ***lf*-NiP2-Br$_2$** (83%), ***lf*-NiP4-Br$_2$** (55%), ***lf*-NiP6-Br$_2$** (27%) and ***lf*-NiP8-Br$_2$** (50%). It is of importance to use UV–vis–NIR absorption spectroscopy to monitor the reaction progress, because an incomplete oxidative fusion reaction gives undesired partially fused product, while addition of excess $AuCl_3$ may chlorinate the desired fused oligomer. After the oxidative fusions, in the last step,

Pd-catalyzed coupling of each fused oligomers with TMS-acetylene resulted in ***lf*-NiP2-TMS$_2$** (86%), ***lf*-NiP4-TMS$_2$** (82%), ***lf*-NiP6-TMS$_2$** (57%) and ***lf*-NiP8-TMS$_2$** (42%). In addition to the fused porphyrin oligomers, a corresponding monomer **NiP1-TMS$_2$** was also prepared following a similar synthetic route.

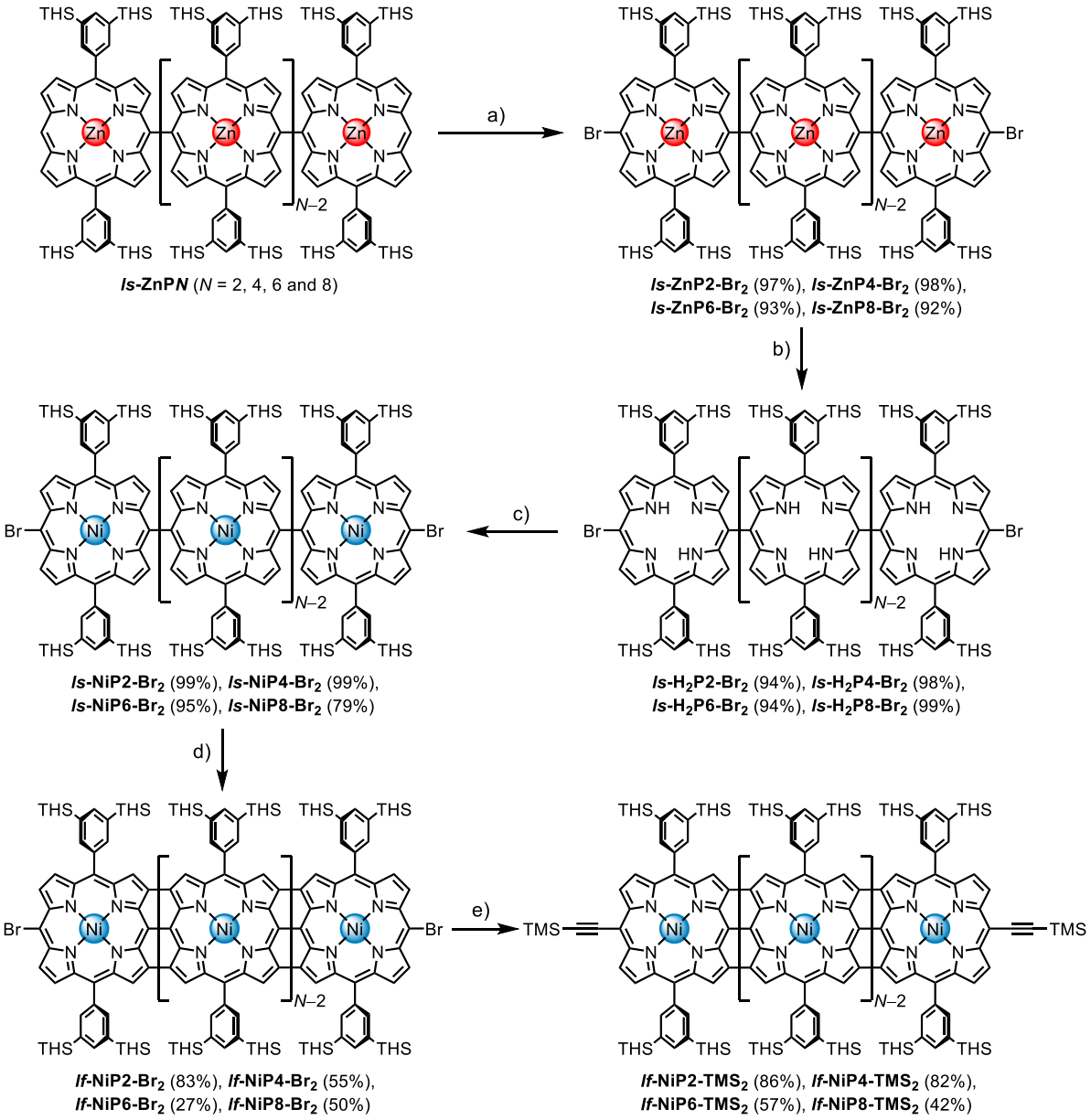

Figure 3.8: Synthesis of ***lf*-NiP*N*-TMS$_2$**. Conditions: (a) NBS, $CHCl_3$, 0 ºC, 5 min; (b) trifluoroacetic acid (TFA), 0 ºC, 5 min; (c) $Ni(acac)_2$ (acac = acetylacetonate), 1,3-xylene, 130 ºC, 2 h; (d) $AuCl_3$, AgOTf (OTf = trifluoromethanesulfonate), 1,2-dichloroethane (DCE), 25 ºC, 15 min; (e) TMS-acetylene, $Pd(PPh_3)_4$, CuI, DIPA/toluene (1:1), 50 ºC, 2–3 h.

3.3.3 ^{1}H NMR Spectroscopy and Mass Spectrometry

The fused porphyrin oligomers ***lf*-NiP*N*-TMS$_2$** were fully characterized by ^{1}H NMR Spectroscopy and MALDI-ToF mass spectrometry. The molecular ion peak of each oligomer observed from its mass spectrum matches the calculated value. For instance, molecular ion peaks at *m*/*z* = 10060 and 13348 were found for ***lf*-NiP6-TMS$_2$** (calc. for $C_{634}H_{1018}N_{24}Ni_6Si_{26}$: 10059) and ***lf*-NiP8-TMS$_2$** (cal. for $C_{842}H_{1350}N_{32}Ni_8Si_{34}$: 13345), respectively (Figure C.34 and C.35 in Appendix C).

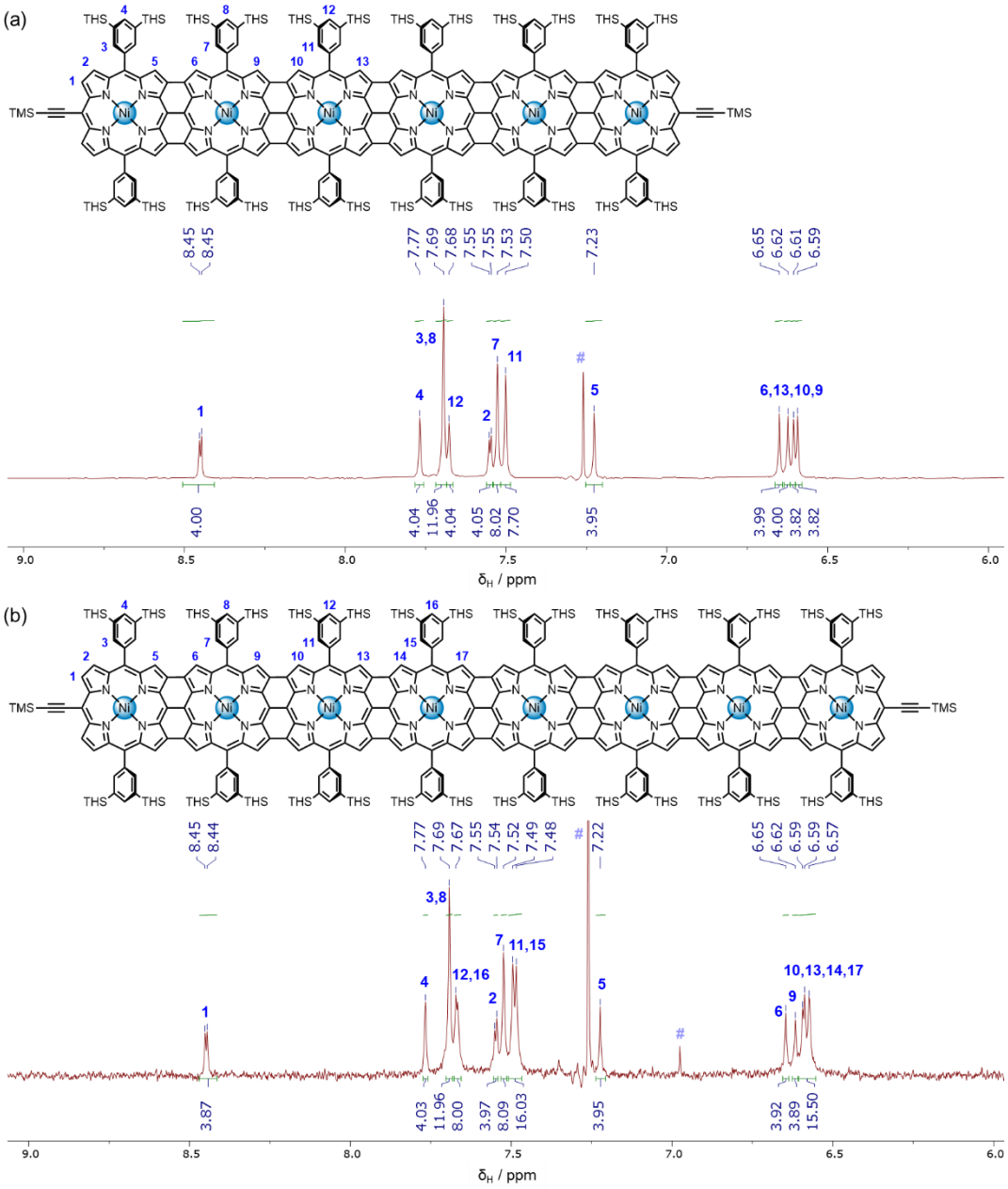

Figure 3.9: Chemical structures and selected sections of diffusion edited ^{1}H NMR spectra (700 MHz, $CDCl_3$, 298 K) of ***lf*-NiP6-TMS$_2$** and ***lf*-NiP6-TMS$_2$**. # = $CHCl_3$.

Selected regions of diffusion edited ^{1}H NMR spectra of ***lf*-NiP6-TMS$_2$** and ***lf*-NiP8-TMS$_2$** are shown in Figure 3.9. The ^{1}H NMR signals are satisfactorily resolved and most of ^{1}H NMR resonances can be unambiguously assigned based on comparison between the whole series of compounds and analysis of the ^{1}H-^{1}H correlations observed from the COSY and NOESY spectra. All ^{1}H resonances of the β protons on the fused porphyrin oligomers are shielded compared to the *meso–meso* singly-linked oligomers, especially for the β protons on the central porphyrin units that exhibit singlet ^{1}H NMR signals at δ_H = 6.5–7.0 ppm (see Appendix C, Section C.4 for ^{1}H NMR data of the singly-linked oligomers ***ls*-NiP*N*-Br$_2$**). This can be rationalized by the weaker aromatic character of the fused porphyrins, and by the paratropic ring current contributed from the central naphthalene unit.[253–259]

Fused porphyrin hexamers and octamers have not previously been characterized by ^{1}H NMR and mass spectra.[71,80,250] The fused oligomers bearing the trihexylsilyl side chains are highly soluble in organic solvents, such as $CHCl_3$, and incorporation of the nickel as the metal centers makes them less susceptible to oxidation by lowering their HOMO energies.

3.3.4 UV–vis–NIR Absorption Spectra

The UV–vis–NIR absorption spectra of the whole set of compounds ***lf*-NiP*N*-TMS$_2$** (N = 1, 2, 4, 6 and 8), measured in $CHCl_3$ at 298 K, are shown in Figure 3.10a. The absorption spectra of fused oligomers exhibit three typical bands, which are labeled as band I, II and III,[35,50] arising from the B_y, B_x and Q_x transitions of a porphyrin monomer, respectively (see Table 3.1 for the peak wavelengths λ_{abs} and molar extinction coefficients ε for each compound). For band I, the peak wavelengths exhibit small hypsochromic shifts by increasing the length of the oligomers (until N = 6), reflecting the influence of the terminal alkyne moieties to the λ_{abs} diminishes for long oligomers. Band II and band III progressively shift to lower energy regions with an increase of the number of porphyrin unit. Band III, according to previous studies, is mainly contributed from the HOMO → LUMO transition.[81] Thus, the progressively red-shifted absorption band III indicates that the optical gaps $E_{g,opt}$ for the fused porphyrin oligomers are continuously narrowing with an increase of the molecular length.

We used the free-electron model (one particle in a box model) to analyze this progressively band shifts with chain length. The free-electron model considers the whole molecule structure as a one-dimensional potential box with an infinite barrier height. The potential energy is zero inside the box and abruptly reaches infinity at the boundary. The energy levels are given as:

$$E_n = \frac{h^2}{8mL^2} n^2 \tag{3.1}$$

where n is the number of π-electrons that scales with the length of the molecule, h is the Planck constant, m is the mass of the electron, and L is the width of the box. In practice, the HOMO–LUMO gap E_g for each oligomer was plotted against $1/N$ (N is number of the repeating unit), and the plots were fitted to the following expression,

$$E_g = a + b\frac{1}{N} + c\frac{1}{N^2} \tag{3.2}$$

where a, b and c are fitting parameters; the intercept a can be regarded as $E_{g,\infty}$, the HOMO–LUMO gap for the infinitely long oligomers (see ref. 260 for the derivation of eqn. 3.2 from eqn. 3.1). The trendline (orange line in Figure 3.10b) implies the optical gap $E_{g,opt}$ decreases steeply with length for the fused porphyrin oligomers. We have also calculated the HOMO–LUMO gaps ($E_{g,DFT}$) for these oligomers by DFT and the excitation energies ($E_{g,TD\text{-}DFT}$) by TD-DFT at B3LYP/6-31G* level of theory (see Table 3.1 for the calculated values). TD-DFT calculations predicted that the $S_0 \rightarrow S_1$ transitions in all oligomers are dipole-forbidden, whereas the excitation energies for the $S_0 \rightarrow S_2$ transition (dominated by the HOMO → LUMO transition) match the values of $E_{g,opt}$ estimated from the experimental absorption spectra. The $E_{g,DFT}$ (or $E_{g,TD\text{-}DFT}$) decreases with length following a similar trend to the $E_{g,opt}$ (light blue line in Figure 3.10b). Both the experimental and calculated energy gaps suggest the ***lf*-NiP*N*-TMS$_2$** are strongly π-conjugated, without reaching saturation at N = 8. This feature also makes them exciting candidates as molecular wires that potentially exhibit weakly length-dependent attenuation of the molecular conductance.

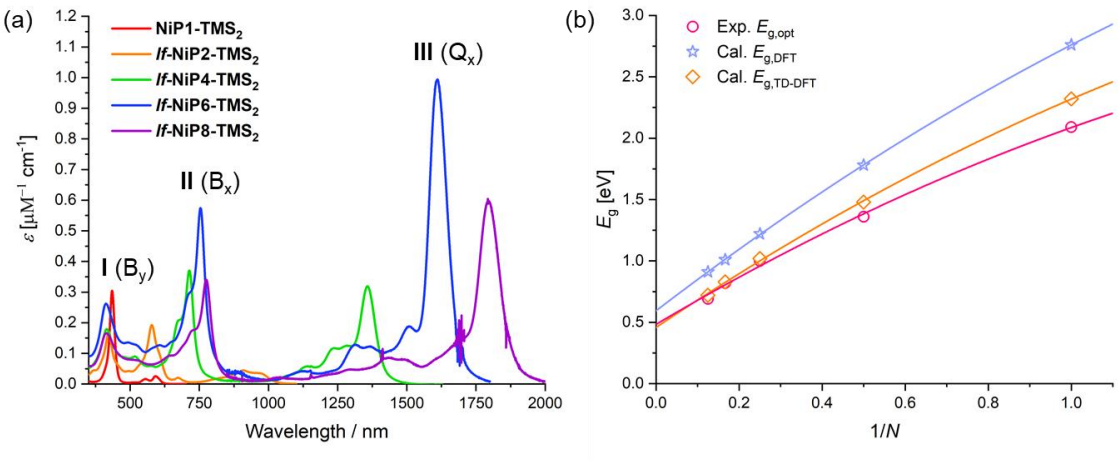

Figure 3.10: (a) UV–vis–NIR absorption spectra of ***lf*-NiP*N*-TMS$_2$**. (b) Plots of experimental and calculated HOMO–LUMO gaps (or excitation energies) vs $1/N$. The lines show the fits to the free-electron model (eqn. 3.2).

Table 3.1: UV–vis–NIR absorption properties[a] and HOMO–LUMO gaps for ***lf*-NiP*N*-TMS$_2$**.

Species	**NiP1-TMS$_2$**	***lf*-NiP2-TMS$_2$**	***lf*-NiP4-TMS$_2$**	***lf*-NiP6-TMS$_2$**	***lf*-NiP8-TMS$_2$**
Band I [nm]	435	423	416	413	413
(ε [μM^{-1} cm^{-1}])	(0.30)	(0.17)	(0.18)	(0.26)	(0.17)
Band II [nm]	—	581	714	754	775
(ε [μM^{-1} cm^{-1}])		(0.19)	(0.37)	(0.58)	(0.34)
Band III [nm]	555, 592	913	1365	1610	1791
(ε [μM^{-1} cm^{-1}])	(0.02, 0.03)	(0.11)	(0.31)	(1.00)	(0.59)
$E_{g,opt}$ [eV][b]	2.23, 2.09	1.36	1.00	0.82	0.69
$E_{g,DFT}$ [eV][c]	2.76	1.78	1.22	1.01	0.91
$E_{g,TD\text{-}DFT}$ [eV][d]	2.34, 2.32	1.48	1.02	0.83	0.72

[a] Measurements were performed in $CHCl_3$ at 298 K. [b] HOMO–LUMO gaps (optical gaps) estimated from the peak wavelength of band III (the lowest-energy absorption band). [c] HOMO–LUMO gaps calculated from DFT at B3LYP/6-31G* level of theory. [d] TD-DFT excitation energies (for the lowest-energy absorption band) calculated at B3LYP/6-31G* level of theory using the PCM solvent model ($CHCl_3$). In DFT and TD-DFT calculations, the trimethylsilyl groups on the molecules were replaced by hydrogen to simplify the calculation.

3.4 Single-Molecule Conductance for *lf*-NiP*N*-TMS$_2$

The single-molecule conductance for the whole series of compounds ***lf*-NiP*N*-TMS$_2$** (N = 1, 2, 4, 6 and 8) were measured using the STM-BJ technique. The measured conductance (G) vs distance (z) traces were separated using data-clustering algorithms. The longest plateau groups for the fixed bias $G(z)$ measurements (V_{bias} = 0.2 V) were plotted in Figure 3.11a and 3.11c. The all plateau data are summarized in Figure 3.11b.

The plateau-containing traces reflect that the TMS end capping groups on the oligomers cleaved *in situ*, which enabled formation of the molecular junctions with Au–acetylene contacts. As shown in the 2D conductance histograms (Figure 3.11a), the plateaus become longer for each progressive compound (from N = 1 to N = 8), although those for the long oligomers do not all reach the expected distance for the junction. Several groups of plateaus are observed from the 2D conductance histograms for monomer and dimer, ranging from $10^{-1.5}$ to $10^{-3.5}$ G_0. The plateaus for long oligomers (N = 4, 6 and 8) express broader conductance range (10^{-2} to $10^{-5.5}$ G_0). The 1D conductance histograms (Figure 3.11b and 3.11c) show that the molecular conductance for monomer and dimer are similar (estimated from the peak positions), while the conductance becomes lower from the tetramer (N = 4) — the most probable conductance is about 10^{-3} G_0 for the tetramer and $10^{-4.5}$ G_0 for the octamer (Figure 3.11c).

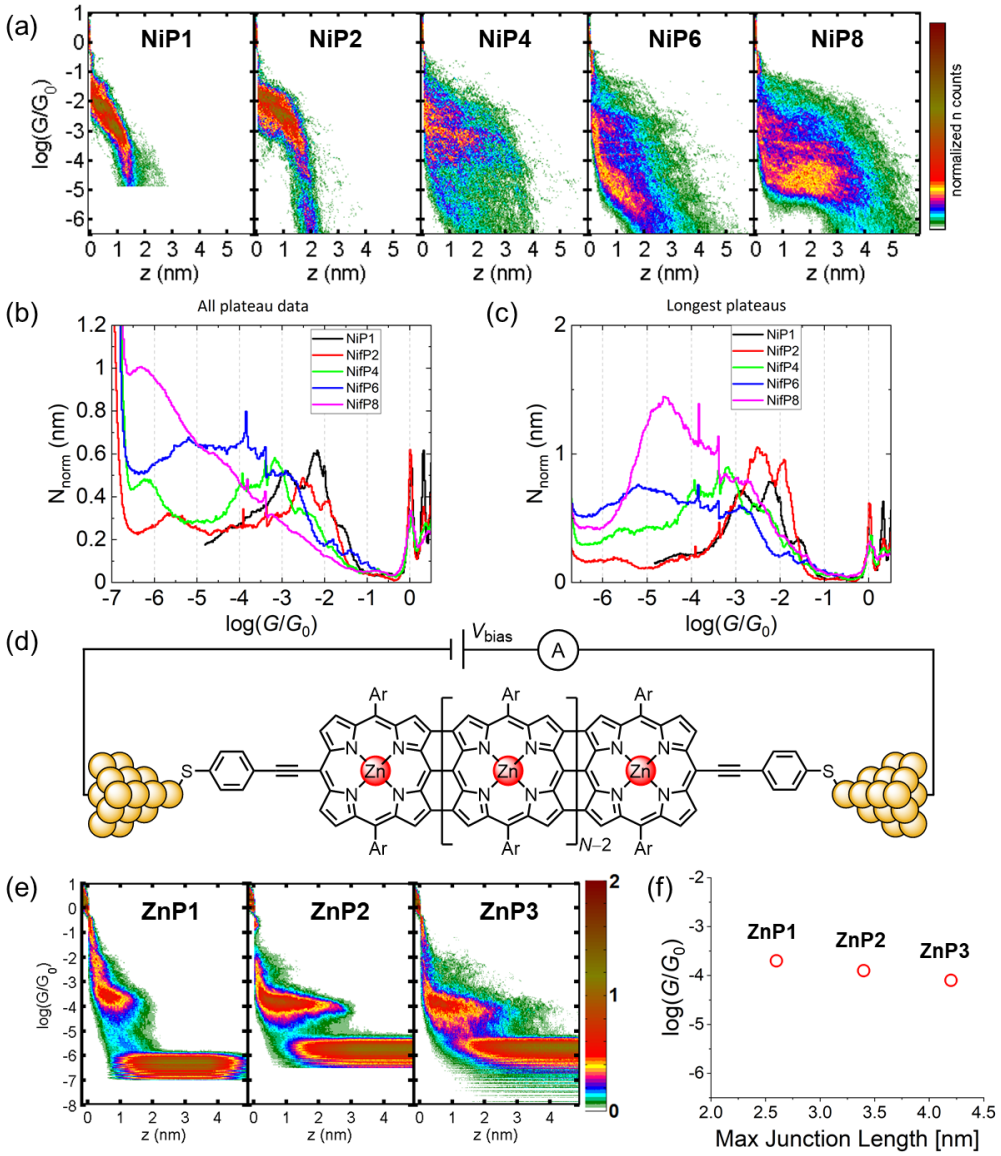

Figure 3.11: (a) 2D conductance histograms for the longest plateau groups for ***lf*-NiP*N*-TMS2** recorded at V_{bias} = 0.2 V. (b) and (c) 1D conductance histograms for all plateau data and the longest plateaus for ***lf*-NiP*N*-TMS2**. $N_{norm} = N_{points}/n_{curves}/v_p/\Delta \log G$, where N_{points} is the number of points recorded in each bin, n_{curves} is the total number of G versus z curves included in the histogram, v_p is the number of points recorded per unit of length in z, and $\Delta \log G$ is the bin size.[261] (d) Schematic showing molecular junctions for ***lf*-ZnP*N*-SAc2** connected to gold electrodes via Au–S link. The acetyl groups cleave *in situ* to produce Au–S bonds on the gold surface in the measurements. (e) 2D conductance histograms for the longest plateau groups for ***lf*-ZnP*N*-SAc2** recorded at V_{bias} = 0.1 V (for N = 1) and 0.2 V (for N = 2, 3). (f) Plots of conductance peak positions for each compound (***lf*-ZnP*N*-SAc2**) against max junction length (measured between two Au atoms bonded to the terminal S atoms). Data were recorded and analyzed by Dr. Edmund Leary.

The conductance histograms for ***lf*-NiP*N*-TMS$_2$** are compared to those recorded for ***lf*-ZnP*N*-SAc$_2$** (N = 1–3; Figure 3.11d–f) in previous work.[63] The conductance distributions of the plateaus shown in Figure 3.11a are broader than those for ***lf*-ZnP*N*-SAc$_2$**, implying that the binding geometries for the junctions bearing direct Au–C link are less well-defined compared to the Au–S linkage.[63] The single-molecule conductances for ***lf*-ZnP1-SAc$_2$** ($10^{-3.7}$ G_0) and ***lf*-ZnP2-SAc$_2$** ($10^{-3.9}$ G_0) are one to two orders of magnitude lower than those for ***lf*-NiP*N*-TMS$_2$** (N = 1 and 2). The conductance for ***lf*-ZnP3-SAc$_2$** ($10^{-4.1}$ G_0) are similar to (or slightly higher than) those for ***lf*-NiP*N*-TMS$_2$** (N = 6 and 8), while the latter two oligomers are typically longer than ***lf*-ZnP3-SAc$_2$**. These results indicate that replacement of the Au–S linkage with direct Au–C contacts significantly lower the contact resistance of the molecular junctions, and hence increases the single-molecule conductance for junctions on the same length scale.

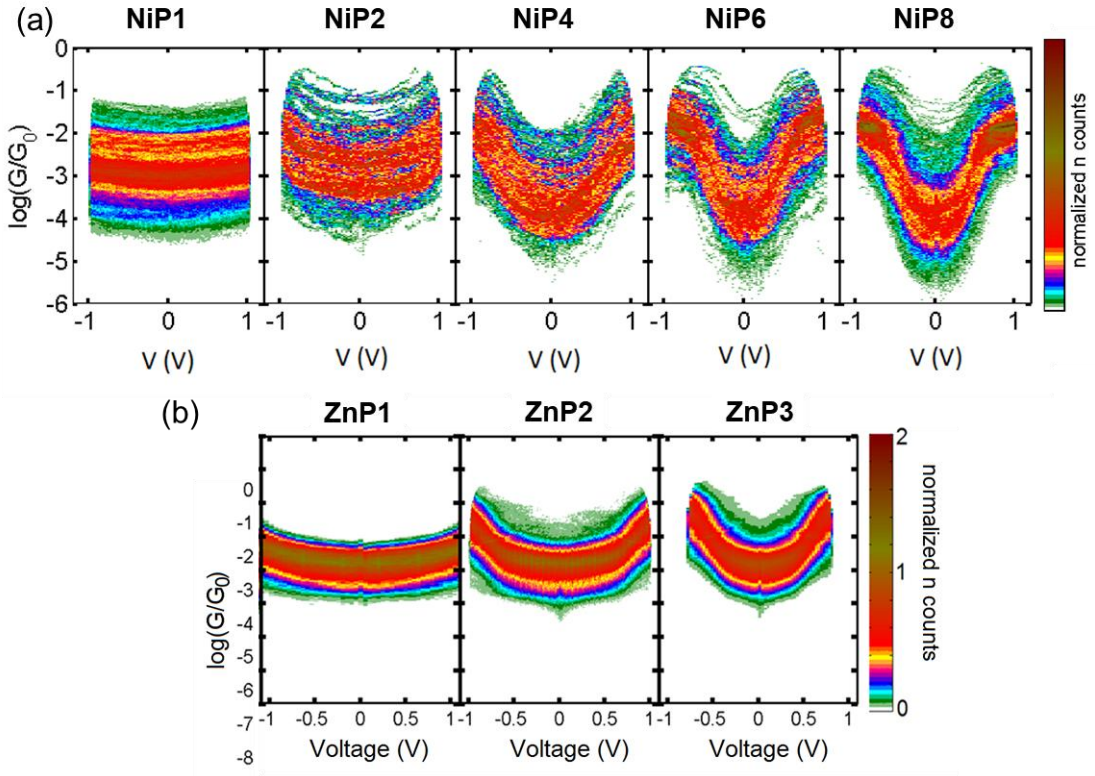

Figure 3.12: log(G/G_0)−V 2D histograms generated from I–V traces recorded for ***lf*-NiP*N*-TMS$_2$** (N = 1, 2, 4, 6 and 8) and ***lf*-ZnP*N*-SAc$_2$** (N = 1, 2, 3).[63] I–V curves were measured at set intervals by sweeping the applied bias voltage. V_{bias} = −1.0 to 1.0 V for ***lf*-NiP*N*-TMS$_2$** (N = 1, 2, 4, 6 and 8) and ***lf*-ZnP*N*-SAc$_2$** (N = 1, 2); V_{bias} = −0.7 to 0.7 V for ***lf*-ZnP3-SAc$_2$**. Data were recorded and analyzed by Dr. Edmund Leary.

After establishing the low-bias behaviors, we next investigated the voltage-dependent transport behaviors of the compounds. The $\log(G/G_0)$−V 2D histograms (Figure 3.12a) summarize the U-shaped traces for compounds ***lf*-NiP*N*-TMS$_2$** obtained from the I−V measurements by sweeping the bias between –1.0 and 1.0 V. The $\log(G/G_0)$−V traces are flat for the monomer and become progressively tilted for longer oligomers. Given that the HOMO–LUMO gaps for ***lf*-NiP*N*-TMS$_2$** decrease steeply with length (Section 3.3.4), at the same bias, for the longer oligomers, the molecular frontier orbital energies (energies for the HOMOs) are expected to align closer with the electrode Fermi levels. We interpret that a transition from off-resonant to resonant transport occurs at high bias ($\geq$ 0.7 V) for long oligomers ($N \geq 4$). At V_{bias} = 0.3–0.7 V, the single-molecule conductance increases with voltage for all compounds and the magnitude of increase is more pronounced for longer oligomers, and thereby all the oligomers express similar conductance (~10^{-3} G_0). At low-bias (0–0.3 V), monomer and dimer exhibit similar molecular conductance (10^{-2} to 10^{-3} G_0). There is a gentle decay (about one order of magnitude) in conductance from the tetramer onward (conductance in 10^{-3} to $10^{-4.5}$ G_0 for N = 4–8), which is similar to that observed from the fixed bias $G(z)$ measurements.

The bias-driven conductance increase has been observed in Zn(II) porphyrin tapes up to a trimer (about 4 nm in length) before (Figure 3.12b).[63] In this study, we are able to probe this behavior in molecular junctions up to an 8 nm long fused porphyrin octamer. The length of the fused porphyrin octamer single-molecule junction is significantly longer than the typical crossover length (~4 nm) between tunnelling and hopping regimes.[262] We ascribe the observation of the long-range coherent tunnelling transport in these molecular junctions to the strong electronic coupling between neighboring porphyrin units in the fused porphyrin oligomers and the intermediate molecule–electrode coupling provided by the Au–acetylene contacts.

3.5 Conclusion

In this chapter, we have prepared a series of fused porphyrin oligomers ***lf*-NiP*N*-TMS$_2$** up to an octamer with about 8 nm in length and explored the single-molecule conductance of each ***lf*-NiP*N*-TMS$_2$** using the STM-BJ method. The ***lf*-NiP*N*-TMS$_2$** were prepared and well-characterized by ^{1}H NMR, UV–vis–NIR absorption spectroscopy, as well as mass spectrometry. The Ni(II) porphyrin tapes with 3,5-bis(trihexylsilyl)phenyl groups are chemically stable and highly soluble in organic solvents (e.g., $CHCl_3$), which allows acquisition of the well-resolved ^{1}H NMR spectra and mass spectra for long oligomers (N = 6 and 8). The experimental and calculated HOMO–LUMO gaps for the whole set of oligomers are progressively narrowing with length, reflecting the molecules are strongly π-conjugated, without reaching saturation at N = 8.

In molecular conductance measurements, we discovered that molecules can be connected to the gold electrodes via covalent Au−C link after *in situ* cleavage of the TMS end capping groups. This condition, which has not yet been reported in STM-BJ measurements, was found by comparison of the effectiveness of junction formation using a family of porphyrin monomers with various end capping groups. At low-bias, the single-molecule conductances for **NiP1-TMS$_2$** and **NiP2-TMS$_2$** are about 10^{-2} to 10^{-3} G_0. For long oligomers ($N \geq 4$), a gentle decay of the measured conductance (to 10^{-3} to $10^{-4.5}$ G_0) was found. At high-bias (($\geq$ 0.7 V), the molecular conductance increases for each oligomer because the Fermi levels of the electrodes approach the molecular frontier orbital energy levels, leading to a transition from off-resonant to resonant transport. There have been few reports on single-molecule junctions with > 4 nm in length that exhibiting efficient charge transport (> 10^{-4} G_0),[223,263–265] and we are able to observe fused porphyrin junctions (about 8 nm in length) with low-bias molecular conductance ranging from 10^{-3} to 10^{-5} G_0. This reflects weakly distance-dependent attenuation feature for the fused porphyrin oligomers and the covalent Au−C contacts that exhibit low effective contact resistance.

4

Phase-Coherent Transport and Quantum Interference in a Fused Porphyrin Octamer-Graphene Junction

4.1 Introduction 108

4.1.1 Device Architecture and Fabrication 108

4.1.2 Charge Transport 110

4.1.3 Kondo Effect 112

4.1.4 Fabry-Pérot Interference Effect 112

4.1.5 Project Aim 113

4.2 Molecular Design, Synthesis and Chemical Characterization 114

4.2.1 Molecular Design 114

4.2.2 Synthesis and Chemical Characterization of *lf*-NiP8-TAP$_2$ 114

4.3 Charge Transport Measurements 117

4.3.1 Device Fabrication and Molecule Deposition 117

4.3.2 Conductance Measurements 118

4.3.3 Fabry-Pérot Interference within the Graphene Channel 119

4.3.4 Phase-Coherent Molecular Transport 121

4.4 Conclusion 125

Most of the work in this chapter was published in:

Chen, Z.;† Deng, J.-R.;† Hou, S.; Bian, X.; Swett, J. L.; Wu, Q.; Baugh, J.; Briggs, G. A. D.; Mol, J. A.; Lambert, C. J.; Anderson, H. L.; Thomas, J. O. Phase-Coherent Charge Transport Through a Porphyrin Nanoribbon-Graphene Junction. *arXiv* **2022**, DOI: 10.48550/arXiv.2205.08499.

4.1 Introduction

Quantum interference manifests in conductance measurements when there are multiple coherent pathways for electron propagation through a single molecule or nanostructure.[31,34,38,235,266] Exploring and manipulating quantum interference in molecular-scale electronic devices could lead to applications in reduced energy computing and efficient thermoelectric energy harvesting.[235,266] To realize such ambitious goals, it is necessary to experimentally demonstrate phase-coherent molecular transport, and to understand the hierarchy of quantum interference phenomena that are possible within a given junction. We demonstrated that monodisperse fused nickel(II) porphyrin oligomers, up to an octamer, can be modularly synthesized and structurally characterized in Chapter 3. In this chapter, we investigate the charge transport and quantum interference in a fused porphyrin octamer single-molecule transistor with graphene electrodes. Functionalization of the porphyrin core with pyrene anchors allows binding of the molecule to the graphene source and drain electrodes via π-stacking. The resulting intermediate molecule–electrode coupling leads to observation of off-resonant transport, a Kondo resonance and a wide range of quantum interference phenomena, such as Fabry-Pérot and Fano resonances in conductance measurements. These results clearly inply that the charge transport through the fused porphyrin octamer (~8 nm in length) is phase coherent.

4.1.1 Device Architecture and Fabrication

In this chapter, we performed the charge transport measurement by integrating the molecule (i.e., a fused porphyrin octamer) into a graphene-based device, which is different from the STM break junctions with gold electrodes described in previous chapter, mainly due to the presence of a third electrode – an electrostatic gate, which allows additional insight into the charge transport properties of the molecular devices. Graphene is a good material for the source and drain electrodes in a three-terminal device, because, unlike the relatively bulky three-dimensional (3D) metallic electrodes (e.g., gold electrodes), it is atomically thin. This results in a weaker screening of an applied gate electric field and gives stronger coupling of the molecular energy levels to the gate electrode.[267–269]

A typical graphene-based three-terminal device architecture is shown in Figure 4.1a.[268,270] In each device, a graphene nanogap is fabricated by feedback-controlled electroburning of a graphene tape containing a bowtie-shaped constriction. The electroburning process starts with ramping up of the voltage across the graphene constriction at a given rate (5–10 V s^{-1}), while the current is continuously monitored (Figure 4.1b). Once an abrupt decrease of the current is

observed, the voltage is rapidly ramped back to 0 V (2300–5000 V s^{-1}). This cycle repeats for several times until a resistance of 500–2000 MΩ is reached. After the electroburning, the size of the nanogap (that determines the distance between the graphene source and drain electrodes) can be estimated by fitting the measured I–V_{sd} curve (Figure 4.1c, red dots) to the Simmons model (Figure 4.1c, black line).[270] The typical size is 1–2 nm. This device is fabricated on a silicon substrate, which serves as a global back gate (gate electrode). A dielectric layer (SiO_2, 300 nm) is sandwiched between the gate electrode and the graphene nanogap, which ensures the gate couples only electrostatically to the molecule. The gate potential provides an additional parameter to tune the alignment of the energy levels of the molecule with respect to the Fermi energy of the graphene leads, making it possible to test charge transport through energy levels far from the Fermi energy. This is difficult to achieve using the STM-BJ method. After the electroburning, molecules are deposited upon the graphene nanogap. The molecules can be attached to graphene electrodes via covalent link (e.g., amide bond)[269,271] or non-covalent interactions (e.g., π-stacking).[267,268,270] In this chapter, we focus on π-stacking interaction, which leads to weak or intermediate molecule–electrode coupling Γ.[270,272]

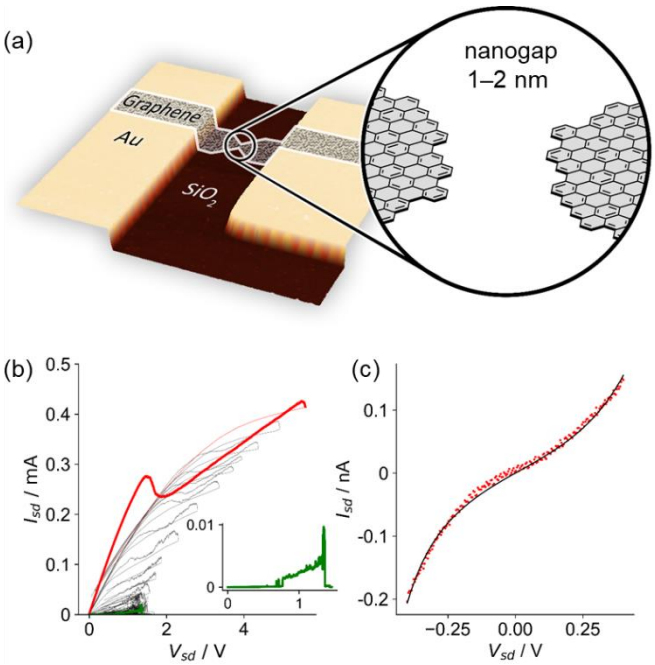

Figure 4.1: (a) Schematic showing the device architecture before deposition of the molecule. The graphene is patterned into a bowtie-shape and electroburned to form a nanogap. (b) Typical feedback-controlled electroburning traces. The first and last traces are indicated in red and green, respectively. Inset: the last electroburning trace. (c) Typical I–V_{sd} trace after electroburning (red dots), and the corresponding fit to the asymmetric Simmons model (black line, gap size: 1.17 nm).[270] Reproduced with permission from ref. 270.

4.1.2 Charge Transport

Figure 4.2a shows a typical three-terminal device constituting a porphyrin monomer with pyrene anchor groups that interface with the graphene source and drain electrodes via π-stacking. Γ_s and Γ_d characterize the molecule–electrode coupling to the source and drain electrodes respectively. C_t is the sum of the capacitances to the source C_s, drain C_d and gate C_g. V_{sd} and V_g are the applied bias and gate voltages to the junction. With an applied voltage, the neutral molecule with a number of electrons, N, can be charged or discharged (i.e., oxidized or reduced) to different oxidation states ($N \pm i$). The electrochemical potential diagram (Figure 4.2c) shows a set of electrochemical potentials (energy levels) μ required to oxidized or reduced the molecule.[268,270,234] The electrochemical potential μ is defined as the difference between the total energies of the system U in two oxidation states:

$$\mu_{N-1\pm i \leftrightarrow N\pm i} = U_{N\pm i} - U_{N-1\pm i} \tag{4.1}$$

The energy difference between $\mu_{N-1\pm i \leftrightarrow N\pm i}$ and $\mu_{N\pm i \leftrightarrow N+1\pm i}$ is the charge addition energy E_{add}, a sum of energy spacing between two molecular orbitals δE and the electrostatic contributions to the energy (e.g., charging energy E_C).[234,273]

$$E_{add} = \mu_{N\pm i \leftrightarrow N+1\pm i} - \mu_{N-1\pm i \leftrightarrow N\pm i} \approx \delta E + E_C \tag{4.2}$$

In the weak coupling regime, where $\Gamma << \delta E$, E_C, $k_B T$, charge transport through the molecular junction is mediated by stepwise hopping (also known as sequential electron tunneling).[234] At a given bias, when the energy level $\mu_{N-1\pm i \leftrightarrow N\pm i}$ is located between the electrochemical potentials of the source and drain electrodes (μ_s and μ_d) — within the bias window, electrons sequentially hop on the molecule from one electrode and off to another electrode, creating an electron flow. Figure 4.2d demonstrates charge transport occurs when $\mu_d < \mu_{N-1 \leftrightarrow N} < \mu_s$ at a negative bias. On the contrary, when the energy levels are out of the bias window, electron flow is blocked. Applying a gate voltage allows shifting of the energy levels of the molecule with respect to the Fermi energy of the leads. For example, as shown in Figure 4.2e, a negative gate voltage shifts up the molecular energy levels and thus the electron flow occurs at low bias. In a typical three-terminal measurement, both the bias and gate voltages are sweeping, leading to a current map measured as a function of bias and gate voltages, namely a stability diagram (Figure 4.2b).[234] The red and blue shaded regions correspond to single-electron transport through the junction and the white regions are called Coulomb blockade where the charge transport is suppressed. The values of the charge addition energy E_{add}, gate

coupling α_g and capacitances of the system can be determined by analyzing the stability diagram.

When the molecule–electrode coupling becomes stronger, where Γ, $k_BT \approx \delta E$, E_C, coherent tunneling dominates the charge transport. In this intermediate coupling regime, electron can tunnel through the junction even though the energy level is out of the bias window (i.e., it is termed as off-resonant transport as discussed in Chapter 3), leading to a nonzero background conductance in the Coulomb blockade region observed from the stability diagram.[234] In addition to the off-resonant transport, other effects including quantum interference (e.g., Fabry-Pérot resonance and Fano resonance) and Kondo effects can be observed in this regime.[235] In the following, we briefly introduce the Kondo effect for a spin-½ system, and Fabry-Pérot interference in graphene nanoconstrictions.

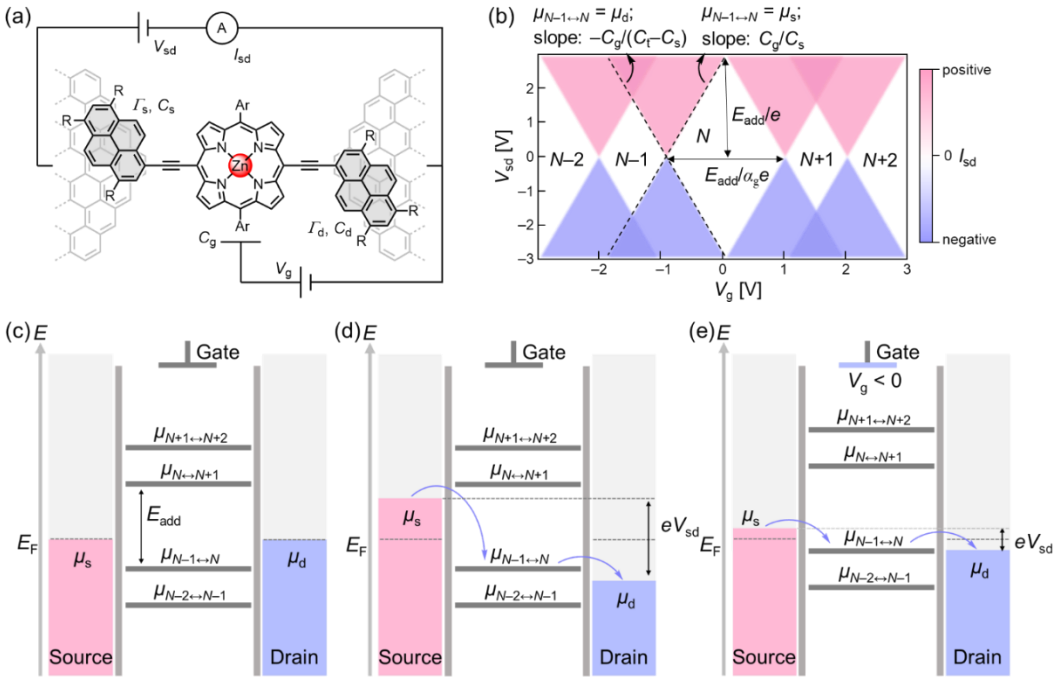

Figure 4.2: (a) Schematic representation of a single-molecule transistor comprising of a porphyrin monomer functionalized with pyrene anchors to bind to graphene electrodes via π-stacking. Ar = 3,5-bis(trihexylsilyl)phenyl groups; R = dodecyloxy solubilizing groups. (b) Stability diagram showing the current I_{sd} map as a function of bias voltage V_{sd} and gate voltage V_g. $\alpha_g = C_g/C_t$ characterizes the gate coupling that can be extracted from the height and width of the Coulomb diamond, or the positive and negative slopes shown in the figure.[268] (c)–(e) Electrochemical potential diagrams of a three-terminal molecular junction with weak molecule–electrode coupling at $V_{sd} = 0$, $V_g = 0$ (c), $V_{sd} < 0$, $V_g = 0$ (d), and $V_{sd} < 0$, $V_g < 0$ (e). Charge transport occurs when $\mu_{N-1\pm i\leftrightarrow N\pm i}$ is located between μ_s and μ_d.

4.1.3 Kondo Effect

The Kondo effect is a many-body phenomenon that occurs when the tunneling electrons interact with an unpaired electron localized in the molecular backbone of the junction.[234,274,275] The unpaired electron can be introduced by incorporation of a paramagnetic atom,[276] oxidation or reduction of the neutral molecule in an odd charge state (e.g., N–1 or N+1),[277,278] or directly using a neutral organic radical.[279] The interaction results in the creation of a many-body singlet state pinned to Fermi level of the leads, which shows up as a zero-bias resonance in the stability diagram. The Kondo resonance is temperature-dependent, and can be characterized by the Kondo temperature T_K. In practice, the value of T_K can be estimated by fitting the temperature-dependent conductance data to the spin-½ Kondo model (eqn. 4.3),[280] or from the full width at half-maximum (FWHM) of the Kondo resonance peak (eqn. 4.4),[281]

$$G_K(T) = \frac{G_{T=0}}{\left[1+(2^{1/s}-1)(T/T_K)^2\right]^s} \tag{4.3}$$

$$\text{FWHM} = \frac{2}{e}\sqrt{(\pi k_B T)^2 + 2(k_B T_K)^2} \tag{4.4}$$

where $G_K(T)$ is the differential conductance at the peak of Kondo resonance, $G_{T=0}$ is the differential conductance of the Kondo peak at zero temperature, and s is an empirical parameter that is about 0.22 for a spin-½ system; k_B is the Boltzmann constant, T is the temperature recorded in each measurement.

4.1.4 Fabry-Pérot Interference Effect

Electrons that are tranported through the graphene channel can be transmitted or reflected at metal contacts,[282] or at potential barriers formed by local changes in doping.[283,284] A pair of partially reflective potential barriers in the channel lead to the formation of an electronic cavity and resulting a "chequerboard"-like interference pattern on the stability diagram (see Figure 4.3b for an example). This effect is called the Fabry-Pérot interference, which may only occur when the length of the cavity is smaller than the phase coherence length of the electrons moving through graphene. The resonance peaks of the Fabry-Pérot cavity can be analyzed by fast Fourier transforms to determine the characteristic periodic energy spacings ΔE_{FP}. The length of the Fabry-Pérot cavity can be estimated using eqn. 4.5, derived from the one particle in a box approximation:[282,284]

$$L = h v_F / 2\Delta E_{FP} \tag{4.5}$$

where v_F is the Fermi velocity, a value of 2.4×10^6 m/s measured for the CVD graphene.[285]

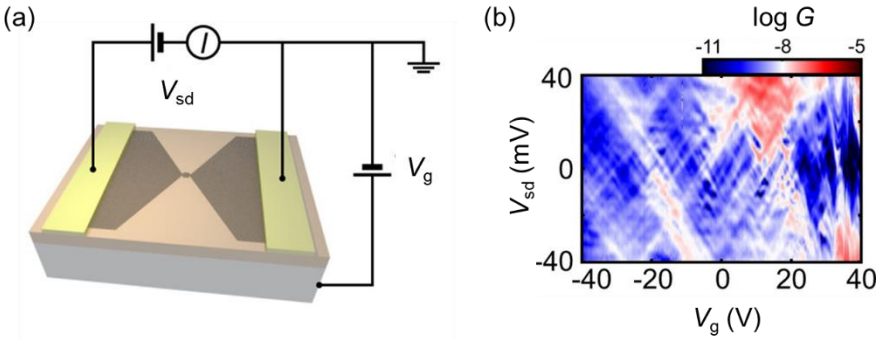

Figure 4.3: (a) Schematic of a graphene nanoconstriction device. (b) Conductance map of a strongly coupled constriction showing a "chequerboard"-like pattern as a manifestation of the Fabry-Pérot interference effect.[284] Reproduced with permission from ref. 284.

The Fabry-Pérot interference effect has been observed in carbon nanotubes,[286] 2D graphene,[282] and graphene nanoconstrictions created by feedback-controlled electroburning (Figure 4.3a),[284] the same technique that we used for device fabrication in this chapter. However, there has been no report on observation of this effect in single-molecule junctions.

4.1.5 Project Aim

In this project, we fabricate a fused porphyrin octamer-graphene single-molecule transistor (Figure 4.4) and explore the charge transport in this device at cryogenic temperatures. Conductance measurements as a function of (source-drain) bias voltage (V_{sd}), gate voltage (V_g), magnetic field, and temperature exhibit a wide range of quantum interference phenomena, such as Fabry-Pérot, Kondo and Fano resonances. Our results show that an 8-nm fused porphyrin octamer molecular junction sustains phase-coherent electron transmission that can be tuned electrostatically, and demonstrate a comprehensive picture of the different quantum-coherent phenomena that arise in a single molecule-graphene transistor.

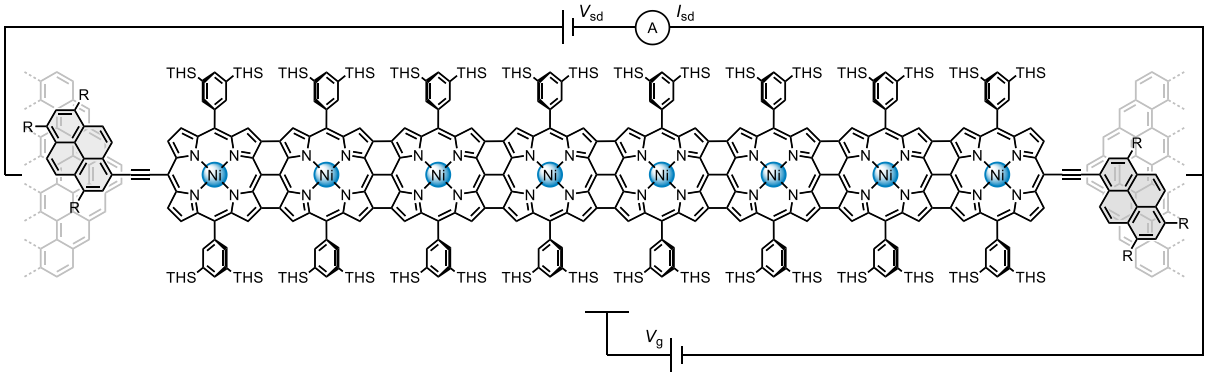

Figure 4.4: Schematic showing a fused porphyrin octamer (***lf*-NiP8-TAP$_2$**)-graphene single-molecule three-terminal device (transistor). R = dodecyloxy solubilizing group.

4.2 Molecular Design, Synthesis and Chemical Characterization

4.2.1 Molecular Design

We use nickel(II) porphyrin octamer ***lf*-NiP8** as the molecular backbone (see Figure 4.4 for the chemical structure), because it exhibits a narrow HOMO–LUMO gap ($E_{g,opt}$ ~ 0.7 eV estimated from lowest energy absorption peak as discussed in Chapter 3, Section 3.3.4), and thus a number of oxidation states are expected to be assessed by applying a gate voltage (within a window ranging from –4.0 V to 4.0 V). In addition, the progressively narrowing of the measured optical gaps $E_{g,opt}$ for the oligomers ***lf*-NiP*N*** with increasing length does not reach a saturation at N = 8. This implies that in ***lf*-NiP8**, the π orbitals of each porphyrin ring are strongly coupled to those in the neighboring units to form delocalized frontier orbitals which could mediate phase-coherent electron transmission through the molecule.

Two tridodecyloxy pyrenyl groups are connected to the ends of the fused porphyrin octamer to serve as anchors to interface the molecule with the graphene source and drain electrodes (Figure 4.4). The trialkoxy pyrenyl (TAP) group is chosen because it showed a relatively high junction formation probability compared to other anchor groups in previous study where a porphyrin monomer **ZnP1** was used as the molecular backbone.[270] Furthermore, it has been incorporated onto fused porphyrin dimer ***lf*-ZnP2** and trimer ***lf*-ZnP3** for charge transport studies.[87,287]

4.2.2 Synthesis and Chemical Characterization of *lf*-NiP8-TAP$_2$

The synthetic route for the fused porphyrin octamer with tridodecyloxy pyrenyl anchor groups ***lf*-NiP8-TAP$_2$** is summarized in Figure 4.5. Bromination of pyrene gave 1,3,6-tribromopyrene **4.1** in 53% yield.[†] This is followed by a nucleophilic aromatic substitution, which yielded tridodecyloxy pyrene **4.2** (3.1%). The yield for the trisubstituted product **4.2** is poor because after each substitution, the pyrene core becomes more electron rich and thereby less reactive toward a further substitution. The TAP-acetylene **4.5** was then readily synthesized by bromination of compound **4.2**, followed by a Pd-catalyzed Sonogashira coupling with TMS-acetylene and removal of the TMS group by treatment compound **4.4** with tetrabutylammonium fluoride (TBAF) solution. The fused porphyrin octamer ***lf*-NiP8-Br$_2$** was prepared following the procedures described in previous chapter (Section 3.3). In the final step, ***lf*-NiP8-TAP$_2$**

[†] Compound **4.1** was made by Dr. Keith G. Andrews (Department of Chemistry, University of Oxford, UK).

(11%) was afforded by Pd-catalyzed Sonogashira coupling of ***lf*-NiP8-Br$_2$** and TAP-acetylene **4.5**. The yield of this reaction is relatively low compared to the similar coupling reaction using TMS-acetylene (which gave ***lf*-NiP8-TMS$_2$** in 42% yield). This is because the TAP-acetylene **4.5** is highly electron rich, which easily undergo oxidative homocoupling during the reaction. Additionally, after attachment of the TAP groups, ***lf*-NiP8-TAP$_2$** becomes less soluble in solvents (e.g., CH_2Cl_2, toluene) compared to ***lf*-NiP8-Br$_2$** or ***lf*-NiP8-TMS$_2$**, which makes the purification difficult (by silica gel column or recycling gel permeation chromatography; see Appendix, Section D.2 for details).

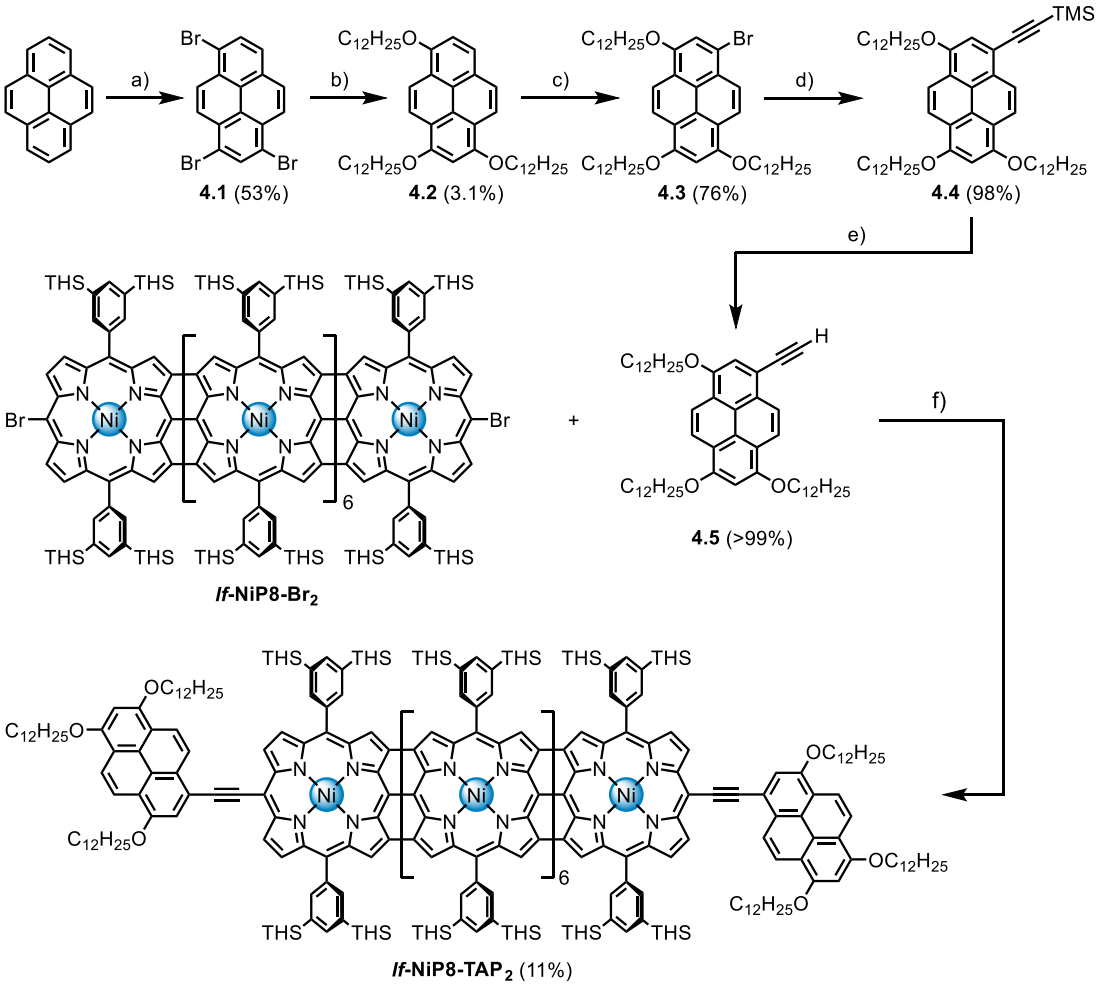

Figure 4.5: Synthesis of ***lf*-NiP8-TAP$_2$**. Conditions: (a) *N*-bromosuccinimide (NBS), DMF, 70–130 ºC, 14 h; (b) dodecan-1-ol, NaH, diglyme, 130 ºC, 5 d; (c) NBS, CH_2Cl_2, 0 ºC, 15 min; (d) $Pd(dppf)Cl_2$ (dppf = 1,1′-bis(diphenylphosphino)ferrocene), CuI, TMS-acetylene, Et_3N/THF (2:1), 85 ºC, 16 h; (e) TBAF, 25 ºC, 15 min; $Pd(PPh_3)_4$, CuI, *i*-Pr_2NH/toluene (1:1), 50 ºC, 22 h. See ref. 270 for the detailed synthetic procedures and characterization data of compounds **4.1**–**4.5**.

Since only a small amount of ***lf*-NiP8-TAP$_2$** (0.11 mg) was isolated and it is less soluble compared to ***lf*-NiP8-Br$_2$** or ***lf*-NiP8-TMS$_2$**, we are only able to identify the isolated product ***lf*-NiP8-TAP$_2$** by observation of its molecular ion peak in mass spectrometry (found *m*/*z* = 13942.67, calc. $C_{940}H_{1494}N_{32}Ni_8O_6Si_{32}$: 14707.52; Figure 4.6a). The measured UV–vis–NIR absorption spectrum of ***lf*-NiP8-TAP$_2$** shows three characteristic bands at 414, 770 and 1728 nm, labeled as band I, II and III, arising from the B_y, B_x and Q_x transitions of a porphyrin monomer, which is similar to that of ***lf*-NiP8-TMS$_2$** described in Section 3.3. The band I and band III for ***lf*-NiP8-TAP$_2$** are broader than those for ***lf*-NiP8-TMS$_2$**, probably as a result from the rotation of two terminal TAP groups around the ethyne bridges (it becomes less π-conjugated when the fused porphyrin octamer core and the pyrene cores of the TAP end groups are twisted from a coplanar conformation).

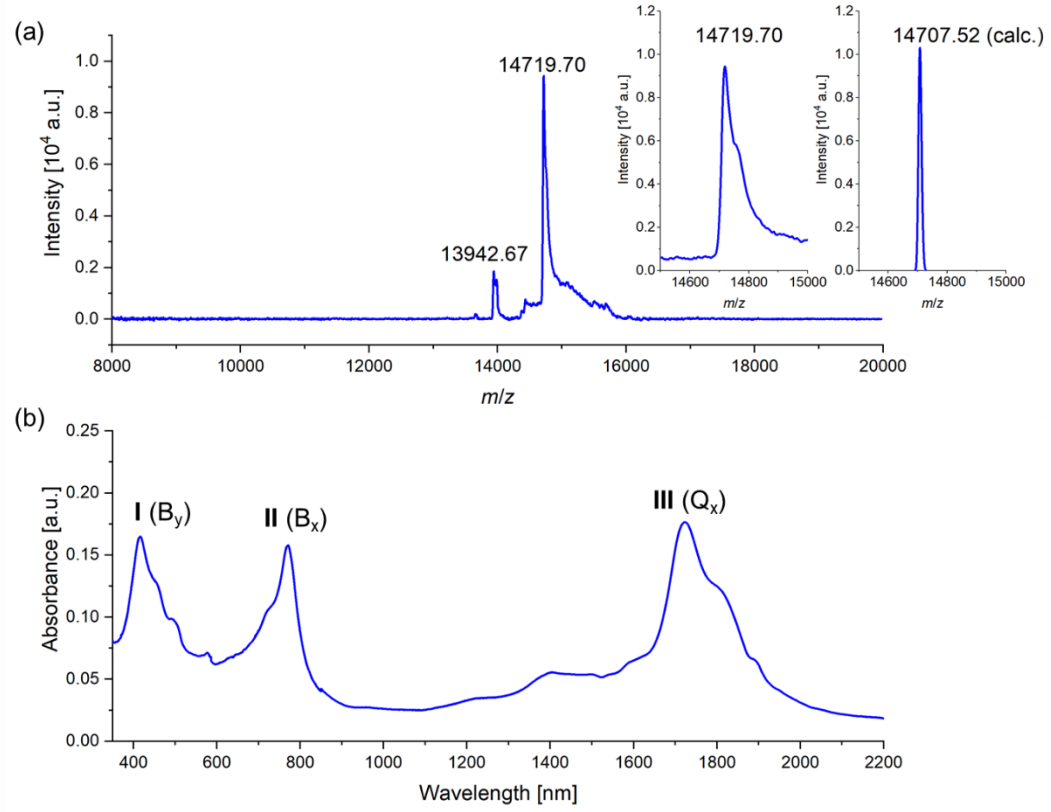

Figure 4.6: (a) MALDI-ToF spectrum of ***lf*-NiP8-TAP$_2$** (found *m*/*z* = 13942.67, calc. $C_{940}H_{1494}N_{32}Ni_8O_6Si_{32}$: 14707.52) with DCTB as matrix. The peak found *m*/*z* = 13942.67 corresponds to the singly coupled side product (calc. $C_{886}H_{1414}N_{32}Ni_8O_3Si_{32}$: 13930.91). (b) UV–vis–NIR absorption spectrum of ***lf*-NiP8-TAP$_2$** measured in $CDCl_3$ at 298 K. λ_{max} = 414, 770 and 1728 nm.

4.3 Charge Transport Measurements[†]

4.3.1 Device Fabrication and Molecule Deposition

Figure 4.7 shows a schematic representation of the device used in this study. It is similar to the general device shown in Figure 4.1, except that a platinum electrostatic gate electrode, covered with a 10 nm HfO_2 dielectric layer is used instead of the global Si/SiO_2 gate to increase the gate coupling to the molecular levels. Compared to previous works,[270] we optimized the fabrication procedures by using a Z-shaped pattern graphene to reduce tension in the constriction, and using a positive, rather than negative, photoresist to reduce contamination. Graphene nanogaps were prepared by feedback-controlled electroburning of the graphene bowtie shape until the resistance of the tunnel junction exceeds 1.3 GΩ (10^{-7} G_0). The empty nanogaps were characterized by measuring a current map as a function of bias voltage (V_{sd}) and gate voltage (V_g) at room temperature in order to exclude devices containing residual graphene quantum dots. Molecules were deposited by dropping a solution of ***lf*-NiP8-TAP$_2$** (1 μM in toluene) upon the device and allowed it to dry in air. Only devices that showed clean current maps before molecule deposition were carried on further measurements. Therefore, new signals appeared after molecule deposition were attributed to transport through molecular junctions. Then, the chip containing molecular devices was connected to a chip holder via wire bonding, loaded in Oxford Instruments 4K PuckTester, and cooled down to cryogenic temperature for detailed measurements.

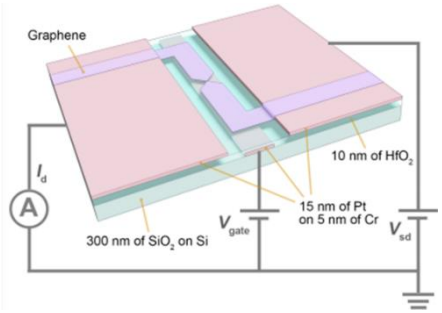

Figure 4.7: Device architecture. The pink rectangular area in the middle represents the local platinum gate electrode under a 10 nm layer of HfO_2; the pink areas at both ends represent the source and drain platinum electrodes, which are in contact with the bowtie-shape graphene (purple). Data were collected and analyzed by Dr. Zhixin Chen and Dr. James O. Thomas.

[†] All conductance measurements and data analysis in this chapter were performed by Dr. Zhixin Chen and Dr. James O. Thomas, in collaboration with Prof. G. Andrew D. Briggs and Prof. Lapo Bogani (Department of Materials, University of Oxford, UK).

4.3.2 Conductance Measurements

The full differential conductance map (G_{sd} = dI_{sd}/dV_{sd}) of the fused porphyrin octamer-graphene device, measured at 4.2 K, displays several Coulomb diamonds and associated resonant tunneling regions (Figure 4.8a). We assign the diamond at V_g = 0 as the *N* state (*N* being the number of electrons on the molecule when it is neutral), because this diamond has a large addition energy (E_{add} = 0.7 eV), that broadly matches the optical HOMO–LUMO gap (energy of the longest wavelength absorption band; 1728 nm, 0.72 eV). There is a zero-bias conductance peak in the neighboring diamond between V_g ~ –0.7 V and V_g ~ –1.4 V, consistent with the experimental signature of a Kondo resonance (discussed in detail below) that results from screening of an unpaired spin on the nanoribbon by electrons within the graphene electrodes.[276,277] The observation of a Kondo resonance is consistent with the assignment of this smaller diamond to the odd *N*–1 state (i.e., molecule is the radical cation, ***lf*-NiP8-TAP$_2^{+\cdot}$** in this Coulomb diamond), and the larger diamond at V_g = 0 to the even *N* state, as the number of electrons on the molecule differs by one between adjacent Coulomb diamonds.[12] The two sequential transport regions with broad edges which flank the *N*–1 diamond are then the *N*–1/*N* charge transition (V_g ~ –0.7 V) and the *N*–2/*N*–1 transition (V_g ~ –1.4 V). Finally, the highly conductive region at positive V_g is the *N*/*N*+1 charge transition. We calculate the coupling of the molecular levels to the gate and source potentials from the slopes of the Coulomb diamonds, as $\alpha_{g,mol}$ = 0.22 eV/V, and $\alpha_{s,mol}$ = 0.65 eV/V respectively, giving the fraction of each applied potential that the molecular levels shift by.[268]

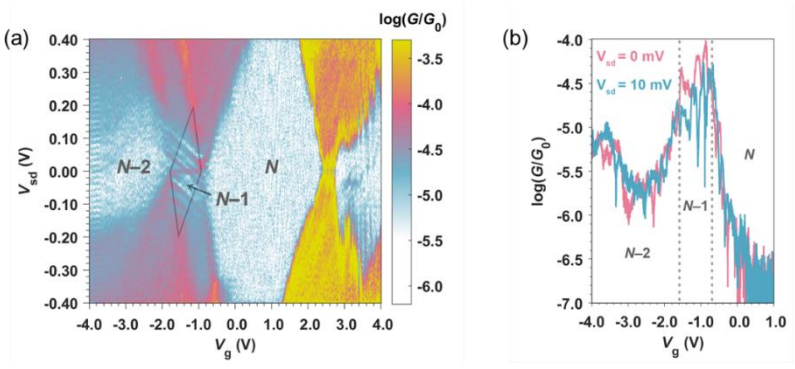

Figure 4.8: (a) Differential conductance (G = dI_{sd}/dV_{sd}) map measured as a function of V_{sd} and V_g. (b) Differential conductance as a function of V_g at V_{sd} = 0 mV (pink curve) and V_{sd} = 10 mV (blue curve) for ***lf*-NiP8-TAP$_2$** device at 4.2 K. The conductance is plotted in logarithmic scale as the ratio to conductance quantum $G_0 = 2e^2/h$ where e is the elementary charge and h is Planck's constant. The *N*–1 charge state is highlighted by a grey diamond. Data were collected and analyzed by Dr. Zhixin Chen and Dr. James O. Thomas.

Considering the measurement temperature is low (4.2 K, k_BT = 0.4 meV), the poor definition in the boundaries of the Coulomb diamonds (FWHM of Coulomb peaks ~ 14 meV, see Appendix D, Section D.4) is attributed to the lifetime broadening that results from intermediate molecule–electrode coupling, a regime consistent with appearance of the Kondo resonance.[288,289] The broad diamond edges suggest there are large regions where the molecular charge state is not well defined, in contrast with a device in the weakly coupled regime (commonly observed for molecules π-stacked to graphene electrodes[87,268,270,287]), where conductance occurs only within the sequential transport regions (when the electrochemical potentials of molecular transitions μ lie within the bias window) separated by Coulomb diamonds. In Figure 4.8a and 4.8b, we observe off-resonant transport features, suggesting that the conductance is not completely suppressed, even at V_{sd} = 10 mV (away from the Kondo peak). Instead, conductance remains above the noise except within the *N* diamond, indicating that there are significant contributions from off-resonant phase-coherent transport around the *N*–1/*N* and *N*–2/*N*–1 transitions of the intermediately coupled ***lf*-NiP8-TAP$_2$** device.[288] As the hybridization between molecule and electrode increases with electronic coupling, transport through an intermediately coupled molecular junction can only be fully understood by considering the entire graphene-molecule-graphene system. We discuss the mixture of effects that arise from this holistic approach in the next four sections with the following order: at first, we discuss the Fabry-Pérot interference observed within the graphene; secondly the Kondo resonance at *N*–1 charge state; thirdly the Fano resonance observed as a result from interference between graphene states and molecular states; and in the final part, we focus on off-resonant molecular transport.

4.3.3 Fabry-Pérot Interference within the Graphene Channel

A high-resolution conductance map of the *N*–2/*N*–1 and *N*–1/*N* transitions is shown in Figure 4.9a. There is periodic structure within the off-resonant conductance, especially in the range ± 100 mV, with a weaker coupling to the gate ($\alpha_{g,FP}$ = 0.054 eV/V) than to the molecular states ($\alpha_{g,mol}$ = 0.22 eV/V). The effect is more obvious in the second derivative of the current (dI^2_{sd}/dV^2_{sd}) map which displays a "chequerboard" pattern (Figure 4.9b). The appearance of this pattern is attributed to the formation of an electronic Fabry-Pérot interferometer within the graphene channel, as observed before in other graphene-based devices.[284,290,291]

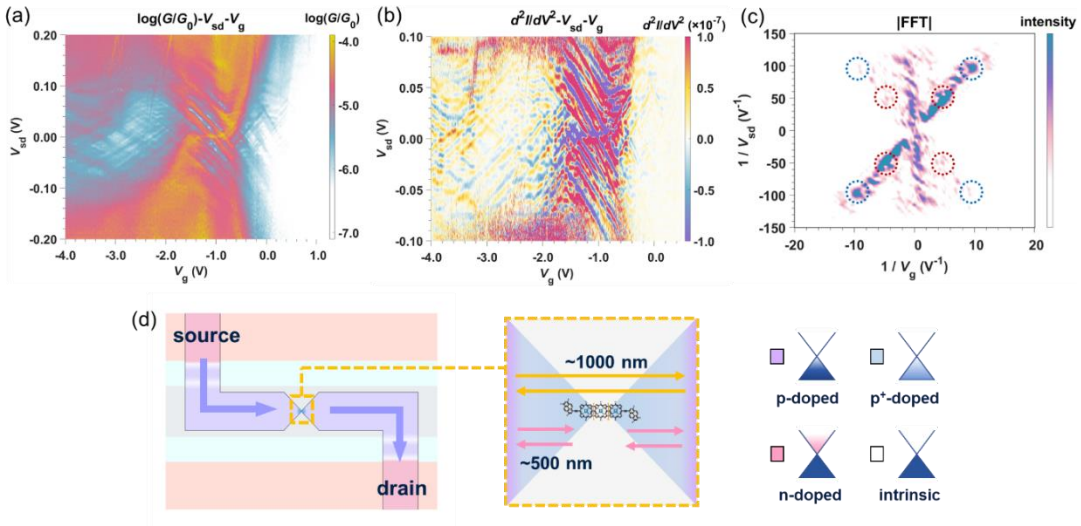

Figure 4.9: Fabry-Pérot interference. (a) Detailed conductance map of the interference pattern overlapping with molecular charge transitions. (b) Derivative of differential conductance (dI^2_d/dV^2_{sd}) measured as a function of V_{sd} and V_g. (c) 2D fast Fourier transform (FFT) of (b), the blue and red dotted circles respectively indicate two groups of hot spots used to estimate the characteristic energy spacings (ΔE_{FP}) of 5 and 10 meV. (d) Schematic showing possible interference conditions. Two possible resonance conditions for Fabry-Pérot interference within the graphene are indicated by arrows within the highly doped region (orange; $L \approx 1000$ nm) and on one of the molecule-graphene interfaces (pink; $L \approx 500$ nm). Data were collected and analyzed by Dr. Zhixin Chen and Dr. James O. Thomas.

There are two features of the conductance oscillations that make up the chequerboard. These two oscillations correspond to two characteristic periodic energy spacings ($\Delta E_{FP} \approx 5$ and 10 meV), as shown in Figure 4.9c, a two-dimensional fast Fourier transform of the dI^2_{sd}/dV^2_{sd} map. Considering resonances within a one-dimensional Fabry-Pérot cavity (eqn. 4.5), our measured ΔE_{FP} of 5 and 10 meV correspond to cavity lengths of $L = h v_F/(2\Delta E_{FP}) = 1000$ and 500 nm, using the Fermi velocity of $v_F = 2.4 \times 10^6$ m/s for CVD graphene.[285] These length scales are two orders of magnitude larger than those associated with reflections within the molecule itself (~ 8 nm in length for ***lf*-NiP8-TAP$_2$**), which indicates that the quantum interference pattern is dominated by reflections within the graphene channel. This can be further verified by magnetoconductance oscillations (Section D.5 in Appendix D).

We reason that the cavity is formed within the graphene by doping induced by interactions with the substrate. Graphene transferred onto HfO_2 is *p*-doped (light purple area),[291] as shown in Figure 4.9d. The electroburning process that is used to create the nanogap anneals the graphene and increases the hole concentration local to the tunnel junction, generating a highly

doped (p^+-doped) region (blue area) of ~ 1000 nm in diameter.[284] Therefore reflections over 500 nm occur between a pp^+ potential step and a molecule–electrode tunnel barrier, as highlighted by pink arrows in Figure 4.9d. As the length of the molecule is much shorter than the graphene cavity, reflections from either side of the molecule-graphene interface are not distinguishable. For the reflections within a 1000 nm cavity (the diameter of the p^+-doped region), the interfaces between *p*-doped and p^+-doped graphene regions generate the potential steps, the electrons are reflected or transmitted within the pp^+p cavity that contains the molecular junction, as indicated by orange arrows in Figure 4.9d. The demonstration of quantum interference within a Fabry-Pérot cavity that contains a molecular junction at the center implies that electron transmission through the molecule is phase coherent.

4.3.4 Phase-Coherent Molecular Transport

Next, we describe the temperature and charge-state dependence of the device conductance. As shown in Figure 4.10a, as the thermal energy increases beyond hv_F/L (5 meV), the Fabry-Pérot interference pattern disappears (at 80 K, k_BT = 6.9 meV) likely due to both the thermal energy being larger than the Fabry-Pérot spacing, as well as the coherence length within the graphene channel decreasing with temperature.[292] Furthermore, the Kondo resonance, clearly visible as a zero-bias conductance enhancement within the *N*–1 state (***lf*-NiP8-TAP$_2^{+\cdot}$**) at 10 K, as shown in Figure 4.9a, is also no longer present in the 80 K data. The resonance results from scattering from a many-body state formed from the spin-1/2 radical on the molecule and electrons of opposite spin at the Fermi surface of the electrodes. As thermal energy increases toward the binding energy of this many-body molecule-electrode state the zero-bias conductance will decay. The characteristic temperature-dependence is parameterized by the Kondo temperature (T_K), the temperature when the conductance is half its value at 0 K. We extract the Kondo temperature of our device at V_g = –0.85 V by fitting the temperature-dependence of the zero-bias conductance to the usual spin-1/2 model: $G_K(T) = G_{T=0}/[1 + (2^{1/s} - 1)\,(T/T_K)^2]^s$ (eqn. 4.3 described in Section 4.1.3).[274] We calculate T_K = 18 ± 1 K and s = 0.30 ± 0.04 from the fit in Figure 4.10b. We also obtain T_K at this gate voltage from the FWHM of the resonance that gives a similar value of 17 ± 1 K. (see Figure 4.10b, inset). There are several parameters that define Kondo temperature of a nanoscale system; it depends on the addition energy E_{add} of the *N*–1 transition (0.12 eV for ***lf*-NiP8-TAP$_2$**), and exponentially on the molecule-electrode coupling, hence its association with the onset of intermediate coupling.[38] A typical gate-dependent measurement of a Kondo resonance would give a smooth conductance decay (or a

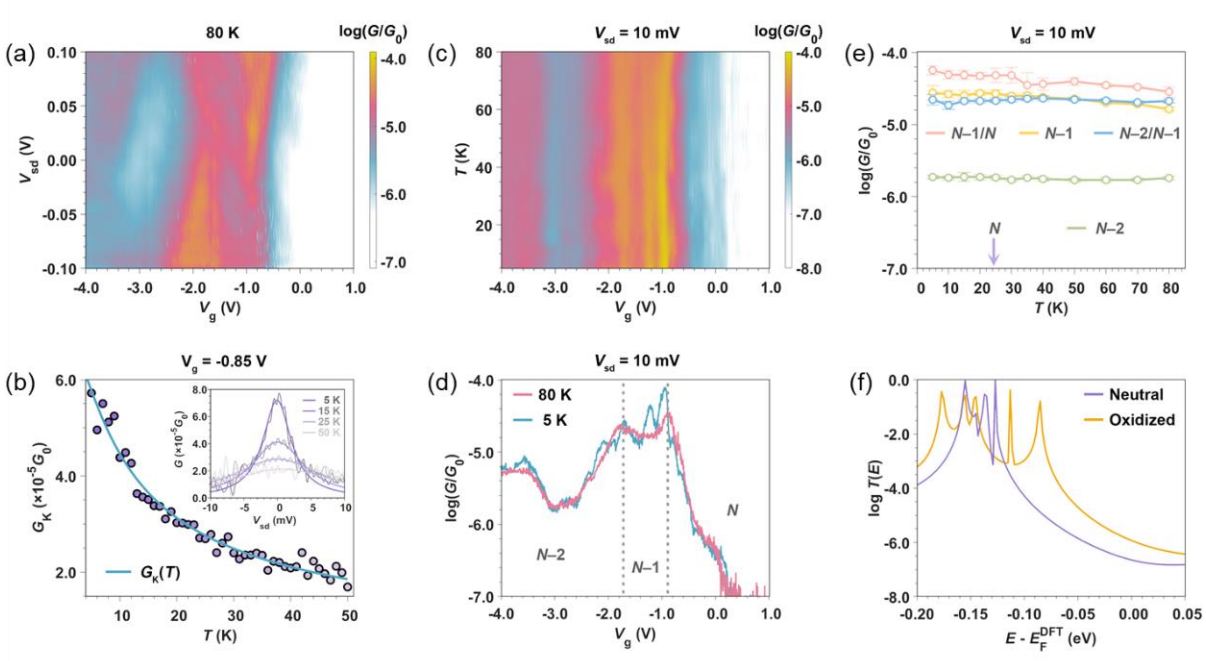

Figure 4.10: Temperature and oxidation-state dependence of molecular conductance. (a) The fluctuations of conductance and Kondo resonances from interference disappear as thermal energy surpasses $h v_F/L$ (5 meV) and the coherence length decreases, shown in the conductance map at 80 K (6.9 meV). (b) Experimental differential conductance of the Kondo peak at V_g = –0.85 V (purple circles) and fit to spin-1/2 Kondo model with T_K = 18 ± 1 K and s = 0.30 ± 0.04 (blue line). Inset: experimental differential conductance as a function of bias voltage (grey curves) and the Lorentzian fits of Kondo peaks (purple curves). (c) Differential conductance map measured as a function of temperature and gate voltage. Indicative of phase coherent transport, the conductance does not show an obvious temperature dependence. (d) Differential conductance as a function of V_g measured at 5 K (blue curve) and 80 K (pink curve) with a fixed bias voltage V_{sd} = 10 mV. (e) Temperature dependence of off-resonant transport measured in the conductance minima of the charge states. The values are average over a 100 mV window around V_g = –2.90 V for N–2, V_g = –1.30 V for N–1, and V_g = 0.6 V for N charge states. We also display the temperature-dependence of the N–2/N–1 (V_g = –1.75 V) and N–1/N (V_g = –0.95 V) Coulomb peaks. Note there is a shift in the position of the Coulomb peaks from Figure 4.9, likely to be a result in a change in trap occupancy in the HfO_2. For (c), (d) and (e), the conductance was measured V_{sd} = 10 mV to exclude the impact of Kondo resonance. (f) Calculated transmission spectra for the neutral state (purple) and oxidized state (orange) of single-molecule junction. Data were collected and analyzed by Dr. Zhixin Chen and Dr. James O. Thomas.

Kondo valley) as V_g is detuned from the resonances, described by the Haldane relation.[274,277] However, as T_K also depends exponentially on the graphene density of states,[294] our gate-dependent measurement of the Kondo peak displays conductance oscillations, as opposed to a smooth valley, within the N–1 state due to the interplay between Kondo and Fabry-Pérot resonances (visible in the pink gate trace in Figure 4.8b and Figure 4.15).

Aside from the Kondo behavior, the conductance of the device, including at the Coulomb peaks show a weak temperature dependence (Figure 4.10c and 4.10d). In the regions of V_g between the Coulomb peaks, the conductance is temperature independent, with some slight decrease in the conductance of N–1 state and the N–1/N peak due to Fermi broadening and consistent with off-resonant phase-coherent transport being the dominant mechanism. This constitutes one of the longest molecular systems (8 nm) with well-defined anchoring over which phase-coherent transport has been measured, resulting from low attenuation factors that are associated with fused porphyrin oligomers.[63]

The data show that off-resonance conductance is strongly dependent on the charge state of ***lf*-NiP8-TAP$_2$**, and depends on V_g within each diamond due to the effect of the gate potential on the level alignments (Figure 4.10d). For the neutral nanoribbon the conductance is below the noise level ($< 10^{-7.0}$ G_0) of our experimental setup away from the Coulomb peaks, but it is $10^{-4.7}$ G_0 in the N–1 state and $10^{-5.8}$ G_0 in N–2 (0.8 V from the N–2/N–1 Coulomb peak), indicating that in the oxidized states of the ***lf*-NiP8-TAP$_2$** off-resonance coherent transport is more efficient than in the neutral state. Charge-state dependence of conductance has been observed previously in STM-BJ measurements of fused porphyrin oligomers,[86] with a similar conductance enhancement of ~100 reported for an edge-fused trimer upon oxidation, similar to the ratio measured in our device that has a quite different geometry. Furthermore, our results are consistent with the general observation in single-molecule conductance measurements that upon oxidation or reduction, a conductance enhancement is observed in the odd-electron number state.[295–297]

As with these previous studies, we can utilize a combination of DFT and quantum transport theory[222,298,299] to calculate the phase-coherent transmission[†] (Section D.6 in Appendix D) to

[†] The theoretical calculations in this section were carried out by Dr. Songjun Hou and Dr. Qingqing Wu, under the supervision of Prof. Colin J. Lambert (Department of Physics, Lancaster University, UK).

support our experimental observations of a change in off-resonant conductance after ***lf*-NiP8-TAP$_2$** oxidation. To model the effect of a gate potential in the calculations, Cl atoms are placed on top of each Ni atom in the fused octamer to enable transmission to be calculated for an oxidized nanoribbon. The transmission coefficient T(E) (orange curve), when eight Cl atoms are present, is plotted in Figure 4.10f, and for comparison, the transmission coefficient (purple curve) of the neutral octamer is also shown. In agreement with our measurements, upon oxidation, a clear increase in $T(E)$ is observed over a large energy range close to Fermi energy, primarily due to a shrinking of the HOMO–LUMO gap (Figure 4.20 in Section D.6). The introduction of Cl atoms does create extra features (spikes) in the transmission that not affect the increasing trend (Figure D.10 in Section D.6). The calculated transmission spectrum based on coherent transport theory show excellent agreement with the experimental measurements of ***lf*-NiP8-TAP$_2$**, particularly at higher temperature.

4.4 Conclusion

In Chapter 3, we used the STM-BJ technique to study the electron transport behaviors of a family of fused porphyrin nanoribbons with different lengths (number of porphyrin units), and show that electron transmission through a fused porphyrin octamer even over a molecular length of 8 nm still expresses phase coherent transport (evidenced by the off-resonant transport behavior observed in the voltage-dependent measurement).

In this chapter, we conducted measurements of charge transport through the fused porphyrin octamer utilizing the graphene nanogap technique. Our findings provide clear evidences about the presence of phase-coherent electron transport persisting through the graphene-porphyrin nanoribbon-graphene junction. The mechanism is confirmed by conductance oscillations from Fabry-Pérot resonances that extend over a graphene-molecule-graphene cavity and the observation of temperature-independent off-resonant conductance in multiple oxidation states of the molecule. The persistency of phase-coherent transport behavior across such extended molecular systems, even within the intermediate (rather than strong) molecule-electrode coupling regime, is important for understanding and designing systems for efficient long-range electron transport, and the measurement of molecular conductance in different charge states provides complementary information to measurements of redox switching in single-molecule devices where such control over the molecular oxidation is not possible. The study of coherent electron transport through a molecular nanoribbon embedded in a Fabry-Pérot cavity opens up prospects for all-electrical interferometric measurements between graphene and molecular pathways, where both transmission magnitude and phase through the device can be determined experimentally. This platform could enable the read-out of molecular topological qubits, for which nanoribbons have demonstrated potential,[300] therefore providing an interesting research direction in exploring nanoribbon-graphene hybrid devices for quantum information processing.

5

Polaron Delocalization in the Radical Cations of Fused Porphyrin Oligomers

5.1 Introduction 127

5.1.1 Optical Signatures of Organic Mixed Valence Systems 128

5.1.2 Spin Delocalization Probed by EPR Spectroscopy 131

5.2 Molecular Design, Synthesis and Chemical Characterization 132

5.2.1 Molecular Design 132

5.2.2 Syntheses of *lf*-ZnP*N*-TIPS$_2$ 133

5.2.3 Chemical Characterizations of *lf*-ZnP*N*-TIPS$_2$ 134

5.3 Spectroelectrochemistry Measurements 136

5.4 EPR Measurements 141

5.4.1 Continuous Wave EPR 141

5.4.2 ^{1}H and ^{14}N ENDOR 143

5.4.3 Oxidation of *lf*-ZnP*N*-TIPS$_2$ in Air 144

5.5 Conclusion and Future Works 146

5.1 Introduction

Removal of an electron from a π-conjugated polymer chain (or framework) creates a spin-1/2 radical cation. Interaction of the radical cation with the molecular structure and solvent environment leads to geometrical relaxation and polarization of the molecular framework. The radical cation together with the distortion of the molecular framework is termed as a hole polaron.[301,302] Exploration of the extent of the polaron delocalization in a π-conjugated polymer is important for both the field of organic semiconductors and the research area of single-molecule electronics. For organic semiconductors, where the molecules are used for fabrication of optoelectronic devices (e.g., photovotalics and light-emitting diodes) or field-effect transistors, materials associated with spatially delocalized polarons feature high charge mobility and efficient long-range charge separation, because a delocalized polaron tends to have a smaller reorganization energy for charge transport.[303–306] For single-molecule electronics, recent studies, including the results that we discussed in Chapter 4, suggest that the off-resonant coherent transport becomes more efficient for molecular wires in their oxidized states than in the neutral state.[86,98,295,297] The delocalization length of the polarons in the molecular wires affects their charge transport behaviors.[98]

As discussed in previous chapters, conjugated porphyrin oligomers expressing weakly distance-dependent attenuation in single-molecule conductance are promising candidates as molecular wires for device fabrications. Investigation of the length of polaron delocalization in charged porphyrin oligomers is a primary step to understand the charge transport behaviors of these molecules in electronic devices. In the radical cations of linear butadiyne-linked porphyrin oligomers ***lb*-ZnP*N*$^{+\cdot}$**, the extent of polaron delocalization is about 2–3 porphyrin units (~3 nm), as investigated by Anderson, Timmel and coworkers, using optical and electron paramagnetic resonance (EPR) spectroscopies.[102] Therien and coworkers found that the hole polaron delocalization length in *p*-doped ethyne-linked porphyrin oligomers ***le*-ZnP*N*$^{+\cdot}$** spans up to 7 porphyrin units (~7.5 nm) at room temperature on the EPR time scale, which defines the longest hole polarons yet reported for a π-conjugated organic material in solution.[65,100] This length was recently refined to be ~5 porphyrin units by Timmel, Anderson and coworkers, deduced from low temperature EPR measurements and simulations.[66] Compared to the abovementioned two series of porphyrin oligomers, triply-linked (fused) porphyrin oligomers exhibit extremely strong electronic coupling between the neighboring porphyrin rings and a highly rigid coplanar geometry.[71,76] Therefore, we hypothesized that the hole polarons are coherently delocalized over a long range in the fused porphyrin oligomers.

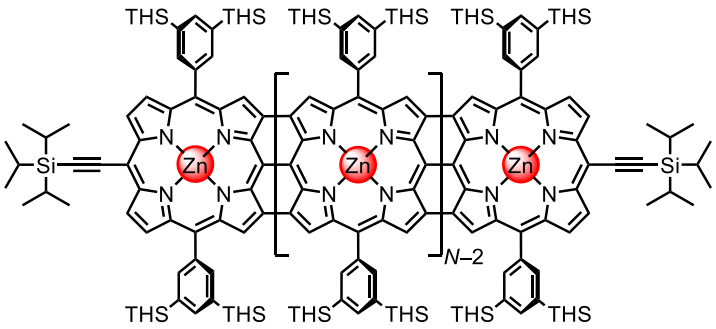

Figure 5.1: Chemical structures of ***lf*-ZnP*N*-TIPS$_2$**; *N* = 1–4, 6 and 10; TIPS = triisopropylsilyl groups, THS = trihexylsilyl solubilizing groups.

To investigate polaron delocalization length in the radical cations of fused porphyrin oligomers, we design and synthesize a family of fused porphyrin oligomers ***lf*-ZnP*N*-TIPS$_2$** (*N* = 1–4, 6 and 10; Figure 5.1), followed by probing the extent of polaron delocalization in the radical cations of these oligomers using vis–NIR–IR and EPR spectroscopies. Before discussing the experimental results, in the following, we briefly introduce the theoretical models that are used to study charge delocalization in the oligomers.

5.1.1 Optical Signatures of Organic Mixed Valence Systems

The two-state Marcus–Hush theory provides a simple model to understand the polaron delocalization in a mixed valence system comprising of two identical sites (a and b), one of which is oxidized.[307–310] The extent of the polaron delocalization varies, depending on the ratio of the electronic coupling H_{ab} between the two states (ψ_a and ψ_b) that describe the situation when the charge is exclusively localized in one site of the system, to the reorganization energy λ for the charge transfer. The free energies of these two localized states ψ_a and ψ_b can be schematically illustrated using two parabolas: λx^2 for ψ_a and $\lambda(x-1)^2$ for ψ_b (Figure 5.2). The free energies G_1 and G_2 for the ground state (Ψ_1) and excited state (Ψ_2) of the system can then be calculated by diagonalizing the following Hamiltonian matrix at a given x (reaction coordinate of electron transfer):

$$\mathbf{H} = \begin{bmatrix} \lambda x^2 & H_{ab} \\ H_{ab} & \lambda(x-1)^2 \end{bmatrix} \tag{5.1}$$

$$\mathbf{G}/\lambda = \mathbf{\Psi}^{-1}(\mathbf{H}/\lambda)\mathbf{\Psi} = \begin{bmatrix} G_1/\lambda & 0 \\ 0 & G_2/\lambda \end{bmatrix} \tag{5.2}$$

$$\mathbf{\Psi} = \begin{bmatrix} c_{11} & c_{21} \\ c_{12} & c_{22} \end{bmatrix} \tag{5.3}$$

where c_{ij} are mixing coefficients related to the population of the polaron on each site of the system.[311]

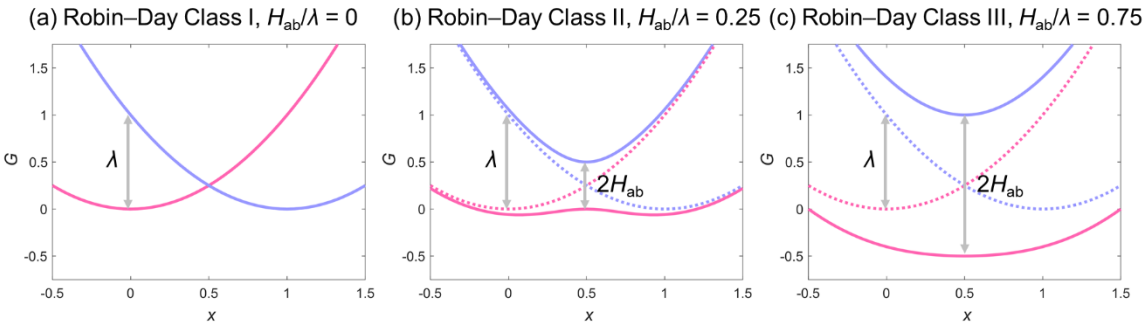

Figure 5.2: Free energy surfaces of the diabatic states (ψ_a and ψ_b; dashed curves) and adiabatic states (Ψ_1 and Ψ_2; solid curves) in the three coupling regimes of the two-state Marcus–Hush model.

If the electronic coupling H_{ab} between two sites is weak ($H_{ab} \approx 0$), the charge is mainly localized on one site of the system and it is classified as a Robin–Day class I compound.[310,312] Since the value of H_{ab} is small, the vertical excitation energy from the minimum of the surface corresponds to the reorganization energy λ (Figure 5.2a). Once the electronic coupling increases ($0 < H_{ab}/\lambda < 0.5$), the two parabolas mix and a gap (with a size of $2H_{ab}$) opens at the crossing point corresponding to a Robin–Day class II compound (Figure 5.2b). [310,312] If the electronic coupling between two states increases even further ($H_{ab}/\lambda > 0.5$), the two parabolas strongly mix to give a single minimum of the ground state free energy surface, and the charge is fully delocalized over both sites, leading to a Robin–Day class III compound (Figure 5.2c).[310,312] For this class of compounds, the vertical excitation energy from the energy minimum of the ground state corresponds to twice of the electronic coupling ($2H_{ab}$). If there are two energy minima in the ground state free energy surface, photoexcitation from one minimum could induce charge transfer from one site to the other, leading to observation of an intervalence charge-transfer (IV-CT) band in the absorption spectrum of a mixed valence compound in practice.[308,310,313,314] To describe an oligomer or polymer comprising of a number of N identical sites, the two-state model can be extended to a generalized multiparabolic model (MPM) by diagonalizing the following Hamiltonian matrix at a given x:[311,315,316]

$$\mathbf{H} = \begin{bmatrix} \lambda x^2 & H & 0 & \cdots & 0 \\ H & \lambda(x-1+2)^2 & H & \ddots & \vdots \\ 0 & H & \ddots & H & 0 \\ \vdots & \ddots & H & \lambda(x-N+2)^2 & H \\ 0 & \cdots & 0 & H & \lambda(x-N+1)^2 \end{bmatrix} \tag{5.4}$$

$$\mathbf{G}/\lambda = \mathbf{\Psi}^{-1}(\mathbf{H}/\lambda)\mathbf{\Psi} = \begin{bmatrix} G_1/\lambda & 0 & \cdots & 0 \\ 0 & G_2/\lambda & \ddots & \vdots \\ \vdots & \ddots & \ddots & 0 \\ 0 & \cdots & 0 & G_N/\lambda \end{bmatrix} \tag{5.5}$$

The vertical excitation energy from the ground state to the excited state *i* is thus given by

$$\Delta E_{\text{abs}} = G_i - G_1 \tag{5.6}$$

which can be used to estimate the H/λ for the system.

Compared to the neutral molecules, the radical monocations, in principle, feature two characteristic low energy absorption bands (electronic transitions), namely P_1 and P_2 bands, which are assigned approximately to HOMO → SOMO and SOMO → LUMO transitions, respectively (Figure 5.3).[317–319] However, in practice, to precisely assign the electronic transitions requires DFT and TD-DFT calculations of the electronic structures. The P_1 band corresponding to the lowest energy absorption peak can be regarded as the IV-CT band of a mixed valence system to estimate the reorganization energy λ for the Robin–Day class I/II compounds or electronic coupling energy H for the Robin–Day class III compounds.

In addition to the MPM model, the optical data obtained for a family of oligomers with different number of repeating units can also be plotted against $1/N$ and fitted to the Meier equation,[320] the Hückel model,[321] or the one particle in a box model[260] to estimate the effective conjugation length N_{ecl} of the oligomers. N_{ecl} characterizes the saturation of the shift of the absorption band and the polaron delocalization length.

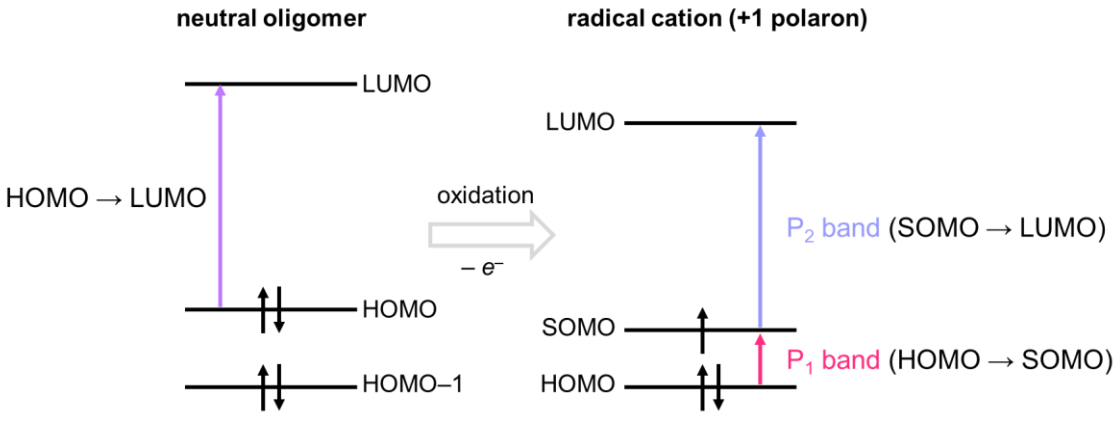

Figure 5.3 Schematic illustration of the optical signatures for a neutral and a charged π-conjugated oligomer.[102] HOMO, LUMO and SOMO are highest occupied molecular orbital, lowest unoccupied molecular orbital, and singly occupied molecular orbital, respectively.

5.1.2 Spin Delocalization Probed by EPR Spectroscopy

The distribution of a spin-½ hole polaron in a polymer chain can be investigated by probing the electron–nuclear hyperfine couplings using EPR spectroscopy.[65,66,100,102,322–325] In principle, the isotropic hyperfine couplings decrease when the spin density spreads over more atoms, because the spin density at each atom becomes lower. A common approach to evaluate the spin density distribution in a family of oligomers with *N* repeating units is to plot the linewidths observed from the measurements as a function of 1/*N* and to compare the plots to the Norris trend:[322]

$$\Delta B_N = \frac{1}{\sqrt{N}} \Delta B_1 \tag{5.7}$$

where ΔB_N is the width of a Gaussian envelope fitted to the continuous wave (cw) EPR spectrum. Norris demonstrated that in the limit of a stochastic, near-barrierless electron transfer between *N* equivalent sites of a chain, the spectral envelope width of an oligomer can be predicted as a function of the envelope width of the monomer repeat unit ΔB_1. Therefore, a good agreement between the experimental trend in ΔB_N and the one predicted by Norris suggests that the spin density is uniformly distributed over the system on the timescale of the measurement. However, only considering the fit to the Norris equation may exaggerate the polaron delocalization length in the oligomers because the polaron may rapidly hop between different units (at room temperature) in the measurement, leading to an average of the spin density over the whole molecule.[65,324] Solely comparing the observed linewidths to the Norris trend may also underestimate the extent of polaron delocalization, because deviations from the trend could arise from an uneven distribution of the spin density across different units in an oligomer.[66] Therefore, to clearly extrapolate the polaron delocalization length from the experimental data requires careful simulation, computational analysis (DFT calculations) and other experimental data (such as ENDOR spectra measured at cryogenic temperatures; ENDOR = electron nuclear double resonance). If the apparent extent of delocalization is independent of temperature, this implies true static delocalization rather than hopping or dynamic migration.

5.2 Molecular Design, Synthesis and Chemical Characterization

5.2.1 Molecular Design

In this project, a family of fused Zn(II) porphyrin oligomers ***lf*-ZnP*N*-TIPS$_2$** (N = 1–4, 6, 10) were prepared and oxidized to investigate the extent of the polaron delocalization (see Figures 5.1 or 5.3 for the chemical structures). By analogy with the fused Ni(II) porphyrin oligomers ***lf*-NiP*N*-TMS$_2$** discussed in Chapter 3, we chose the bulky 3,5-bis(trihexylsilyl)phenyl solubilizing groups to improve the solubility of the fused porphyrin oligomers. To be aligned with the previous studies on the butadiyne and ethyne-linked porphyrin oligomers, we used zinc instead of nickel as metal centers in this work. TIPS-acetylene groups were introduced as the end groups to protect the terminal *meso* positions of the porphyrin oligomers, leading to high efficiencies for the oxidative fusion reactions.

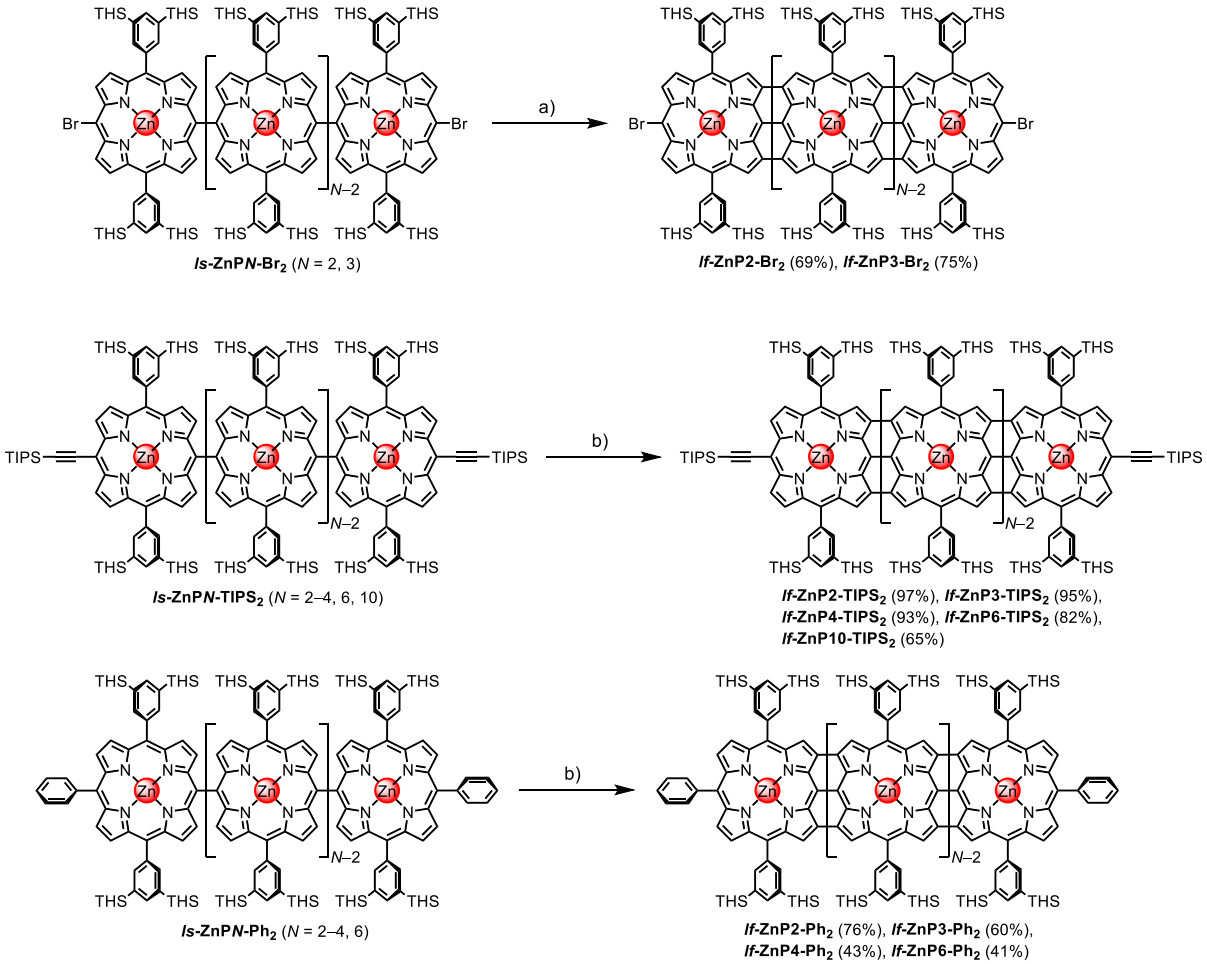

Figure 5.3: Syntheses of ***lf*-ZnP*N*-Br$_2$**, ***lf*-ZnP*N*-TIPS$_2$** and ***lf*-ZnP*N*-Ph$_2$**. Reaction conditions: (a) Fe(OTf)$_3$, CH_2Cl_2, 1–6 h (see ref. 325 for the details); (b) 2,3-dichloro-5,6-dicyano-*p*-benzoquinone (DDQ), Sc(OTf)$_3$, toluene, 80 ºC, 2 h.

5.2.2 Syntheses of *lf*-ZnP*N*-TIPS$_2$

The syntheses of *meso–meso* singly-linked porphyrin oligomers ***ls*-ZnP*N*-Br$_2$** followed the same procedures mentioned in Chapter 3. In previous work, Anderson, Timmel and coworkers showed that Fe(OTf)$_3$ can be used as oxidant to convert ***ls*-ZnP*N*-Br$_2$** to ***lf*-ZnP*N*-Br$_2$** (*N* = 2 and 3) in good yields (Figure 5.3).[325] However, severe demetalation was observed during the oxidative fusion reaction, and thus remetalation of the partially fused porphyrin oligomers and treatment of metalated intermediates with another portion of Fe(OTf)$_3$ are needed to afford the fully fused products. It is also difficult to covert ***ls*-ZnP*N*-Br$_2$** to ***lf*-ZnP*N*-Br$_2$** using the DDQ/Sc(OTf)$_3$ promoted oxidation reported by Osuka and coworkers.[71,250]

We functionalized the terminal *meso* positions of the singly-linked porphyrin oligomers with several different acetylenes (i.e., TMS, THS, CPDIPS and TIPS-acetylenes; CPDIPS = Si(*i*-Pr)$_2$(CH$_2$)$_3$CN) by Sonogashira coupling reactions and tested the effectiveness of the DDQ/Sc(OTf)$_3$ promoted oxidative fusion reaction. Only oligomers with TIPS end groups (***lf*-ZnP*N*-TIPS$_2$**) yielded the desired products (***lf*-ZnP*N*-TIPS$_2$**) in good to excellent yields (see Figure 5.3 for reaction conditions and yields for each porphyrin oligomers), presumably attributed to the steric bulkiness of the TIPS group compared to other silyl groups.[†] The oxidative fusion reactions were also found to be more efficient for oligomers with TIPS end groups than those with phenyl capping groups that are mostly used to protect the terminal *meso* positions (Figure 5.3 displays the yields for ***lf*-ZnP*N*-Ph$_2$**). In addition, no demetalation was observed in the fusion reactions for oligomers bearing TIPS end groups, which simplifies the purification. Compared to the phenyl groups, the use of TIPS groups provides an additional advantage: it allows functionalization of the alkyne moieties with other groups after cleavage of the silyl groups to study other properties (e.g., charge transport behaviors) of the molecular wires in future works.[63,226] In addition to the fused porphyrin oligomers ***lf*-ZnP*N*-TIPS$_2$** (*N* = 2–4, 6, 10), a porphyrin monomer **ZnP1-TIPS$_2$** was also synthesized as a reference compound for EPR studies.

[†] The first success in synthesis of ***lf*-ZnP2-TIPS$_2$** was made by Dr. Jeff M. Van Raden (Department of Chemistry, University of Oxford).

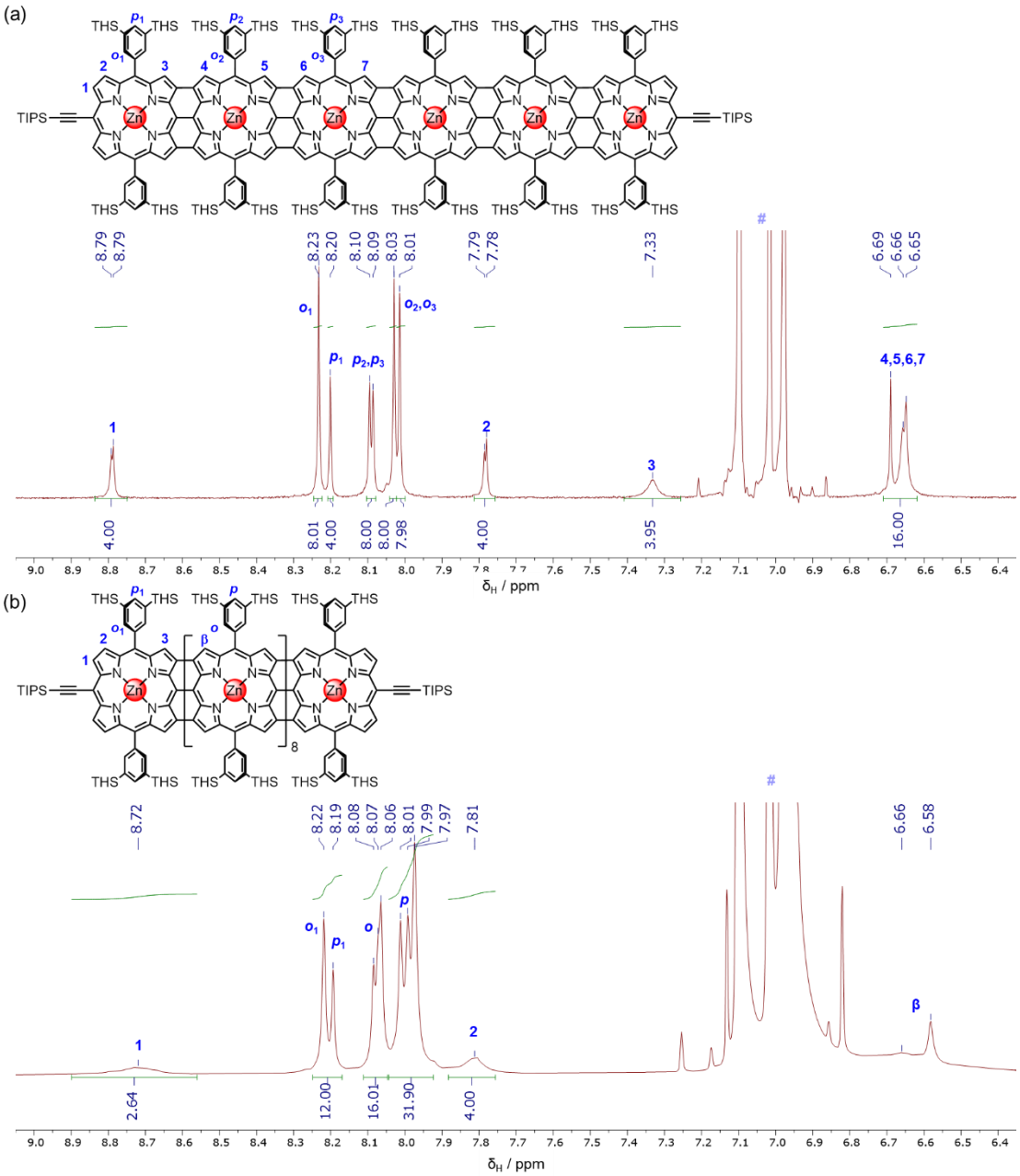

Figure 5.4: (a) Chemical structure and selected section of ^{1}H NMR spectrum (700 MHz, toluene-d_8, 298 K) of ***lf*-ZnP6-TIPS$_2$**. (b) Chemical structure and selected section of ^{1}H NMR spectrum (500 MHz, toluene-d_8, 298 K) of ***lf*-ZnP10-TIPS$_2$**. # = toluene.

5.2.3 Chemical Characterizations of *lf*-ZnP*N*-TIPS$_2$

The fused porphyrin oligomers ***lf*-ZnP*N*-TIPS$_2$** (*N* = 2–4, 6, 10) were initially identified by comparing the observed molecular ion peak in mass spectroscopy for each oligomer to that obtained before the oxidative fusion (i.e., mass spectra for ***ls*-ZnP*N*-TIPS$_2$**). For example, molecular ion peaks at *m*/*z* = 6967 and 6978 were found for ***lf*-ZnP4-TIPS$_2$** (calc. for $C_{438}H_{710}N_{16}Si_{18}Zn_4$: 6967) and ***ls*-ZnP4-TIPS$_2$** (calc. for $C_{438}H_{722}N_{16}Si_{18}Zn_4$: 6979); *m*/*z* =

10268 and 10286 were found for ***lf*-ZnP6-TIPS$_2$** (calc. for $C_{646}H_{1042}N_{24}Si_{26}Zn_6$: 10267) and ***ls*-ZnP6-TIPS$_2$** (calc. for $C_{646}H_{1062}N_{24}Si_{26}Zn_6$: 10287); *m*/*z* = 16877 and 16915 were found for ***lf*-ZnP10-TIPS$_2$** (calc. for $C_{1062}H_{1706}N_{40}Si_{42}Zn_{10}$: 16869) and ***ls*-ZnP10-TIPS$_2$** (calc. for $C_{1062}H_{1742}N_{40}Si_{42}Zn_{10}$: 16905). Although the measured *m*/*z* for ***lf*-ZnP10-TIPS$_2$** deviates from the calculated value (~10 Da), the observed *m*/*z* difference between ***lf*-ZnP10-TIPS$_2$** and ***ls*-ZnP10-TIPS$_2$** (~38 Da) is similar to the expected shift for the oxidative fusion reactions (loss of 36 protons and formation of 18 C–C bonds). More details are described in Appendix E, Sections E.2 and E.3.

The fused oligomers were further characterized by ^{1}H NMR spectroscopy. The ^{1}H NMR signals for short oligomers (*N* = 2–4) are clearly resolved and most of the ^{1}H NMR resonances can be unambiguously assigned based on comparison among the whole series of compounds and analysis of the ^{1}H-^{1}H correlations observed from the COSY and NOESY spectra (see Appendix E, Section E.8 for details). For ***lf*-ZnP6-TIPS$_2$**, the ^{1}H signals are more resolved in comparison to those reported in previous works (Figure 5.4a).[80,249] However, the ^{1}H resonance peaks for the β protons become broadened compared to those for the short oligomers and the fused nickel porphyrin hexamer ***lf*-NiP6-TMS$_2$** discussed in Chapter 3. This is particularly the case for H_3 and one of the protons in the range of 6.6 to 6.7 ppm, leading to a difference of the integrated proton numbers from the expected values. For ***lf*-ZnP10-TIPS$_2$**, while the signals for the protons on the peripheral aryl groups (*ortho* and *para* positions) remain satisfactorily resolved, the peaks for the β protons are seriously broadened (Figure 5.4b). We could not even observe the ^{1}H resonance peak for H_3 from the spectrum. These broadenings could arise from π–π stacking of the long oligomers or the emergence of an open-shell characters of the molecules. Given that the fused nickel porphyrin hexamer and octamer with the same solubilizing side chains display sharp ^{1}H resonance peaks in the measured spectra, the π–π stacking of ***lf*-ZnP6-TIPS$_2$** at a similar concentration is unlikely. However, as the structures of zinc oligomers are flatter than those of nickel complexes, the solubility issue cannot be completely excluded. Given that the HOMO energies for zinc porphyrins are higher than those for nickel porphyrins, we hypothesized that the zinc oligomers can be oxidized by O_2 in air to form radical cations, resulting in a broadening of the ^{1}H NMR signals. The EPR studies of oligomers revealed that spin-½ signals are present in the isolated samples of long oligomers (*N* = 6 and 10), supporting the second hypothesis. Details are discussed later in this chapter.

5.3 Spectroelectrochemistry Measurements[†]

We measured the optical properties of the polarons in radical cations of ***lf*-ZnP*N*-TIPS$_2$** (*N* = 2–4, 6 and 10) by spectroelectrochemistry, a technique combining spectroscopy and electrochemistry. The measurements were performed using an optically transparent thin-layer electrochemical cell (OTTLE; see ref. 327 for the working principles), in which each of the oligomers in a CH_2Cl_2 solution, with 0.1 M tetra-*n*-butylammonium hexafluorophosphate (Bu_4NPF_6) as supporting electrolyte, was oxidized and reduced by running a cyclic voltammogram. The UV–vis–NIR–IR absorption spectra (in the range from 350 to 5000 nm) for oligomers in different oxidation states were collected in parallel with the electrochemical process. The collected data were resolved by multivariate curve resolution using the MCR-ALS toolbox in MATLAB and the deconvoluted spectra for the neutral oligomers and their radical cations (at 1+ oxidation state) are given in Figure 5.5 (light blue curves for ***lf*-ZnP*N*-TIPS$_2$** and pink curves for ***lf*-ZnP*N*-TIPS$_2^{+\cdot}$**).

Table 5.1: Experimental[a] and TD-DFT calculated[b] vis–NIR–IR absorption properties for ***lf*-ZnP*N*-TIPS$_2^Q$** (*Q* = 0 and +1) for longest wavelength absorption bands.

***lf*-ZnP*N*-TIPS$_2$**	*N* = 2	*N* = 3	*N* = 4	*N* = 6	*N* = 10
$\lambda_{abs,III}$ [nm]	1087	1378	1631	2075	2832
($E_{abs,III}$ [eV])	(1.14)	(0.90)	(0.76)	(0.60)	(0.44)
$\lambda_{BLYP35,III}$ [nm]	911	1223	1433	1883	2664
($E_{BLYP35,III}$ [eV])	(1.36)	(1.01)	(0.86)	(0.66)	(0.47)
$\lambda_{LC\text{-}\omega hPBE,III}$ [nm]	979	1245	1474	1860	2423
($E_{LC\text{-}\omega hPBE,III}$ [eV])	(1.27)	(1.00)	(0.84)	(0.67)	(0.51)
***lf*-ZnP*N*-TIPS$_2^{+\cdot}$**	*N* = 2	*N* = 3	*N* = 4	*N* = 6	*N* = 10
$\lambda_{abs,P2}$ [nm]	1674	1822	2161	2785	3600
($E_{abs,P2}$ [eV])	(0.74)	(0.68)	(0.57)	(0.45)	(0.34)
$\lambda_{BLYP35,P2}$ [nm]	1593[c]	1759	2129	2785	4359
($E_{BLYP35,P2}$ [eV])	(0.78)	(0.70)	(0.58)	(0.45)	(0.28)
$\lambda_{LC\text{-}\omega hPBE,P2}$ [nm]	1567[d]	1972	2322	2819	3495
($E_{LC\text{-}\omega hPBE,P2}$ [eV])	(0.79)	(0.63)	(0.53)	(0.44)	(0.35)

[a] Experimental values of λ_{abs} and E_{abs} were estimated from the absorption peak maxima from the deconvoluted absorption spectra shown in Figure 5.5. [b] Theoretically calculated values were obtained from TD-DFT calculations using BLYP35 or LC-ωhPBE (ω = 0.1) functionals, 6-31G* basis set and the PCM solvent model (CH_2Cl_2). [c] It is dipole forbidden from calculation (calculated oscillator strength $f = 0$). [d] It is dominated by HOMO–1 → SOMO transition.

[†] All measurements and data analysis were carried out with Sebastian M. Kopp, in collaboration with Dr. Robert M. J. Jacobs (Department of Chemistry, University of Oxford).

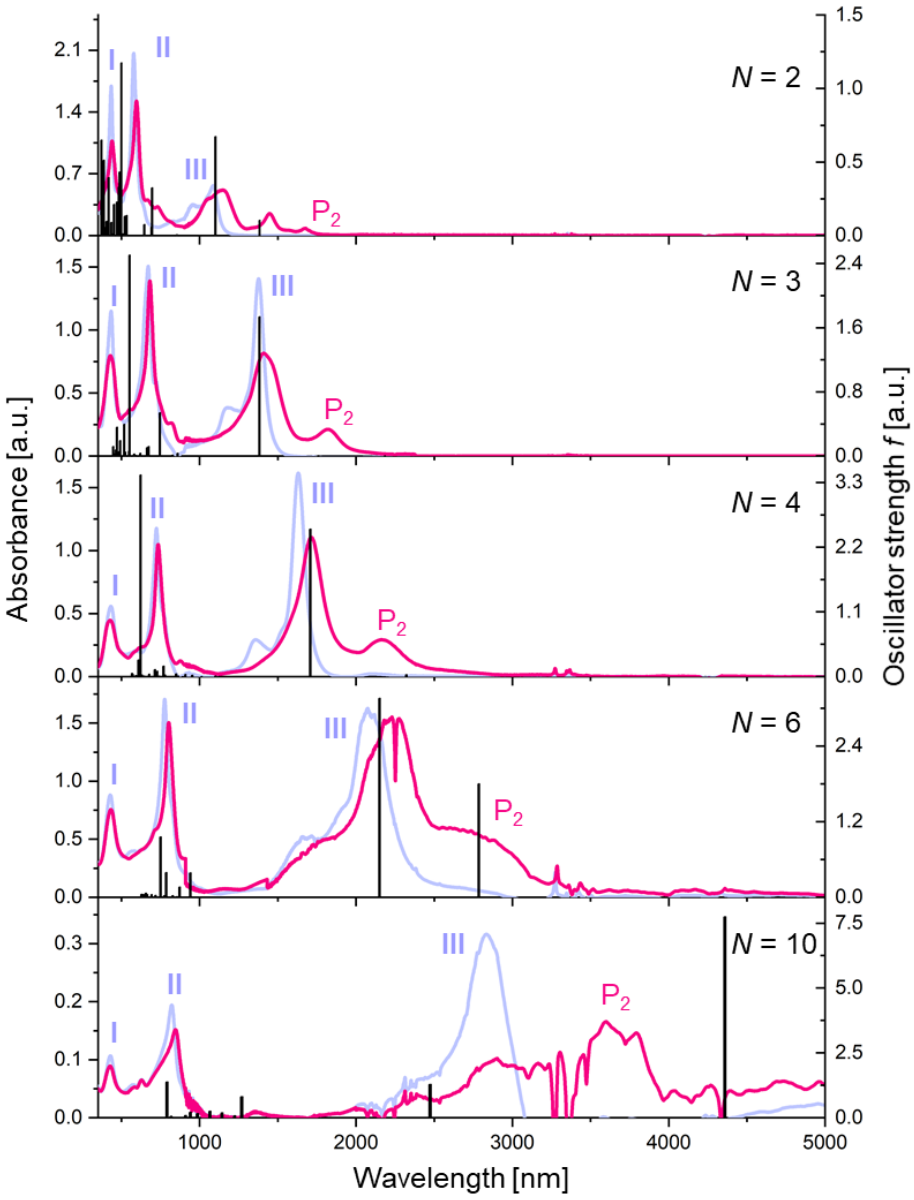

Figure 5.5: Deconvoluted vis–NIR–IR absorption spectra for ***lf*-ZnP*N*-TIPS$_2$** (light blue curves) and ***lf*-ZnP*N*-TIPS$_2^{+\cdot}$** (pink curves), measured in CH_2Cl_2 with 0.1 M Bu_4NPF_6 at 298 K. Black bars: TD-DFT (BLYP35/6-31G*) calculated wavelengths vs. oscillator strengths *f* for ***lf*-ZnP*N*-TIPS$_2$**.

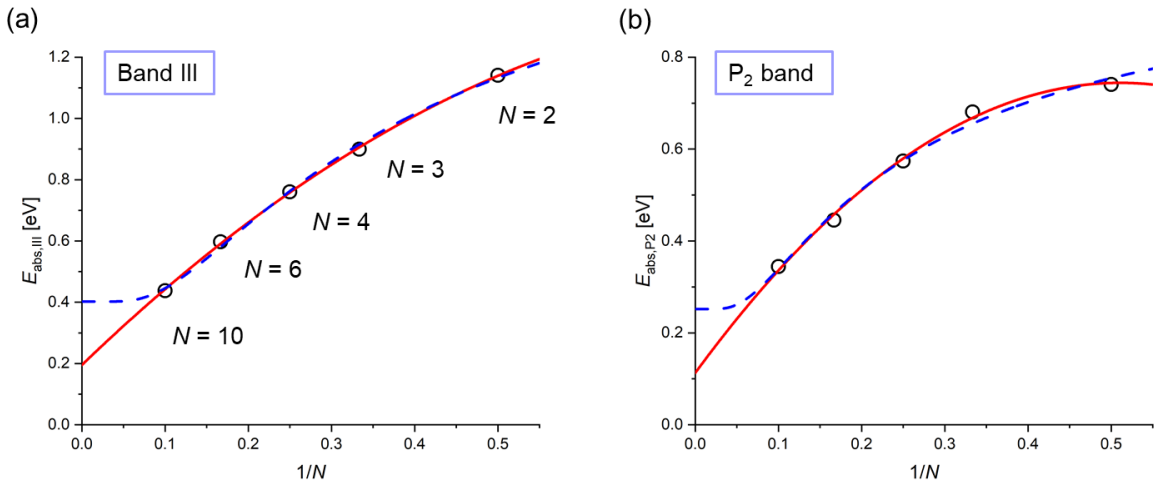

Figure 5.6: (a) and (b) are plots of $E_{abs,III}$ and $E_{abs,P2}$ for ***lf*-ZnP*N*-TIPS$_2$** against 1/*N*, respectively. Blue dash lines and red solid lines are fits to the Meier equation (eqn. 5.8) and eqn.5.9, respectively. Fitted values: (a) $E_{abs}(\infty)$ = 0.40 eV, $E_{abs}(1)$ = 1.44 eV, α = 0.35, R^2 = 0.99541; a = 0.20 eV, b = 2.62 eV, c = –1.46 eV, R^2 = 0.99930; (b) $E_{abs}(\infty)$ = 0.23 eV, $E_{abs}(1)$ = 0.88 eV, α = 0.22, R^2 = 0.97945; (d) a = 0.11 eV, b = 2.47 eV, c = –2.42 eV, R^2 = 0.99197.

The spectra for neutral oligomers exhibit three characteristic peaks, labeled as band I, II and III, which originate from B_y, B_x and Q_x transitions of a porphyrin monomer. The band III is assigned to HOMO → LUMO transition for each oligomer according to the TD-DFT calculations and previous studies.[71,80,81,249] Compared to the neutral oligomers, the spectra for ***lf*-ZnP*N*-TIPS$_2^{+\cdot}$** feature an additional low energy absorption peak for each oligomer, except the dimer which shows two additional peaks. These optical signatures are different from those observed for the oxidized butadiyne-linked porphyrin oligomers ***lb*-ZnP*N*-THS$_2^{+\cdot}$** that feature two characteristic electronic transitions at around 2000–5000 and 1000 nm, characterized as P_1 and P_2 bands for the polarons of the oligomers.[102,328,329] We performed TD-DFT calculations to simulate the electronic transitions for ***lf*-ZnP*N*-TIPS$_2^{+\cdot}$** employing four different functionals (i.e., B3LYP, BLYP35 and LC-ωhPBE, ω = 0.1 and 0.2) that have been generally used for mixed valence systems.[101,102,330,331] The calculated excitation energies using BLYP35 and LC-ωhPBE (ω = 0.1) functionals match the experimental values (Table 5.1), except for the value for ***lb*-ZnP10-TIPS$_2^{+\cdot}$** estimated by BLYP35. Comparison of the calculated excitation energies to those determined from the deconvoluted experimental spectra suggests that the characteristic low energy absorption peaks observed for ***lf*-ZnP*N*-TIPS$_2^{+\cdot}$** mainly arise from SOMO → LUMO transitions and they are labeled as P_2 bands for the hole polarons. The HOMO → SOMO transitions, traditionally named as the P_1 bands, for ***lf*-ZnP*N*-TIPS$_2^{+\cdot}$** are dipole forbidden, merged with the SOMO → LUMO transitions or exhibited in the relatively

higher energy regime, depending on the length of the oligomers and the functionals used for the calculations. Therefore, we focus on the P_2 bands in the rest of this chapter.

We next analyzed the band shifts with the chain length of the oligomers by plotting the measured $E_{abs,III}$ (for neutral oligomers) and $E_{abs,P2}$ (for oligomers in +1 oxidation state) against $1/N$, followed by fitting of the plots to the Meier equation (eqn. 5.8),[320] and eqn. 5.9 derived from the one particle in a box model[260] (or the Hückel model[260,321]):

$$E_{\mathrm{abs}}(N) = E_{\mathrm{abs}}(\infty) + [E_{\mathrm{abs}}(1) - E_{\mathrm{abs}}(\infty)]e^{-\alpha[N-1]} \tag{5.8}$$

where $E_{abs}(N)$ corresponds to the energy estimated from the band observed from experiment for an oligomer with N porphyrin units, $E_{abs}(\infty)$, $E_{abs}(1)$ and α are fitting parameters,

$$E_{\mathrm{abs}}(N) = a + b\frac{1}{N} + c\frac{1}{N^2} \tag{5.9}$$

in which a, b and c are fitting parameters; a is equal to $E_{abs}(\infty)$ in eqn. 5.8.

The plots and the corresponding fits are depicted in Figure 5.6. For the neutral oligomers, both fits (Figure 5.6a) suggest that the progressively bathochromic shifts of the band III do not reach a saturation up to $N = 10$, although the estimated limits $E_{abs}(\infty)$ (or a) vary depending on the equation used. Since the band III corresponds to the HOMO → LUMO transitions for the neutral oligomers, the continuously bathochromic shifts of the band III infer the effective conjugative length N_{ecl} for ***lf*-ZnP*N*-TIPS$_2$** is beyond 10 porphyrin units, also supported by previous studies.[71,80,81,249] For the radical cations, the plots for the P_2 bands as functions of $1/N$ (Figure 5.6b) express similar trends to those for the neutral oligomers (clear shifts to low energy for the whole series of oligomers), which implies $N_{ecl} \geq 10$ for ***lf*-ZnP*N*-TIPS$_2^{+\cdot}$**.

We next employed the MPM model to estimate the ratio of the electronic coupling to the reorganization energy H/λ. A modified Hamiltonian matrix (compared to eqn. 5.4) was used to describe the system:[311,315,316]

$$\mathbf{H} = \begin{bmatrix} \lambda x^2 - \varepsilon & H & 0 & \cdots & 0 \\ H & \lambda(x-1+2)^2 & H & \ddots & \vdots \\ 0 & H & \ddots & H & 0 \\ \vdots & \ddots & H & \lambda(x-N+2)^2 & H \\ 0 & \cdots & 0 & H & \lambda(x-N+1)^2 - \varepsilon \end{bmatrix} \tag{5.10}$$

in which ε is a fitting parameter introduced to account for the effect from the end groups (i.e., the electron-withdrawing features of TIPS-acetylenes may destabilize the hole polaron on the terminal porphyrins). After diagonalizing the matrix for each oligomer (N = 3, 4, 6 and 10), the values of $\Delta G_{abs}(N)/\lambda$ were normalized and fitted to the $E_{abs,P2}$ observed from experiment, where

$\Delta G_{abs}(N)/\lambda = G_{abs,3}(N) - G_{abs,1}(N)$ are energies corresponding to electronic transition from ground state to the second excited state, modeling the P_2 band.

The calculated parabolas for each oligomer are depicted in Figures 5.7 a–d, in which the red arrows correspond to the modeled P_2 bands. The simulated values of $\Delta G_{abs}(N)/\lambda$ using H/λ = 6.2 and ε/λ = –0.64 match the normalized experimental excitation energies of the P_2 bands (Figure 5.7e). A negative value of ε/λ agrees with the destabilization of the hole polaron on the end porphyrins caused by the TIPS-acetylene end groups. The value of H/λ is significantly greater than 0.5, implying that ***lf*-ZnP*N*-TIPS$_2^{+\cdot}$** are in Robin–Day class III and that the polarons are fully delocalized in these oligomers.

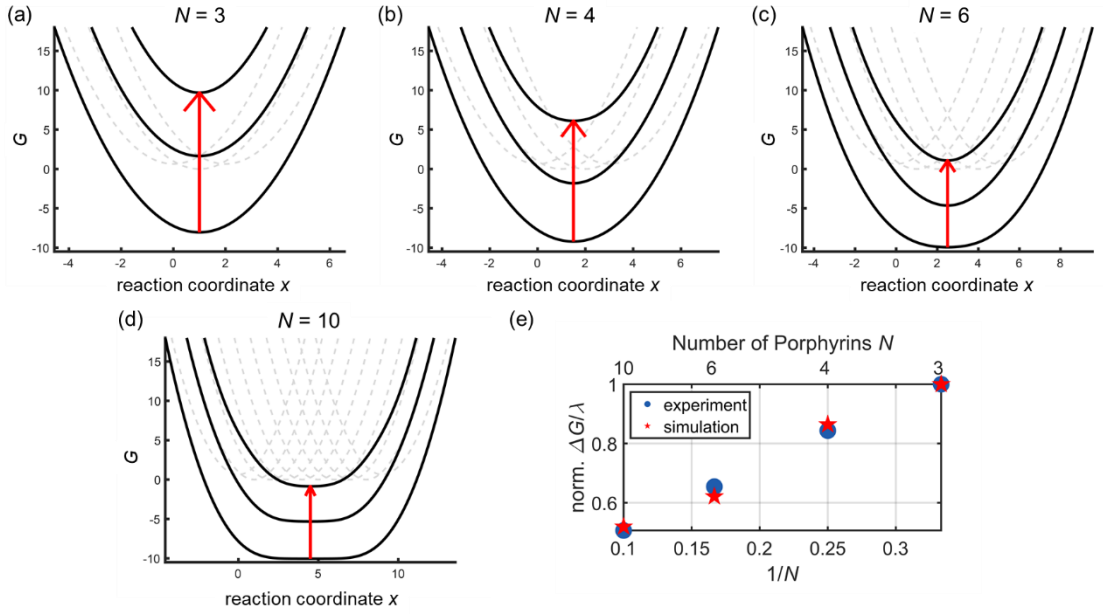

Figure 5.7: (a)–(d) MPM simulations for ***lf*-ZnP*N*-TIPS$_2^{+\cdot}$** (N = 3, 4, 6 and 10) using H/λ = 6.2, ε/λ = –0.64. (e) Normalized experimental energies (blue dots) and MPM simulated $\Delta G_{abs}(N)/\lambda$ (red stars) of the P_2 bands as a function of chain length. The simulations were performed with H/λ = 6.2, ε/λ = –0.64, obtained by least squares fitting of the simulated $\Delta G_{abs}(N)/\lambda$ to the experimental P_2 bands (RMSD = 0.02). RMSD is the root-mean-square deviation.

5.4 EPR Measurements†

5.4.1 Continuous Wave EPR

We probed the extent of spin delocalization in the radical cations of ***lf*-ZnP*N*-TIPS$_2$** (N = 1–4, 6 and 10) by EPR spectroscopy. The radical cations were generated by addition of tris(4-bromophenyl)ammoniumyl hexachloroantimonate (BAHA, 0.5 equivalent) as a chemical oxidant to the neutral oligomers in solution (CD_2Cl_2/toluene-d_8/THF-d_8 = 1:1:1). Figure 5.8a shows the room temperature (295 K) X-band cw-EPR spectra of ***lf*-ZnP*N*-TIPS$_2^{+\cdot}$**. The hyperfine structure of the monomer is dominated by the coupling to four equivalent ^{14}N nuclei of the porphyrin. While the dimer exhibits partially resolved hyperfine couplings, the hyperfine couplings for longer oligomers (N > 2) are no longer resolved, resulting in inhomogeneous broadening and a phenomenological Gaussian lineshape of the spectra.

We extracted the envelope widths ΔB_N for oligomers by fitting each experimental spectrum to a Gaussian envelop (Figure 5.8b, blue lines), and plotted them as a function of $(1/N)^{0.5}$, as shown in Figure 5.8e (black circles). The envelope widths are progressively narrowing with length for the whole series of radical cations. However, this trend deviates significantly from the Norris relationship predicted by eqn. 5.7, where the experimental ΔB_1 was used for the prediction. This observed deviation is similar to that obtained from the measurements of the ethyne-linked porphyrin oligomers ***le*-ZnP*N*-CPDIPS$_2^{+\cdot}$**,[66] arising from the inhomogeneous population of the ^{14}N spin density within individual porphyrin units in the oligomers. To elucidate the reason for the deviation, we simulated the EPR spectra by relating the isotropic part of the hyperfine couplings $A_{\mathrm{iso},i}$ to the DFT calculated Mulliken spin densities on the ^{14}N nuclei ρ_i using the McConnell relationship:[332]

$$A_{\mathrm{iso},i} = c\rho_i \tag{5.10}$$

where c is the McConnell constant that was determined using the monomer result (see ref. 35 for more details). The simulated spectra and the corresponding envelop widths replicate the experimental data (Figures 5.8c and 5.8e, red circles). The calculations also suggest that the spin on each radical cation is delocalized across the whole π-conjugated system, whereas the spin densities on ^{14}N nuclei are inhomogeneously distributed within each porphyrin unit in the

† All EPR measurements and data analysis were conducted by Sebastian M. Kopp, working with Ashley J. Redman, under the supervision of Prof. Christiane R. Timmel (Department of Chemistry, University of Oxford).

oligomers (except for the monomer and the central porphyrin in the trimer). For example, the plot of the relative spin densities on the ^{14}N nuclei of ***lf*-ZnP4-TIPS$_2^{+\cdot}$** (blue shades in Figure 5.8d) reveal that on each porphyrin, the spin densities on the peripheral ^{14}N nuclei are much larger than those on the central ^{14}N atoms. The same motif of alternating regions of high and low spin densities along the backbones is found in all oligomers (see Appendix E for the plots for other oligomers). Based on the simulation data and DFT calculation results, the deviation of the experimental data from an ideal Norris trend is due to the inhomogeneity of the ^{14}N spin density on each porphyrin unit, but not arising from reduced spin delocalization across the wire.

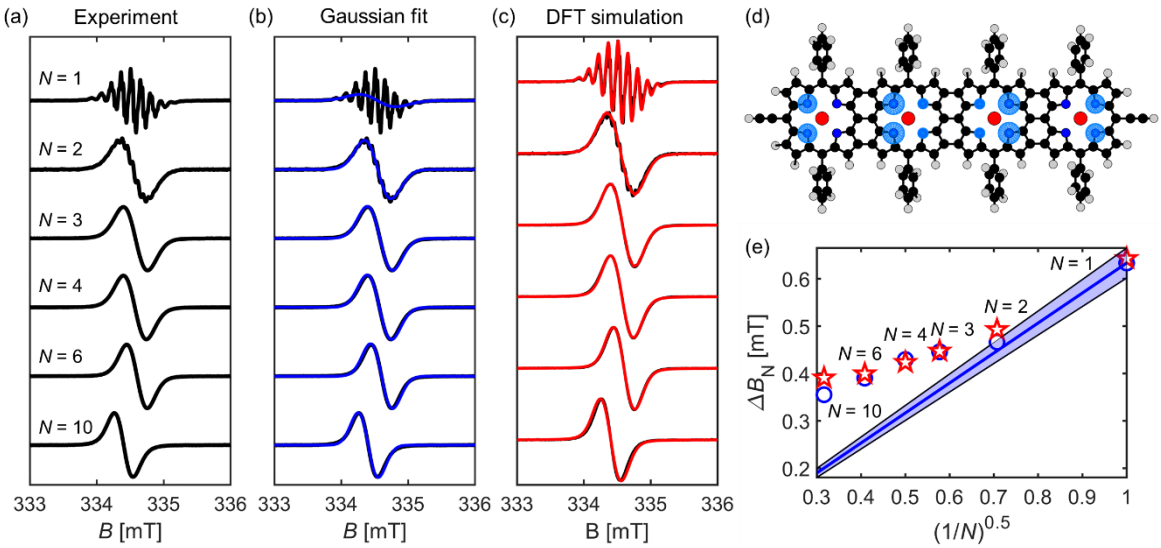

Figure 5.8: (a) Experimental X-band cw-EPR spectra of the radical cations ***lf*-ZnP*N*-TIPS$_2^{+\cdot}$** (N = 1–4, 6 and 10) acquired at room temperature (black lines). (b) Experimental spectra (black lines) overlaid with spectral envelopes (blue lines) obtained by fitting each spectrum to a derivative Gaussian function. (c) Experimental spectra (black lines) overlaid with simulated EPR spectra (red lines) using the ^{14}N spin densities from DFT calculations at the B3LYP/6-31G* level of theory. (d) Schematic visualization of the DFT calculated relative spin densities (blue shades) on the ^{14}N nuclei of ***lf*-ZnP4-TIPS$_2^{+\cdot}$**. The calculated spin densities ρ_i for the four sets of ^{14}N nuclei are 0.0177, 0.0362, 0.0003 and 0.0319 (from the central to the peripheral ^{14}N nuclei). (e) Widths of the experimental (black circles) and DFT Gaussian envelopes (red stars) vs $(1/N)^{1/2}$. The blue line shows the predicted Norris trend with 95% certainty range (light blue shades). Data collected and analyzed by Sebastian M. Kopp.

5.4.2 ^{1}H and ^{14}N ENDOR

We next investigated the hyperfine couplings in more detail by measuring the W-band ^{1}H and ^{14}N Mims ENDOR spectra of ***lf*-ZnP*N*-TIPS$_2^{+\cdot}$** at 50 K, where thermally induced hopping and dynamic polaron migration typically don't contribute to the spin density distribution on the EPR time scale (see Figures 5.9a–c for the spectra). The full width at half maximum (FWHM) of the measured ^{14}N Mims ENDOR spectra (Figure 5.9c, dark blue lines) are progressively narrowing with increasing oligomer length.

Simulations of the spectra were guided by DFT calculated spin density distributions that were used to derive both the isotropic and anisotropic hyperfine couplings,

$$\mathbf{A}_i = A_{\mathrm{iso},i}\begin{bmatrix}1 & 0 & 0\\ 0 & 1 & 0\\ 0 & 0 & 1\end{bmatrix} + \mathbf{T}_i \qquad (5.11)$$

where the isotropic part $A_{\mathrm{iso},i}$ is proportional to the spin density on the nucleus i (eqn. 5.10).

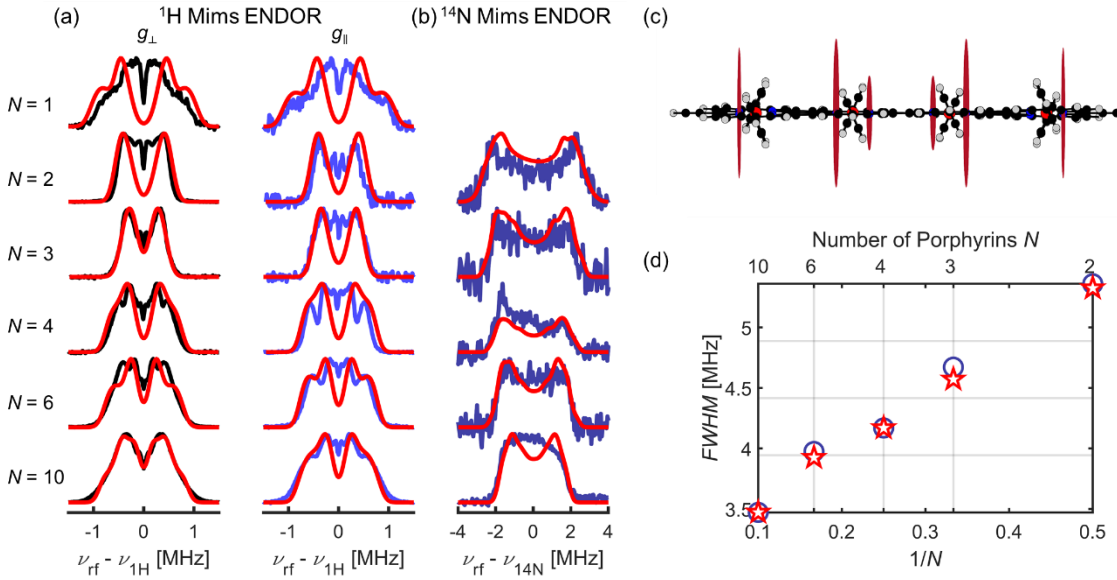

Figure 5.9: (a) and (b) Experimental (black, blue and dark blue lines) and simulated (red lines) ^{1}H and ^{14}N Mims ENDOR spectra for ***lf*-ZnP*N*-TIPS$_2^{+\cdot}$**. The experimental spectra were recorded at 50 K in a frozen solution at W-band. The ^{1}H Mims ENDOR spectra were measured at the two principal positions of the anisotropic g-tensor ($g_\perp$ and $g_\parallel$). The ^{14}N Mims ENDOR were recorded at the field position corresponding to the maximum of the spectrum ($g_\perp$). (c) Schematic visualization of the DFT (B3LYP/EPR-II) calculated anisotropic ^{14}N hyperfine coupling tensors for ***lf*-ZnP4-TIPS$_2^{+\cdot}$**. (d) FWHM of the experimental (dark blue circles) and simulated (red stars) ^{14}N ENDOR spectra for ***lf*-ZnP*N*-TIPS$_2^{+\cdot}$** as a function of chain length (1/*N*). Data collected and analyzed by Sebastian M. Kopp.

The anisotropic part $\mathbf{T}_i$, in a point-dipole approximation, is given by:

$$\mathbf{T}_i = \frac{\mu_0}{4\pi\hbar} g_e \mu_e g_n \mu_n \sum_{k \neq i} \rho_k \frac{\vec{n}_k \vec{n}_k^T - \mathbf{1}}{R_k} \tag{5.12}$$

in which R_k is the distance between nuclei i and k, ρ_k is the spin density on the nucleus k, $\vec{n}_k$ is a unit vector defining the orientation of R_k, g_e is the electron g-factor, β_e is Bohr magneton, g_n is the nuclear g-factor, β_n is the nuclear magneton, μ_0 corresponds to the vacuum permeability.

The simulated spectra qualitatively reproduce the appearance of the experimental data (Figures 5.9a, 5.9b and 5.9e). These simulations are based on a spin density distribution over the entire length of each oligomers, guided by DFT calculations at the B3LYP/6-31G* level of theory (see Appendix E, Section E.5 for the Mulliken spin density distributions on ***lf*-ZnP*N*-TIPS$_2^{+\cdot}$** used for the spectra simulations). The calculated anisotropic ^{14}N hyperfine coupling tensors exhibit different principal magnitudes perpendicular to the porphyrin planes (Figure 5.9c and Figure E.3 in Appendix E), which is consistent with the alternating regions of high and low spin densities on the ^{14}N nuclei found from the cw-EPR spectra simulations (Figure 5.8d and Figure E.1 in Appendix E). The good simulation of the ^{14}N ENDOR spectra with these tensors is further evidence for the non-uniform spin density distribution in the radical cations of the fused porphyrin oligomers.

To briefly summarize, the measured cw-EPR and Mims ENDOR spectra for ***lf*-ZnP*N*-TIPS$_2^{+\cdot}$** are interpreted based on simulations of the hyperfine couplings, accompanied by DFT calculations. The continuous narrowing of the measured spectra widths (cw-EPR and ^{14}N ENDOR), together with the DFT calculated spin density distributions that span over the entire wires, suggests that the spin delocalization in ***lf*-ZnP*N*-TIPS$_2^{+\cdot}$** does not reach saturation at N = 10.

5.4.3 Oxidation of *lf*-ZnP*N*-TIPS$_2$ in Air

To verify the hypothesis given in Section 5.2.3 that the long oligomers (N = 6, 10) are partially oxidized under ambient conditions (in air, at ~298 K), we measured the cw-EPR and pulsed EPR spectra for the oligomers before and after addition of BAHA (0.5 equivalent).

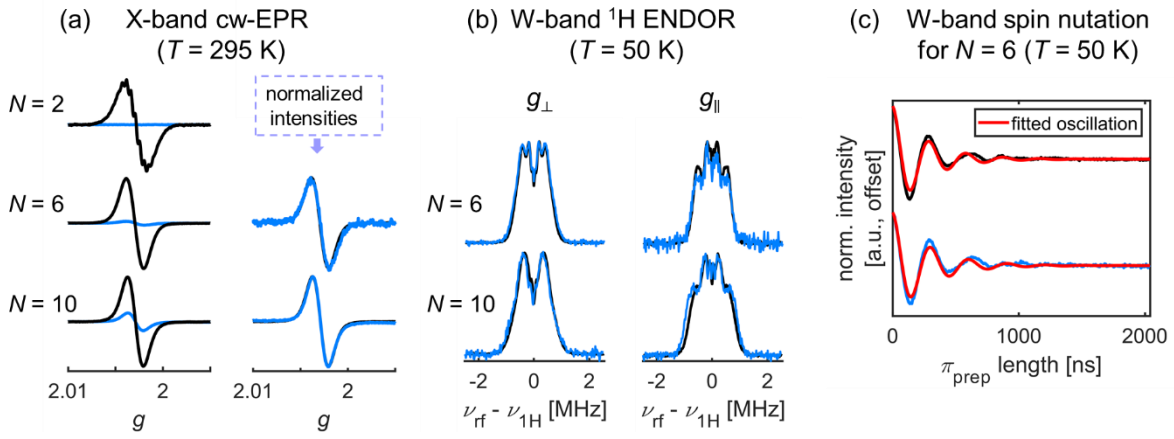

Figure 5.10: cw-EPR and pulsed EPR spectra for fused porphyrin oligomers before (blue lines) and after (black lines) addition of chemical oxidant BAHA (0.5 equivalent). (a) Left: X-band room temperature cw-EPR spectra for N = 2, 6 and 10. Right: intensity normalized spectra for N = 6 and 10. (b) Intensity normalized W-band ^{1}H Mims ENDOR EPR spectra for N = 6 and 10 measured at 50 K and at two principal positions of the anisotropic g-tensor ($g_{\perp}$ and $g_{\parallel}$). (c) Intensity normalized transient spin nutation curves for N = 6 (black and blue lines). Red lines express fits of the experimental curves to a damped cosine oscillation. Oscillation periods 2π = 304 and 296 ns were obtained from the fits for the hexamer before and after addition of BAHA, respectively. Data collected and analyzed by Sebastian M. Kopp.

Figure 5.10a display X-band cw-EPR spectra measured at room temperature for N = 2, 6 and 10. For N = 2, no EPR signal was found before addition of BAHA (blue line), which is consistent with the expected closed-shell configuration of the neutral dimer. On the contrary, we found that the measured spectra for N = 6 and 10 before addition of BAHA express EPR signals with identical shapes and g-values to those observed for chemically oxidized oligomers as evident from the intensity normalized spectra. This implies that radical cations are present in the "neutral" samples. A quantitative analysis of the intensities of the cw-EPR spectra shows that 2% of ***lf*-ZnP6-TIPS$_2$** and 12% of ***lf*-ZnP10-TIPS$_2$** are in the form of the respective radical cations before the addition of BAHA. These results are aligned with the trend of peak broadening observed in ^{1}H NMR measurements, which shows the ^{1}H resonance peaks for the β protons become broadened for the hexamer and severely broadened for the decamer.

Pulsed EPR measurements were conducted to provide more insights into the radical cations observed for the oligomers before addition of chemical oxidant. The intensity normalized W-band ^{1}H Mims ENDOR spectra for oligomers with = 6 and 10 before addition of BAHA again replicate those measured for oligomers after doping. The transient spin nutation experiments

for N = 6 show that the samples before and after addition of BAHA exhibit very similar oscillation patterns and oscillation periods (2π = 304 and 296 ns), which further corroborates the presence of spin-1/2 radical cations in the sample before addition of chemical oxidant. More evidences are provided in the Appendix E, Section E.5.

Given that zinc porphyrins possess high-lying HOMO energies and the measured optical gaps for fused porphyrin oligomers are progressively narrowing across the whole series of oligomers, the presence of the radical cations ***lf*-ZnP*N*-TIPS$_2^{+\cdot}$** (N = 6 and 10) in the isolated ***lf*-ZnP*N*-TIPS$_2$** is attributed to the chemical oxidation of the neutral oligomers in air (presumably by $^1O_2$). Distribution of the unpaired electron spin over the entire π-conjugated system on the porphyrins causes the peak broadenings observed for the β protons in ^{1}H NMR measurements, whereas the protons on the peripheral aryl groups are less affected, expressing more resolved signals in the spectra.

5.5 Conclusion and Future Works

In this chapter, we prepared a series of fused porphyrin oligomers ***lf*-ZnP*N*-TIPS$_2$** with up to 10 porphyrin units, and investigated the extent of polaron delocalization in their radical cations ***lf*-ZnP*N*-TIPS$_2^{+\cdot}$** using UV–vis–NIR–IR and EPR spectroscopies, in combination with computational simulations. We found that the polaron states are coherently delocalized over the entire oligomers across the series of radical cations, as evidenced by the following results:

(*i*) The P_2 bands observed from the deconvoluted absorption spectra for ***lf*-ZnP*N*-TIPS$_2^{+\cdot}$** (N = 2–4, 6 and 10) progressively shift to low energy with increasing oligomer length, without reaching a saturation at N = 10.

(*ii*) Simulations using the MPM models reproduce the excitation energies of the P_2 bands. The calculated ratio of the electronic coupling to the reorganization energy H/λ = 6.2 infers that the whole family of ***lf*-ZnP*N*-TIPS$_2^{+\cdot}$** is in Robin–Day class III.

(*iii*) The linewidths of the experimental cw-EPR spectra (at 295 K) and ^{14}N Mims ENDOR spectra (at 50 K) for ***lf*-ZnP*N*-TIPS$_2^{+\cdot}$** (N = 1–4, 6 and 10) are continuously narrowing with length, suggesting the spin density is distributed over more porphyrin units for longer oligomers.

(*iv*) The simulated spectra guided by DFT calculated spin density distributions reproduce the experimental EPR spectra. The calculated spin density spreads over the entire π-conjugated system of each oligomer, suggesting that the polaron state is fully delocalized.

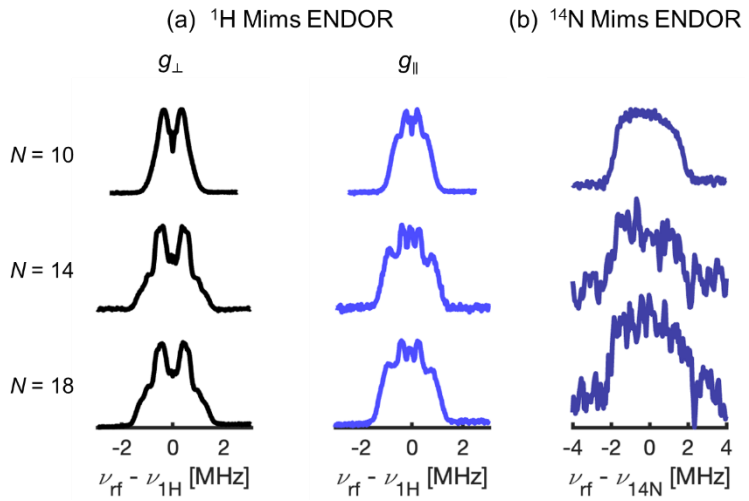

Figure 5.11: ^{1}H (a) and ^{14}N (b) W-band Mims ENDOR spectra for ***lf*-ZnP*N*-TIPS$_2^{+\cdot}$** (N = 10, 14 and 18), recorded at 50 K. Data collected and analyzed by Sebastian M. Kopp.

Recently, we have synthesized ***lf*-ZnP14-TIPS$_2$** and ***lf*-ZnP18-TIPS$_2$** to explore the limit of the hole polaron delocalization in ***lf*-ZnP*N*-TIPS$_2^{+\cdot}$**. Preliminary results from EPR studies (Figure 5.11) suggest that the polaron delocalization length reaches a saturation in between 10 and 14 porphyrin units (N_{ecl} = 10–14). The estimated length of the π-conjugated system for a fused porphyrin decamer is about 8.5 nm from the DFT-optimized geometry, which sets a new record for the extent of intrachain polaron delocalization in a π-conjugated organic material in solution.[65,66,100,102,311,333,334]

The calculated value of H/λ = 6.2 for the fused porphyrin oligomers is significantly greater than that of the butadiyne-linked oligomers (H/λ = 1.2).[102] Since we could not observe the P_1 bands ($E_{abs,P1} = 2H$ for Robin–Day class III compounds) for ***lf*-ZnP*N*-TIPS$_2^{+\cdot}$**, we estimated the value of H as half the splitting of the HOMO levels in a fused porphyrin dimer made of two monomers in the neutral state (i.e., $2H = E_{HOMO} - E_{HOMO-3}$; E_i is the DFT calculated energy for a molecular level; see Section E.7 for more details).[335,336] The calculated H (0.41 eV) for the fused porphyrin oligomers is about 60% larger than that of butadiyne-linked oligomers (H = 0.24 eV estimated from the experimental $E_{abs,P1}$, and 0.24 eV from calculation using the same method). Therefore, the reorganization energy λ for the fused oligomers are two times smaller than the butadiyne-linked oligomers. This could be explained the more rigid triply-linked coplanar geometry for the fused porphyrin oligomers, which increases the π-overlap between the neighboring porphyrin rings and minimize the reorganization of the molecular structure after the oxidation.

In addition to the extent of the polaron delocalization, we also discovered that spin-1/2 radical cations are present in the isolated samples of long porphyrin oligomers ($N \geq 6$), which results in the broadening of the measured ^{1}H resonance peaks in NMR studies and appearance of signals before addition of a chemical oxidant in EPR studies. It has been reported that long fused porphyrin oligomers suffer from oxidative degradation due to their high-lying HOMOs for more than a decade.[255,337,338] However, there is no previous report on what the "degraded" product is. Here, we proved that spin-1/2 radical cations are formed in the isolated "neutral" oligomers using a series of EPR techniques, providing a primary understanding to the results from the oxidation of ***lf*-ZnP*N*-TIPS$_2$** in air. These findings are also aligned with the results described in Chapter 3 that replacement of zinc with nickel stabilize the porphyrin tapes from chemical oxidation under aerobic conditions.

As discussed in Chapter 4 and ref. 86, the off-resonance coherent transport is more efficient in the charged fused porphyrin oligomers (i.e., trimer and octamer) than in the neutral state. This implies the presence of a state closely aligning with the Fermi level of the electrodes. Our findings in this chapter reveal that the polaron wavefunction in the fuse porphyrin radical cations coherently span over 10 porphyrin units, which supports the phase-coherent charge transport behaviors observed from the fused porphyrin oligomers molecular junctions.

Appendix A — Overview of Compound Descriptors

In this thesis, the porphyrin (**P**) oligomers mentioned are identified by the following descriptors:

TopologyLinker-MetalP*N*$_{Ar}$-End

The prefix "topology" describes whether the oligomers are linear (***l***) or cyclic (***c***). "linker" specifies how the porphyrin units are connected. Typical linkers mentioned in this thesis are summarized in Figure A.1. The prefix "metal" indicates the central metal ion in the porphyrin core, where free base porphyrin is described by "**H**$_2$". "***N***" is the number of porphyrin units in this molecule. "**Ar**" specify the solubilizing group incorporated ("*t*-Bu", "Oct", and "THS" are 3,5-bis(*tert*-butyl)phenyl, 3,5-bis(tert-butyl)phenyl, and 3,5-bis(trihexylsilyl)phenyl groups, respectively). "**End**" describes the end groups attached to the peripheral porphyrin *meso* positions.

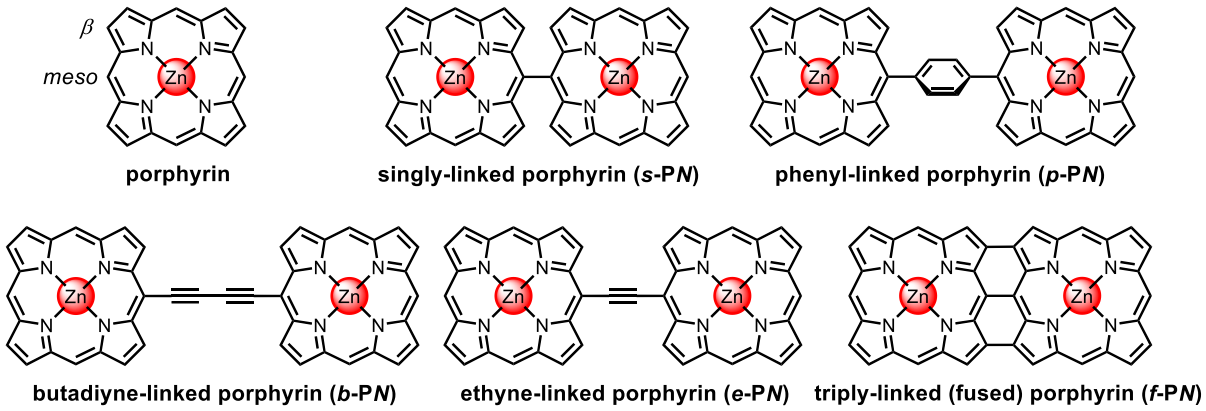

Figure A.1: Examples of porphyrin oligomers connected by different linkers.

When the porphyrin oligomers bind to one or more templates to form complexes, the complexes are named as "**P*N*·T*M*$_x$**", where "**T*M***" specifies the template and "*x*" is the number of templates bound to the porphyrin oligomer **P*N***. For example, the synthesis and properties of porphyrin nanoring-template complex ***cs*[*b*$_1$]-P24·(T12e)$_2$** are detailed (Figure A.2). The compound descriptor ***cs*[*b*$_1$]-P24·(T12e)$_2$** indicates the complex is formed by porphyrin nanoring ***cs*[*b*$_1$]-P24** and two equivalents of template **T12e**, where the porphyrin nanoring ***cs*[*b*$_1$]-P24** consists of 24 porphyrin units which are *meso–meso* singly-linked ("***s***") and a butadiyne link ("*b*").

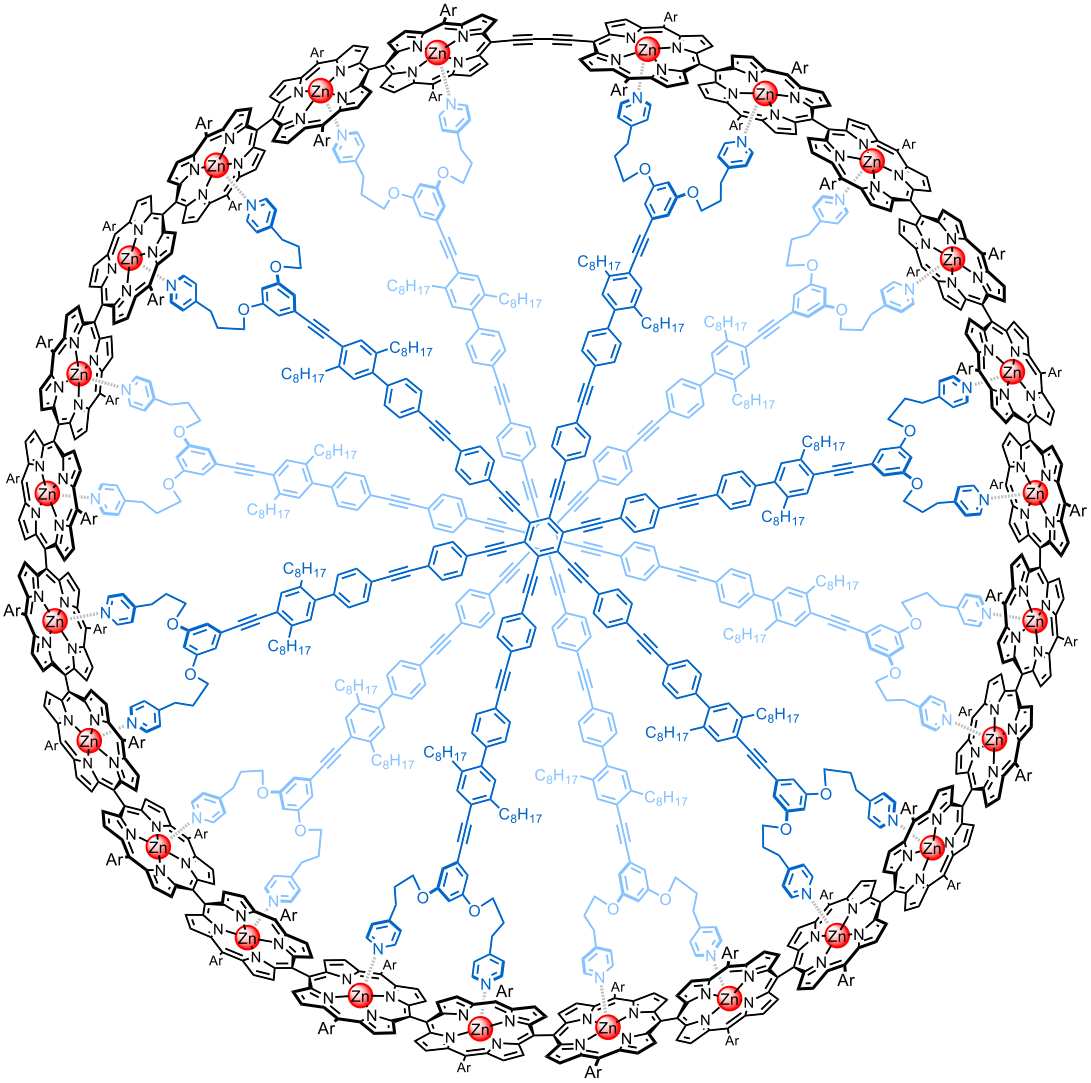

***cs*[b_1]-P24·(T12e)$_2$**

Figure A.2: Schematic showing the chemical structure of porphyrin nanoring-template complex ***cs*[b_1]-P24·(T12e)$_2$**.

Appendix B — Experimental Procedures and Supplementary Details for Chapter 2

B.1 General Methods

Solvents for reactions were obtained from an MBraun MBSPS-5-BenchTop solvent purification system kept under nitrogen. Chloroform-*d* for NMR was stored over K_2CO_3 prior to use. All other reagents and solvents were obtained from commercial suppliers and used as received unless otherwise stated. Thin-layer chromatography (TLC) was carried out using aluminum sheets precoated with silica gel with fluorescence indicator from Merck and visualized under UV light at 254 or 365 nm. Purification by column chromatography was carried out on silica gel (SiO_2, 60 Å, 40−63 μm). Petroleum ether (PE) of boiling range: 40−60°C was used for chromatography. Size exclusion chromatography (SEC) was carried out using Bio-Rad Bio-Beads S-X1 (40–80 μm bead size). Analytical GPC was carried out using JAIGEL-3H-A (8 × 500 mm) and JAIGEL-4H-A (8 × 500 mm) columns in THF + 1% pyridine as eluent with a flow rate of 1.0 mL/min. Semi-preparative GPC was carried out on a Shimadzu recycling GPC system equipped with a LC-20 AD pump, SPD-20A UV detector and a set either of JAIGEL 3H (20 × 600 mm) and JAIGEL 4H (20 × 600 mm) columns in either toluene + 1% pyridine or THF + 1% pyridine as eluent at a flow rate of 3.5 mL/min. Retention times of porphyrin oligomers and rings were obtained from analytical GPC traces (conditions above) using monomer, **P1** (retention time = 37.7 minutes), as reference.

NMR spectra were recorded on either a Bruker AVIII HD 400, a Bruker AVIII HD 500, a Bruker NEO 600 with a broadband helium cryoprobe, or a Bruker AVIII 700 with an inverse TCI $^{1}H/^{13}C/^{15}N$ cryoprobe. Chemical shift values are quoted in ppm and coupling constants (*J*) in Hertz to the nearest 0.1 Hz. ^{1}H and ^{13}C NMR spectra are referenced against the residual solvent peak ($CHCl_3$ δ_H = 7.26 ppm, $CDCl_3$ δ_C = 77.16 ppm). Unless stated otherwise, NMR spectra were recorded at 298 K. Diffusion experiments were carried out using the double stimulated echo sequence with bipolar gradients for convection compensation.[340] Diffusion coefficients were obtained by fitting signal intensity decays to the Stejskal-Tanner equation: $I = I_0 \cdot \exp[(\gamma_H \cdot \delta \cdot G)^2 \cdot D \cdot (\Delta - \delta/3)]$, where I and I_0 represent signal areas in the presence and absence of gradient pulses, respectively, D is the diffusion coefficient, G is the gradient strength, γ_H is the ^{1}H magnetogyric ratio, δ is the gradient pulse duration, and Δ is the diffusion time.

MALDI-ToF spectra were measured using a Bruker MALDI Autoflex Speed instrument. *Trans*-2-[3-(4-*tert*-butylphenyl)-2-methyl-2-propenylidene]malononitrile (DCTB) was used as

matrix. ESI spectra were measured at the University of Oxford on a Thermo Orbitrap Exactive mass spectrometer.

Optical spectroscopic measurements were carried out on solutions in toluene containing 1% pyridine (or neat toluene in the case of **T12e** and ***cs*[*b*$_1$]-P24·(T12e)$_2$**), in silica cuvettes of size 3.5 × 10.0 mm or 10.0 × 10.0 mm, at a concentration of 0.25–2.0 μM for steady-state measurements and 0.25–2.0 mM for time-resolved experiments. Steady-state UV–vis–NIR absorption spectra were acquired on either a Perkin Elmer Lambda 20 spectrometer at 298 K with temperature control by a PTP-1 Peltier unit from Perkin Elmer or a Perkin Elmer Lambda 25 spectrometer at 298 K with a PTP-A Peltier unit from Perkin Elmer. Steady-state fluorescence spectra were acquired using an Edinburgh Instruments FS5 spectrofluorometer operating Fluoracle® software, equipped with a xenon arc lamp (providing 230–1000 nm excitation range), a thermostatic sample holder (SC-20) and both an R13456 PMT detector (200–950 nm spectral coverage, Hamamatsu) and an InGaAs analogue NIR detector (850–1650 nm spectral coverage).

B.2 Known Compounds

4-(3-Bromopropyl)pyridine[341] was prepared as reported previously. This compound degrades to an insoluble brown oil upon concentration from a $CHCl_3$ solution, following aqueous workup. For this reason, the compound was stored as a solution in DMF and used without further purification.

1,4-Dibromo-2,5-dioctylbenzene,[342] 5-iodoresorcinol,[343] [(3-cyanopropyl)diisopropylsilyl]-acetylene (CPDIPS-acetylene),[344] trihexylsilylacetylene (THS-acetylene),[345] hexakis[(trimethylsilyl)-ethynyl]benzene,[346] hexakis(4-bromophenyl)benzenebenzene,[347] 1,2,3,4,5,6-hexakis((4-iodophenyl)-ethynyl)benzene (Core-I$_6$),[124] zinc 5,15-bis-(3,5-bis(octyloxy)phenyl)porphyrin (**P1**),[79] were prepared as reported previously.

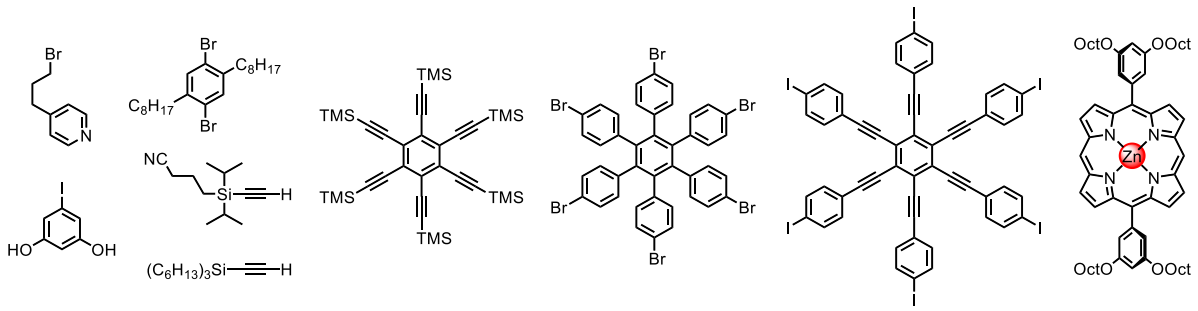

Figure B.1: An overview of synthesized known compounds.

B.3 Syntheses of *ls*-P*N*

B.3.1 PIFA-mediated oligomerization of P1

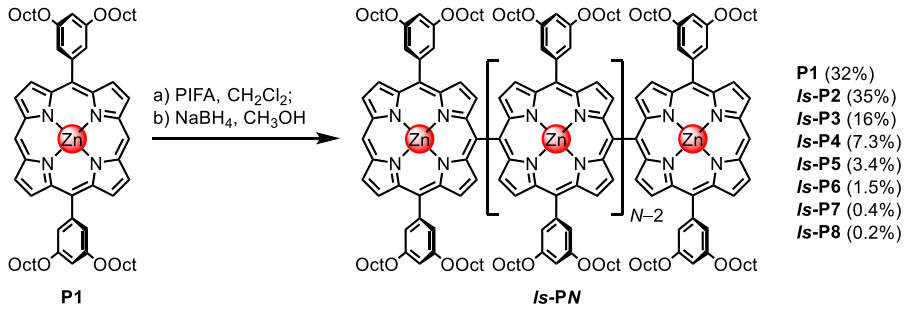

To a solution of **P1**[79] (2.0 g, 1.8 mmol, 1.0 equiv.) in dry CH_2Cl_2 (250 mL), [bis(trifluoro-acetoxy)iodo]benzene (PIFA, 0.39 g, 0.91 mmol, 0.5 equiv.) was added and the mixture was stirred at 25 °C. The progress of the coupling was monitored by analytical GPC (Figure 2.8b). After 2 h, a suspension of $NaBH_4$ (0.69 g, 18 mmol, 10 equiv.) in CH_3OH (50 mL) was added and the reaction mixture was stirred at 25 °C for 30 minutes. The reaction mixture was passed through a silica column (gradient elution: CH_2Cl_2/pentane 1:1 to 7:3) and the filtrate was concentrated under reduced pressure. The crude was dissolved in $CHCl_3$ (300 mL) and a solution of $Zn(OAc)_2{\cdot}2H_2O$ (2.35 g, 11 mmol) in CH_3OH (25 mL) was added. After stirring for 1 h at 40 °C, the mixture was passed through a silica column ($CHCl_3$), and the filtrate was concentrated under reduced pressure. The resulting crude was separated by size-exclusion chromatography (Bio-Beads, S-X1, toluene + 1% pyridine) followed by recycling GPC (toluene + 1% pyridine). Each of the separated fractions was passed through a silica column (gradient elution: CH_2Cl_2/pentane 3:7 to 7:3) and the filtrates were concentrated under reduced pressure. Precipitation from CH_3OH /$CHCl_3$ (9:1) by layered addition of CH_3OH onto a solution of oligomer in $CHCl_3$, afforded the isolated porphyrin oligomers as powders (red to brown in color depending on oligomer size).

Isolated yields: **P1** (630 mg, 32%), ***ls*-P2** (696 mg, 35%), ***ls*-P3** (321 mg, 16%), ***ls*-P4** (145 mg, 7.3%), ***ls*-P5** (67 mg, 3.4%), ***ls*-P6** (29 mg, 1.5%).

P1:

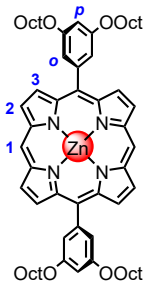

^{1}H NMR (600 MHz, $CDCl_3$, 298 K) δ_H = 10.31 (s, 2H, H_1), 9.43 (d, *J* = 4.4 Hz, 4H, H_2), 9.26 (d, *J* = 4.4 Hz, 4H, H_3), 7.43 (d, *J* = 2.2 Hz, 4H, H_o), 6.92 (t, *J* = 2.2 Hz, 2H, H_p), 4.15 (t, *J* = 6.7 Hz, 8H, H_{Oct}), 1.93–1.84 (m, 8H, H_{Oct}), 1.56–1.48 (m, 8H, H_{Oct}), 1.41–1.23 (m, 32H, H_{Oct}), 0.87 (t, *J* = 6.9 Hz, 12H, H_{Oct}) ppm.

MALDI-ToF *m*/*z* 1036.621 (calculated for $[C_{64}H_{84}N_4O_4Zn]^{\bullet+}$ = $(M)^{\bullet+}$: 1036.578).

UV–vis–NIR ($CDCl_3$, 298 K) λ_{max} (ε / 10^6 M^{-1} cm^{-1}): 409 (0.53), 565 (0.03) nm.

Retention time: 37.7 min.

***ls*-P2:**

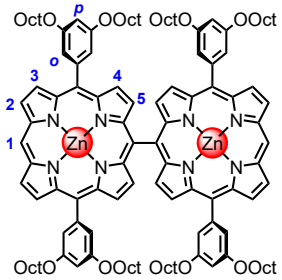

^{1}H NMR (600 MHz, $CDCl_3$, 298 K): δ_H = 10.38 (s, 2H, H_1), 9.49 (d, *J* = 4.5 Hz, 4H, H_2), 9.27 (d, *J* = 4.5 Hz, 4H, H_3), 8.82 (d, *J* = 4.7 Hz, 4H, H_4), 8.10 (d, *J* = 4.7 Hz, 4H, H_5), 7.42 (d, *J* = 2.3 Hz, 8H, H_o), 6.81 (t, *J* = 2.3 Hz, 4H, H_p), 4.13–4.00 (m, 16H, H_{Oct}), 1.83–1.75 (m, 16H, H_{Oct}), 1.47–1.39 (m, 16H, H_{Oct}), 1.36–1.15 (m, 64H, H_{Oct}), 0.81 (t, *J* = 6.9 Hz, 24H, H_{Oct}) ppm.

MALDI-ToF *m*/*z* 2074.854 (calculated for $[C_{128}H_{166}N_8O_8Zn_2]^{\bullet+}$ = $(M)^{\bullet+}$: 2074.141).

UV–vis–NIR ($CDCl_3$, 298 K) λ_{max} (ε / 10^6 M^{-1} cm^{-1}): 414 (0.29), 446 (0.22), 551 (0.059), 589 (0.0092) nm.

Retention time: 36.4 min.

***ls*-P3:**

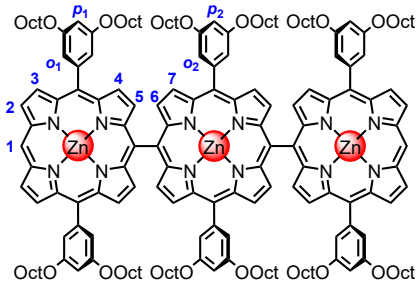

^{1}H NMR (600 MHz, $CDCl_3$, 298 K) δ_H = 10.40 (s, 2H, H_1), 9.51 (d, *J* = 4.4 Hz, 4H, H_2), 9.30 (d, *J* = 4.3 Hz, 4H, H_3), 8.90 (d, *J* = 4.5 Hz, 4H, H_4), 8.81 (d, *J* = 4.8 Hz, 4H, H_7), 8.25 (d, *J* = 4.2 Hz, 4H, H_5), 8.14 (d, *J* = 4.8 Hz, 4H, H_6), 7.46 (s, 8H, H_{o1}), 7.39 (s, 4H, H_{o2}), 6.84 (s, 4H, H_{p1}), 6.68 (d, *J* = 2.4 Hz, 2H, H_{p2}), 4.10 (t, *J* = 6.8 Hz, 16H, H_{Oct}), 3.96 (t, *J* = 6.7 Hz, 8H, H_{Oct}), 1.83 (t, *J* = 7.2 Hz, 16H, H_{Oct}), 1.76–1.63 (m, 8H, H_{Oct}), 1.47–1.08 (m, 120H, H_{Oct}), 0.82 (t, *J* = 6.8 Hz, 24H, H_{Oct}), 0.73 (t, *J* = 6.8 Hz, 12H, H_{Oct}) ppm.

MALDI-ToF *m*/*z* 3109.847 (calculated for $[C_{192}H_{248}N_{12}O_{12}Zn_3]^{\bullet+}$ = $(M)^{\bullet+}$: 3109.707).

UV–vis–NIR ($CDCl_3$, 298 K) λ_{max} (ε / 10^6 M^{-1} cm^{-1}): 411 (0.45), 472 (0.35), 563 (0.11) nm.

Retention time: 35.6 min.

***ls*-P4:**

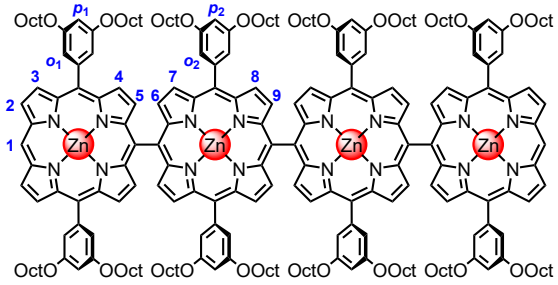

^{1}H NMR (600 MHz, $CDCl_3$, 298 K) δ_H = 10.41 (s, 2H, H_1), 9.51 (d, *J* = 4.4 Hz, 4H, H_2), 9.30 (d, *J* = 4.5 Hz, 4H, H_3), 8.91 (d, *J* = 4.6 Hz, 4H, H_4), 8.89 (d, *J* = 4.7 Hz, 4H, H_7), 8.83 (d, *J* = 4.6 Hz, 4H, H_8), 8.29 (d, *J* = 4.7 Hz, 4H, H_6), 8.27 (d, *J* = 4.6 Hz, 4H, H_5), 8.15 (d, *J* = 4.7 Hz, 4H, H_9), 7.47 (d, *J* = 2.3 Hz, 8H, H_{o1}), 7.43 (d, *J* = 2.5 Hz, 8H, H_{o2}), 6.85 (t, *J* = 2.3 Hz, 4H, H_{p1}), 6.71 (t, *J* = 2.3 Hz, 4H, H_{p2}), 4.10 (t, *J* = 6.7 Hz, 16H, H_{Oct}), 4.00 (t, *J* = 6.6 Hz, 16H, H_{Oct}), 1.86–1.79 (m, 16H, H_{Oct}), 1.75–1.69 (m, 16H, H_{Oct}), 1.50–1.43 (m, 16H, H_{Oct}), 1.40–1.11 (m, 144H, H_{Oct}), 0.82 (t, *J* = 6.8 Hz, 24H, H_{Oct}), 0.74 (t, *J* = 6.8 Hz, 24H, H_{Oct}) ppm.

MALDI-ToF *m*/*z* 4148.269 (calculated for $[C_{256}H_{330}N_{16}O_{16}Zn_4]^{\bullet+}$ = $(M)^{\bullet+}$: 4148.265).

UV–vis–NIR ($CDCl_3$, 298 K) λ_{max} (ε / 10^6 M^{-1} cm^{-1}): 411 (0.44), 483 (0.36), 569 (0.14) nm.

Retention time: 34.9 min.

***ls*-P5:**

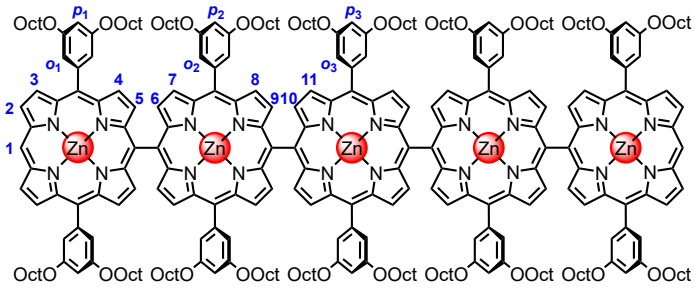

^{1}H NMR (600 MHz, $CDCl_3$, 298 K) δ_H = 10.41 (s, 2H, H_1), 9.52 (d, J = 4.3 Hz, 4H, H_2), 9.30 (d, J = 4.3 Hz, 4H, H_3), 8.94 – 8.88 (m, 12H, $H_{4,8,11}$), 8.83 (d, J = 4.7 Hz, 4H, H_7), 8.31 (d, J = 4.6 Hz, 8H, $H_{9,10}$), 8.27 (d, J = 4.5 Hz, 4H, H_5), 8.15 (d, J = 4.7 Hz, 4H, H_6), 7.47 (d, J = 2.3 Hz, 12H, $H_{o1,o3}$), 7.44 (d, J = 2.3 Hz, 8H, H_{o2}), 6.85 (t, J = 2.3 Hz, 4H, H_{p1}), 6.75 (t, J = 2.3 Hz, 2H, H_{p3}), 6.72 (t, J = 2.4 Hz, 4H, H_{p2}), 4.11 (t, J = 6.7 Hz, 16H, H_{Oct}), 4.06 – 3.98 (m, 24H, H_{Oct}), 1.88–1.80 (m, 16H, H_{Oct}), 1.78–1.69 (m, 16H, H_{Oct}), 1.50–1.11 (m, 200H, H_{Oct}), 0.82 (t, J = 6.8 Hz, 24H, H_{Oct}), 0.78–0.73 (m, 36H, H_{Oct}) ppm.

MALDI-ToF m/z 5184.339 (calculated for $[C_{320}H_{412}N_{20}O_{20}Zn_5]^{\bullet+}$ = $(M)^{\bullet+}$: 5185.831).

UV–vis–NIR ($CDCl_3$, 298 K) λ_{max} (ε / 10^6 M^{-1} cm^{-1}): 411 (0.68), 490 (0.42), 571 (0.28) nm.

Retention time: 34.3 min.

***ls*-P6:**

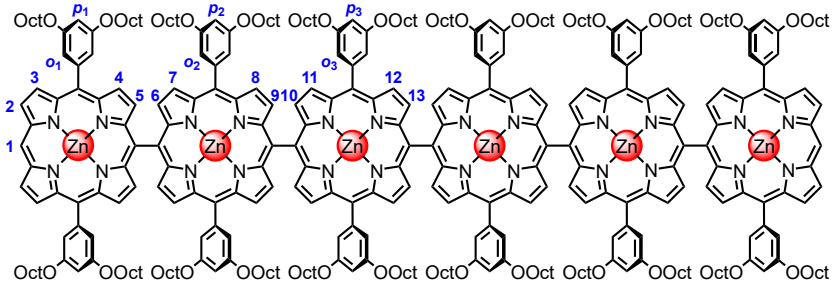

^{1}H NMR (600 MHz, $CDCl_3$, 298 K) δ_H = 10.42 (s, 2H, H_1), 9.52 (d, J = 4.5 Hz, 4H, H_2), 9.31 (d, J = 4.5 Hz, 4H, H_3), 8.99–8.89 (m, 16H, $H_{4,8,11,12}$), 8.85 (d, J = 4.7 Hz, 4H, H_7), 8.37–8.31 (m, 12H, $H_{9,10,13}$), 8.28 (d, J = 4.5 Hz, 4H, H_5), 8.17 (d, J = 4.6 Hz, 4H, H_6), 7.51–7.46 (m, 16H, $H_{o1,o3}$), 7.45 (d, J = 2.3 Hz, 8H, H_{o2}), 6.86 (t, J = 2.3 Hz, 4H, H_{p1}), 6.76 (t, J = 2.3 Hz, 4H, H_{p3}),

6.73 (t, J = 2.3 Hz, 4H, H_{p2}), 4.11 (t, J = 6.7 Hz, 16H, H_{Oct}), 4.07–3.98 (m, 32H, H_{Oct}), 1.87–1.81 (m, 12H, H_{Oct}), 1.80–1.70 (m, 32H, H_{Oct}), 1.50–1.13 (m, 240H, H_{Oct}), 0.83 (t, J = 6.8 Hz, 24H, H_{Oct}), 0.79–0.73 (m, 48H, H_{Oct}) ppm.

MALDI-ToF m/z 6224.616 (calculated for $[C_{384}H_{494}N_{24}O_{24}Zn_6]^{\bullet+}$ = $(M)^{\bullet+}$: 6222.395).

UV–vis–NIR ($CDCl_3$, 298 K) λ_{max} (ε / 10^6 M^{-1} cm^{-1}): 411 (0.65), 494 (0.57), 576 (0.29) nm.

Retention time: 33.8 min.

***ls*-P7:**

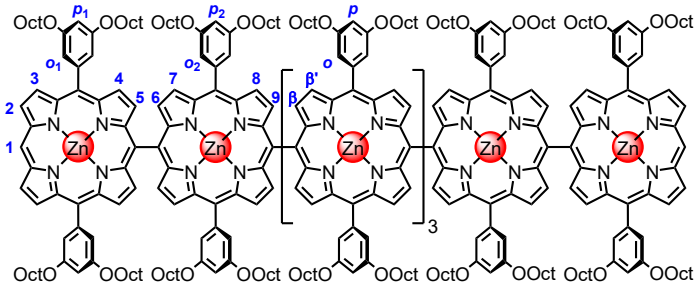

^{1}H NMR (600 MHz, $CDCl_3$, 298 K) δ_H = 10.42 (s, 2H, H_1), 9.53 (d, J = 4.3 Hz, 4H, H_2), 9.32 (d, J = 4.3 Hz, 4H, H_3), 8.98–8.89 (m, 20H, $H_{4,8,\beta'}$), 8.86 (d, J = 4.7 Hz, 4H, H_7), 8.39–8.31 (m, 16H, $H_{9,\beta}$), 8.29 (d, J = 4.4 Hz, 4H, H_5), 8.18 (d, J = 4.7 Hz, 4H, H_6), 7.52–7.47 (m, 20H, $H_{o1,o}$), 7.46 (d, J = 2.3 Hz, 8H, H_{o2}), 6.86 (t, J = 2.4 Hz, 4H, H_{p1}), 6.79–6.75 (m, 6H, H_p), 6.73 (t, J = 2.4 Hz, 4H, H_{p2}), 4.16–3.98 (m, 56H, H_{Oct}), 1.88–1.71 (m, 56H, H_{Oct}), 1.49–1.14 (m, 280H, H_{Oct}), 0.83 (t, J = 6.8 Hz, 16H, H_{Oct}), 0.80–0.74 (m, 56H, H_{Oct}) ppm.

MALDI-ToF m/z 7260.579 (calculated for $[C_{448}H_{576}N_{28}O_{28}Zn_7]^{\bullet+}$ = $(M)^{\bullet+}$: 7258.958).

UV–vis–NIR ($CDCl_3$, 298 K) λ_{max} (ε / 10^6 M^{-1} cm^{-1}): 411 (0.73), 496 (0.65), 575 (0.37) nm.

Retention time: 33.3 min.

B.3.2 PIFA-mediated oligomerization of *ls*-P2

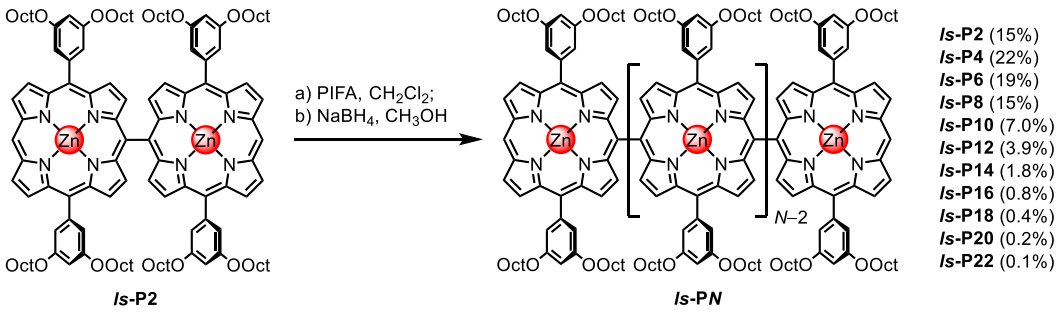

ls-P2 *ls*-P*N*

To a solution of ***ls*-P2** (1.65 g, 0.795 mmol, 1.0 equiv.) in dry CH_2Cl_2 (200 mL), [bis(trifluoro-acetoxy)iodo]benzene (PIFA, 0.171 g, 0.397 mmol, 0.5 equiv.) was added and the mixture was stirred at 25 °C. The progress of the coupling was monitored by analytical GPC (Figure 2.32). After 2 h, a suspension of $NaBH_4$ (0.301 g, 7.95 mmol, 10 equiv.) in CH_3OH (20 mL) was added and the reaction mixture was stirred at 25 °C for 30 min. The reaction mixture was passed through a silica column (gradient elution: $CHCl_3$/pentane 1:1 to 7:3) and the filtrate was concentrated under reduced pressure. The crude was dissolved in $CHCl_3$ (250 mL) and a solution of $Zn(OAc)_2 \cdot 2H_2O$ (1.94 g, 9.1 mmol) in CH_3OH (20 mL) was added. After stirring for 1 h at 40 °C, the mixture was passed through a silica column ($CHCl_3$), and the filtrate was concentrated under reduced pressure. The resulting crude was separated by size-exclusion chromatography (S-X1, toluene + 1% pyridine) followed by recycling GPC (toluene + 1% pyridine). Each of the separated fractions were passed through a silica column (gradient elution: $CHCl_3$:pentane 3:7 to 7:3) and the filtrates was concentrated under reduced pressure. Precipitation from $CH_3OH/CHCl_3$ (9:1) by layered addition of CH_3OH onto a solution of oligomer in $CHCl_3$, afforded the isolated porphyrin oligomers as powders (red to brown in color depending on oligomer size).

Isolated yields: ***ls*-P2** (242 mg, 15%), ***ls*-P4** (356 mg, 22%), ***ls*-P6** (311 mg, 19%), ***ls*-P8** (246 mg, 15%), ***ls*-P10** (115 mg, 7.0%), ***ls*-P12** (64 mg, 3.9%), ***ls*-P14** (30 mg, 1.8%), ***ls*-P16** (14 mg, 0.8%), ***ls*-P18** (6.8 mg, 0.4%), ***ls*-P20** (3.9 mg, 0.2%), ***ls*-P22** (1.6 mg, 0.1%).

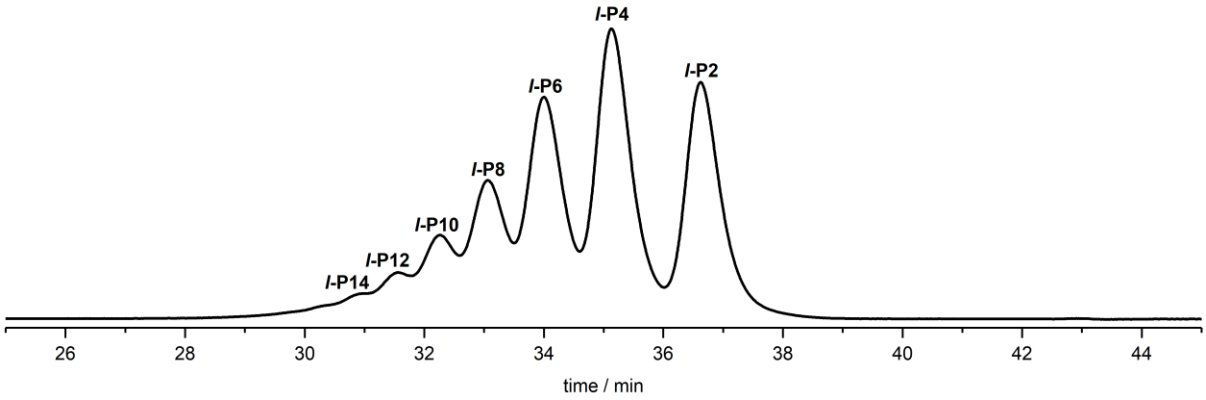

Figure B.2: Analytical GPC trace of the crude reaction mixture from PIFA oligomerization of ***l*-P2** (THF + 1% pyridine, λ = 420 nm).

***ls*-P8:**

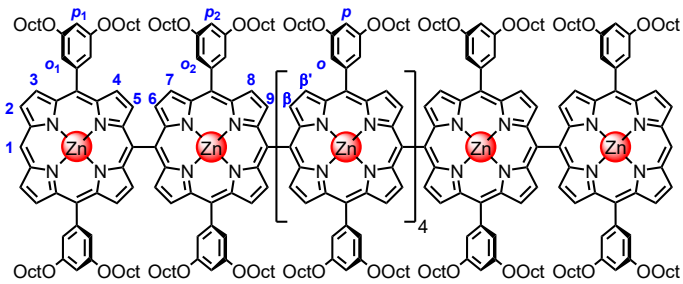

^{1}H NMR (600 MHz, $CDCl_3$, 298 K) δ_H = 10.42 (s, 2H, H_1), 9.53 (d, *J* = 4.3 Hz, 4H, H_2), 9.32 (d, *J* = 4.3 Hz, 4H, H_3), 9.00–8.90 (m, 24H, $H_{4,8,\beta'}$), 8.86 (d, *J* = 4.5 Hz, 4H, H_7), 8.39–8.31 (m, 20H, $H_{9,\beta}$), 8.29 (d, *J* = 4.4 Hz, 4H, H_5), 8.18 (d, *J* = 4.5 Hz, 4H, H_6), 7.52–7.44 (m, 32H, $H_{o1,o2,o}$), 6.88–6.85 (m, 4H, H_{p1}), 6.80–6.76 (m, 8H, H_p), 6.74 (d, *J* = 2.3 Hz, 4H, H_{p2}), 4.15–3.98 (m, 64H, H_{Oct}), 1.88–1.70 (m, 64H, H_{Oct}), 1.48–1.13 (m, 320H, H_{Oct}), 0.83 (t, *J* = 7.0 Hz, 24H, H_{Oct}), 0.81–0.73 (m, 72H, H_{Oct}) ppm.

MALDI-ToF *m*/*z* 8294.738 (calculated for $[C_{512}H_{658}N_{32}O_{32}Zn_8]^{\bullet+}$ = $(M)^{\bullet+}$: 8295.521).

UV–vis–NIR ($CDCl_3$, 298 K) λ_{max} (ε / 10^6 M^{-1} cm^{-1}): 411 (0.74), 498 (0.67), 576 (0.40) nm.

Retention time: 32.9 min.

***ls*-P10:**

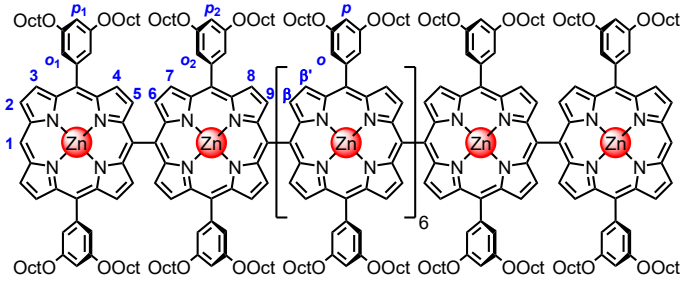

^{1}H NMR (600 MHz, $CDCl_3$, 298 K) δ_H = 10.42 (s, 2H, H_1), 9.53 (d, *J* = 4.6 Hz, 4H, H_2), 9.32 (d, *J* = 4.2 Hz, 4H, H_3), 9.03–8.89 (m, 32H, $H_{4,8,\beta'}$), 8.86 (d, *J* = 4.9 Hz, 4H, H_7), 8.39–8.33 (m, 28H, $H_{9,\beta}$), 8.29 (d, *J* = 4.9 Hz, 4H, H_5), 8.18 (d, *J* = 5.0 Hz, 4H, H_6), 7.54–7.45 (m, 40H, $H_{o1,o2,o}$), 6.86 (s, 4H, H_{p1}), 6.81–6.76 (m, 12H, H_p), 6.74 (s, 4H, H_{p2}), 4.15–3.99 (m, 80H, H_{Oct}), 1.87–1.71 (m, 80H, H_{Oct}), 1.49–1.14 (m, 400H, H_{Oct}), 0.86–0.82 (m, 24H, H_{Oct}), 0.82–0.73 (m, 96H, H_{Oct}) ppm.

MALDI-ToF *m*/*z* 10,370.405 (calculated for $[C_{640}H_{822}N_{40}O_{40}Zn_{10}]^{\bullet+}$ = $(M)^{\bullet+}$: 10,368.648).

Retention time: 32.1 min.

***ls*-P12:**

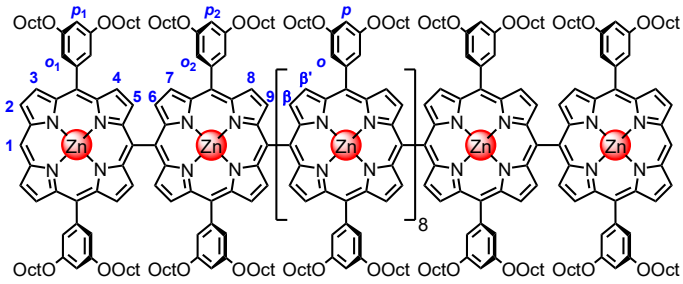

^{1}H NMR (600 MHz, $CDCl_3$, 298 K) δ_H = 10.42 (s, 2H, H_1), 9.53 (d, *J* = 4.2 Hz, 4H, H_2), 9.32 (d, *J* = 4.2 Hz, 4H, H_3), 9.00–8.90 (m, 40H, $H_{4,8,\beta'}$), 8.86 (d, *J* = 4.5 Hz, 4H, H_7), 8.42–8.31 (m, 36H, $H_{9,\beta}$), 8.29 (d, *J* = 4.4 Hz, 4H, H_5), 8.18 (d, *J* = 4.5 Hz, 4H, H_6), 7.55–7.44 (m, 48H, $H_{o1,o2,o}$), 6.88–6.83 (m, 4H, H_{p1}), 6.82–6.75 (m, 16H, H_p), 6.75–6.71 (m, 4H, H_{p2}), 4.14–3.99 (m, 96H, H_{Oct}), 1.87–1.71 (m, 96H, H_{Oct}), 1.50–1.14 (m, 480H, H_{Oct}), 0.83 (t, *J* = 6.9 Hz, 24H, H_{Oct}), 0.81–0.74 (m, 120H, H_{Oct}) ppm.

MALDI-ToF *m*/*z* 12,440.091 (calculated for $[C_{768}H_{986}N_{48}O_{48}Zn_{12}]^{\bullet+}$ = $(M)^{\bullet+}$: 12,442.775).

UV–vis–NIR ($CDCl_3$, 298 K) λ_{max} (ε / 10^6 M^{-1} cm^{-1}): 414 (1.11), 505 (1.03), 585 (0.66) nm.

Retention time: 31.3 min.

***ls*-P14:**

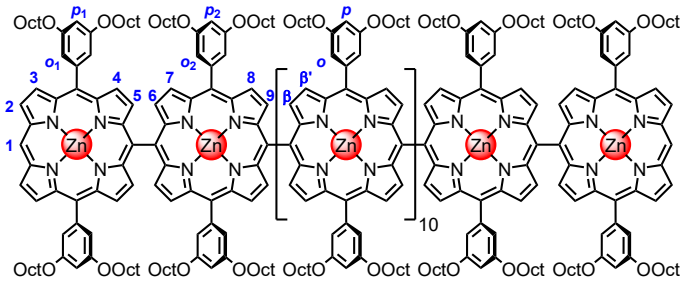

^{1}H NMR (600 MHz, $CDCl_3$, 298 K) δ_H = 10.42 (s, 2H, H_1), 9.53 (d, *J* = 4.2 Hz, 4H, H_2), 9.31 (d, *J* = 4.2 Hz, 4H, H_3), 9.01–8.89 (m, 48H, $H_{4,8,\beta'}$), 8.85 (d, *J* = 4.7 Hz, 4H, H_7), 8.47–8.31 (m, 44H, $H_{9,\beta}$), 8.29 (d, *J* = 4.5 Hz, 4H, H_5), 8.17 (d, *J* = 4.5 Hz, 4H, H_6), 7.54–7.44 (m, 56H, $H_{o1,o2,o}$), 6.86 (s, 4H, H_{p1}), 6.81–6.76 (m, 20H, H_p), 6.73 (s, 4H, H_{p2}), 4.15–3.99 (m, 112H, H_{Oct}), 1.88–1.71 (m, 112H, H_{Oct}), 1.49–1.14 (m, 560H, H_{Oct}), 0.83 (t, *J* = 6.8 Hz, 24H, H_{Oct}), 0.81–0.73 (m, 144H, H_{Oct}) ppm.

MALDI-ToF *m/z* 14,515.204 (calculated for $[C_{896}H_{1150}N_{56}O_{56}Zn_{14}]^{\bullet+}$ = $(M)^{\bullet+}$: 14,515.901).

Retention time: 30.8 min.

***ls*-P16:**

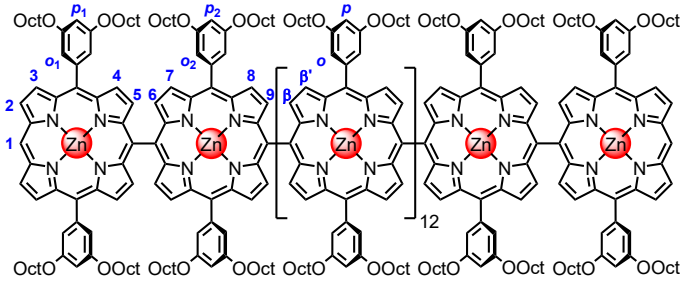

^{1}H NMR (600 MHz, $CDCl_3$, 298 K) δ_H = 10.42 (s, 2H, H_1), 9.53 (d, *J* = 4.2 Hz, 4H, H_2), 9.32 (d, *J* = 4.1 Hz, 4H, H_3), 9.03–8.90 (m, 56H, $H_{4,8,\beta'}$), 8.86 (d, *J* = 4.3 Hz, 4H, H_7), 8.42–8.32 (m, 52H, $H_{9,\beta}$), 8.29 (d, *J* = 4.3 Hz, 4H, H_5), 8.18 (d, *J* = 4.4 Hz, 4H, H_6), 7.55–7.44 (m, 64H, $H_{o1,o2,o}$), 6.86 (t, *J* = 2.3 Hz, 4H, H_{p1}), 6.81–6.76 (m, 24H, H_p), 6.74 (t, *J* = 2.3 Hz, 4H, H_{p2}), 4.20–3.96 (m, 128H, H_{Oct}), 1.88–1.71 (m, 128H, H_{Oct}), 1.49–1.13 (m, 640H, H_{Oct}), 0.84 (t, *J* = 6.9 Hz, 24H, H_{Oct}), 0.82–0.73 (m, 168H, H_{Oct}) ppm.

MALDI-ToF *m/z* 16,589.711 (calculated for $[C_{1024}H_{1314}N_{64}O_{64}Zn_{16}]^{\bullet+}$ = $(M)^{\bullet+}$: 16,590.028).

Retention time: 30.2 min.

***ls*-P18:**

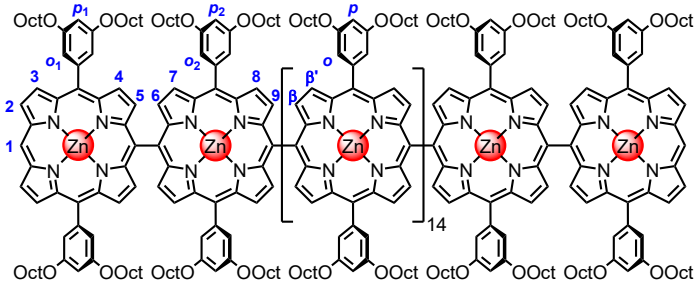

^{1}H NMR (600 MHz, $CDCl_3$, 298 K) δ_H = 10.41 (s, 2H, H_1), 9.52 (d, *J* = 4.0 Hz, 4H, H_2), 9.31 (d, *J* = 4.0 Hz, 4H, H_3), 9.02–8.89 (m, 64H, $H_{4,8,\beta'}$), 8.85 (d, *J* = 4.3 Hz, 4H, H_7), 8.42–8.30 (m, 60H, $H_{9,\beta}$), 8.28 (d, *J* = 4.7 Hz, 4H, H_5), 8.16 (d, *J* = 4.5 Hz, 4H, H_6), 7.54–7.44 (m, 72H, $H_{o1,o2,o}$), 6.88–6.84 (m, 4H, H_{p1}), 6.81–6.75 (m, 28H, H_p), 6.74–6.72 (m, 4H, H_{p2}), 4.17–3.96 (m, 144H, H_{Oct}), 1.88–1.71 (m, 144H, H_{Oct}), 1.50–1.12 (m, 720H, H_{Oct}), 0.93–0.72 (m, 216H, H_{Oct}) ppm.

MALDI-ToF *m/z* 18,662.517 (calculated for $[C_{1152}H_{1478}N_{72}O_{72}Zn_{18}]^{\bullet+}$ = $(M)^{\bullet+}$: 18,663.155).

Retention time: 29.7 min.

***ls*-P20:**

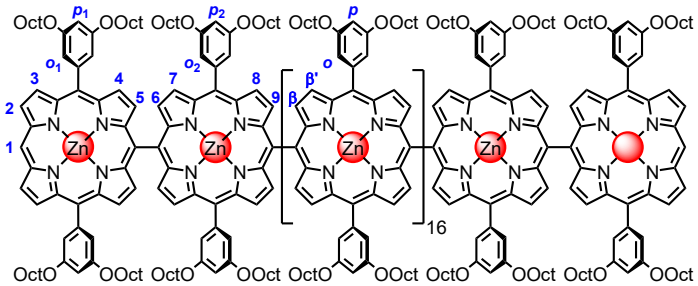

^{1}H NMR (600 MHz, $CDCl_3$, 298 K) δ_H = 10.42 (s, 2H, H_1), 9.53 (d, *J* = 4.0 Hz, 4H, H_2), 9.32 (d, *J* = 3.9 Hz, 4H, H_3), 9.05–8.89 (m, 72H, $H_{4,8,\beta'}$), 8.86 (d, *J* = 4.5 Hz, 4H, H_7), 8.42–8.31 (m, 68H, $H_{9,\beta}$), 8.29 (d, *J* = 4.4 Hz, 4H, H_5), 8.18 (d, *J* = 4.7 Hz, 4H, H_6), 7.60–7.44 (m, 80H, $H_{o1,o2,o}$), 6.87–6.85 (m, 4H, H_{p1}), 6.81–6.75 (m, 32H, H_p), 6.74–6.72 (m, 4H, H_{p2}), 4.20–3.96 (m, 160H, H_{Oct}), 1.89–1.70 (m, 160H, H_{Oct}), 1.50–1.13 (m, 800H, H_{Oct}), 0.86–0.73 (m, 240H, H_{Oct}) ppm.

MALDI-ToF *m/z* 20,759.173 (calculated for $[C_{1280}H_{1642}N_{80}O_{80}Zn_{20}]^{\bullet+}$ = $(M)^{\bullet+}$: 20,737.282).

Retention time: 29.2 min.

***ls*-P22:**

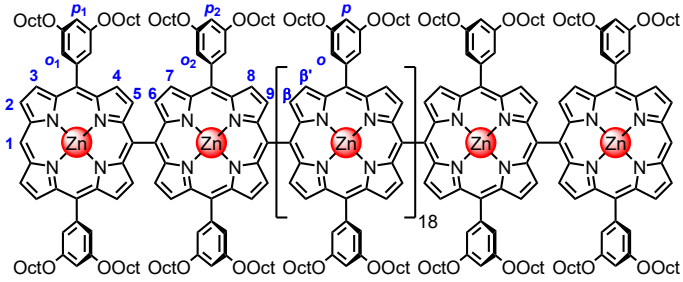

^{1}H NMR (600 MHz, $CDCl_3$, 298 K): δ_H = 10.42 (s, 2H, H_1), 9.52 (d, J = 3.9 Hz, 4H, H_2), 9.33–9.30 (m, 4H, H_3), 9.02–8.90 (m, 80H, $H_{4,8,\beta'}$), 8.87–8.84 (m, 4H, H_7), 8.42–8.32 (m, 76H, $H_{9,\beta}$), 8.30–8.27 (m, 4H, H_5), 8.19–8.15 (m, 4H, H_6), 7.56–7.44 (m, 88H, $H_{o1,o2,o}$), 6.87–6.85 (m, 4H, H_{p1}), 6.81–6.76 (m, 4H, H_p), 6.74–6.72 (m, 4H, H_{p2}), 4.26–3.89 (m, 176H, H_{Oct}), 1.87–1.70 (m, 176H, H_{Oct}), 1.49–1.15 (m, 880H, H_{Oct}), 0.87–0.73 (m, 264H, H_{Oct}) ppm.

MALDI-ToF *m*/*z* 22,838.975 (calculated for $[C_{1408}H_{1806}N_{88}O_{88}Zn_{22}]^{\bullet+}$ = $(M)^{\bullet+}$: 22,810.408).

Retention time: 28.9 min.

B.3.3 PIFA-mediated oligomerization of *ls*-P6

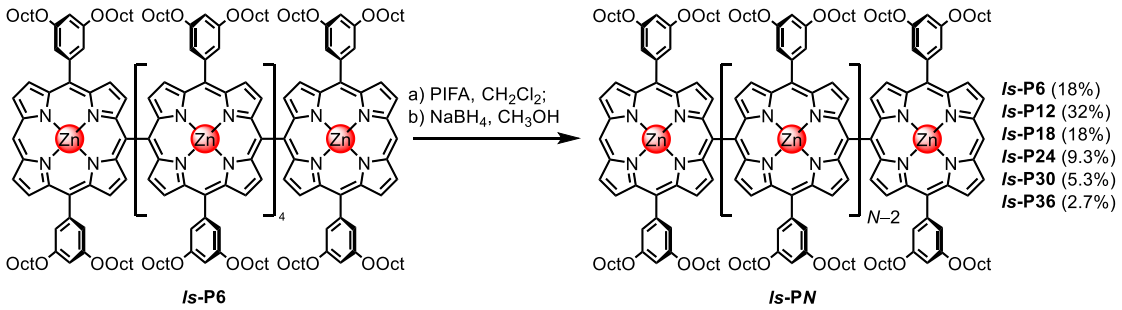

To a solution of ***ls*-P6** (300 mg, 0.046 mmol, 1.0 equiv.) in dry CH_2Cl_2 (50 mL), [bis(trifluoroacetoxy)iodo]benzene (PIFA, 9.84 mg, 0.023 mmol, 0.5 equiv.) was added and the mixture was stirred at 25 °C. The progress of the coupling was monitored by analytical GPC (Figure 2.33). After 2 h, a suspension of $NaBH_4$ (17 mg, 0.46 mmol, 10 equiv.) in CH_3OH (5 mL) was added and the reaction mixture was stirred at 25 °C for 30 min. The reaction mixture was passed through a silica column (gradient elution: $CHCl_3$/pentane 1:1 to 7:3) and the filtrate was concentrated under reduced pressure. The crude was dissolved in $CHCl_3$ (50 mL) and a solution of $Zn(OAc)_2{\cdot}2H_2O$ (353 mg, 1.66 mmol) in CH_3OH (5 mL) was added. After stirring for 1 hour at 40 °C, the mixture was passed through a silica column ($CHCl_3$), and the filtrate was concentrated under reduced pressure. The resulting crude was separated by size-exclusion chromatography (Bio-Beads, S-X1, toluene + 1% pyridine) followed by recycling GPC (toluene + 1% pyridine). Each of the separated fractions was passed through a silica column (gradient elution: $CHCl_3$/pentane 3:7 to 7:3) and the filtrates were concentrated under reduced pressure. Precipitation from $CH_3OH/CHCl_3$ (9:1) by layered addition of CH_3OH onto a solution of oligomer in $CHCl_3$, afforded the isolated porphyrin oligomers as powders.

Isolated yields: ***ls*-P6** (54 mg, 18%), ***ls*-P12** (95 mg, 32%), ***ls*-P18** (53 mg, 18%), ***ls*-P24** (28 mg, 9.3%), ***ls*-P30** (16 mg, 5.3%), ***ls*-P36** (7.7 mg, 2.7%).

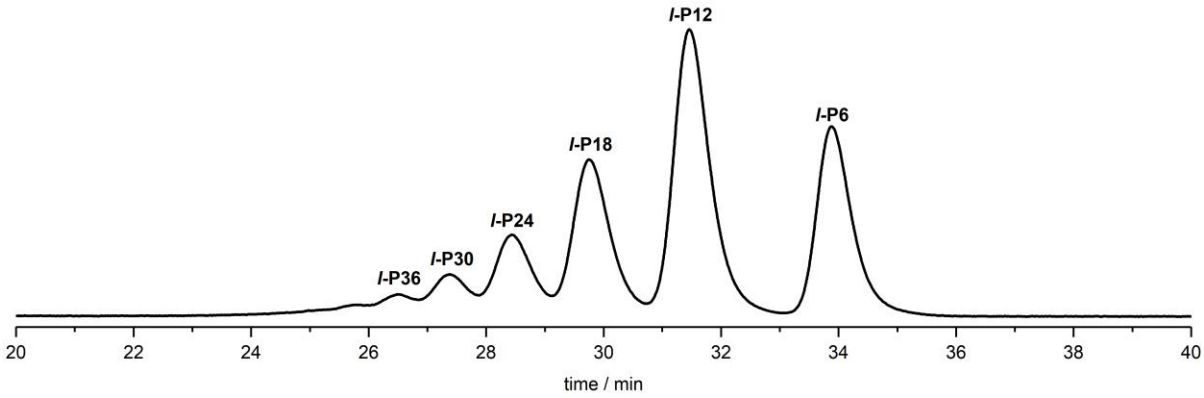

Figure B.3: Analytical GPC trace of the crude reaction from PIFA oligomerization of ***ls*-P6** (THF + 1% pyridine, λ = 420 nm).

***ls*-P24:**

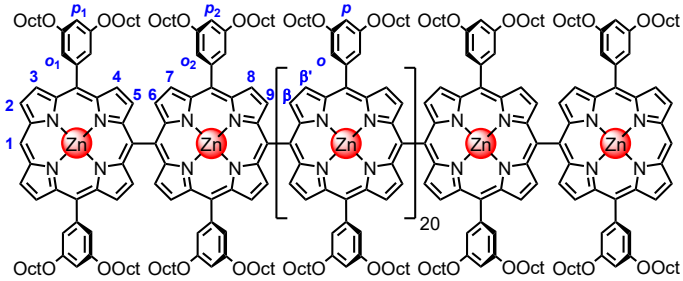

^{1}H NMR (700 MHz, $CDCl_3$, 298 K): δ_H = 10.42 (s, 2H, H_1), 9.53 (d, J = 3.9 Hz, 4H, H_2), 9.34–9.29 (m, 4H, H_3), 9.01–8.90 (m, 88H, $H_{4,8,\beta'}$), 8.86 (d, J = 4.3 Hz, 4H, H_7), 8.41–8.33 (m, 84H, $H_{9,\beta}$), 8.31–8.26 (m, 4H, H_5), 8.18 (d, J = 4.1 Hz, 4H, H_6), 7.56–7.44 (m, 96H, $H_{o1,o2,o}$), 6.88–6.85 (m, 4H, H_{p1}), 6.82–6.76 (m, 40H, H_p), 6.75–6.72 (m, 4H, H_{p2}), 4.20–3.93 (m, 192H, H_{Oct}), 1.88–1.72 (m, 192H, H_{Oct}), 1.50–1.13 (m, 960H, H_{Oct}), 0.87–0.73 (m, 288H, H_{Oct}) ppm.

^{1}H Diffusion NMR (500 MHz, $CDCl_3$, 298 K) $D = 9.40 \cdot 10^{-11}$ m^2 s^{-1}.

MALDI-ToF *m/z* 24,883.667 (calculated for $[C_{1536}H_{1970}N_{96}O_{96}Zn_{24}]^{\bullet+}$ = $(M)^{\bullet+}$: 24,883.534).

UV–vis–NIR ($CDCl_3$, 298 K) λ_{max} (ε / 10^6 M^{-1} cm^{-1}): 411 (2.37), 504 (2.60), 579 (1.86) nm.

Retention time: 28.4 min.

***ls*-P30:**

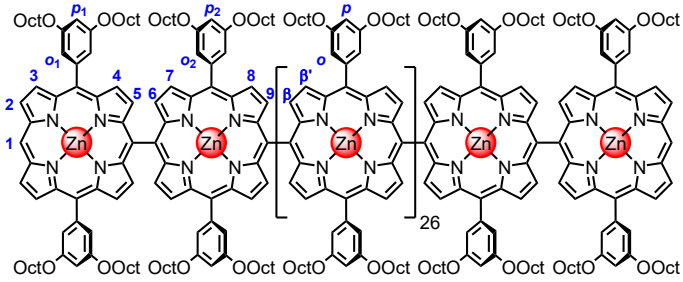

^{1}H NMR (600 MHz, $CDCl_3$, 298 K): δ_H = 10.43 (s, 2H, H_1), 9.61–9.47 (m, 4H, H_2), 9.37–9.28 (m, 4H, H_3), 9.12–8.88 (m, 112H, $H_{4,8,\beta'}$), 8.87–8.83 (m, 4H, H_7), 8.48–8.32 (m, 108H, $H_{9,\beta}$), 8.31–8.28 (m, 4H, H_5), 8.19–8.16 (m, 4H, H_6), 7.57–7.45 (m, 120H, $H_{o1,o2,o}$), 6.88–6.85 (m, 4H, H_{p1}), 6.83–6.76 (m, 52H, H_p), 6.75–6.73 (m, 4H, H_{p2}), 4.36–3.82 (m, 240H, H_{Oct}), 1.91–1.69 (m, 240H, H_{Oct}), 1.48–1.08 (m, 1200H, H_{Oct}), 0.86–0.74 (m, 360H, H_{Oct}) ppm.

MALDI-ToF *m*/*z* 31,090.715 (calculated for $[C_{1920}H_{2462}N_{120}O_{120}Zn_{30}]^{\bullet+}$ = $(M)^{\bullet+}$: 31,103.915).

Retention time: 27.4 min.

***ls*-P36:**

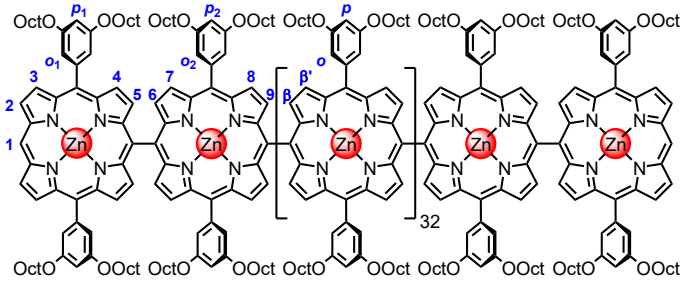

^{1}H NMR (600 MHz, $CDCl_3$, 298 K) δ_H = 10.43 (s, 2H, **H_1**), 9.53 (d, *J* = 4.1 Hz, 4H, **H_2**), 9.37–9.28 (m, 4H, **H_3**), 9.03–8.91 (m, 136H, **$H_{4,8,\beta'}$**), 8.87–8.85 (m, 4H, **H_7**), 8.42–8.33 (m, 132H, **$H_{9,\beta}$**), 8.29 (d, *J* = 4.6 Hz, 4H, **H_5**), 8.20–8.17 (m, 4H, **H_6**), 7.58–7.44 (m, 144H, **$H_{o1,o2,o}$**), 6.88–6.85 (m, 4H, **H_{p1}**), 6.82–6.77 (m, 64H, **H_p**), 6.75–6.73 (m, 4H, **H_{p2}**), 4.45–3.83 (m, 288H, **H_{Oct}**), 1.91–1.69 (m, 288H, **H_{Oct}**), 1.49–1.13 (m, 1440H, **H_{Oct}**), 0.88–0.73 (m, 432H, **H_{Oct}**) ppm.

MALDI-ToF *m*/*z* 37,333.64 (calculated for $[C_{2304}H_{2954}N_{144}O_{144}Zn_{36}]^{\bullet+}$ = **$(M)^{\bullet+}$**: 37,325.304).

Retention time: 26.5 min.

B.4 Syntheses of T2, T12a, T12b and T12e

B.4.1 Synthesis of T2

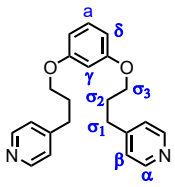

To a solution of 4-(3-bromopropyl)pyridine[341] (2.91 g, 14.4 mmol) and resorcinol (0.400 g, 3.63 mmol) in DMF (15 mL) was added K_2CO_3 (4.02 g, 29.1 mmol), and the reaction mixture was heated to 50 °C. After 5 h, the reaction mixture was diluted with Et_2O (200 mL), washed with water (5 × 50 mL), dried over Na_2SO_4, filtered, and concentrated under reduced pressure. The crude mixture was purified by flash column chromatography (SiO_2, gradient elution: 50% EtOAc/$CHCl_3$; then 5% CH_3OH/$CHCl_3$) and fractions containing product were concentrated under reduced pressure. To the residual oil was added hexane (25 mL), the suspension was sonicated for 10 minutes, and cooled to –78 °C for 30 min. The precipitate was collected by vacuum filtration, washed with additional *n*-hexane (3 × 10 mL), and dried to give the title compound as a white solid (643 mg, 51%).

^{1}H NMR (600 MHz, $CDCl_3$, 298 K) δ_H = 8.50 (d, *J* = 6.0 Hz, 4H, **α**), 7.16 (t, *J* = 8.2 Hz, 1H, **a**), 7.14 (d, *J* = 6.0 Hz, 4H, **β**), 6.48 (dd, *J* = 8.2, 2.4 Hz, 2H, **δ**), 6.42 (t, *J* = 2.4 Hz, 1H, **γ**), 3.94 (t, *J* = 6.1 Hz, 4H, **σ$_3$**), 2.84–2.79 (m, 4H, **σ$_1$**), 2.15–2.07 (m, 4H, **σ$_2$**) ppm.

^{13}C NMR (151 MHz, $CDCl_3$, 298 K) δ_C = 160.22, 150.59, 149.97, 130.10, 124.10, 106.97, 101.67, 66.64, 31.73, 29.87 ppm.

HRMS (ESI) *m*/*z* calculated for $C_{22}H_{25}N_2O_2^+$ ($[M+H]^+$) 349.1911, found 349.1910.

B.4.2 Synthesis of T12a

Compound T12$_I$:

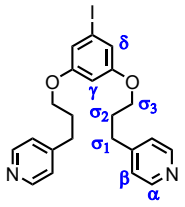

To a solution of 4-(3-bromopropyl)pyridine[341] (2.99 g, 14.9 mmol) and 5-iodoresorcinol[343] (0.882 g, 3.74 mmol) in DMF (12 mL) was added K_2CO_3 (4.13 g, 29.9 mmol), and the reaction mixture was heated to 40–45 °C. After 4 h, complete conversion to the title compound was confirmed by TLC ($CH_3OH/CHCl_3$ 5:95). The reaction mixture was diluted with Et_2O (200 mL), washed with water (5 × 50 mL), dried over Na_2SO_4, filtered, and concentrated under reduced pressure. Purification by flash column chromatography (SiO_2, gradient elution: 50% EtOAc/$CHCl_3$; then 5% $CH_3OH/CHCl_3$) gave the title compound (1.64 g, 93%) as a pale green oil.

^{1}H NMR (400 MHz, $CDCl_3$, 298 K) δ_H = 8.51 (d, *J* = 6.1 Hz, 4H, **α**), 7.13 (d, *J* = 6.1 Hz, 4H, **β**), 6.84 (d, *J* = 2.2 Hz, 2H, **δ**), 6.35 (t, *J* = 2.2 Hz, 1H, **γ**), 3.90 (t, *J* = 6.1 Hz, 4H, **σ$_3$**), 2.79 (dd, *J* = 8.5, 6.8 Hz, 4H, **σ$_1$**), 2.15–2.03 (m, 4H, **σ$_2$**) ppm.

^{13}C NMR (101 MHz, $CDCl_3$, 298 K) δ_C = 160.45, 150.36, 150.04, 124.07, 116.58, 101.63, 94.30, 66.91, 31.64, 29.74 ppm.

HRMS (ESI) *m*/*z* calculated for $C_{22}H_{24}O_2N_2I^+$ ($[M+H]^+$) 475.0877, found 475.0878.

Template T12a:

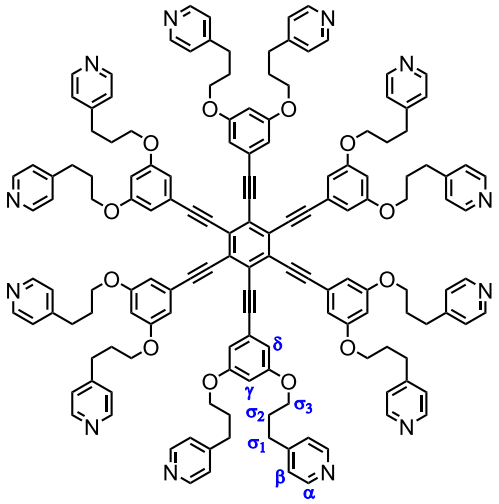

Hexakis[(trimethylsilyl)ethynyl]benzene[346] (0.155 g, 0.237 mmol, 1.0 equiv.) was added to a 25 mL round bottom flask equipped with a stir bar followed by dissolution in THF/CH_3OH 9:1 (10 mL) and addition of K_2CO_3 (0.327 g, 2.37 mmol). The reaction mixture was stirred for 30 minutes at which point the contents were diluted with diethyl ether (10 mL). The contents were then transferred to a separatory funnel and the organic phase was washed with H_2O (3 × 5 mL), brine (1 × 10 mL), and then dried over sodium sulfate. The solvent was reduced to approximately 1 mL, at which point it was transferred to a Schlenk flask, followed by the addition of aryl iodide **T2I** (0.900 g, 1.89 mmol 8.0 equiv.) in THF (5 mL) and Et_3N (2 mL). The contents were subjected to three freeze-pump-thaw cycles, and while frozen, CuI (27.0 mg, 0.142 mmol) and $Pd(PPh_3)_4$ (0.165 g, 0.142 mmol) were added, and the contents were again subjected to three freeze-pump-thaw cycles. The reaction was stirred at 25 °C for 24 h at which point the solvent was removed. Purification by column chromatography (SiO_2, 5% to 20% $CH_3OH/CHCl_3$) gave the desired product as a yellow, fluorescent solid (0.261 g, 48%).

^{1}H NMR (500 MHz, $CDCl_3$, 298 K) δ_H = 8.50–8.44 (m, 24H, **α**), 7.09–7.02 (m, 24H, **β**), 6.77 (d, *J* = 2.3 Hz, 12H, **δ**), 6.41 (t, *J* = 2.3 Hz, 6H, **γ**), 3.82 (t, *J* = 6.1 Hz, 24H, **σ3**), 2.74–2.65 (m, 24H, **σ1**), 2.04–1.96 (m, 24H, **σ2**) ppm.

^{13}C NMR (126 MHz, $CDCl_3$, 298 K) δ_C = 160.03, 150.24, 150.03, 127.71, 124.57, 123.94, 110.38, 103.48, 99.64, 86.92, 66.97, 31.63, 29.78 ppm.

HRMS (ESI) *m/z* calculated for $C_{150}H_{139}N_{12}O_{12}^+$ ($[M+H]^+$) 2300.0630, found 2300.0570.

B.4.3 Synthesis of T12b

Compound T2$_{Bpin}$:

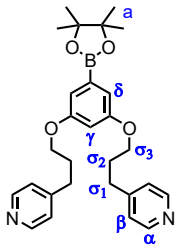

To a deoxygenated mixture of aryl iodide **T2$_I$** (1.27 g, 2.68 mmol), bis(pinacolato)diboron (0.782 g, 3.08 mmol), and KOAc (0.788 g, 8.03 mmol) in dioxane (20 mL) was added Pd(dppf)Cl_2·CH_2Cl_2 (109 mg, 0.134 mmol), the reaction mixture was further degassed stirring at 90 °C for 5 d. The reaction mixture was filtered through a short pad of silica (CH_3OH/$CHCl_3$ 15:85) and concentrated under reduced pressure. The crude was purified by flash column chromatography (SiO_2, gradient elution: 2–5% CH_3OH/$CHCl_3$) affording the title compound (1.18 g, 93%) as an orange oil with minor impurities, and was used without further purification.

^{1}H NMR (400 MHz, $CDCl_3$, 298 K) δ_H = 8.43 (d, *J* = 6.1 Hz, 4H, α), 7.08 (d, *J* = 6.1 Hz, 4H, β), 6.87 (d, *J* = 2.4 Hz, 2H, δ), 6.46 (t, *J* = 2.4 Hz, 1H, γ), 3.91 (t, *J* = 6.0 Hz, 4H, σ_3), 2.79–2.70 (m, 4H, σ_1), 2.07–1.99 (m, 4H, σ_2), 1.27 (s, 12H, a) ppm.

^{13}C NMR (101 MHz, $CDCl_3$, 298 K) δ_C = 159.79, 150.78, 149.85, 124.17, 112.58, 105.31, 84.08, 66.64, 31.71, 29.95, 25.00, 24.74 ppm.

HRMS (ESI) *m*/*z* calculated for $C_{28}H_{36}BN_2O_4^+$ ($[M+H]^+$) 475.2763, found 475.2763.

Template T12b:

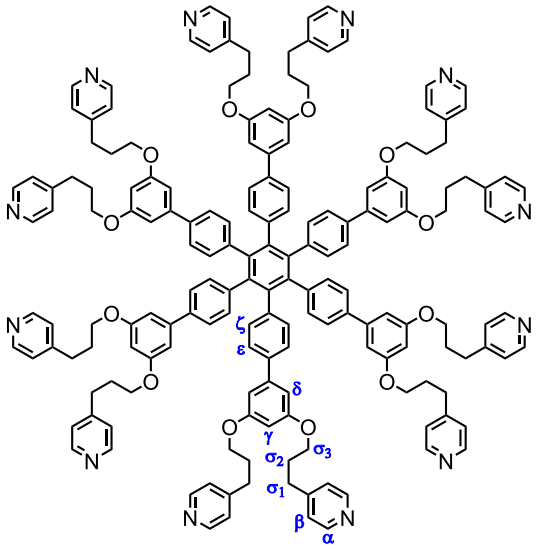

A mixture of boronic acid pinacol ester **T2$_{Bpin}$** (141 mg, 0.298 mmol), hexa(4-bromophenyl)benzene[347] (15.0 mg, 0.015 mmol), and XPhos Pd G2 (7.0 mg, 8.9 μmol) in dioxane (2 mL) was subjected to three freeze-pump-thaw cycles, after which an argon-purged aqueous solution of K_3PO_4 (0.5 mL, 0.5 mmol, 1.0 M) was added. The reaction mixture was heated to 50 °C for 3 h, followed by heating to 90 °C for 3 d. The reaction mixture was filtered through a short pad of silica ($CH_3OH/CHCl_3$ 15:85 + 1% Et_3N) and concentrated under reduced pressure. The crude was purified by column chromatography (SiO_2, gradient elution: 15% $CH_3OH/CHCl_3$; then 15% $CH_3OH/CHCl_3$ + 1% Et_3N). Fractions containing product were concentrated, dissolved in $CHCl_3$ (50 mL), washed with saturated Na_2CO_3 (4 × 25 mL), dried over Na_2SO_4, and concentrated once more. The residue was dissolved in THF (5 mL) and pipetted into *n*-hexane (50 mL). The resulting suspension was sonicated for 1 minute, after which the precipitate was allowed to settle over 30 min and collected by vacuum filtration, washed with additional *n*-hexane (2 × 10 mL) and pentane (2 × 10 mL), and dried to give the title compound (24 mg, 62%) as a white solid.

^{1}H NMR (500 MHz, $CDCl_3$, 298 K) δ_H = 8.53–8.40 (m, 24H, **α**), 7.13 (d, *J* = 8.5 Hz, 12H, **ε**/**ζ**), 7.11–7.06 (m, 24H, **β**), 6.94 (d, *J* = 8.5 Hz, 12H, **ε**/**ζ**), 6.56 (d, *J* = 2.2 Hz, 12H, **δ**), 6.29 (t, *J* = 2.2 Hz, 6H, **γ**), 3.89 (t, *J* = 6.0 Hz, 24H, **σ$_3$**), 2.75 (t, *J* = 7.4 Hz, 24H, **σ$_1$**), 2.08–1.99 (m, 24H, **σ$_2$**) ppm.

^{13}C NMR (126 MHz, $CDCl_3$, 298 K) δ_C = 160.31, 150.50, 149.95, 142.90, 140.36, 140.17, 137.43, 131.98, 125.45, 124.08, 105.69, 100.10, 66.66, 31.66, 29.84 ppm.

HRMS (ESI) *m*/*z* calculated for $C_{174}H_{163}O_{12}N_{12}^+$ ($[M+H]^+$) 2612.2508, found 2612.2462.

B.4.4 Synthesis of T12e

Compound 2.1:

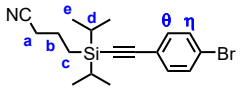

A Schlenk flask containing 4-bromoiodobenzene (1.60 g, 5.66 mmol), $Pd(PPh_3)_2Cl_2$ (198 mg, 0.283 mmol), CuI (54 mg, 0.28 mmol) in THF (50 mL) and *i*-Pr_2NH (10 mL) was subjected to three freeze-pump-thaw cycles and while frozen, CPDIPS-acetylene[344] (1.23 g, 5.94 mmol) was added. The reaction mixture was subjected to additional two freeze-pump-thaw cycles and stirred at room temperature for 12 h. The reaction mixture was filtered through a pad of silica ($CHCl_3$/petroleum ether 1:1) and concentrated under reduced pressure. Purification by flash column chromatography (SiO_2, gradient elution from 30–50% $CHCl_3$/petroleum ether) gave the title compound (1.69 g, 82%) as a clear oil.

^{1}H NMR (400 MHz, $CDCl_3$, 298 K) δ_H = 7.44 (d, *J* = 8.5 Hz, 2H, **θ/η**), 7.32 (d, *J* = 8.5 Hz, 2H, **θ/η**), 2.43 (t, *J* = 7.0 Hz, 2H, **a**), 1.92–1.80 (m, 2H, **b**), 1.13–1.05 (m, 14H, **d**+**e**), 0.87–0.79 (m, 2H, **c**) ppm.

^{13}C NMR (101 MHz, $CDCl_3$, 298 K) δ_C = 133.61, 131.69, 123.10, 122.04, 119.84, 106.82, 90.94, 21.41, 20.92, 18.33, 18.09, 11.83, 9.74 ppm.

HRMS (ESI) *m*/*z* calculated for $C_{18}H_{24}NBrNaSi^+$ ($[M+Na]^+$) 384.0754, found 384.0755.

Compound 2.2:

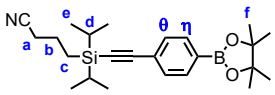

To a deoxygenated mixture of aryl bromide **2.1** (1.69 g, 4.65 mmol), bis(pinacolato)diboron (1.77 g, 6.97 mmol), and KOAc (1.37 g, 14.0 mmol) in dioxane (30 mL) was added $Pd(dppf)Cl_2{\cdot}CH_2Cl_2$ (327 mg, 0.465 mmol), the reaction mixture was further degassed by a stream of argon, before stirring at 90 °C for 1.5 d. The reaction mixture was filtered through a short pad of silica ($CHCl_3$) and concentrated under reduced pressure. The crude was purified by flash column chromatography (SiO_2, 50% $CHCl_3$/petroleum ether) affording the title compound (2.37 g, ≥99%) as an orange oil containing some impurities (unreacted B_2pin_2 and pinacol), and was used without further purification.

^{1}H NMR (400 MHz, $CDCl_3$, 298 K) δ_H = 7.74 (d, *J* = 8.1 Hz, 2H, **θ/ε**), 7.45 (d, *J* = 8.1 Hz, 2H, **θ/ε**), 2.43 (t, *J* = 6.9 Hz, 2H, **a**), 1.93–1.81 (m, 2H, **b**), 1.34 (s, 12H, f), 1.14–1.03 (m, 14H, **d**+**e**), 0.87–0.79 (m, 2H, **c**) ppm.

^{13}C NMR (101 MHz, $CDCl_3$, 298 K) δ_C = 134.65, 131.32, 125.72, 119.90, 108.11, 90.88, 84.14, 83.65, 25.01, 21.41, 20.93, 18.35, 18.11, 11.88, 9.76 ppm.

HRMS (ESI) *m/z* calculated for $C_{24}H_{36}O_2NBNaSi^+$ ($[M+Na]^+$) 431.2537, found 431.2541.

Compound 2.3:

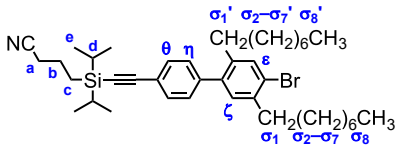

A mixture of boronic acid pinacol ester **2.2** (1.080 g, 2.64 mmol), 1,4-dibromo-2,5-dioctylbenzene[342] (2.43 g, 5.28 mmol), and K_2CO_3 (2.19 g, 15.8 mmol) in dioxane (50 mL) was subjected to three freeze-pump-thaw cycles, and while still frozen, $Pd(PPh_3)_2Cl_2$ (185 mg, 0.264 mmol) was added. The reaction mixture was subjected to additional three freeze-pump-thaw cycles and heated to 90 °C. After 16 h, the reaction mixture was filtered through a short pad of silica ($CHCl_3$) and concentrated under reduced pressure. Purification by flash column chromatography (SiO_2, gradient elution: 10–50% $CHCl_3$/petroleum ether) gave the title compound (0.785 g, 45%) as an orange oil, with some impurities. It was used without further purification.

^{1}H NMR (400 MHz, $CDCl_3$, 298 K) δ_H = 7.51 (d, *J* = 8.2 Hz, 2H, **θ/η**), 7.44 (s, 1H, **ε/ζ**), 7.23 (d, *J* = 8.3 Hz, 2H, **θ/η**), 6.99 (s, 1H, **ε/ζ**), 2.73–2.66 (m, 2H, **σ$_1$/σ$_1$'**), 2.50–2.42 (m, 4H, **a**+**σ$_1$/σ$_1$'**), 1.95–1.85 (m, 2H, **b**), 1.65–1.56 (m, 2H, **σ$_2$/σ$_2$'**), 1.50–1.16 (m, 22H, **σ$_2$/σ$_2$'**+**σ$_3$–σ$_7$**+**σ$_3$'–σ$_7$'**), 1.15–1.08 (m, 14H, **d**+**e**), 0.90–0.82 (m, 8H, **c**+**σ$_8$/σ$_8$'**) ppm.

^{13}C NMR (151 MHz, $CDCl_3$, 298 K) δ_C = 141.78, 140.35, 139.79, 139.45, 133.33, 131.98, 131.53, 129.26, 123.77, 121.76, 119.91, 107.94, 89.84, 35.86, 32.50, 32.03, 31.95, 31.31, 30.15, 29.59, 29.54, 29.47, 29.39, 29.36, 29.23, 22.81, 22.78, 21.48, 20.92, 18.36, 18.13, 14.25, 14.25, 11.92, 9.82 ppm.

HRMS (ESI) *m/z* calculated for $C_{40}H_{60}NBrNaSi^+$ ($[M+Na]^+$) 684.3571, found 684.3728.

Compound 2.4

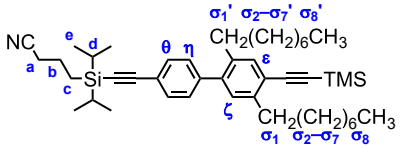

A mixture of aryl bromide **2.3** (785 mg, 1.18 mmol), $Pd(PPh_3)_2Cl_2$ (84 mg, 0.12 mmol), and CuI (11.3 mg, 0.059 mmol) in Et_3N (6.0 mL) was subjected to three freeze-pump-thaw cycles, and while still frozen, TMS-acetylene (2.50 mL, 15.2 mmol) was added. The reaction flask was subjected to additional three freeze-pump-thaw cycles, then closed, and heated to 50 °C. After 3 d, complete conversion was indicated by ^{1}H-NMR. The reaction mixture was filtered through a short pad of silica ($CHCl_3$) and concentrated under reduced pressure. Purification by flash column chromatography (SiO_2, gradient elution: 10–50% $CHCl_3$/petroleum ether) gave the title compound (716 mg, 89%) as a yellow oil.

^{1}H NMR (400 MHz, $CDCl_3$, 298 K) δ_H = 7.50 (d, *J* = 8.5 Hz, 2H, θ/η), 7.35 (s, 1H, ε/ζ), 7.23 (d, *J* = 8.5 Hz, 2H, θ/η), 6.96 (s, 1H, ε/ζ), 2.78–2.69 (m, 2H, σ_1/σ_1'), 2.51–2.42 (m, 4H, e+σ_1/σ_1'), 1.95–1.84 (m, 2H, a), 1.69–1.58 (m, 2H, σ_2/σ_2'), 1.48–1.39 (m, 2H, σ_2/σ_2'), 1.39–1.15 (m, 20H, σ_3–σ_7+σ_3'–σ_7'), 1.15–1.08 (m, 14H, d+e), 0.94–0.80 (m, 8H, c+σ_8/σ_8'), 0.27 (s, 9H, TMS) ppm.

^{13}C NMR (126 MHz, $CDCl_3$, 298 K) δ_C = 142.93, 142.31, 141.42, 137.61, 133.29, 131.90, 130.26, 129.24, 121.84, 121.62, 119.91, 108.00, 104.23, 97.75, 89.74, 34.51, 32.49, 32.03, 31.96, 31.38, 30.89, 29.85, 29.63, 29.52, 29.46, 29.38, 29.25, 22.81, 22.78, 21.47, 20.92, 18.36, 18.13, 14.25, 11.91, 9.81, 0.19 ppm.

HRMS (ESI) *m/z* calculated for $C_{45}H_{70}NSi_2^+$ ($[M+H]^+$) 680.5041, found 680.5040.

Compound 2.5

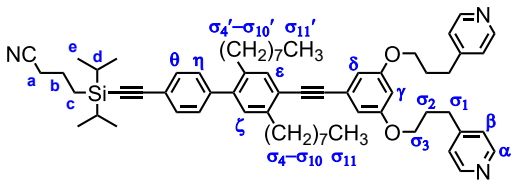

To a solution of **2.4** (716 mg, 1.05 mmol) in THF (30 mL) and CH_3OH (30 mL) was added K_2CO_3 (436 mg, 3.16 mmol). After 2 h, complete desilylation was confirmed by TLC (5% EtOAc/petroleum ether). The reaction mixture was filtered through a short pad of silica ($CHCl_3$)

and concentrated under reduced pressure. The remaining oil was dissolved in THF (4 mL) and transferred to a Schlenk flask containing **T2$_{Br}$** (574 mg, 1.21 mmol) in THF (12 mL) and Et_3N (4 mL). The solution was purged by N_2 bubbling for 20 minutes, then subjected to freeze-pump-thaw cycles (3), and while still frozen and under argon, $Pd_2(dba)_3$ (96 mg, 0.110 mmol), $AsPh_3$ (258 mg, 0.842 mmol), and CuI (20.0 mg, 0.105 mmol) were added. The reaction flask was subjected to additional freeze-pump-thaw cycles (3) and warmed to room temperature. After 16 hours, the reaction mixture was filtered through a short pad of silica ($CH_3OH/CHCl_3$ 1:9) and concentrated under reduced pressure. Purification by gravity column chromatography (SiO_2, gradient elution: 2–5% $CH_3OH/CHCl_3$) gave the title compound (942 mg, 94%) as a pale-yellow oil.

^{1}H NMR (500 MHz, $CDCl_3$, 298 K) δ_H = 8.52 (br s, 4H, **α**), 7.52 (d, *J* = 8.3 Hz, 2H, **η**/**θ**), 7.41 (s, 1H, **ε**/**ζ**), 7.26 (d, *J* = 8.2 Hz, 2H, **η**/**θ**), 7.18 (d, *J* = 5.2 Hz, 4H, **β**), 7.01 (s, 1H, **ε**/**ζ**), 6.68 (d, *J* = 2.2 Hz, 2H, **δ**), 6.41 (t, *J* = 2.3 Hz, 1H, **γ**), 3.98 (t, *J* = 6.0 Hz, 4H, **σ$_3$**), 2.87–2.83 (m, 4H, **σ$_1$**), 2.83–2.79 (m, 2H, **σ$_4$**/**σ$_4$'**), 2.54–2.48 (m, 2H, **σ$_4$**/**σ$_4$'**), 2.45 (t, *J* = 7.0 Hz, 2H, **a**), 2.17–2.09 (m, 4H, **σ$_2$**), 1.94–1.85 (m, 2H, **b**), 1.73–1.65 (m, 2H, **σ$_5$**/**σ$_5$'**), 1.49–1.41 (m, 2H, **σ$_5$**/**σ$_5$'**), 1.42–1.16 (m, 20H, **σ$_6$**–**σ$_{10}$**+**σ$_6$'**–**σ$_{10}$'**), 1.16–1.09 (m, 14H, **d**+**e**), 0.89–0.81 (m, 8H, **c**+**σ$_{11}$**/**σ$_{11}$'**) ppm.

^{13}C NMR (126 MHz, $CDCl_3$, 298 K) δ_C = 159.92, 151.06, 149.56, 142.46, 142.25, 141.44, 137.81, 133.14, 131.95, 130.41, 129.26, 125.24, 124.24, 121.70, 119.93, 110.08, 107.97, 102.47, 92.71, 89.82, 88.34, 66.78, 34.46, 32.55, 32.04, 31.97, 31.79, 31.41, 30.94, 29.83, 29.81, 29.65, 29.54, 29.48, 29.42, 29.27, 22.82, 22.80, 21.48, 20.94, 18.37, 18.14, 14.27, 11.92, 9.82 ppm (two signals missing, presumably due to overlap).

HRMS (ESI) *m*/*z* calculated for $C_{64}H_{84}O_2N_3Si^+$ ($[M+H]^+$) 954.6327, found 954.6318.

Template T12e:

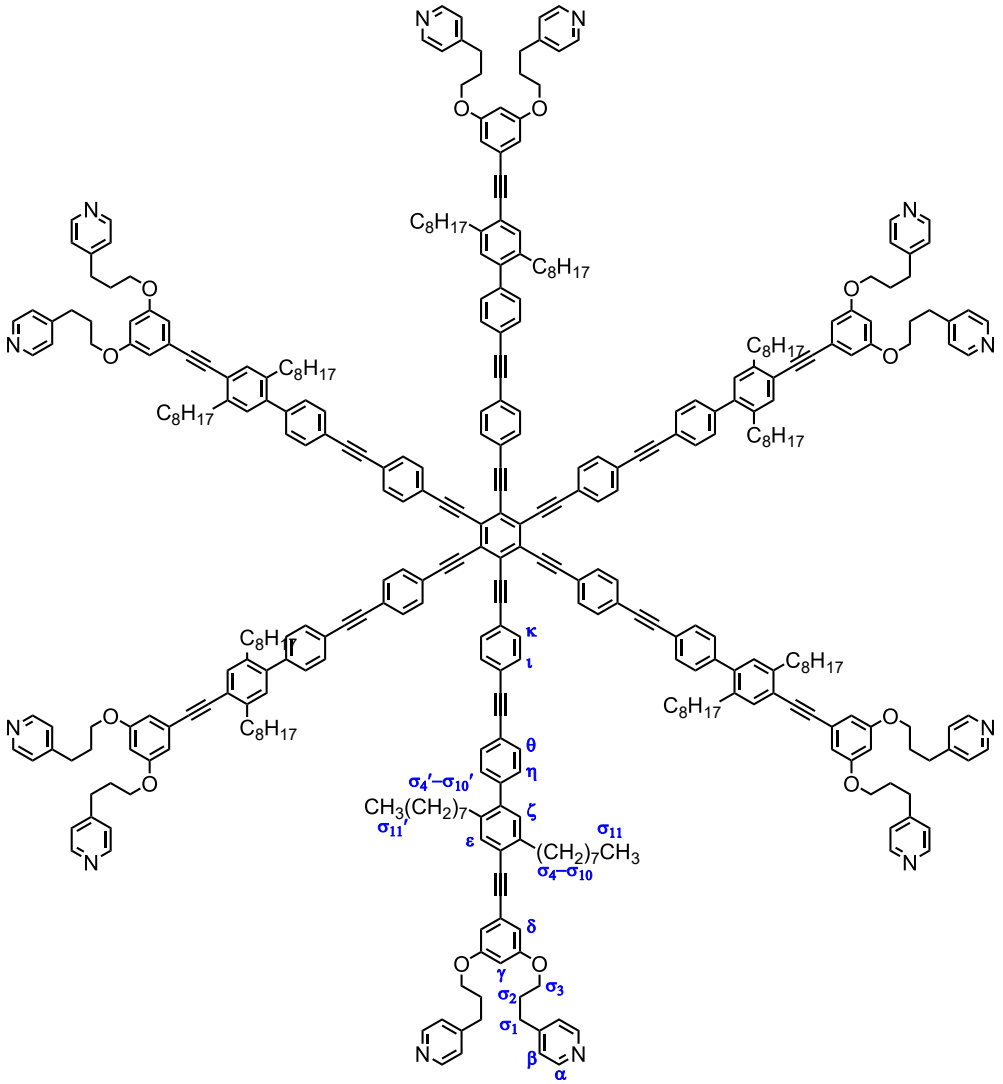

To a solution of **2.5** (399 mg, 0.418 mmol) in THF (20 mL) was added TBAF solution (1.46 mL, 1.46 mmol, 1.0 M in THF). After 1 h, complete desilylation was indicated by ^{1}H NMR. The reaction mixture was filtered through a short pad of silica ($CH_3OH/CHCl_3$ 1:9) and concentrated under reduced pressure. The residue was dissolved in THF (5 mL) and transferred to a Schlenk flask containing 1,2,3,4,5,6-hexakis((4-iodophenyl)ethynyl)benzene (Core-I_6)[124] (50.0 mg, 0.035 mmol) in THF (30 mL) and *i*-Pr_2NH (5 mL). The contents were purged by argon bubbling for 20 min, followed by three freeze-pump-thaw-cycles, and while still frozen and under argon, $Pd(PPh_3)_4$ (22 mg, 0.019 mmol) and CuI (4.0 mg, 0.021 mmol) were added. The reaction flask was subjected to additional three freeze-pump-thaw-cycles cycles and heated to 40 °C. After 3 days, the reaction mixture was filtered through a short pad of silica ($CH_3OH/CHCl_3$ 1:9) and concentrated under reduced pressure. The crude mixture was purified by size-exclusion chromatography (Bio-Beads S-X1, $CHCl_3$), followed by column

chromatography (SiO_2, neutralized prior to loading using one column volume of $CHCl_3$ + 5% Et_3N, followed by two column volumes of $CHCl_3$; crude eluted with 7% $CH_3OH/CHCl_3$). The title compound eluded as a yellow band, exhibiting turquoise fluorescence under UV irradiation (λ = 365 nm). Fractions containing product were concentrated under reduced pressure, dissolved in THF (5 mL) and pipetted into *n*-hexane (100 mL). The resulting suspension was sonicated for 1 minute and the precipitate was allowed to settle over 30 minutes, after which it was collected by vacuum-filtration, washed with additional *n*-hexane (2 × 10 mL) and pentane (2 × 10 mL), and dried to give the title compound as a yellow solid (104 mg, 56%).

^{1}H NMR (500 MHz, $CDCl_3$, 298 K) δ_H = 8.62–8.40 (m, 24H, α), 7.66 (d, *J* = 8.2 Hz, 12H, ι/κ), 7.64–7.58 (m, 24H, $\iota/\kappa+\theta$), 7.43 (s, 6H, ε), 7.32 (d, *J* = 8.0 Hz, 12H, η), 7.15 (d, *J* = 5.7 Hz, 24H, β), 7.06 (s, 6H, ζ), 6.68 (d, *J* = 2.2 Hz, 12H, δ), 6.42 (t, *J* = 2.1 Hz, 6H, γ), 3.97 (t, *J* = 6.0 Hz, 24H, σ_3), 2.89–2.77 (m, 36H, $\sigma_1+\sigma_4/\sigma_4$'), 2.54 (t, *J* = 8.0 Hz, 12H, σ_4/σ_4'), 2.17–2.08 (m, 24H, σ_2), 1.71 (p, *J* = 7.7 Hz, 12H, σ_5/σ_5'), 1.51–1.14 (m, 132H, $\sigma_5/\sigma_5'+\sigma_6-\sigma_{10}+\sigma_6'-\sigma_{10}$'), 0.86 (t, *J* = 7.1 Hz, 18H, σ_{11}/σ_{11}'), 0.84 (t, *J* = 6.9 Hz, 18H, σ_{11}/σ_{11}') ppm.

^{1}H Diffusion NMR (500 MHz, $CDCl_3$, 298 K) $D = 1.86 \cdot 10^{-10}$ m^2 s^{-1}.

^{13}C NMR (126 MHz, $CDCl_3$, 298 K) δ_C = 159.94, 150.48, 150.01, 142.50, 142.18, 141.44, 137.86, 133.19, 131.95, 131.92, 131.56, 130.41, 129.43, 127.67, 125.20, 124.29, 124.10, 122.83, 121.73, 121.66, 110.09, 102.47, 99.71, 92.76, 92.08, 89.60, 89.11, 88.30, 66.80, 34.49, 32.60, 32.04, 31.99, 31.71, 31.41, 30.98, 29.85, 29.83, 29.65, 29.56, 29.48, 29.40, 29.29, 22.82, 14.28, 14.26 ppm (one signal coincident or not observed in aliphatic region) ppm.

UV–vis–NIR ($CDCl_3$, 298 K) λ_{max} (ε / 10^6 M^{-1} cm^{-1}): 318 (0.32), 386 (0.30) nm.

HRMS (ESI) *m*/*z* calcd for $C_{378}H_{404}N_{12}O_{12}^{2+}$ ($[M+2H]^{2+}$) 2653.5747, found 2653.5722.

B.5 Attempted Syntheses of *cs*-P12 and *cs*[b_1]-P12

B.5.1 Syntheses of *ls*-P12-Br$_2$ and *ls*-P12-THS$_2$

***ls*-P12-Br$_2$:**

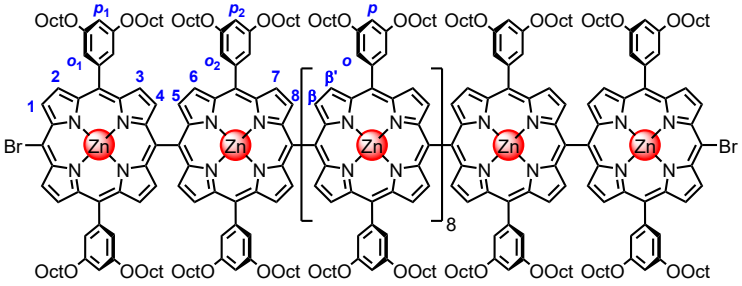

To a stirred solution of ***ls*-P12** (12 mg, 0.96 µmol) in $CHCl_3$ (5.0 mL) with pyridine (50 µL) in an ice bath (0 °C), a solution of *N*-bromosuccinimide (0.36 mg, 2.0 µmol) in $CHCl_3$ (1.0 mL) was added dropwise. The reaction was conducted at 0 °C for 5 minutes, and acetone (0.1 mL) was added to quench the excess *N*-bromosuccinimide. The resulting mixture was purified by flash column chromatography on silica gel using CH_2Cl_2/pentane 1:1 as eluent to give the desired product ***ls*-P12-Br$_2$** (11 mg, 87%).

^{1}H NMR (600 MHz, $CDCl_3$, 298 K): δ_H = 9.89 (d, *J* = 4.4 Hz, 4H, **H$_1$**), 9.21 (d, *J* = 4.4 Hz, 4H, **H$_2$**), 9.01–8.89 (m, 36H, **H$_{7,\beta'}$**), 8.87 (d, *J* = 4.4 Hz, 4H, **H$_6$**), 8.83 (d, *J* = 4.3 Hz, 4H, **H$_3$**), 8.40–8.29 (m, 36H, **H$_{8,\beta}$**), 8.22 (d, *J* = 4.5 Hz, 4H, **H$_4$**), 8.18 (d, *J* = 4.1 Hz, 4H, **H$_5$**), 7.55–7.47 (m, 32H, **H$_o$**), 7.47–7.41 (m, 16H, **H$_{o1,o2}$**), 6.86–6.83 (m, 4H, **H$_{p1}$**), 6.80–6.75 (m, 16H, **H$_p$**), 6.75–6.72 (m, 4H, H$_{p2}$), 4.14–3.98 (m, 96H, **H$_{Oct}$**), 1.88–1.71 (m, 96H, **H$_{Oct}$**), 1.50–1.14 (m, 480H, **H$_{Oct}$**), 0.87–0.72 (m, 144H, **H$_{Oct}$**) ppm.

UV–vis–NIR ($CDCl_3$, 298 K) λ_{max} (ε / 10^6 M^{-1} cm^{-1}): 418 (1.08), 504 (1.07), 585 (0.67) nm.

MALDI-ToF *m*/*z* 12,601.859 (calculated for $[C_{768}H_{984}Br_2N_{48}O_{48}Zn_{12}]^{\bullet+}$ = $(M)^{\bullet+}$: 12,600.594).

***ls*-P12-THS$_2$:**

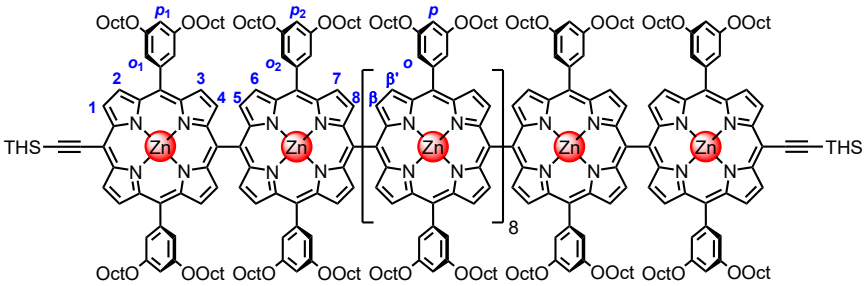

A mixture of ***ls*-P12-Br$_2$** (20 mg, 1.6 µmol), Pd(PPh$_3$)$_4$ (0.73 mg, 0.63 µmol) and CuI (0.12 mg, 0.63 µmol) in dry toluene (1.5 mL) and *i*-Pr$_2$NH (1.5 mL) was degassed by three freeze-pump-thaw cycles. After that, THS-acetylene[345] (3.6 µL, 9.6 µmol) was added to the mixture and the reaction was conducted at 50 °C under argon for 3 h. After the reaction, the resulting mixture was concentrated and purified by flash column chromatography on silica gel using pentane/CH_2Cl_2 (1:1) as eluent to give the crude product. The crude product was recrystallized by layer addition (CH_2Cl_2/CH_3OH) to give the title compound (17 mg, 85% yield).

^{1}H NMR (600 MHz, $CDCl_3$, 298 K) δ_H = 9.88 (d, *J* = 4.4 Hz, 4H, **H$_1$**), 9.19 (d, *J* = 4.4 Hz, 4H, **H$_2$**), 9.00–8.89 (m, 36H, **H$_{7,\beta'}$**), 8.86 (d, *J* = 4.6 Hz, 4H, **H$_6$**), 8.80 (d, *J* = 4.5 Hz, 4H, **H$_3$**), 8.43–8.29 (m, 36H, **H$_{8,\beta}$**), 8.23–8.16 (m, 8H, **H$_{4,5}$**), 7.54–7.48 (m, 32H, **H$_o$**), 7.47–7.41 (m, 16H, **H$_{o1,o2}$**), 6.87–6.83 (m, 4H, **H$_{p1}$**), 6.81–6.75 (m, 16H, **H$_p$**), 6.75–6.72 (m, 4H, **H$_{p2}$**), 4.13–4.00 (m, 96H, **H$_{Oct}$**), 1.89–1.72 (m, 108H, **H$_{Oct,THS}$**), 1.66–1.58 (m, 12H, **H$_{THS}$**), 1.50–1.14 (m, 504H, **H$_{Oct,THS}$**), 1.13–1.08 (m, 12H, **H$_{THS}$**), 0.96 (t, *J* = 7.0 Hz, 16H, **H$_{THS}$**), 0.86–0.73 (m, 144H, **H$_{Oct}$**) ppm.

UV–vis–NIR ($CDCl_3$, 298 K) λ_{max} (ε / 10^6 M^{-1} cm^{-1}): 415 (1.93), 504 (2.18), 585 (1.36) nm.

MALDI-ToF *m*/*z* 13,056.045 (calculated for $[C_{808}H_{1062}N_{48}O_{48}Si_2Zn_{12}]^{\bullet+}$ = $(M)^{\bullet+}$: 13,055.324).

B.5.2 Macrocyclization of *ls*-P12 Using Ag(I)-Mediated Oxidative Coupling

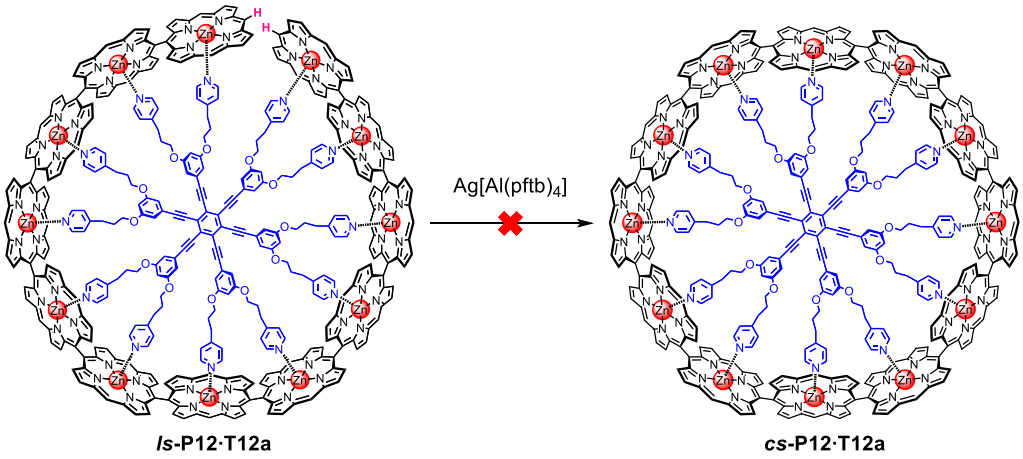

A mixture of ***ls*-P12** (1.24 mg, 0.1 μmol, 1.0 equiv.) and **T12a** (0.23 mg, 0.1 μmol, 1.0 equiv.) in dry $CHCl_3$ (1.0 mL) with 1% dimethylacetamide (DMA, 10 μL) was degassed by three freeze-pump-thaw cycles. After that, under argon, a solution of $Ag[Al(pftb)_4]$[198] (pftb = perfluoro-*tert*-butoxy, 0.11 mg, 0.1 μmol, 1.0 equiv.) in dry $CHCl_3$ (0.1 mL) was added and the reaction mixture was stirred at 25 ºC. The progress of the reaction was monitored by analytical GPC, showing no desired product formed after 6 h (Figure 2.14b). A solution of $Ag[Al(pftb)_4]$ (1.1 mg, 1.0 μmol, 10 equiv.) in dry $CHCl_3$ (1.0 mL) was added to the reaction mixture and the mixture was stirred at 50 ºC for 2 h. Again, no desired product was observed from the analytical GPC trace of the reaction mixture. Then, a solution of $Ag[Al(pftb)_4]$ (11 mg, 10 μmol, 100 equiv.) in dry $CHCl_3$ (10 mL) was added and indicated by the analytical GPC trace, no cyclic product formed after another 6 h.

B.5.3 Macrocyclization of *ls*-P12 Using PIFA-Mediated Oxidative Coupling

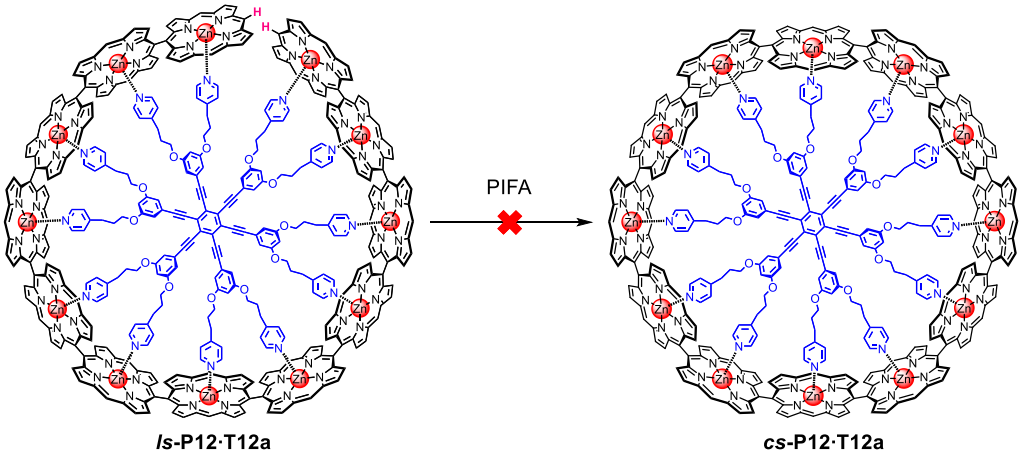

Condition A: To a solution of ***ls*-P12** (5.0 mg, 0.4 μmol, 1.0 equiv.) and **T12a** (0.92 mg, 0.4 μmol, 1.0 equiv.) in dry CH_2Cl_2 (3.0 mL), [bis(trifluoroacetoxy)iodo]benzene (PIFA, 0.09 mg, 0.2 μmol, 0.5 equiv.) was added and the mixture was stirred at 25 °C. The progress of the coupling was monitored by analytical GPC, showing no cyclic product formed after 40 h (Figure 2.14c).

Condition B: To a solution of ***ls*-P12** (5.0 mg, 0.4 μmol, 1.0 equiv.) and **T12a** (0.92 mg, 0.4 μmol, 1.0 equiv.) in dry CH_2Cl_2 (3.0 mL), [bis(trifluoroacetoxy)iodo]benzene (PIFA, 0.09 mg, 0.2 μmol, 0.5 equiv.) was added and the mixture was stirred at 25 ºC. The progress of the coupling was monitored by analytical GPC, showing the linear 12-mer was barely converted after 1 h. PIFA (0.26 mg, 0.6 μmol, 1.5 equiv.) was added to the reaction mixture and trace amount of linear 24-mer was observed after 1 h. Then, PIFA (0.34 mg, 0.8 μmol, 2.0 equiv.) was subjected to the reaction mixture, resulting in precipitation of the starting materials without formation of desired cyclic product.

B.5.4 Macrocyclization of *ls*-P12-Br_2 Using Yamamoto Coupling

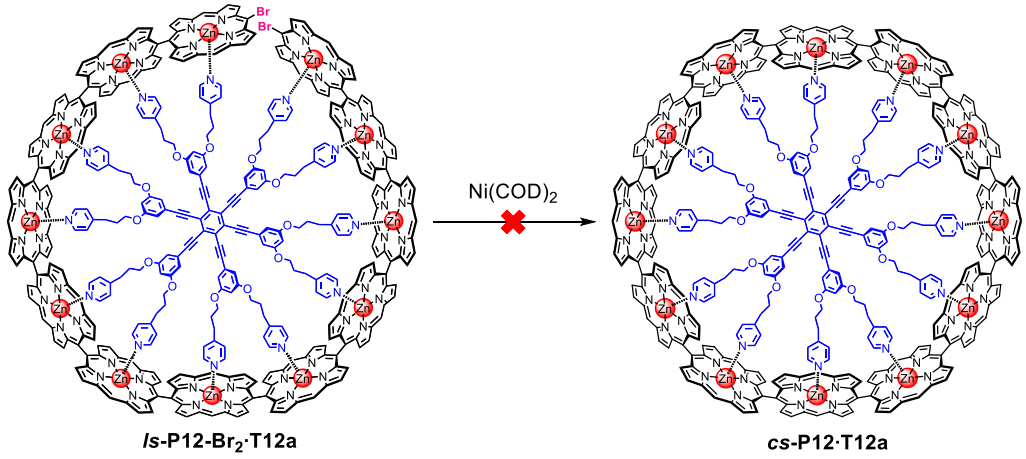

Condition A: A mixture of ***ls*-P12-Br_2** (1.26 mg, 0.1 μmol, 1.0 equiv.) and **T12a** (0.23 mg, 0.1 μmol, 1.0 equiv.) in $CHCl_3$ (2.0 mL) was concentrated under reduced pressure to give self-assembled complex ***ls*-P12-Br_2·T12a**. After that, the preformed complex and $Ni(COD)_2$ were suspended in dry DMF (1.0 mL) and the mixture was degassed by three freeze-pump-thaw cycles. Then, the reaction mixture was stirred at 80 ºC under argon. The progress was monitored by analytical GPC, which suggested no expected product formed after 24 h.

Condition B: To a solution of ***ls*-P12-Br$_2$** (1.26 mg, 0.1 μmol, 1.0 equiv.) and **T12a** (0.23 mg, 0.1 μmol, 1.0 equiv.) in dry toluene (0.5 mL) was added dry DMF (0.5 mL) and the mixture was degassed by three freeze-pump-thaw cycles. After that, the reaction mixture was stirred at 80 ºC under argon. The progress was monitored by analytical GPC (Figure 2.15c), which suggested no expected product formed after 24 h.

B.5.5 Macrocyclization Using Suzuki Coupling of *ls*-P3-Bpin$_2$ and *ls*-P9-Br$_2$

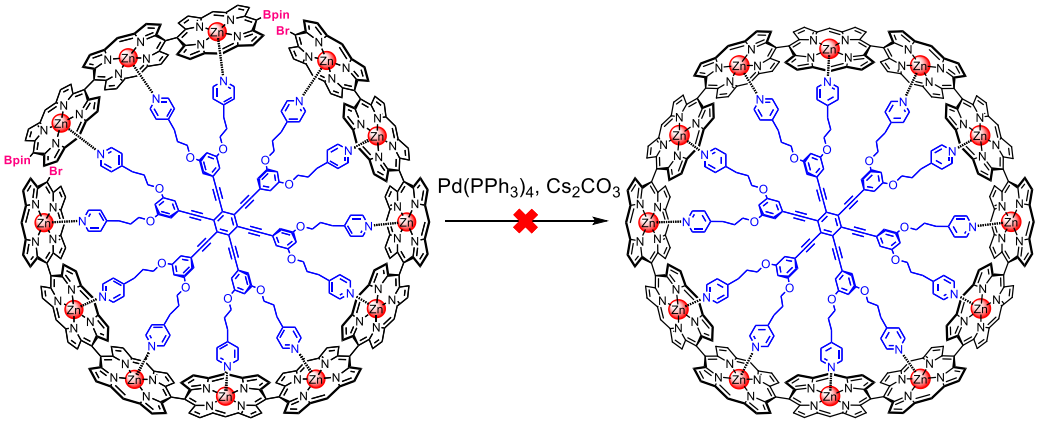

A solution of ***ls*-P3-Bpin$_2$** (1.4 mg, 0.4 μmol, 1.0 equiv.), ***ls*-P9-Br$_2$** (4.0 mg, 0.4 μmol, 1.0 equiv.) and **T12a** (0.96 mg, 0.4 μmol, 1.0 equiv.) in $CHCl_3$ (5.0 mL) was concentrated under reduced pressure to preform self-assembled complex. The preformed complex, $Pd(PPh_3)_4$ (9.7 mg, 8.4 μmol, 20 equiv.) and Cs_2CO_3 (2.7 mg, 8.4 μmol, 20 equiv.) were suspended in dry toluene (0.8 mL) and DMF (0.2 mL). The suspension was degassed by three freeze-pump-thaw cycles. After that, the reaction mixture was stirred at 80 ºC under argon for 20 h and the progress was monitored by analytical GPC after 20 h (Figure 2.15d), showing no desired cyclic product formed.

B.5.6 Attempted Syntheses of *cs*[b_1]-P12

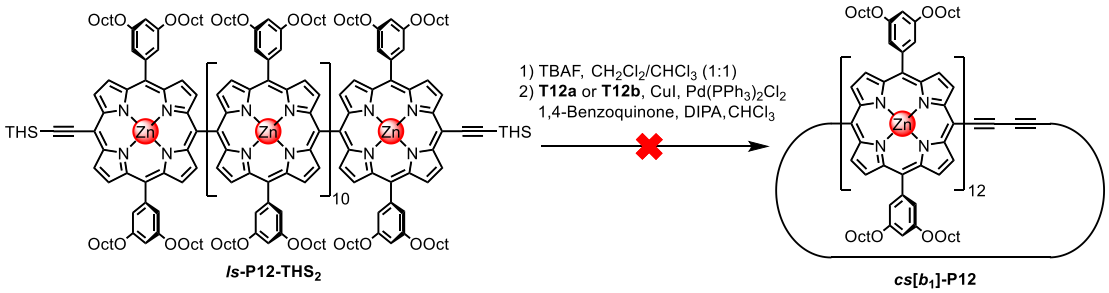

To a solution of ***ls*-P12-THS$_2$** (5.0 mg, 0.38 μmol) in CH_2Cl_2 (1 mL) was added TBAF (1.0 M in THF, 11 μL, 11 μmol). After stirring for 1 h, AcOH (1 μL) was added, and the reaction mixture was passed through a short pad of silica (CH_2Cl_2/pentane 1:1), giving deprotected linear 12-mer ***ls*-P12-*e*$_2$** (4.7 mg, 98%).

Condition A: *ls*-P12-*e*$_2$ (0.1 mg, 8.0 nmol, 1.0 equiv.) was dissolved in $CHCl_3$ (2.0 mL) in a 7-mL vial and a solution of **T12a** template (18 μg, 8.0 nmol, 1.0 equiv.) in $CHCl_3$ (2.0 mL) was added. A catalyst mixture was prepared by dissolving CuI (0.42 mg, 2.2 μmol), $Pd(PPh_3)_2Cl_2$ (0.50 mg, 0.43 μmol), and 1,4-benzoquinone (0.92 mg, 8.5 μmol) in *i*-Pr_2NH (9.2 μL) and $CHCl_3$ (0.38 mL) using sonication. The catalyst mixture was added to the reaction flask and it was left stirring exposed to the atmosphere. Progress was monitored by analytical GPC, showing no expected cyclic product formed after 24 h.

Condition B: *ls*-P12-*e*$_2$ (0.1 mg, 8.0 nmol, 1.0 equiv.) was dissolved in $CHCl_3$ (2.0 mL) in a 7-mL vial and a solution of **T12b** template (21 μg, 8.0 nmol, 1.0 equiv.) in $CHCl_3$ (2.0 mL) was added. A catalyst mixture was prepared by dissolving CuI (0.42 mg, 2.2 μmol), $Pd(PPh_3)_2Cl_2$ (0.50 mg, 0.43 μmol), and 1,4-benzoquinone (0.92 mg, 8.5 μmol) in *i*-Pr_2NH (9.2 μL) and $CHCl_3$ (0.38 mL) using sonication. The catalyst mixture was added to the reaction flask and it was left stirring exposed to the atmosphere. Progress was monitored by analytical GPC, showing no expected cyclic product formed after 24 h.

B.6 Synthesis of *cs*[*b*$_1$]-P24

Nanoring *cs*[*b*$_1$]-P24:

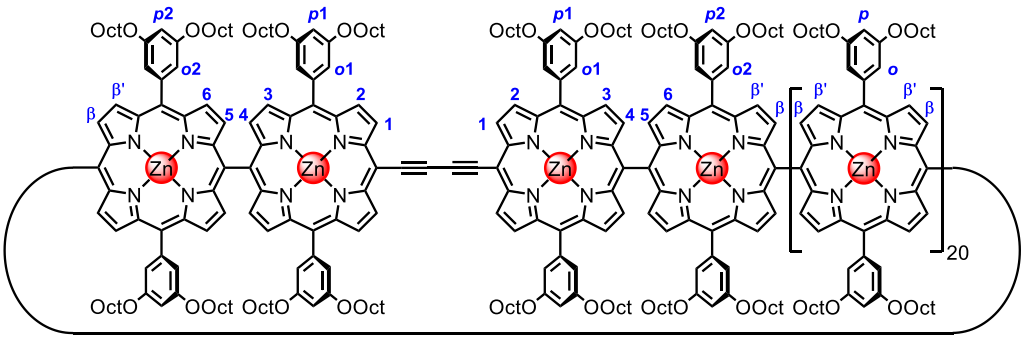

To a solution of ***ls*-P24-THS$_2$** (14.3 mg, 0.57 μmol) in CH_2Cl_2 (6 mL) and $CHCl_3$ (6 mL) was added TBAF (1.0 M in THF, 1.4 mL, 1.4 mmol). After stirring for 1 h, AcOH (1.4 mL) was added, and the reaction mixture was passed through a short pad of silica ($CHCl_3$). Toluene (30 mL) was added to the filtrate, and the chlorinated solvents were removed under reduced pressure. The remaining toluene solution was washed with saturated aq. Na_2CO_3 (3 × 25 mL), H_2O (1 × 25 mL), dried over Na_2SO_4, filtered, and concentrated under reduced pressure. The deprotected 24-mer was passed through a size-exclusion column (Bio-Beads, S-X1, $CHCl_3$). The isolated yield of 24-mer ***ls*-P24-*e*$_2$** was determined as 12.5 mg (89%). ***ls*-P24-*e*$_2$** (12.5 mg, 0.50 μmol) was dissolved in $CHCl_3$ (250 mL) in a 1 L flask and a solution of **T12e** template (5.32 mg, 1.0 μmol, 2.0 equiv.) in $CHCl_3$ (220 mL) was added. A catalyst mixture was prepared by dissolving CuI (54 mg, 284 μmol), $Pd(PPh_3)_2Cl_2$ (39 mg, 56 μmol), and 1,4-benzoquinone (121 mg, 1120 μmol) in *i*-Pr_2NH (1.2 mL) and $CHCl_3$ (48 mL) using sonication. The catalyst mixture was added to the reaction flask and it was left stirring exposed to the atmosphere. Progress was monitored by analytical GPC (Figure 2.20). After 18 h, THF + 1% pyridine (50 mL) was added to the reaction mixture and it was concentrated under reduced pressure to a volume of ca. 10 mL. The solution was passed through a short size-exclusion column (Bio-Beads S-X1, THF + 1% pyridine), removing unreacted 1,4-benzoquinone (orange band), and concentrated under reduced pressure. Purification by recycling GPC (loaded in THF + 20% pyridine; eluted in THF + 1% pyridine), followed by further size-exclusion chromatography (Bio-Beads S-X1, $CHCl_3$) gave the title compound (3.22 mg, 26%).

^{1}H NMR (700 MHz, $CDCl_3$, 298 K) δ_H = 10.14 (d, J = 4.3 Hz, 4H, **H_1**), 9.60–8.53 (m, 104H, **$H_{2,3,6,\beta'}$** + **H_β**), 8.53–8.11 (m, 56H, **$H_{4,5,\beta}$**), 8.10–6.96 (m, 120H, **H_β** + **H_o**), 6.98–6.52 (m, 48H, **$H_{p1,p2,p}$**), 4.60–3.36 (m, 192H, OCH_2), 1.94–1.60 (m, 192H, CH_2), 1.60–1.06 (m, 960H, 5 x CH_2), 0.96–0.60 (m, 288H, CH_3) ppm.

^{1}H Diffusion NMR (700 MHz, $CDCl_3$, 298 K) $D = 1.33 \times 10^{-10}$ m^2 s^{-1}.

^{13}C NMR (151 MHz, $CDCl_3$, 298 K) δ_C = 158.38 ($C_{Ar,meta}$), 154.99 ($C_{1'}$), 150.26 ($C_{2'}$), 144.48 ($C_{meso'}$), 134.27 (C_1), 132.25 (C_2), 122.94 (C_{meso}), 120.29 ($C_{Ar,ipso}$), 114.28 (C_o), 101.19 (C_p), 68.44 (OCH_2), [32.09, 31.93, 31.90, 31.87, 31.86] (CH_2), [29.86, 29.82, 29.53, 29.52, 29.48, 29.46, 29.36, 29.33, 29.30] (2 x CH_2), [26.26, 26.20] (CH_2), [22.85, 22.77, 22.71] (CH_2), [14.27, 14.20, 14.15] (CH_2) ppm (signals corresponding to the butadiyne link were not observed).

UV–vis–NIR ($CDCl_3$, 298 K) λ_{max} (ε / 10^6 M^{-1} cm^{-1}): 411 (1.71), 503 (2.12), 578 (1.19), 683 (0.10) nm.

MALDI-ToF *m*/*z* 24,927.485 (calculated for $[C_{1540}H_{1968}N_{96}O_{96}Zn_{24}]^{\bullet+}$ = $(M)^{\bullet+}$: 24,929.930).

Retention time: 29.7 min.

Complex *cs*[*b*$_1$]-P24·(T12e)$_2$:

The complex of ***cs*[*b*$_1$]-P24** with two **T12e** templates was formed in an NMR tube: ***cs*[*b*$_1$]-P24** (2.25 mg, 0.090 μmol) was dissolved in $CDCl_3$ (500 μL) and an excess of **T12e** was added in small increments (115 μL in total, 1.8 mM in $CDCl_3$, 2.25 equiv). Near the end of the titration (at 2.0 equiv. of T12), pyridine-d_5 was added (5 μL, 0.125 M in $CDCl_3$) to break-up any non-equilibrated (precipitated) material of ***cs*[*b*$_1$]-P24** and **T12e**. The point of saturation was marked by the appearance of free **T12e** ^{1}H resonances (at 2.25 equiv. of T12) as shown in Figure 2.35. Unbound **T12e** was removed by repeated size-exclusion chromatography (Bio-Beads, S-X1, $CHCl_3$), affording the ***cs*[*b*$_1$]-P24·(T12e)$_2$** complex (3.11 mg, 97%).

^{1}H NMR (700 MHz, $CDCl_3$, 298 K) δ_H = 10.11–9.96 (m, 2H, **H_1**), 9.93–9.77 (m, 2H, **$H_{1'}$**), 9.61–8.67 (m, 96H, **$H_{\beta'}$**), 8.66–7.44 (m, 120H, **H_o** + **η**/**θ**), 7.46–6.98 (m, 60H, ε + **η**/**θ** + **ι**/**κ**), 6.97–6.70 (m, 60H, **H_p** + **ζ**), 6.68–6.21 (m, 60H, **ι**/**κ** + **δ** + **γ**), 6.00–5.56 (m, 48H, **β_{Py}**), 4.45–3.37 (m, 240H, OCH_2 Oct + **σ_3**), 3.35–2.86 (m, 48H, **α_{Py}**), 2.84–2.49 (m, 24H, **σ_4**), 2.48–2.24 (m, 24H, **σ_4'**), 2.24–0.40 (m, 1848H, aliphatic) ppm.

^{1}H Diffusion NMR (700 MHz, $CDCl_3$, 298 K) $D = 1.37 \times 10^{-10}$ m^2 s^{-1}.

UV–vis–NIR ($CDCl_3$, 298 K) λ_{max} (ε / 10^6 M^{-1} cm^{-1}): 319 (1.24), 421 (2.15), 512 (2.19), 594 (1.16), 628 (0.26), 651 (0.19), 721 (0.086) nm.

MALDI-ToF *m/z* 35,664.706 (calculated for $[C_{2296}H_{2772}N_{120}O_{120}Zn_{24}]^{\bullet+}$ = $(M)^{\bullet+}$: 35,539.767).

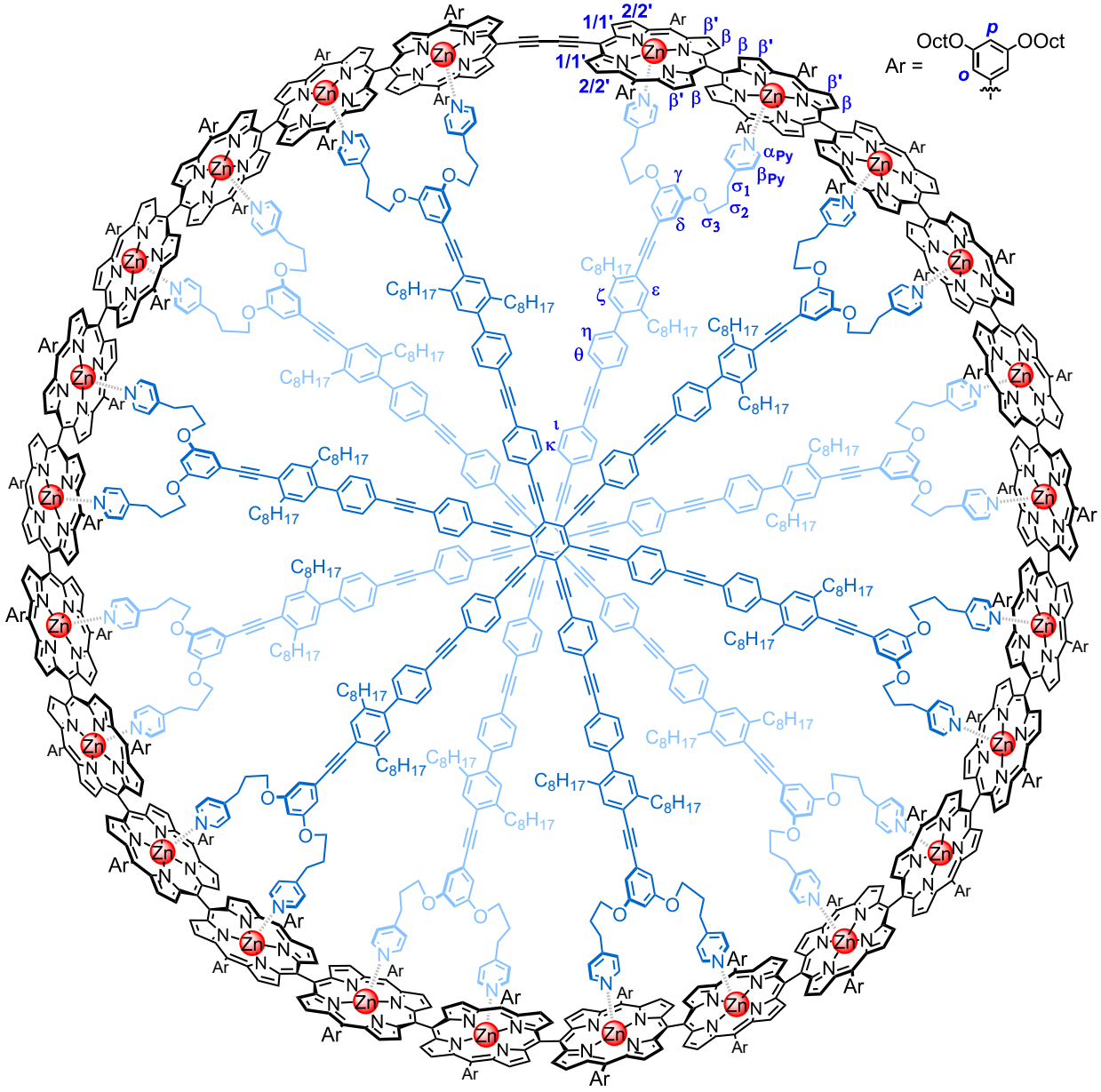

Figure B.4: Chemical structure of ***cs*[*b*$_1$]-P24·(T12e)$_2$**.

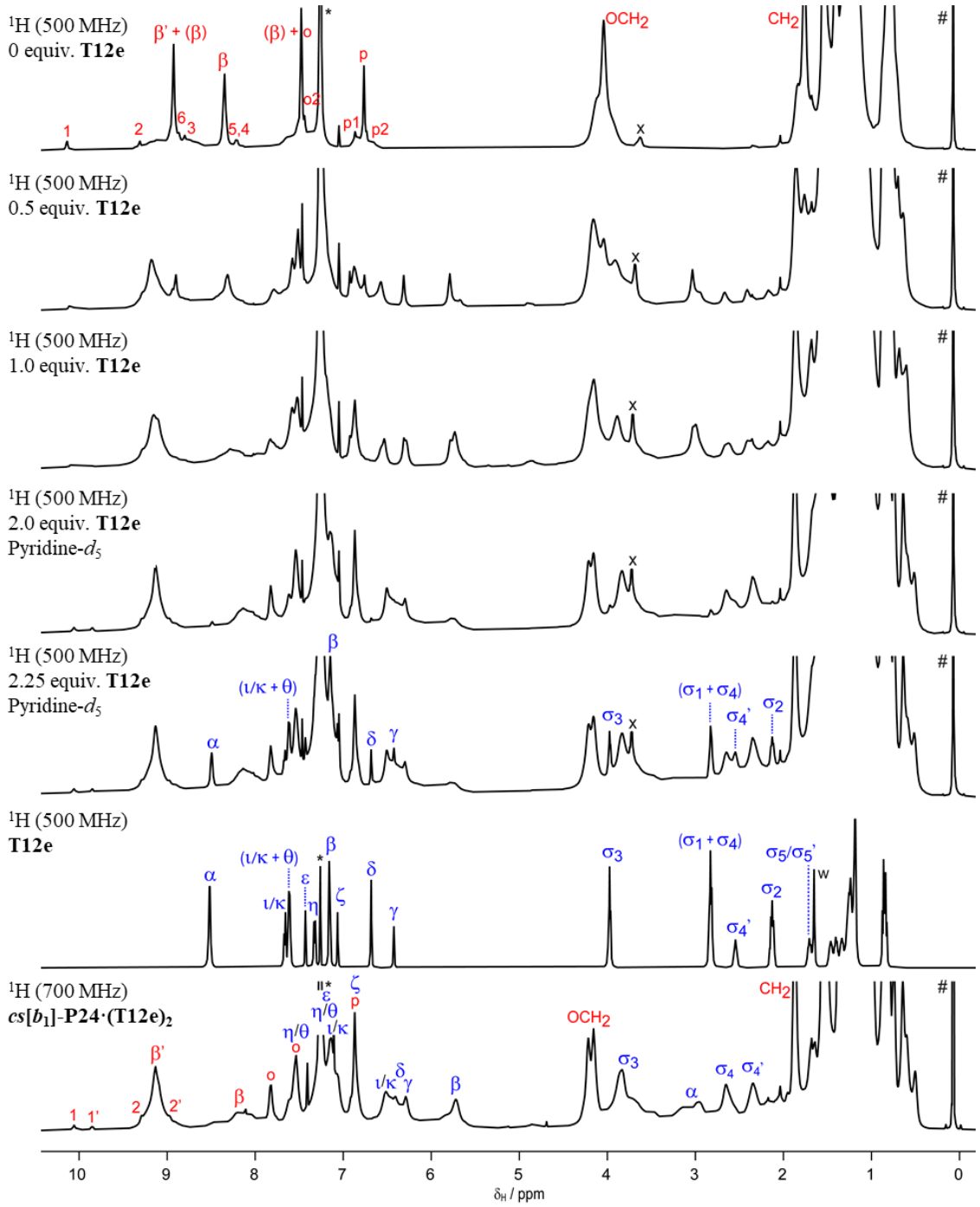

Figure B.5: Formation titration of the complex ***cs*[*b*$_1$]-P24·(T12e)$_2$**. From top to bottom: ^{1}H NMR spectra (500 or 700 MHz, $CDCl_3$, 298 K) at the incremental stages 0 equiv., 0.5 equiv., 1.0 equiv., 2.0 equiv., and 2.25 equiv. of **T12e**, isolated **T12e**, and isolated ***cs*[*b*$_1$]-P24·(T12e)$_2$** complex after size-exclusion chromatography. ^{1}H resonances, corresponding with unbound **T12e**, are highlighted in the spectrum with 2.25 equiv. of **T12e** added. * = $CHCl_3$; w = water; # = silicone grease; x = THF.

B.7 Syntheses of *lb*-P2 and *ls*[b_1]-P4

P1-CPDIPS:

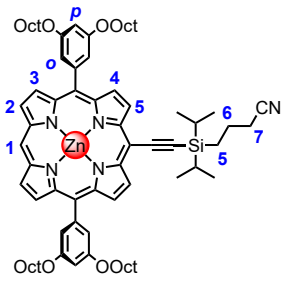

To a solution of **P1**[79] (100 mg, 96.3 µmol) in $CHCl_3$ (8.0 mL) and pyridine (80 µL) at 0 °C was added a solution of *N*-bromosuccinimide (17.1 mg, 96.3 µmol). The reaction mixture was stirred for 1 h and quenched by addition of acetone (0.1 mL). The resulting mixture was filtered through a pad of silica (CH_2Cl_2/pentane 1:1), and concentrated under reduced pressure. The crude containing **P1**, mono-, and dibrominated **P1**, was subjected directly to the next step. The crude mixture together with $Pd(PPh_3)_4$ (28 mg, 24 µmol) and CuI (1.8 mg, 9.6 µmol) was dissolved in dry *i*-Pr_2NH (2 mL) and toluene (2 mL), and subjected to three freeze-pump-thaw cycles. After that, CPDIPS-acetylene[344] (80 mg, 385 µmol) was added and the reaction mixture was stirred at 50 °C under argon for 2 h. The reaction mixture was separated by column chromatography (SiO_2, gradient elution: CH_2Cl_2/pentane 1:1 to CH_2Cl_2, giving the title compound (70 mg, 58%).

^{1}H NMR (600 MHz, $CDCl_3$, 298 K) δ_H = 10.20 (s, 1H, $\mathbf{H_1}$), 9.78 (d, *J* = 4.4 Hz, 2H, $\mathbf{H_5}$), 9.34 (d, *J* = 4.4 Hz, 2H, $\mathbf{H_2}$), 9.17 (d, *J* = 4.5 Hz, 2H, $\mathbf{H_4}$), 9.15 (d, *J* = 4.4 Hz, 2H, $\mathbf{H_3}$), 7.37 (d, *J* = 2.2 Hz, 4H, $\mathbf{H_o}$), 6.90 (t, *J* = 2.2 Hz, 2H, $\mathbf{H_p}$), 4.13 (t, *J* = 6.7 Hz, 8H, $\mathbf{H_{Oct}}$), 2.59 (t, *J* = 6.9 Hz, 2H, H_7), 2.27–2.21 (m, 2H, $\mathbf{H_6}$), 1.88 (p, *J* = 7.6 Hz, 8H, $\mathbf{H_{Oct}}$), 1.51 (p, *J* = 7.6 Hz, 8H, $\mathbf{H_{Oct}}$), 1.48–1.24 (m, 46H, $\mathbf{H_{Oct}}$+$\mathbf{H_{Si\text{-}\textit{i}\text{-}Pr}}$), 1.21–1.16 (m, 2H, $\mathbf{H_5}$), 0.87 (t, *J* = 6.8 Hz, 12H, $\mathbf{H_{Oct}}$) ppm.

^{13}C NMR (151 MHz, $CDCl_3$, 298 K) δ_C = 158.50, 152.46, 150.55, 149.88, 149.82, 144.11, 133.29, 132.80, 132.13, 130.89, 121.66, 119.94, 114.49, 110.61, 107.86, 101.16, 99.73, 96.50, 68.57, 31.96, 29.56, 29.39, 26.28, 22.80, 21.87, 21.19, 18.82, 18.55, 14.23, 12.51, 10.33 ppm.

UV–vis–NIR ($CDCl_3$, 298 K) λ_{max} (ε / 10^6 M^{-1} cm^{-1}): 407 (0.068), 426 (0.57), 490 (0.0018), 516 (0.0039), 555 (0.024), 592 (0.011) nm.

MALDI-ToF *m/z* 1241.641 (calculated for $[C_{76}H_{103}N_5O_4SiZn]^{\bullet+}$ = $(M)^{\bullet+}$: 1241.7065).

***ls*-P2-CPDIPS:**

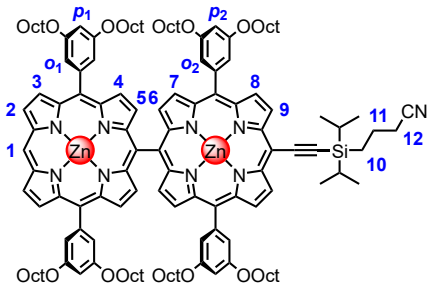

To a solution of ***ls*-P2** (60 mg, 29 μmol) in $CHCl_3$ (5.0 mL) and pyridine (50 μL) at 0 °C was added a solution of *N*-bromosuccinimide (5.1 mg, 29 μmol) in $CHCl_3$ (1.0 mL). The reaction mixture was stirred for 5 min and quenched by addition of acetone (0.1 mL). The resulting mixture was filtered through a pad of silica (CH_2Cl_2/pentane 1:1), and concentrated under reduced pressure. The crude containing ***ls*-P2**, mono-, and dibrominated ***ls*-P2**, was subjected directly to the next step. The crude mixture together with $Pd(PPh_3)_4$ (3.3 mg, 2.9 μmol) and CuI (0.6 mg, 2.9 μmol) was dissolved in dry *i*-Pr_2NH (2.5 mL) and toluene (2.5 mL), and subjected to three freeze-pump-thaw cycles. After that, CPDIPS-acetylene[344] (12 mg, 58 μmol) was added and the reaction mixture was stirred at 50 °C under argon for 2 hours. The reaction mixture was separated by column chromatography (SiO_2, gradient elution: CH_2Cl_2/pentane 1:1 to 3:1, giving the title compound (35 mg, 53%).

^{1}H NMR (600 MHz, $CDCl_3$, 298 K) δ_H = 10.38 (s, 1H, $\mathbf{H_1}$), 9.83 (d, *J* = 4.6 Hz, 2H, $\mathbf{H_9}$), 9.48 (d, *J* = 4.5 Hz, 2H, $\mathbf{H_2}$), 9.26 (d, *J* = 4.5 Hz, 2H, $\mathbf{H_3}$), 9.18 (d, *J* = 4.6 Hz, 2H, $\mathbf{H_8}$), 8.82 (d, *J* = 4.7 Hz, 2H, $\mathbf{H_4}$), 8.69 (d, *J* = 4.7 Hz, 2H, $\mathbf{H_7}$), 8.12 (d, *J* = 4.7 Hz, 2H, $\mathbf{H_5}$), 8.00 (d, *J* = 4.7 Hz, 2H, $\mathbf{H_6}$), 7.41 (d, *J* = 2.3 Hz, 4H, $\mathbf{H_{o1}}$), 7.36 (d, *J* = 2.3 Hz, 4H, $\mathbf{H_{o2}}$), 6.80 (t, *J* = 2.3 Hz, 2H, $\mathbf{H_{p1}}$), 6.78 (t, *J* = 2.3 Hz, 2H, $\mathbf{H_{p2}}$), 4.09 – 4.00 (m, 16H, $\mathbf{H_{Oct}}$), 2.64 (t, *J* = 6.9 Hz, 2H, $\mathbf{H_{12}}$), 2.34–2.26 (m, 2H, $\mathbf{H_{11}}$), 1.83–1.74 (m, 16H, $\mathbf{H_{Oct}}$), 1.55–1.38 (m, 20H, $\mathbf{H_{\textit{i}\text{-}Pr,Oct}}$), 1.33–1.15 (m, 58H, $\mathbf{H_{10,Oct}}$), 0.80 (t, *J* = 6.9 Hz, 24H, $\mathbf{H_{Oct}}$) ppm.

UV–vis–NIR ($CDCl_3$, 298 K) λ_{max} (ε / 10^6 M^{-1} cm^{-1}): 433 (0.20), 462 (0.25), 550 (0.030), 575 (0.037), 619 (0.019) nm.

MALDI-ToF *m*/*z* 2280.092 (calculated for $[C_{140}H_{185}N_9O_8SiZn_2]^{\bullet+}$ = $(M)^{\bullet+}$: 2280.270).

***lb*-P2:**

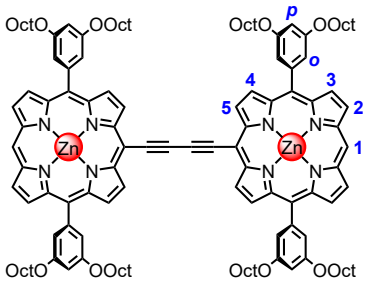

Tetrabutylammonium fluoride solution (1.0 M in THF, 0.16 mL, 0.16 mmol) was added to a solution of **P1-CPDIPS** (40 mg, 32 μmol) in CH_2Cl_2/$CHCl_3$ 1:1 (8 mL). After stirring for 2 hours, AcOH (0.2 mL) was added and the reaction mixture was filtered through a pad of silica (CH_2Cl_2/pentane 1:1). After evaporation of the solvents, the desilylated residue was dissolved in *i*-Pr_2NH (0.75 mL) and toluene (3 mL) and a catalyst mixture of CuI (3.1 mg, 16 μmol), 1,4-benzoquinone (7.0 mg, 64 μmol), and $Pd(PPh_3)_2Cl_2$ (2.3 mg, 3.2 μmol) in *i*-Pr_2NH (0.75 mL) and toluene (3 mL) was added. The reaction mixture was stirred vigorously in an open flask and after 1 hour filtered through a pad of silica (CH_2Cl_2/petroleum ether 1:1), and the solvents were evaporated under reduced pressure. Purification by recycling GPC (toluene + 1% pyridine), followed by precipitation from $CHCl_3$/CH_3OH gave the title compound (35 mg, 51%) as a green powder.

^{1}H NMR (600 MHz, $CDCl_3$, 298 K) δ_H = 10.11 (s, 2H, **H_1**), 10.02 (d, *J* = 4.5 Hz, 4H, **H_5**), 9.29 (d, *J* = 3.5 Hz, 4H, **H_2**), 9.25 (d, *J* = 4.5 Hz, 4H, **H_4**), 9.14 (d, *J* = 3.5 Hz, 4H, **H_3**), 7.45–7.41 (m, 8H, **H_o**), 6.95–6.90 (m, 4H, **H_p**), 4.16 (t, *J* = 7.0 Hz, 16H, **H_{Oct}**), 1.93–1.86 (m, 16H, **H_{Oct}**), 1.56–1.50 (m, 16H, **H_{Oct}**), 1.42–1.36 (m, 16H, **H_{Oct}**), 1.36–1.24 (m, 48H, **H_{Oct}**), 0.89–0.84 (m, 24H, **H_{Oct}**) ppm.

^{13}C NMR (151 MHz, $CDCl_3$, 298 K) δ_C = 158.55, 153.21, 150.72, 149.75, 149.73, 144.05, 133.52, 132.82, 132.14, 131.01, 122.01, 114.54, 108.19, 101.30, 99.03, 87.47, 82.27, 68.62, 31.97, 29.59, 29.41, 26.30, 14.24 ppm.

UV–vis–NIR ($CDCl_3$, 298 K) λ_{max} (ε / 10^6 M^{-1} cm^{-1}): 438 (0.269), 446 (0.316), 478 (0.245), 562 (0.039), 613 (0.041), 660 (0.065) nm.

MALDI-ToF *m*/*z* 2123.103 (calculated for $[C_{132}H_{166}N_8O_8Zn_2]^{\bullet+}$ = $(M)^{\bullet+}$: 2123.141).

***ls*[*b*$_1$]-P4:**

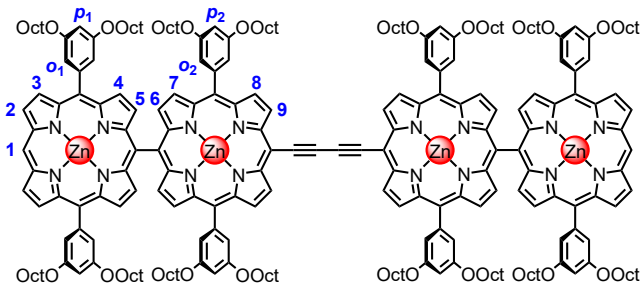

Tetrabutylammonium fluoride solution (1.0 M in THF, 0.10 mL, 0.10 mmol) was added to a solution of ***ls*-P2-CPDIPS** (25 mg, 11 μmol) in CH_2Cl_2 (1.0 mL). After stirring for 30 min, AcOH (10 μL) was added and the reaction mixture was filtered through a pad of silica (CH_2Cl_2/pentane 1:1). After evaporation of the solvents, the desilylated residue was dissolved in *i*-Pr_2NH (1.0 mL) and $CHCl_3$ (4.0 mL) and a catalyst mixture of CuI (1.0 mg, 5.5 μmol, 0.5), 1,4-benzoquinone (2.4 mg, 22 μmol), and $Pd(PPh_3)_2Cl_2$ (0.5 mg, 0.8 μmol) in *i*-Pr_2NH (1.0 mL) and $CHCl_3$ (4.0 mL) was added. The reaction mixture was stirred vigorously in an open flask and after 1 h filtered through a pad of silica (CH_2Cl_2/pentane 1:1), and the solvents were evaporated under reduced pressure. Purification by recycling GPC (toluene + 1% pyridine), followed by precipitation from $CHCl_3$/CH_3OH gave the title compound (17 mg, 76%).

^{1}H NMR (600 MHz, $CDCl_3$) δ_H = 10.40 (s, 2H, **H$_1$**), 10.18 (d, *J* = 4.6 Hz, 4H, **H$_9$**), 9.50 (d, *J* = 4.5 Hz, 4H, **H$_2$**), 9.32 (d, *J* = 4.6 Hz, 4H, **H$_8$**), 9.29 (d, *J* = 4.5 Hz, 4H, **H$_3$**), 8.88 (d, *J* = 4.6 Hz, 4H, **H$_4$**), 8.73 (d, *J* = 4.6 Hz, 4H, **H$_7$**), 8.19 (d, *J* = 4.7 Hz, 4H, **H$_5$**), 8.04 (d, *J* = 4.7 Hz, 4H, **H$_6$**), 7.49–7.40 (m, 16H, **H$_{o1,o2}$**), 6.86–6.80 (m, 8H, **H$_{p1,p2}$**), 4.14–4.04 (m, 32H, **H$_{Oct}$**), 1.88–1.78 (m, 32H, **H$_{Oct}$**), 1.49–1.42 (m, 32H, **H$_{Oct}$**), 1.36–1.19 (m, 128H, **H$_{Oct}$**), 0.87–0.78 (m, 48H, **H$_{Oct}$**) ppm.

UV–vis–NIR ($CDCl_3$) λ_{max} (ε / 10^6 M^{-1} cm^{-1}): 412 (0.27), 480 (0.20), 497 (0.27), 546 (0.067), 582 (0.054), 631 (0.048), 679 (0.069) nm.

MALDI-ToF *m*/*z* 4196.123 (calculated for $[C_{260}H_{330}N_{16}O_{16}Zn_4]^{\bullet+}$ = $(M)^{\bullet+}$: 4196.268).

B.8 Scanning Tunnelling Microscopy

STM details: All STM images were acquired with an Omicron STM-1 system operating under ultra-high vacuum (UHV) conditions with a base pressure of 2×10^{-9} mbar. Images were acquired at room temperature in constant current mode using electrochemically etched tungsten tips, coated in gold during tip optimization. All images taken at –1.8 V sample-bias, 20 pA set-point current.

Au(111) on mica surfaces (Georg Albert PVD GmbH) were prepared by cycles or Ar ion sputtering (0.76 keV for 30 min at a pressure of 8.6×10^{-6} mbar) and annealing (~500 °C, 25 min).

Electrospray deposition: *cs*[*b*$_1$]-P24 was synthesized as outlined above and deposited upon a clean Au(111) substrate via electrospray ionization. A 50 µg/mL solution of ***cs*[*b*$_1$]-P24** in toluene/methanol (3:1 ratio) was prepared and deposited with a solution flow rate of between 0.1 and 0.03 µL/hour for 45 minutes using a potential of 1.2 kV to initiate the electrospray event (base pressure during deposition was 1×10^{-7} mbar).

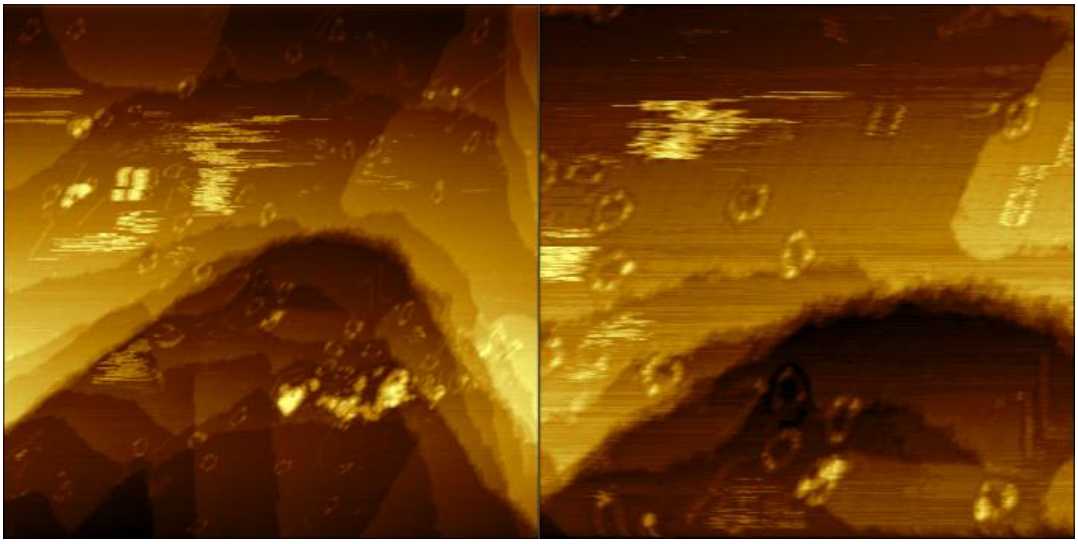

Figure B.6: Perspective images of ***cs*[*b*$_1$]-P24** deposited on to Au(111)/mica via electrospray deposition (image sizes: 200 × 200 nm and 100 × 100 nm). Images display a low coverage of ***cs*[*b*$_1$]-P24** rings, with individual species being observed on terraces and at step-edges. The 'fuzzy'/discontinuous appearance of several rings is attributed to molecular motion at a rate faster than the acquisition time for a single STM image. Data were collected and analyzed by Dr. Alex Saywell et al.

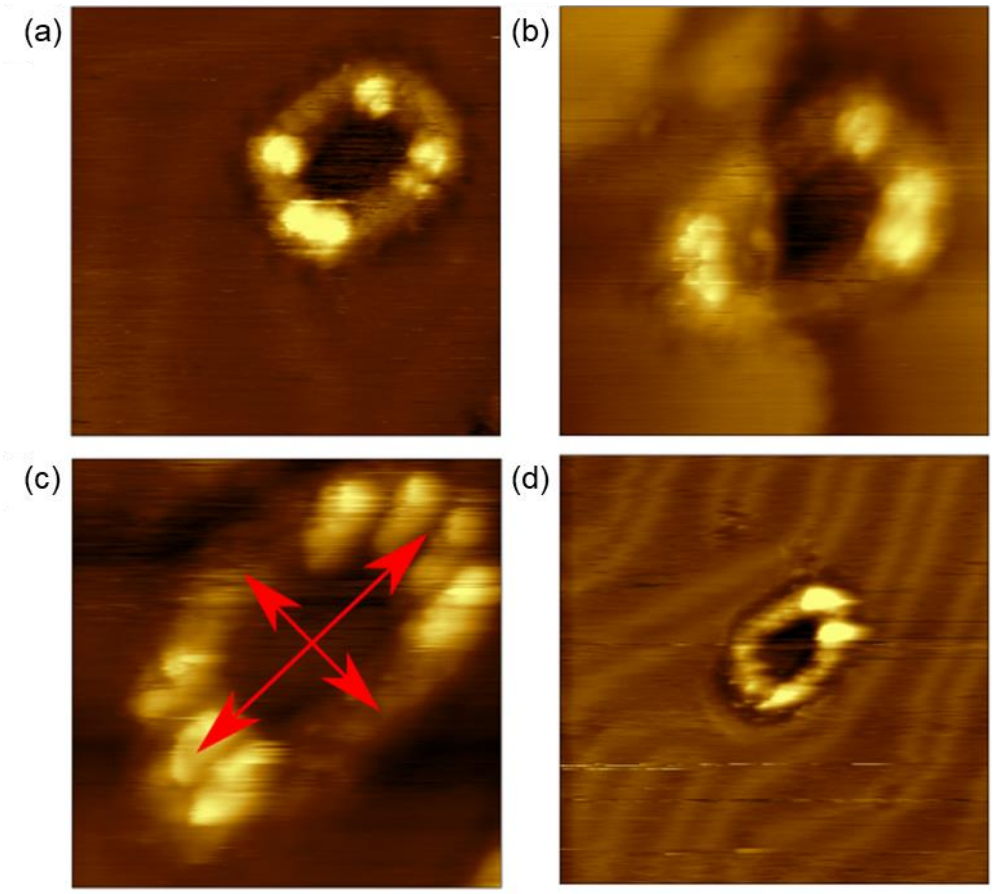

Figure B.7: Close-up STM images of individual ***cs*[*b*$_1$]-P24** rings on Au(111) [image sizes (a)–(d) : 15 × 15 nm, 12.2 × 12.2 nm, 9.6 × 9.6 nm, 28.9 × 28.9 nm]. The 'bright' features observed around the rings are attributed to the non-planar orientation of several porphyrin sub-units. Measurements of the ring dimensions were acquired from this type of image (measurement positions indicated by red arrows). The measured dimensions were obtained from line profiles taken across the 'long' and 'short' axis of the ring with the center of the peaks (corresponding to the mid-point within the annulus described by the cyclic molecule) used to define the dimensions. Data were collected and analyzed by Dr. Alex Saywell et al.

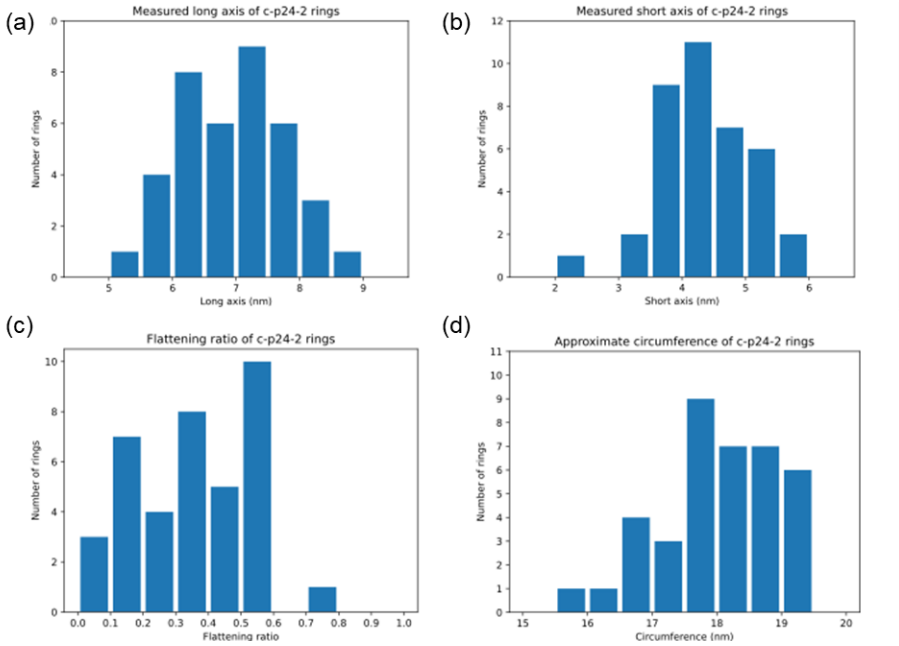

Figure B.8: (a) and (b) Histograms of the long (*a*) and short (*b*) axis distances, as well as, (c), the flattening factor (f = 1–b/a), for 38 individual ***cs*[*b*$_1$]-P24** rings. Average lengths are taken from the forward and backward scans to compensate for thermal drift and piezoelectric creep: STM dimensions are calibrated using the known dimensions of substrate features. The wide range of values for the flattening ratio indicates that the nanorings exhibit a high degree of flexibility. The average values (and standard deviation, SD) obtain from the data sets are: a = 6.9 nm (SD = 0.9 nm), b = 4.4 nm (SD = 0.7 nm), f = 0.4 (SD = 0.2). (d) Histogram showing calculated circumference values for 40 ***c*-P24b** rings. The circumference length is estimated from the Ramanujan approximation $c \approx \pi \left[3\left(\frac{a}{2}+\frac{b}{2}\right) - \sqrt{\left(3\frac{a}{2}+\frac{b}{2}\right)\left(3\frac{b}{2}+\frac{a}{2}\right)}\right]$. Data were collected and analyzed by Dr. Alex Saywell et al.

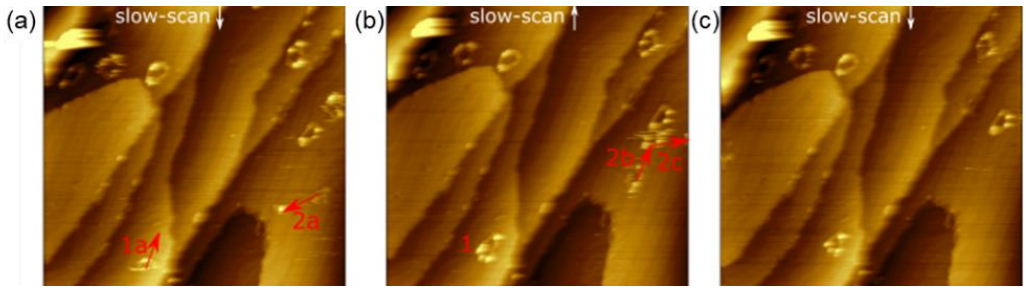

Figure B.9: A sequence of three consecutive STM images showing the diffusion of ***cs*[*b*$_1$]-P24** nanorings on Au(111). The acquisition time for each image is 750 s (image size 100 × 100 nm). The motion of two nanorings is identified (labeled 1 and 2); with molecule-1 moving a short distance (1a) and molecule-2 observed to move through several points (2a–c) during the first two images and is seen to have moved outside of the scan-range in the final image. Mobility is likely due to interaction with the STM tip and linked to the non-planar conformation of ***cs*[*b*$_1$]-P24**. Data were collected and analyzed by Dr. Alex Saywell et al.

B.9 UV–vis–NIR Titrations

B.9.1 Formation Titrations

Reference titrations with porphyrin monomer (P1) and 4-ethyl Pyridine (EtPy)

The binding curves were fitted with eqn. 2.5 to give formation constant K_f = (1.19 ± 0.09) × 10^4 M^{-1}.

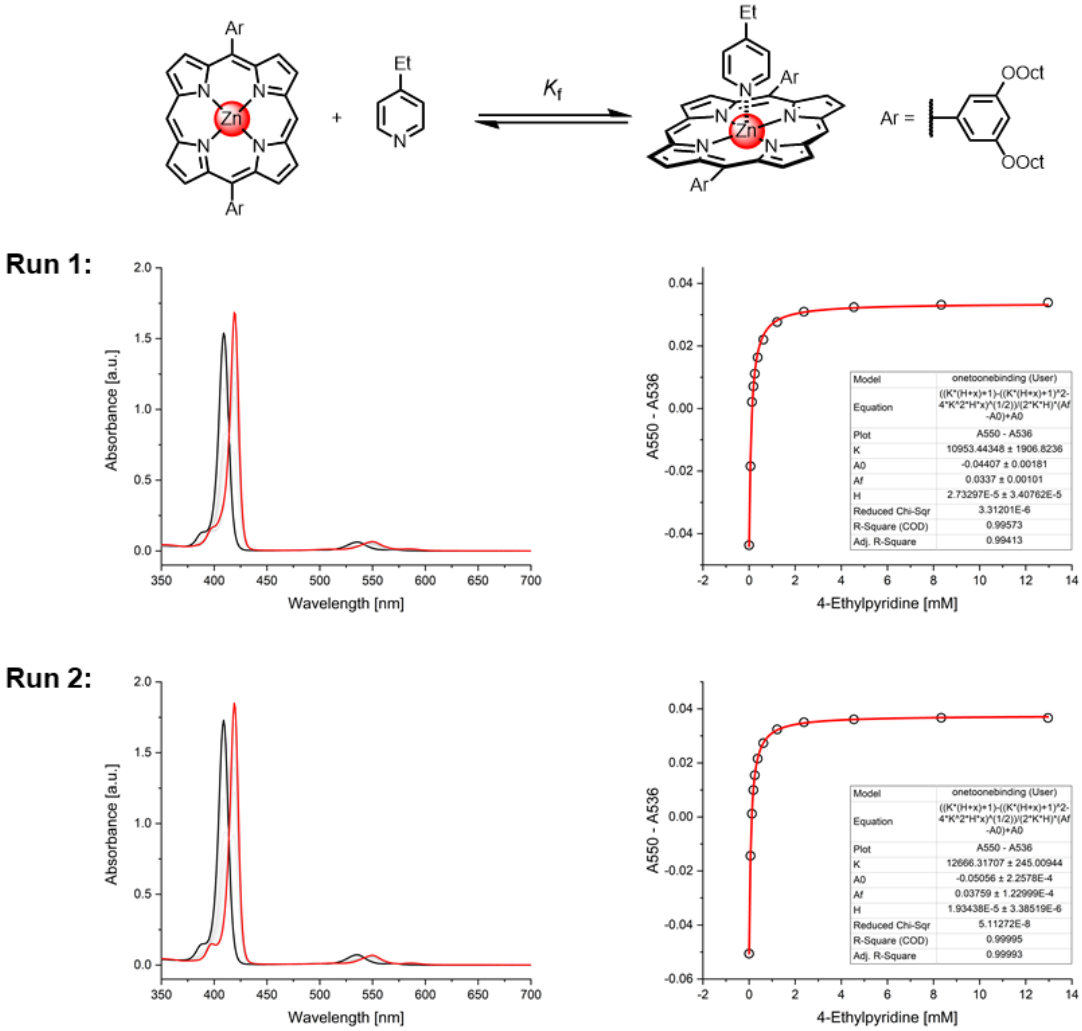

Figure B.10: UV–vis titration of **P1** with **EtPy**. Run 1: K_f = 1.10 × 10^4 M^{-1}, R^2 = 0.99413; Run 2: K_f = 1.27 × 10^4 M^{-1}, R^2 = 0.99993 ($CDCl_3$, 298 K, [**P1**] = 3.00 × 10^{-6} M).

Reference titrations with porphyrin monomer (P1) and Quinuclidine (Q)

The binding curves were fitted with eqn. 2.5 to give formation constant K_Q = (3.89 ± 0.27) × 10^5 M^{-1}.

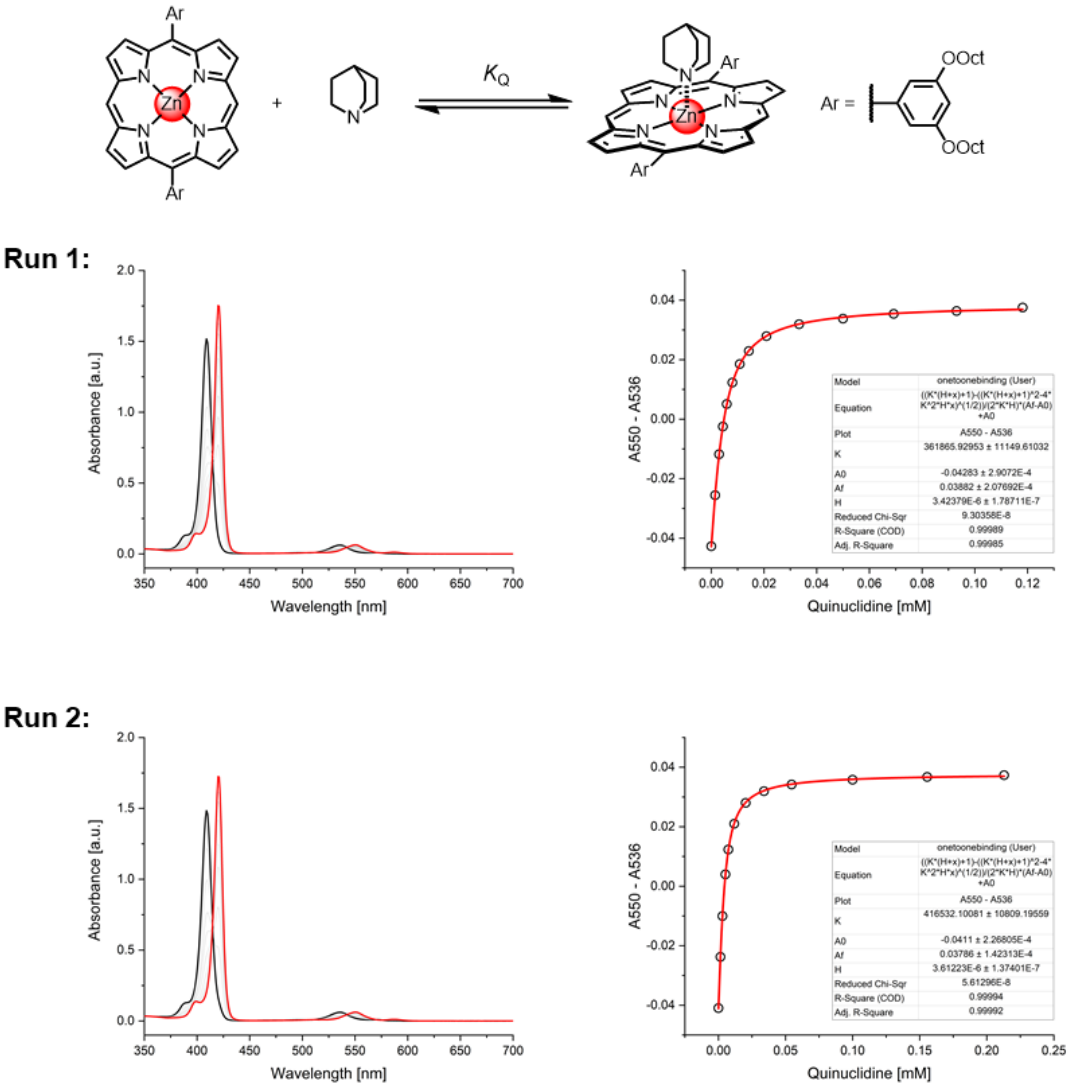

Figure B.11: UV–vis titration of **P1** with **Q**. Run 1: K_f = 3.62 × 10^5 M^{-1}, R^2 = 0.99985; Run 2: K_f = 4.16 × 10^5 M^{-1}, R^2 = 0.99992 ($CDCl_3$, 298 K, [**P1**] = 3.00 × 10^{-6} M).

B.9.2 Denaturation Titrations

Determination of formation constants from denaturation titrations

The formation constant of the porphyrin nanoring ***cs*[*b*$_1$]-P24** with template **T12e** was determined by fluorescence denaturation titrations with a large excess of the competing ligand quinuclidine (**Q**). The fluorescence of template **T12e** is quenched when bound to the porphyrin nanoring ***cs*[*b*$_1$]-P24**. Turn-on fluorescence response is measured when the bound template **T12e** is knocked out from the complex by the competing ligand. Followed by determination the denaturation constant (K_{dn}), the formation constant (K_f) can be calculated using the following equation:

$$K_f = \frac{{K_Q}^N}{K_{dn}} \tag{B.1}$$

where N is the number of quinuclidine binding sites involved (N = 24), and K_Q is the formation constant of the porphyrin monomer and quinuclidine, which is determined by direct formation reference titration.

Analysis of the 1:2 binding of porphyrin nanoring *cs*[*b*$_1$]-P24 to template T12e using a two-step model

Assuming there are two equilibria in the denaturation process as shown below, the denaturation constants $K_{dn,1}$ and $K_{dn,2}$ can be expressed using eqn. B.4 and B.5, where [***cs*[*b*$_1$]-P24·(T12e)$_2$**], [***cs*[*b*$_1$]-P24·T12e·Q$_{12}$**], [***cs*[*b*$_1$]-P24·Q$_{24}$**], [**T12e**] and [**Q**] are the concentrations of the species present during the denaturation.

$$\textit{cs}[b_1]\text{-P24}\cdot(\text{T12e})_2 + 12\text{Q} \rightleftharpoons \textit{cs}[b_1]\text{-P24}\cdot\text{T12e}\cdot\text{Q}_{12} + \text{T12e} \tag{B.2}$$

$$\textit{cs}[b_1]\text{-P24}\cdot\text{T12e}\cdot\text{Q}_{12} + 12\text{Q} \rightleftharpoons \textit{cs}[b_1]\text{-P24}\cdot\text{Q}_{24} + 2\text{T12e} \tag{B.3}$$

$$K_{dn,2} = \frac{[\textit{cs}[b_1]\text{-P24}\cdot\text{T12e}\cdot\text{Q}_{12}][\text{T12e}]}{[\textit{cs}[b_1]\text{-P24}\cdot(\text{T12e})_2][\text{Q}]^{12}} \tag{B.4}$$

$$K_{dn,1} = \frac{[\textit{cs}[b_1]\text{-P24}\cdot\text{Q}_{24}][\text{T12e}]}{[\textit{cs}[b_1]\text{-P24}\cdot\text{T12e}\cdot\text{Q}_{12}][\text{Q}]^{12}} \tag{B.5}$$

The [***cs*[*b*$_1$]-P24·(T12e)$_2$**] can be expressed using the [***cs*[*b*$_1$]-P24·(T12e)$_2$**]$_0$ (initial concentration of complex ***cs*[*b*$_1$]-P24·(T12e)$_2$**), [***cs*[*b*$_1$]-P24·T12e·Q$_{12}$**] and [***cs*[*b*$_1$]-P24·Q$_{24}$**] as eqn. B.6. The template concentration [**T12e**] is correlated to [***cs*[*b*$_1$]-P24·T12e·Q$_{12}$**] and [***cs*[*b*$_1$]-P24·Q$_{24}$**] as eqn. B.7. As the concentration of the free quinuclidine [**Q**] present in the denaturation is much larger than that of the bound quinuclidine, we assume it can be substituted with the [**Q**]$_0$ (concentration of quinuclidine added; eqn. B.8).

$$[\textit{cs}[\textit{b}_1]\text{-P24}\cdot(\text{T12e})_2] = [\textit{cs}[\textit{b}_1]\text{-P24}\cdot(\text{T12e})_2]_0 - [\textit{cs}[\textit{b}_1]\text{-P24}\cdot\text{T12e}\cdot\text{Q}_{12}] - [\textit{cs}[\textit{b}_1]\text{-P24}\cdot\text{Q}_{24}] \quad \text{(B.6)}$$

$$[\mathbf{T12e}] = [\textit{cs}[\textit{b}_1]\text{-P24}\cdot\text{T12e}\cdot\text{Q}_{12}] + 2[\textit{cs}[\textit{b}_1]\text{-P24}\cdot\text{Q}_{24}] \quad \text{(B.7)}$$

$$[\mathbf{Q}] \approx [\mathbf{Q}]_0 \quad \text{(B.8)}$$

Inserting the eqn. B.6– B.8 to the eqn. B.4– B.5 to eliminate the [***cs*[*b*$_1$]-P24·T12e·Q$_{12}$**] and [***cs*[*b*$_1$]-P24·Q$_{24}$**] gives a cubic equation of [**T12e**] as eqn. B.9.

$$[\mathbf{T12e}]^3 + K_{\mathrm{dn},2}[\mathbf{Q}]_0{}^{12}[\mathbf{T12e}]^2 + \left(K_{\mathrm{dn},2}K_{\mathrm{dn},1}[\mathbf{Q}]_0{}^{24} - K_{\mathrm{dn},2}[\textit{cs}[\textit{b}_1]\text{-P24}\cdot(\text{T12e})_2]_0[\mathbf{Q}]_0{}^{12}\right)\cdot [\mathbf{T12e}] - 2K_{\mathrm{dn},2}K_{\mathrm{dn},1}[\textit{cs}[\textit{b}_1]\text{-P24}\cdot(\text{T12e})_2]_0[\mathbf{Q}]_0{}^{24} = 0 \quad \text{(B.9)}$$

The change in fluorescence at 472 nm during denaturation is directly proportional to [**T12e**] as can be expressed by eqn. B.10 and B.11. Inserting the root of [**T12e**] to the following eqn. B.11 gives the relationship between the observed fluorescence intensity (*F*) and the [**Q**]$_0$ (concentration of quinuclidine added).

$$\frac{F-F_0}{F_\mathrm{f}-F_0} = \frac{[\mathbf{T12e}]}{[\mathbf{T12e}]_\mathrm{f}} = \frac{[\mathbf{T12e}]}{2[\textit{cs}[\textit{b}_1]\text{-P24}\cdot(\text{T12e})_2]_0} \quad \text{(B.10)}$$

$$F = \frac{[\mathbf{T12e}]}{2[\textit{cs}[\textit{b}_1]\text{-P24}\cdot(\text{T12e})_2]_0} \times (F_\mathrm{f} - F_0) + F_0 \quad \text{(B.11)}$$

B.9.3 Summary of formation and denaturation of *cs*[*b*$_1$]-P24·(T12e)$_2$

Table B.1: Summary of denaturation constants (K_{dn}), formation constants (K_f) and Hill constants (n_H) for ***c*-P24b·(T12)$_2$** from two-step model.

	log $K_{dn,1}$	log $K_{dn,2}$	log $K_{f,1}$	log $K_{f,2}$	n_H (exp)	n_H (calc)
Run 1	25.88	26.70	41.19 ± 0.36[b]	40.37 ± 0.36[b]	5.9	7.6
Run 2	25.86	26.83	41.21 ± 0.36[b]	40.23 ± 0.36[b]	5.4	7.1
Average	25.87 ± 0.09[a]	26.77 ± 0.09[a]	41.20 ± 0.37[b]	40.30 ± 0.37[b]	5.7	7.4

[a] 20% standard deviation errors were estimated for the denaturation titrations and data analysis. [b] Errors were determined by propagating the errors from the K_Q values used and the estimated errors of K_{dn}.

Table B.2: Summary of denaturation constants (K_{dn}), formation constants (K_f) and Hill constants (n_H) for ***cs*[*b*$_1$]-P24·(T12e)$_2$** from one-step (all-or-nothing) model.

	log K_{dn}	log K_f	n_H (exp)	n_H (calc)
Run 1	52.31	81.85 ± 0.73[b]	5.9	11.6
Run 2	52.87	81.29 ± 0.73[b]	5.4	11.7
average	52.59 ± 0.09[a]	81.57 ± 0.73[b]	5.7	11.7

[a] 20% standard deviation errors were estimated for the denaturation titrations and data analysis. [b] Errors were determined by propagating the errors from the K_Q values used and the estimated errors of K_{dn}.

B.9.4 Calculation of statistical factors

To understand the stability constants of different complexes, it is useful to factor out statistical contributions. A measured (or apparent) equilibrium constant K_{eq} (or K_{app}) can be factorized into its statistical component K_σ and its statistically corrected value K_{chem} according to the following equation:

$$wA + xB \rightleftharpoons yC + zD \tag{B.12}$$

$$K_{app} = \frac{{Q_C}^y {Q_D}^z}{{Q_A}^w {Q_B}^x} = \left(\frac{{\sigma_A}^w {\sigma_B}^x}{{\sigma_C}^y {\sigma_D}^z}\right)\left(\frac{{Q'_C}^y {Q'_D}^z}{{Q'_A}^w {Q'_B}^x}\right) = K_\sigma K_{\mathrm{chem}} \tag{B.13}$$

where for each species i, Q_i is the partition coefficient, Q'_i is the statistically corrected partition coefficient, and σ_i is the symmetry number.[368–370]

Values of K_σ were calculated using Benson's symmetry number method.[368] The symmetry number (σ) of each species is the product of its external symmetry number, σ_{ext}, (calculated from the point group of the molecule) and its internal symmetry number, σ_{int}, (calculated from the number of degenerate internal rotors). The external symmetry number is defined as the number of different but indistinguishable atomic arrangements that can be obtained by rotating a given molecule as a whole as a rigid object. The internal symmetry number is defined as the number of different but indistinguishable atomic arrangements that can be obtained by internal rotations around single bonds.

The intermediates and isomers in formation of the ***cs*[b_1]-P24·(T12e)$_2$** complex is illustrated in Figure B.12. There are several paths in forming the 1:2 complex, involving three isomers of ***cs*[b_1]-P24·T12e** (namely species ***b***–***d***) and two isomers of ***cs*[b_1]-P24·(T12e)$_2$** (namely species ***e*** and ***f***). The values of σ for all the species involved are shown in Table B.3.

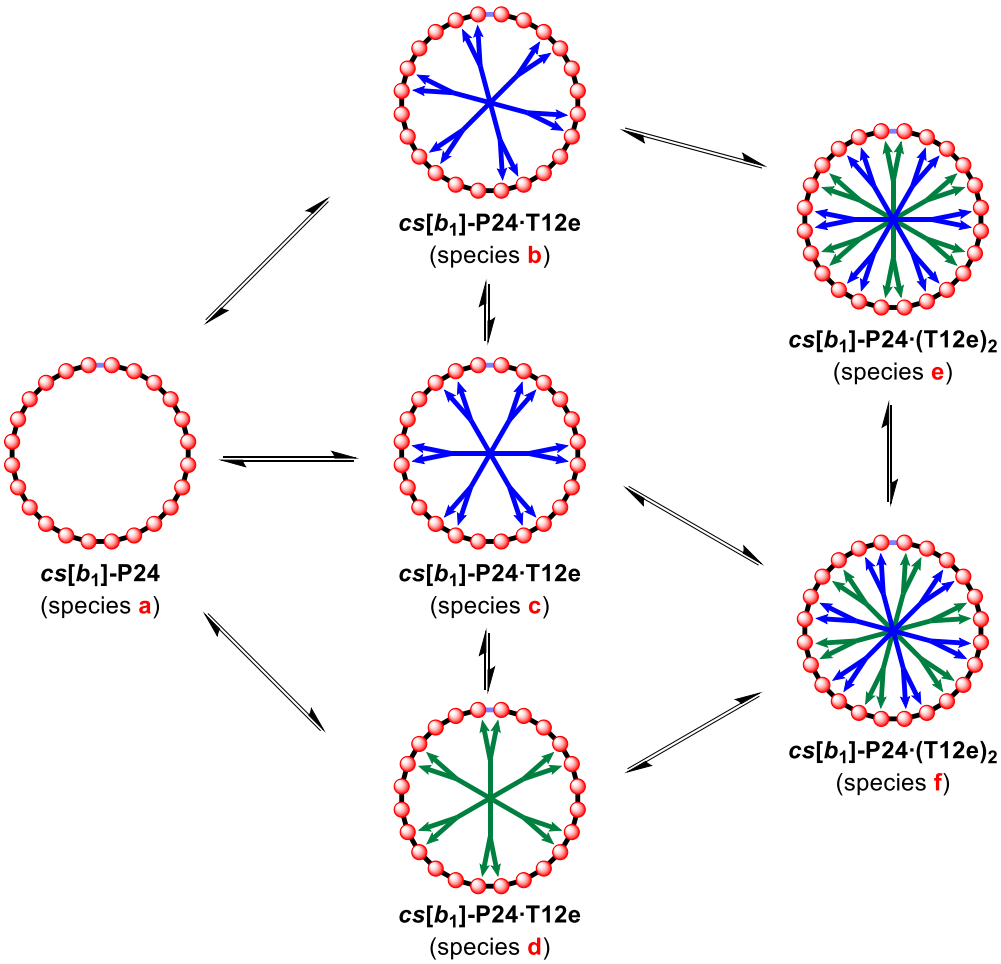

Figures B.12: Schematic diagram showing three possible paths: A (orange), B (light blue) and C (hot pink) in formation of the 1:2 complex ***cs*[b_1]-P24·(T12e)$_2$**.

Table B.3: Internal, external and total symmetry numbers for each component.[a]

Species *i*	Compound	Point group	σ_{ext}	σ_{int}	σ_i	σ_{app}
a	***cs*[b_1]-P24**	C_2	2	2	4	—
b	***cs*[b_1]-P24·T12e**	C_1	1	1	1	$\frac{1}{2}$
c	***cs*[b_1]-P24·T12e**	C_2	2	1	2	
d	***cs*[b_1]-P24·T12e**	C_2	2	1	2	
e	***cs*[b_1]-P24·(T12e)$_2$**	C_2	2	1	2	$\frac{2}{3}$
f	***cs*[b_1]-P24·(T12e)$_2$**	C_1	1	1	1	
T	**T12e**	D_{6h}	12	2^6	768	—

[a] Note that when counting internal rotations and calculating σ_{int}, we do not include rotors that are unaffected by the binding process, such as the *para*-phenylene links in **T12e**, because if a rotor is unaffected by the binding process, it has no influence on K_σ.

For reactions involving a mixture of different isomers *i* (e.g., three isomers for ***cs*[b_1]-P24·T12e**), an apparent symmetry number must be determined using the symmetry numbers of the individual isomers:[370]

$$\sigma_{app} = \frac{1}{\sum \frac{1}{\sigma_i}} \tag{B.14}$$

As shown in Figure B.12, the formation of ***cs*[b_1]-P24·(T12e)$_2$** is described by a two-step process:

$$K_\mathrm{f} = K_{\mathrm{f},1}K_{\mathrm{f},2} = \left(K_{\sigma,1}K_{\mathrm{chem},1}\right)\left(K_{\sigma,2}K_{\mathrm{chem},2}\right) = \left(K_{\sigma,1}K_{\sigma,2}\right)\left(K_{\mathrm{chem},1}K_{\mathrm{chem},2}\right) = K_\sigma K_\mathrm{chem} \tag{B.15}$$

in which K_f, $K_{\mathrm{f},1}$ and $K_{\mathrm{f},2}$ are measured (apparent) association constants; K_chem, $K_{\mathrm{chem},1}$ and $K_{\mathrm{chem},2}$ are statistically corrected association constants; K_σ, $K_{\sigma,1}$ and $K_{\sigma,2}$ are apparent statistical factors, which are calculated by the following equations:

$$K_{\sigma,1} = K_{\sigma,\mathrm{a}} + K_{\sigma,\mathrm{b}} + K_{\sigma,\mathrm{c}} = \frac{\sigma_a\sigma_\mathrm{T}}{\sigma_b} + \frac{\sigma_a\sigma_\mathrm{T}}{\sigma_c} + \frac{\sigma_a\sigma_\mathrm{T}}{\sigma_d} = \sigma_a\sigma_\mathrm{T}\left(\frac{1}{\sigma_b} + \frac{1}{\sigma_c} + \frac{1}{\sigma_d}\right) = \frac{\sigma_a\sigma_\mathrm{T}}{\sigma_{app,1}} \tag{B.16}$$

$$\sigma_{app}K_\sigma = K_{\sigma,\mathrm{e}} + K_{\sigma,\mathrm{f}} = \frac{\sigma_a{\sigma_\mathrm{T}}^2}{\sigma_e} + \frac{\sigma_a{\sigma_\mathrm{T}}^2}{\sigma_f} = \sigma_a{\sigma_\mathrm{T}}^2\left(\frac{1}{\sigma_e} + \frac{1}{\sigma_f}\right) = \frac{\sigma_a{\sigma_\mathrm{T}}^2}{\sigma_{app,2}} \tag{B.17}$$

$$K_{\sigma,2} = \frac{K_\sigma}{K_{\sigma,1}} \tag{B.18}$$

The cooperativity factor α for the system is estimated:

$$\alpha = \frac{K_{\mathrm{chem},2}}{K_{\mathrm{chem},1}} = \frac{K_{\sigma,1}}{K_{\sigma,2}}\frac{K_{\mathrm{f},2}}{K_{\mathrm{f},1}} = \frac{{K_{\sigma,1}}^2}{K_\sigma}\frac{K_{\mathrm{f},2}}{K_{\mathrm{f},1}} = \frac{\sigma_a\sigma_{app,2}}{{\sigma_{app,1}}^2}\frac{K_{\mathrm{f},2}}{K_{\mathrm{f},1}} = 10.67 \cdot 0.126 \approx 1.3$$

B.10 Steady-State Absorption and Fluorescence Spectroscopy

Fluorescence quantum yields were determined by the relative method,[351] using tetraphenylporphyrin (**H_2TPP**) (Φ_F = 0.070, toluene, non-deaerated) as reference dye,[352] using the formula:

$$\Phi_s = \Phi_r \cdot \frac{F_s}{F_r} \cdot \frac{[1-10^{-A(\lambda_{Ex})}]_r}{[1-10^{-A(\lambda_{Ex})}]_s} \cdot \frac{n_s^2}{n_r^2} \quad \text{(B.19)}$$

in which sample (*s*) and reference (*r*) are designated by subscripts, Φ is the quantum yield, *F* is the integral photon flux, $1–10^{-A(\lambda Ex)}$ is the absorption factor at the wavelength of excitation, and *n* is the refractive index of the solvent.

Table B.4: Summary of photophysical parameters. Measurements of ***l*-P2b**, ***l*-P4b**, ***l*-P24**, and ***c*-P24b** were performed in toluene + 1% pyridine, while those on ***cs*[b_1]-P24·(T12e)$_2$** and **T12e** were performed in neat toluene, all at 25 °C.

Compound	$\lambda_{abs,max}$ / nm	ε_{max} / 10^6 M^{-1} cm^{-1}	$\lambda_{Em,max}$ / nm	Φ_F[a]	τ_F[b]/ ns
***ls*-P2**	425, 453, 485, 570, 634, 693	0.17, 0.33, 0.27, 0.026, 0.047, 0.074	699	0.12	1.02
***ls*[b_1]-P4**	420, 485, 506, 561, 655, 715	0.36, 0.27, 0.40, 0.085, 0.072, 0.11	723	0.11	0.99
***ls*-P24**	419, 516, 594, 635	2.13, 2.36, 1.60, 0.30	651	0.085	1.32
***cs*[b_1]-P24**	419, 514, 593, 635, 717	1.74, 2.24, 1.19, 0.26, 0.12	729	0.050	0.91
***cs*[b_1]-P24·(T12e)$_2$**	320, 420, 512, 593, 628, 651, 723	1.20, 2.15, 2.21, 1.16, 0.23, 0.17, 0.073	679, 727	0.086	0.84
T12e	317, 386	0.33, 0.31	470	0.26[c]	-

[a] Fluorescence quantum yields are determined using **H_2TPP** as reference dye.[352] [b] These fluorescence lifetimes were measured using the Edinburgh Instruments FS5 spectrofluorometer in time-correlated single photon counting (TCSPC) mode using a picosecond pulsed diode laser (EPL-475) as the excitation source; excitation wavelength: 473 nm. Exponential reconvolution fits incorporating the measured instrument response function were used to extract fluorescence lifetimes. [c] The fluorescence quantum yield of **T12e** was measured using an integrating sphere.

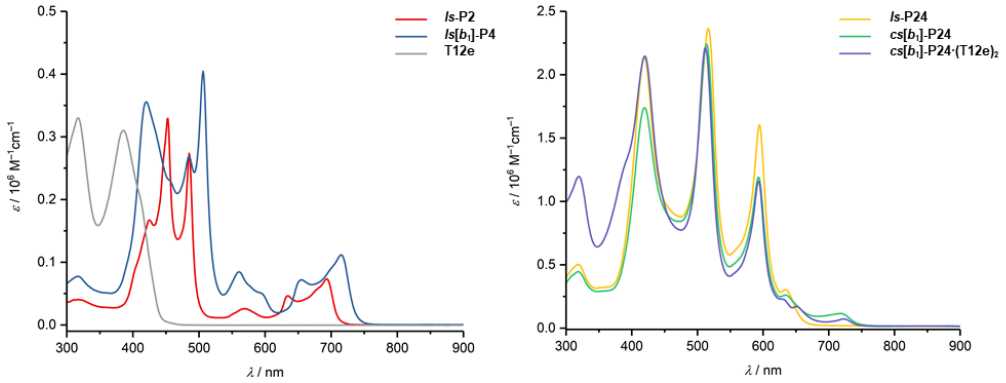

Figure B.13. Absorption spectra (ε vs. λ) of ***lb*-P2**, ***ls*[b_1]-P4**, and **T12e** (left) and of ***ls*-P24**, ***cs*[b_1]-P24b**, and ***cs*[b_1]-P24b·(T12e)$_2$** (right). Spectra of ***lb*-P2**, ***ls*[b_1]-P4**, ***ls*-P24**, and ***cs*[b_1]-P24b** were recorded in toluene + 1% pyridine, while the spectra of ***cs*[b_1]-P24b·(T12e)$_2$** and **T12e** were recorded in neat toluene.

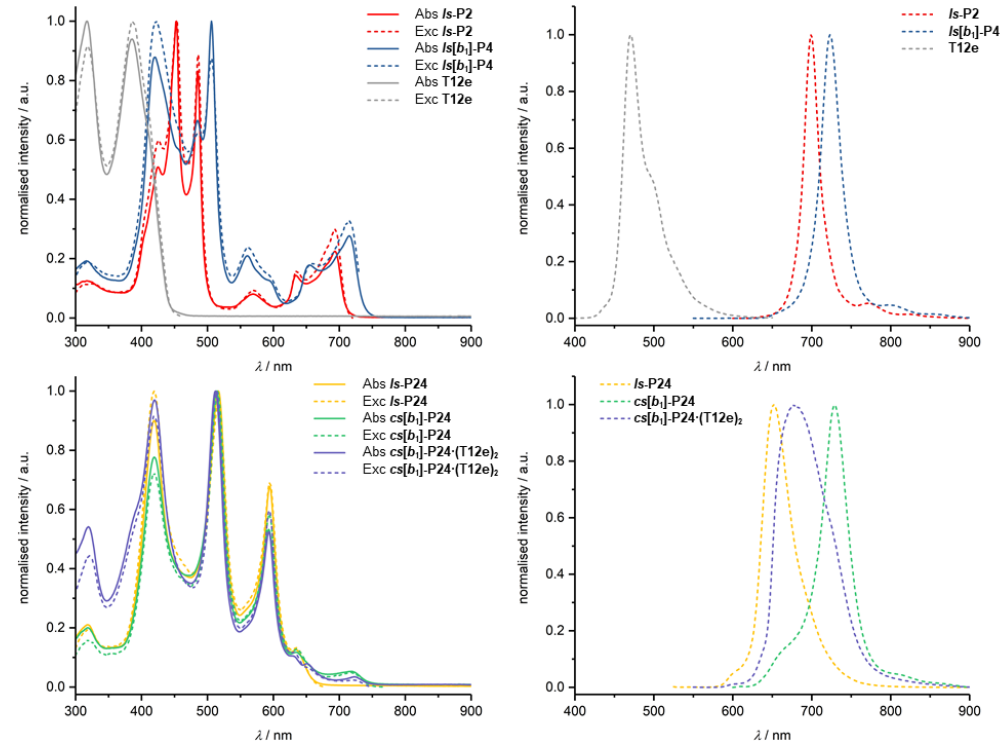

Figure B.14: Left: Normalized absorption (full lines) and excitation (dashed lines) spectra of ***lb*-P2**, ***ls*[b_1]-P4**, and **T12e** (top) and of ***ls*-P24**, ***cs*[b_1]-P24**, and ***cs*[b_1]-P24·(T12e)$_2$** (bottom). Right: Normalized emission spectra of ***lb*-P2**, ***ls*[b_1]-P4**, and **T12e** (top) and of ***ls*-P24**, ***cs*[b_1]-P24**, and ***cs*[b_1]-P24·(T12e)$_2$** (bottom). Fluorescence spectra were recorded with excitation at the following wavelengths: ***lb*-P2**: 485 nm, ***ls*[b_1]-P4**: 505 nm, **T12e**: 385 nm, ***ls*-P24**: 515 nm, ***cs*[b_1]-P24**: 515 nm, and ***cs*[b_1]-P24·(T12e)$_2$**: 510 nm. Spectra of ***lb*-P2**, ***ls*[b_1]-P4**, ***ls*-P24**, and ***cs*[b_1]-P24** were recorded in toluene + 1% pyridine, while the spectra of ***cs*[b_1]-P24·(T12e)$_2$** and **T12e** were recorded in neat toluene.

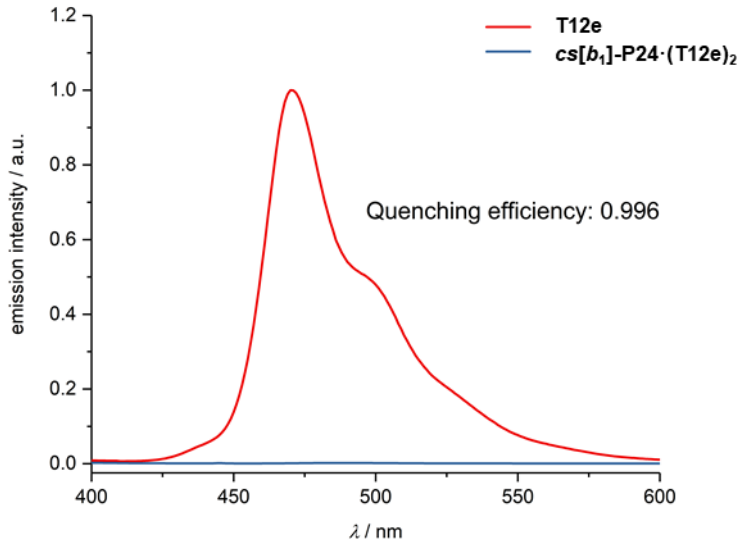

Figure B.15: Estimation of template fluorescence quenching efficiency in ***cs*[*b*$_1$]-P24·(T12e)$_2$**. Emission spectra of **T12e** (red line, c = 1.6 × 10^{-7} M) and ***cs*[*b*$_1$]-P24·(T12e)$_2$** (blue line, c = 0.8 × 10^{-8} M) were measured at identical template concentrations ([**T12**] = 1.6 × 10^{-7} M) and by excitation at λ_{Ex} = 318 nm in both cases. The quenching efficiency, E, was calculated from the integrated emission spectra (400–600 nm), according to: $E = 1 - (I_{Em,complex}/I_{em,T12})$, where $I_{Em,complex}$ and $I_{Em,T12}$ denote the integrated emission from the template in the ***cs*[*b*$_1$]-P24·(T12e)$_2$** complex and in the **T12e** template, respectively. Spectra were measured in toluene at 25 °C.

B.11 Time-Resolved Fluorescence Spectroscopy

Ultrafast time-resolved measurements were conducted using the photoluminescence upconversion (PL UC) technique. Samples were excited with a 410 nm pulse, generated by frequency doubling of a Ti:sapphire oscillator 820 nm output (Spectra Physics Mai-Tai, 100 fs, 80 MHz). The side-excitation configuration was adopted to avoid possible artefacts caused by self-absorption. In this configuration, the excitation beam entered the cuvette close to its front surface and PL was collected in the perpendicular direction with respect to the excitation beam by a pair of off-axis parabolic mirrors. The PL signal was then focused onto a beta-barium borate (BBO) crystal, mounted on a rotation stage to allow tuning of the phase-matching angle, and optically gated by a vertically polarized gate beam (820 nm) arriving at the BBO crystal at controllable time delays. The resulting PL UC signal generated by sum-frequency generation was then spectrally dispersed by a monochromator (Triax 190, Jobin-Yvon) and detected by a nitrogen-cooled CCD. A Schott filter UG11 was used to filter scattering from excitation and gate beams. The resulting time resolution was around 350 fs. Time-resolved spectra were corrected for instrument response by using a filament lamp of known emissivity.

Time-integrated photoluminescence (TI PL) was measured by using the same spectrometer and CCD detector, while removing the BBO crystal and UG11 filter.

Time-resolved PL dynamics at longer delay times (>1 ns) were measured by using time-correlated single-photon counting (TCSPC) technique. Here, emission was detected with a silicon single-photon avalanche diode and electrically gated using a Becker & Hickl module. The resulting temporal resolution was around 40 ps.

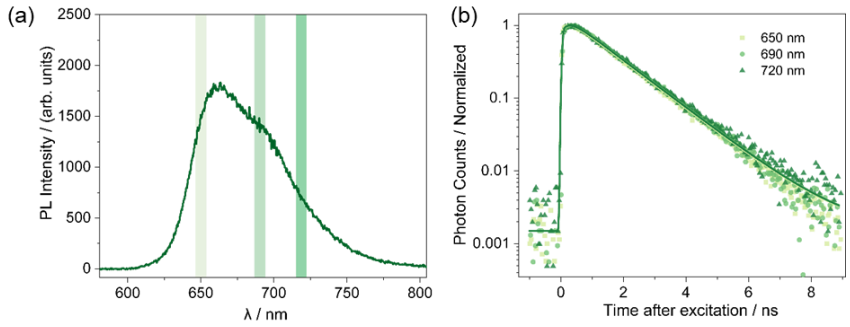

Figure B.16: Time-integrated spectrum and time-resolved photoluminescence dynamics for ***ls*-P24** at long (> 1 ns) time delays. Time-integrated spectrum (a) and time-resolved photoluminescence (b) dynamics for ***ls*-P24** under 410 nm excitation at a fluence of 400 nJ cm^{-2}. Solid lines represent multi-exponential fitting convoluted with a Gaussian response function. TCSPC reveals an emission wavelength-independent lifetime dominated by a $\tau = 1.30 \pm 0.05$ ns decay component. The fitted instrument response function (IRF) is ~0.04 ns, and an initial slower rise of 0.2 ns is observed, related to the system response. Data were collected and analyzed by Dr. Marcello Righetto and Prof. Laura M. Herz.

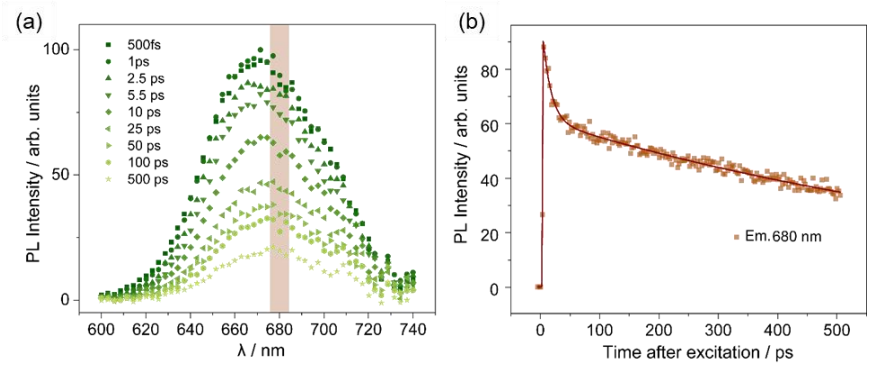

Figure B.17: (a) Time-resolved photoluminescence spectra for ***ls*-P24** following 410 nm pulsed excitation at a fluence of 2.5 µJ cm^{-2}. Different symbols represent spectra taken at different times after the excitation, in the range 500 fs (dark green squares) to 500 ps (light green stars). (b) Photoluminescence intensity dynamics for ***ls*-P24**, measured at an emission wavelength of 680 nm under the same excitation conditions. Corresponding measured wavelength is indicated as a shaded area in the full spectra in part (a). Fitting results are consistent with the observation of a 1.3 ns lifetime and also reveal the presence of a 14 ps lifetime component, not detectable with TCSPC. This fast process has been observed previously in similar molecules and is attributed to excited state energy migration from nonorthogonal S_1 state conformers to a perfectly orthogonally arranged emitting state of the porphyrin arrays.[165] Data were collected and analyzed by Dr. Marcello Righetto and Prof. Laura M. Herz.

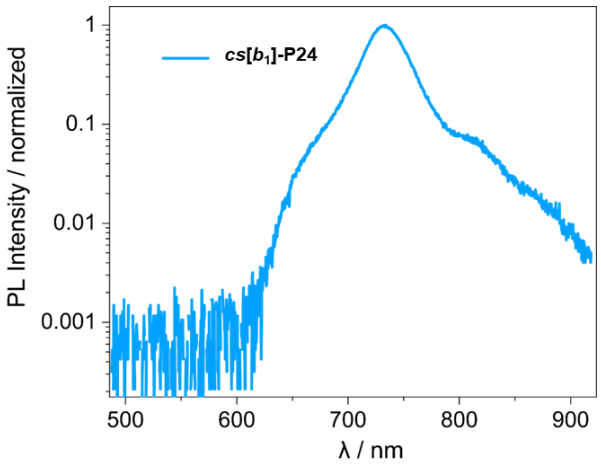

Figure B.18: Time-integrated photoluminescence spectrum for ***cs*[*b*$_1$]-P24**. Logarithmic scale plot of steady-state PL spectrum for ***cs*[*b*$_1$]-P24** under 410 nm excitation at 400 nJ cm^{-2}. A side-band between 670 and 690 nm can be observed. Such signal is related to the emission originating from the *meso–meso* linked porphyrins as measured in time-resolved spectra. Data were collected and analyzed by Dr. Marcello Righetto and Prof. Laura M. Herz.

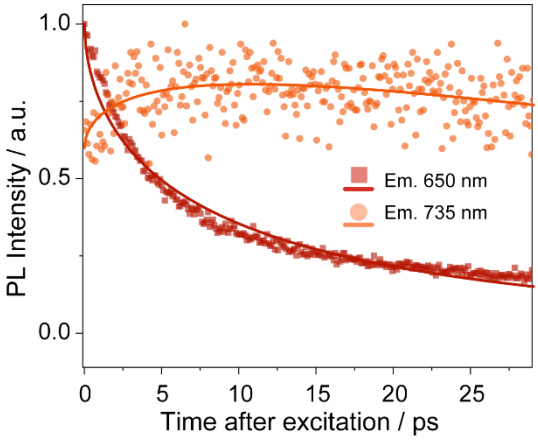

Figure B.19: Time-resolved photoluminescence dynamics for ***cs*[*b*$_1$]-P24** – additional acceptor wavelength. Comparison between normalized photoluminescence intensity dynamics for ***cs*[*b*$_1$]-P24**, measured at an emission wavelength of 650 nm (red squares) and 735 nm (orange circles) following pulsed 410 nm wavelength excitation at a fluence of 2.5 µJ cm^{-2}). Solid lines represent fits to the model described in the supplementary note on energy transfer dynamics (below). Here, the numerical solution to eqn. B.20 is fitted to the PL decays detected at 650, 735 nm. Data were collected and analyzed by Dr. Marcello Righetto and Prof. Laura M. Herz.

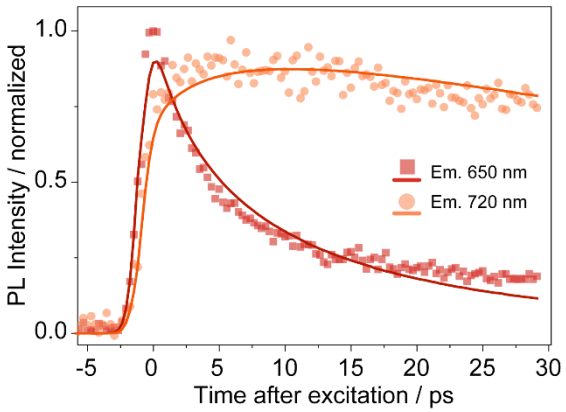

Figure B.20: Time-resolved photoluminescence dynamics for ***cs*[*b*$_1$]-P24** – fit of initial rise. Comparison between normalized photoluminescence intensity dynamics for ***cs*[*b*$_1$]-P24**, measured at an emission wavelength of 650 nm (red squares) and 720 nm (orange circles) following pulsed 410 nm wavelength excitation at a fluence of 2.5 µJ cm^{-2}). Solid lines represent fits to the model described in the supplementary note on energy transfer dynamics (below). Here, the numerical solution to eqn. B.21 is fitted to the PL decays detected at 650, 720 nm. Data were collected and analyzed by Dr. Marcello Righetto and Prof. Laura M. Herz.

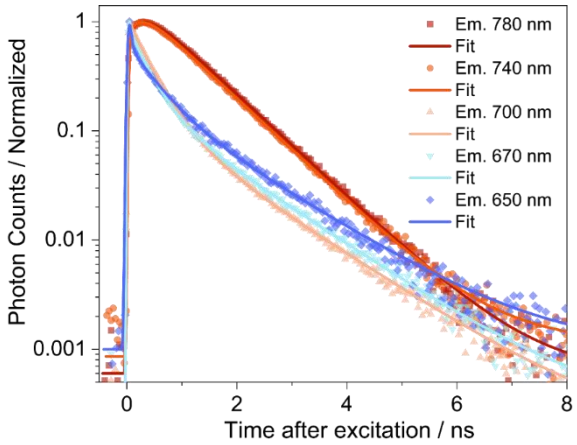

Figure B.21: Time-resolved photoluminescence dynamics for ***cs*[*b*$_1$]-P24** at long (> 1 ns) time delays. Time-resolved photoluminescence dynamics for ***cs*[*b*$_1$]-P24** under 410 nm excitation at 0.4 µJ cm^{-2}. Solid lines represent multi-exponential fitting convoluted with a Gaussian response function. Different colors represent dynamics measured at different wavelengths. Emission at the longer wavelengths can be described by a 0.2 ns rise time followed by a single exponential decay $\tau_2 = 0.90 \pm 0.08$ ns. On the other hand, emission at shorter wavelengths can be described by a bi-exponential decay with $\tau_1 = 0.38 \pm 0.06$ ns and $\tau_2 = 1.33 \pm 0.05$ ns. Data were collected and analyzed by Dr. Marcello Righetto and Prof. Laura M. Herz.

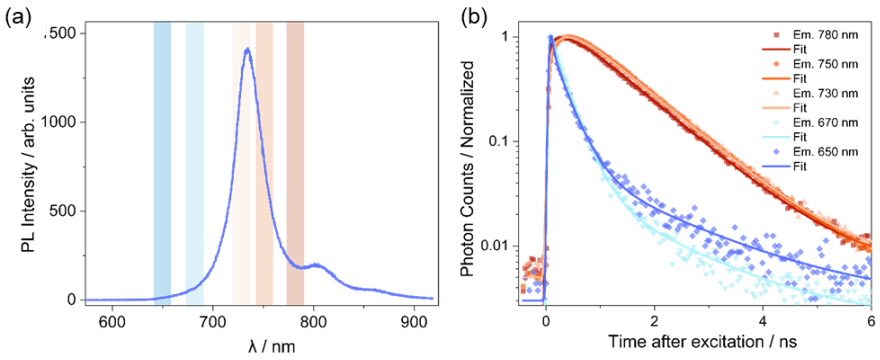

Figure B.22: Time-integrated spectrum and time-resolved photoluminescence dynamics for ***ls*[b_1]-P4** at long (> 1 ns) time delays. Time-integrated spectrum (a) and time-resolved photoluminescence (b) dynamics for ***ls*[b_1]-P4** under 410 nm excitation at a fluence of 400 nJ cm^{-2}. Solid lines represent multi-exponential fitting convoluted with a Gaussian response function. Corresponding detection wavelengths are indicated as shaded areas in the full spectra in sub-figure (a). TCSPC reveals emission wavelength-dependent PL dynamics. Emission at longer wavelengths can be described by a 0.2 ns rise time followed by a single exponential decay $\tau_2 = 0.97 \pm 0.2$ ns. On the other hand, emission at shorter wavelengths can be described by a bi-exponential decay with $\tau_1 = 0.27 \pm 0.04$ ns and $\tau_2 = 1.5 \pm 0.2$ ns. Data were collected and analyzed by Dr. Marcello Righetto and Prof. Laura M. Herz.

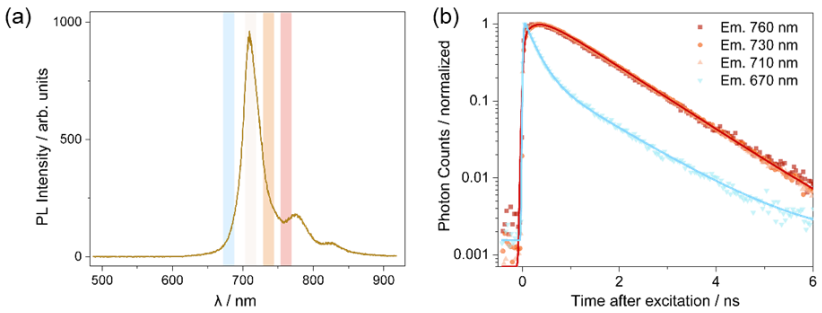

Figure B.23: Time-integrated spectrum and time-resolved photoluminescence dynamics for ***lb*-P2** at long (> 1 ns) time delays. Time-integrated spectrum (a) and time-resolved photoluminescence dynamics (b) for ***lb*-P2** under 410 nm excitation at a fluence of 400 nJ cm^{-2}. Solid lines represent multi-exponential fitting convoluted with a Gaussian response function. Corresponding detection wavelengths are indicated as shaded areas in the full spectra in sub-figure (a). TCSPC reveals an emission-wavelength-dependent PL dynamics. Longer emission wavelength can be described by a 0.25 ns rise time followed by a single exponential decay $\tau_2 = 1.03 \pm 0.03$ ns. On the other hand, emission at shorter wavelengths can be described by a bi-exponential decay with $\tau_1 = 0.23 \pm 0.06$ ns and $\tau_2 = 1.15 \pm 0.03$ ns. Data were collected and analyzed by Dr. Marcello Righetto and Prof. Laura M. Herz.

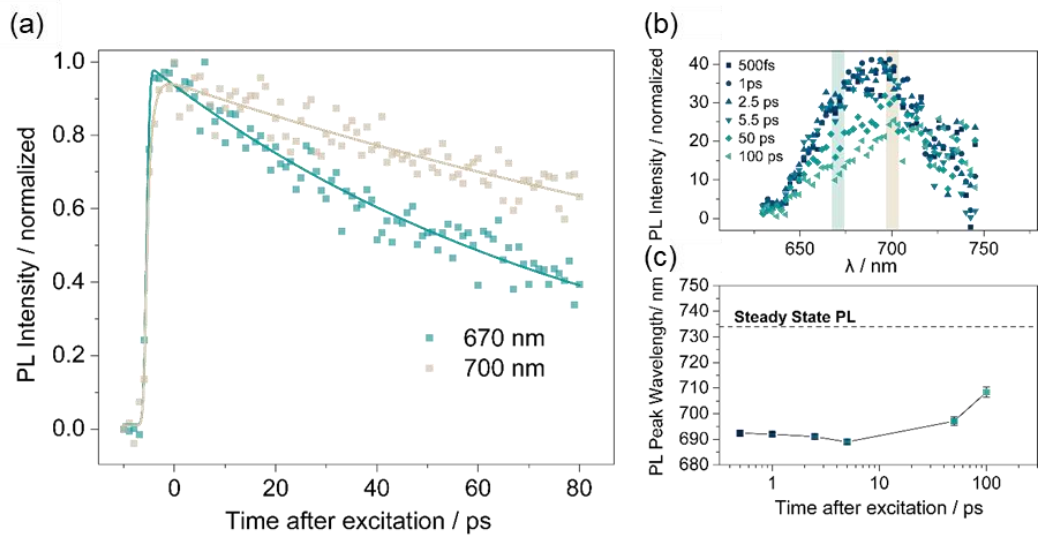

Figure B.24: Time-resolved photoluminescence spectra and dynamics for *ls*[b_1]-P4. (a) Comparison between normalized photoluminescence intensity dynamics for ***ls*[b_1]-P4**, measured at an emission wavelength of 670 nm (cyan squares) and 720 nm (grey squares) under 410-nm wavelength excitation at 2.5 μJ cm^{-2}. Corresponding detection wavelengths are indicated as shaded areas in the full time-resolved spectra in part (a). Solid lines represent fits to a multiexponential function convoluted with a Gaussian instrument response function. The 670 nm transient can be described by a single exponential decay with $\tau_1 = 90$ ps. On the other hand, the 700 nm transient is dominated by a slower decay $\tau_2 = 200$ ps, and an additional exponential rise with $\tau_1 = 1$ ps can also be observed. (b) Time-resolved photoluminescence spectra for ***ls*[b_1]-P4** following 410-nm wavelength pulsed excitation at a fluence of 2.5 μJ cm^{-2}. Different symbols represent spectra taken at different times after the excitation, in the range 500 fs (dark blue square) to 100 ps (grey triangle). (c) Time evolution of the peak wavelength of the photoluminescence spectra for and ***ls*[b_1]-P4**. Data points are extracted through Gaussian fitting of the time-resolved photoluminescence spectra measured under the same excitation conditions (410 nm, 2.5 μJ cm^{-2}) as a function of time after excitation. Dashed lines are guides for the eye. The time-dependent shift of the PL peak position and the faster decay of the blue side and slower decay of the red side is attributed to excited state planarization of the butadiyne-linked porphyrin dimer.[353] The observation of the full planarization dynamics beyond 500 ps for ***ls*[b_1]-P4** is hindered by the weaker sensitivity of the experimental setup used to measure the PL UC signal. However, similar dynamics are observed for ***ls*[b_1]-P4** (see Figure B.25), whose blue-shifted emission with respect to ***ls*[b_1]-P4** allows for a clearer observation of this process. Data were collected and analyzed by Dr. Marcello Righetto and Prof. Laura M. Herz.

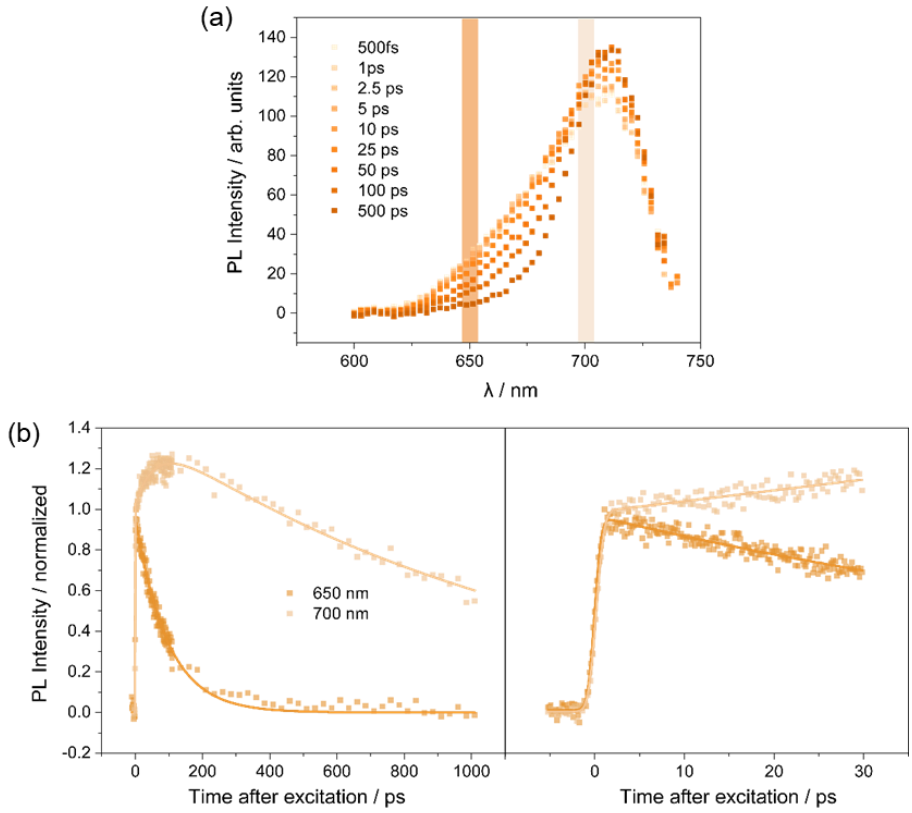

Figure B.25: Time-resolved photoluminescence spectra and dynamics for *lb*-P2. (a) Time-resolved photoluminescence spectra for ***lb*-P2** following 410-nm wavelength pulsed excitation at a fluence of 2.5 µJ cm^{-2}. Different colors represent spectra taken at different times after the excitation, in the range 500 fs (linen square) to 500 ps (orange squares). (b) Comparison between normalized photoluminescence intensity dynamics for ***lb*-P2**, measured at an emission wavelength of 650 nm (linen squares) and 700 nm (dark yellow squares) under 410 nm wavelength excitation at 2.5 µJ cm^{-2}. The two different sub-figures represent measurements with different time resolutions. Corresponding detection wavelengths are indicated as shaded areas in the full spectra in sub-figure (a). Solid lines represent fits to a multiexponential function convoluted with a Gaussian instrument response function. The 650 nm transient can be described by a single exponential decay single exponential decay $\tau_1 = 95$ ps. On the other hand, the 700 nm transient can be well described by an exponential rise $\tau_1 = 60$ ps and a subsequent decay $\tau_2 = 1200$ ps. The obtained Gaussian broadening associated with the instrument response and internal conversion processes was $\sigma = 0.7$ ps. The evident coupled decay of the blue side and growth of the red side of the PL is significantly slower than what was observed for ***cs*[*b*$_1$]-P24** and is attributed to excited state planarization of the butadiyne-linked porphyrin dimer.[353] Data were collected and analyzed by Dr. Marcello Righetto and Prof. Laura M. Herz.

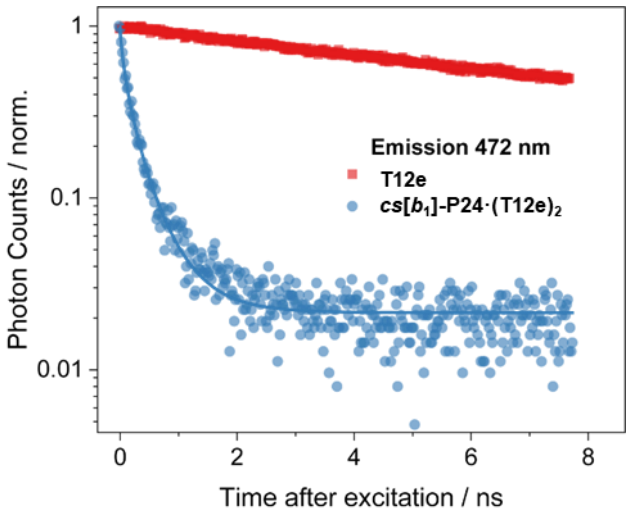

Figure B.26: Time-resolved photoluminescence dynamics for **T12e** and ***cs*[b_1]-P24·(T12e)$_2$**. (**a**) Comparison between normalized photoluminescence intensity dynamics for **T12e** and ***cs*[b_1]-P24·(T12e)$_2$**, measured at an emission wavelength of 472 nm following 380-nm wavelength pulsed excitation at a fluence of 350 nJ cm^{-2}. The detected emission wavelength corresponds to the characteristic emission peak of **T12e** and its quenched dynamics in ***cs*[b_1]-P24·(T12e)$_2$** confirms the presence of energy transfer between the template and the porphyrin nanoring. Solid lines represent fits to the experimental data. **T12e** exhibits a monoexponential decay with time constant $\tau = 8 \pm 1$ ns. The template emission can be fitted with a stretched exponential decay with characteristic time and stretching exponent $\tau = 0.15 \pm 0.04$ ns and $\beta = 0.7$, respectively. This faster decay can be reasonably assigned to energy transfer (i.e., excitations are funneled from the template onto the ring) and confirms previous deductions of efficient energy transfer from fluorescence excitation spectra.

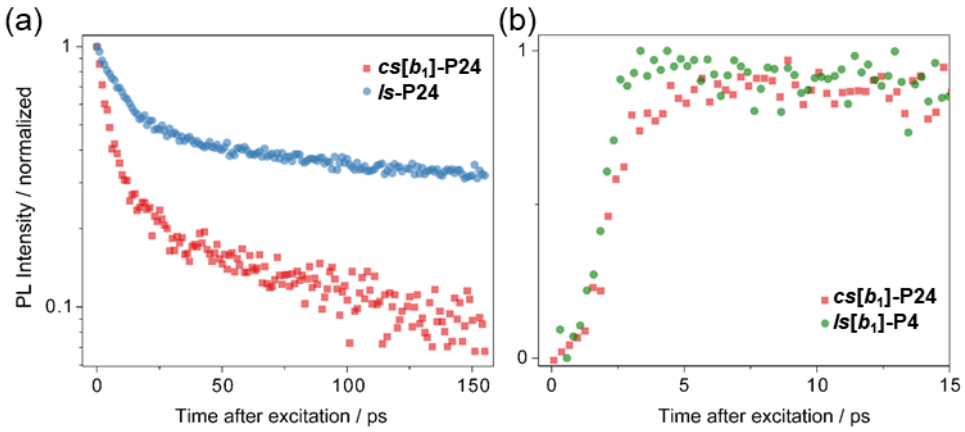

Figure B.27: Comparison of photoluminescence dynamics for ***ls*-P24**, ***cs*[b_1]-P24** and ***ls*[b_1]-P4**. (a) Comparison between normalized photoluminescence intensity dynamics for ***cs*[b_1]-P24** and ***ls*-P24**, measured at an emission wavelength of 650 nm (***cs*[b_1]-P24**) and 680 nm (***ls*-P24**) following pulsed 410 nm wavelength excitation at a fluence of 2.5 µJ cm^{-2}. The comparison shows the quenching of the emission from meso-meso linked porphyrins in a linear chain (***ls*-P24**) and a ring with an acceptor unit (***cs*[b_1]-P24**). (b) Comparison between normalized photoluminescence intensity dynamics for ***cs*[b_1]-P24** and ***ls*[b_1]-P4**, measured at an emission wavelength of 720 nm (***cs*[b_1]-P24**) and 700 nm (***ls*[b_1]-P4**) following pulsed 410 nm wavelength excitation at a fluence of 2.5 µJ cm^{-2}. The comparison shows the slower rise of ***cs*[b_1]-P24** photoluminescence to its relative maximum with respect to the rise of ***ls*[b_1]-P4**. This delayed rise further validates the presence of an excitation transfer process, where excitation generated on the meso-meso linked porphyrins are transferred to the ***ls*[b_1]-P4** emissive unit.

Supplementary note on energy transfer dynamics in *cs*[b_1]-P24

Here we provide a more in-depth discussion of the investigation of EET dynamics in ***cs*[b_1]-P24**. We investigated this process through ultrafast time-resolved photoluminescence spectroscopy (Figure 2.29 c–e). By using 410 nm wavelength pump pulses, excitations in ***cs*[b_1]-P24** can be generated on any of the 12 non-equivalent porphyrin sub-units and then migrate through a hopping-like transfer process between individual porphyrins to the butadiyne-linked porphyrin dimer unit. Hence, we expect the intramolecular energy transfer dynamics in ***cs*[b_1]-P24** to be a complex multi-step process, which cannot be described by a single time-independent energy transfer rate. In particular, transfer times for any individual excitation will depend sensitively on the distance along the ring circumference by which the excitation was created with respect to the acceptor. By measuring the temporal evolution of ***cs*[b_1]-P24** spectra, we observed a

time-dependent shift of the emission from 690 to 730 nm in the first 500 ps after excitation (Figure 2.29d and 2.29e). Considering the peak wavelength of steady-state emission for ***ls*-P24** (donor model molecule) and ***ls*[b_1]-P4** (acceptor model molecule), we can interpret the early-time PL spectra as originating from the individual *meso–meso* linked porphyrin sub-units, and the time-dependent shift as representative of the energy transfer dynamics to the butadiyne-linked porphyrin unit. Therefore, the coupled dynamics in ***cs*[b_1]-P24** emission detected at 650 and 720 nm can be used to describe the population dynamics of the donor and the acceptor, respectively.

The time-dependent population of donor n_d and acceptor n_a can be described by the following coupled rate equations:

$$\begin{cases} \frac{dn_d}{dt} = -\left(\frac{1}{\tau_d} + k(t)\right) n_d(t) \\ \frac{dn_a}{dt} = k(t) n_d(t) - \frac{n_a(t)}{\tau_a} \end{cases} \tag{B.20}$$

where $k(t)$ is the time-dependent energy transfer rate and τ_d and τ_a are the exciton decay lifetimes for the isolated donor and acceptor, respectively. Several theoretical and experimental studies on exciton transfer dynamics in complex systems have found that the energy transfer rate exhibiting a stretched (or Kohlrausch) exponential behavior can satisfactorily account for the observed dispersive dynamics.[354-356] Hence, to describe the energy transfer in ***cs*[b_1]-P24**, we adopt the Kohlrausch-Williams-Watts (KWW) decay rate $k(t) = \beta \tau_0^{-\beta} t^{\beta-1}$,[216,357] which, in the absence of any other deexcitation processes, yields stretched-exponential transients $I(t) = I_0 \exp[-(t/\tau_0)^{\beta}]$. Here, the stretching parameter β gauges deviations from the canonical single exponential decay, and can vary between 0 and 1, with $\beta \to 1$ being the single exponential case.[216]

Figure 2.29c and Figure B.19 show the global fitting of the numerical solution to eqn. B.20 to the PL transients detected at 650, 720 nm and 650, 735 nm, respectively. The dispersive energy transfer rate approach provides an excellent description of the observed behavior. The average extracted parameters are $\beta = 0.54 \pm 0.04$, $\tau_0 = 8.5 \pm 0.6$ ps, and $\tau_a = 40 \pm 7$ ps, while the donor lifetime in the absence of the acceptor was set to $\tau_d = 1.3$ ns.

Crucially, the stretching exponential β is significantly below 1 and accounts for a distribution of energy transfer characteristic times. Thus, we can interpret the extracted energy transfer characteristic time (~ 8 ps) as an average time constant; however, in the ensemble, energy transfer events will occur on both faster and slower timescales, depending on how far

away from the acceptor the original excitation was placed. As the KWW decay rate stated above indicates, for values of β that are significantly smaller than 1, as is the case here, the instantaneous decay rate at very early times after excitation is significantly faster than that described by τ_0, representing early-time transfer processes associated with excitations generated on porphyrin donors right adjacent to the acceptor unit. As time progresses, the instantaneous KWW transfer rate declines, describing the EET processes occurring from porphyrins located further and further away from the acceptor.

Based on this consideration, we further discuss the presence of ultrafast energy transfer components, occurring with time constants below our temporal resolution (350 fs), and also the presence of initial acceptor excitation.

To deconvolve and better quantify these effects, which occur within the time resolution of our system, we introduced an exciton generation function $g(t)$ for both rate equations in eqn. B.20, approximated to a Gaussian function of time $g_{d/a}(t) = A_{d/a}\frac{1}{\sigma\sqrt{2\pi}}e^{-\frac{t^2}{2\sigma^2}}$, where $A_{d/a}$ is the amplitude term and σ is the broadening parameter.

$$\begin{cases} \frac{dn_d}{dt} = g_d(t) - \left(\frac{1}{\tau_d} + k(t)\right)n_d(t) \\ \frac{dn_a}{dt} = g_a(t) + k(t)n_d(t) - \frac{n_a(t)}{\tau_a} \end{cases} \quad \text{(B.21)}$$

Figure 2.50 shows the global fitting of the numerical solution to eqn. B.21 to the complete PL decay for both donor and acceptor, with Gaussian amplitude and broadening as free parameters, while the decay parameters were fixed to the value extracted from the tail fit (eqn. B.20, Figure 2.29c). From the fit, we obtained $\sigma \approx 0.7$ ps and $A_a/A_d \approx 0.4$.

The resulting Gaussian amplitude terms $A_{d/a}$ quantify the initial donor and acceptor PL intensity. Therefore, the ratio A_a/A_d is proportional to the initial PL ratio. This ratio contains information about direct acceptor excitation in our experiment and about ultrafast EET processes that may transfer excitations to the acceptor within the instrumental time resolution. Thus, the obtained non-zero A_a/A_d value suggests that excitations are initially generated also on the acceptor or transferred to the acceptor within the instrumental time resolution.

The resulting A_a/A_d value is proportional to the number of excitations on the acceptor via the radiative rate k_r, i.e., $I(t=0) \propto k_r n$. However, we note that a precise estimate of the radiative constant of the donor and acceptor is needed in order to estimate the initial donor to acceptor population ratio $n_a(t=0)/n_d(t=0)$ and to deconvolute ultrafast energy transfer

and initial acceptor excitation effects. Unfortunately, estimating the radiative constants for different emitting moieties of the ***cs*[*b*$_1$]-P24** molecule is a challenging task. The needed k_r values cannot easily be inferred from the radiative constants for donor and acceptor model molecules (e.g., ***lb*-P2**, ***ls*[*b*$_1$]-P4**, ***ls*-P24**) because conformation changes as a result of the incorporation in the ***cs*[*b*$_1$]-P24** could significantly impact the observed rates.

Nevertheless, the presence of direct acceptor excitation can be further confirmed and quantified by looking at the absorption coefficients of the different donor and acceptor model compounds at the excitation wavelength (i.e., 410 nm). The molar absorption coefficient of the compounds at 410 nm are as follows: ***lb*-P2**: ε = 0.11 μM^{-1} cm^{-1}; ***ls*[*b*$_1$]-P4**: ε = 0.27 μM^{-1} cm^{-1}; ***ls*-P24**: ε = 1.80 μM^{-1} cm^{-1}; ***cs*[*b*$_1$]-P24**: ε = 1.49 μM^{-1} cm^{-1}. These values imply that the initial donor to acceptor population ratio $n_a(t=0)/n_d(t=0)$ is 0.086 ± 0.005, as expected from the fact that donor is 22 porphyrins and the acceptor consists of 2 porphyrins, i.e., $n_a(t=0)/n_d(t=0) \approx 1/11$.

If we make the approximation that the donor and acceptor have the same radiative rate, then comparing $A_a/A_d \approx 0.4$ from eqn. B.21 with $n_a/n_d \approx 0.09$ at $t = 0$ from the absorption spectra implies that about 30% of the energy is transferred within the time resolution of our measurements (350 fs).

Furthermore, we note that the obtained σ value for temporal broadening is significantly higher than the temporal resolution of our system (350 fs). We attribute this slowing of the initial rise in ***cs*[*b*$_1$]-P24** photoluminescence to a combination of internal conversion, as already reported for ***ls*-P24**,[70] and ultrafast energy transfer from neighboring porphyrins.

We hypothesize that such a combination of ultrafast energy transfer and initial acceptor excitation also underlies the initial emission wavelength shift observed when comparing ***cs*[*b*$_1$]-P24** and ***ls*-P24** emission. Although it could be expected that the initial emission peaks for these two molecules are at similar wavelengths immediately after excitation, the emission of ***cs*[*b*$_1$]-P24** already shows a 20 nm red-shift at $t = 0$ (see Figure 2.29e). However, considering that we are directly exciting a fraction of acceptor sub-units and that ultrafast energy transfer from neighboring porphyrins may occur within the temporal resolution of our system, we believe that under our experimental conditions, the initial population of the acceptor is not negligible and therefore may contribute to the emission observed at nominal zero time.

Supplementary note on the radiative coherence length in *ls*-P24

Although coherence in energy transfer processes can emerge in multiple ways (e.g., path interferences, system-bath correlations, excitonic delocalization, and non-Markovian phenomena),[358] an indication of possible coherent interactions in ***cs*[*b*$_1$]-P24** can be obtained by looking at the model ***ls*-P24**. Specifically, as demonstrated by Van Grondelle and coworkers for light-harvesting complexes[359] and by Osuka and coworkers for linear porphyrin arrays,[360] exciton superradiance is a spectroscopic observable related to exciton delocalization. The exciton interactions between chromophores in an array enhance the radiative rate as a result of chromophores radiating in phase. Therefore, the so-called "superradiance (or radiative) coherence length" can be obtained as $N_c = k_{r,array}/k_{r,monomer}$. A value $N_c > 1$ implies the presence of delocalization of the exciton wavefunction over several chromophores. Furthermore, in the case of parallel dipoles within the assembly, this value directly estimates the exciton delocalization length.[163] Thus, by applying this to the case of ***ls*-P24**, we can estimate a value for N_c by considering the radiative rate of ZnTPP as the monomer. The measured radiative rate for ***ls*-P24** is $k_{r,\textbf{\textit{ls}}\text{-P24}} = (15\ \text{ns})^{-1}$, while the well-known value for ZnTPP is $k_{r,ZnTPP} = (70\ \text{ns})^{-1}$,[352] thus resulting in $N_c \approx 4.5$. This N_c value is significantly larger than unity, implying a delocalized nature of exciton wavefunction in ***ls*-P24**. Therefore, it is reasonable to assume that the first step is the EET of the macrocycle will involve the migration of delocalized excitations along the porphyrin array.

B.12 Computational Modeling

B.12.1 DFT calculations

Strain analysis

All the DFT calculations were performed using Gaussian 09/A.03 or Gaussian 16/A.03.[361] The porphyrin *meso* aryl groups were replaced with hydrogen atoms. Geometries of molecular models ***ls*-P4**, ***ls*-P5**, ***lf*-P4**, ***lf*-P5**, ***lb*-P4-*e*$_2$**, ***lb*-P5-*e*$_2$**, ***cs*-P12**, ***cs*-P24**, ***cf*-P12**, ***cf*-P24**, ***cs*[*b*$_1$]-P12**, ***cs*[*b*$_1$]-P18** and ***cs*[*b*$_1$]-P24** were optimized at PBE0+GD3BJ/Def2SVP level of theory.[362,363] Due to the large size of the cyclic oligomers, we were only able to rigorously confirm the minima with frequency calculations on the linear oligomers, which gave no imaginary frequency.

The theoretical predicted strain energies (E_{strain}) were estimated by homodesmotic reactions,[188] where the calculated electronic energies were subtracted according to eqn. 2.2–2.4. The predicted strain energies are summarized in Table B.5.

Table B.5: Electronic and strain energies for the cyclic and linear porphyrin oligomers.

Compound	Energy / Ha	Strain energy / kJ mol^{-1}
***ls*-P4**	–11058.770946	–
***ls*-P5**	–13823.169308	–
***lf*-P4**	–11051.761024	–
***lf*-P5**	–13813.823538	–
***lb*-P4-*e*$_2$**	–11666.853741	–
***lb*-P5-*e*$_2$**	–14583.279225	–
***cs*-P12**	–33172.720757	156.4
***cs*-P24**	–66345.530016	80.5
***cf*-P12**	–33144.681540	180.2
***cf*-P24**	–66289.470465	78.4
***cs*[*b*$_1$]-P12**	–33324.754238	139.8
***cs*[*b*$_1$]-P18**	-49911.160297	98.0
***cs*[*b*$_1$]-P24**	–66497.558937	75.8

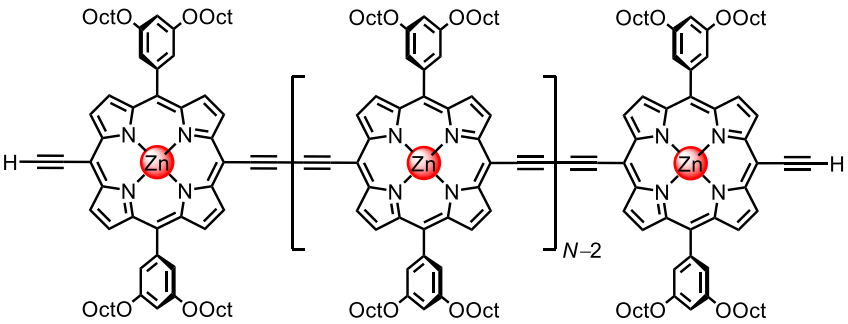

***lb*-P*N*-*e*$_2$**

Figure B.28: Chemical structure of ***lb*-P*N*-*e*$_2$**.

NICS calculations

DFT geometry optimizations of nanobelts ***cf*-P12**, ***cf*-P13**, ***cf*-P24**, ***cf*-P25** and ***cf*[b_1]-P12** were first performed using the BLYP35/6-31G* functional/basis set.[330,331] NICS/susceptibility calculations were performed using the GIAO method, as implemented in Gaussian16/A.03 with BLYP35/6-31G* functional/basis set.[143] For nanobelts ***cf*-P12**, ***cf*-P13** and ***cf*[b_1]-P12**, NICS grids were calculated with 1 Å resolution on a 25 Å × 25 Å grid. For large nanobelts ***cf*-P24** and ***cf*-P25**, NICS grids were calculated with 1 Å resolution on a 50 Å × 50 Å grid.

B.12.2 Molecular Mechanics and Molecular Dynamics Calculations

Parameterization

In this work, we developed a non-bonded/bonded hybrid model for the interaction of zinc porphyrins and pyridine ligands for the AMBER force field where the zinc ion has bonded terms to the nitrogen atoms of the porphyrin but only non-bonded terms to the nitrogen of pyridine ligands. Previous parameters for zinc porphyrin systems were either not parameterized for the interaction with pyridine ligands[364] or used a fully bonded approach[365] which limits the scope of binding property investigations.

The zinc porphyrin complex was parameterized using the LEaP program (AMBER20 tools)[366] in conjunction with MCPB.py[367] with default settings. This is a tool for generation of force field parameters for metal ions from DFT calculations and utilizes RESP charge calculations and derivation of force constants from the Hessian matrix (Seminario method).[368] DFT calculations were carried out in Gaussian 09 (B3LYP/6-31G*).[369] Other parameters were obtained using the LEaP program to assign GAFF parameters and AM1-BCC charges. See ref. 370 for more details.

Methodology of the molecular dynamic simulations

All molecular dynamics (MD) simulations were performed in an isothermal-isobaric (NPT) ensemble at 300 K and 1 bar with a time step of 2 fs using GROMACS (v. 2019.2).[371] Simulations employed the General AMBER force field[372] with modifications to parameters for zinc ions and porphyrin connections as described above. Systems were minimized using the steepest descent algorithm for 5000 steps or until the maximum force on any atom was below 1000 kJ mol^{-1} nm^{-1} and subsequently equilibrated using a velocity-rescaling thermostat[373] and

Parrinello-Rahman barostat.[374] All simulations were performed in explicit chloroform[375] with three-dimensional periodic boundary conditions. The box sizes were chosen by leaving 1 nm distance between solute and box boundary. Long-range electrostatic interactions were calculated using the particle mesh Ewald method.[376] All bond lengths involving hydrogen atoms were constrained with the LINCS algorithm.[376] All MD simulations were performed with the complete molecule, including 3,5-bis(octyloxy)phenyl solubilizing groups.

Flexibility of *cs*[*b*$_1$]-P24

Structural parameters of the free ***cs*[*b*$_1$]-P24** ring and template complex ***cs*[*b*$_1$]-P24·(T12e)$_2$** were obtained from MD simulations and are shown in Figure B.29. A long axis *a* and a short axis *b* were defined as the longest and shortest zinc to zinc distances of opposite porphyrins to determine the ellipticity of the porphyrin ring by calculating the flattening factor *f*. MM parameters of the porphyrin structures were obtained for the condensed phase and therefore may not be suitable to describe phase dynamics, for example due to over polarization of charges. However, it may still be instructive to compare STM results to solution-phase simulation data. Five simulations were run for 100 ns each.

In agreement with STM imaging, MD simulations show that the ***cs*[*b*$_1$]-P24** rings persist in an approximately circular shape but are quite flexible with a distribution of different flattening factors. The average flattening factor from simulations is 0.16 ± 0.07 compared to 0.37 ± 0.11 from experiment and accordingly *b* is larger (5.8 ± 0.3 nm compared to 5.2 ± 1.2 nm) and *a* is smaller on average (6.9 ± 0.3 nm compared to 8.3 ± 1.4 nm). However, this is likely to be due to the different conditions of the condensed phase simulations with explicit solvent compared to ultra-high vacuum in STM imaging. Introducing templates in the simulation rigidifies the ring structure which causes the short and long axes to only differ by 4 % on average.

Concerted rotation of porphyrin units in *cs*[*b*$_1$]-P24

Simulations of the free ***cs*[*b*$_1$]-P24** ring were run to investigate the flexibility of individual porphyrins in the ring. To follow their rotation, a dihedral angle was defined by the center of mass of all zinc ions and three points in the plane of the porphyrin as indicated in Figure B.30 for each of the 24 porphyrins. Five simulations were run for 100 ns each.

All porphyrins populate dihedral angles from –180° to +180° but have different equilibrium distributions because of the bias of the butadiyne link. Due to the *meso-meso* link, the rotation of any one porphyrin requires a concerted motion of all porphyrins. While they do not complete a full concerted rotation on the time scale of the simulation, they rotate back and forth, sweeping the entire range of dihedral angles from –180° to +180° (Figure B.30c). However, porphyrins adjacent to the butadiyne link have a preference to be coplanar and at an angle of about 90° to the plane of the ring and this in turn leads to a bias for the following dihedral angle distributions as the relative angle between neighboring porphyrins is restricted to about 70–90°. Introduction of the T12 templates locks the porphyrin units into a certain orientation, leading to a narrow spread of dihedral angles and well-defined environments (Figure B.30d and B.30e).

Viability of ring-closure reactions

MD simulations of different complexes between templates and linear porphyrin chains were run for 40 ns and repeated 4 times to investigate the geometry of the terminal alkynes. The 2D normalized histograms show the distance d between carbons of the terminal acetylenes and the angle θ between the alkyne units (Figure B.31). A computational study on the Glaser-Hay coupling by Fomina et al.[200] found a bond distance of 2.00 Å between the terminal carbon atoms in the pre-bond-formation intermediate. Mode A and B of the ***ls*-P24-*e*$_2$·(T12e)$_2$** complex have very similar binding properties, although mode B has a slightly smaller average distance between the terminal porphyrins and a less steep angle. In both binding modes, the complexes spend time in configurations with relatively short distances ($d \leq 4$ Å) that are suitable for Glaser coupling. In contrast, a single **T12e** template does not bring the alkyne ends sufficiently close together, and also holds the terminal alkynes at a smaller angle relative to each other as a result of the partially open complex. The 12-mer porphyrin system has a shorter average end-to-end distance than the 24-mer system with a similar distribution of angles.

Quality of template fit

Distances between templates and the plane of the porphyrin ring as well as distances between zinc ions and pyridine nitrogens were used to assess the quality of template binding. These properties were analyzed for the linear and cyclic complexes from 40 ns MD simulations. The plane of the ring is the average plane of all 24 zinc atoms defined by the center of mass of the zinc ions and an average normal vector to the planes defined by three zinc ions.

While the optimized structure of ***cs*[*b*$_1$]-P24·(T12e)$_2$** shows the templates close to the plane of the ring, both templates are spending the majority of the time out of the plane of the ring on one side during MD simulations (Figure B.31). Switches between which side the templates lie on are infrequent and associated with an energy barrier, as it requires a concerted motion of all porphyrins when the templates move through the plane of the ring. In contrast, the linear complex has no size restrictions. Therefore, one of the templates can lie in the plane of the ring and also there is a frequent switch of which template is more central. The templates move in a highly concerted way and the average distance between templates is 3.5 Å in both the linear and the cyclic complexes. To eliminate effects caused by the interactions between the two bound templates, simulations were also run for complexes with just one **T12e** molecule. In these simulations, the single template stayed in the plane of the ring for the linear complex, but again remained out of the plane for the cyclic complex. However, the average zinc ion to pyridyl nitrogen distance is 2.10 Å in both the linear and the cyclic complex compared to 2.13 Å in the zinc-porphin pyridyl reference system, which indicates efficient binding. (Note that the molecular mechanics system was parameterized in such a way that variation of the zinc ion to pyridyl ion distance is easily possible and detaching of pyridyl ligand was commonly observed in strained systems such as ***ls*-P12-*e*$_2$·T12a**). Therefore, the template successfully strikes the balance between rigidity, to give a cyclic shape to the linear porphyrin chain, and flexibility, to be able to move out of the way and not prevent a decrease in circumference during the ring-closure reaction.

Strain analysis

The energies for strain calculations were obtained from MM calculations carried out in Gromacs 2019 with a double precision installation.[371] Structures were minimized using the steepest descent algorithm with a step size of 0.01 nm, a convergence threshold of 1 kJ mol^{-1} and a maximum number of steps of 50000. Minimization was done in vacuum with no periodic boundary condition and no cut-off for non-bonded interactions.

The theoretical predicted strain energies (E_{strain}) were estimated by homodesmotic reactions,[188] where the calculated electronic energies were subtracted according to eqn. 2.2–2.4. The predicted strain energies are summarized in Table B.6.

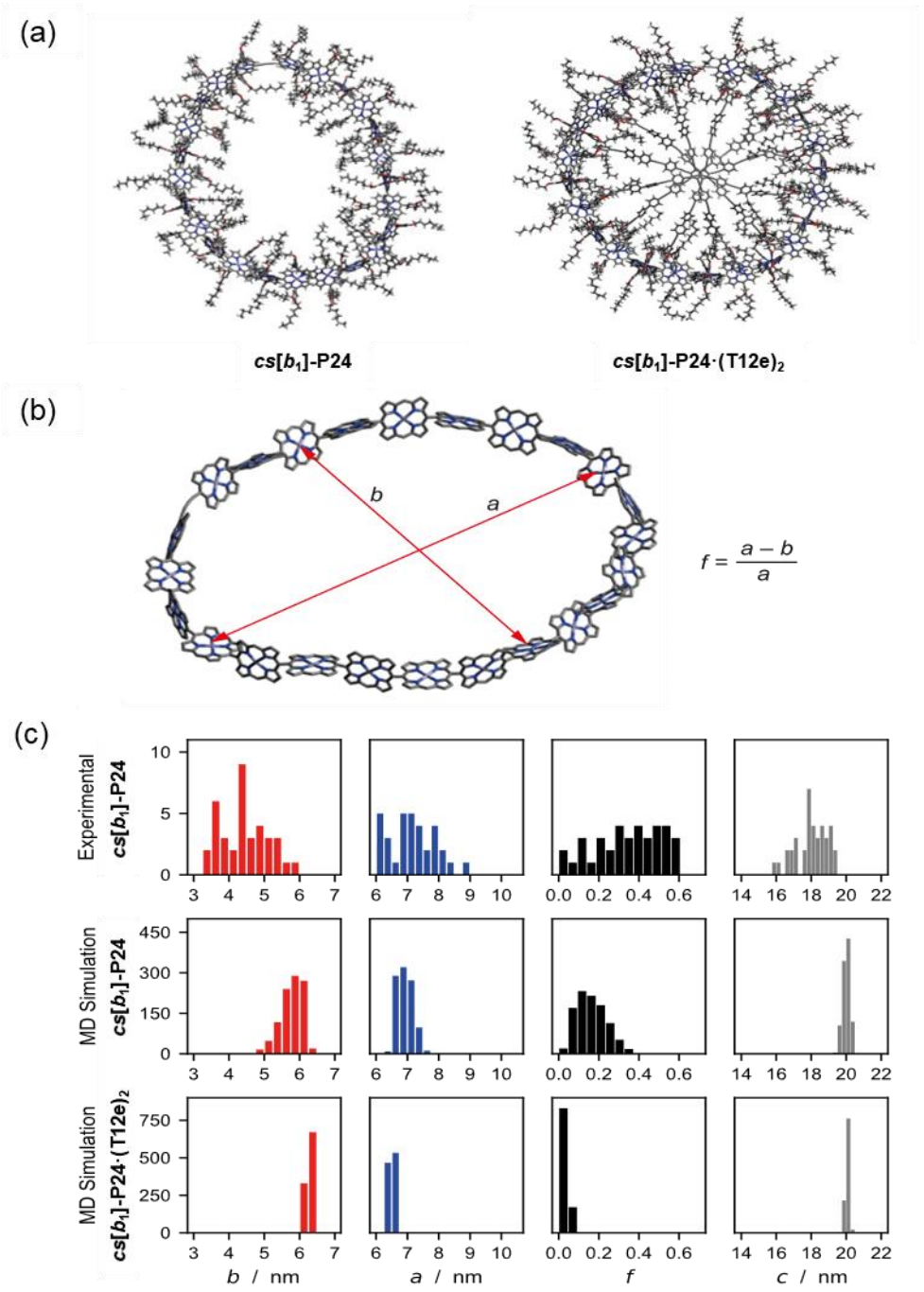

Figure B.29: (a) Models of systems used in simulations. (b) Structural parameters of porphyrin ring to describe its ellipticity: long axis *a*, short axis *b*, and flattening factor *f*. (c) Distributions of parameters for STM experiments and MD simulations. Data were collected and analyzed by Janko Hergenhahn.

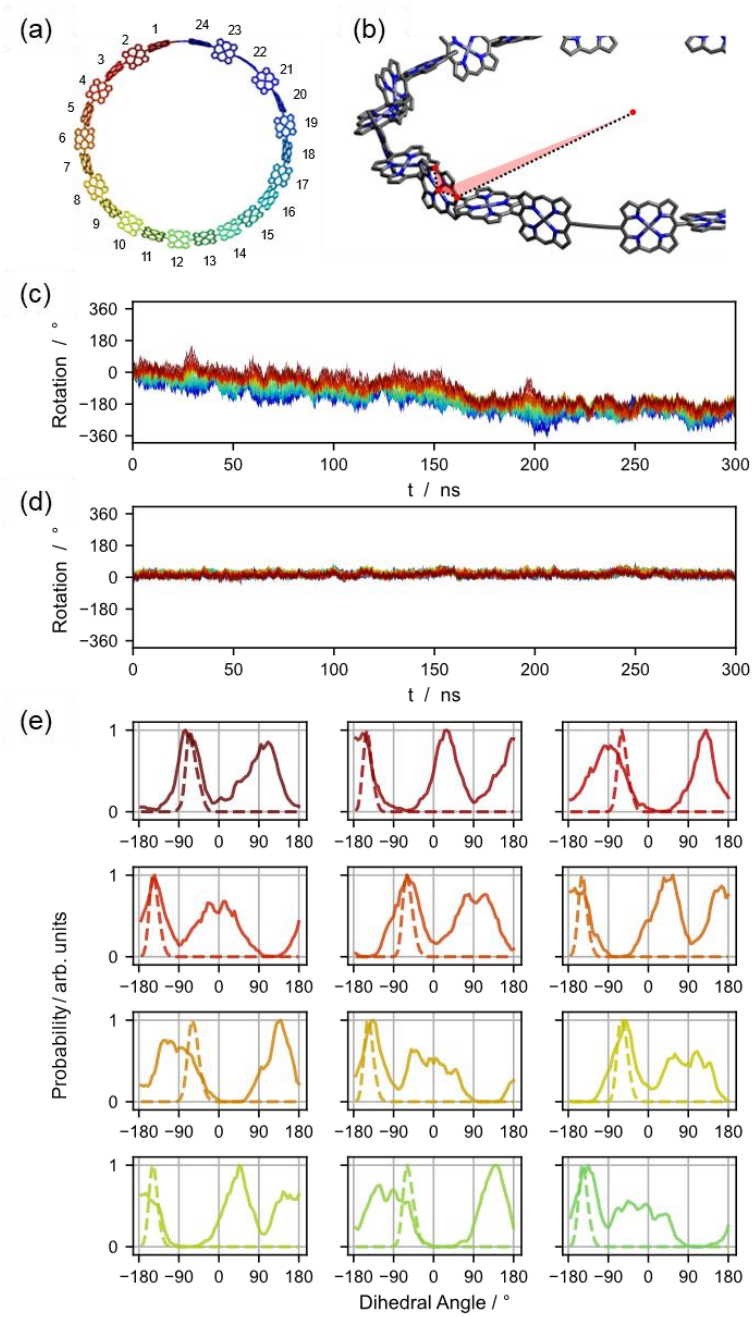

Figure B.30: (a) Numbering of porphyrin units in ***cs*[*b*$_1$]-P24**, hydrogens and solubilizing groups are omitted for clarity. (b) Dihedral angle used to define the porphyrin rotation, shown for porphyrin unit number 3. (c) Rotation of porphyrins relative to t = 0 over a 150 ns MD simulation for the free ***cs*[*b*$_1$]-P24** ring, and (d) the template complex ***cs*[*b*$_1$]-P24·(T12e)$_2$**. (e) Distribution of dihedral angles for porphyrins 1 to 12. Porphyrins 13 to 24 are related to these by symmetry. Solid lines show distributions for the free ring ***cs*[*b*$_1$]-P24** and dashed lines for the template complex. Data were collected and analyzed by Janko Hergenhahn.

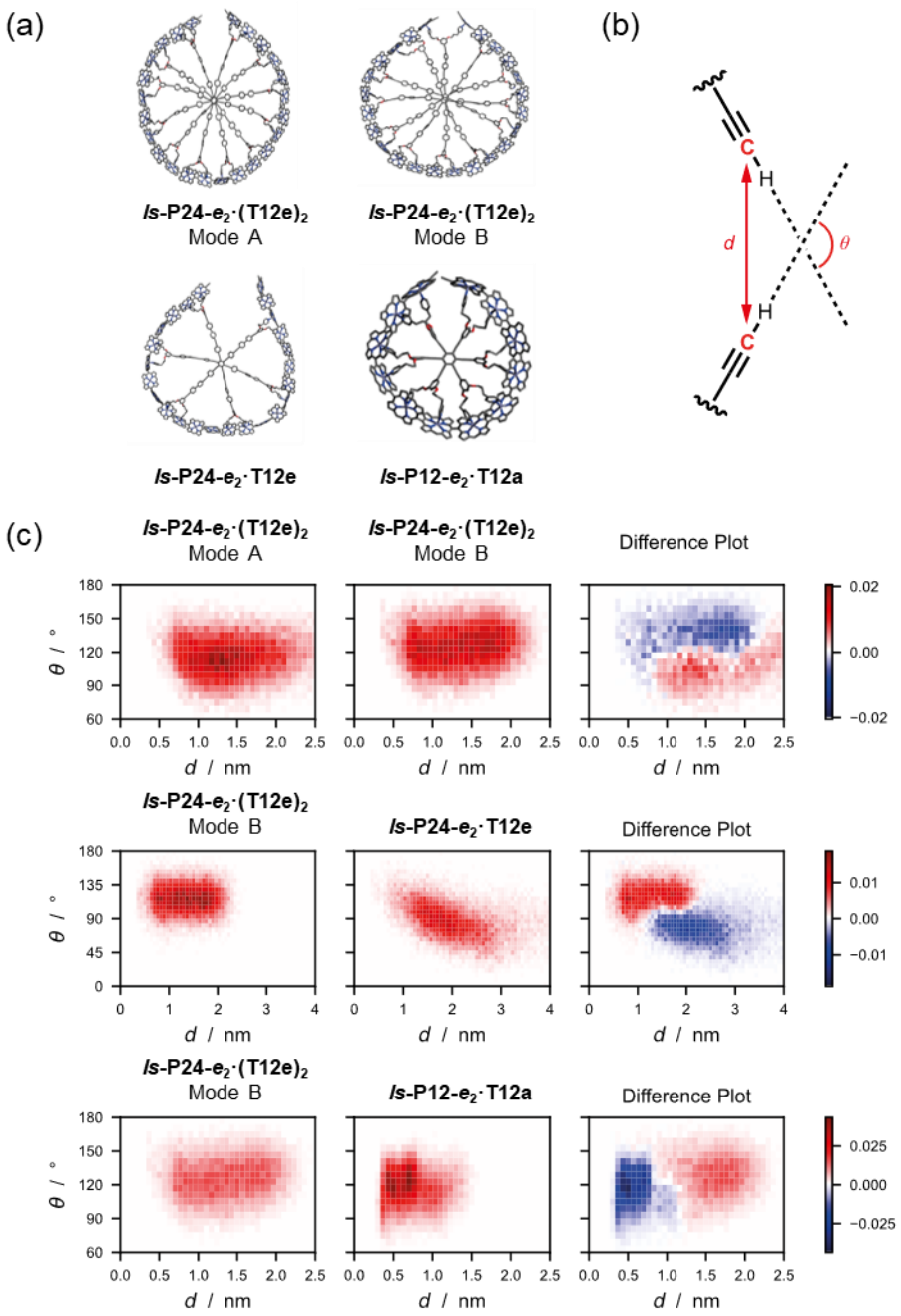

Figure B.31. (a) Structures used in simulations, hydrogens and solubilizing groups are omitted for clarity. (b) End-to-end distance, which is defined as the distance between carbons of terminal acetylenes, and acetylene angle used for analysis of binding behavior. (c) Distributions of end-to-end distances and angles for a selection of template complexes (regions in which the second complex gives a higher probability density are colored blue). Data were collected and analyzed by Janko Hergenhahn.

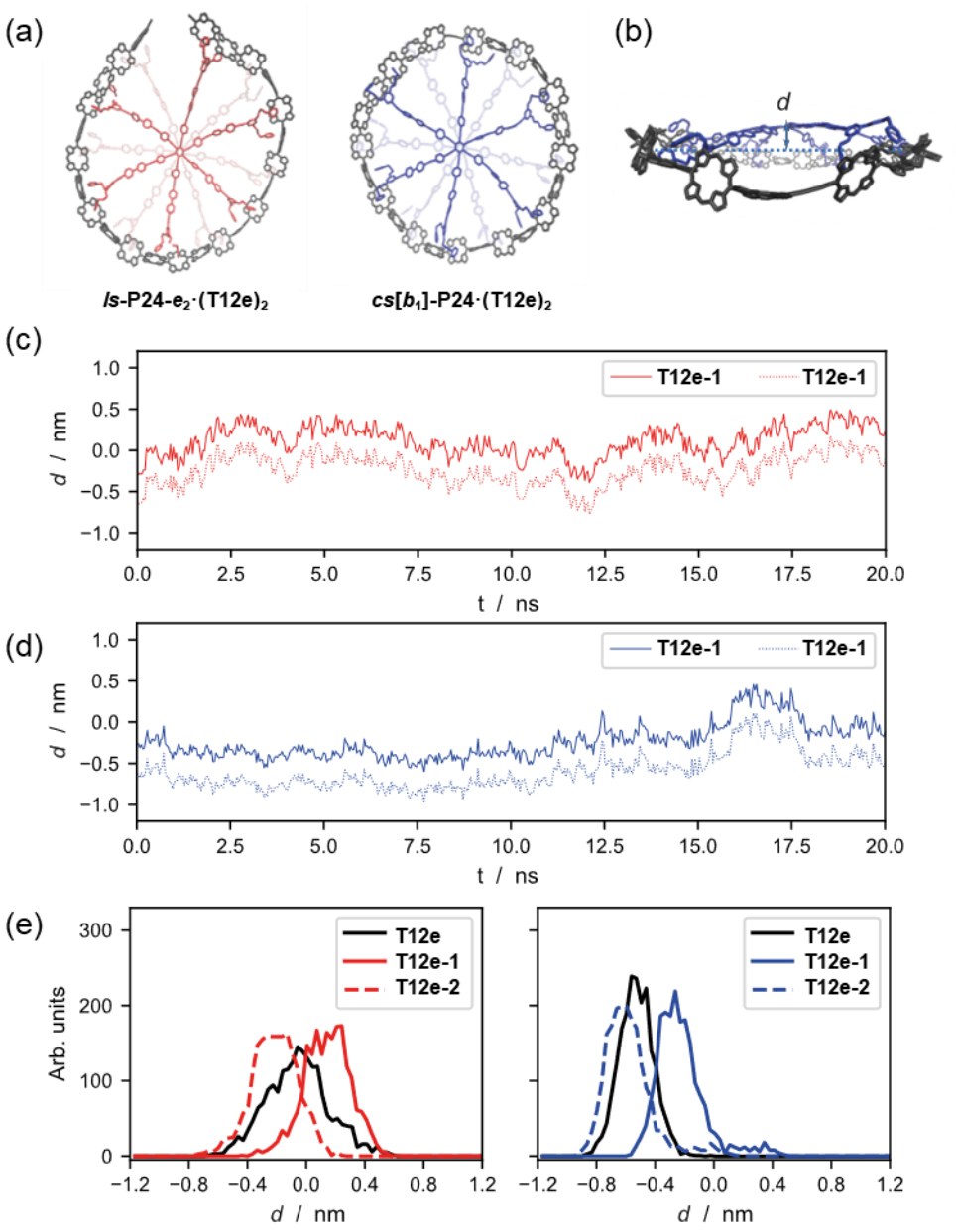

Figure B.32: (a) Structures used in simulations, hydrogens and solubilizing groups omitted for clarity. (b) Distance *d* between ring plane and template core. Evolution of *d* during 20 ns of MD simulation for (c) linear and (d) cyclic complex. (e) Distributions of distances for linear (left) and cyclic (right) complexes. The figure also shows the distances of a single template with a solid black line for both systems. Data were collected and analyzed by Janko Hergenhahn.

Table B.6: Optimized energies and strain energies for the linear and cyclic oligo porphyrin compounds from molecular mechanics calculations.

Species	Energy / kJ mol^{-1}	Strain energy / kJ mol^{-1}	Species	Energy / kJ mol^{-1}	Strain energy / kJ mol^{-1}
***ls*-P4**	-2460.387	–	***cs*[b_1]-P14**	-10414.497	125.5
***ls*-P5**	-3045.522	–	***cs*[b_1]-P15**	-11189.209	116.6
***lb*-P4-e_2**	-3365.366	–	***cs*[b_1]-P16**	-11961.074	110.4
***lb*-P5-e_2**	-4131.126	–	***cs*[b_1]-P17**	-12734.335	102.9
***lf*-P4**	-2790.982	–	***cs*[b_1]-P18**	-13503.486	99.6
***lf*-P5**	-3401.686	–	***cs*[b_1]-P19**	-14275.823	93.0
***cs*-P9**	-6671.462	220.4	***cs*[b_1]-P20**	-15045.093	89.5
***cs*-P10**	-7469.540	188.1	***cs*[b_1]-P21**	-15815.910	84.4
***cs*-P11**	-8242.284	181.1	***cs*[b_1]-P22**	-16583.561	82.5
***cs*-P12**	-9033.308	155.8	***cs*[b_1]-P23**	-17354.488	77.4
***cs*-P13**	-9803.993	150.9	***cs*[b_1]-P24**	-18121.854	75.7
***cs*-P14**	-10585.203	135.4	***cs*[b_1]-P25**	-18892.253	71.1
***cs*-P15**	-11354.524	131.9	***cs*[b_1]-P26**	-19658.958	70.2
***cs*-P16**	-12134.640	117.5	***cs*[b_1]-P27**	-20428.665	66.2
***cs*-P17**	-12903.159	114.8	***cs*[b_1]-P28**	-21195.583	65.1
***cs*-P18**	-13677.766	105.9	***cs*[b_1]-P29**	-21965.082	61.3
***cs*-P19**	-14445.718	103.7	***cs*[b_1]-P30**	-22731.134	61.0
***cs*-P20**	-15221.055	94.1	***cs*[b_1]-P31**	-23500.125	57.8
***cs*-P21**	-15988.387	92.6	***cs*[b_1]-P32**	-24266.594	57.1
***cs*-P22**	-16760.027	86.7	***cf*-P9**	-5258.696	237.6
***cs*-P23**	-17527.107	85.4	***cf*-P10**	-5895.409	211.6
***cs*-P24**	-18299.570	78.7	***cf*-P11**	-6527.115	190.6
***cs*-P25**	-19066.575	77.4	***cf*-P12**	-7155.098	173.3
***cs*-P26**	-19836.120	73.6	***cf*-P13**	-7780.236	158.9
***cs*-P27**	-20603.157	72.4	***cf*-P14**	-8403.184	146.7
***cs*-P28**	-21374.010	67.3	***cf*-P15**	-9024.404	136.1
***cs*-P29**	-22140.548	66.5	***cf*-P16**	-9644.164	127.1
***cs*-P30**	-22909.324	63.5	***cf*-P17**	-10262.838	119.1
***cs*-P31**	-23675.887	62.7	***cf*-P18**	-10880.565	112.1
***cs*-P32**	-24445.599	58.7	***cf*-P19**	-11497.465	105.9
***cs*[b_1]-P9**	-6524.957	186.2	***cf*-P20**	-12113.765	100.3
***cs*[b_1]-P10**	-7307.265	169.7	***cf*-P21**	-12729.514	95.3
***cs*[b_1]-P11**	-8087.141	155.6	***cf*-P22**	-13344.748	90.7
***cs*[b_1]-P12**	-8865.009	143.5	***cf*-P23**	-13959.537	86.6
***cs*[b_1]-P13**	-9641.654	132.6	***cf*-P24**	-14573.948	82.9

B.12.3 NMR and Mass Spectra

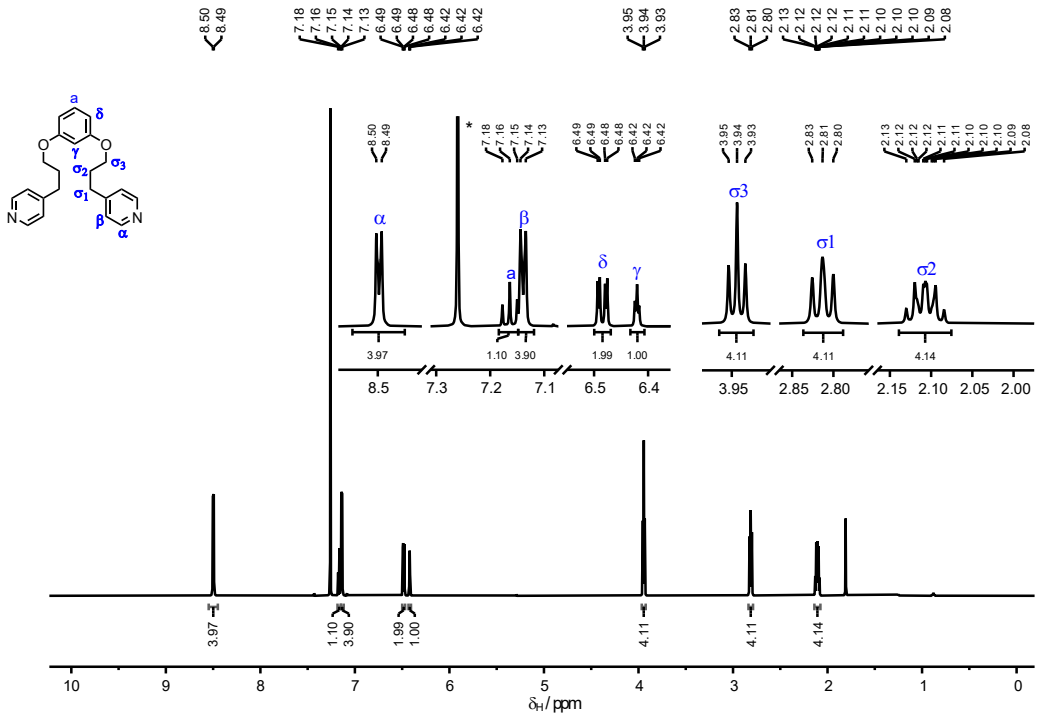

Figure B.33: ^{1}H NMR spectrum of **T2** (600 MHz, $CDCl_3$, 298 K). * = $CHCl_3$.

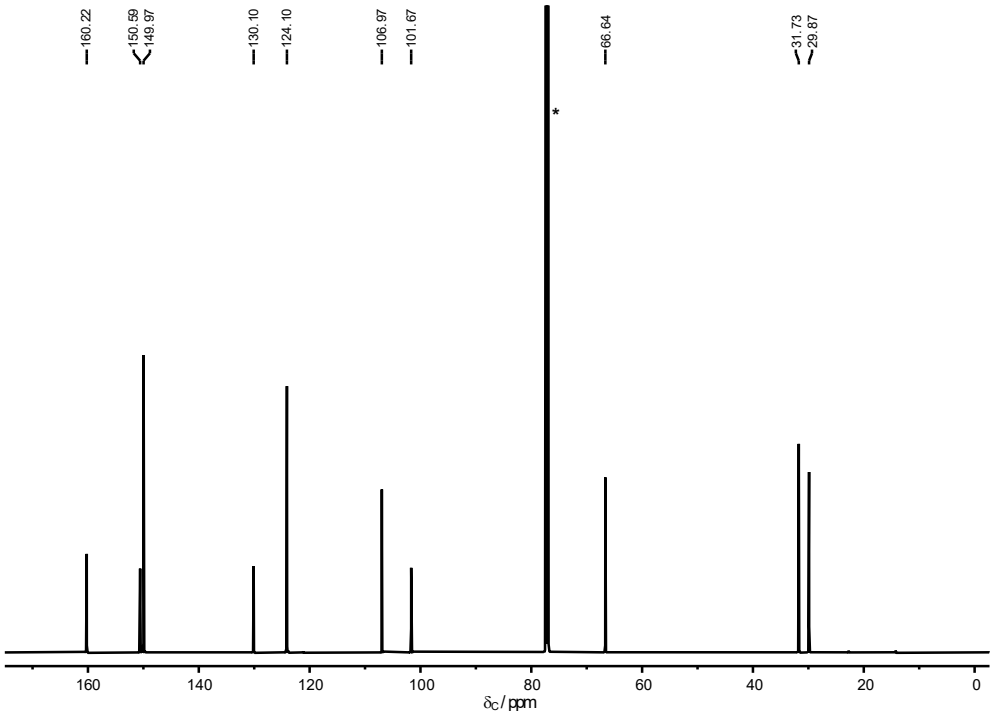

Figure B.34: ^{13}C NMR spectrum of **T2** (151 MHz, $CDCl_3$, 298 K). * = $CDCl_3$.

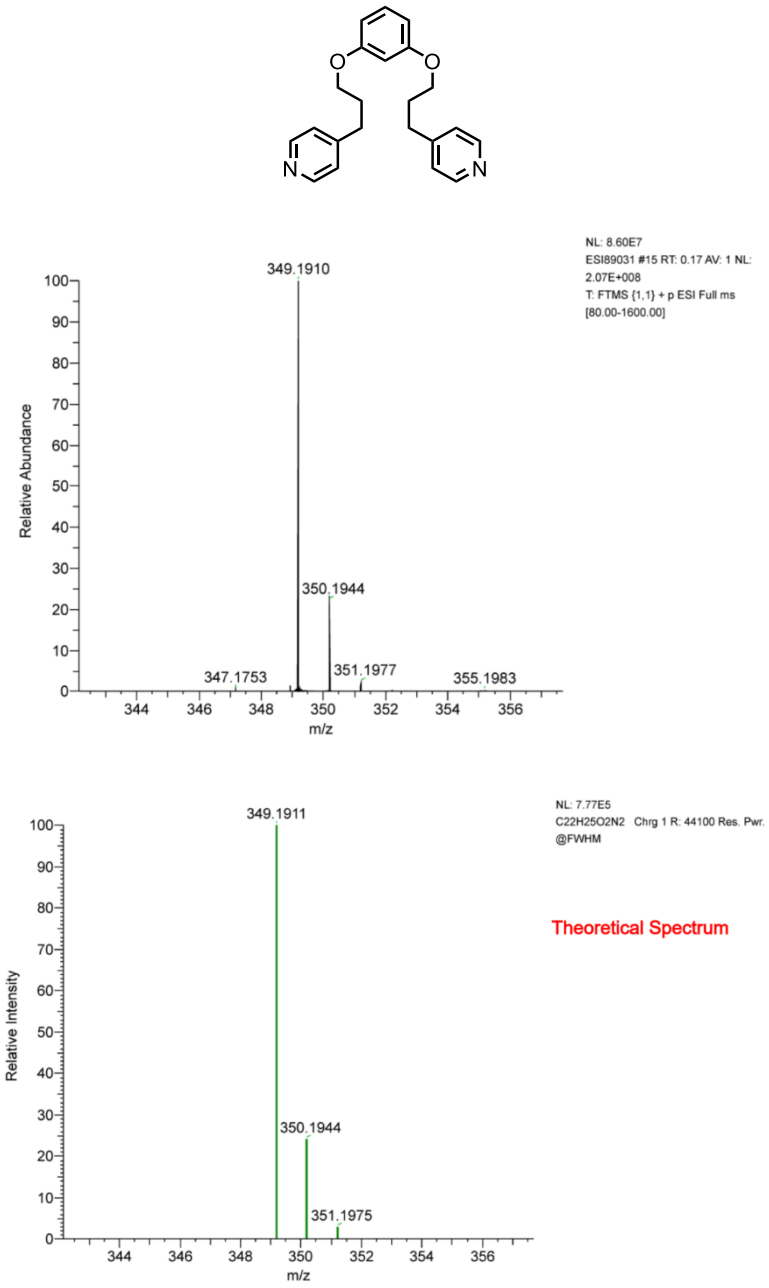

Figure B.35: ESI mass spectra of **T2**.

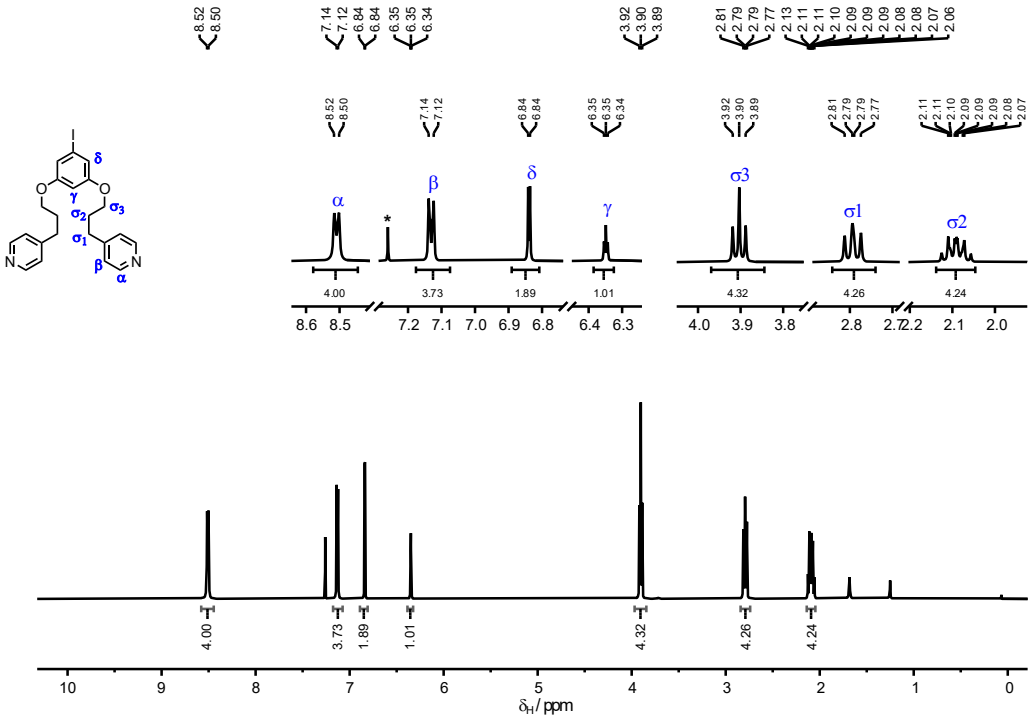

Figure B.36: ^{1}H NMR spectrum of **T2I** (400 MHz, $CDCl_3$, 298 K). * = $CHCl_3$.

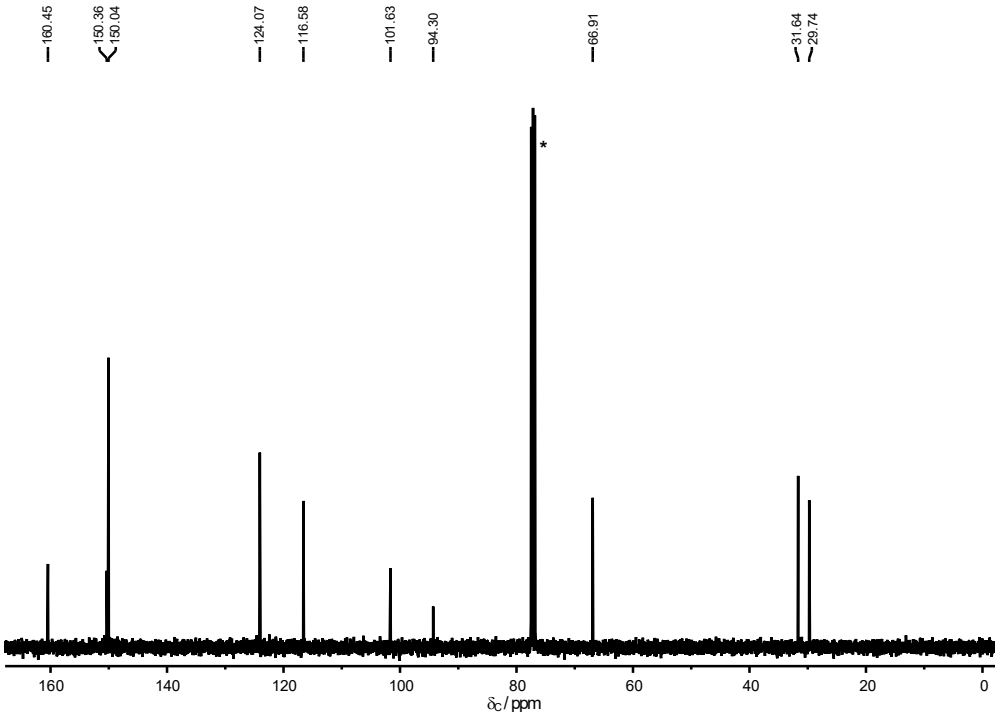

Figure B.37: ^{13}C NMR spectrum of **T2I** (101 MHz, $CDCl_3$, 298 K). * = $CDCl_3$.

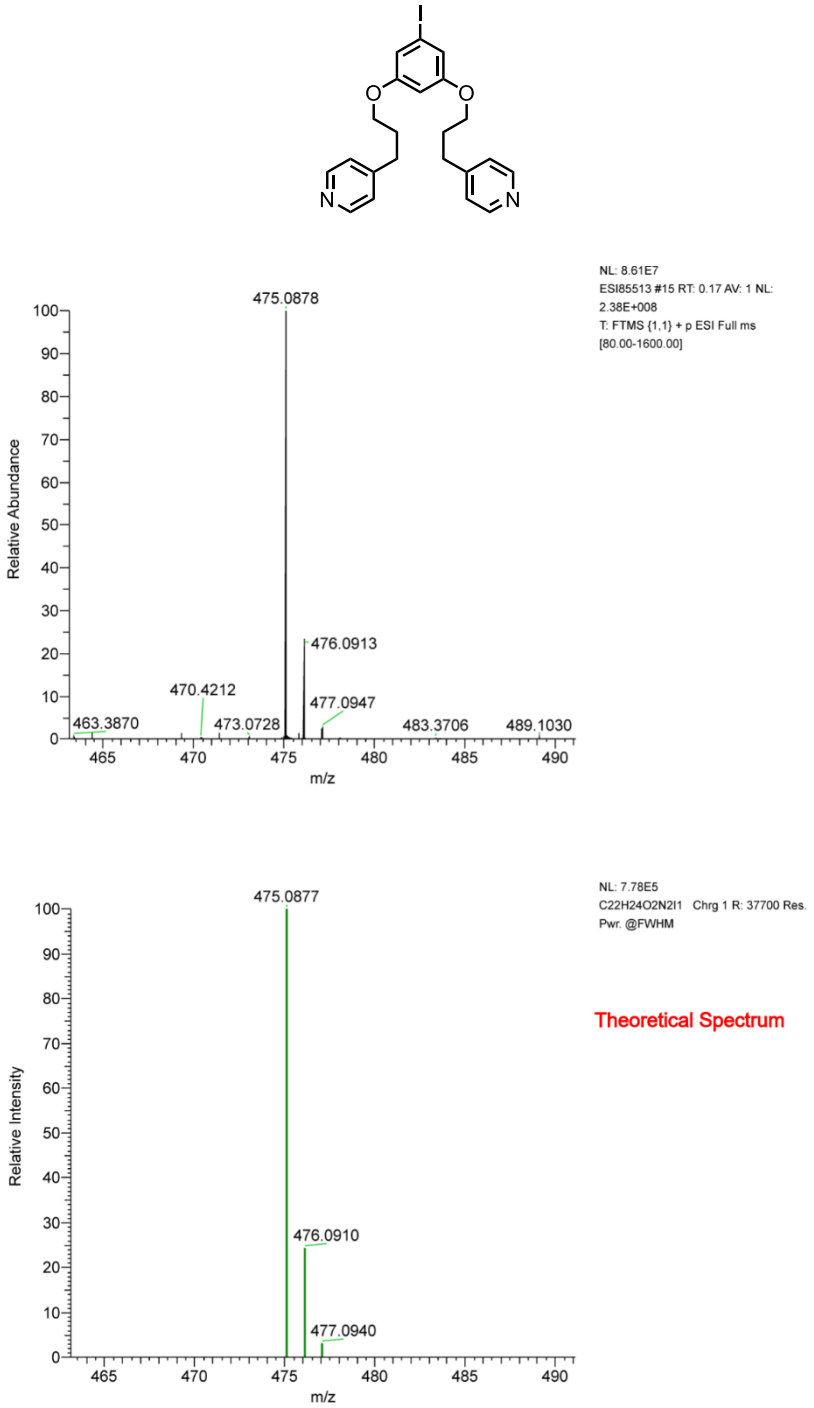

Figure B.38: ESI mass spectra of **T2$_I$**.

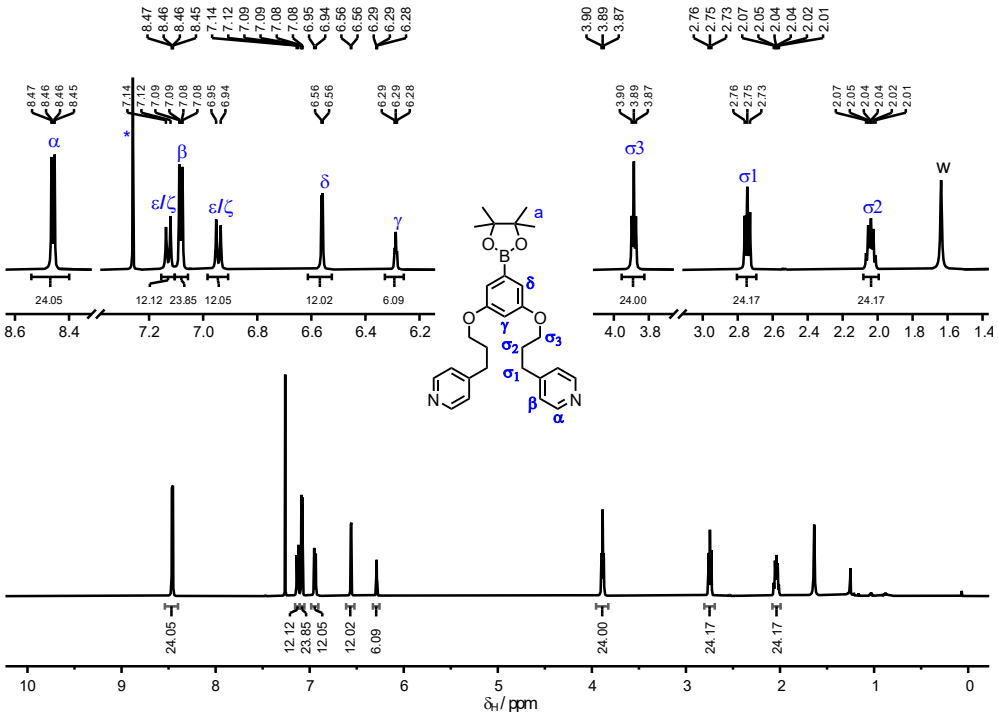

Figure B.39: ^{1}H NMR spectrum of **T2$_{Bpin}$** (400 MHz, $CDCl_3$, 298 K). * = $CHCl_3$; # = unidentified impurity.

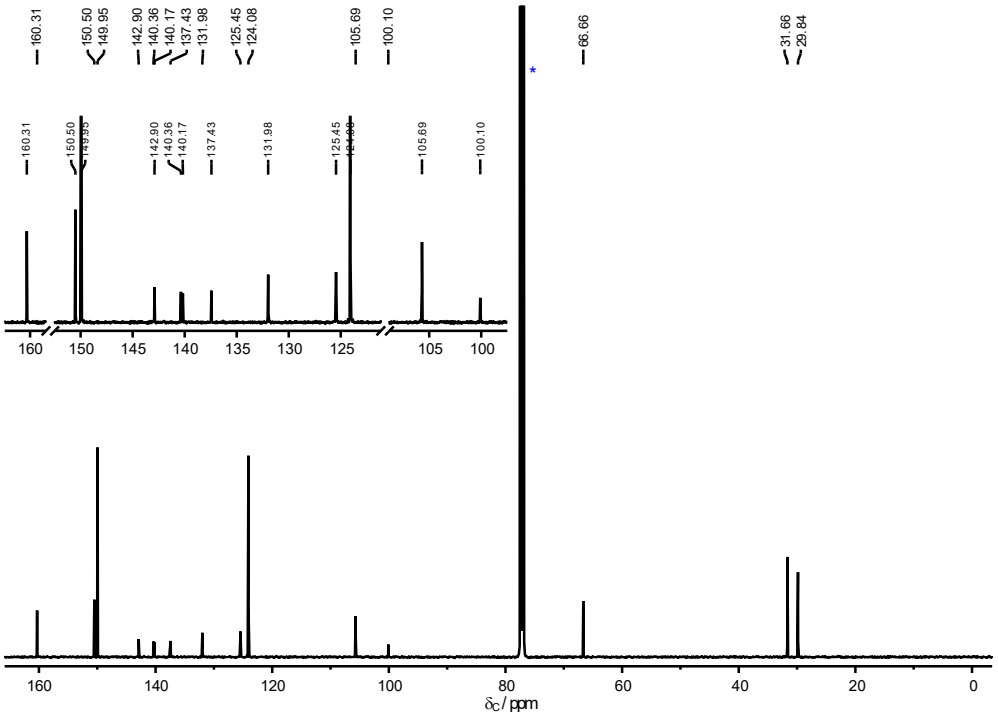

Figure B.40: ^{13}C NMR spectrum of **T2$_{Bpin}$** (101 MHz, $CDCl_3$, 298 K). * = $CDCl_3$.

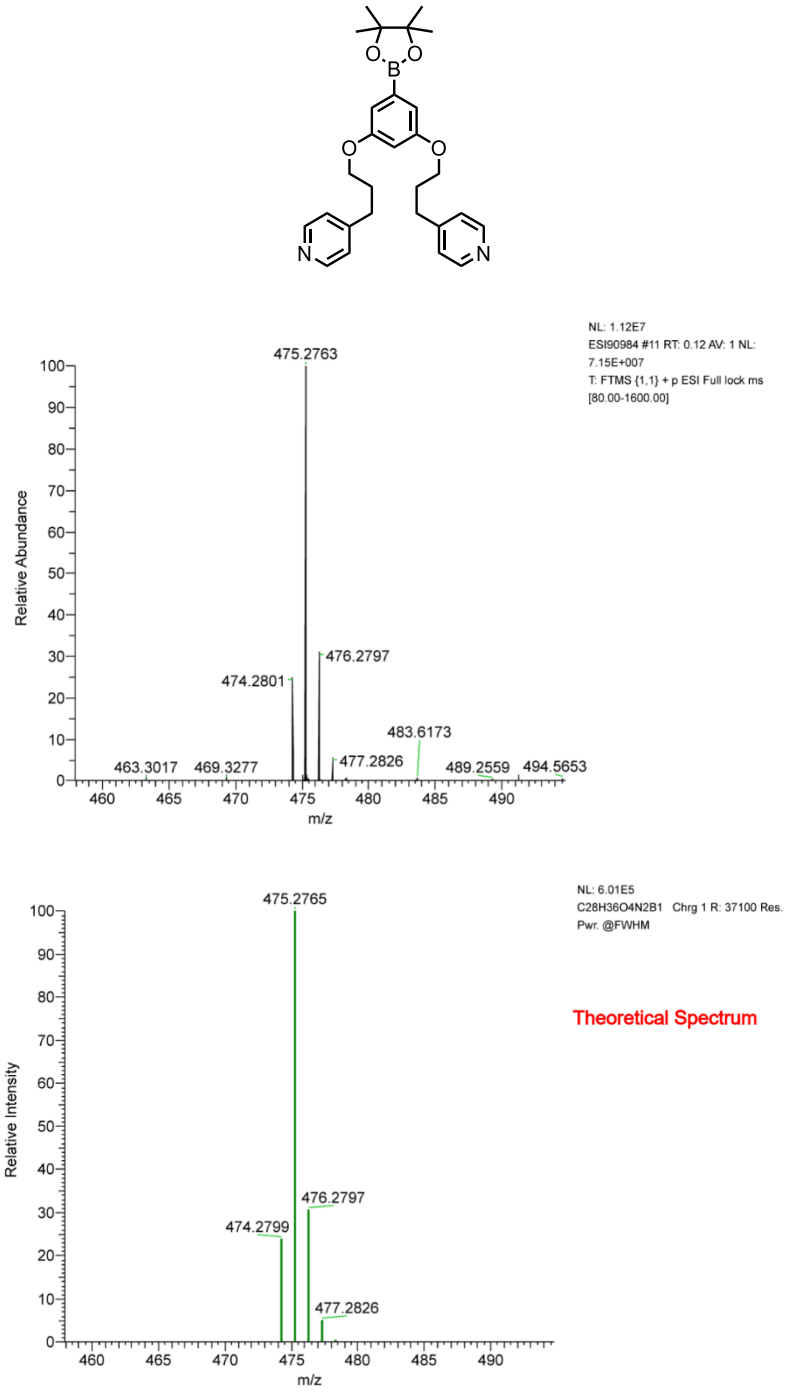

Figure B.41: ESI mass spectra of **T2$_{Bpin}$.**

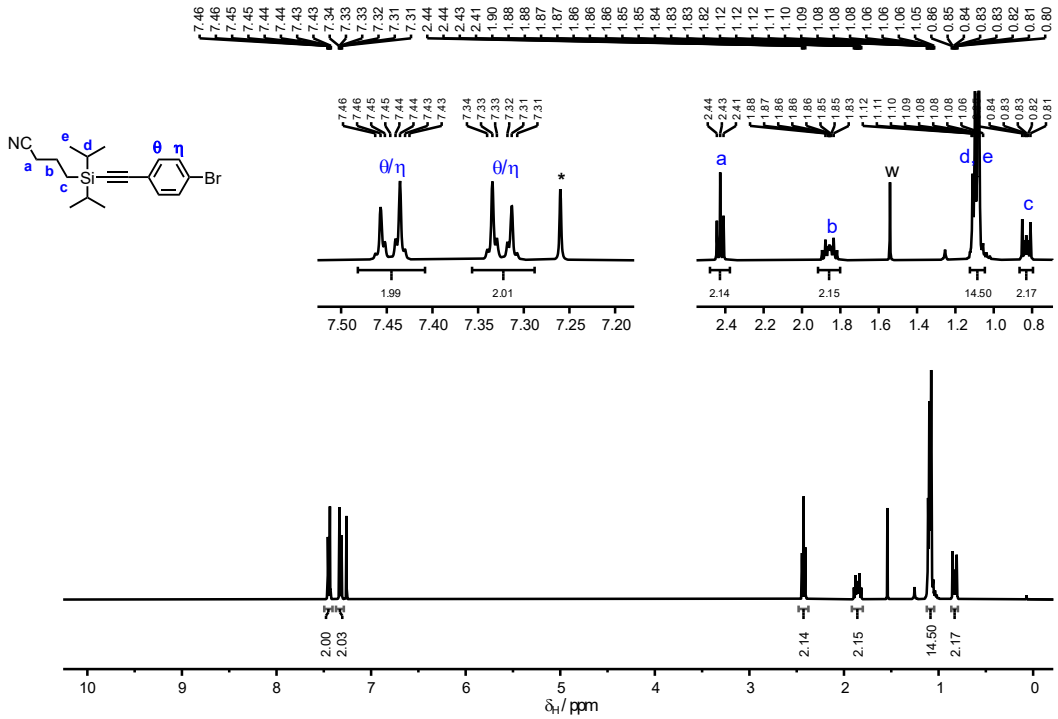

Figure B.42: ^{1}H NMR spectrum of **2.1** (400 MHz, $CDCl_3$, 298 K). * = $CHCl_3$; w = water.

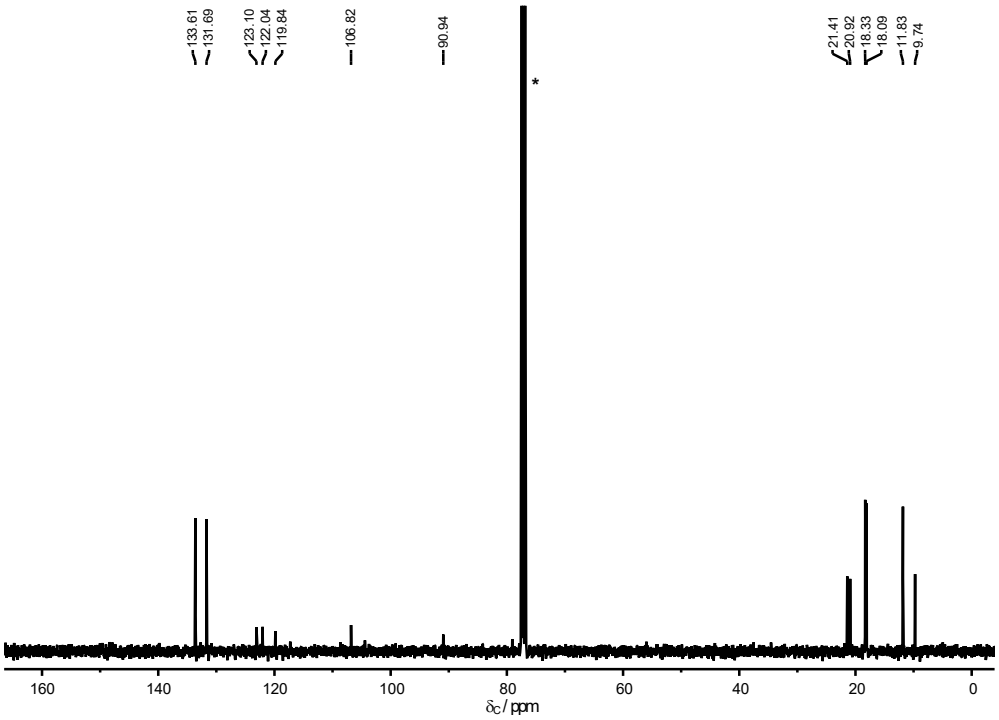

Figure B.43: ^{13}C NMR spectrum of **2.1** (101 MHz, $CDCl_3$, 298 K). * = $CDCl_3$.

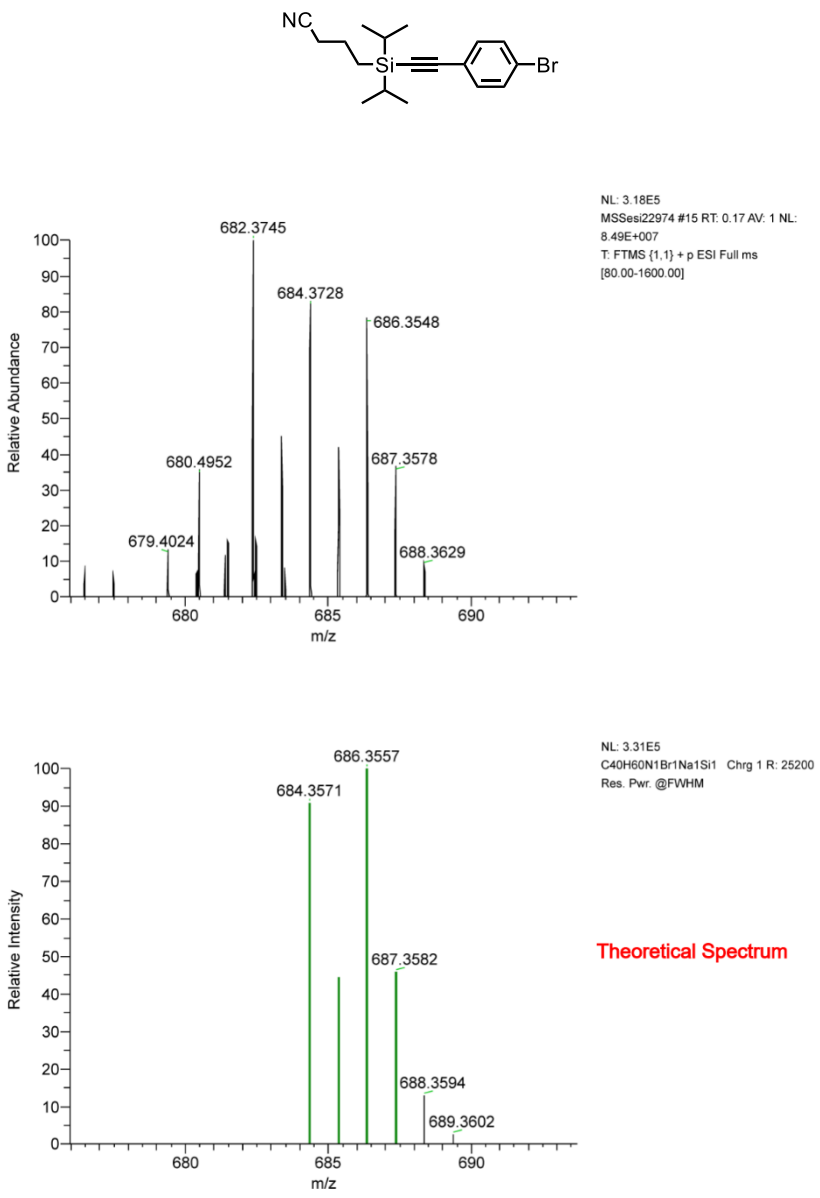

Figure B.44: ESI mass spectra of **2.1**.

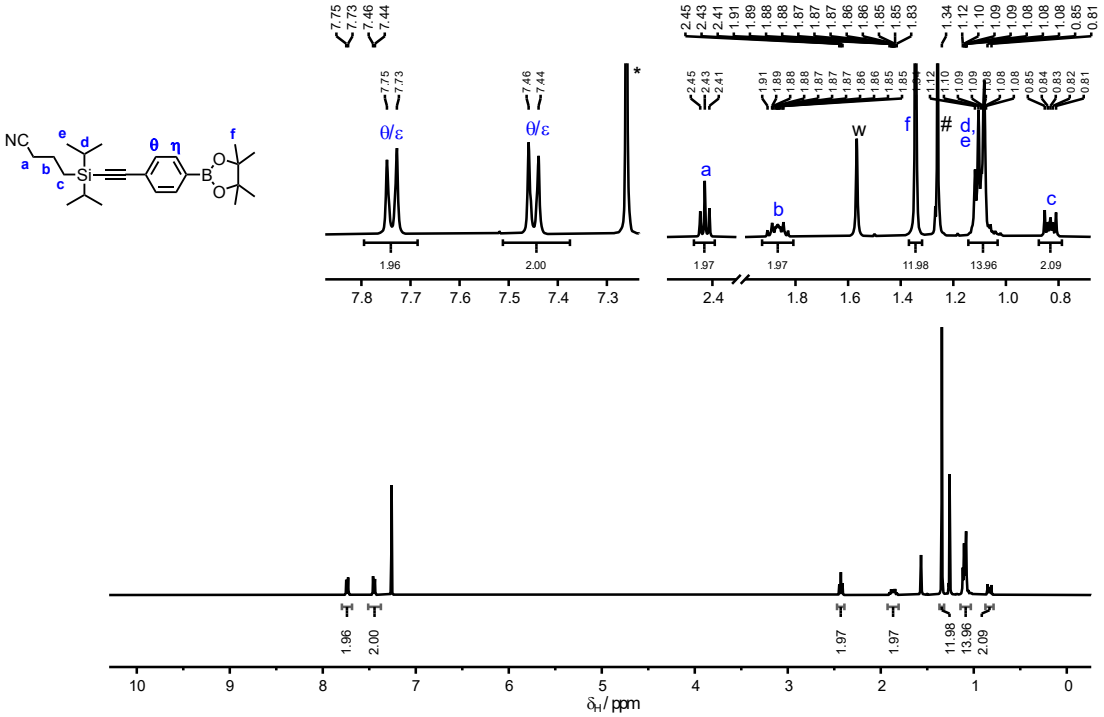

Figure B.45: ^{1}H NMR spectrum of **2.2** (400 MHz, $CDCl_3$, 298 K). * = $CHCl_3$; w = water; # = B_2pin_2.

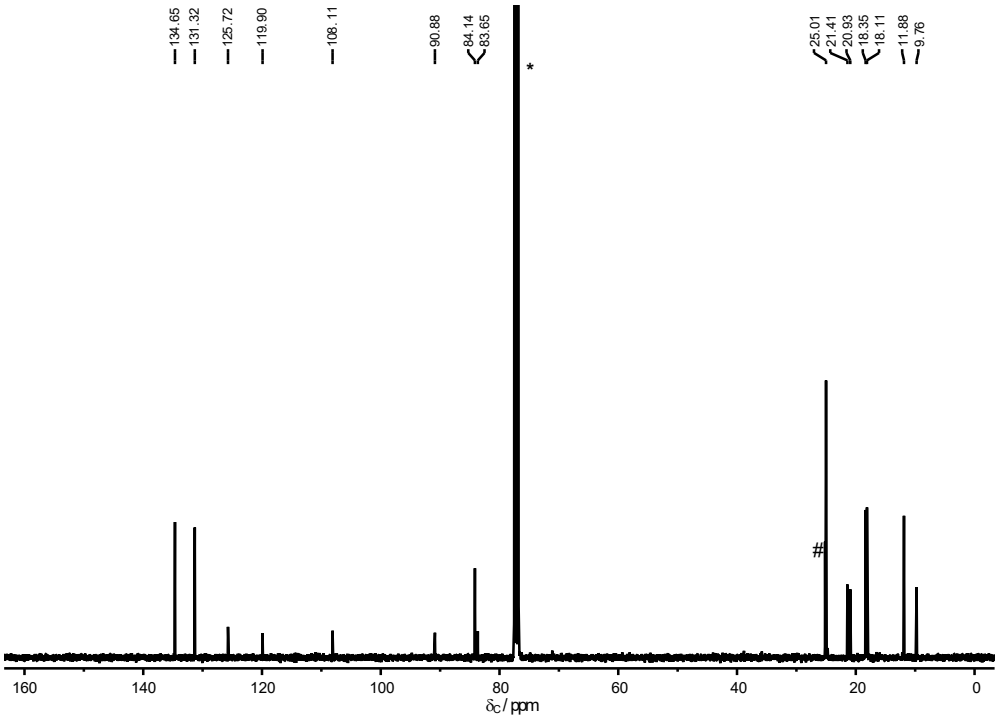

Figure B.46: ^{13}C NMR spectrum of **2.2** (101 MHz, $CDCl_3$, 298 K). * = $CDCl_3$; # = B_2pin_2.

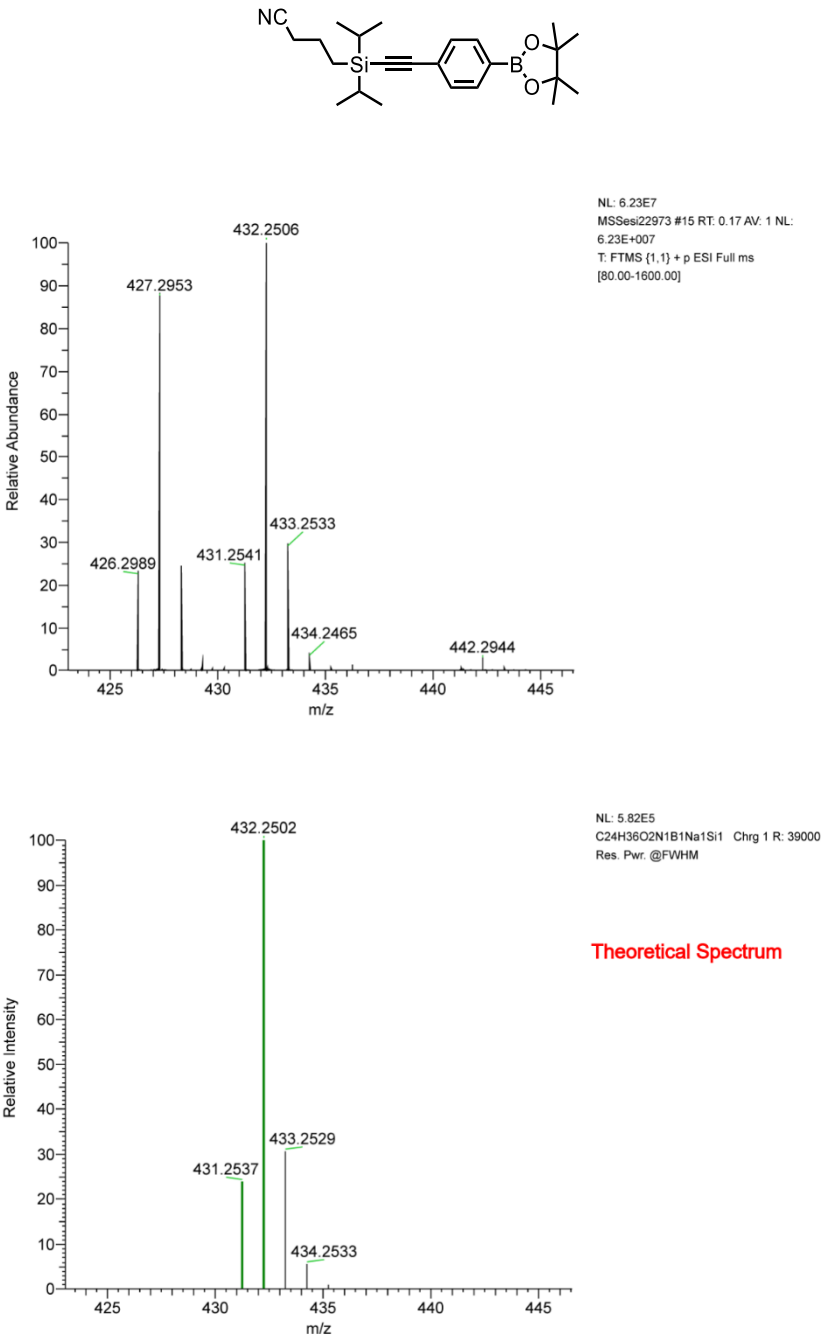

Figure B.47: ESI mass spectra of **2.2**.

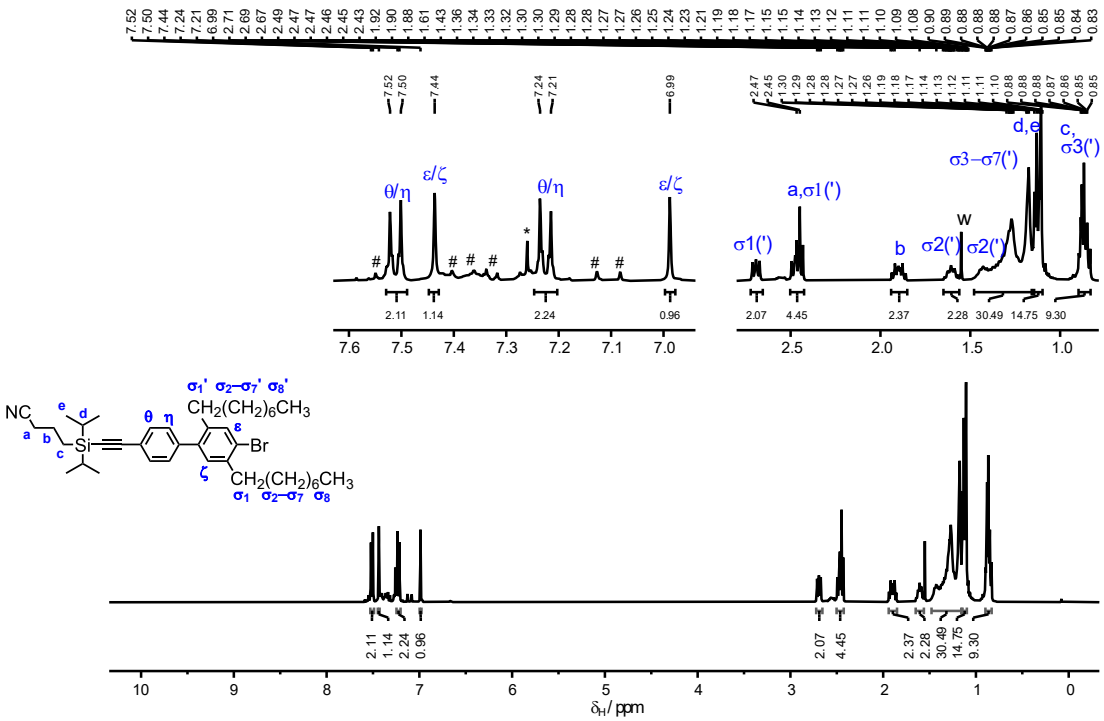

Figure B.48: ^{1}H NMR spectrum of **2.3** (400 MHz, $CDCl_3$, 298 K). * = $CHCl_3$; w = water # = unidentified impurity.

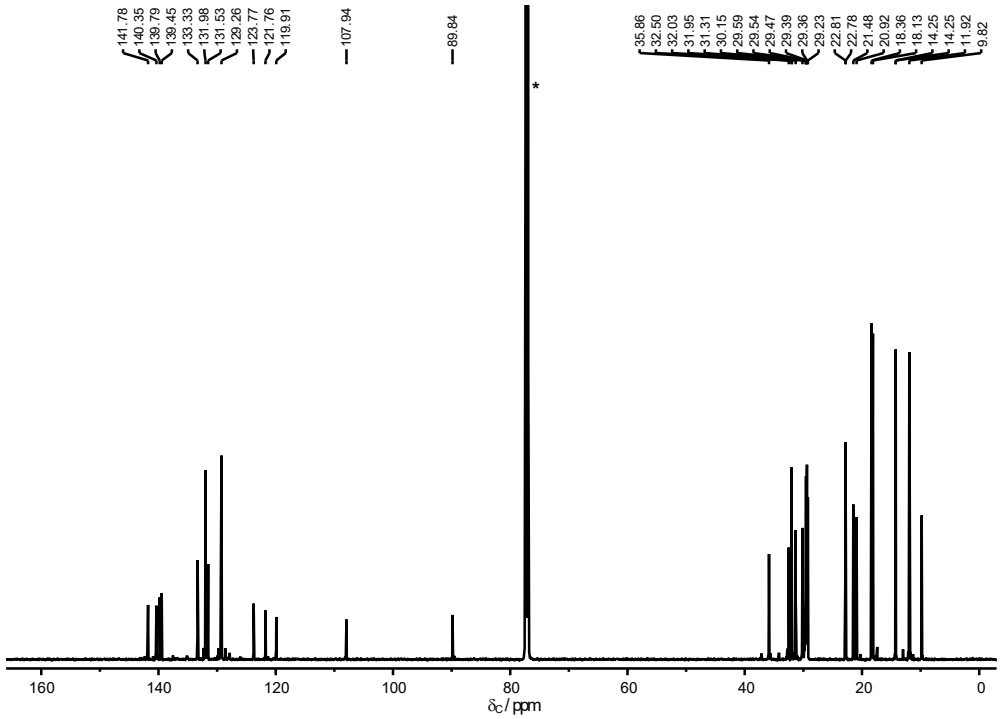

Figure B.49: ^{13}C NMR spectrum of **2.3** (101 MHz, $CDCl_3$, 298 K). * = $CDCl_3$.

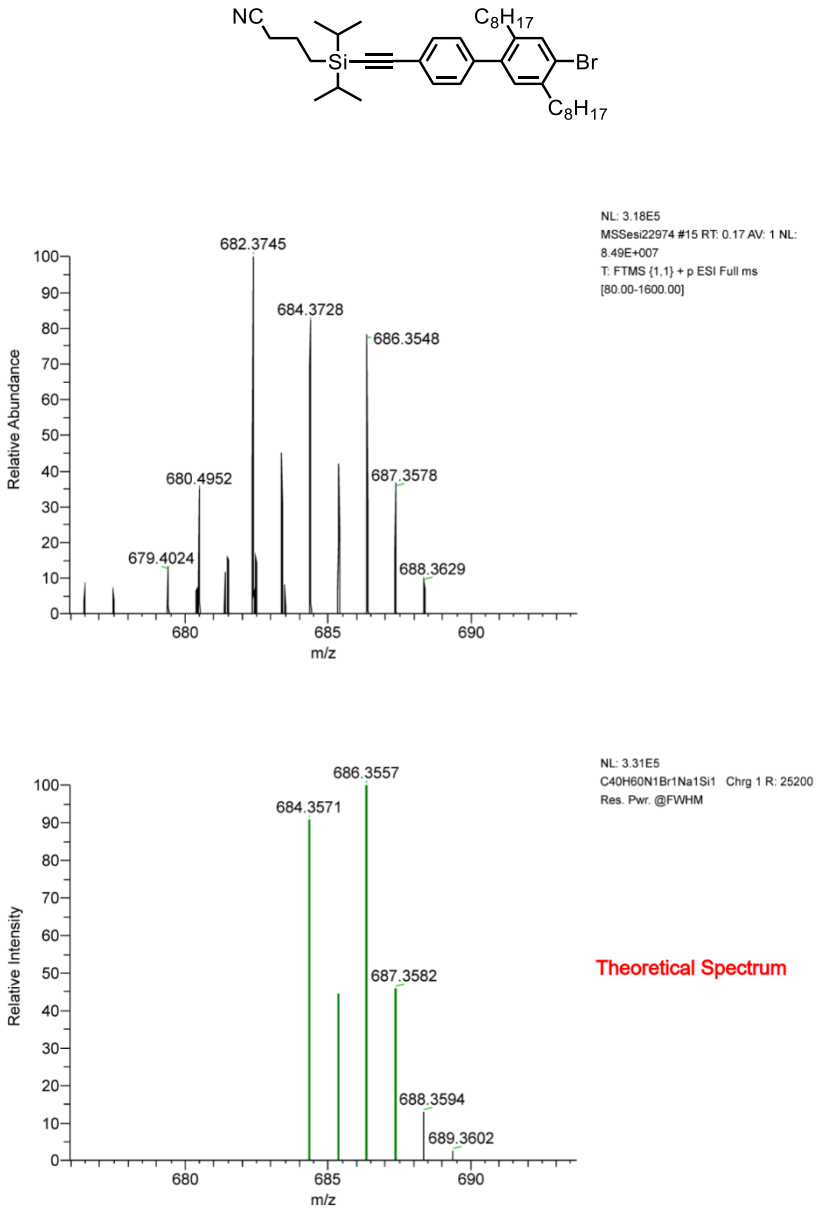

Figure B.50: ESI mass spectra of **2.3**.

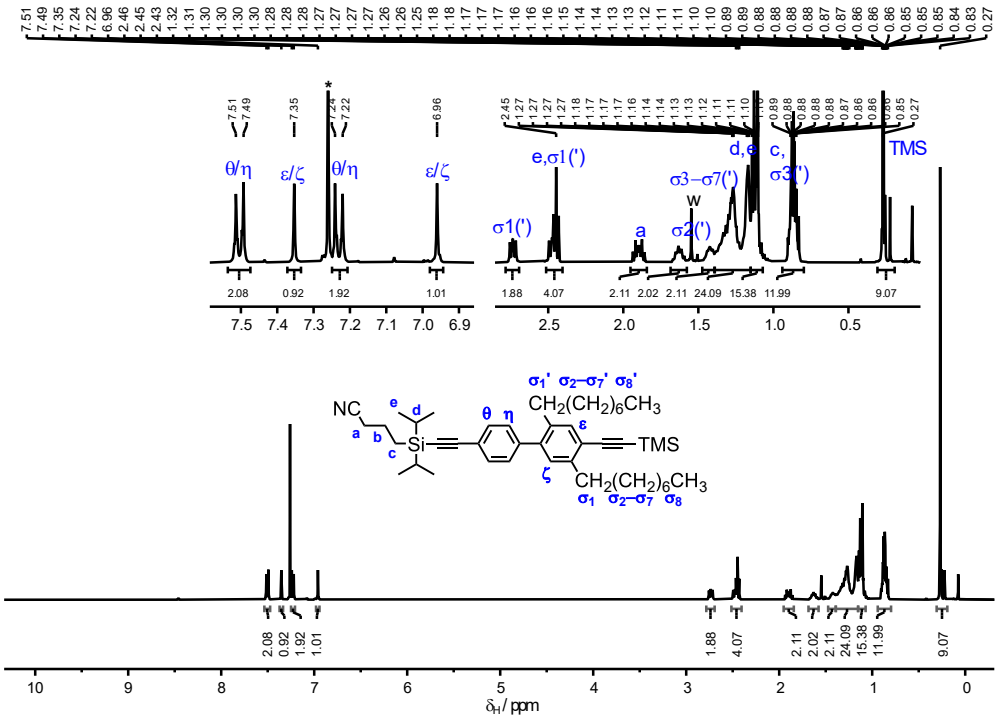

Figure B.51: ^{1}H NMR spectrum of **2.4** (400 MHz, $CDCl_3$, 298 K). * = $CHCl_3$; w = water.

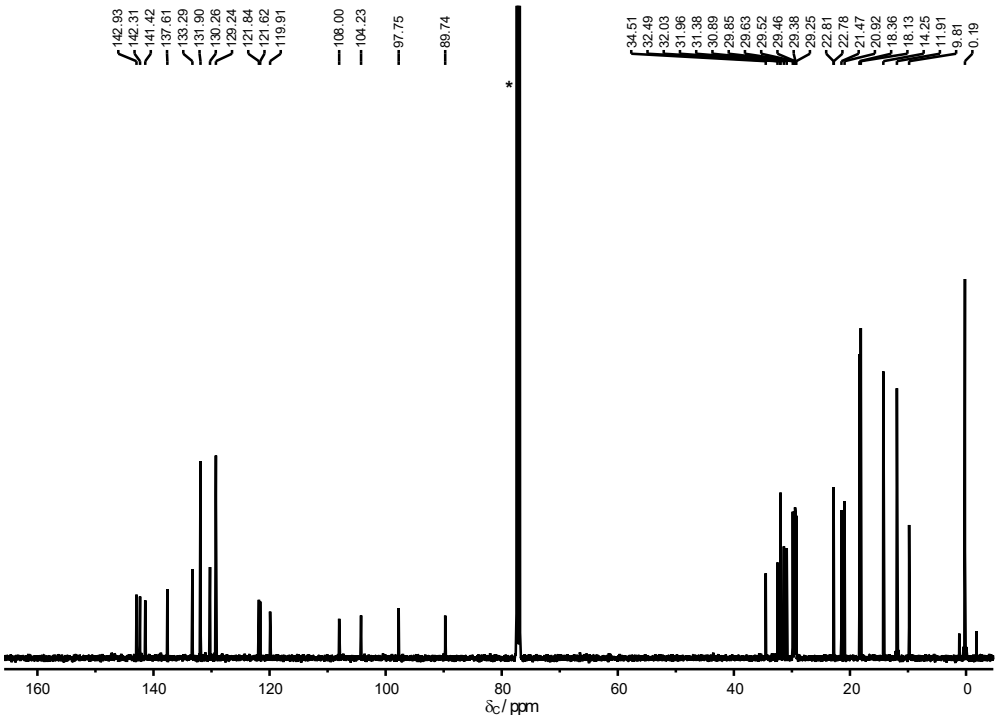

Figure B.52: ^{13}C NMR spectrum of **2.4** (101 MHz, $CDCl_3$, 298 K). * = $CDCl_3$.

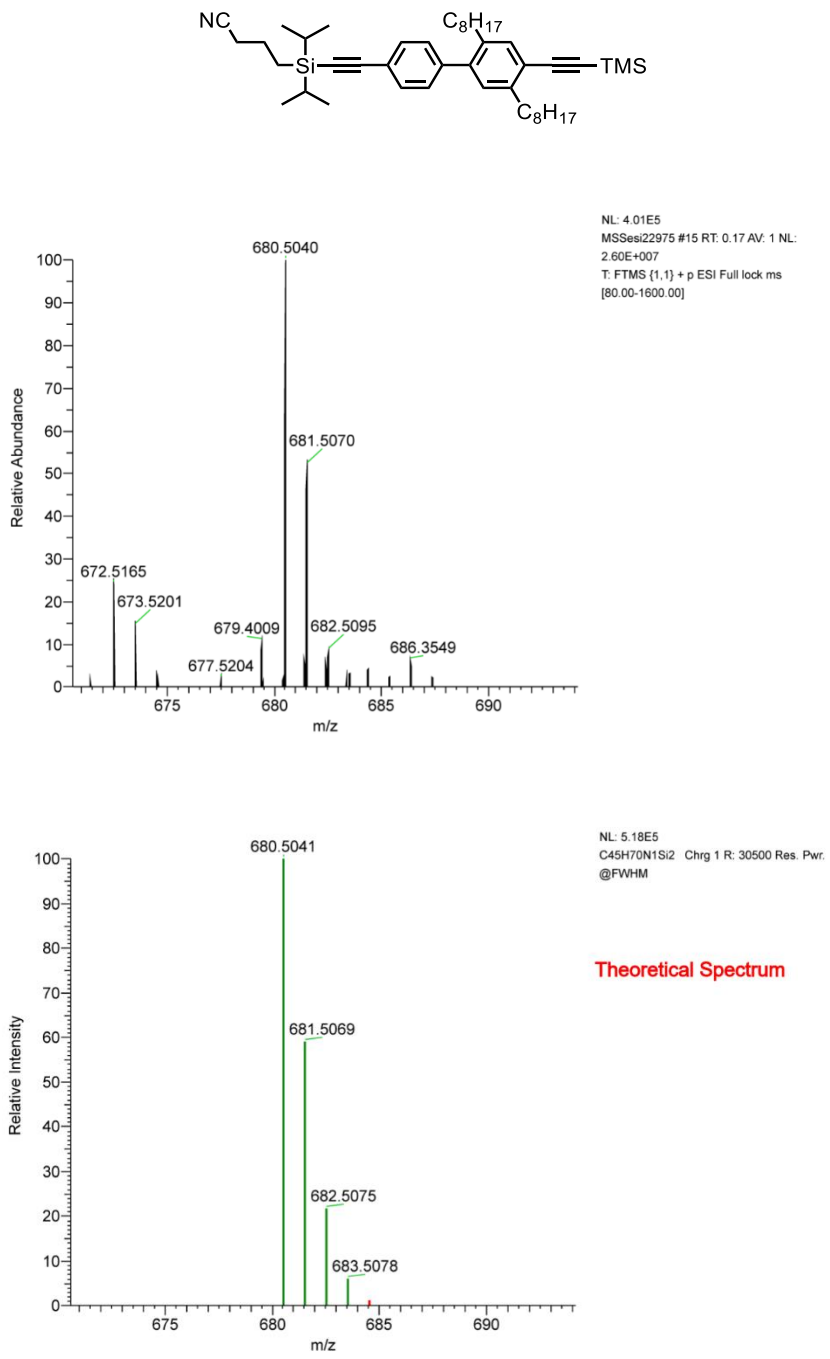

Figure B.53: ESI mass spectra of **2.4**.

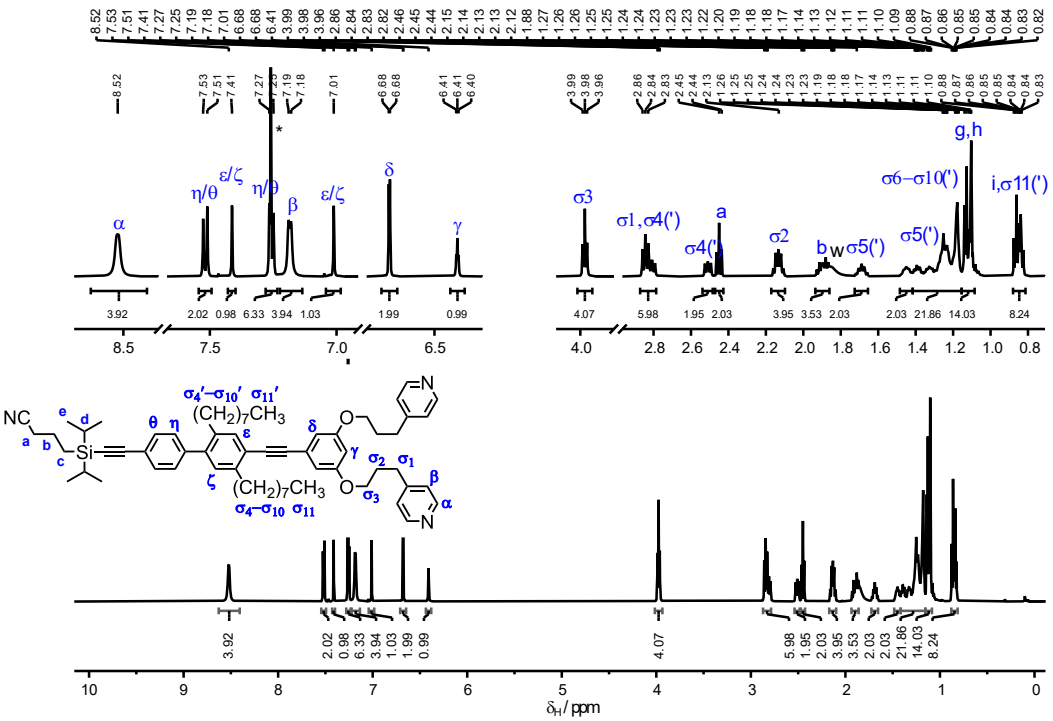

Figure B.54: ^{1}H NMR spectrum of **2.5** (500 MHz, $CDCl_3$, 298 K). * = $CHCl_3$; w = water.

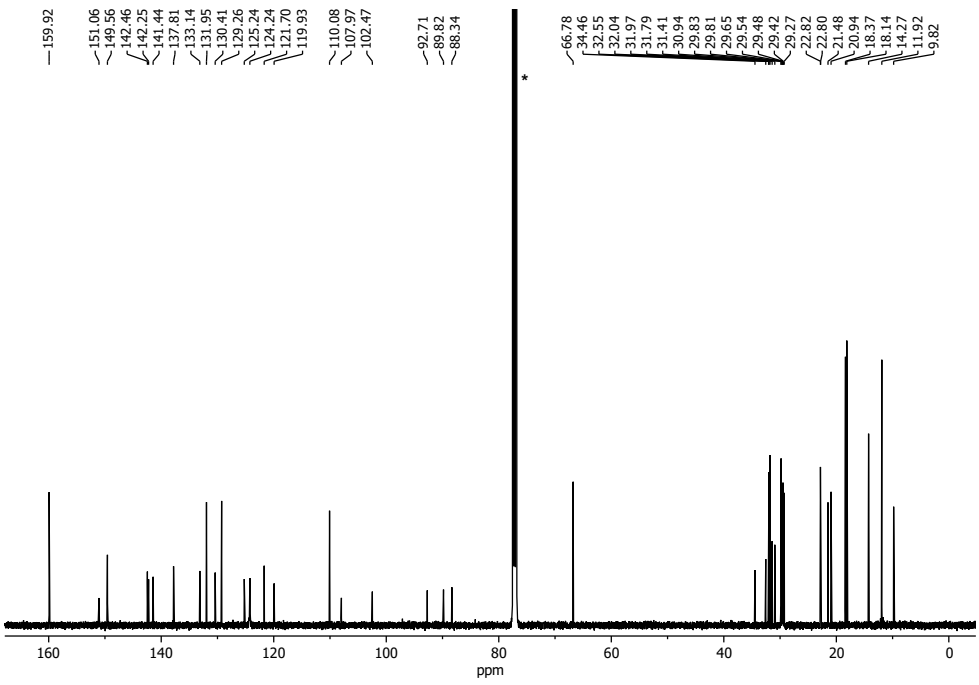

Figure B.55: ^{13}C NMR spectrum of **2.5** (126 MHz, $CDCl_3$, 298 K). * = $CDCl_3$.

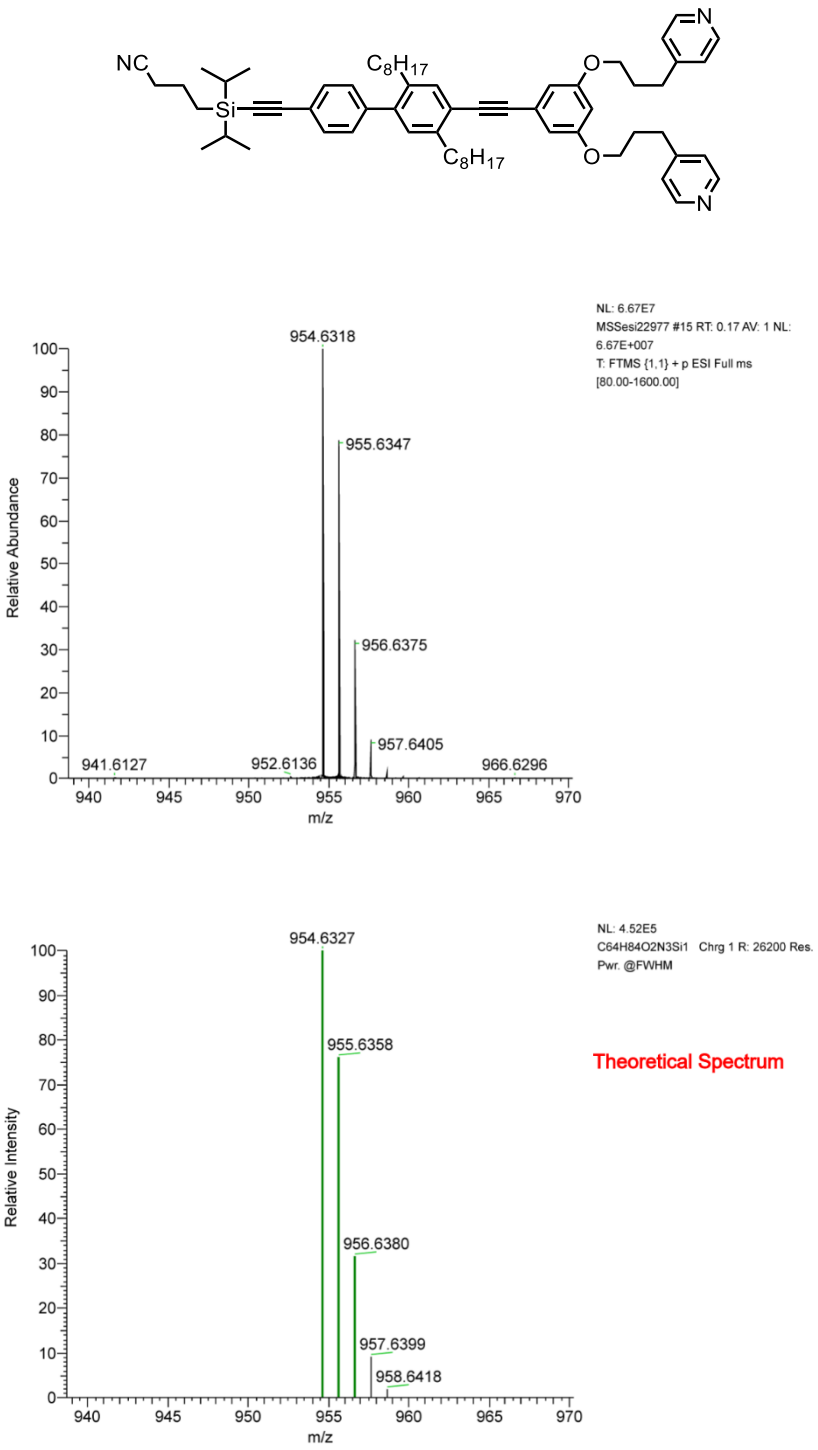

Figure B.56: ESI mass spectra of **2.5**.

Table B.7: ^{1}H NMR assignment and 2D correlations of the **T12e** template. Key ^{1}H-^{1}H NOE correlations are indicated with double-headed arrows.

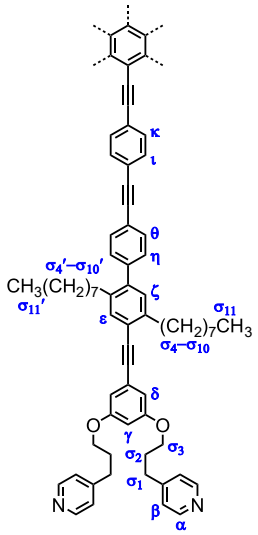

#	Assign.	^{1}H	Mult.	COSY	NOESY[a]	HSQC	HMBC[a]
1	α	8.62–8.40	(m, 4H)	6	s: 6	150.48 (CH)	s: 150.48, 124.10
2	ι/κ	7.66	(d, *J* = 8.2 Hz, 2H)	3	s: 3	131.95/131.92 (CH)	s: 131.95/131.92, 124.29, 99.71; m: 131.56
3	ι/κ + θ	7.64–7.58	(m, 4H)	2, 5	s: 5; m: 12	131.95/131.92+131.56 (CH)	s: 142.18, 131.95/131.92, 131.56, 122.83, 92.08, 89.60+89.11; m: 129.43
4	ε	7.43	(s, 1H)	-	s: 12; m: 8;	133.19 (CH)	s: 142.50, 142.18, 141.44, 88.30, 32.60; w: 130.41, 34.49
5	η	7.32	(d, *J* = 8.0 Hz, 2H)	3	w: 12	129.43 (CH)	s: 129.43, 121.66; m: 141.44, 131.56; w: 92.08
6	β	7.15	(d, *J* = 5.7 Hz, 4H)	1	m: 11, 13; w: 10	124.10 (CH)	s: 150.01, 124.10, 31.71
7	ζ	7.06	(s, 1H)	-	s: 11; m: 3, 5	130.41 (CH)	s: 142.18, 137.86, 121.73, 34.49; m: 133.19
8	δ	6.68	(d, *J* = 2.2 Hz, 2H)	9	m: 4, 9, 11; w: 10, 13	110.09 (CH)	s: 159.94, 110.09, 102.47, 92.76
9	γ	6.42	(t, *J* = 2.1 Hz, 1H)	8	m: 8, 10; w: 11, 13	102.47 (CH)	s: 159.94, 110.09; w: 125.20
10	σ_3	3.97	(t, *J* = 6.0 Hz, 4H)	13	s: 13; m: 9, 11; w: 6, 8	66.80 (CH_2)	s: 159.94, 31.71, 29.85/29.83
11	σ_1+σ_4	2.89–2.77	(m, 6H)	13, 14	s: 7, 13; m: 6, 8, 10, 14; w: 9	34.49+31.71 (CH_2)	s: 150.48, 124.10, 66.80, 29.85/29.83; m: 142.50, 130.41, 30.98; w: 121.66
12	σ_4’	2.54	(t, *J* = 8.0 Hz, 2H)	15	s: 4; m: 15; w: 3, 5	32.60 (CH_2)	s: 133.19; m: 137.86, 31.41; w: 141.44, [29.65, 29.56, 29.48, 29.40, 29.29]
13	σ_2	2.17–2.08	(m, 4H)	10, 11	s: 10, 11; m: 6; w: 9	29.85+29.83 (CH_2)	s: 150.48, 66.80, 31.71
14	σ_5/σ_5’	1.71	(p, *J* = 7.7 Hz, 2H)	11, 15	m: 11, 15; w: 8	30.98 (CH_2)	w: 142.50, 34.49, [29.85, 29.83]
15	σ_5/σ_5’ σ_6-σ_{10} σ_6’-σ_{10}’	1.51–1.14	(m, 22H)	12, 14, 16, 17	s: 16, 17; m: 12, 14	32.04, 31.99, 31.41, 29.85, 29.65, 29.56, 29.48, 29.40, 29.29, 22.82 (CH_2)	s: [32.04, 31.99], [29.65, 29.56, 29.48, 29.40, 29.29]; m: 22.82, [14.28, 14.26]
16	σ_{11}/σ_{11}’ (CH_3)	0.86	(t, *J* = 7.1 Hz, 3H)	15	s: 15	14.28/14.26 (CH_3)	s: [32.04, 31.99], 22.82
17	σ_{11}/σ_{11}’ (CH_3)	0.84	(t, *J* = 6.9 Hz, 3H)	15	s: 15	14.28/14.26 (CH_3)	s: [32.04, 31.99], 22.82

[a] Relative intensities of NOE and HMBC correlations are labeled as s, m, or w for strong, medium, or weak.

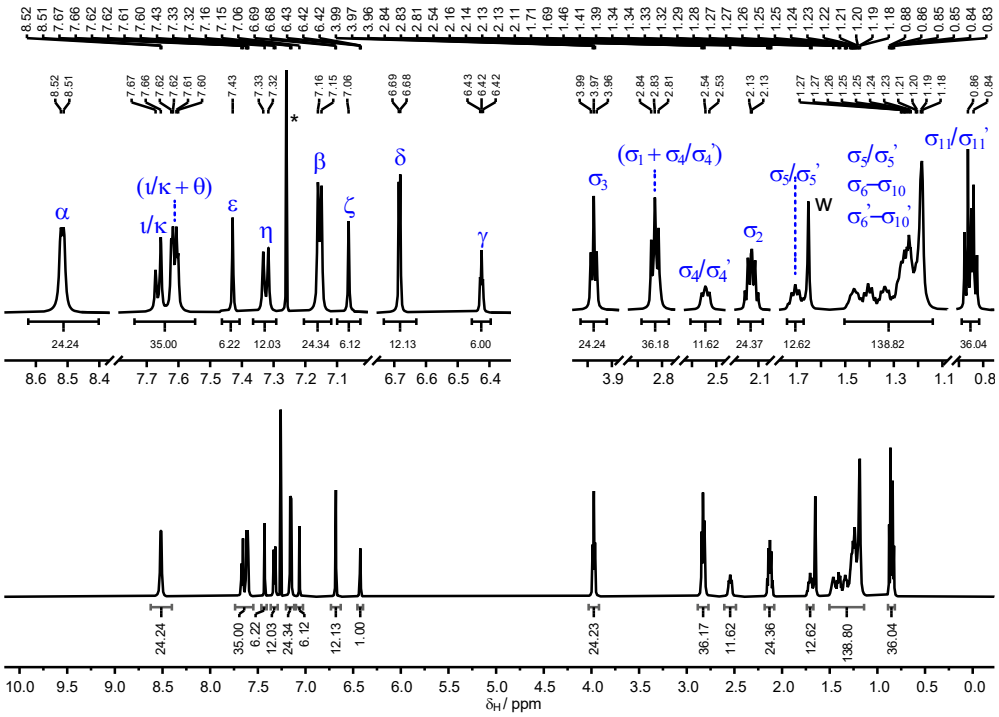

Figure B.57: ^{1}H NMR spectrum of **T12e** (500 MHz, $CDCl_3$, 298 K). * = $CHCl_3$; w = water.

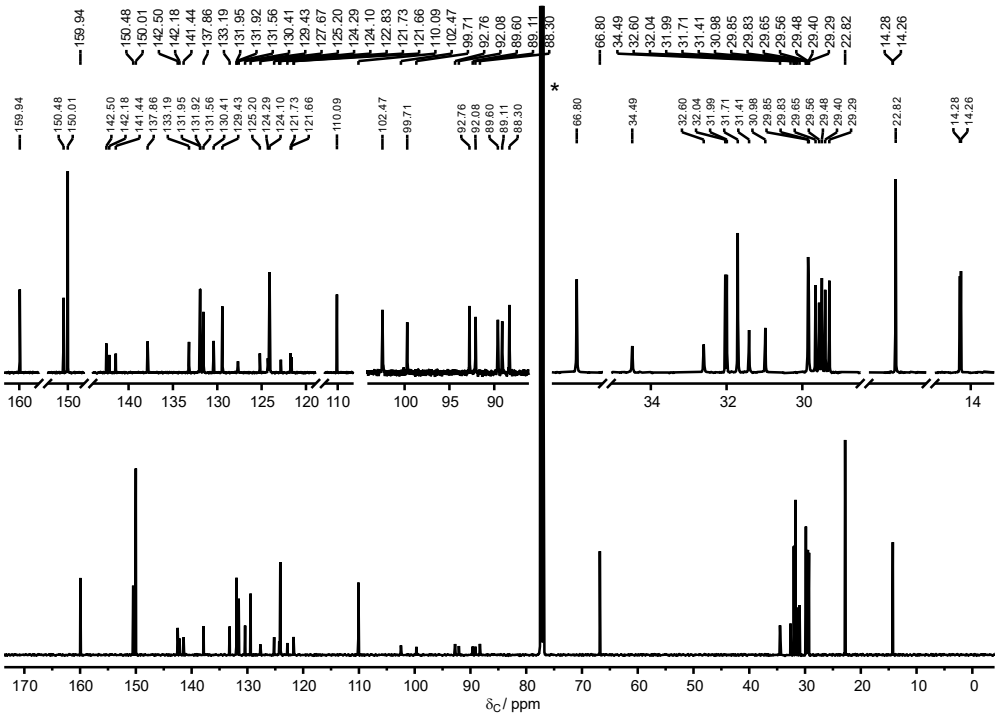

Figure B.58: ^{13}C NMR spectrum of **T12e** (126 MHz, $CDCl_3$, 298 K). * = $CDCl_3$.

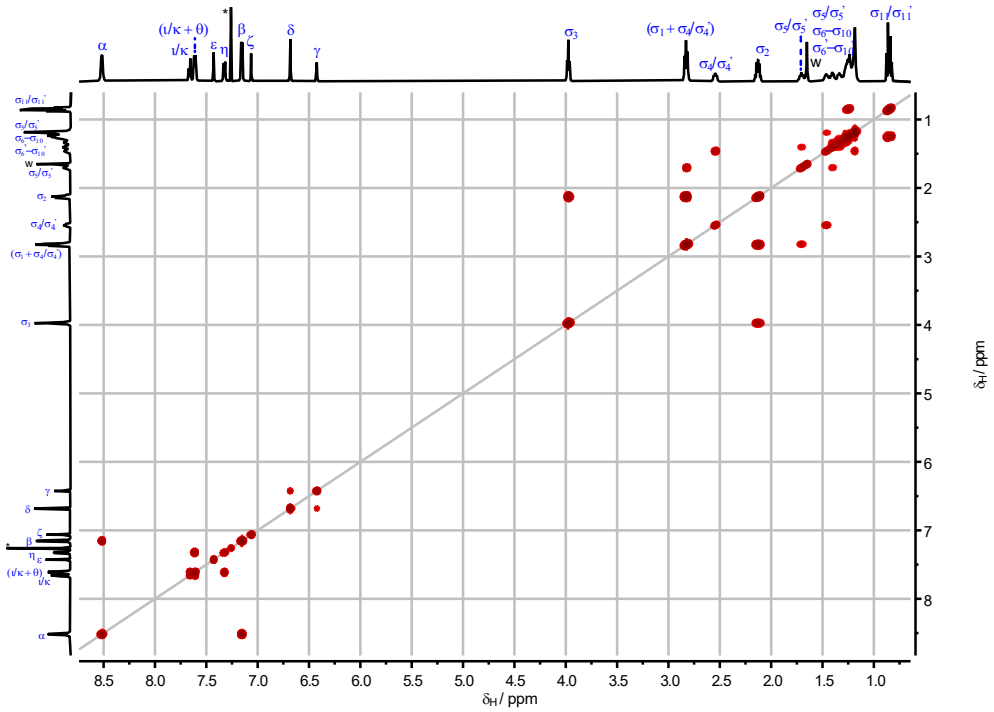

Figure B.59: COSY spectrum of **T12e** (500 MHz, $CDCl_3$, 298 K). * = $CHCl_3$; w = water.

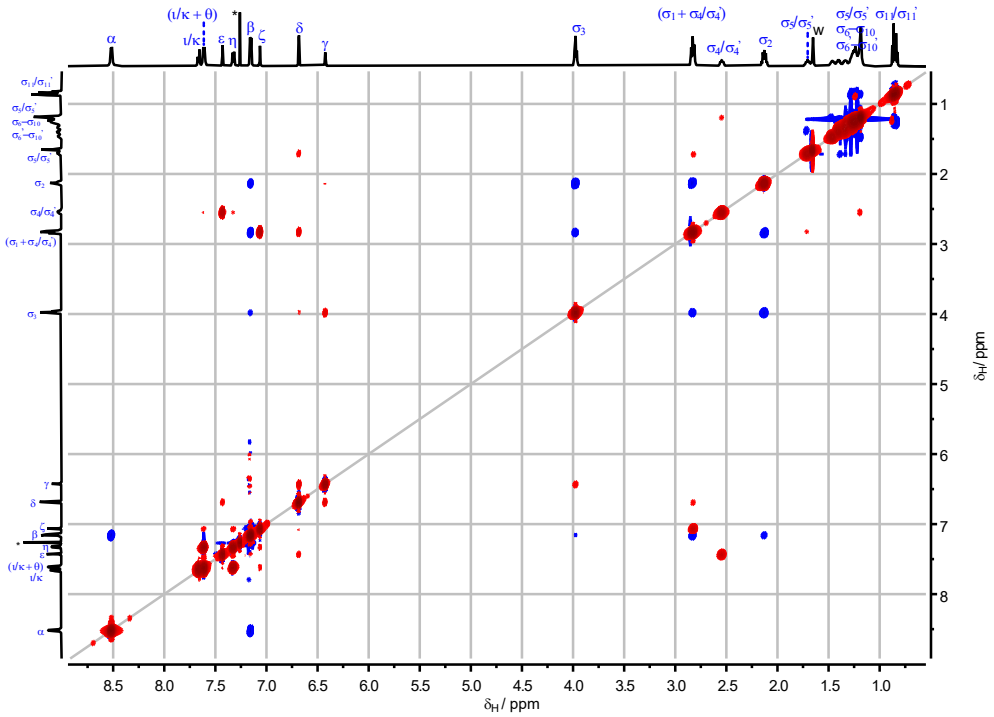

Figure B.60: NOESY spectrum of **T12e** (500 MHz, $CDCl_3$, 298 K, t_{mix} = 800 ms). * = $CHCl_3$; w = water.

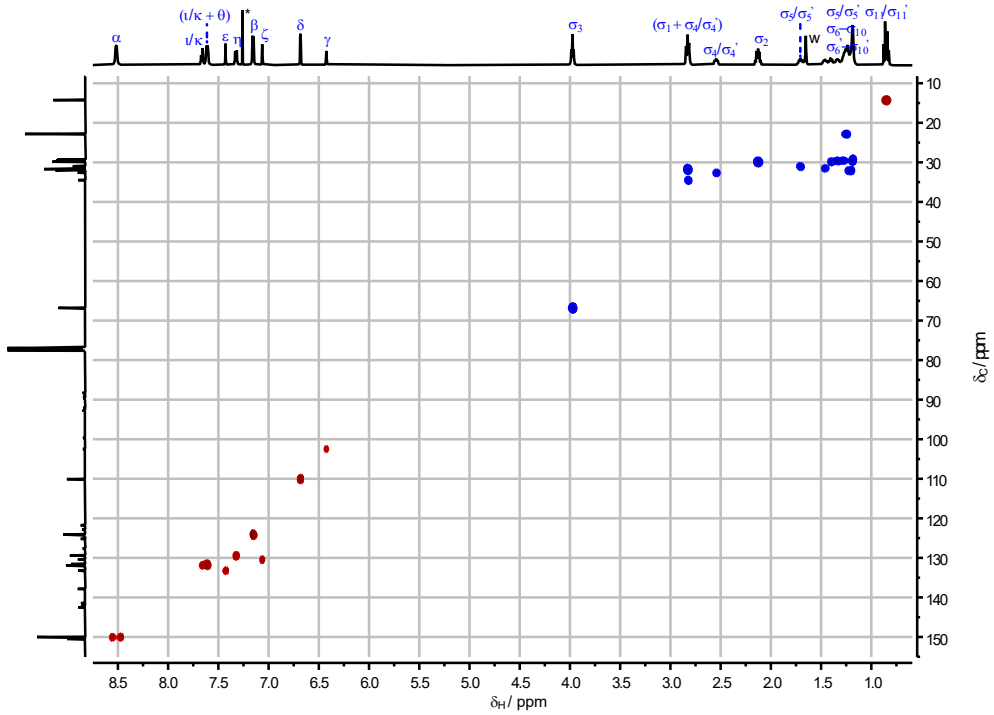

Figure B.61: HSQC spectrum of **T12e** (500 MHz, $CDCl_3$, 298 K). * = $CHCl_3$; w = water.

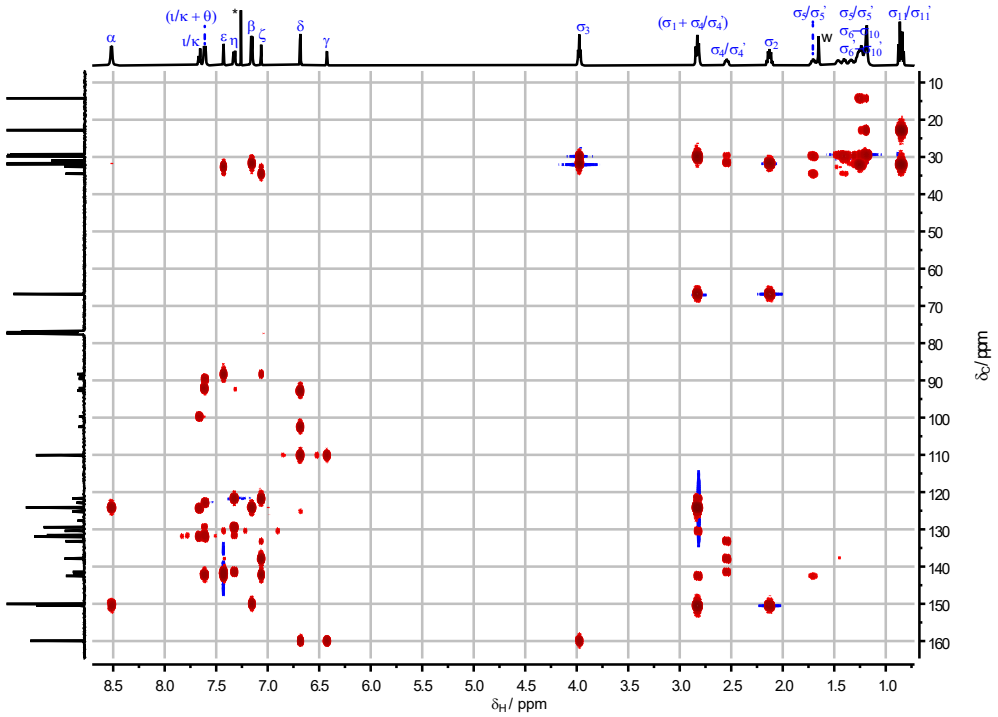

Figure B.62: HMBC spectrum of **T12e** (500 MHz, $CDCl_3$, 298 K). * = $CHCl_3$; w = water.

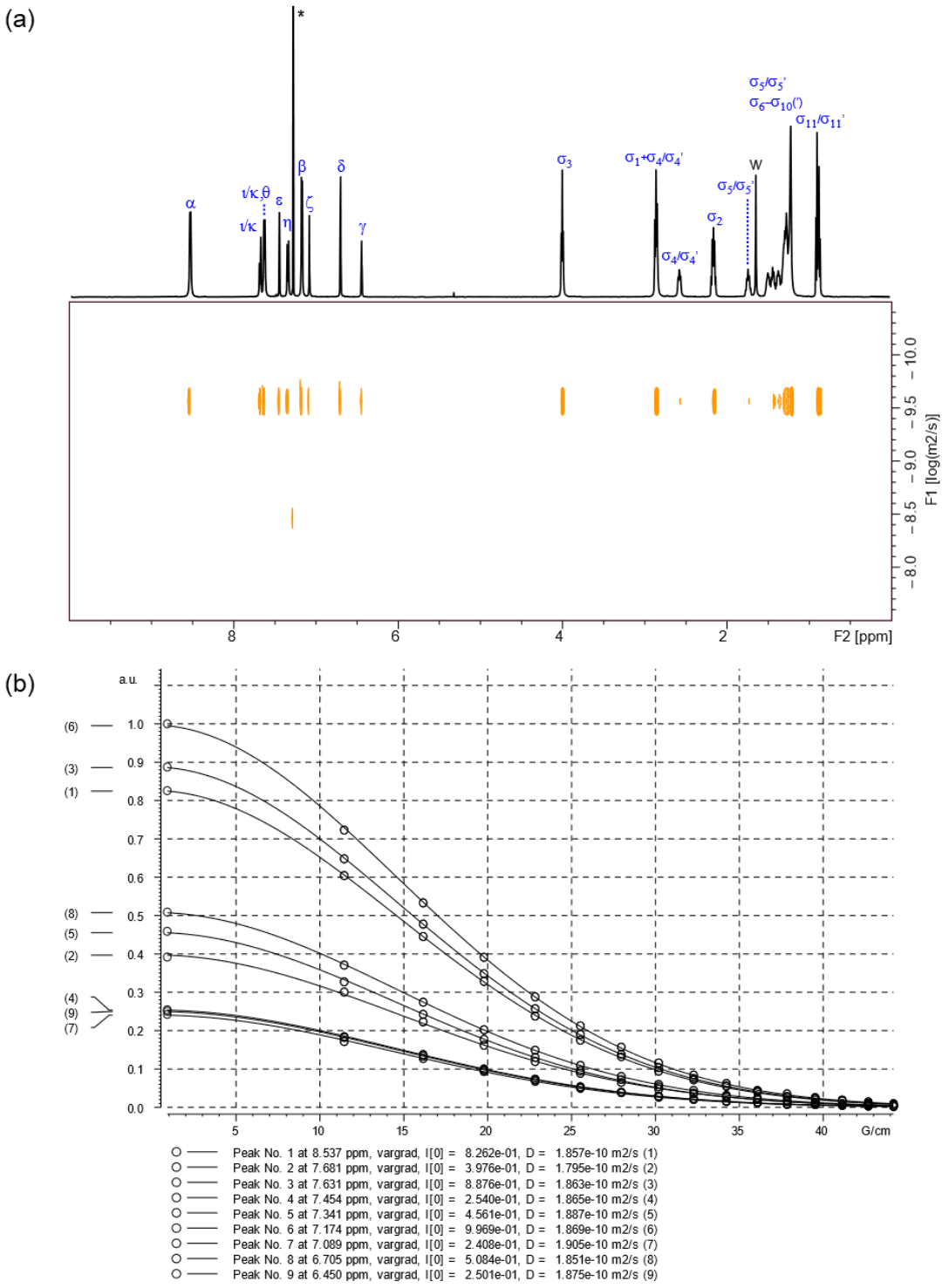

Figure B.63: ^{1}H diffusion NMR (500 MHz, $CDCl_3$, 298 K) of **T12e**. (a) ^{1}H DOSY plot. (b) Diffusion decay plots fitted to the Stejskal Tanner equation and the resulting diffusion coefficients obtained. Acquisition parameters: G = 0.90–44.19 G/cm, D = 0.1 s, and d = 4400 µs. The average diffusion coefficient $D = 1.86 \cdot 10^{-10}$ m^2s^{-1}. * = residual solvent peak, w = water peak.

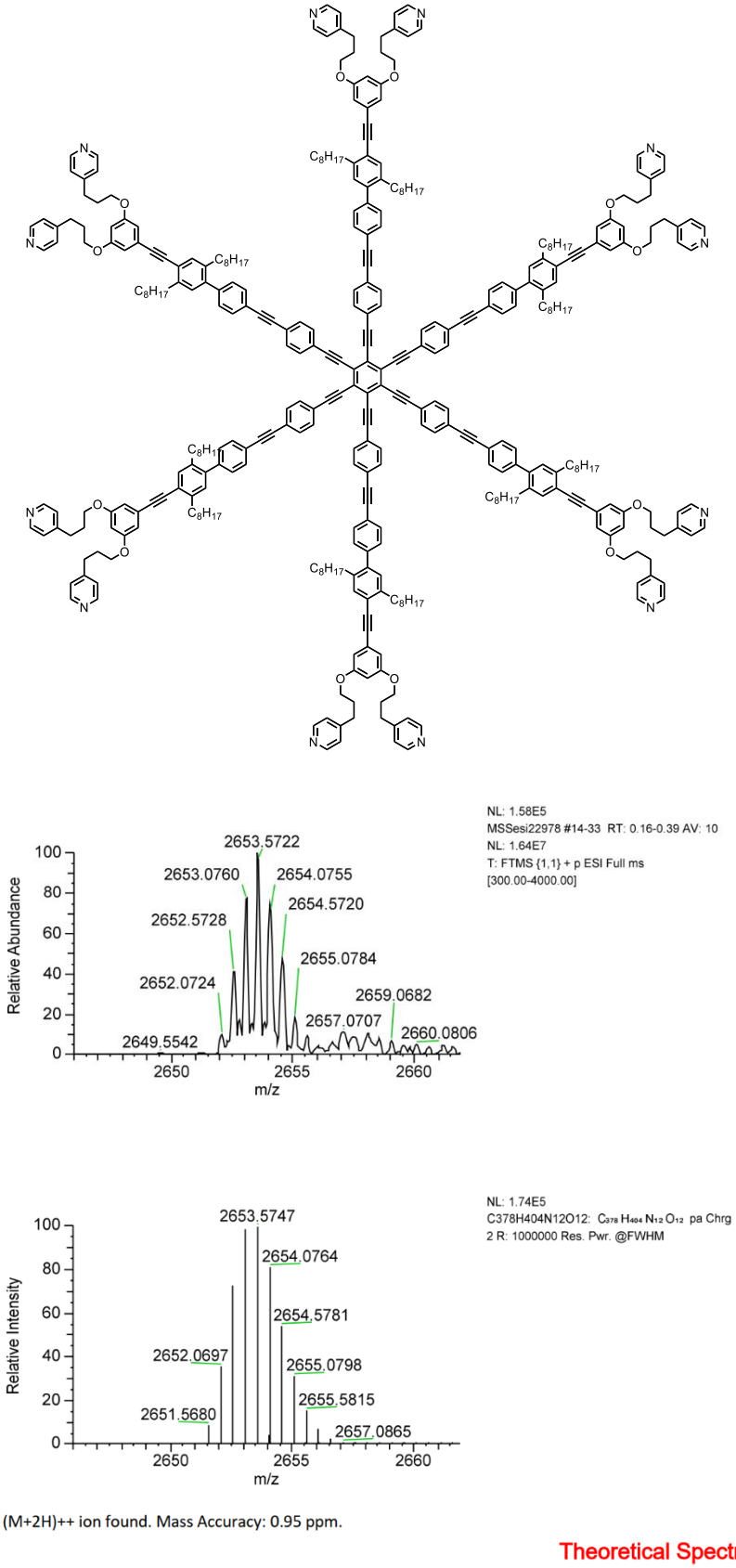

Figure B.64: ESI mass spectrum of **T12e**.

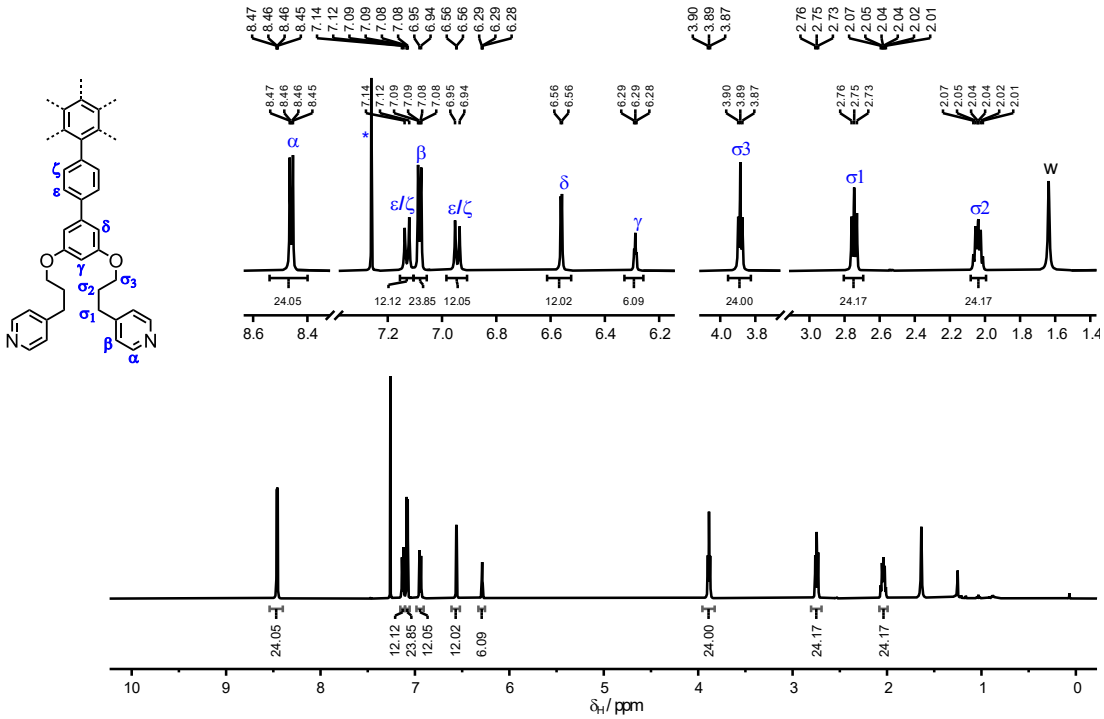

Figure B.65: ^{1}H NMR spectrum of **T12b** (500 MHz, $CDCl_3$, 298 K). * = $CHCl_3$; w = water.

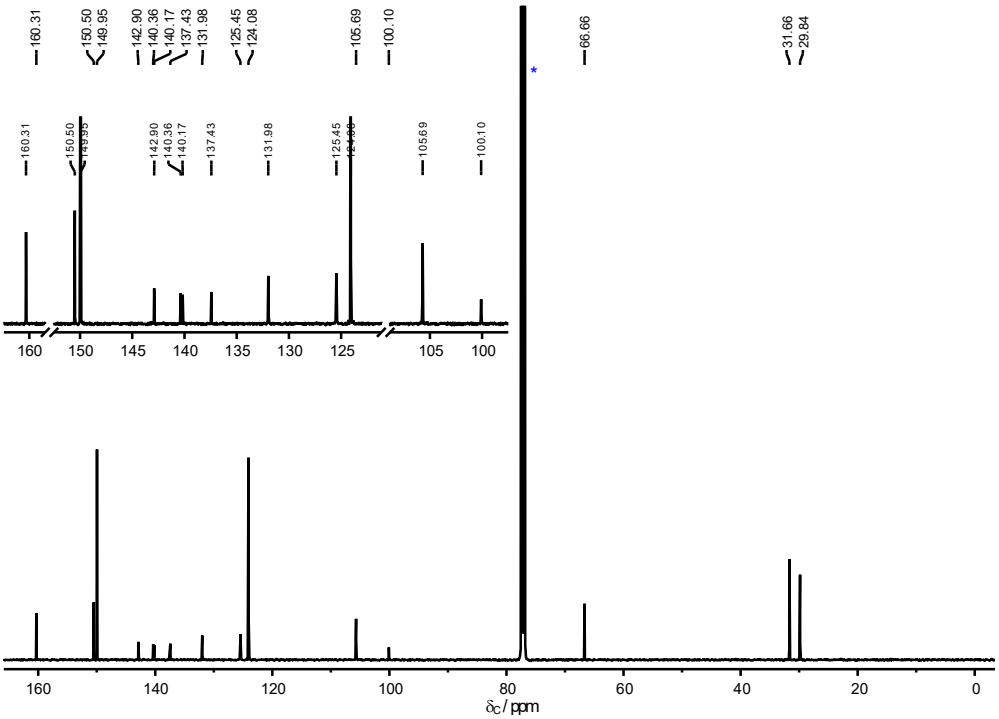

Figure B.66: ^{13}C NMR spectrum of **T12b** (126 MHz, $CDCl_3$, 298 K). * = $CDCl_3$.

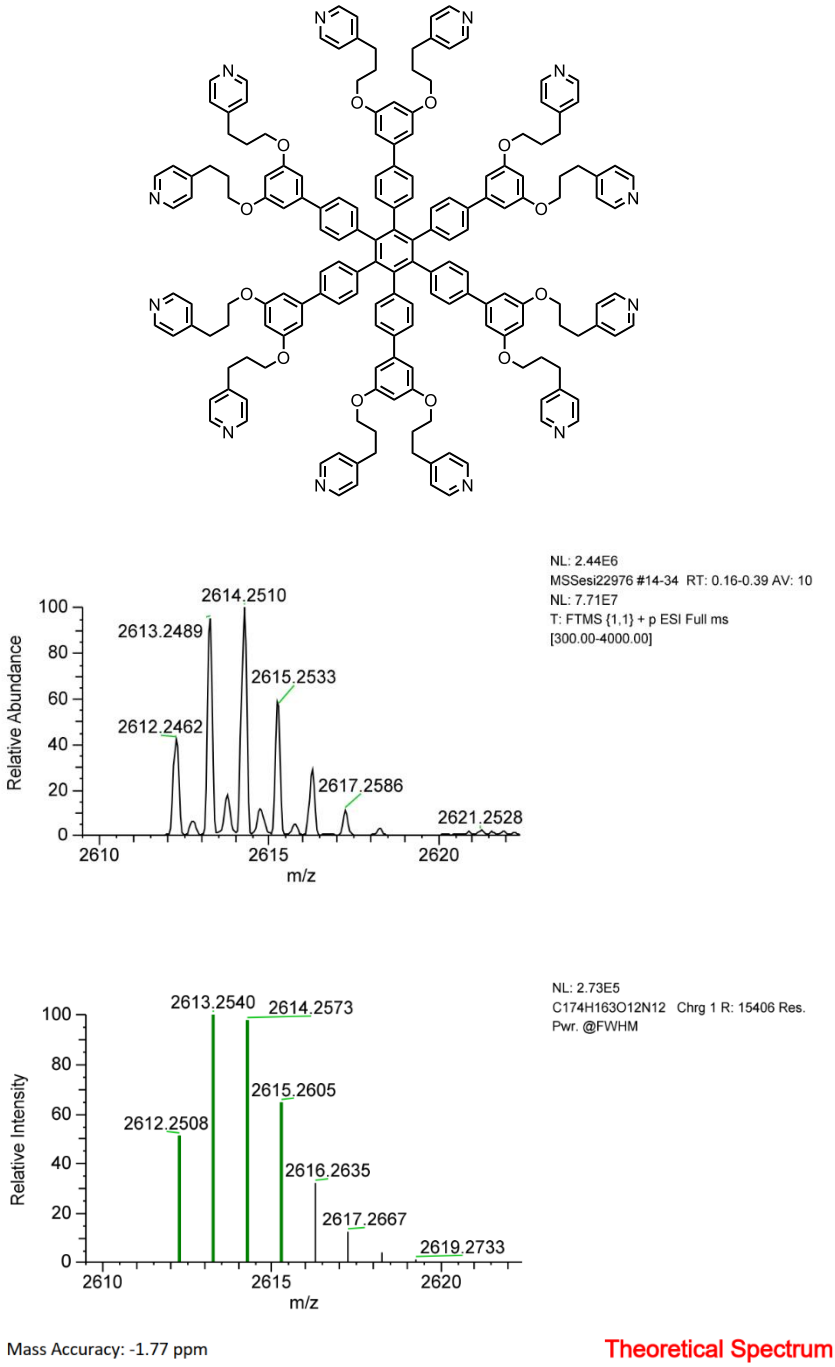

Figure B.67: ESI mass spectrum of **T12b**.

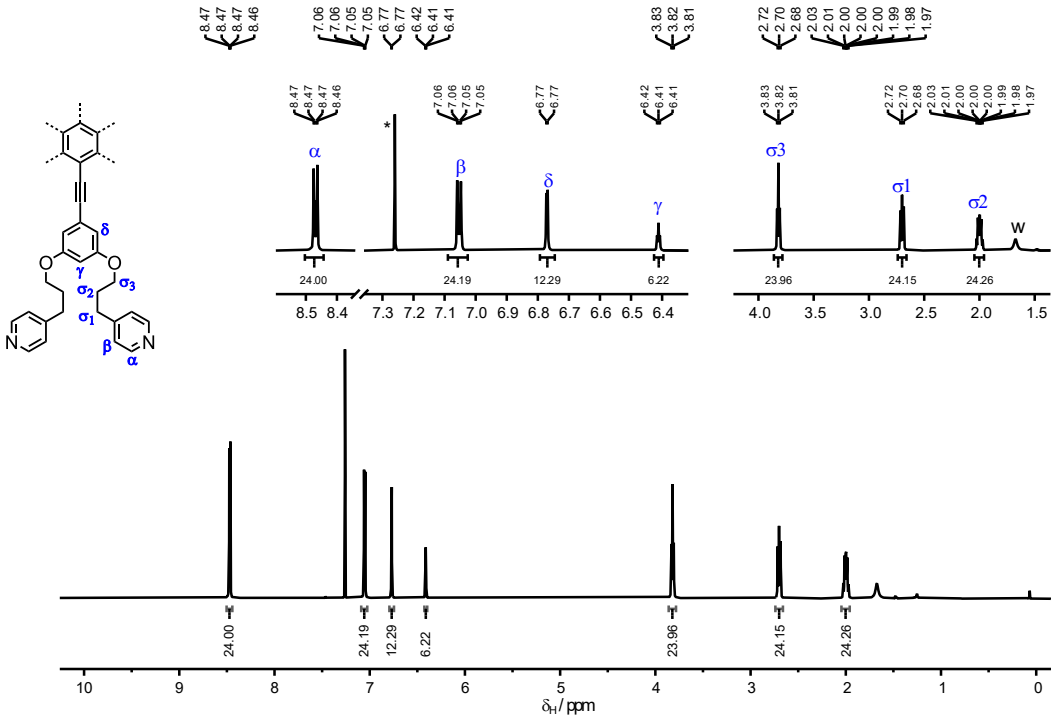

Figure B.68: ^{1}H NMR spectrum of **T12a** (500 MHz, $CDCl_3$, 298 K). * = $CHCl_3$; w = water.

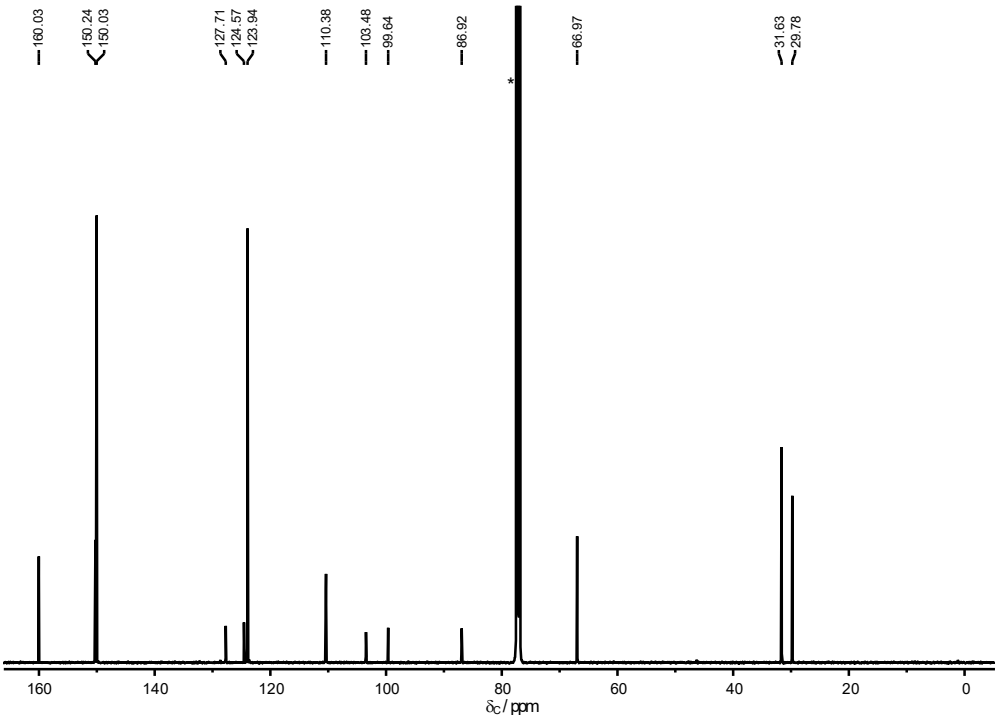

Figure B.69: ^{13}C NMR spectrum of **T12a** (126 MHz, $CDCl_3$, 298 K). * = $CDCl_3$.

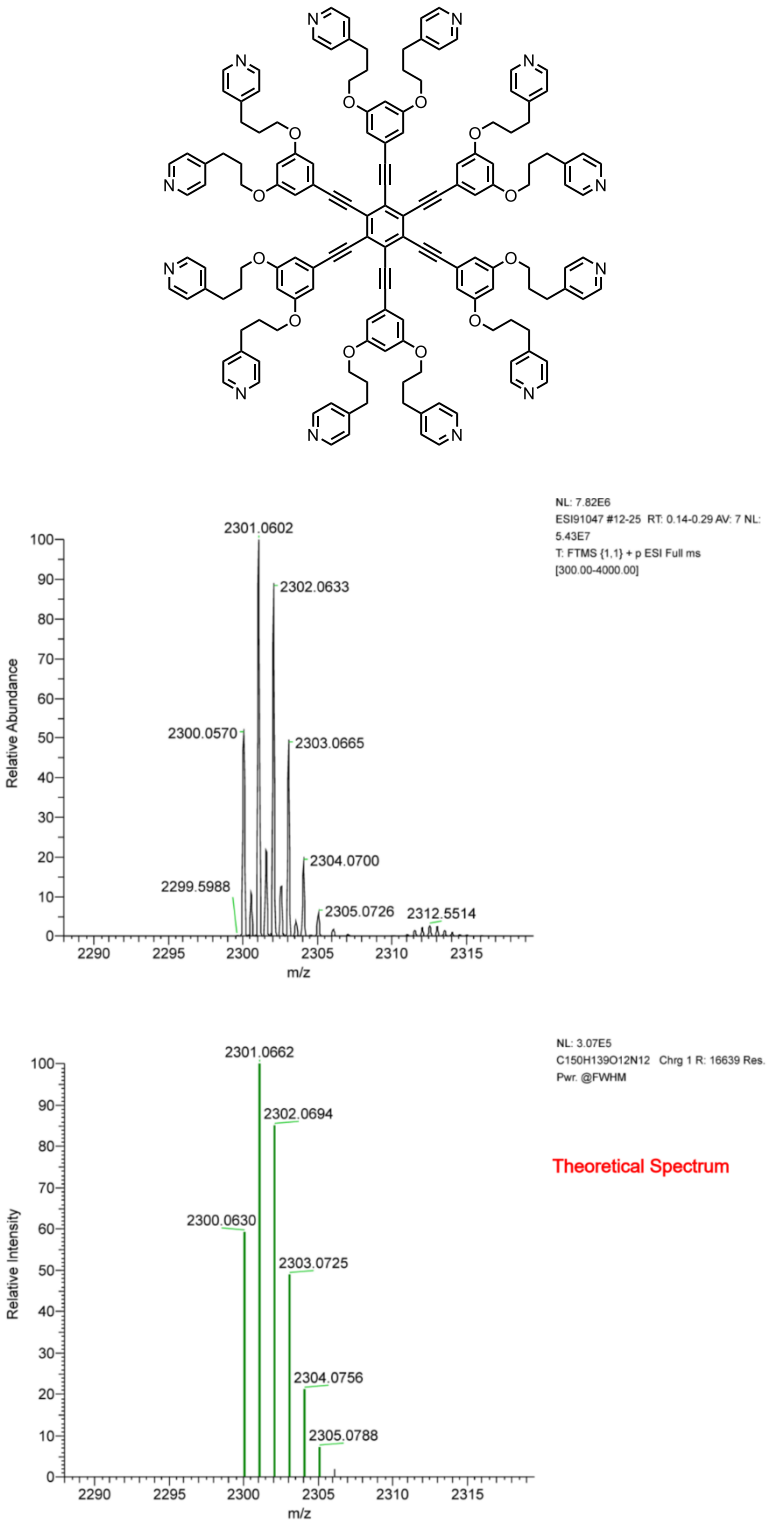

Figure B.70: ESI mass spectrum of **T12a**.

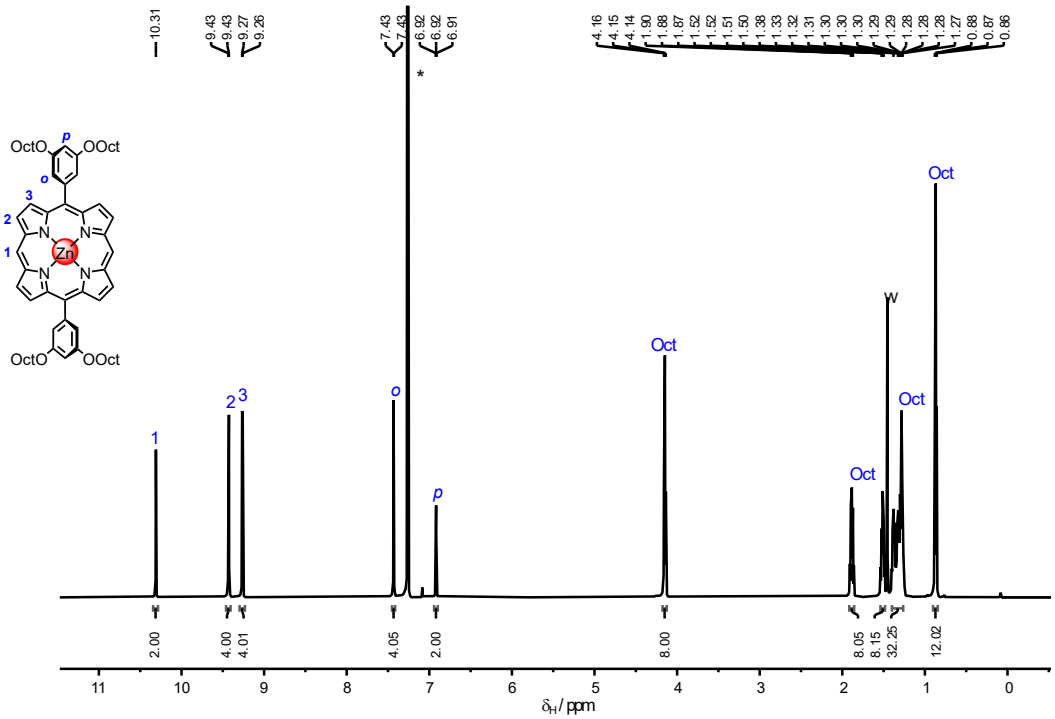

Figure B.71: ^{1}H NMR spectrum of **P1** (600 MHz, $CDCl_3$, 298 K). * = $CHCl_3$; w = water.

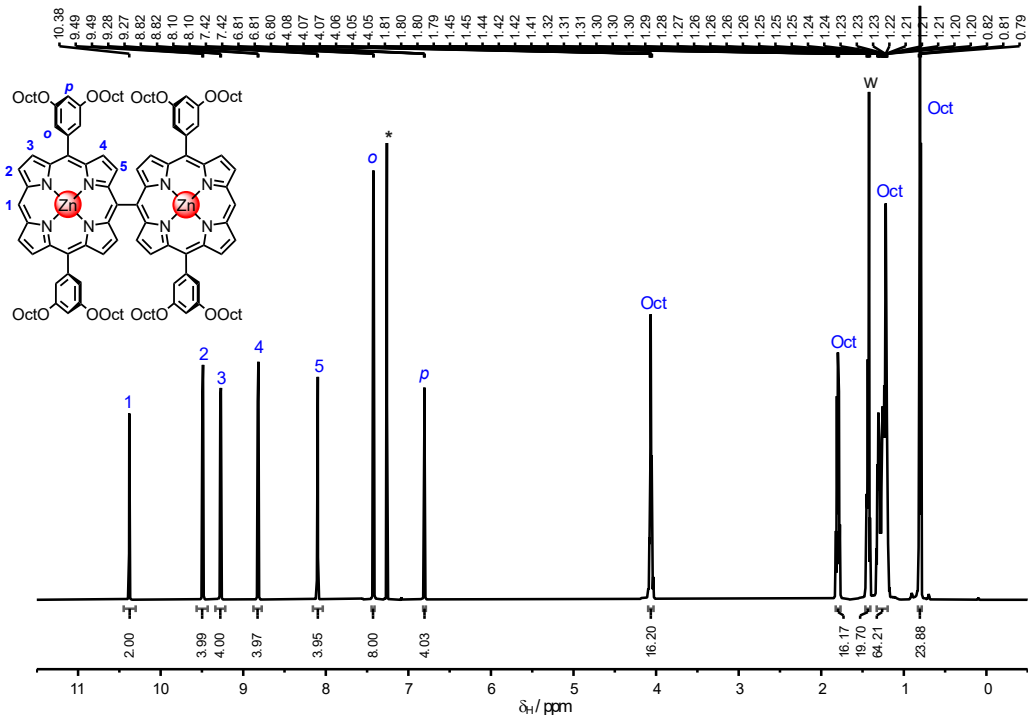

Figure B.72: ^{1}H NMR spectrum of ***ls*-P2** (600 MHz, $CDCl_3$, 298 K). * = $CHCl_3$; w = water.

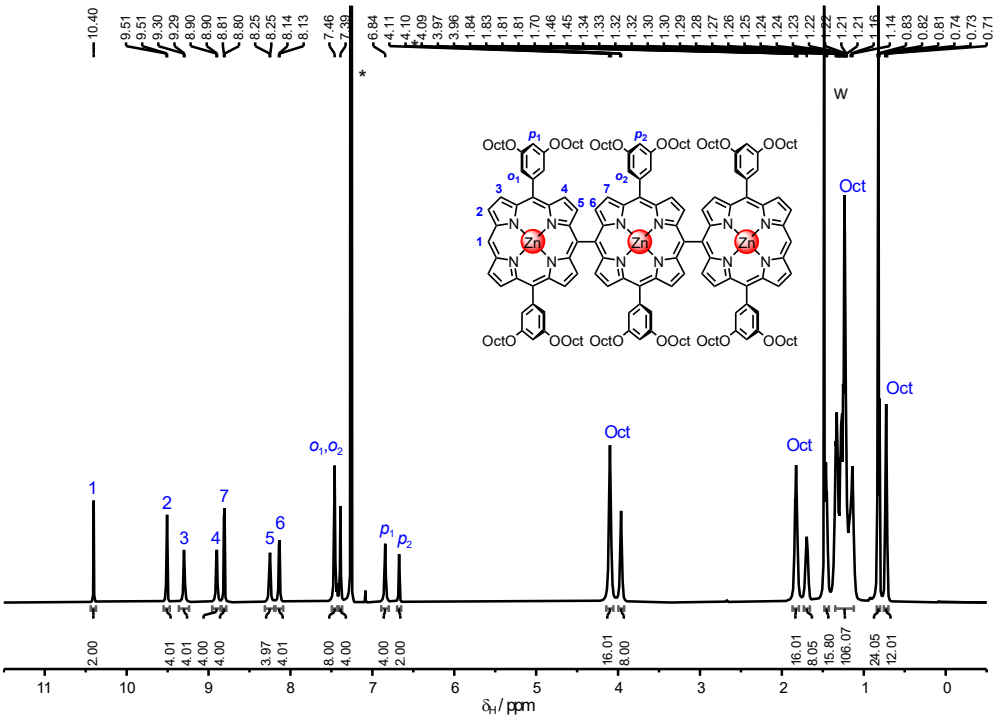

Figure B.73: ^{1}H NMR spectrum of ***ls*-P3** (600 MHz, $CDCl_3$, 298 K). * = $CHCl_3$; w = water.

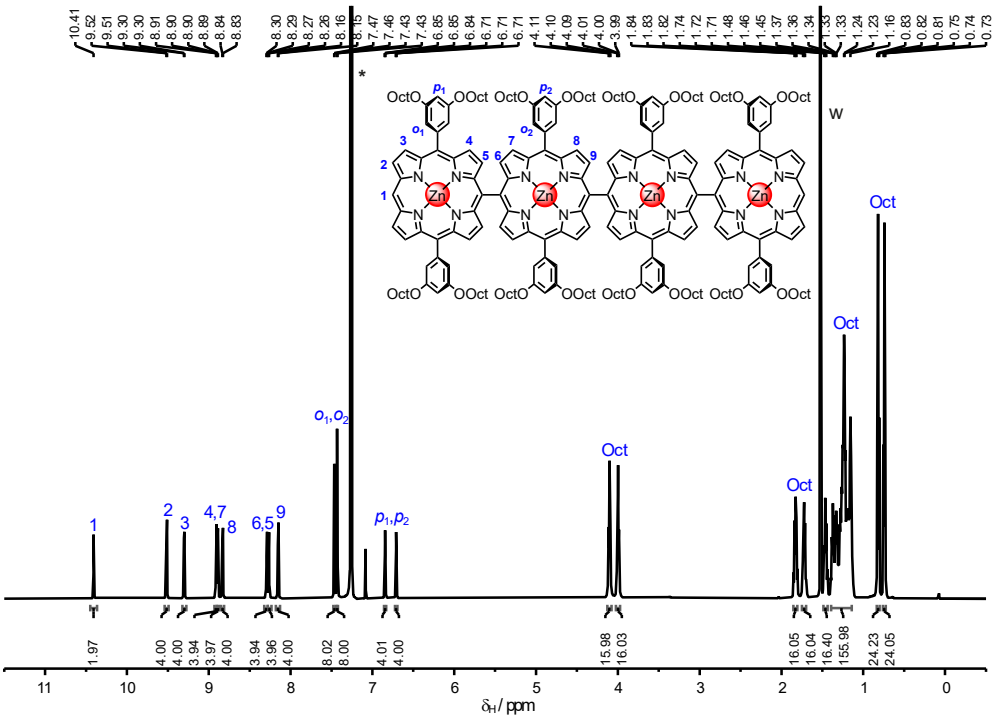

Figure B.74: ^{1}H NMR spectrum of ***ls*-P4** (600 MHz, $CDCl_3$, 298 K). * = $CHCl_3$; w = water.

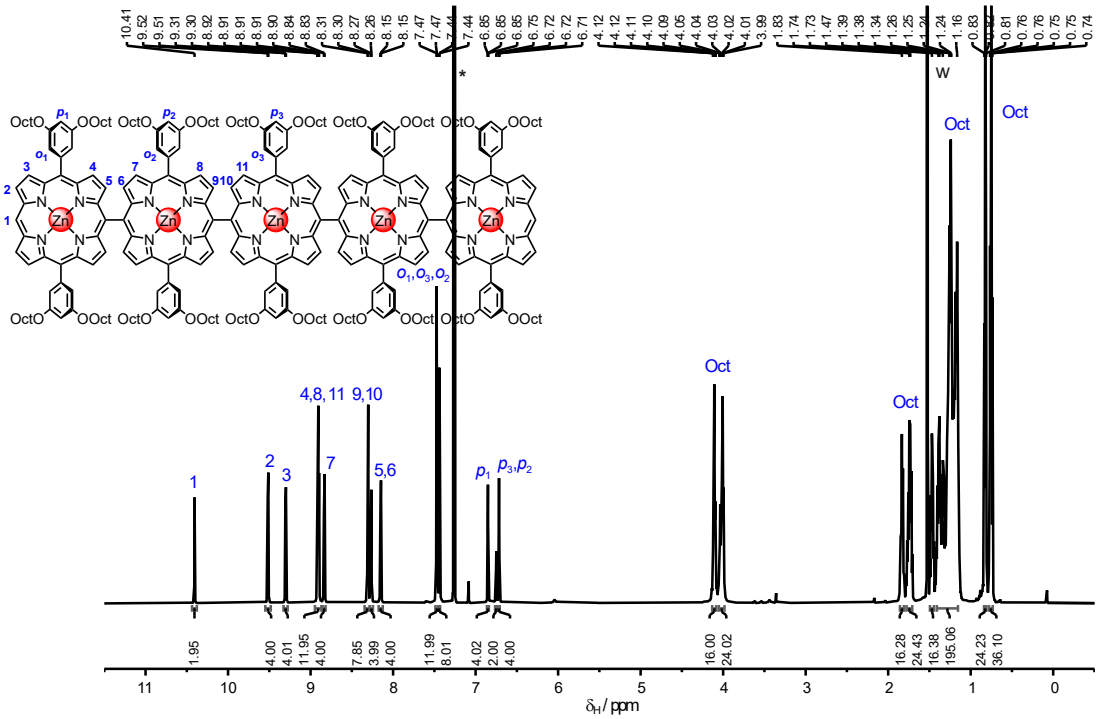

Figure B.75: ^{1}H NMR spectrum of ***ls*-P5** (600 MHz, $CDCl_3$, 298 K). * = $CHCl_3$; w = water.

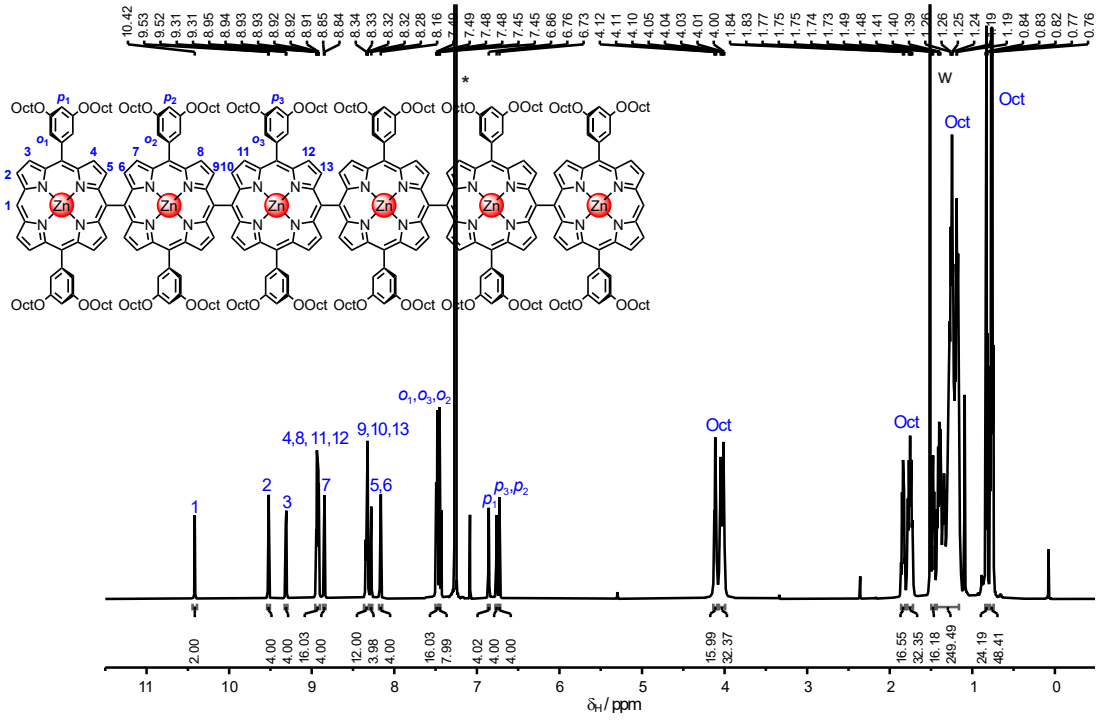

Figure B.76: ^{1}H NMR spectrum of ***ls*-P6** (600 MHz, $CDCl_3$, 298 K). * = $CHCl_3$; w = water.

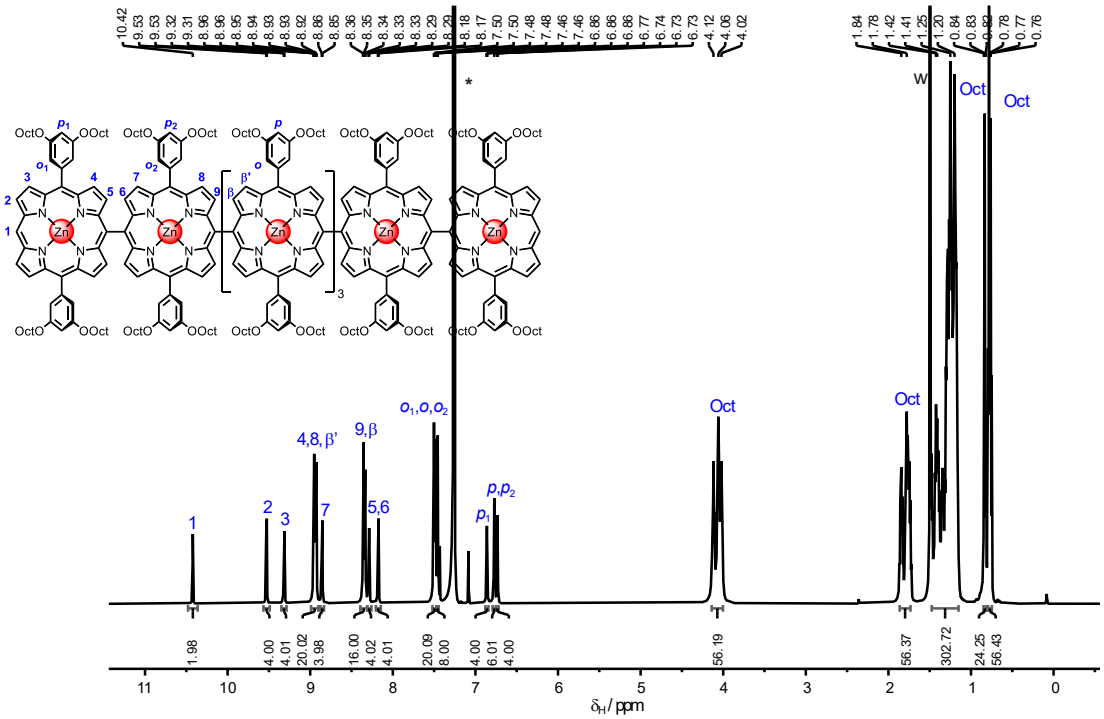

Figure B.77: ^{1}H NMR spectrum of ***ls*-P7** (600 MHz, $CDCl_3$, 298 K). * = $CHCl_3$; w = water.

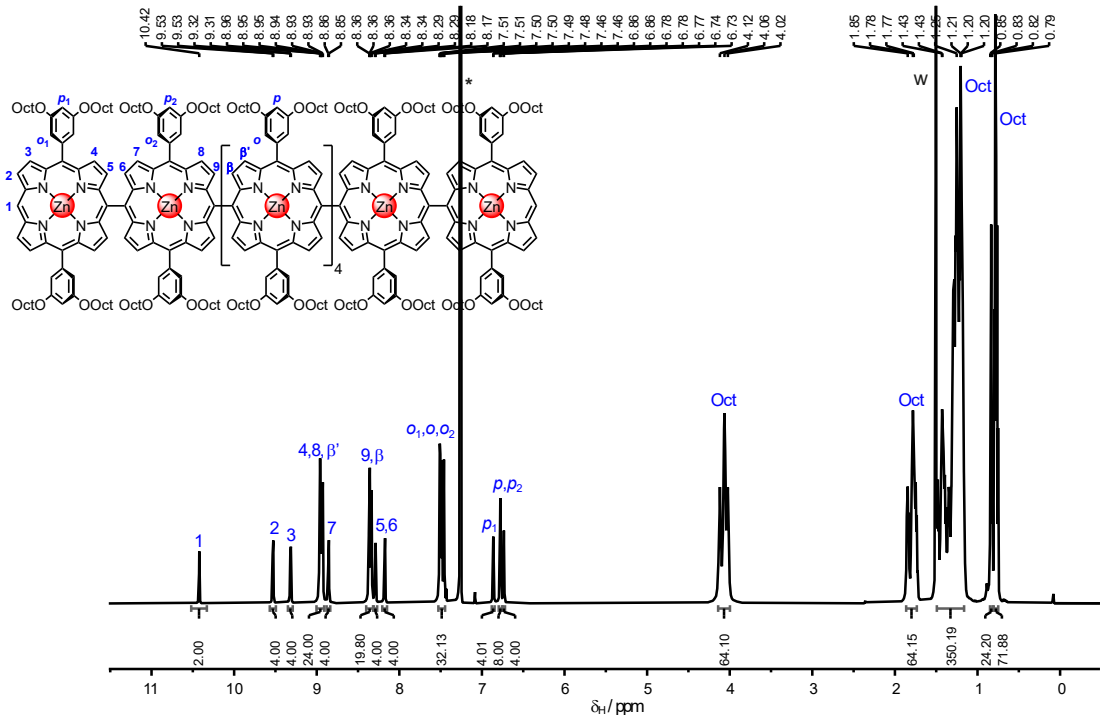

Figure B.78: ^{1}H NMR spectrum of ***ls*-P8** (600 MHz, $CDCl_3$, 298 K). * = $CHCl_3$; w = water.

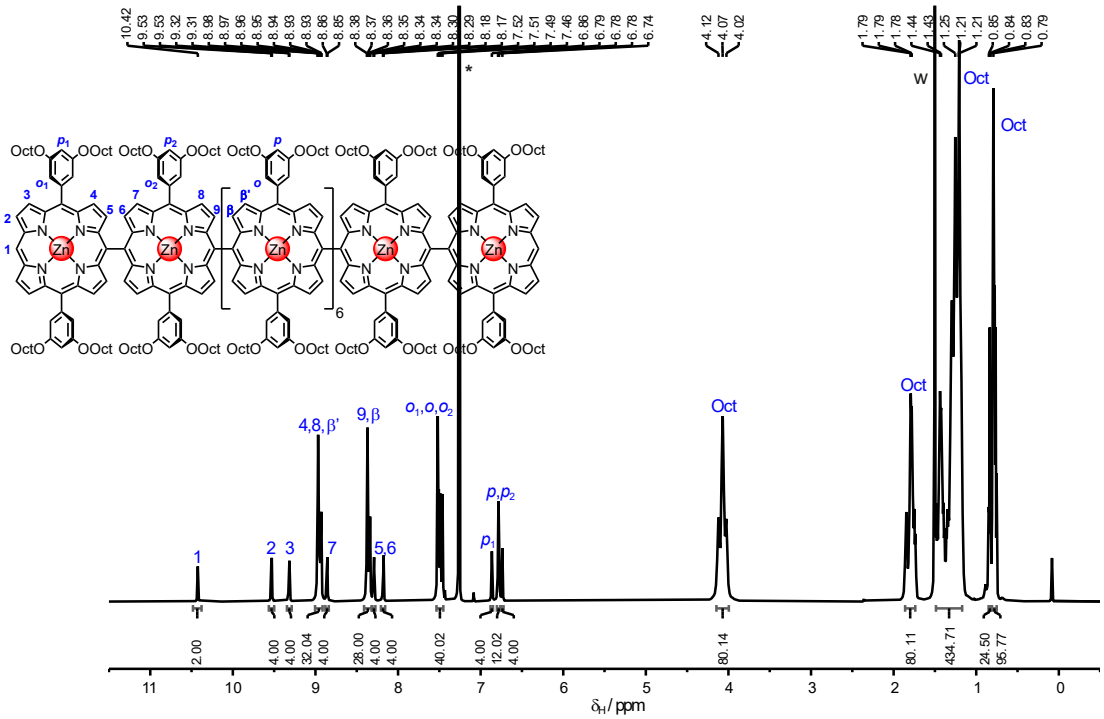

Figure B.79: ^{1}H NMR spectrum of ***ls*-P10** (600 MHz, $CDCl_3$, 298 K). * = $CHCl_3$; w = water.

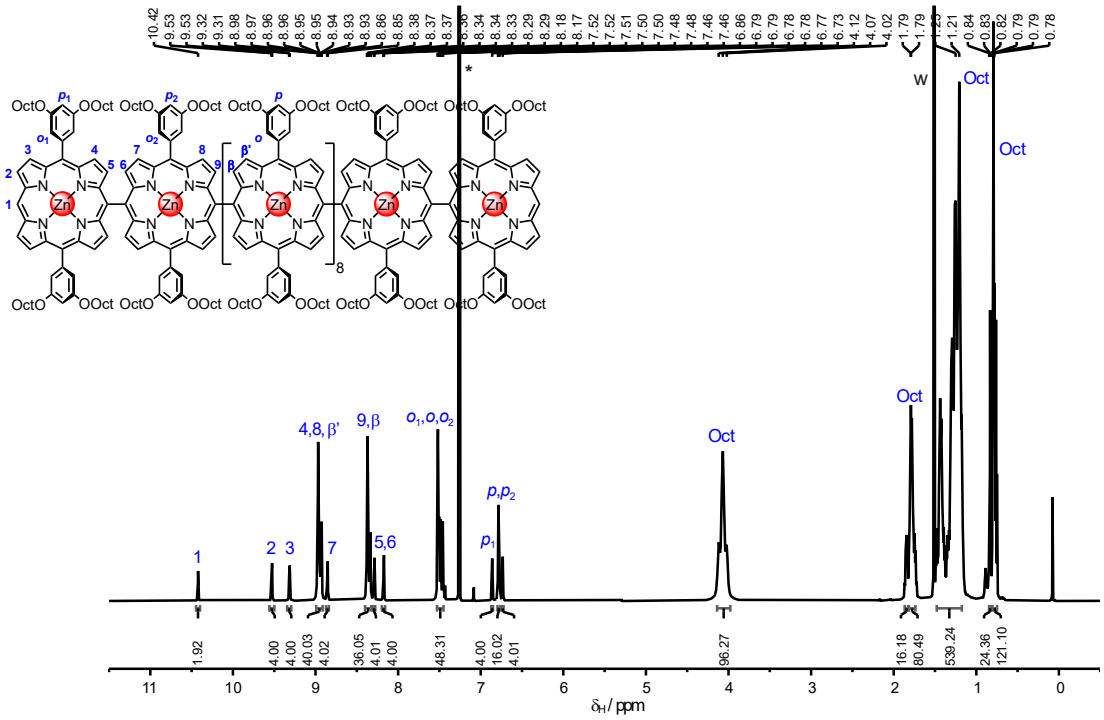

Figure B.80: ^{1}H NMR spectrum of ***ls*-P12** (600 MHz, $CDCl_3$, 298 K). * = $CHCl_3$; w = water.

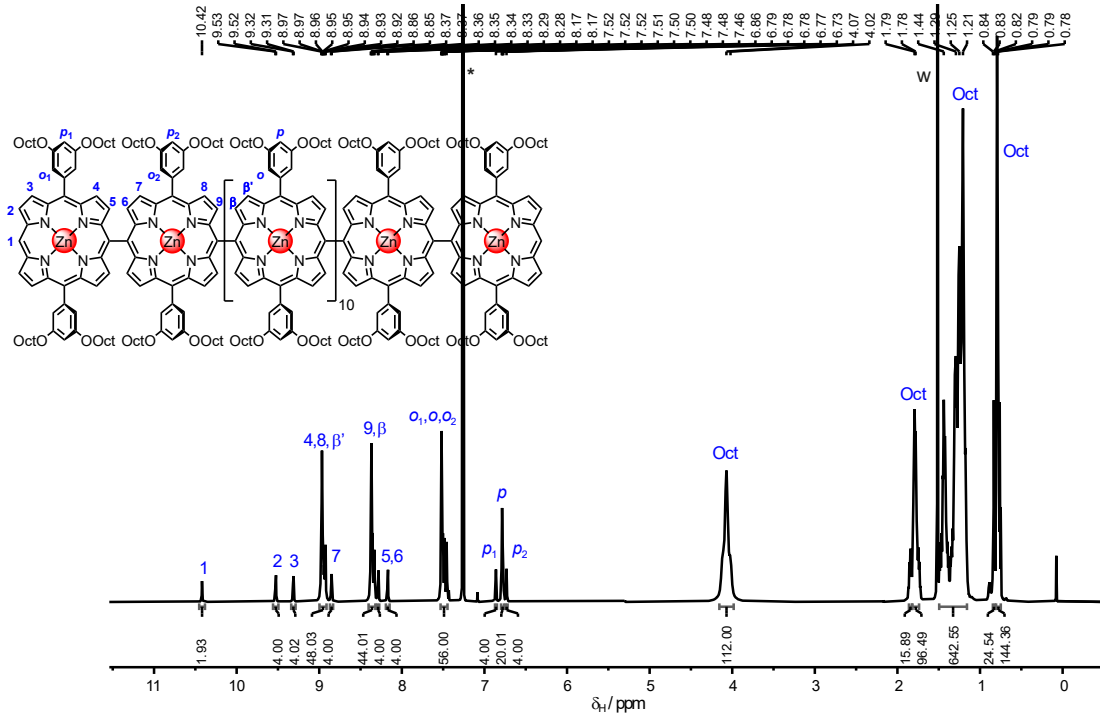

Figure B.81: ^{1}H NMR spectrum of ***ls*-P14** (600 MHz, $CDCl_3$, 298 K). * = $CHCl_3$; w = water.

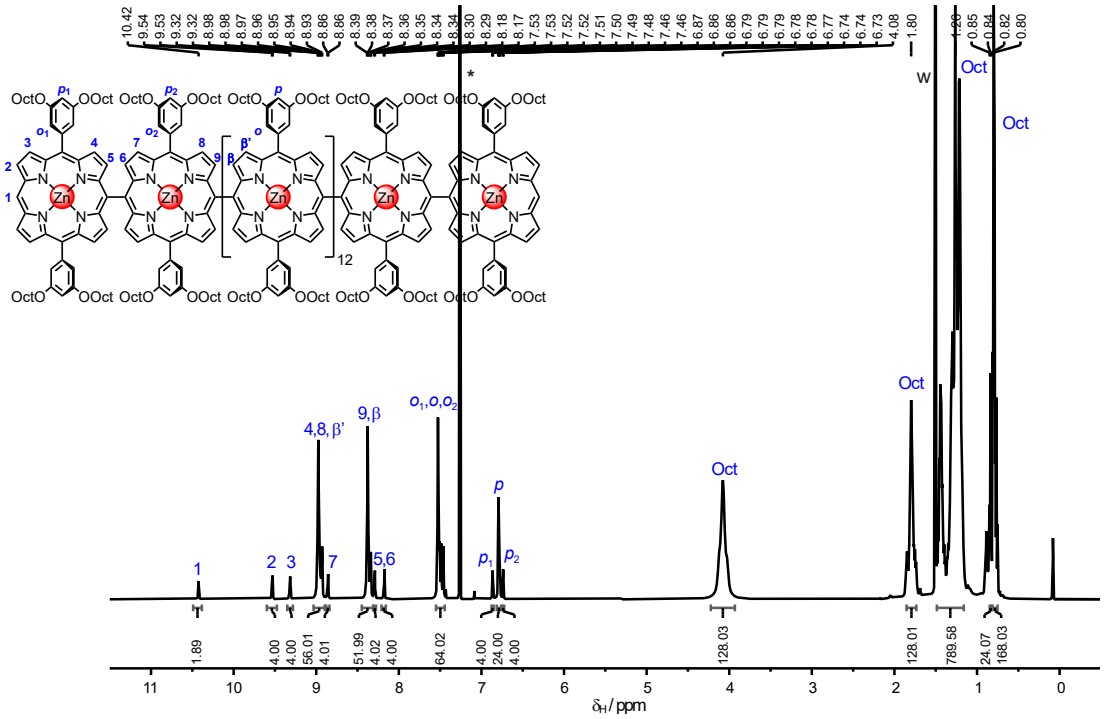

Figure B.82: ^{1}H NMR spectrum of ***ls*-P16** (600 MHz, $CDCl_3$, 298 K). * = $CHCl_3$; w = water.

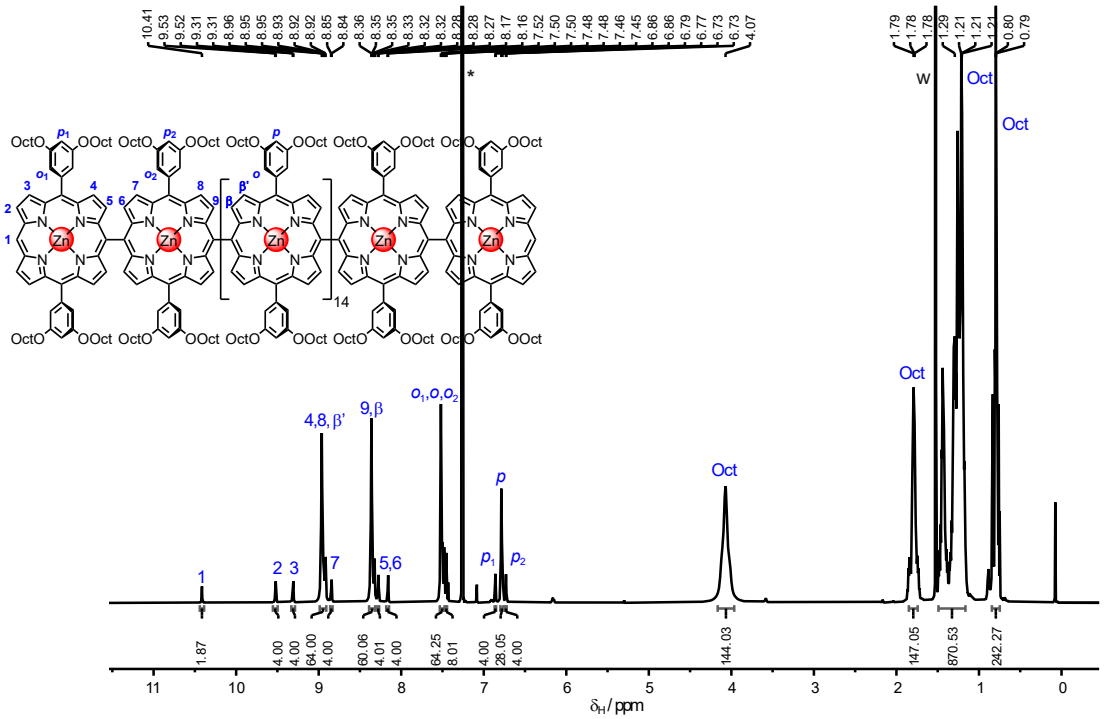

Figure B.83: ^{1}H NMR spectrum of ***ls*-P18** (600 MHz, $CDCl_3$, 298 K). * = $CHCl_3$; w = water.

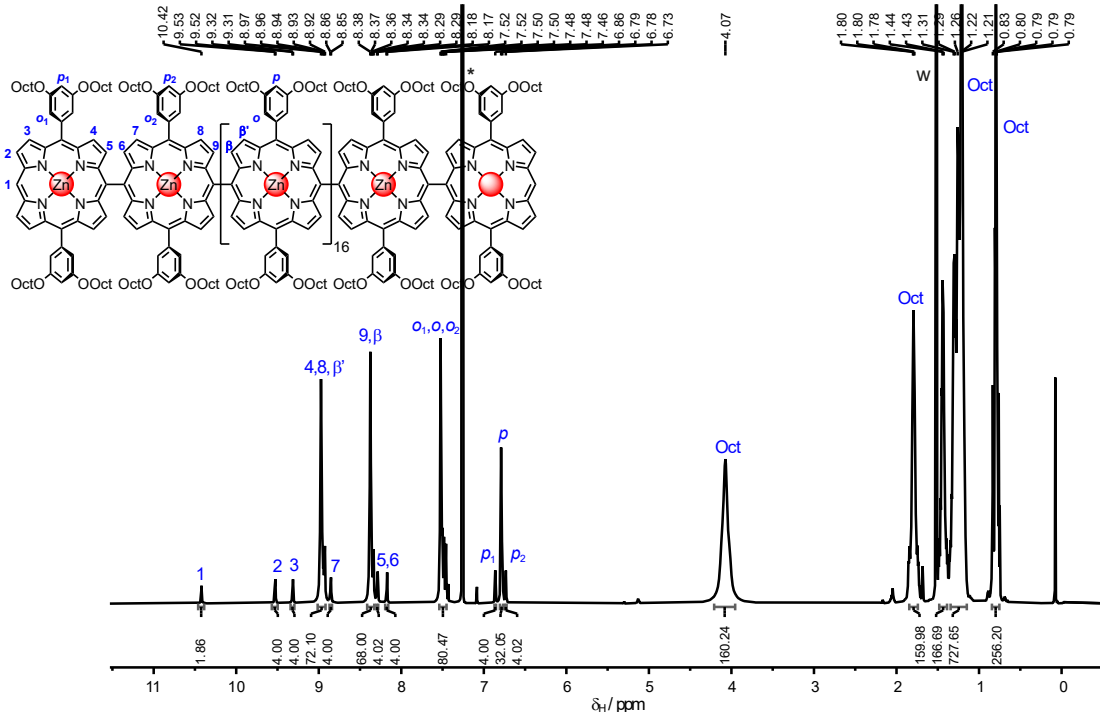

Figure B.84: ^{1}H NMR spectrum of ***ls*-P20** (600 MHz, $CDCl_3$, 298 K). * = $CHCl_3$; w = water.

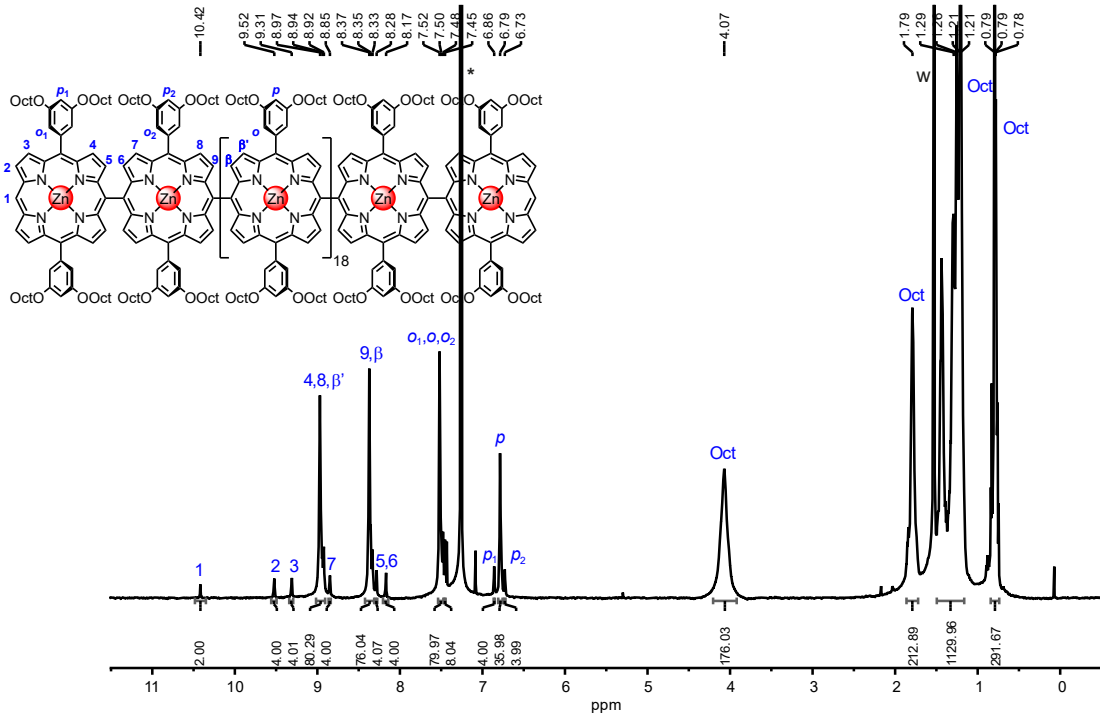

Figure B.85: ^{1}H NMR spectrum of ***ls*-P22** (600 MHz, $CDCl_3$, 298 K). * = $CHCl_3$; w = water.

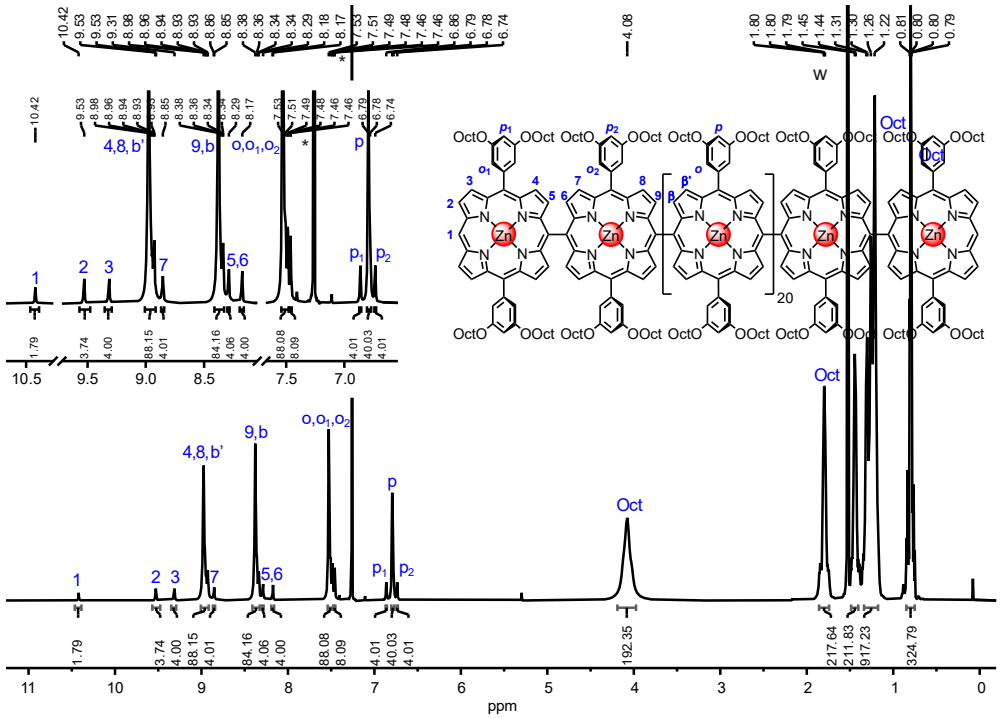

Figure B.86: ^{1}H NMR spectrum of ***ls*-P24** (600 MHz, $CDCl_3$, 298 K). * = $CHCl_3$; w = water.

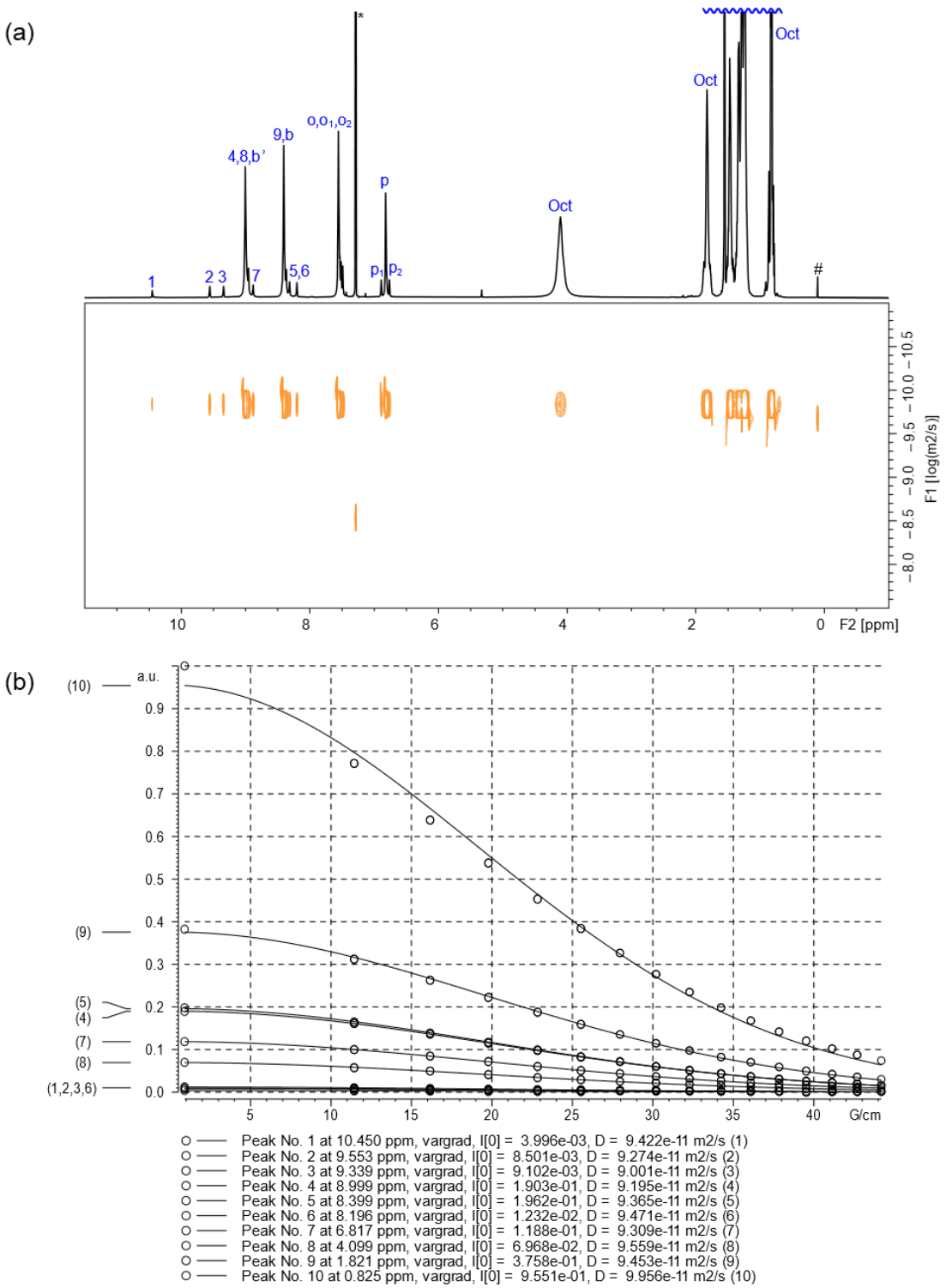

Figure B.87: ^{1}H diffusion NMR (500 MHz, $CDCl_3$, 298 K) of ***ls*-P24**. (a) ^{1}H DOSY plot. (b) Diffusion decay plots fitted to the Stejskal Tanner equation and the resulting diffusion coefficients obtained. Acquisition parameters: G = 0.90–44.19 G/cm, D = 0.10 s, and d = 4600 µs. The average diffusion coefficient $D = 9.40 \cdot 10^{-11}$ m^2s^{-1}. * = residual solvent peak, # = silicone grease peak.

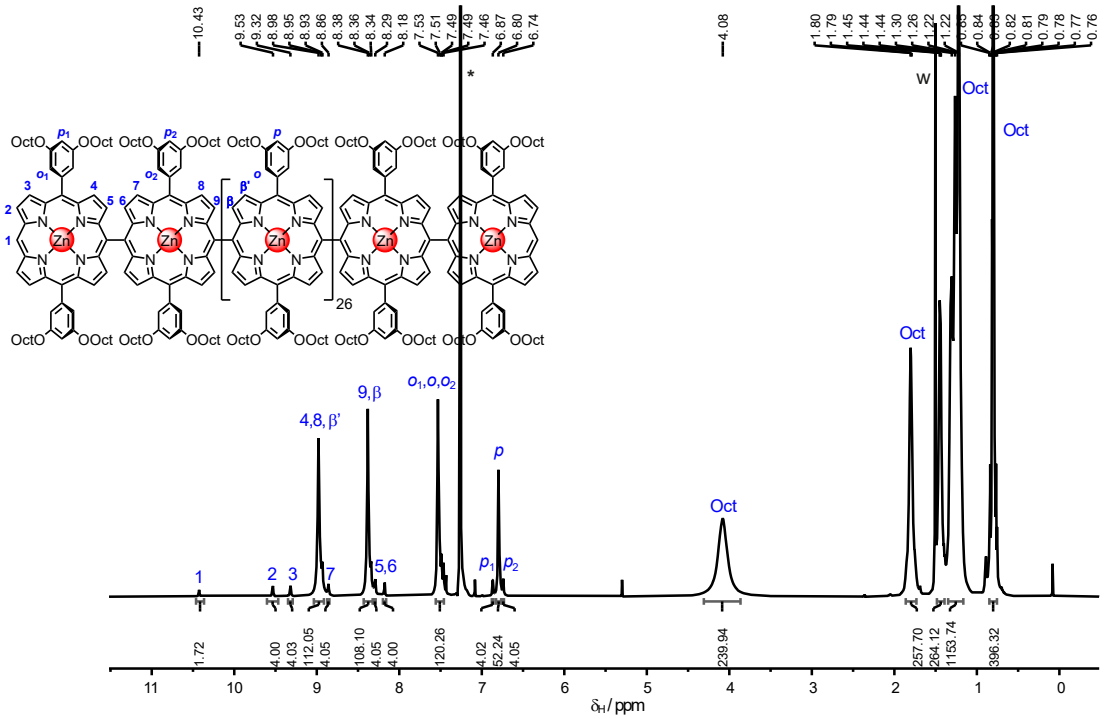

Figure B.88: ^{1}H NMR spectrum of ***l*-P30** (600 MHz, $CDCl_3$, 298 K). * = $CHCl_3$; w = water.

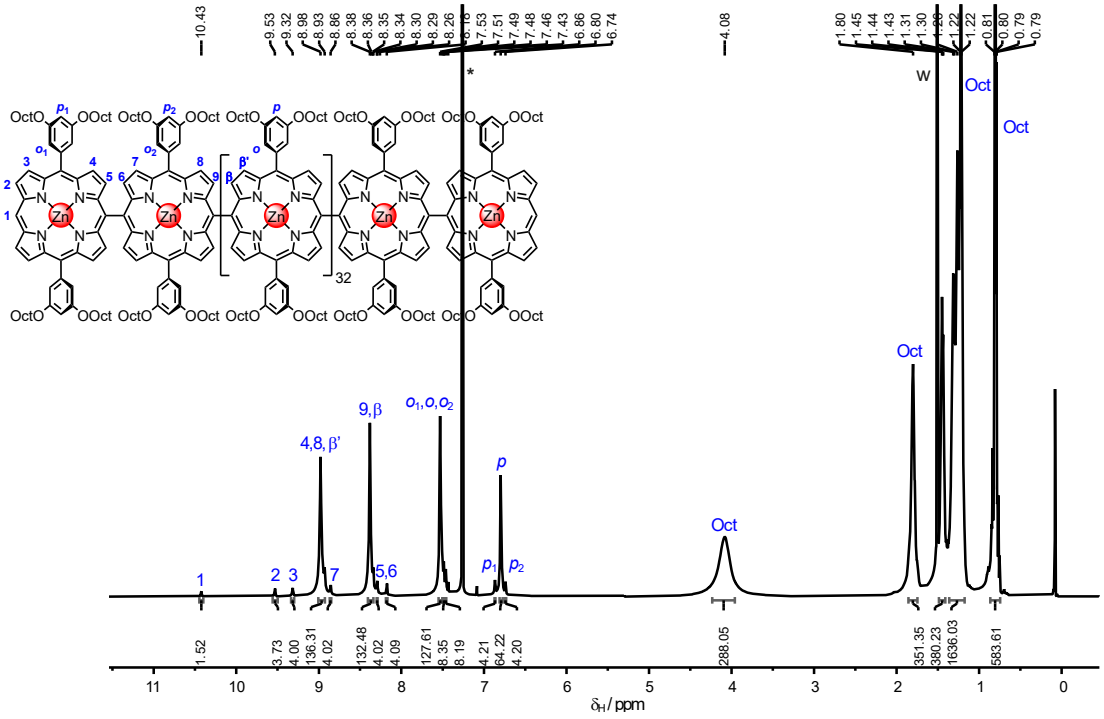

Figure B.89: ^{1}H NMR spectrum of ***ls*-P36** (600 MHz, $CDCl_3$, 298 K). * = $CHCl_3$; w = water.

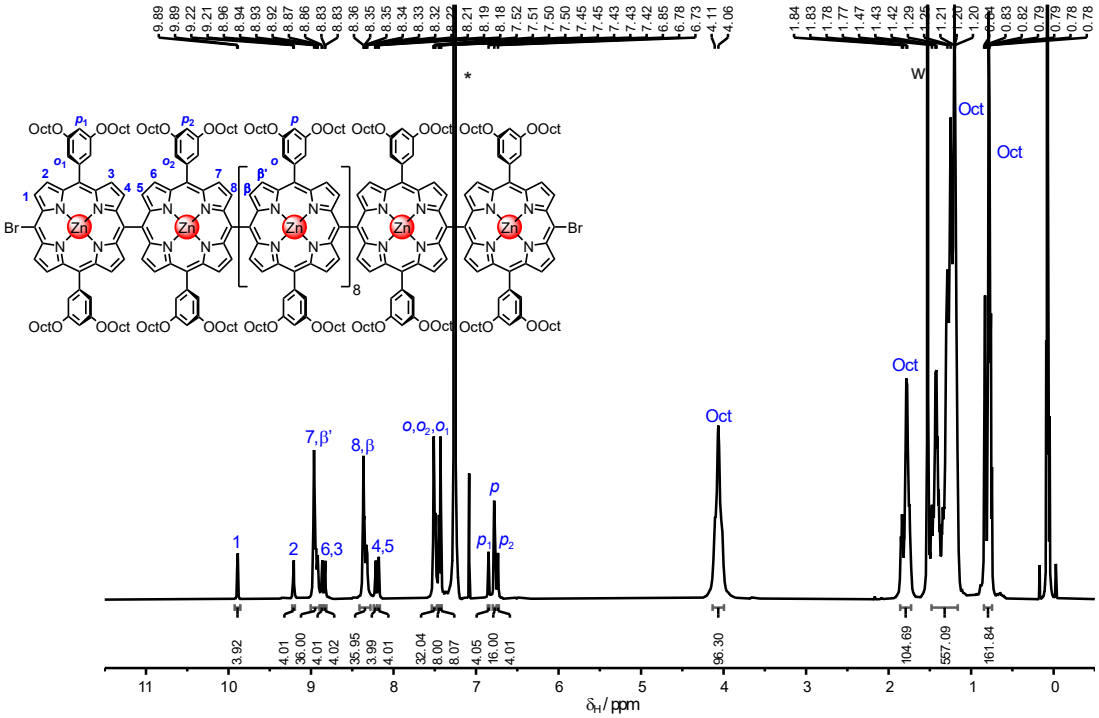

Figure B.90: ^{1}H NMR spectrum of ***ls*-P12-Br$_2$** (600 MHz, $CDCl_3$, 298 K). * = $CHCl_3$; w = water.

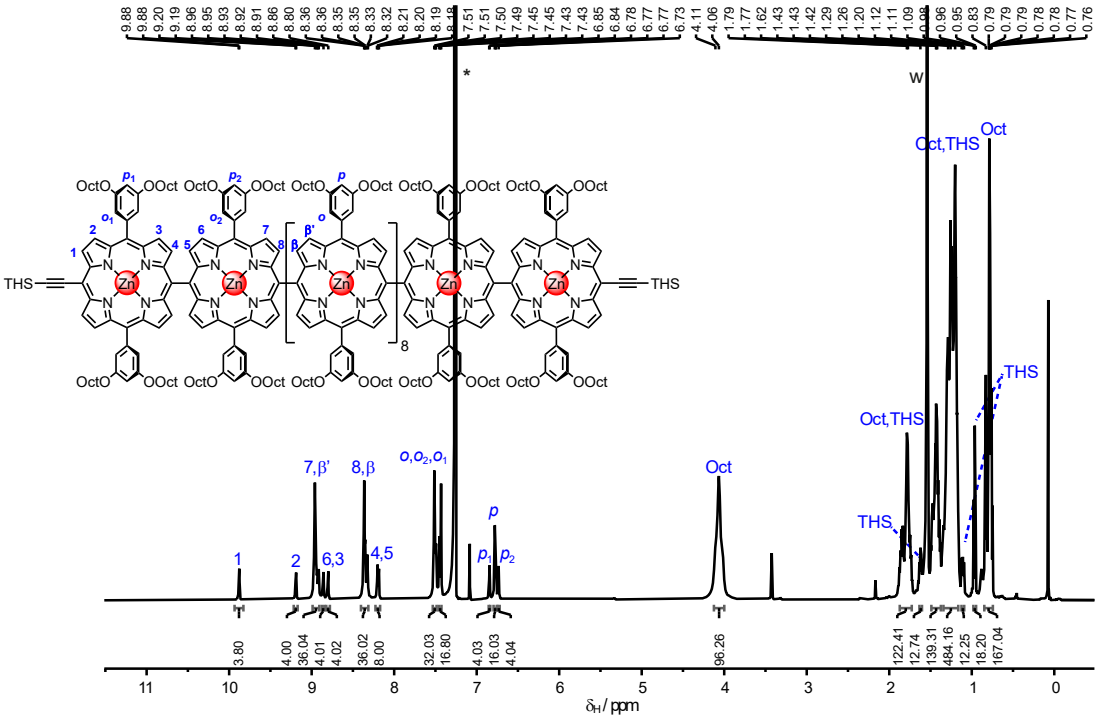

Figure B.91: ^{1}H NMR spectrum of ***ls*-P12-THS$_2$** (600 MHz, $CDCl_3$, 298 K). * = $CHCl_3$; w = water.

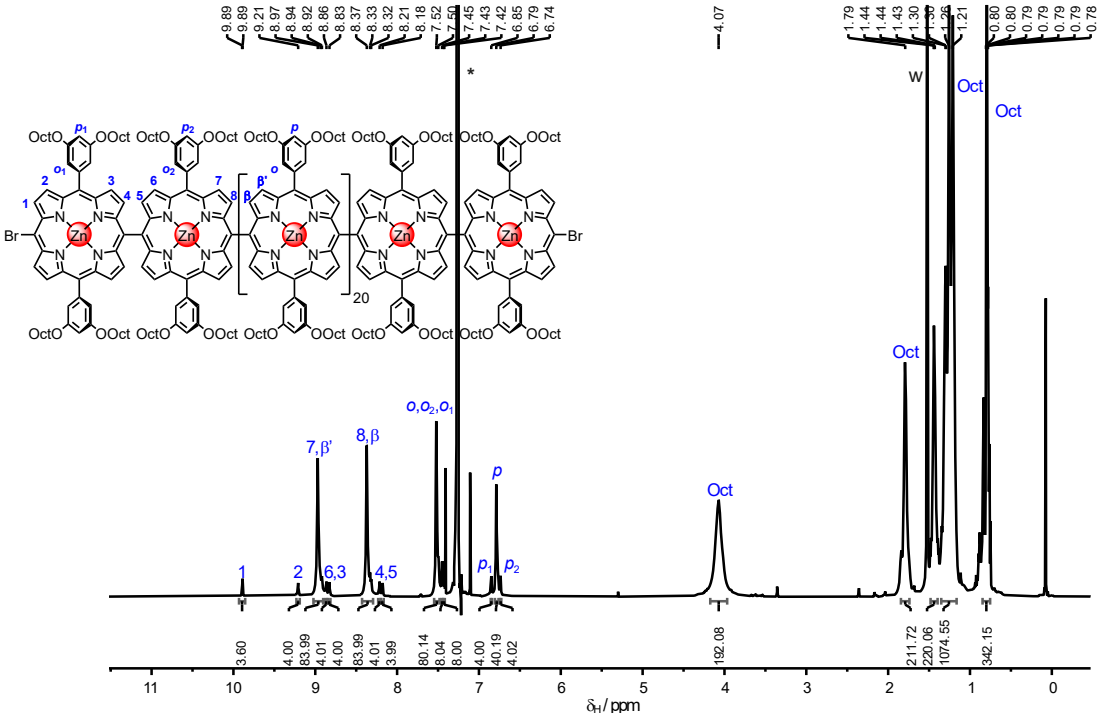

Figure B.92: ^{1}H NMR spectrum of ***ls*-P24-Br$_2$** (600 MHz, $CDCl_3$, 298 K). * = $CHCl_3$; w = water.

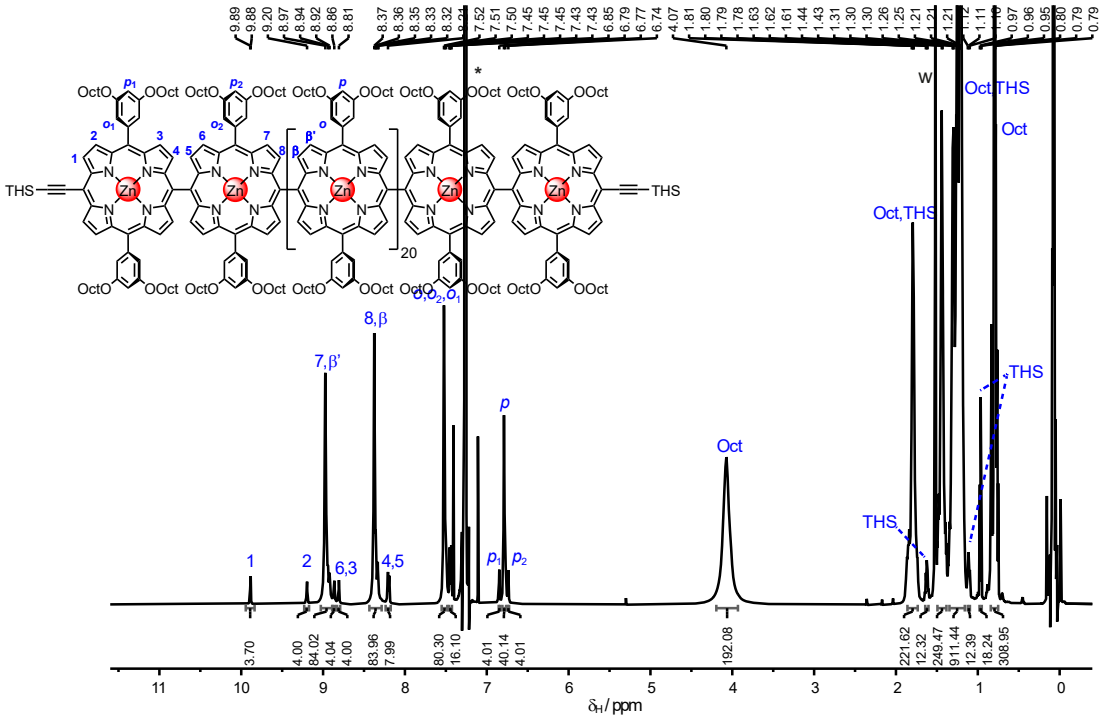

Figure B.93: ^{1}H NMR spectrum of ***ls*-P24-THS$_2$** (600 MHz, $CDCl_3$, 298 K). * = $CHCl_3$; w = water.

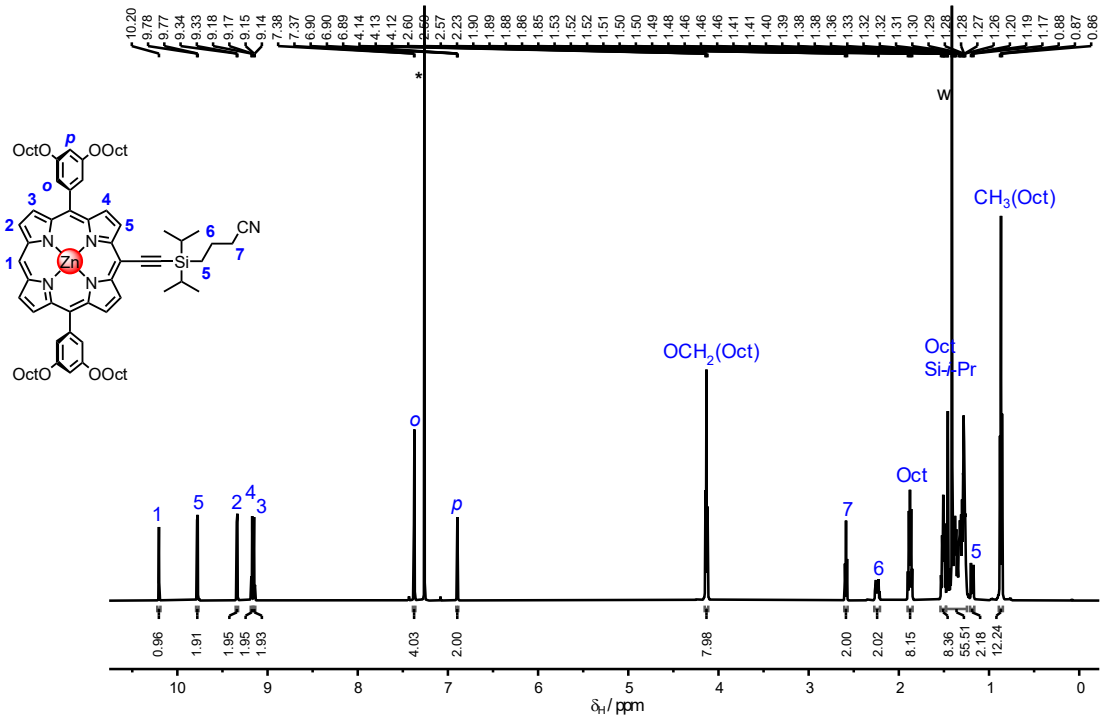

Figure B.94: ^{1}H NMR spectrum of **P1-CPDIPS** (600 MHz, $CDCl_3$, 298 K). * = $CHCl_3$; w = water.

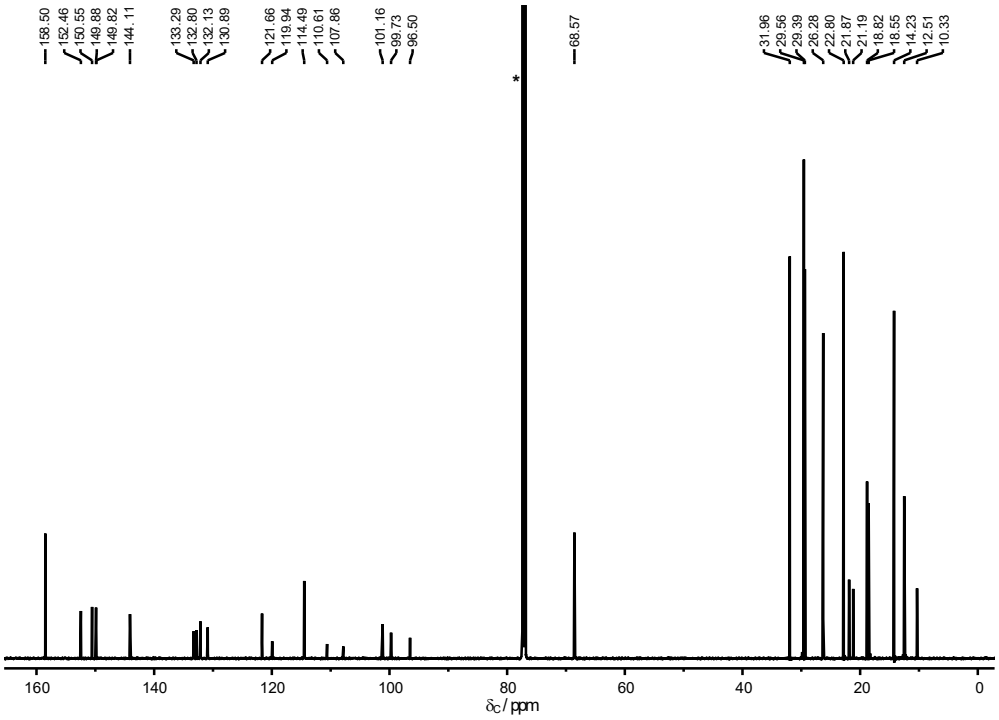

Figure B.95: ^{13}C NMR spectrum of **P1-CPDIPS** (151 MHz, $CDCl_3$, 298 K). * = $CDCl_3$.

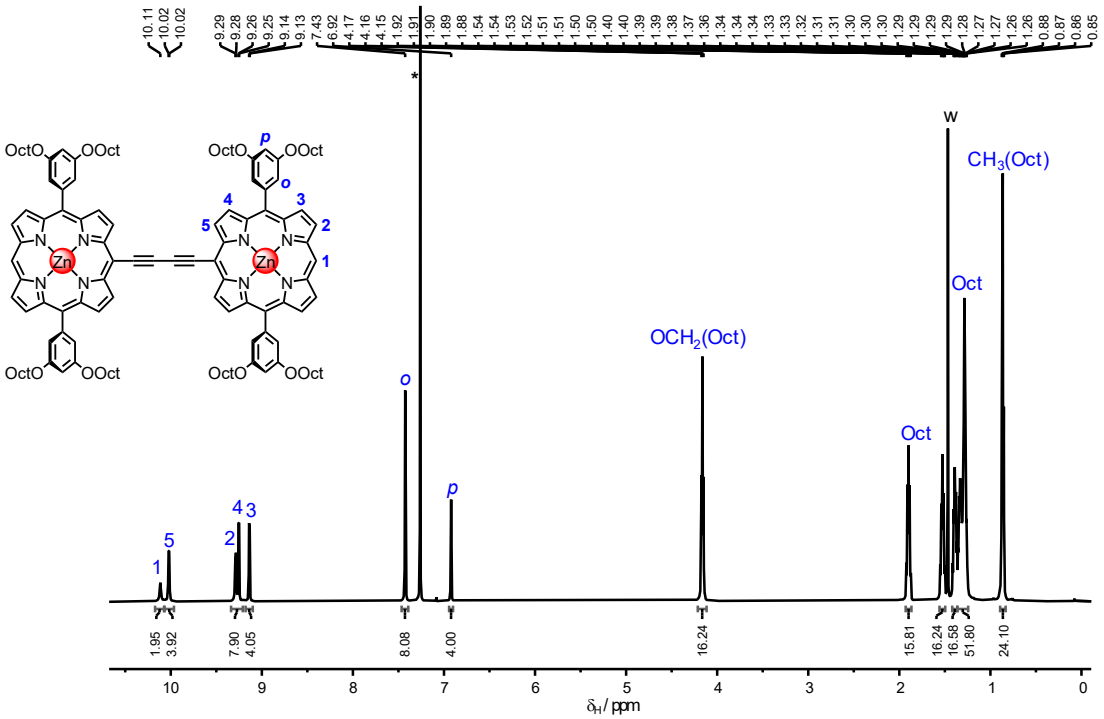

Figure B.96: ^{1}H NMR spectrum of ***lb*-P2** (600 MHz, $CDCl_3$, 298 K). * = $CHCl_3$; w = water.

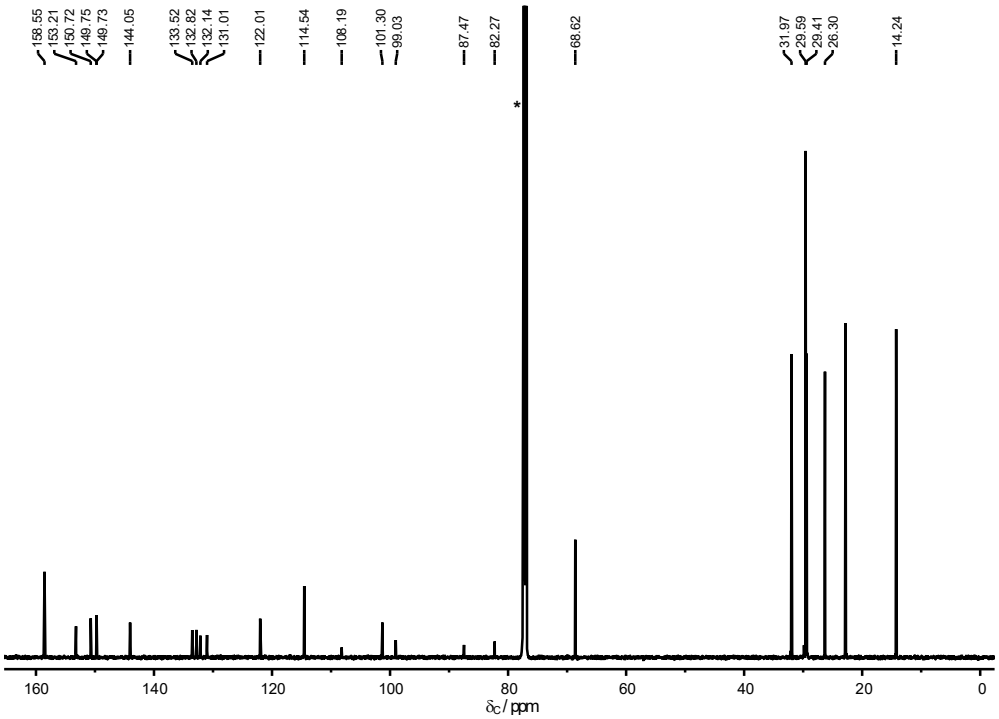

Figure B.97: ^{13}C NMR spectrum of ***lb*-P2** (151 MHz, $CDCl_3$, 298 K). * = $CDCl_3$.

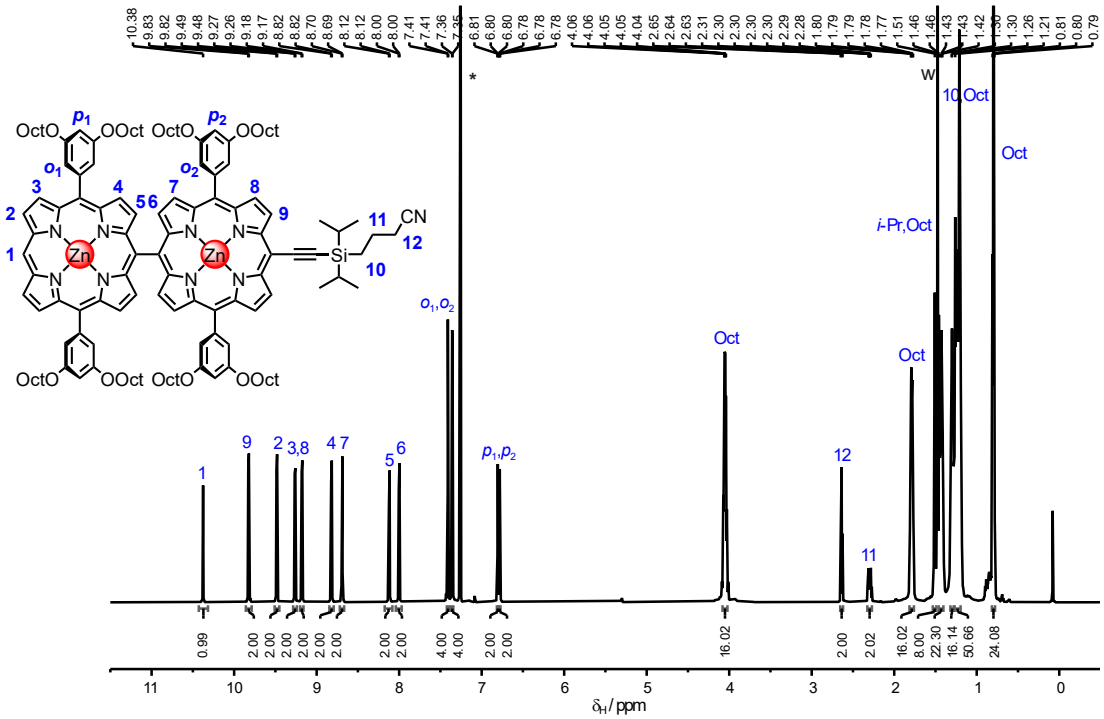

Figure B.98: ^{1}H NMR spectrum of ***ls*-P2-CPDIPS** (600 MHz, $CDCl_3$, 298 K). * = $CHCl_3$; w = water.

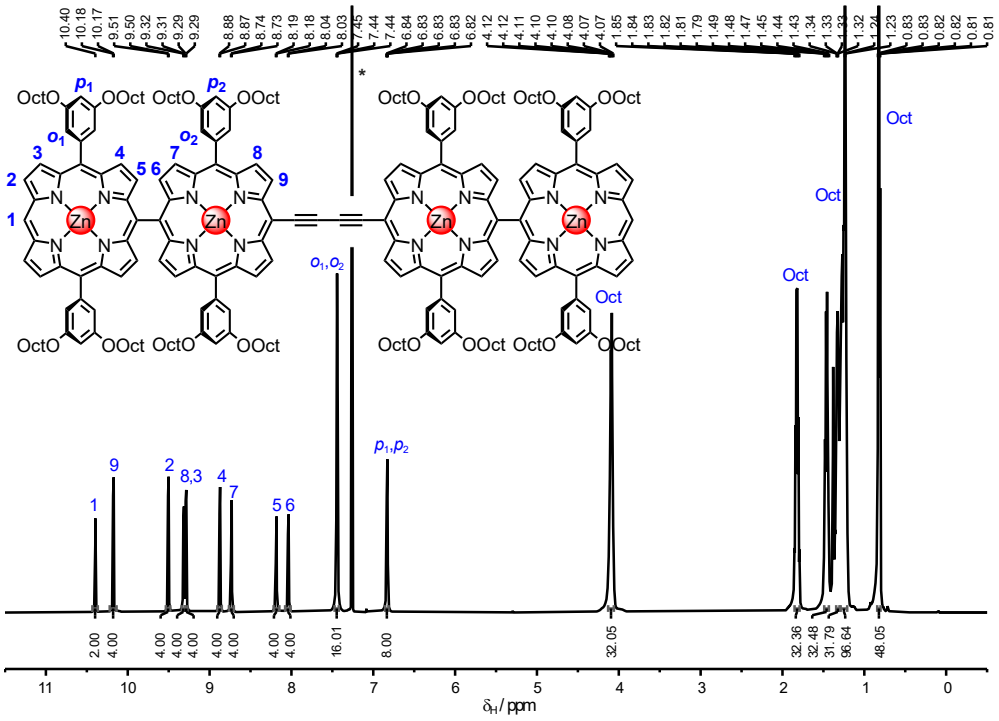

Figure B.99: ^{1}H NMR spectrum of ***ls*[*b*$_1$]-P4** (600 MHz, $CDCl_3$, 298 K). * = $CHCl_3$; w = water.

Table B.8: ^{1}H NMR assignment and 2D correlations for ***cs*[*b*$_1$]-P24**.

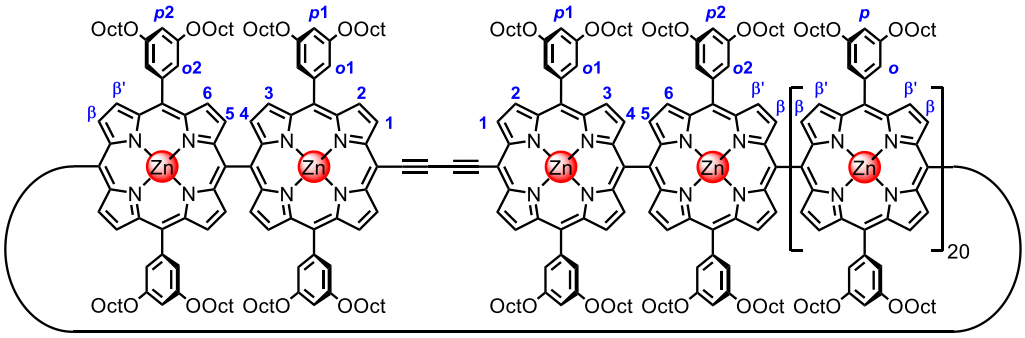

#	Assign.	^{1}H	Mult.	COSY[a]	NOESY[a]	HSQC
1	H1	10.14	d, *J* = 4.3 Hz, 4H	m: 3; w: 9	s: 3; m: 9, 14; w: 5	131.2
2	β' (+β)	9.60–8.53	m, 104H	s: 6; m: 9; w: 14	s: 6, 9, 11, 14; m: 9, 15, 16	132.2
3	H2	9.33–9.30	m, 4H	m: 1; w: 9	s: 1, 9; m: 14; w: 5, 12	133.7
4	H6	8.88–8.85	m, 4H	m: 7; w: 9	m: 7, 10; w: 13	132.1
5	H3	8.82–8.79	m, 4H	m: 8; w: 9	m: 9; w: 1, 3, 8, 12	132.1
6	β	8.53–8.11	m, 56H	s: 2; w: 9	s: 2, 9, 14; 11: m; 11; w: 15	134.2
7	H5	8.25–8.22	m, 4H	m: 4	m: 4, 10	134.2
8	H4	8.22–8.19	m, 4H	m: 5	m: 9; w: 5	134.2
9	*o* (+β)	8.10–6.96	m, 120H	s: 14; m: 2; w: 1, 3, 4, 5, 6, 12, 16	s: 2, 3, 6, 11, 14; m: 1, 2, 5, 8, 15, 16	114.2
10	*o*2	7.44	s, 4H	w: 13	s: 13; m: 4, 7	114.2
11	*p*	6.98–6.52	m, 48H	s: 14; w: 16	s: 2, 9, 14; m: 6, 15, 16	101.2
12	p1	6.87	s, 2H	w: 9	w: 3, 5	101.2
13	p2	6.73	s, 2H	w: 10	s: 10; w: 4	101.1
14	OCH_2	4.60–3.36	m, 192H	s: 9, 11, 15, 16; w: 2	s: 2, 6, 9, 11, 15, 16; m: 1, 3	68.4
15	OCH_2-CH_2	1.94–1.60	m, 192H	s: 14, 16	s: 14, 16; m: 2, 9, 11; w: 6	29.6, 29.5, 29.4
16	$(CH_2)_5$	1.60–1.06	m, 960H	s: 14, 15, 17; w: 9, 11	s: 14, 15, 17; m: 2, 9, 11	31.8, 29.5, 29.3, 26.2, 22.7
17	CH_3	0.96–0.60	m, 288H	s: 16	s: 16	14.1

[a] Relative intensities of COSY and NOE correlations are labeled as s, m, or w for strong, medium, or weak.

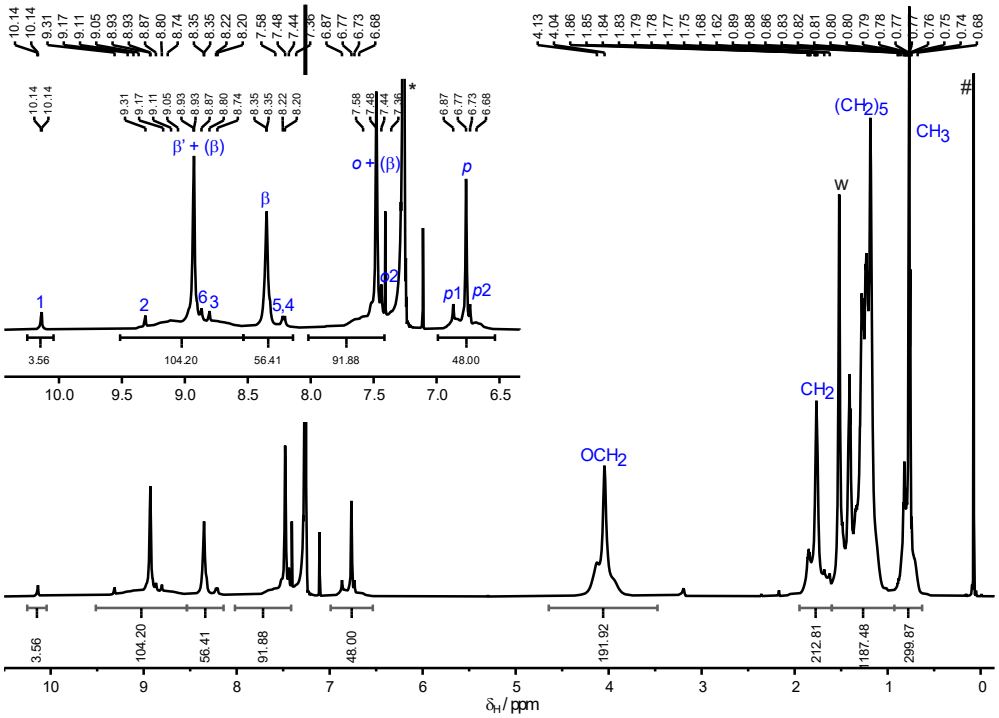

Figure B.100: ^{1}H NMR spectrum of ***cs*[*b*$_1$]-P24** (700 MHz, $CDCl_3$, 298 K). * = $CHCl_3$; w = water; # = silicone grease.

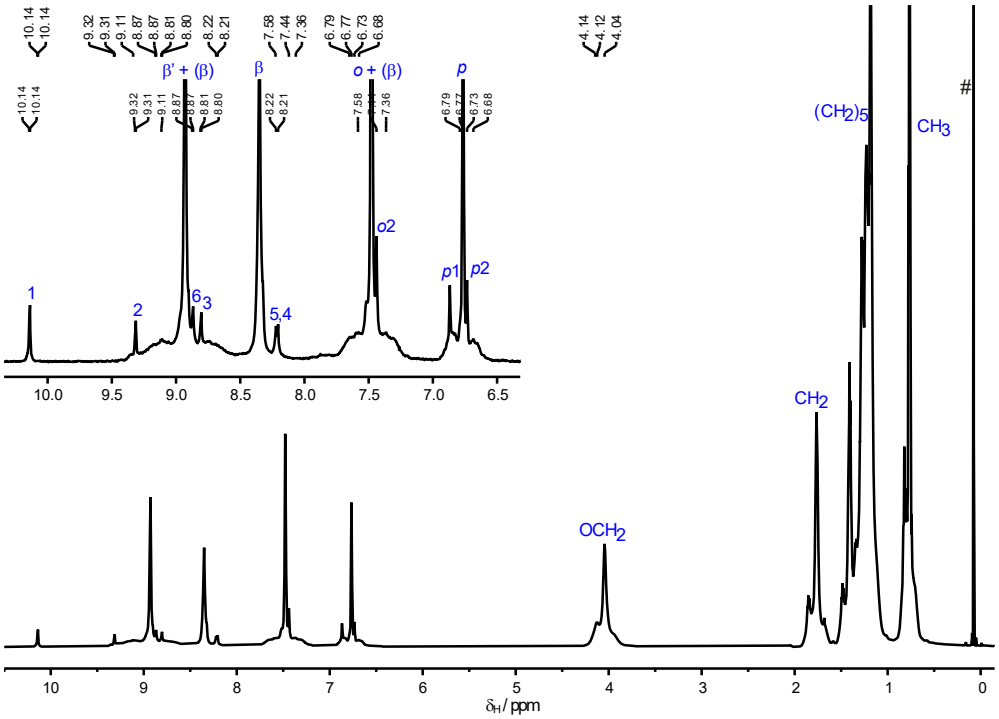

Figure B.101: Diffusion-edited ^{1}H NMR spectrum of ***cs*[*b*$_1$]-P24** (700 MHz, $CDCl_3$, 298 K). # = silicone grease. G = 32.1 G/cm, D = 0.1 s, and d = 1500 μs.

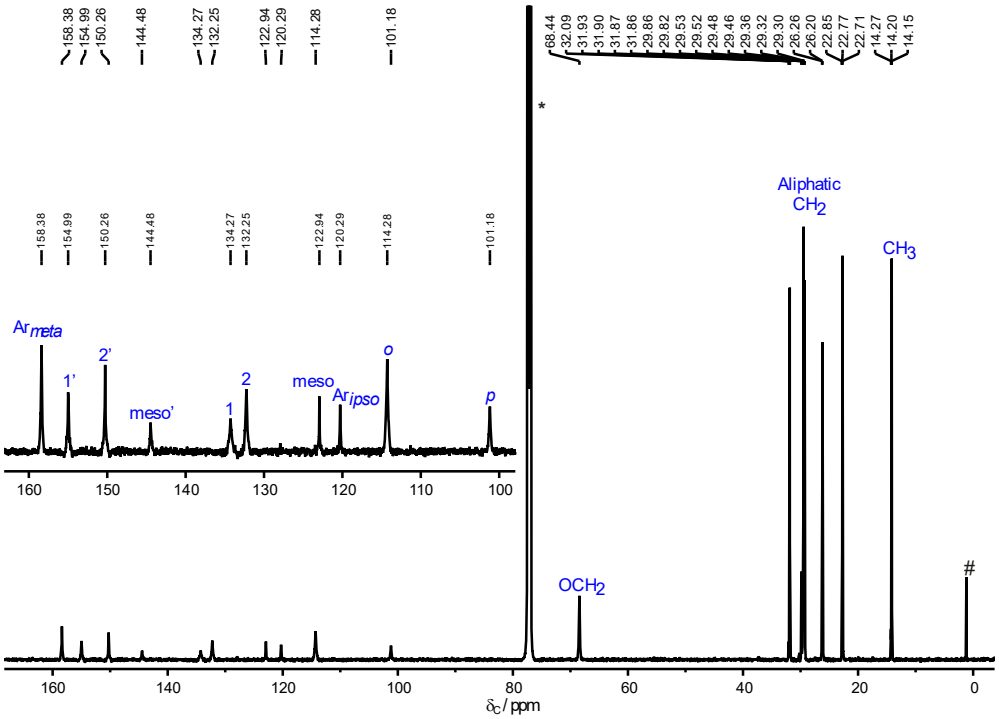

Figure B.102: ^{13}C NMR spectrum of ***cs*[*b*$_1$]-P24** (151 MHz, $CDCl_3$, 298 K). * = $CDCl_3$; # = silicone grease.

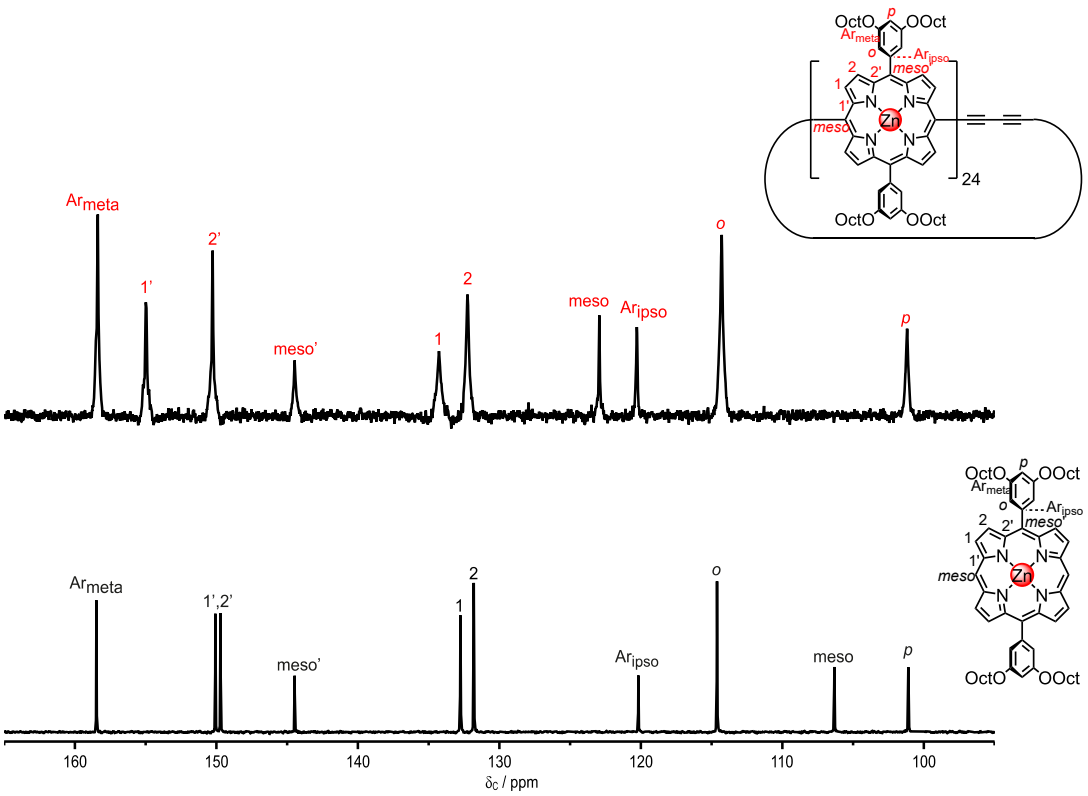

Figure B.103: Comparison of ^{13}C NMR spectra (151 MHz, $CDCl_3$, 298 K) of ***cs*[*b*$_1$]-P24** (top) and **P1** (bottom).

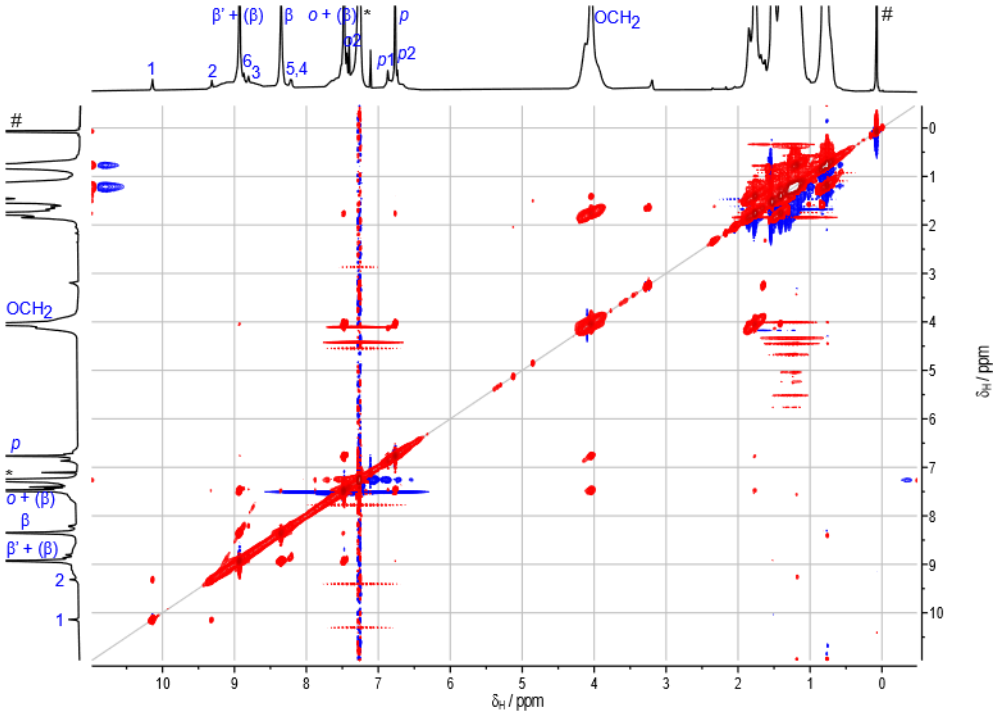

Figure B.104: Full CLIP-COSY spectrum (700 MHz, $CDCl_3$, 298 K) of ***cs*[*b*$_1$]-P24**. * = $CHCl_3$.

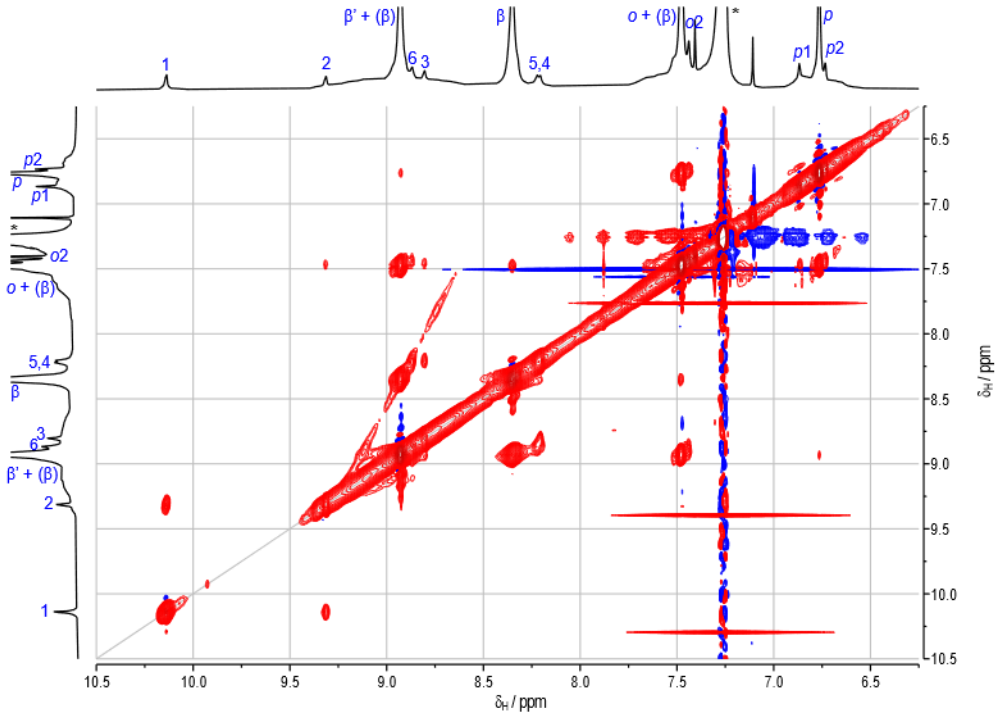

Figure B.105: Ar-region of CLIP-COSY spectrum (700 MHz, $CDCl_3$, 298 K) of ***cs*[*b*$_1$]-P24**. * = $CHCl_3$.

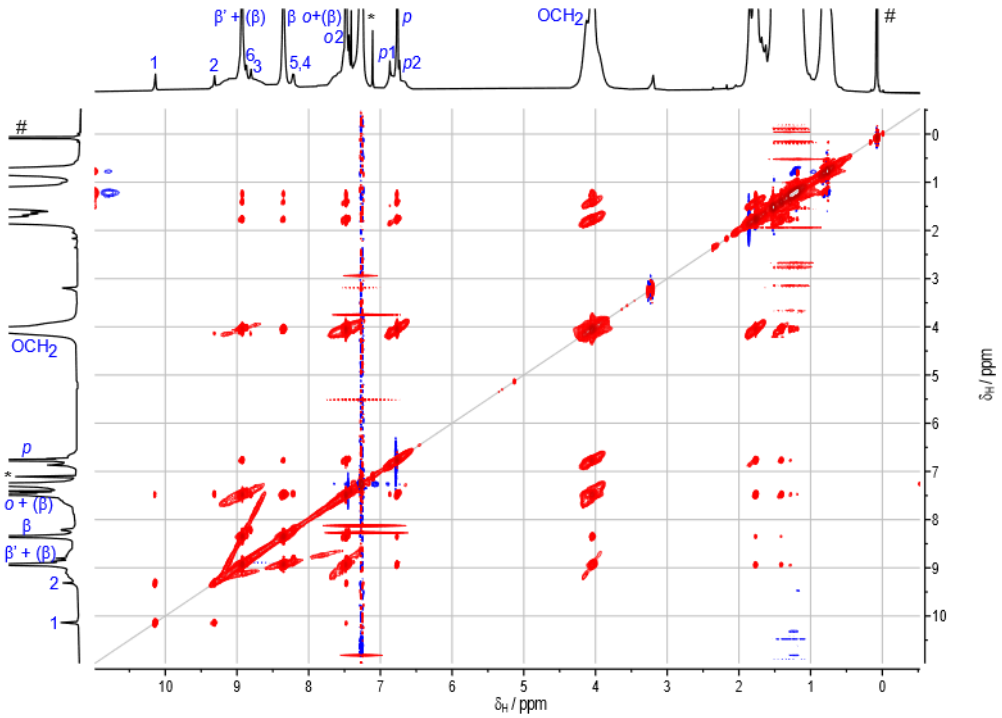

Figure B.106: Full NOESY (700 MHz, $CDCl_3$, 298 K) spectrum of ***cs*[*b*$_1$]-P24**. Mixing time = 400 ms. * = $CHCl_3$; # = silicone grease.

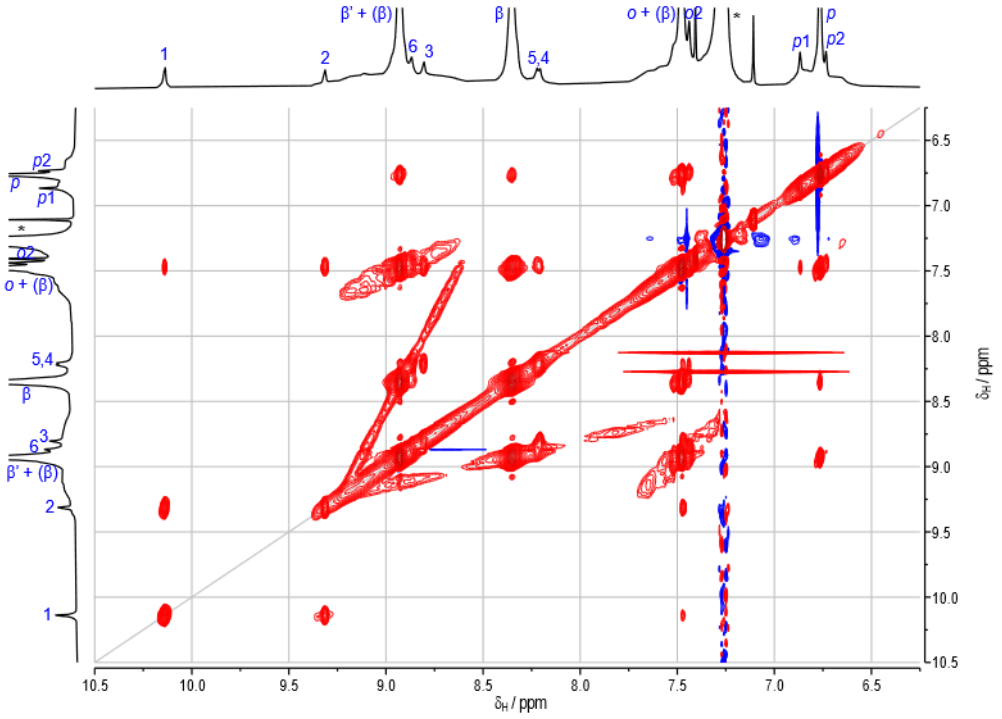

Figure B.107: Ar-region of NOESY spectrum (700 MHz, $CDCl_3$, 298 K) of ***cs*[*b*$_1$]-P24**. Mixing time = 400 ms. * = $CHCl_3$; # = silicone grease.

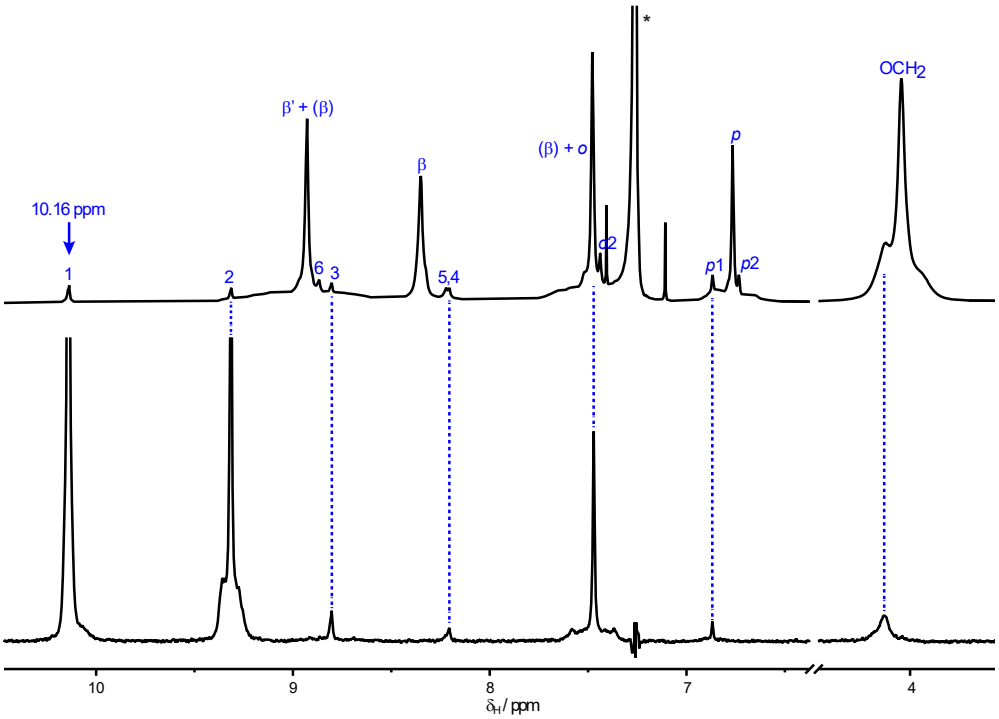

Figure B.108: Ar-region of the ^{1}H spectrum (top) and 1D selective NOESY spectrum (bottom) (700 MHz, $CDCl_3$, 298 K) of ***cs*[*b*$_1$]-P24**. Mixing time = 800 ms; selective pulse at 10.16 ppm (indicated by arrow). * = $CHCl_3$.

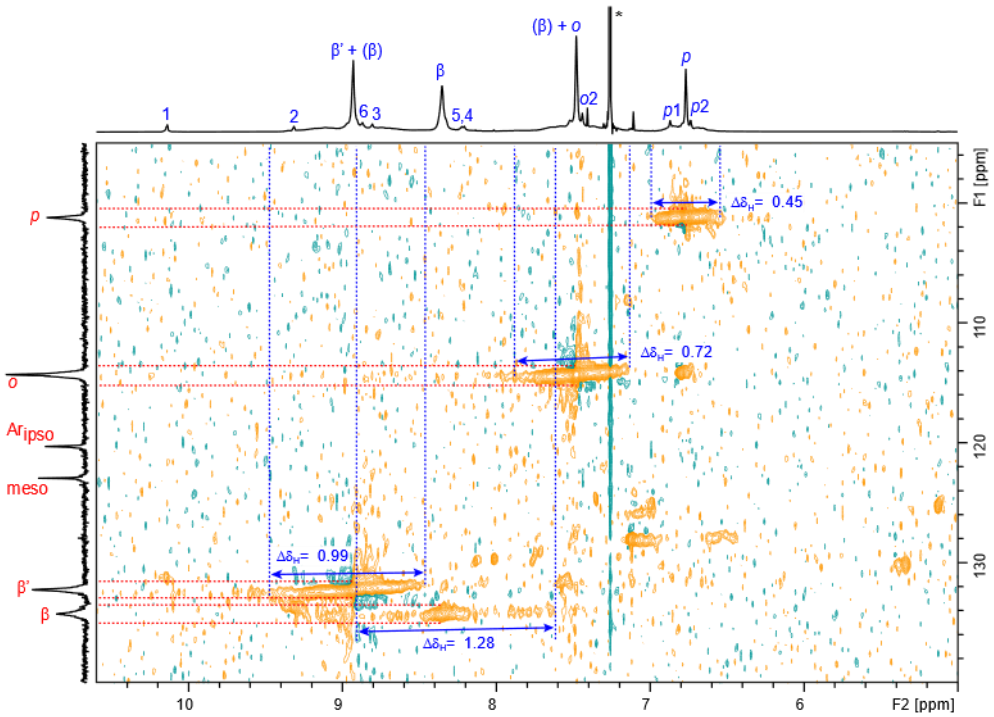

Figure B.109: Ar-region of HSQC spectrum (700 MHz, $CDCl_3$, 298 K) of ***cs*[*b*$_1$]-P24**.

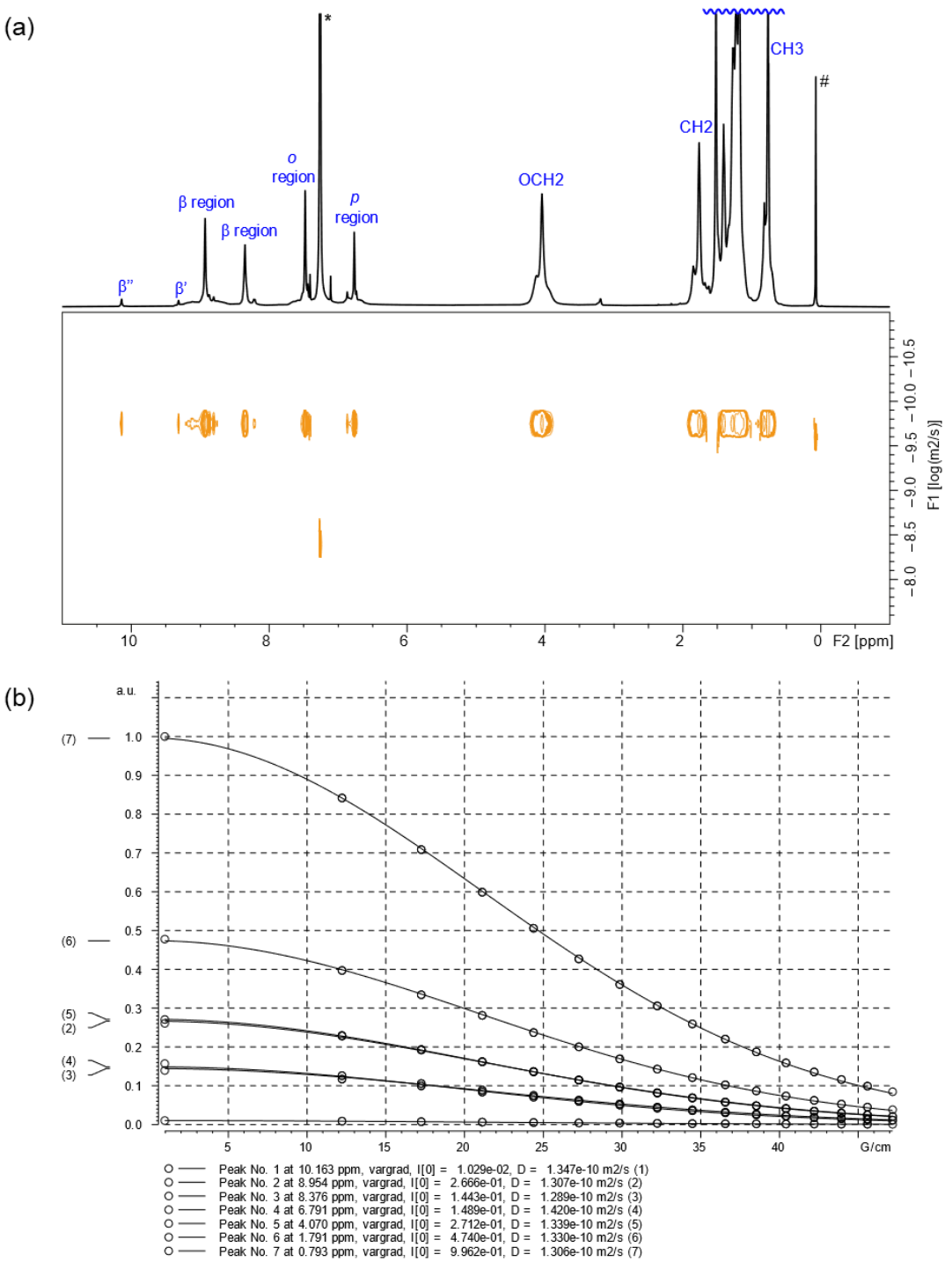

Figure B.110: ^{1}H diffusion NMR (700 MHz, $CDCl_3$, 298 K) of ***cs*[*b*$_1$]-P24**. (a) ^{1}H DOSY plot. (b) Diffusion decay plots fitted to the Stejskal Tanner equation and the resulting diffusion coefficients obtained. Acquisition parameters: G = 9.63–47.19 G/cm, D = 0.1 s, and d = 3600 µs. The average diffusion coefficient D = 1.33·10^{-10} m^{2}s^{-1}. * = residual solvent peak, # = silicone grease peak.

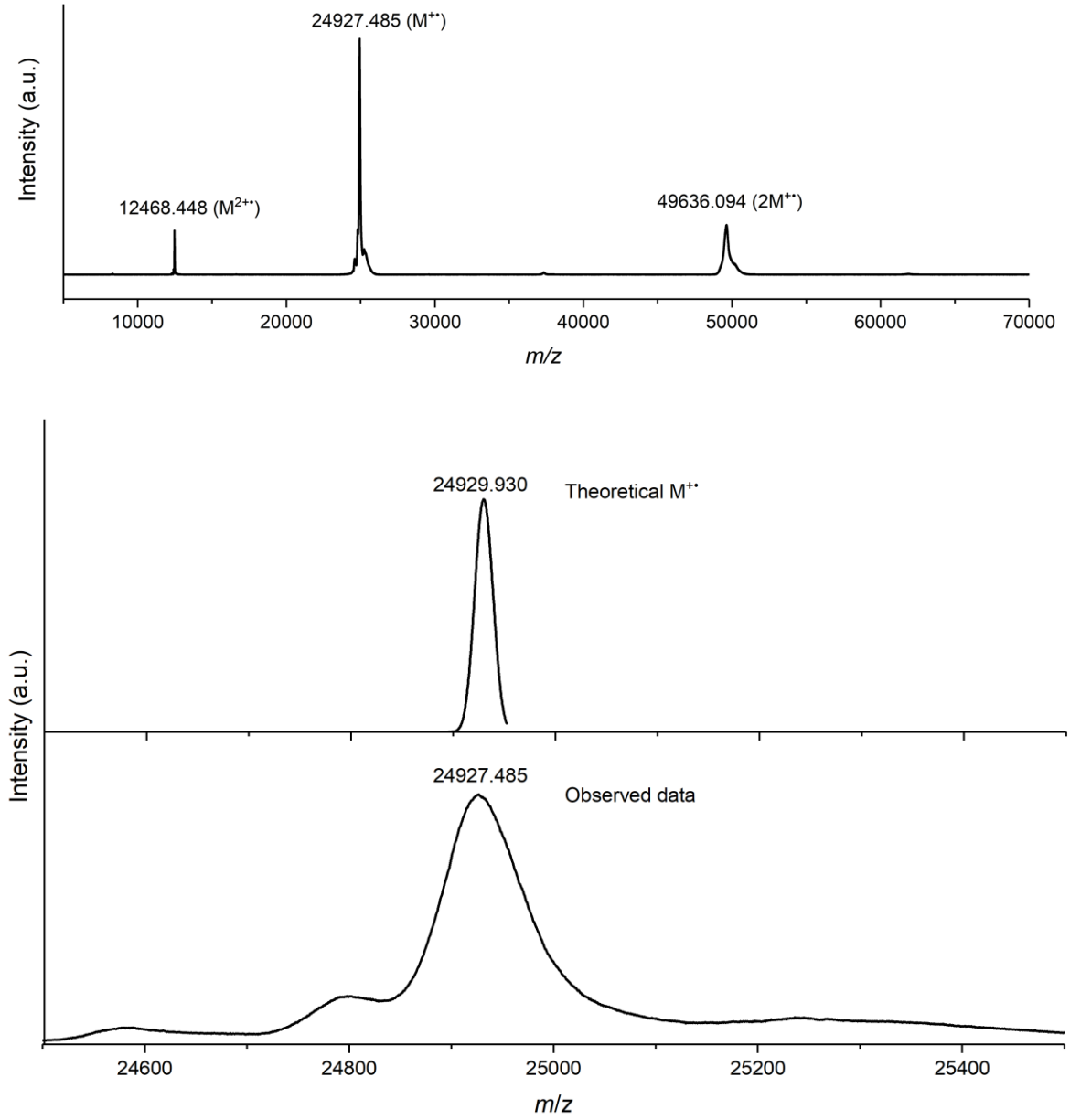

Figure B.111: MALDI-ToF spectrum of ***cs*[*b*$_1$]-P24** with DCTB as matrix. Overview (top) and zoomed-view of the $M^{+\bullet}$ region (bottom).

Table B.9: Complete ^{1}H NMR assignment and 2D correlations for the complex, ***cs*[*b*$_1$]-P24·(T12e)$_2$**.

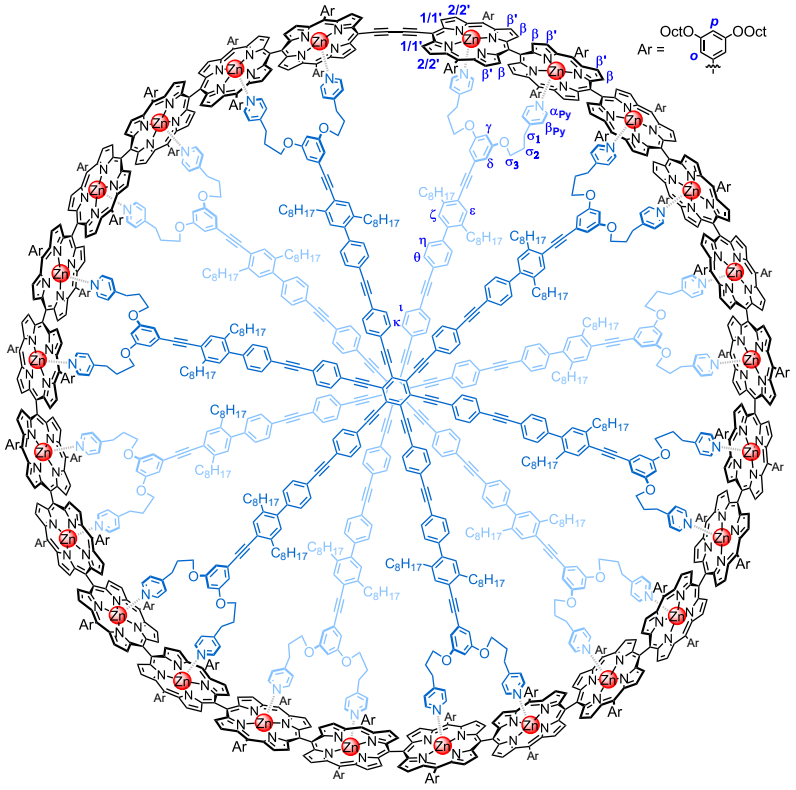

#	Assign.	^{1}H	Mult.	TOCSY[a]	NOESY[a]	HSQC
1	1	10.11–9.96	m, 2H	s: 2	s: 3(2); m: 2, 5, 6, 11	-
2	1’	9.93–9.77	m, 2H	s: 3(2’)	s: 3(2’); m: 1, 7, 11	-
3	2, β’, 2’	9.61–8.67	m, 96H	s: 1, 2	2 m: 5, 6, 11; w: 8 β’ s: 1, 2, 5, 6, 8, 11; m: 10, 12; w: 4 2’ m: 7, 11	131.5
4	β	8.73–7.93[b]	m	-	m: 11; w: 3(β’)	-
5	*o*	7.92–7.74	m, 120H	s: 8; m: 6	s: 3(β’), 11; m: 1, 3(2), 6, 8; w: 12	115.3
6	*o* + η/θ	7.73–7.49		s: 7, 8; m: 5	s: 3(β’), 7, 11; m: 3(2), 5, 8, 14	131.3, 113.9
7	ε + η/θ + ι/κ	7.46–6.98	m, 60H	s: 6, 9; w: 10	s: 6, 14, 11; m: 2, 3(2’), 8; w: 13	132.8, 131.4, 128.9, 127.8, 125.6
8	*p* + ζ	6.97–6.70	m, 60H	s: 5	s: 3(β’), 11, 13; m: 5, 6, 7; w: 3(2)	129.8, 100.4
9	ι/κ + δ + γ	6.68–6.21	m, 60H	s: 7	s: 11; m: 10, 13	127.6, 100.0
10	β_{Py}	6.00–5.56	m, 48H	m: 12; w: 7	s: 12; m: 3(β’), 9	123.4
11	OCH_2 Oct + σ_3	4.45–3.37	m, 240H	s: 15	s: 5, 7, 8, 9; m: 1, 2, 3(2), 3(2’), 4; w: 12	68.3, 68.3, 68.1
12	α_{Py}	3.35–2.86	m, 48H	m: 10	s: 10; m: 3(β’); w: 5, 11	143.4
13	σ_4	2.84–2.49	m, 24H	s: 15	s: 8; m: 9; w: 7	34.2
14	σ_4'	2.48–2.24	m, 24H	s: 15	s: 7; m: 6	32.3
15	aliphatic	2.24–0.40	m, 1848H	s: 11, 13, 14	n/a	n/a

[a] Relative intensities of TOCSY and NOE correlations are labeled as s, m, or w for strong, medium, or weak. [b] Most likely this region only covers a fraction of the β protons.

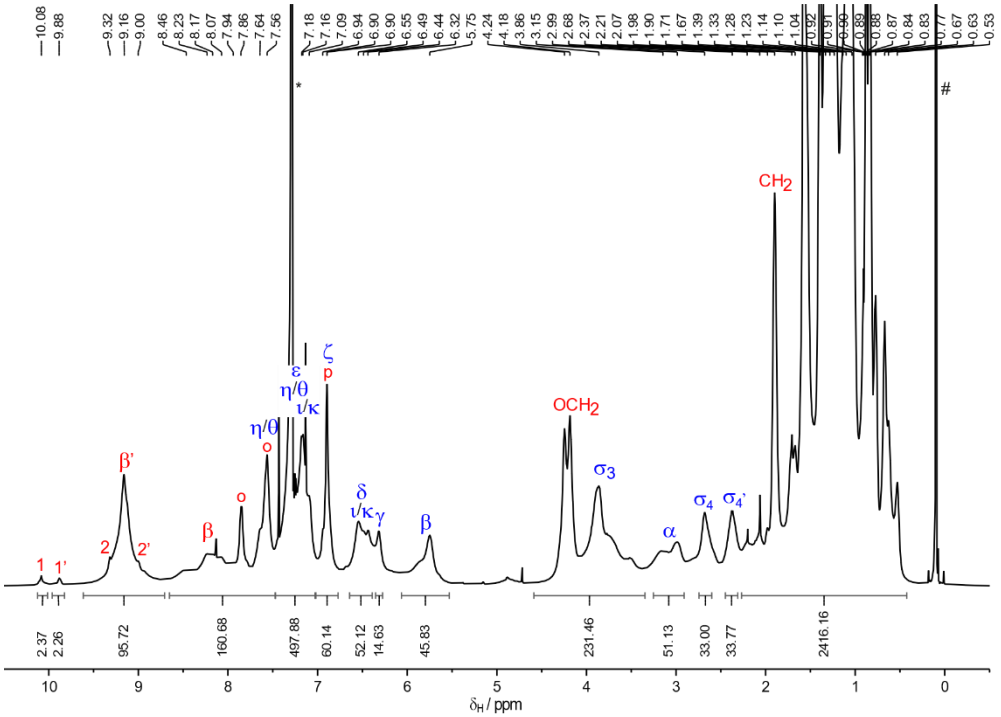

Figure B.112: ^{1}H NMR spectrum of ***cs*[*b*$_1$]-P24·(T12e)$_2$** (700 MHz, $CDCl_3$, 298 K). * = $CHCl_3$; # = silicone grease.

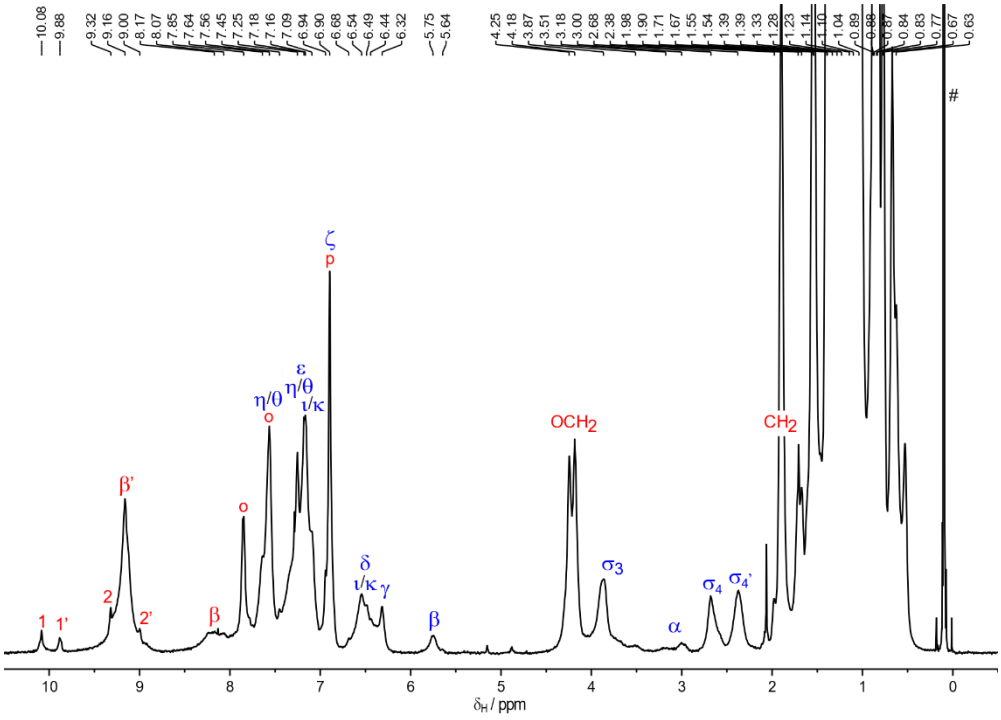

Figure B.113: Diffusion-edited ^{1}H NMR spectrum of ***cs*[*b*$_1$]-P24·(T12e)$_2$** (700 MHz, $CDCl_3$, 298 K). # = silicone grease. G = 18.7 G/cm, D = 0.19 s, and d = 1500 μs.

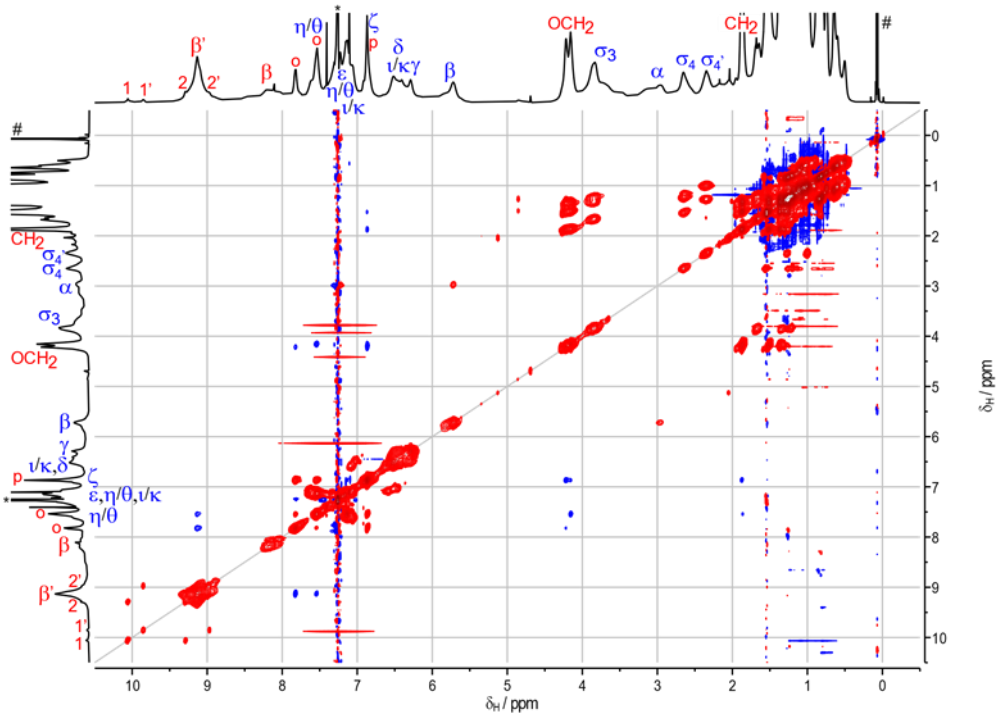

Figure B.114: Full TOCSY spectrum (700 MHz, $CDCl_3$, 298 K) of ***cs*[*b*$_1$]-P24·(T12e)$_2$**. * = $CHCl_3$; # = silicone grease. Negatively phased correlations (in blue) stem from NOE artefacts.

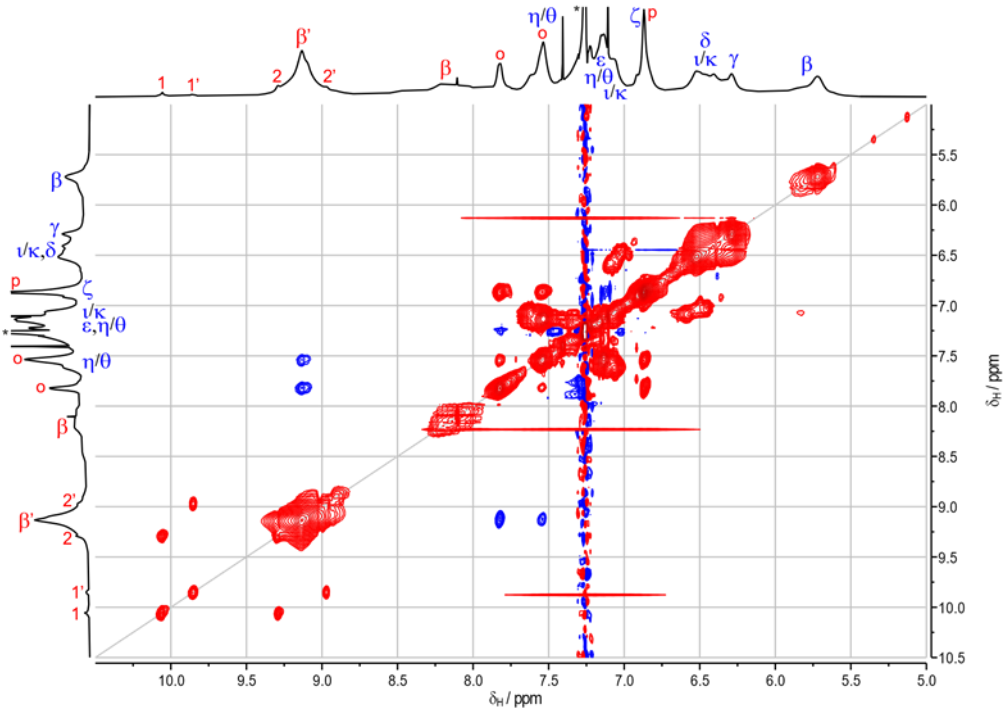

Figure B.115: Ar-region of TOCSY spectrum (700 MHz, $CDCl_3$, 298 K) of ***cs*[*b*$_1$]-P24·(T12e)$_2$**. * = $CHCl_3$.

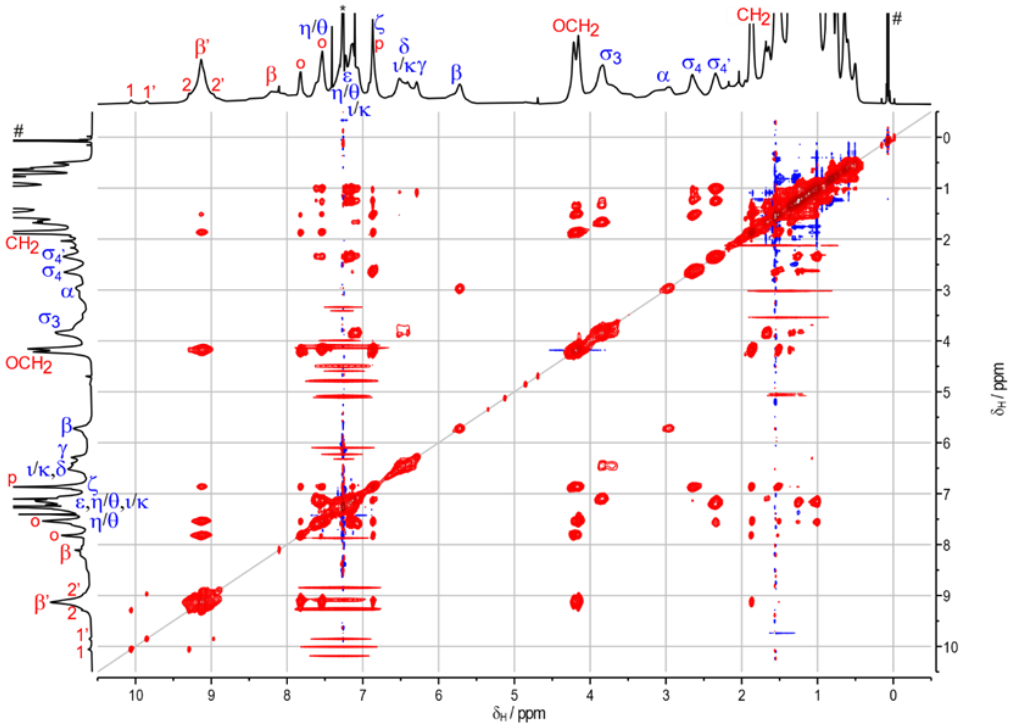

Figure B.116: Full NOESY (700 MHz, $CDCl_3$, 298 K) spectrum of ***cs*[*b*$_1$]-P24·(T12e)$_2$**. Mixing time = 400 ms. * = $CHCl_3$; # = silicone grease.

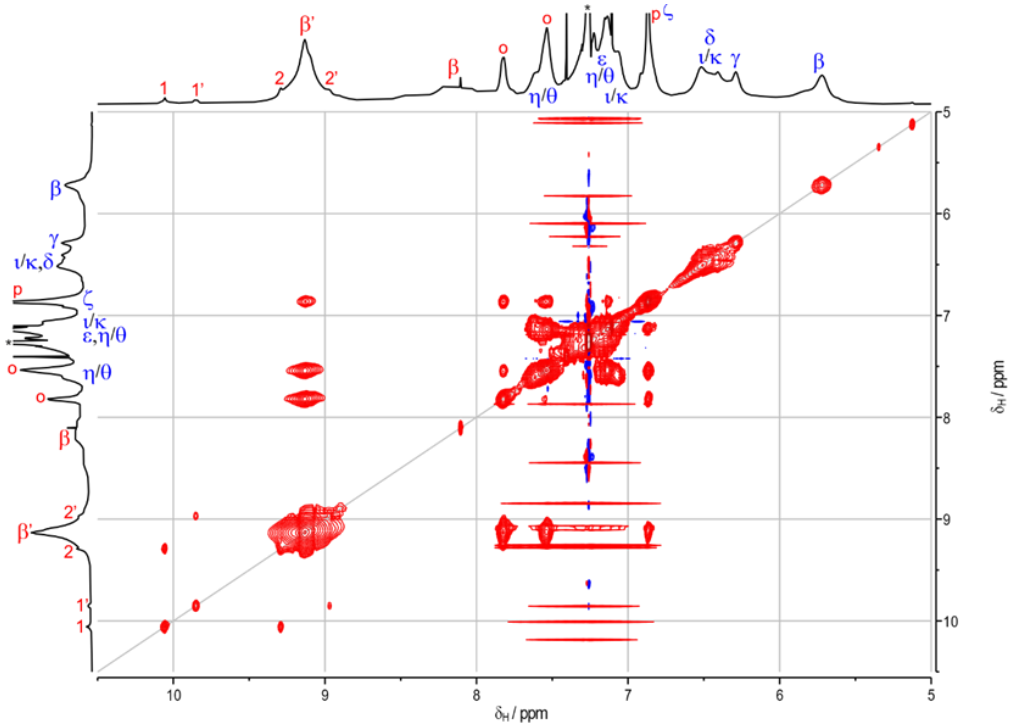

Figure B.117: Ar-region of NOESY spectrum (700 MHz, $CDCl_3$, 298 K) of ***cs*[*b*$_1$]-P24·(T12e)$_2$**. Mixing time = 400 ms. * = $CHCl_3$; # = silicone grease.

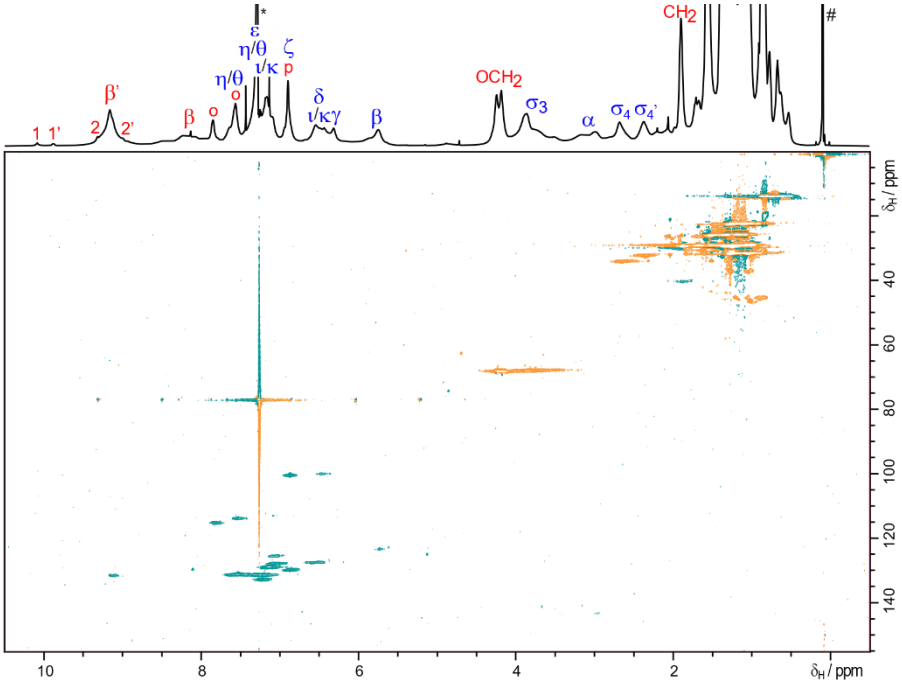

Figure B.118: Full HSQC spectrum (700 MHz, $CDCl_3$, 298 K) of ***cs*[*b*$_1$]-P24·(T12e)$_2$**.

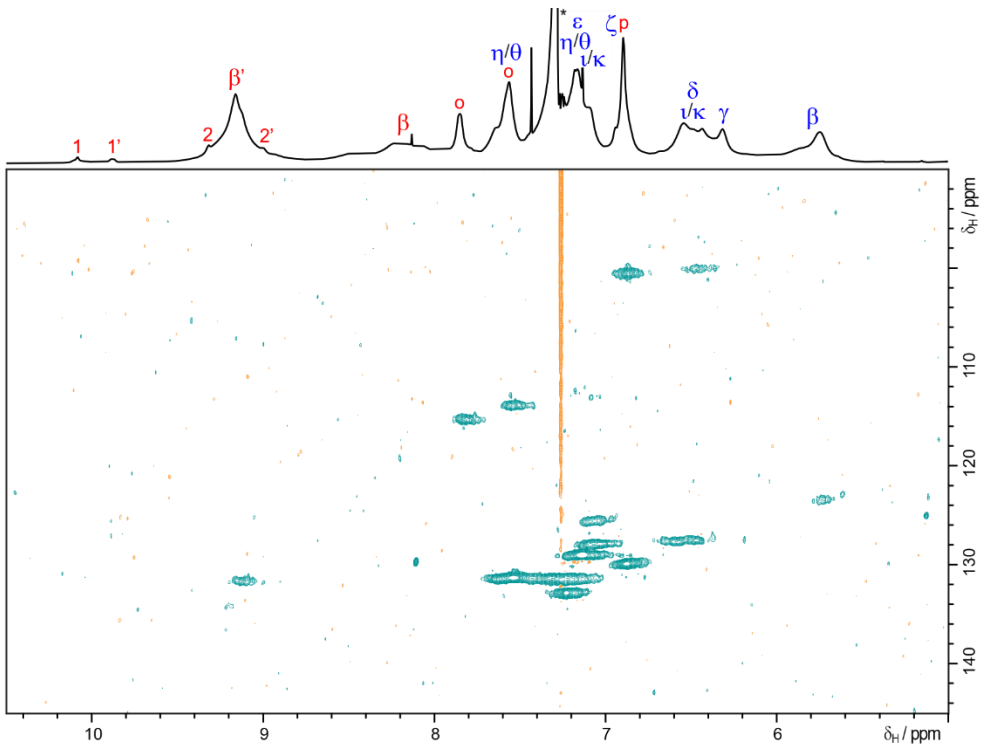

Figure B.119: Ar-region of HSQC spectrum (700 MHz, $CDCl_3$, 298 K) of ***cs*[*b*$_1$]-P24·(T12e)$_2$**.

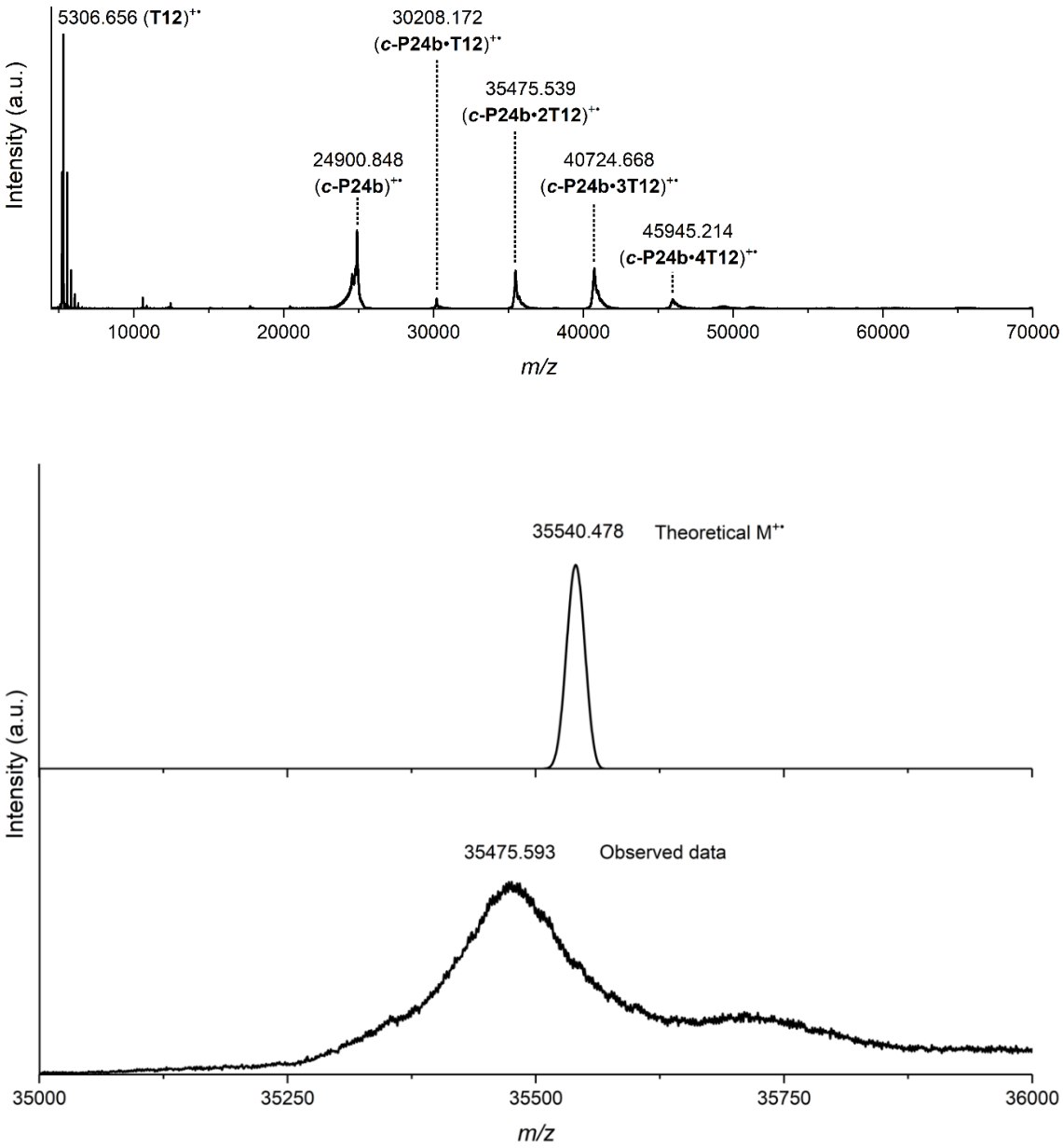

Figure B.120: MALDI-ToF spectrum of the complex, ***cs*[b_1]-P24·(T12e)$_2$**, with DCTB as matrix. Overview (top) and zoomed-view of the $M^{+\bullet}$ region (bottom).

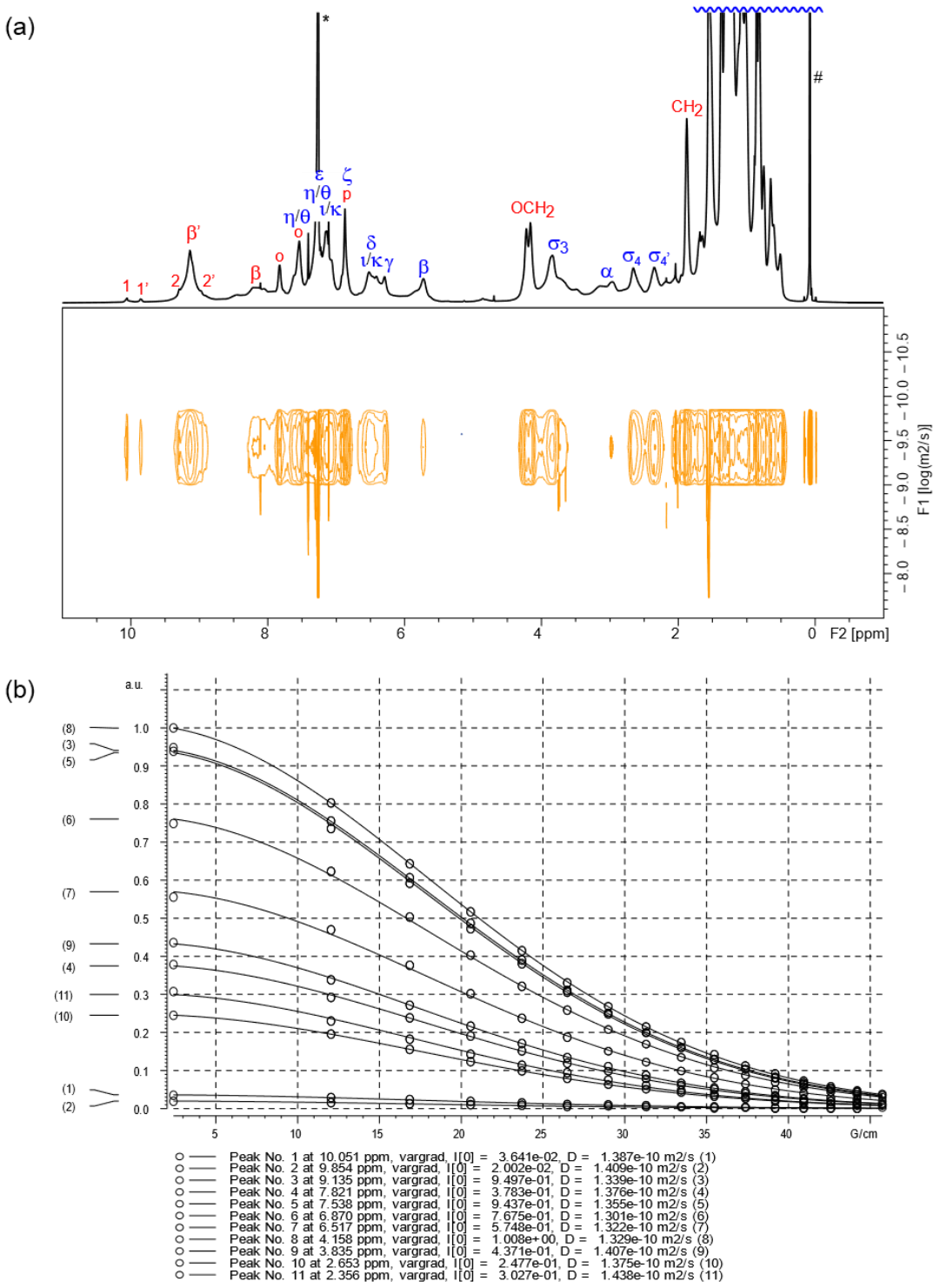

Figure B.121: ^{1}H diffusion NMR (700 MHz, $CDCl_3$, 298 K) of ***cs*[*b*$_1$]-P24·(T12e)$_2$**. (a) ^{1}H DOSY plot. (b) Diffusion decay plots fitted to the Stejskal Tanner equation and the resulting diffusion coefficients obtained. Acquisition parameters: G = 2.41–45.74 G/cm, D = 0.19 s, and d = 3000 µs. The average diffusion coefficient $D = 1.37 \cdot 10^{-10}$ m^{2}s^{-1}. * = residual solvent peak, # = silicone grease peak.

Appendix C — Experimental Procedures and Supplementary Details for Chapter 3

C.1 General Method

All reagents were purchased as reagent grade and used without further purification. Solvents for column chromatography were used in HPLC grade. Dry toluene and diisopropylamine (*i*-Pr_2NH) were obtained from the solvent drying system MBraun MBSPS-5-BenchTop under nitrogen atmosphere (H_2O content < 20 ppm as determined by Karl-Fischer titration). Flash column chromatography was carried out using SiO_2 (60 Å, 230–400 mesh) under positive pressure. Analytical thin-layer chromatography was carried out on aluminum-backed silica gel 60 F254 plate. Evaporation in vacuum was performed at 25–80 ºC and 10–900 mbar. Size exclusion chromatography (SEC) was carried out using Bio-Rad Bio-Beads S-X1 (40–80 μm bead size). Semi-preparative gel permeation chromatography (GPC) was carried out on a Shimadzu recycling GPC system equipped with a LC-20 AD pump, SPD-20A UV detector and a set either of JAIGEL 3H (20 × 600 mm) and JAIGEL 4H (20 × 600 mm) columns using toluene/pyridine (99:1) as eluent at a flow rate of 3.5 mL/min. Reported yields refer to spectroscopically and chromatographically pure compounds that were dried under high vacuum (0.01–0.005 mbar) before analytical characterization.

NMR spectra were recorded at 298 K using a Bruker AVIII HD 400, a Bruker AVIII HD 500, a Bruker NEO 600 with a broadband helium cryoprobe, or a Bruker AVIII 700 with an inverse TCI $^{1}H/^{13}C/^{15}N$ cryoprobe. ^{1}H NMR spectrum is reported in ppm; coupling constants are given in Hertz, to the nearest 0.1 Hz. The solvent used was $CDCl_3$ which was calibrated to residual $CHCl_3$ at 7.26 ppm. Multiplicity (s = singlet, d = doublet, t = triplet, q = quartet, m = multiplet) and coupling constants were reported whenever possible. ^{1}H NMR signals were assigned based on comparison between compounds, chemical shifts, integrals and coupling constants.

MALDI-ToF spectra were measured using a Bruker MALDI Autoflex Speed spectrometer, or at the EPSRC National Mass Spectrometry service (Swansea) using a Bruker MicroflexTM LRF spectrometer. *Trans*-2-[3-(4-*tert*-butylphenyl)-2-methyl-2-propenylidene]-malononitrile (DCTB) was employed as matrix.

UV–vis–NIR absorbance measurement was recorded with a Perkin-Elmer Lambda 20 spectrophotometer or a Jasco V770 spectrophotometer using an Infrasil® Quartz 1 cm cuvette. Measurements were carried out at 298 K under ambient conditions.

C.2 Syntheses of ZnP1-R$_2$

C.2.1 Synthesis of ZnP1-TMS$_2$

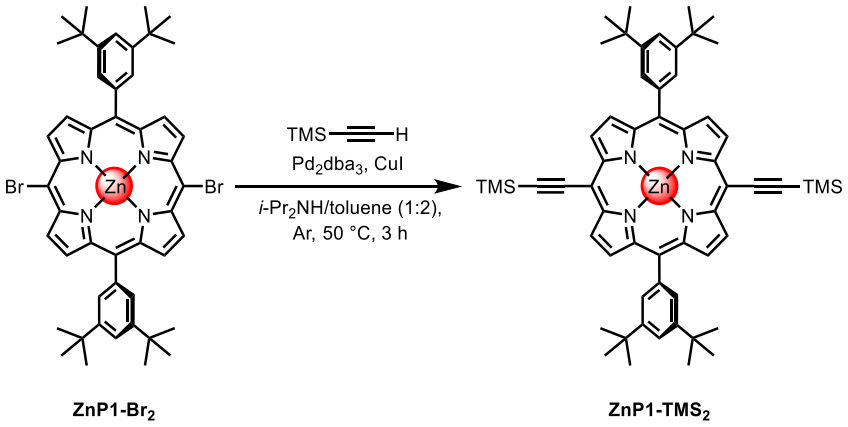

A mixture of **ZnP1-Br$_2$** (64 mg, 0.07 mmol, 1.0 equiv.), tris(dibenzylideneacetone)-dipalladium(0) (Pd_2dba_3, 6.4 mg, 7 µmol, 10 mol%), CuI (2.8 mg, 14 µmol, 20 mol%) and PPh_3 (3.6 mg, 14 µmol, 20 mol%) in dry toluene (4.5 mL), pyridine (0.13 mL) and *i*-Pr_2NH (2.4 mL) was degassed by three freeze-pump-thaw cycles. After that, TMS-acetylene (54 µL, 0.42 mmol, 6.0 equiv.) was added to the mixture and the reaction was stirred at 50 ºC for 3 h. After reaction, the resulting mixture was concentrated and purified by flash column chromatography on silica gel using petroleum ether/CH_2Cl_2 (3:1) as eluent to give the crude product. The crude product was recrystallized by layer addition (CH_2Cl_2/CH_3OH) to give the desired product **ZnP1-TMS$_2$** (50 mg, 76% yield).

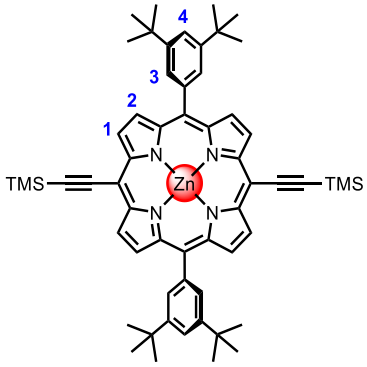

^{1}H NMR (400 MHz, $CDCl_3$, 298 K): δ 9.62 (d, *J* = 4.6 Hz, 4H, **H$_1$**), 8.87 (d, *J* = 4.6 Hz, 4H, **H$_2$**), 7.99 (d, *J* = 1.8 Hz, 4H, **H$_3$**), 7.78 (d, *J* = 1.8 Hz, 2H, H$_4$), 1.53 (s, 36H, **H$_{t\text{-Bu}}$**), 0.57 (s, 18H, **H$_{TMS}$**).

MALDI-ToF: *m*/*z* = 940.361 ($C_{58}H_{68}N_4Si_2Zn$, $M^{+\bullet}$ requires 940.427).

C.2.2 Synthesis of ZnP1-TIPS$_2$

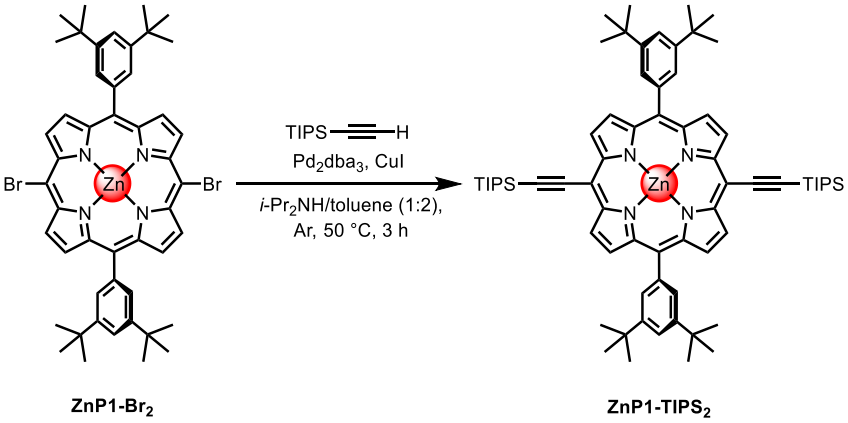

A mixture of **ZnP1-Br$_2$** (100 mg, 0.11 mmol, 1.0 equiv.), Pd_2dba_3 (10.2 mg, 11 µmol, 10 mol%), CuI (5.0 mg, 22 µmol, 20 mol%) and PPh_3 (5.5 mg, 22 µmol, 20 mol%) in toluene (6.0 mL), pyridine (0.17 mL) and *i*-Pr_2NH (3.0 mL) was degassed by three freeze-pump-thaw cycles. After that, TIPS-acetylene (74 µL, 0.33 mmol, 3.0 equiv.) was added to the mixture and the reaction was conducted at 50 ºC for 3 h. After the reaction, the resulting mixture was concentrated and purified by flash column chromatography on silica gel using petroleum ether/CH_2Cl_2 (3:1) as eluent to give the crude product. The crude product was recrystallized by layer addition (CH_2Cl_2/CH_3OH) to give the desired product **ZnP1-TIPS$_2$** (118 mg, 96%).

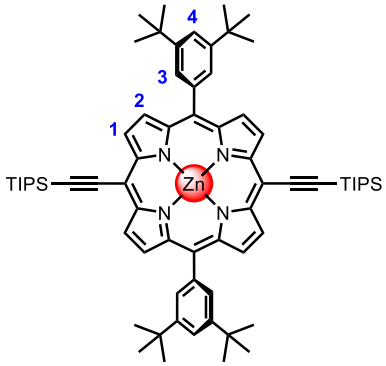

^{1}H NMR (400 MHz, $CDCl_3$, 298 K) δ 9.76 (d, *J* = 4.6 Hz, 4H, **H$_1$**), 8.97 (d, *J* = 4.6 Hz, 4H, **H$_2$**), 8.03 (d, *J* = 1.8 Hz, 4H, **H$_3$**), 7.82 (s, 2H, H$_4$), 1.55 (s, 36H, **H$_{t\text{-Bu}}$**), 1.52–1.40 (m, 42H, **H$_{TIPS}$**).

MALDI-TOF: *m*/*z* = 1111 ($C_{70}H_{92}N_4Si_2Zn$, $M^{+\bullet}$ requires 1111).

C.2.3 Synthesis of ZnP1-H_2

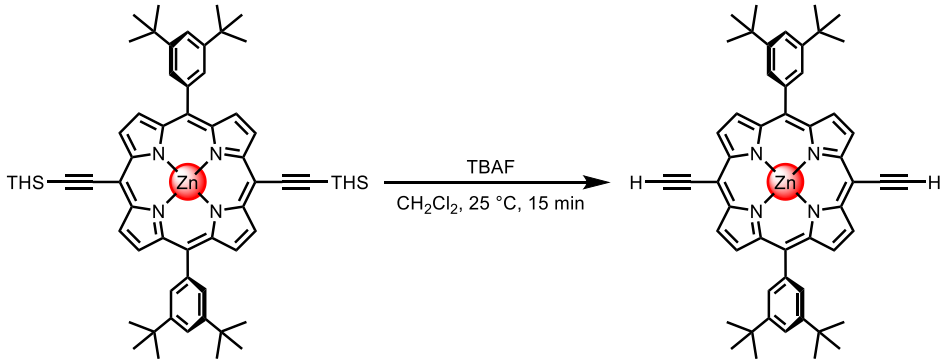

To a solution of **ZnP1-THS_2** (228 mg, 0.166 mmol, 1.0 equiv.) in CH_2Cl_2 (30 mL), tetrabutylammonium fluoride solution (1.0 M in THF, 1.66 mL, 1.66 mmol, 10 equiv.) was added dropwise. The reaction was stirred at 25 ºC for 15 min. After the reaction, the resulting mixture was purified by flash column chromatography on silica gel using $CHCl_3$/pyridine (99:1) as eluent to give the crude product. The crude product was recrystallized by layer addition (CH_2Cl_2/CH_3OH) to give the desired product **ZnP1-H_2** (117 mg, 88%).

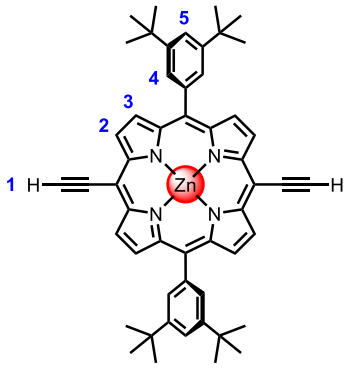

^{1}H NMR (400 MHz, $CDCl_3$ + 1% pyridine-d_5, 298 K): δ 9.60 (d, *J* = 4.6 Hz, 4H, **H_2**), 8.84 (d, *J* = 4.6 Hz, 4H, **H_3**), 7.93 (d, *J* = 1.8 Hz, 4H, **H_4**), 7.72 (t, *J* = 1.8 Hz, 2H, **H_5**), 4.07 (s, 2H, **H_1**), 1.47 (s, 36H, **$H_{t\text{-}Bu}$**).

MALDI-ToF: *m*/*z* = 796.312 ($C_{52}H_{52}N_4Zn$, $M^{+\bullet}$ requires 796.348).

C.2.4 Synthesis of ZnP1-(AuPPh$_3$)$_2$

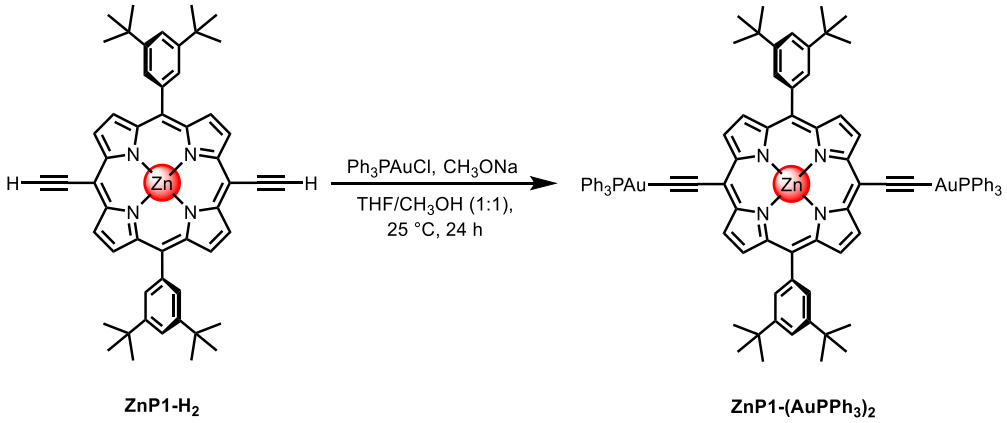

To a solution of **ZnP1-H$_2$** (4.0 mg, 5.0 μmol, 1.0 equiv.) and Ph$_3$PAuCl (4.9 mg, 10 μmol, 2.0 equiv.) in THF (2.0 mL), a suspension of sodium methoxide (1.4 mg, 25 μmol, 5.0 equiv.) in CH$_3$OH (2.0 mL) was added and the mixture was stirred at 25 ºC for 24 h. After reaction, H$_2$O (8.0 mL) was dropwise added to the reaction mixture to precipitate the crude product. The crude product as solids was collected after removal of the solvent by filtration, and recrystallized by layer addition (CHCl$_3$/CH$_3$OH) to give the desired product **ZnP1-(AuPPh$_3$)$_2$** (7.2 mg, 84%).

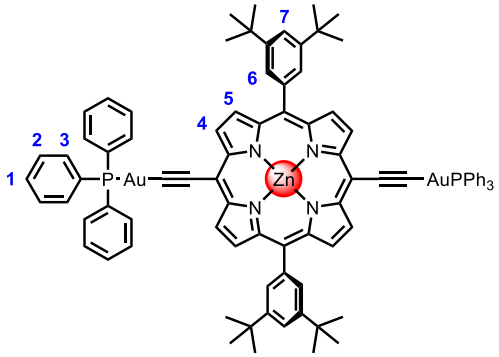

^{1}H NMR (500 MHz, CDCl$_3$, 298 K): δ 9.95 (d, *J* = 4.5 Hz, 4H, **H$_4$**), 8.90 (d, *J* = 4.6 Hz, 4H, **H$_5$**), 8.08 (d, *J* = 1.9 Hz, 4H, **H$_6$**), 7.78 (t, *J* = 1.9 Hz, 2H, **H$_7$**), 7.72 (ddd, *J* = 12.7, 7.6, 1.7 Hz, 12H, **H$_3$**), 7.60 – 7.50 (m, 18H, **H$_{1,2}$**), 1.55 (s, 36H, **H$_{t\text{-Bu}}$**).

^{31}P NMR (162 MHz, CDCl$_3$, 298 K) δ 42.46.

MALDI-TOF: *m*/*z* = 1713 ($C_{312}H_{512}N_{12}Si_{12}Zn_3$, $M^{+\bullet}$ requires 1712).

C.2.5 Synthesis of ZnP1-(AuP(OMe)$_3$)$_2$

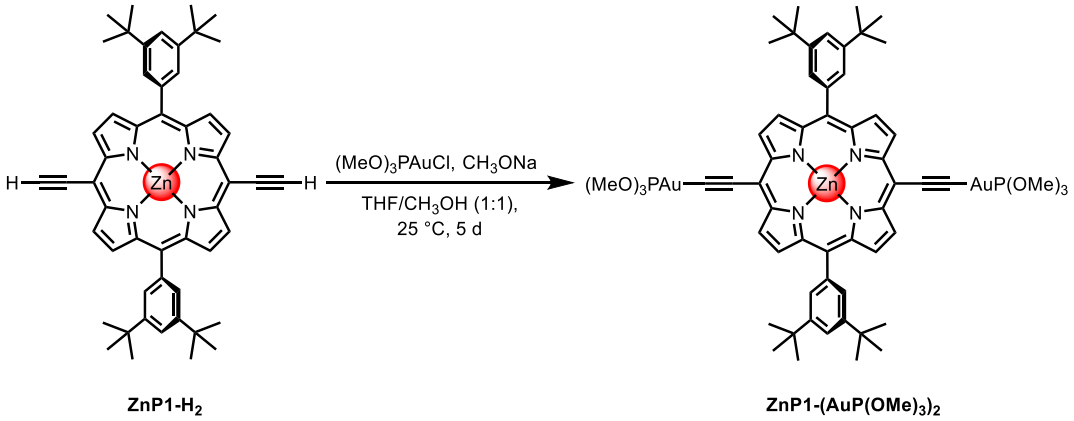

To a solution of **ZnP1-H$_2$** (4.0 mg, 5.0 µmol, 1.0 equiv.) and (MeO)$_3$PAuCl (3.6 mg, 10 µmol, 2.0 equiv.) in THF (2 mL), a suspension of CH_3ONa (5.2 mg, 100 µmol, 20 equiv.) in CH_3OH (2.0 mL) was added and the mixture was stirred at 25 ºC for 5 d. After reaction, the resulting mixture was concentrated *in vacuo*. The resulting solids were dissolved in dichloromethane (5 mL) and filtered. The filtrate collected was concentrated *in vacuo* and the crude product was recrystallized by layer addition ($CHCl_3$/CH_3OH) to give the desired product **ZnP1-(AuP(OMe)$_3$)$_2$** (3.8 mg, 53%).

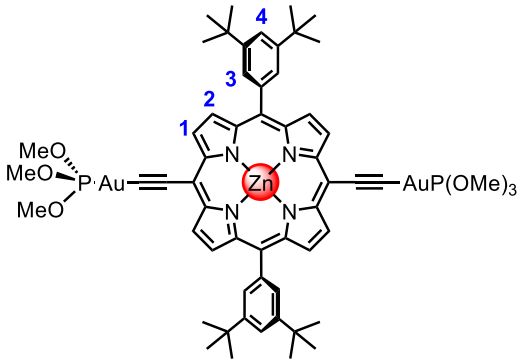

^{1}H NMR (400 MHz, $CDCl_3$, 298 K): δ 9.87 (d, *J* = 4.6 Hz, 4H, **H$_1$**), 8.89 (d, *J* = 4.6 Hz, 4H, **H$_2$**), 8.07 (d, *J* = 1.8 Hz, 4H, **H$_3$**), 7.79 (t, *J* = 1.8 Hz, 2H, **H$_4$**), 3.92 (d, *J* = 13.4 Hz, 18H, **H$_{OMe}$**), 1.55 (s, 36H, **H$_{t\text{-}Bu}$**).

^{31}P NMR (162 MHz, $CDCl_3$, 298 K) δ 150.67.

MALDI-TOF: *m*/*z* = 1437 ($C_{312}H_{512}N_{12}Si_{12}Zn_3$, $M^{+\bullet}$ requires 1436).

C.3 Syntheses of *ls*-ZnP*N*

C.3.1 $AgPF_6$-Mediated Oligomerization of ZnP1

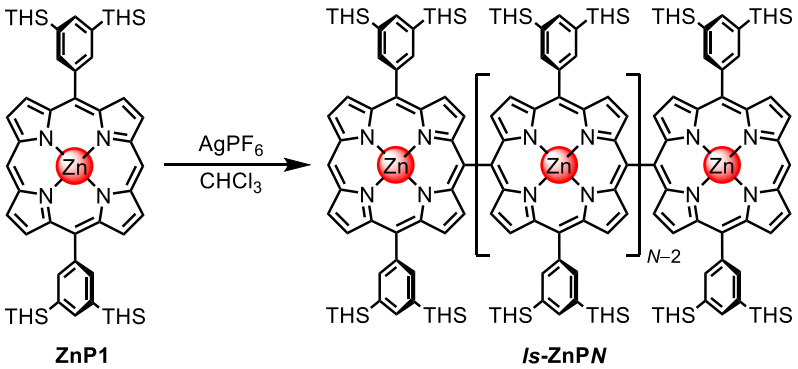

To a solution of **ZnP1** (190 mg, 0.11 mmol, 1.0 equiv.) in dry $CHCl_3$ (30 mL) with *N*,*N*-dimethylacetamide (DMA, 0.3 mL), under argon, $AgPF_6$ solution (0.24 M in dry CH_3CN, 1.4 mL, 0.34 mmol, 3.0 equiv.) was added and the mixture was heated at reflux. After 3 h, $AgPF_6$ solution (0.24 M in dry acetonitrile, 1.4 mL, 0.34 mmol, 3.0 equiv.) was added and the mixture was kept stirring at reflux. The aforementioned step of addition of the $AgPF_6$ solution repeated twice after 24 h and 27 h relative to the reaction start time. After reaction, the resulting mixture was concentrated and purified by flash column chromatography (SiO_2) using petroleum ether/CH_2Cl_2 (97:3) as eluent, followed by size-exclusion chromatography (Bio-Beads, S-X1) with toluene/pyridine (99:1) as eluent to give a crude mixture of different oligomers. The crude mixture was further subjected to recycling GPC to separate the desired products ***ls*-ZnP2** (36 mg, 19%), ***ls*-ZnP3** (15 mg, 7.9% yield), ***ls*-ZnP4** (8.2 mg, 4.3% yield), ***ls*-ZnP5** (5.9 mg, 3.1%), ***ls*-ZnP6** (2.3 mg, 1.2%) and ***ls*-P7** (2.2 mg, 1.2% yield).

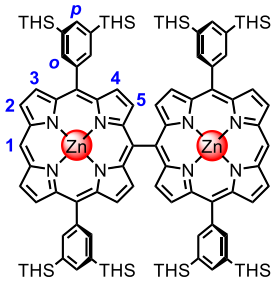

^{1}H NMR (600 MHz, $CDCl_3$, 298 K): δ 10.40 (s, 2H, $\mathbf{H_1}$), 9.48 (d, *J* = 4.5 Hz, 4H, $\mathbf{H_2}$), 9.11 (d, *J* = 4.5 Hz, 4H, $\mathbf{H_3}$), 8.69 (d, *J* = 4.7 Hz, 4H, $\mathbf{H_4}$), 8.31 (d, *J* = 1.3 Hz, 8H, $\mathbf{H_o}$), 8.10 (d, *J* = 4.7 Hz, 4H, $\mathbf{H_5}$), 7.89 (d, *J* = 1.3 Hz, 4H, $\mathbf{H_p}$), 1.41 – 0.61 (m, 312H, $\mathbf{H_{THS}}$).

MALDI-ToF: *m*/*z* = 3310.526 ($C_{208}H_{342}N_8Si_8Zn_2$, $M^{+\bullet}$ requires 3310.377).

UV–vis–NIR ($CDCl_3$, 298 K) λ_{max} / nm (ε / μM^{-1} cm^{-1}): 415 (0.30), 447 (0.23), 553 (0.06).

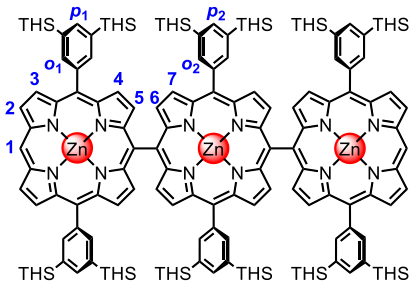

^{1}H NMR (600 MHz, $CDCl_3$, 298 K): δ 10.42 (s, 2H, **H$_1$**), 9.50 (d, *J* = 4.4 Hz, 4H, **H$_2$**), 9.13 (d, *J* = 4.4 Hz, 4H, **H$_3$**), 8.78 (d, *J* = 4.5 Hz, 4H, **H$_4$**), 8.66 (d, *J* = 4.8 Hz, 4H, **H$_7$**), 8.35 (s, 8H, **H$_{o1}$**), 8.29 – 8.25 (m, 8H, **H$_{5,o2}$**), 8.15 (d, *J* = 4.8 Hz, 4H, **H$_6$**), 7.93 (s, 4H, **H$_{p1}$**), 7.76 (s, 2H, **H$_{p2}$**), 1.46 – 0.35 (m, 468H, **H$_{THS}$**).

MALDI-ToF: *m*/*z* = 4964.926 ($C_{312}H_{512}N_{12}Si_{12}Zn_3$, $M^{+\bullet}$ requires 4964.558).

UV–vis–NIR ($CDCl_3$, 298 K) λ_{max} / nm (ε / μM^{-1} cm^{-1}): 415 (0.42), 475 (0.32), 567 (0.10).

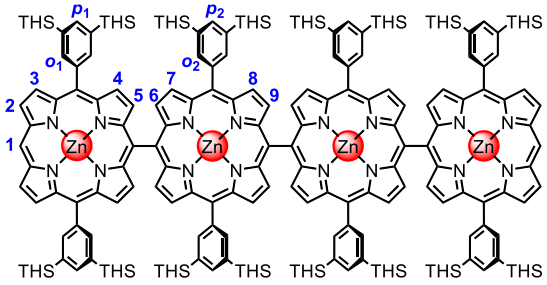

^{1}H NMR (600 MHz, $CDCl_3$, 298 K): δ 10.42 (s, 2H, **H$_1$**), 9.50 (d, *J* = 4.5 Hz, 4H, **H$_2$**), 9.13 (d, *J* = 4.5 Hz, 4H, **H$_3$**), 8.79 (d, *J* = 4.6 Hz, 4H, **H$_4$**), 8.74 (d, *J* = 4.6 Hz, 4H, **H$_8$**), 8.67 (d, *J* = 4.7 Hz, 4H, **H$_7$**), 8.35 (s, 8H, **H$_{o1}$**), 8.32 – 8.27 (m, 16H, **H$_{5,9,o2}$**), 8.16 (d, *J* = 4.7 Hz, 4H, **H$_6$**), 7.93 (s, 4H, **H$_{p1}$**), 7.79 (s, 4H, **H$_{p2}$**), 1.46 – 0.36 (m, 624H, **H$_{THS}$**).

MALDI-ToF: *m*/*z* = 6618.621 ($C_{416}H_{682}N_{16}Si_{16}Zn_4$, $M^{+\bullet}$ requires 6618.739).

UV–vis–NIR ($CDCl_3$, 298 K) λ_{max} / nm (ε / μM^{-1} cm^{-1}): 412 (0.52), 482 (0.37), 567 (0.15).

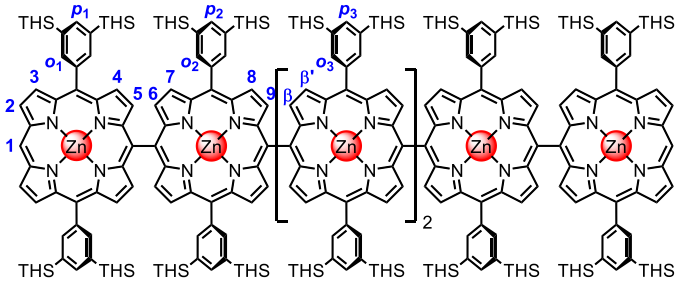

^{1}H NMR (600 MHz, $CDCl_3$, 298 K): δ 10.43 (s, 2H, **H$_1$**), 9.51 (d, *J* = 4.4 Hz, 4H, **H$_2$**), 9.15 (d, *J* = 4.4 Hz, 4H, **H$_3$**), 8.80 (d, *J* = 4.6 Hz, 4H, **H$_4$**), 8.79 – 8.75 (m, 12H, **H$_{8,\beta'}$**), 8.69 (d, *J* = 4.6 Hz, 4H, **H$_7$**), 8.38 – 8.29 (m, 40H, **H$_{5,9,\beta,o1,o2,o3}$**), 8.17 (d, *J* = 4.8 Hz, 4H, **H$_6$**), 7.94 (s, 4H, **H$_{p1}$**), 7.84 (s, 4H, **H$_{p3}$**), 7.81 (s, 4H, **H$_{p2}$**), 1.45 – 0.41 (m, 936H, **H$_{THS}$**).

MALDI-ToF: *m*/*z* = 9926.701 ($C_{624}H_{1022}N_{24}Si_{24}Zn_6$, $M^{+\bullet}$ requires 9927.101).

UV–vis–NIR ($CDCl_3$, 298 K) λ_{max} / nm (ε / μM^{-1} cm^{-1}): 412 (0.70), 492 (0.61), 573 (0.31).

C.3.2 $AgPF_6$-Mediated Oligomerization of *ls*-ZnP2

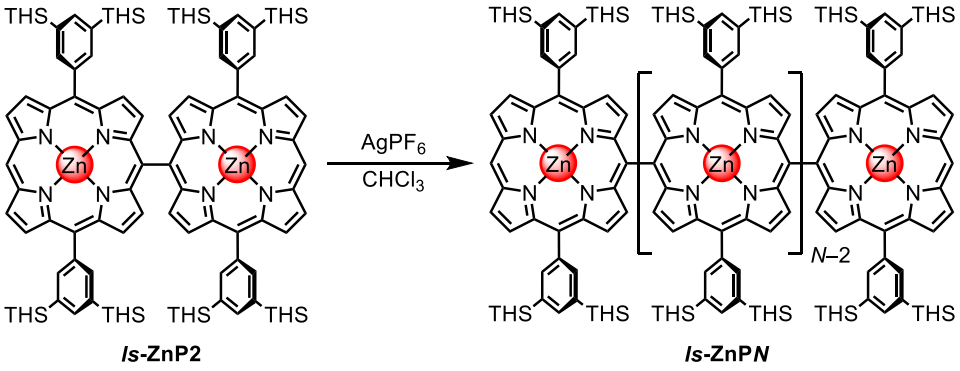

To a solution of ***ls*-ZnP2** (40 mg, 12 μmol, 1.0 equiv.) in dry $CHCl_3$ (20 mL) with DMA (0.1 mL), under argon, a $AgPF_6$ solution (0.24 M in dry CH_3CN, 0.4 mL, 96 μmol, 6.0 equiv.) was added and the mixture was heated at reflux. After 3 d, a $AgPF_6$ solution (0.24 M in dry CH_3CN, 1.0 mL, 240 μmol, 15 equiv.) was added and the mixture was kept stirring at reflux. After 1 d, an additional portion of $AgPF_6$ solution (0.24 M in dry CH_3CN, 1.0 mL, 240 μmol, 15 equiv.) was added. After reaction, the resulting mixture was concentrated and passed through flash column chromatography (SiO_2) using petroleum ether/CH_2Cl_2 (97:3) as eluent, followed by size-exclusion chromatography (Bio-Beads, S-X1) with toluene/pyridine (99:1) as eluent to give a crude mixture of different oligomers. The crude mixture was further subjected to recycling GPC to separate the desired products ***ls*-ZnP4** (4.7 mg, 12%), ***ls*-ZnP6** (1.4 mg, 3.5%) and ***ls*-ZnP8** (1.0 mg, 2.5%).

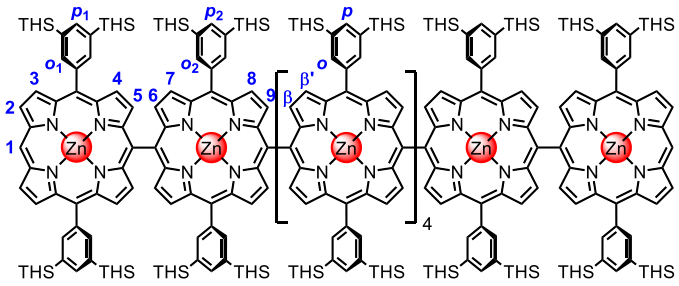

^{1}H NMR (600 MHz, $CDCl_3$, 298 K): δ 10.44 (s, 2H, **H_1**), 9.52 (d, *J* = 4.4 Hz, 4H, **H_2**), 9.15 (d, *J* = 4.4 Hz, 4H, **H_3**), 8.84 – 8.74 (m, 24H, **$H_{4,8,\beta'}$**), 8.69 (d, *J* = 4.6 Hz, 4H, **H_7**), 8.39 – 8.30 (m, 56H, **$H_{5,9,\beta,o1,o2,o}$**), 8.18 (d, *J* = 4.6 Hz, 4H, **H_6**), 7.95 (s, 4H, **H_{p1}**), 7.89 – 7.83 (m, 8H, **H_p**), 7.81 (s, 4H, **H_{p2}**), 1.46 – 0.32 (m, 1184H, **H_{THS}**).

MALDI-ToF: *m*/*z* = 13237.28 ($C_{832}H_{1362}N_{32}Si_{32}Zn_8$, $M^{+\bullet}$ requires 13235.463).

UV–vis–NIR ($CDCl_3$, 298 K) λ_{max} / nm (ε / μM^{-1} cm^{-1}): 412 (0.77), 497 (0.70), 575 (0.41).

C.3.3 Ag[Al(pftb)$_4$]-Mediated Oligomerization of ZnP1

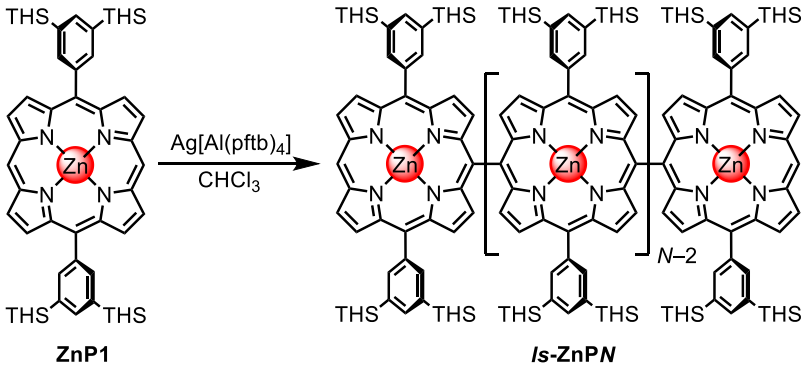

A solution of **ZnP1** (1.8 g, 1.1 mmol, 1.0 equiv.) in dry $CHCl_3$ (200 mL) with DMA (2.5 mL) was evacuated and backfilled with argon for five times. A solution of Ag[Al(pftb)$_4$] (2.3 g, 2.2 mmol, 2.0 equiv.) in dry $CHCl_3$ (50 mL) was evacuated and backfilled with argon for five times. Under argon, the Ag[Al(pftb)$_4$] solution was transferred to the **ZnP1** solution and the mixture was stirred at 25 ºC for 30 min. After reaction, the resulting mixture was concentrated and passed through flash column chromatography (SiO_2) using pentane/CH_2Cl_2 (19:1) as eluent, followed by size-exclusion chromatography (Bio-Beads, S-X1) with toluene/pyridine (99:1) as eluent to give a crude mixture of different oligomers. The crude mixture was further subjected to reversible recycling GPC to separate the desired products ***ls*-ZnP2** (1.5 g, 82%) and ***ls*-ZnP3** (48 mg, 2.7%).

C.3.4 Synthesis of *ls*-ZnP2-Br$_2$

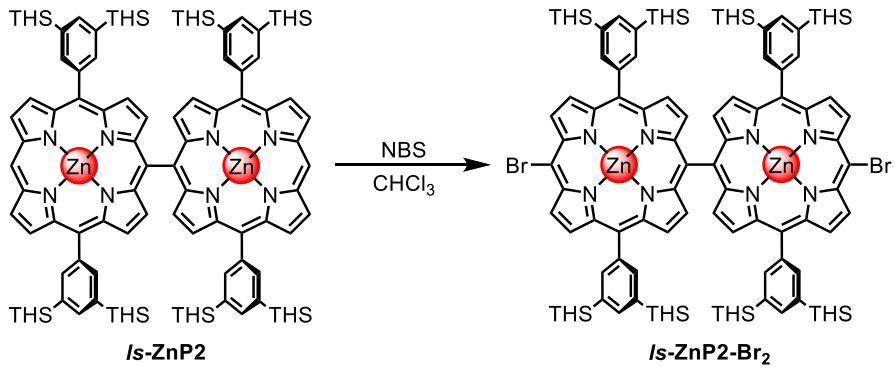

To a solution of ***ls*-ZnP2** (1.4 g, 0.42 mmol, 1.0 equiv.) in $CHCl_3$ (40 mL) with pyridine (0.50 mL) in an ice bath (0 ºC), a solution of *N*-bromosuccinimide (NBS, 0.16 g, 0.88 mmol, 2.1 equiv.) in $CHCl_3$ (10 mL) was added dropwise. The reaction was conducted at 0 ºC for 5 min, and acetone (0.1 mL) was added to quench the excess NBS. The resulting mixture was purified by flash column chromatography (SiO_2) using pentane/CH_2Cl_2 (9:1) as eluent to give the desired product ***ls*-ZnP2-Br$_2$** (1.4 g, 96%).

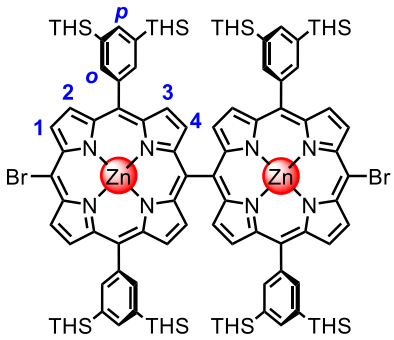

^{1}H NMR (500 MHz, $CDCl_3$, 298 K): δ 9.86 (d, *J* = 4.8 Hz, 4H, **H$_1$**), 9.01 (d, *J* = 4.8 Hz, 4H, **H$_2$**), 8.62 (d, *J* = 4.7 Hz, 4H, **H$_3$**), 8.26 (d, *J* = 1.2 Hz, 8H, **H$_o$**), 8.06 (d, *J* = 4.8 Hz, 4H, **H$_4$**), 7.90 (d, *J* = 1.2 Hz, 4H, **H$_p$**), 1.42 – 0.58 (m, 312H, **H$_{THS}$**).

MALDI-ToF: *m*/*z* = 3468.843 ($C_{208}H_{340}Br_2N_8Si_8Zn_2$, $M^{+\bullet}$ requires 3468.196).

UV–vis–NIR ($CDCl_3$, 298 K) λ_{max} / nm (ε / μM^{-1} cm^{-1}): 424 (0.32), 458 (0.28), 603 (0.01).

C.3.5 Oligomerization of *ls*-ZnP2-Br$_2$

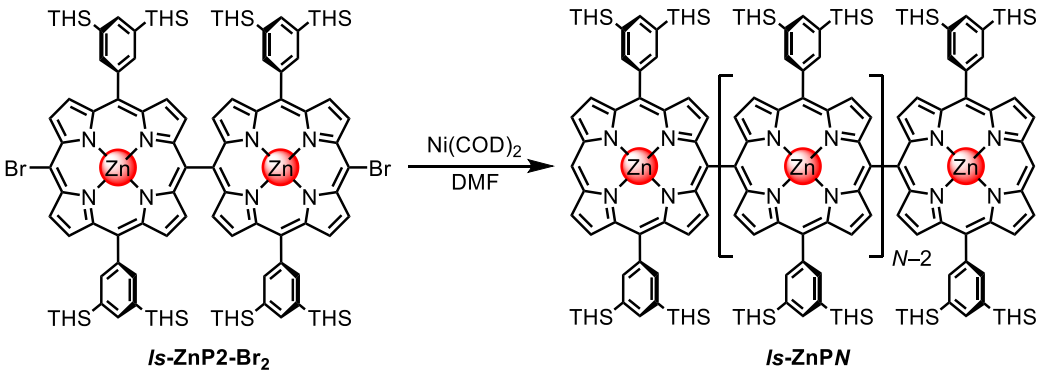

A mixture of ***ls*-ZnP2-Br$_2$** (500 mg, 144 µmol, 1.0 equiv.), Ni(COD)$_2$ (159 mg, 577 µmol, 4.0 equiv.) in dry DMF (150 mL) with pyridine (1.5 mL) was evacuated and backfilled with argon for five times. The reaction mixture was stirred at 50 ºC under argon for 24 h. After reaction, the mixture was concentrated, dissolved in pentane/CH_2Cl_2 (19:1), purified by flash column chromatography (SiO_2) using pentane/CH_2Cl_2 (9:1) as eluent, followed by size-exclusion chromatography (Bio-Beads, S-X1) with toluene/pyridine (99:1) as eluent to give a crude mixture of different oligomers. The crude mixture was further subjected to recycling GPC with toluene/pyridine (99:1) as eluent to separate the desired products ***ls*-ZnP2** (17 mg, 3.5%), ***ls*-ZnP4** (23 mg, 4.8%), ***ls*-ZnP6** (24 mg, 5.1%), ***ls*-ZnP8** (56 mg, 12%), ***ls*-ZnP10** (27 mg, 5.6%), ***ls*-ZnP12** (23 mg, 4.9%) and ***ls*-ZnP14** (12 mg, 2.6%).

C.4 Syntheses of *lf*-NiP*N*-TMS$_2$

C.4.1 Synthesis of NiP1-TMS$_2$

ZnP1-Br$_2$:

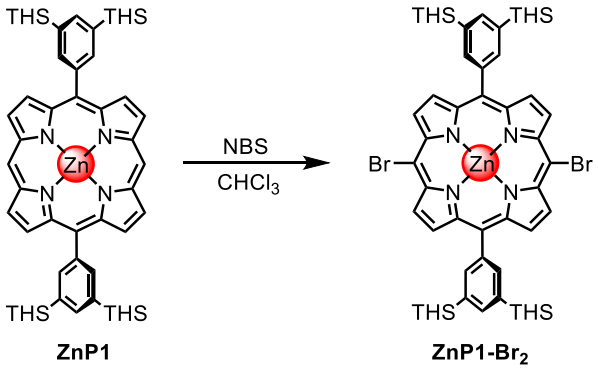

To a solution of **ZnP1** (225 mg, 0.14 mmol, 1.0 equiv.) in $CHCl_3$ (8.0 mL) with pyridine (100 µL) in an ice bath (0 ºC), a solution of NBS (51 mg, 0.29 mmol, 2.1 equiv.) in $CHCl_3$ (2.0 mL) was added dropwise. The reaction was conducted at 0 ºC for 15 min, and acetone (0.1 mL) was added to quench the excess NBS. The resulting mixture was purified by flash column chromatography (SiO_2) using pentane/CH_2Cl_2 (9:1) as eluent to give the desired product **ZnP1-Br$_2$** (226 mg, 92%).

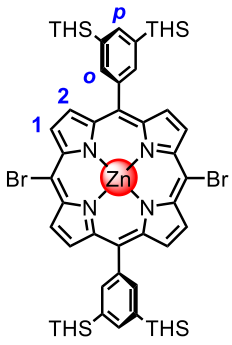

^{1}H NMR (600 MHz, $CDCl_3$, 298 K): δ 9.74 (d, *J* = 4.6 Hz, 4H, **H$_1$**), 8.94 (d, *J* = 4.6 Hz, 4H, **H$_1$**), 8.24 (d, *J* = 1.2 Hz, 4H, **H$_o$**), 8.01 (t, *J* = 1.2 Hz, 2H, **H$_p$**), 1.52 – 0.80 (m, 156H, **H$_{THS}$**).

MALDI-ToF: *m*/*z* = 1813.033 ($C_{104}H_{170}Br_2N_4Si_4Zn$, $M^{+\bullet}$ requires 1813.015).

H_2P1-Br_2:

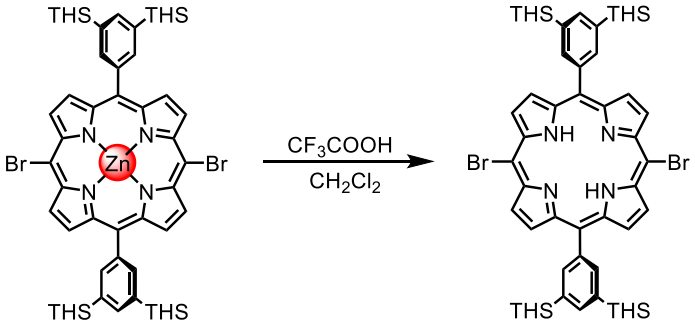

To a solution of **ZnP1-Br_2** (50 mg, 28 µmol) in CH_2Cl_2 (2.5 mL) in an ice bath (0 ºC), a solution of CF_3COOH (100 µL) in CH_2Cl_2 (2.5 mL) was added dropwise. The reaction mixture was stirred at 0 ºC for 5 min, followed by addition of triethylamine (1.0 mL) to quench the excess CF_3COOH. After that, the resulting mixture was purified by flash column chromatography on silica gel using pentane/CH_2Cl_2 (9:1) as eluent to give the desired product **H_2P1-Br_2** (45 mg, 93% yield).

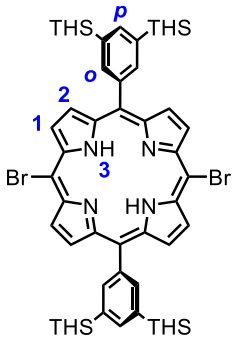

^{1}H NMR (600 MHz, $CDCl_3$, 298 K): δ 9.63 (d, *J* = 4.7 Hz, 4H, **H_1**), 8.84 (d, *J* = 4.7 Hz, 4H, **H_2**), 8.25 (d, *J* = 1.2 Hz, 4H, **H_o**), 8.02 (d, *J* = 1.2 Hz, 2H, **H_p**), 1.51 – 0.85 (m, 156H, **H_{THS}**), – 2.63 (s, 2H, **H_3**).

MALDI-ToF: *m*/*z* = 1751.398 ($C_{104}H_{172}Br_2N_4Si_4$, $M^{+\bullet}$ requires 1751.103).

NiP1-Br$_2$:

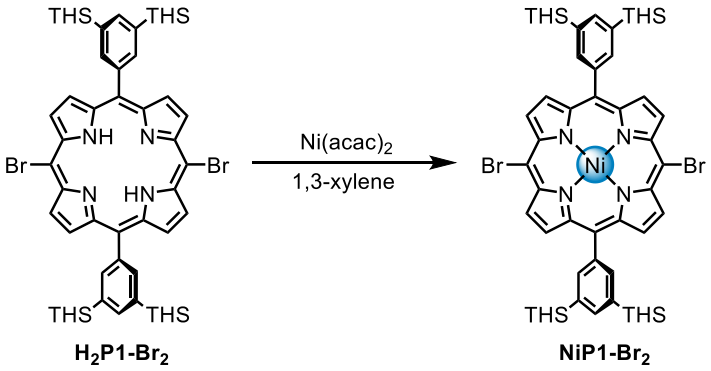

A mixture of **P1-Br$_2$** (110 mg, 69 μmol, 1.0 equiv.) and Ni(acac)$_2$ (532 mg, 2.1 mmol, 30 equiv.) in 1,3-xylene (10 mL) was evacuated and backfilled with argon for three times, followed by stirring at 130 ºC under argon for 2 h. After reaction, the resulting mixture was concentrated and purified by flash column chromatography (SiO_2) using pentane as eluent to give the desired product **NiP1-Br$_2$** (104 mg, 91%).

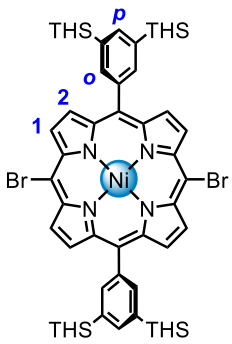

^{1}H NMR (600 MHz, $CDCl_3$, 298 K): δ 9.46 (d, *J* = 5.0 Hz, 4H, **H$_1$**), 8.73 (d, *J* = 5.0 Hz, 4H, **H$_2$**), 8.04 (d, *J* = 1.2 Hz, 4H, **H$_o$**), 7.94 (t, *J* = 1.2 Hz, 2H, **H$_p$**), 1.50 – 0.85 (m, 156H, **H$_{THS}$**).

MALDI-ToF: *m*/*z* = 1807.456 ($C_{104}H_{170}Br_2N_4NiSi_4$, $M^{+\bullet}$ requires 1807.022).

NiP1-TMS$_2$:

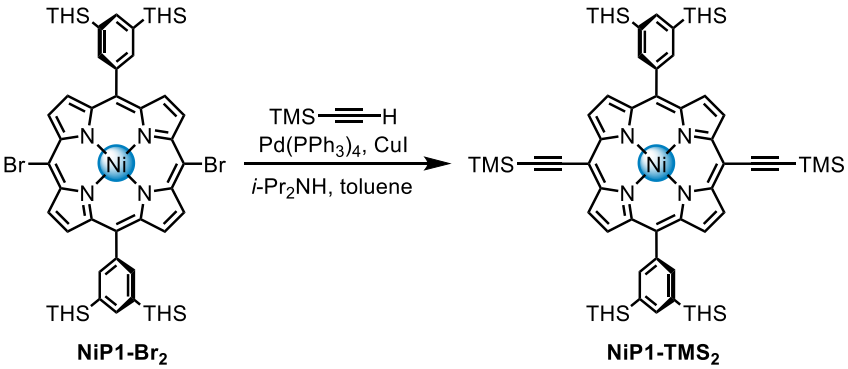

A mixture of **NiP1-Br$_2$** (25 mg, 14 µmol, 1.0 equiv.), Pd(PPh$_3$)$_4$ (3.2 mg, 2.8 µmol, 20 mol%), CuI (0.53 mg, 2.8 µmol, 20 mol%) in dry toluene (1.0 mL) and *i*-Pr$_2$NH (1.0 mL) was degassed by three freeze-pump-thaw cycles. After that, TMS-acetylene (12 µL, 83 µmol, 6.0 equiv.) was added to the mixture and the reaction was stirred at 50 °C under argon for 3 h. After reaction, the resulting mixture was concentrated and purified by flash column chromatography (SiO$_2$) using pentane as eluent to give the desired product **NiP1-TMS$_2$** (22 mg, 85%).

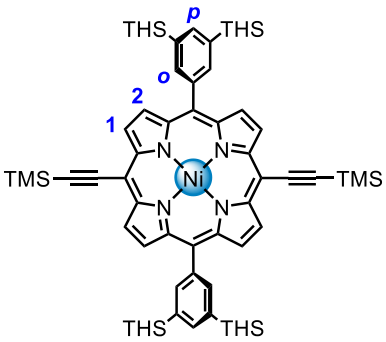

^{1}H NMR (500 MHz, $CDCl_3$, 298 K): δ 9.44 (d, *J* = 4.8 Hz, 4H, **H$_1$**), 8.70 (d, *J* = 4.9 Hz, 4H, **H$_2$**), 8.04 (d, *J* = 1.1 Hz, 4H, **H$_o$**), 7.92 (t, *J* = 1.1 Hz, 2H, **H$_p$**), 1.49 – 0.82 (m, 156H, **H$_{THS}$**), 0.52 (s, 18H, **H$_{TMS}$**).

MALDI-ToF: *m*/*z* = 1842 ($C_{114}H_{188}N_4NiSi_6$, $M^{+\bullet}$ requires 1841).

UV–vis–NIR ($CHCl_3$, 298 K) λ_{max} / nm (ε / 10^6 M^{-1} cm^{-1}): 592 (0.03), 555 (0.02), 435 (0.30).

C.4.2 Synthesis of *lf*-NiP2-TMS$_2$

***ls*-H$_2$P2-Br$_2$:**

H$_2$P1-Br$_2$:

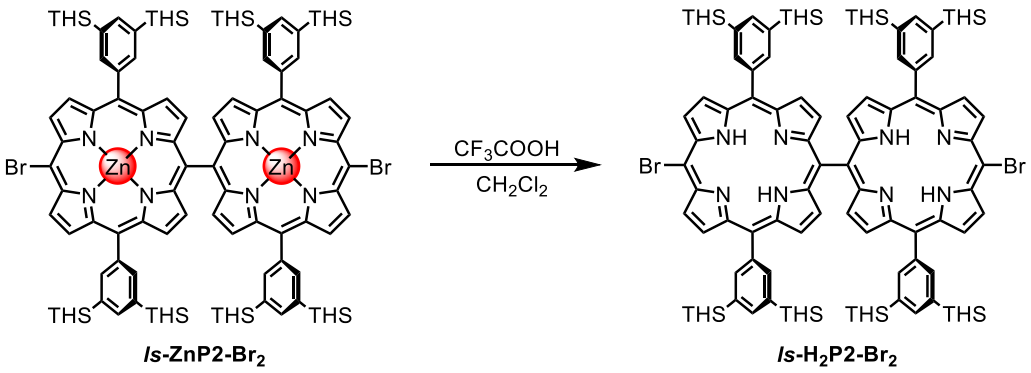

To a solution of **ZnP1-Br$_2$** (55 mg, 28 µmol) in CH_2Cl_2 (2.5 mL) in an ice bath (0 ºC), a solution of CF_3COOH (100 µL) in CH_2Cl_2 (2.5 mL) was added dropwise. The reaction mixture was stirred at 0 ºC for 5 min, followed by addition of triethylamine (1.0 mL) to quench the excess CF_3COOH. After that, the resulting mixture was purified by flash column chromatography on silica gel using pentane/CH_2Cl_2 (9:1) as eluent to give the desired product **H$_2$P2-Br$_2$** (53 mg, 99% yield).

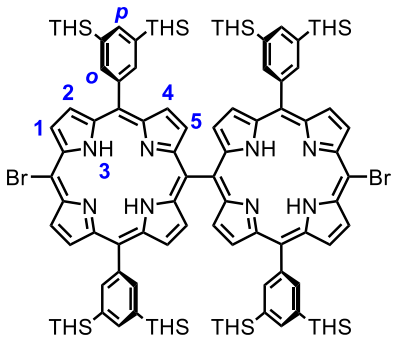

^{1}H NMR (500 MHz, $CDCl_3$, 298 K): δ 9.75 (d, *J* = 4.9 Hz, 4H, **H$_1$**), 8.90 (d, *J* = 4.9 Hz, 4H, **H$_2$**), 8.52 (d, *J* = 4.9 Hz, 4H, **H$_4$**), 8.25 (s, 8H, **H$_o$**), 8.01 (d, J = 4.9 Hz, 4H, **H$_5$**), 7.90 (s, 4H, **H$_p$**), 1.44 – 0.61 (m, 312H, **H$_{THS}$**), –2.14 (s, 4H, **H$_3$**).

MALDI-ToF: *m*/*z* = 3341.482 ($C_{208}H_{344}Br_2N_8Si_8$, $M^{+\bullet}$ requires 3341.373).

UV–vis–NIR ($CDCl_3$, 298 K) λ_{max} / nm (ε / µM^{-1} cm^{-1}): 426 (0.26), 456 (0.27), 532 (0.05), 569 (0.02), 605 (0.02), 664 (0.01).

***ls*-NiP2-Br$_2$:**

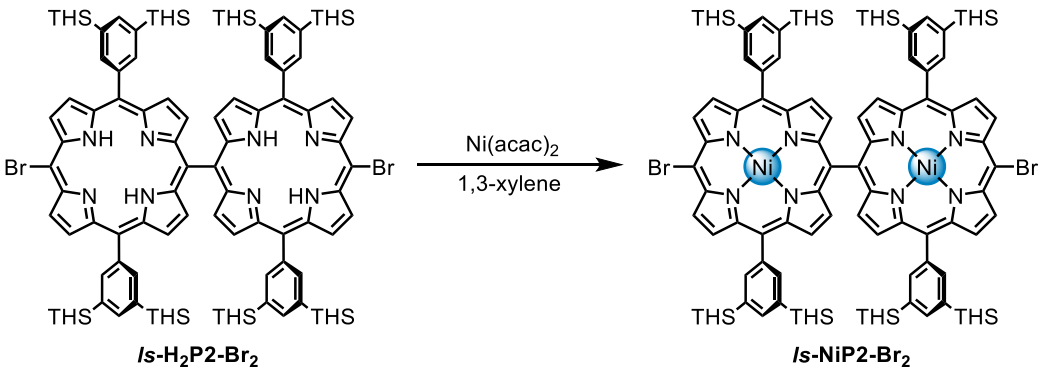

A mixture of ***ls*-H$_2$P2-Br$_2$** (50 mg, 0.62 μmol, 1.0 equiv.) and Ni(acac)$_2$ (116 mg, 0.45 mmol, 30 equiv.) in 1,3-xylene (5.0 mL) was evacuated and backfilled with argon for three times, followed by stirring at 130 ºC under argon for 2 h. After reaction, the resulting mixture was concentrated and purified by flash column chromatography (SiO_2) using pentane as eluent to give the desired product ***ls*-NiP2-Br$_2$** (51 mg, 99%).

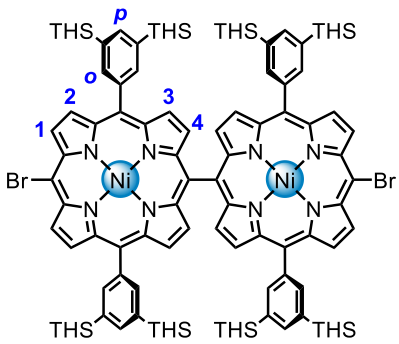

^{1}H NMR (600 MHz, $CDCl_3$, 298 K): δ 9.60 (d, *J* = 5.0 Hz, 4H, **H$_1$**), 8.80 (d, *J* = 5.0 Hz, 4H, **H$_2$**), 8.54 (d, *J* = 5.0 Hz, 4H, **H$_3$**), 8.10 – 8.02 (m, 12H, **H$_{4,o}$**), 7.88 (d, *J* = 1.2 Hz, 4H, **H$_p$**), 1.44 – 0.66 (m, 312H, **H$_{THS}$**).

MALDI-ToF: *m*/*z* = 3454.507 ($C_{208}H_{340}Br_2N_8Ni_2Si_8$, $M^{+\bullet}$ requires 3454.210).

UV–vis–NIR ($CDCl_3$, 298 K) λ_{max} / nm (ε / μM^{-1} cm^{-1}): 424 (0.16), 450 (0.18), 541 (0.04).

***lf*-NiP2-Br$_2$:**

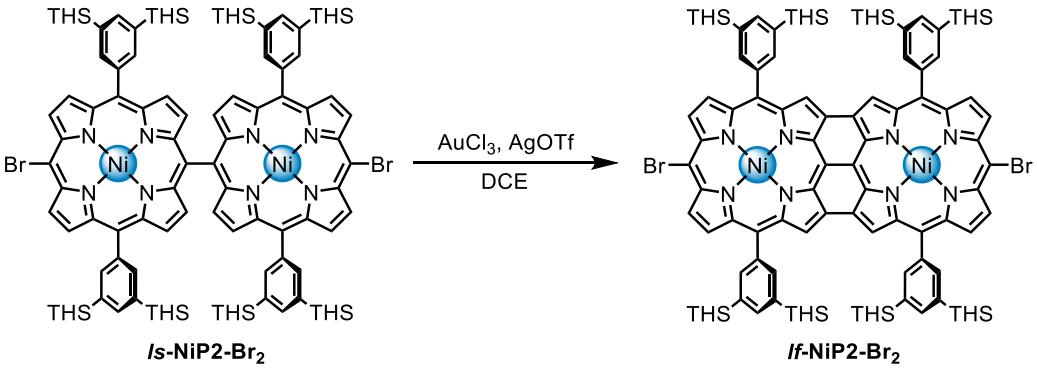

To a solution of ***ls*-NiP2-Br$_2$** (50 mg, 15 µmol, 1.0 equiv.) in dry 1,2-dichloroethane (DCE, 5.0 mL), a suspension of $AuCl_3$ (8.8 mg, 29 µmol, 2.0 equiv.) and AgOTf (37 mg, 0.15 mmol, 10 equiv.) in dry DCE (5.0 mL) was added dropwise and the reaction mixture was stirred at 25 ºC for 15 min. After reaction, triethylamine (1.0 mL) was added to the reaction mixture. The resulting mixture purified by flash column chromatography (SiO_2) using pentane as eluent to give the desired product ***lf*-NiP2-Br$_2$** (41 mg, 83% yield).

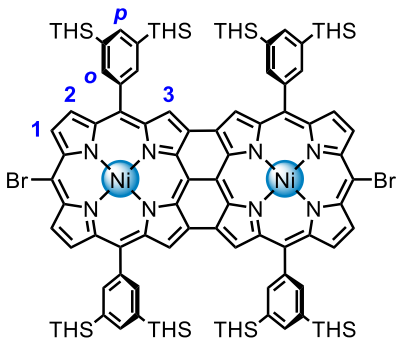

^{1}H NMR (600 MHz, $CDCl_3$, 298 K): δ 8.53 (d, *J* = 4.9 Hz, 4H, **H$_1$**), 7.82 (s, 4H, **H$_p$**), 7.76 (s, 8H, **H$_o$**), 7.63 (d, *J* = 4.9 Hz, 4H, **H$_2$**), 7.45 (s, 4H, **H$_3$**), 1.45 – 0.68 (m, 312H, **H$_{THS}$**).

MALDI-ToF: *m*/*z* = 3450.235 ($C_{208}H_{336}Br_2N_8Ni_2Si_8$, $M^{+\bullet}$ requires 3450.178).

***lf*-NiP2-TMS$_2$:**

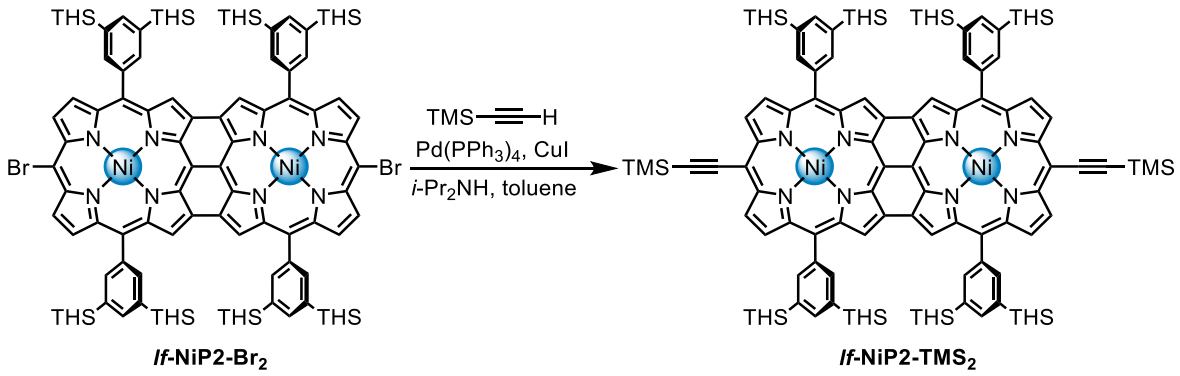

A mixture of ***lf*-NiP4-Br$_2$** (15 mg, 4.4 µmol, 1.0 equiv.), $Pd(PPh_3)_4$ (2.0 mg, 1.7 µmol, 40 mol%), CuI (0.32 mg, 1.7 µmol, 40 mol%) in dry toluene (1.0 mL) and *i*-Pr_2NH (1.0 mL) was degassed by three freeze-pump-thaw cycles. After that, TMS-acetylene (3.6 µL, 26 µmol, 6.0 equiv.) was added to the mixture and the reaction was conducted at 50 °C under argon for 3 h. After reaction, the resulting mixture was concentrated and purified by flash column chromatography (SiO_2) using pentane as eluent to give the desired product ***lf*-NiP2-TMS$_2$** (13 mg, 86%).

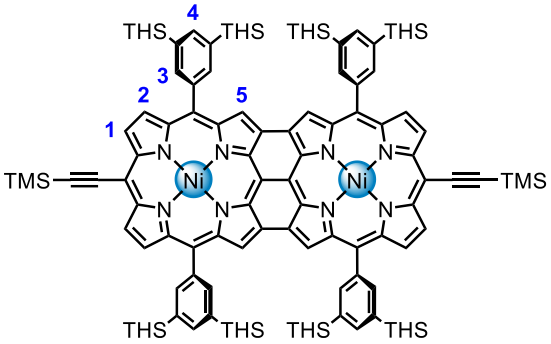

^{1}H NMR (500 MHz, $CDCl_3$, 298 K): δ 8.44 (d, *J* = 4.8 Hz, 4H, **H$_1$**), 7.80 (t, *J* = 1.2 Hz, 4H, **H$_4$**), 7.74 (d, *J* = 1.2 Hz, 8H, **H$_3$**), 7.57 (d, *J* = 4.9 Hz, 4H, **H$_2$**), 7.31 (s, 4H, **H$_5$**), 1.45 – 0.73 (m, 312H, **H$_{THS}$**), 0.39 (s, 18H, **H$_{TMS}$**).

MALDI-ToF: *m/z* = 3487 ($C_{218}H_{354}N_8Ni_2Si_{10}$, $M^{+\bullet}$ requires 3484).

UV–vis–NIR ($CDCl_3$, 298 K) λ_{max} / nm (ε / μM^{-1} cm^{-1}): 913 (0.11), 581 (0.19), 423 (0.17)

C.4.3 Synthesis of *lf*-NiP4-TMS$_2$

***ls*-ZnP4-Br$_2$:**

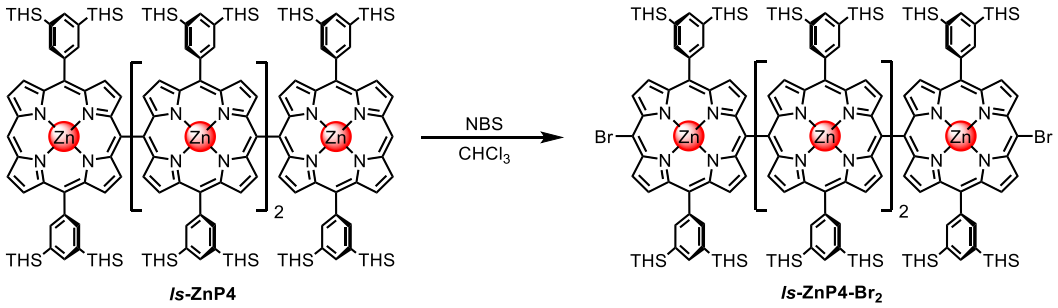

To a solution of ***ls*-ZnP4** (90 mg, 14 μmol, 1.0 equiv.) in $CHCl_3$ (8.0 mL) with pyridine (0.10 mL) in an ice bath (0 ºC), a solution of NBS (5.1 mg, 29 μmol, 2.1 equiv.) in $CHCl_3$ (2.0 mL) was added dropwise. The reaction was conducted at 0 ºC for 5 min, and acetone (0.1 mL) was added to quench the excess NBS. The resulting mixture was purified by flash column chromatography (SiO_2) using pentane/CH_2Cl_2 (9:1) as eluent to give the desired product ***ls*-ZnP4-Br$_2$** (90 mg, 98%).

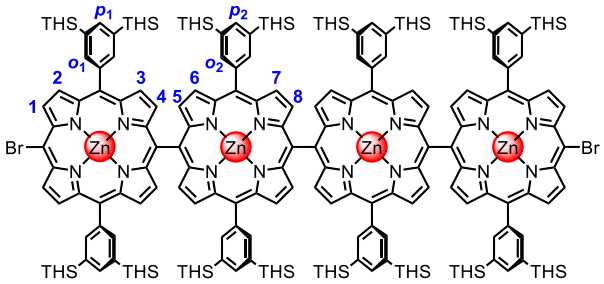

^{1}H NMR (600 MHz, $CDCl_3$, 298 K): δ 9.88 (d, *J* = 4.7 Hz, 4H, **H$_1$**), 9.03 (d, *J* = 4.7 Hz, 4H, **H$_2$**), 8.74 (d, *J* = 4.7 Hz, 4H, **H$_7$**), 8.70 – 8.67 (m, 8H, **H$_{3,6}$**), 8.31 – 8.28 (m, 20H, **H$_{o1,o2,8}$**), 8.22 (d, *J* = 4.7 Hz, 4H, **H$_3$**), 8.17 (d, *J* = 4.7 Hz, 4H, **H$_6$**), 7.93 (s, 4H, **H$_{p1}$**), 7.80 (s, 4H, **H$_{p2}$**), 1.45 – 0.39 (m, 624H, **H$_{THS}$**).

MALDI-ToF: *m*/*z* = 6776.509 ($C_{416}H_{680}Br_2N_{16}Si_{16}Zn_4$, $M^{+\bullet}$ requires 6776.558).

UV–vis–NIR ($CDCl_3$, 298 K) λ_{max} / nm (ε / μM^{-1} cm^{-1}): 420 (0.48), 484 (0.39), 569 (0.17).

***ls*-H_2P4-Br_2:**

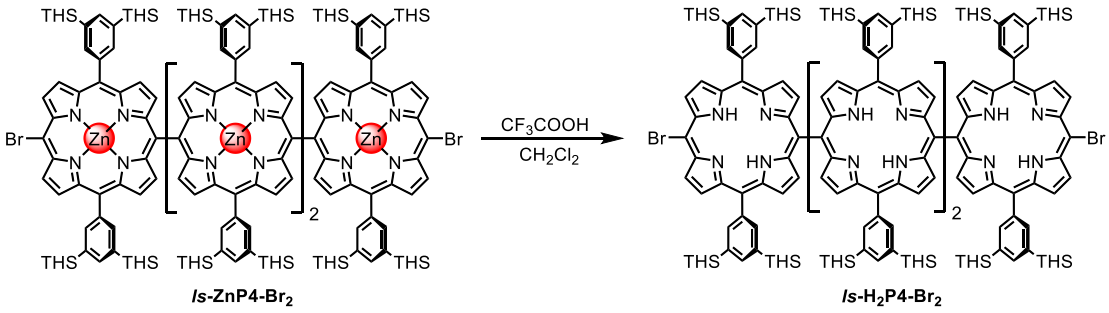

To a solution of ***ls*-ZnP4-Br_2** (90 mg, 13 μmol) in CH_2Cl_2 (5.0 mL) in an ice bath (0 ºC), a solution of CF_3COOH (200 μL) in CH_2Cl_2 (5.0 mL) was added dropwise. The reaction mixture was stirred at 0 ºC for 5 min, followed by addition of triethylamine (1.0 mL) to quench the excess CF_3COOH. After that, the resulting mixture was purified by flash column chromatography (SiO_2) using pentane/CH_2Cl_2 (9:1) as eluent to give the desired product ***ls*-H_2P4-Br_2** (85 mg, 98%).

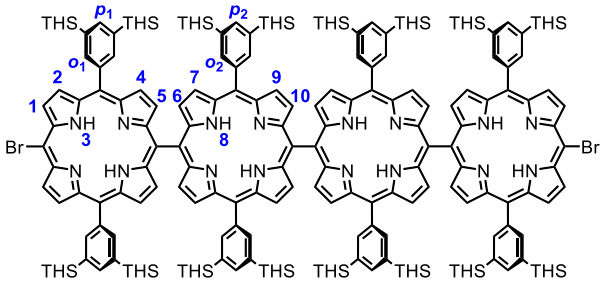

^{1}H NMR (600 MHz, $CDCl_3$, 298 K): δ 9.76 (d, *J* = 4.7 Hz, 4H, **H_1**), 8.90 (d, *J* = 4.7 Hz, 4H, **H_2**), 8.64 (d, *J* = 4.8 Hz, 4H, **H_9**), 8.61 – 8.55 (m, 8H, **$H_{4,7}$**), 8.30 – 8.26 (m, 16H, **$H_{o1,o2}$**), 8.24 (d, J = 4.8 Hz, 4H, **H_{10}**), 8.16 (d, *J* = 4.7 Hz, 4H, **H_5**), 8.12 (d, *J* = 4.7 Hz, 4H, **H_6**), 7.93 (s, 4H, **H_{p1}**), 7.80 (s, 4H, **H_{p2}**), 1.47 – 0.35 (m, 624H, **H_{THS}**), –1.59 (s, 4H, **H_8**), –2.08 (s, 4H, **H_3**).

MALDI-ToF: *m*/*z* = 6523.669 ($C_{416}H_{688}Br_2N_{16}Si_{16}$, $M^{+\bullet}$ requires 6522.911).

UV–vis–NIR ($CDCl_3$, 298 K) λ_{max} / nm (ε / μM^{-1} cm^{-1}): 419 (0.35), 480 (0.26), 535 (0.12), 601 (0.04), 660 (0.02).

***ls*-NiP4-Br$_2$:**

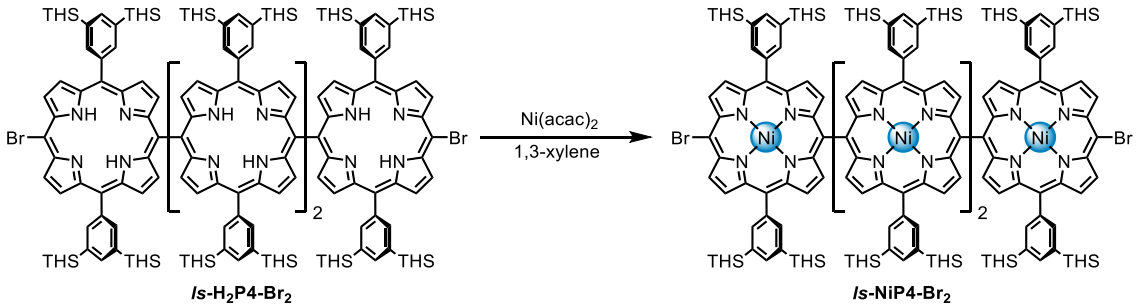

A mixture of ***ls*-H$_2$P4-Br$_2$** (85 mg, 13 μmol, 1.0 equiv.) and Ni(acac)$_2$ (100 mg, 0.39 mmol, 30 equiv.) in 1,3-xylene (5.0 mL) was evacuated and backfilled with argon for three times, followed by stirring at 120 ºC under argon for 2 h. After reaction, the resulting mixture was concentrated and purified by flash column chromatography (SiO_2) using pentane as eluent to give the desired product ***ls*- NiP4-Br$_2$** (88 mg, 99%).

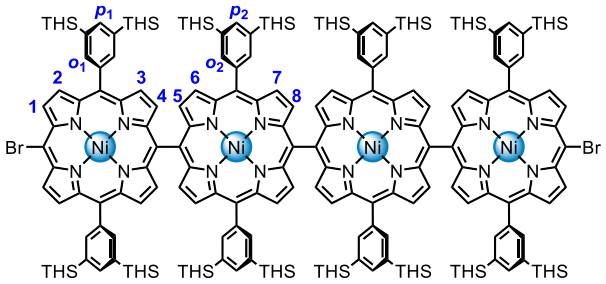

^{1}H NMR (600 MHz, $CDCl_3$, 298 K): δ 9.58 (d, *J* = 4.9 Hz, 4H, **H$_1$**), 8.77 (d, *J* = 4.9 Hz, 4H, **H$_2$**), 8.58 (d, *J* = 4.9 Hz, 4H, **H$_7$**), 8.56 (d, *J* = 4.9 Hz, 4H, **H$_3$**), 8.54 (d, *J* = 5.0 Hz, 4H, **H$_6$**), 8.20 (d, *J* = 4.9 Hz, 4H, **H$_8$**), 8.15 (d, *J* = 4.9 Hz, 4H, **H$_4$**), 8.11 (d, *J* = 5.0 Hz, 4H, **H$_5$**), 8.08 (s, 8H, **H$_{o1}$**), 8.07 (s, 8H, **H$_{o2}$**), 7.86 (s, 4H, **H$_{p1}$**), 7.77 (s, 4H, **H$_{p2}$**), 1.42 – 0.48 (m, 624H, **H$_{THS}$**).

MALDI-ToF: *m*/*z* = 5323.781 ($C_{334}H_{552}N_{12}Si_{14}Zn_3$, $M^{+\bullet}$ requires 5324.826).

UV–vis–NIR ($CDCl_3$, 298 K) λ_{max} / nm (ε / μM^{-1} cm^{-1}): 430 (0.34), 479 (0.39), 572 (0.11), 615 (0.04).

***lf*-NiP4-Br$_2$:**

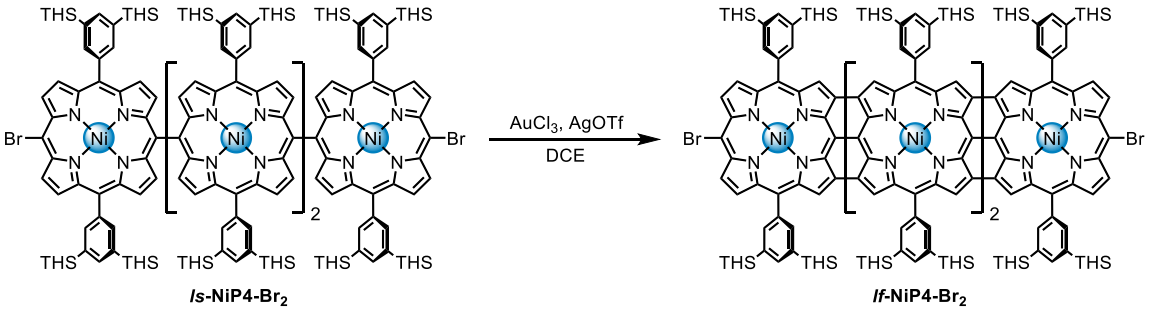

To a solution of ***ls*-NiP4-Br$_2$** (40 mg, 5.9 µmol, 1.0 equiv.) in dry DCE (5.0 mL), a suspension of $AuCl_3$ (11 mg, 36 µmol, 6.0 equiv.) and AgOTf (46 mg, 0.18 mmol, 30 equiv.) in dry DCE (5.0 mL) was added dropwise and the reaction mixture was stirred at 25 ºC for 15 min. After reaction, triethylamine (1.0 mL) was added to the reaction mixture. The resulting mixture was purified by flash column chromatography (SiO_2) using pentane as eluent to give the desired product ***lf*-NiP4-Br$_2$** (22 mg, 55%).

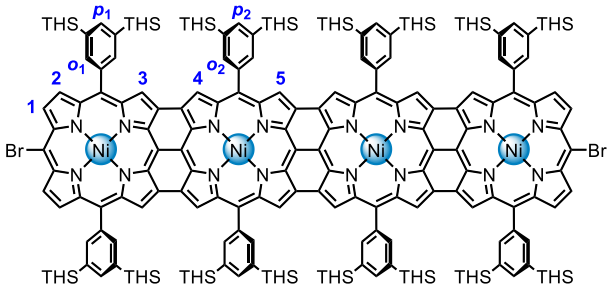

^{1}H NMR (600 MHz, $CDCl_3$, 298 K): δ 8.50 (d, *J* = 4.9 Hz, 4H, **H$_1$**), 7.78 (s, 4H, **H$_{p1}$**), 7.74 – 7.66 (m, 12H, **H$_{p2,o1}$**), 7.59 – 7.54 (m, 12H, **H$_{2,o2}$**), 7.29 (s, 4H, **H$_3$**), 6.76 (s, 4H, **H$_4$**), 6.68 (s, 4H, **H$_5$**), 1.43 – 0.69 (m, 624H, **H$_{THS}$**).

MALDI-ToF: *m*/*z* = 6736.308 ($C_{416}H_{668}Br_2N_{16}Ni_4Si_{16}$, $M^{+\bullet}$ requires 6737.491).

***lf*-NiP4-TMS$_2$:**

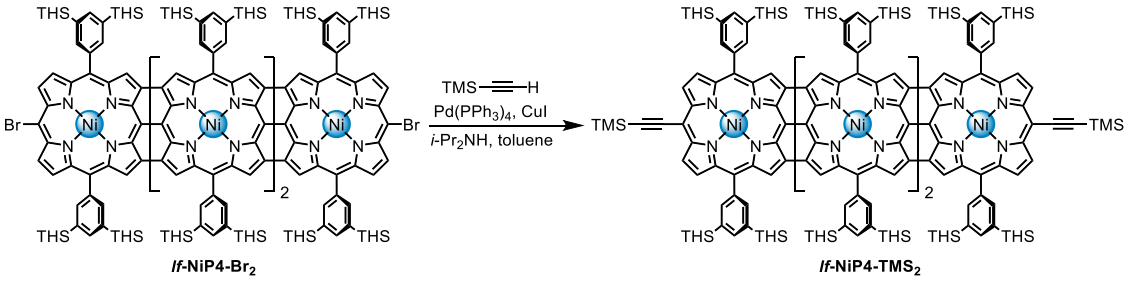

A mixture of ***lf*-NiP4-Br$_2$** (15 mg, 2.2 µmol, 1.0 equiv.), $Pd(PPh_3)_4$ (1.0 mg, 0.88 µmol, 40 mol%), CuI (0.16 mg, 0.88 µmol, 40 mol%) in dry toluene (1.0 mL) and *i*-Pr_2NH (1.0 mL) was degassed by three freeze-pump-thaw cycles. After that, TMS-acetylene (3.6 µL, 26 µmol, 12 equiv.) was added to the mixture and the reaction was conducted at 50 °C under argon for 3 h. After reaction, the resulting mixture was concentrated and purified by flash column chromatography (SiO_2) using pentane as eluent to give the desired product ***lf*-NiP4-TMS$_2$** (12 mg, 82%).

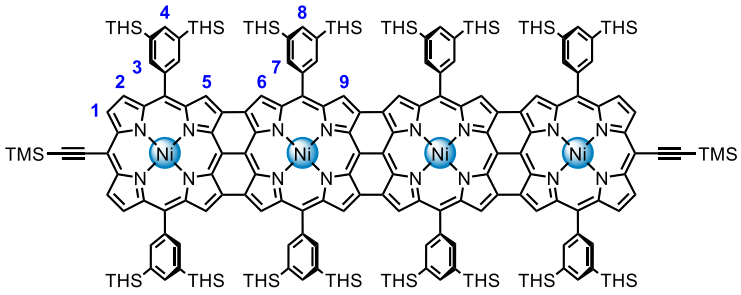

^{1}H NMR (500 MHz, $CDCl_3$, 298 K): δ 8.46 (d, *J* = 4.8 Hz, 4H, **H$_1$**), 7.77 (s, 4H, **H$_4$**), 7.72–7.68 (m, 12H, **H$_{3,8}$**), 7.57 – 7.52 (m, 12H, **H$_{2,7}$**), 7.24 (s, 4H, **H$_5$**), 6.68 (s, 4H, **H$_6$**), 6.64 (s, 4H, **H$_9$**), 1.47–0.67 (m, 624H, **H$_{THS}$**), 0.37 (s, 18H, **H$_{TMS}$**).

MALDI-ToF: *m*/*z* = 6771 ($C_{426}H_{686}N_{16}Ni_4Si_{18}$, $M^{+\bullet}$ requires 6772).

UV–vis–NIR ($CDCl_3$, 298 K) λ_{max} / nm (ε / μM^{-1} cm^{-1}): 1365 (0.31), 714 (0.37), 416 (0.18)

C.4.4 Synthesis of *lf*-NiP6-TMS$_2$

***ls*-ZnP6-Br$_2$:**

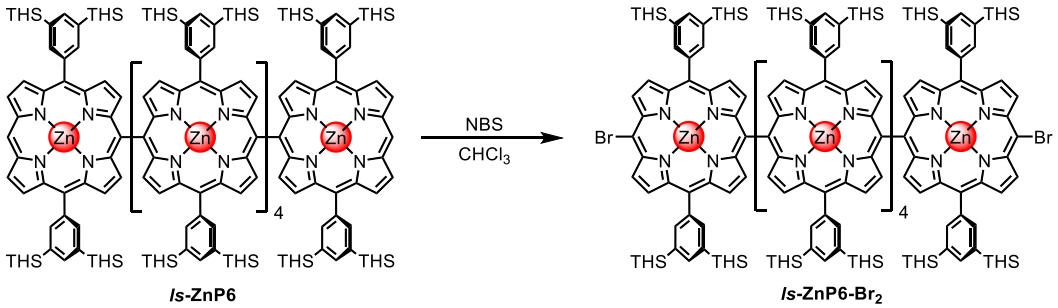

To a solution of ***ls*-ZnP6** (20 mg, 2.0 µmol, 1.0 equiv.) in $CHCl_3$ (4.0 mL) with pyridine (50 µL) in an ice bath (0 ºC), a solution of NBS (0.75 mg, 4.2 µmol, 2.1 equiv.) in $CHCl_3$ (1.0 mL) was added dropwise. The reaction was conducted at 0 ºC for 5 min, and acetone (0.1 mL) was added to quench the excess NBS. The resulting mixture was purified by flash column chromatography (SiO_2) using pentane/CH_2Cl_2 (9:1) as eluent to give the desired product ***ls*-ZnP6-Br$_2$** (20 mg, 99%).

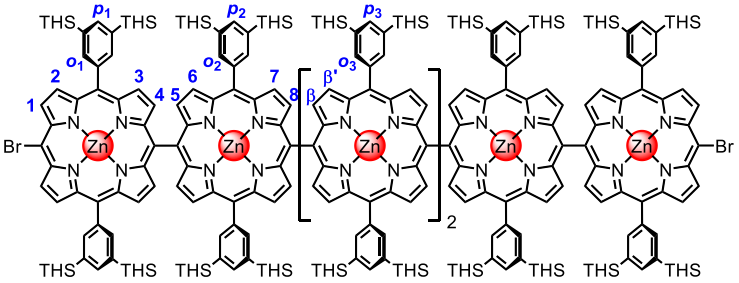

^{1}H NMR (600 MHz, $CDCl_3$, 298 K): δ 9.89 (d, *J* = 4.6 Hz, 4H, **H$_1$**), 9.04 (d, *J* = 4.6 Hz, 4H, **H$_2$**), 8.80 – 8.73 (m, 12H, **H$_{7,\beta'}$**), 8.72 – 8.66 (m, 8H, **H$_{3,6}$**), 8.37 – 8.28 (m, 36H, **H$_{o1,o2,o3,8,\beta}$**), 8.24 (d, *J* = 4.6 Hz, 4H, **H$_4$**), 8.18 (d, *J* = 4.6 Hz, 4H, **H$_5$**), 7.94 (s, 4H, **H$_{p1}$**), 7.84 (s, 4H, **H$_{p3}$**), 7.81 (s, 4H, **H$_{p2}$**), 1.46 – 0.35 (m, 936H, **H$_{THS}$**).

MALDI-ToF: *m*/*z* = 10084.977 ($C_{624}H_{1020}Br_2N_{24}Si_{24}Zn_6$, $M^{+\bullet}$ requires 10084.920).

UV–vis–NIR ($CDCl_3$, 298 K) λ_{max} / nm (ε / µM^{-1} cm^{-1}): 418 (0.79), 493 (0.73), 573 (0.39).

***ls*-H$_2$P6-Br$_2$:**

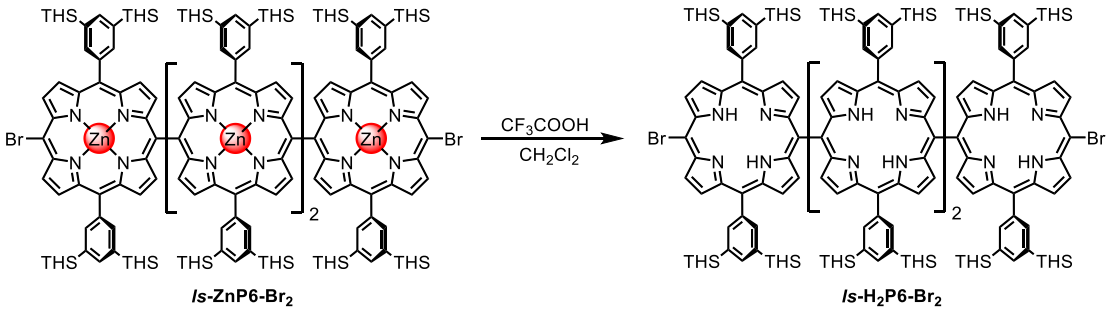

To a solution of ***ls*-ZnP6-Br$_2$** (8.0 mg, 0.80 µmol) in CH_2Cl_2 (2.5 mL) in an ice bath (0 ºC), a solution of CF_3COOH (100 µL) in CH_2Cl_2 (2.5 mL) was added dropwise. The reaction mixture was stirred at 0 ºC for 5 min, followed by addition of triethylamine (1.0 mL) to quench the excess CF_3COOH. After that, the resulting mixture was purified by flash column chromatography (SiO_2) using pentane/CH_2Cl_2 (9:1) as eluent to give the desired product ***ls*-H$_2$P6-Br$_2$** (7.8 mg, 98%).

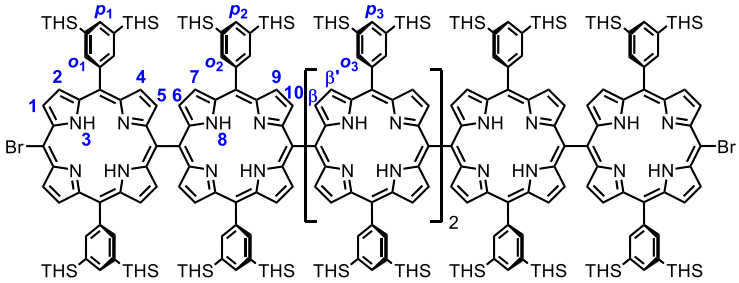

^{1}H NMR (600 MHz, $CDCl_3$, 298 K): δ 9.77 (d, *J* = 4.7 Hz, 4H, **H$_1$**), 8.91 (d, *J* = 4.7 Hz, 4H, **H$_2$**), 8.70 – 8.64 (m, 12H, **H$_{9,β'}$**), 8.62 – 8.58 (m, 8H, **H$_{4,7}$**), 8.32 (s, 8H, **H$_{o3}$**), 8.31 – 8.24 (m, 28H, **H$_{o1,o2,10,β}$**), 8.18 (d, *J* = 4.7 Hz, 4H, **H$_5$**), 8.14 (d, *J* = 4.8 Hz, 4H, **H$_6$**), 7.94 (s, 4H, **H$_{p1}$**), 7.84 (s, 4H, **H$_{p3}$**), 7.81 (s, 4H, **H$_{p2}$**), 1.45 – 0.42 (m, 956H, **H$_{THS}$**), –1.51 (s, 4H, **H$_{NH}$**), –1.56 (s, 4H, **H$_8$**), –2.06 (s, 4H, **H$_3$**).

MALDI-ToF: *m*/*z* = 9705.821 ($C_{624}H_{1032}Br_2N_{24}Si_{24}$, $M^{+\bullet}$ requires 9704.449).

UV–vis–NIR ($CDCl_3$, 298 K) λ_{max} / nm (ε / µM^{-1} cm^{-1}): 418 (0.41), 490 (0.34), 541 (0.21), 603 (0.07), 662 (0.03).

***ls*-NiP6-Br$_2$:**

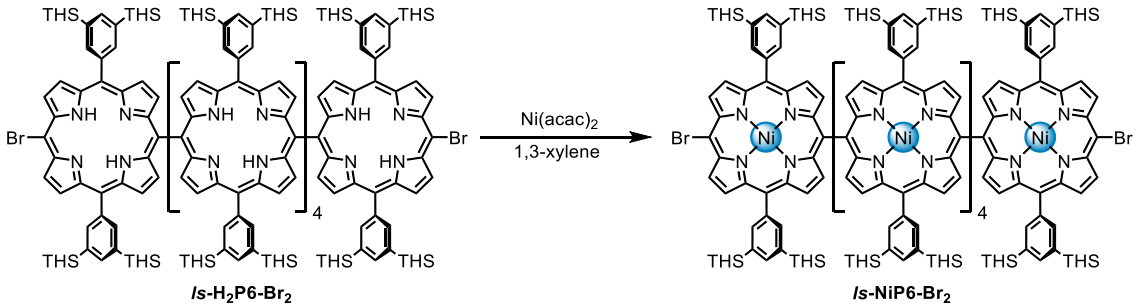

A mixture of ***ls*-H$_2$P4-Br$_2$** (4.8 mg, 0.49 μmol, 1.0 equiv.) and Ni(acac)$_2$ (3.9 mg, 15 μmol, 30 equiv.) in 1,3-xylene (5.0 mL) was evacuated and backfilled with argon for three times, followed by stirring at 120 ºC under argon for 2 h. After reaction, the resulting mixture was concentrated and purified by flash column chromatography (SiO_2) using pentane as eluent to give the desired product ***ls*- NiP6-Br$_2$** (4.6 mg, 92%).

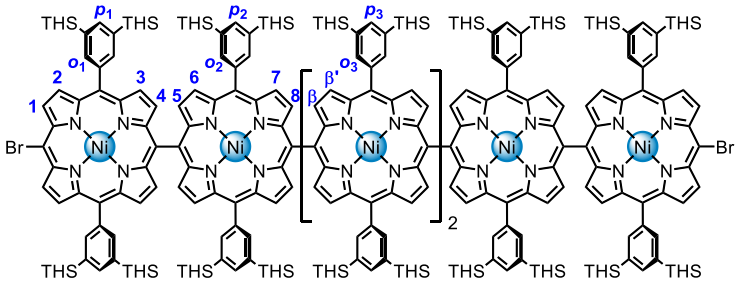

^{1}H NMR (600 MHz, $CDCl_3$, 298 K): δ 9.58 (d, *J* = 4.9 Hz, 4H, **H$_1$**), 8.77 (d, *J* = 4.9 Hz, 4H, **H$_2$**), 8.64 – 8.58 (m, 12H, **H$_{7,\beta'}$**), 8.57 (d, *J* = 4.9 Hz, 4H, **H$_3$**), 8.55 (d, *J* = 5.0 Hz, 4H, **H$_6$**), 8.25 – 8.21 (m, 12H, **H$_{8,\beta}$**), 8.16 (d, *J* = 4.9 Hz, 4H, **H$_4$**), 8.14 – 8.06 (m, 28H, **H$_{o3,5,o2,o1}$**), 7.87 (s, 4H, **H$_{p1}$**), 7.80 (s, 4H, **H$_{p3}$**), 7.78 (s, 4H, **H$_{p2}$**), 1.42 – 0.47 (m, 936H, **H$_{THS}$**).

MALDI-ToF: *m*/*z* = 10084.977 ($C_{624}H_{1020}Br_2N_{24}Si_{24}Zn_6$, $M^{+\bullet}$ requires 10084.920).

UV–vis–NIR ($CDCl_3$, 298 K) λ_{max} / nm (ε / μM^{-1} cm^{-1}): 414 (0.41), 479 (0.44), 550 (0.21).

***lf*-NiP6-Br$_2$:**

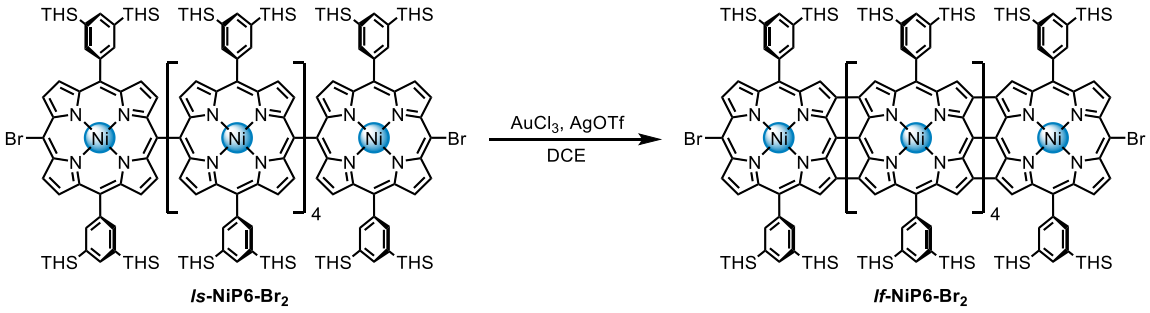

To a solution of ***ls*-NiP6-Br$_2$** (3.8 mg, 0.38 µmol, 1.0 equiv.) in dry DCE (10 mL), a suspension of $AuCl_3$ (1.2 mg, 3.8 µmol, 10 equiv.) and AgOTf (4.9 mg, 19 µmol, 50 equiv.) in dry DCE (5.0 mL) was added dropwise and the reaction mixture was stirred at 25 °C for 15 min. After that, a suspension of $AuCl_3$ (0.22 mg, 0.76 µmol, 2.0 equiv.) and AgOTf (0.97 mg, 3.8 µmol, 10 equiv.) in dry DCE (1.0 mL) was added dropwise to the reaction mixture and the reaction was monitored by UV–vis–NIR spectroscopy with CH_2Cl_2 + 1% triethylamine as solvent. After completion, the resulting mixture was purified by flash column chromatography (SiO_2) using pentane as eluent to give the desired product ***lf*-NiP6-Br$_2$** (2.3 mg, 61%).

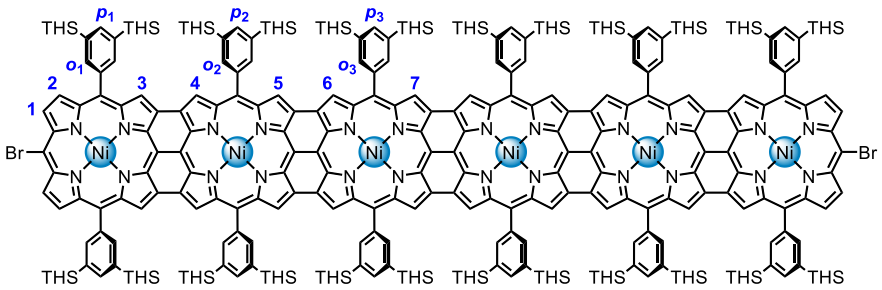

^{1}H NMR (500 MHz, $CDCl_3$, 298 K): δ 8.50 (d, *J* = 4.9 Hz, 4H, **H$_1$**), 7.77 (s, 4H, **H$_{p1}$**), 7.72 – 7.65 (m, 16H, **H$_{o1,p2,p3}$**), 7.57 (d, *J* = 4.9 Hz, 4H, **H$_2$**), 7.54 (s, 8H, **H$_{o2}$**), 7.50 (s, 8H, **H$_{o3}$**), 7.28 (s, 4H, **H$_3$**), 6.72 (s, 4H, **H$_4$**), 6.64 (s, 4H, **H$_{6/7}$**), 6.62 (s, 4H, **H$_5$**), 6.61 (s, 4H, **H$_{6/7}$**), 1.39 – 0.66 (m, 936H, **H$_{THS}$**).

MALDI-ToF: *m*/*z* = 10022.340 ($C_{624}H_{1000}Br_2N_{24}Ni_6Si_{24}$, $M^{+\bullet}$ requires 10023.803).

***lf*-NiP6-TMS$_2$:**

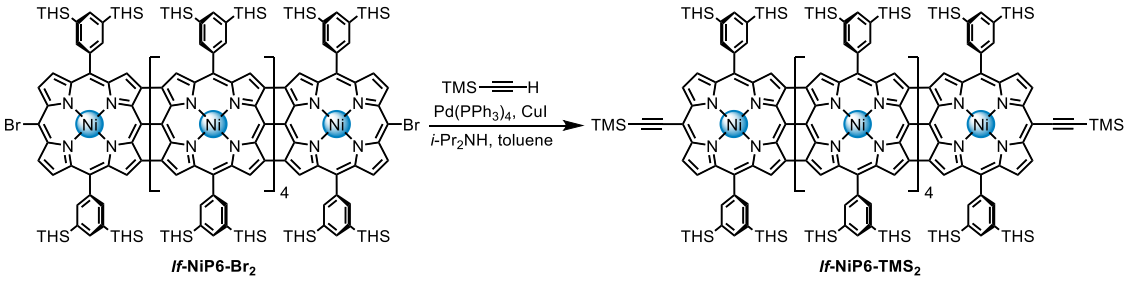

A mixture of ***lf*-NiP6-Br$_2$** (1.0 mg, 0.1 µmol, 1.0 equiv.), $Pd(PPh_3)_4$ (1.1 mg, 1.6 µmol, 16 equiv.), CuI (0.3 mg, 1.6 µmol, 16 equiv.) in dry toluene (1.0 mL) and *i*-Pr_2NH (1.0 mL) was degassed by three freeze-pump-thaw cycles. After that, TMS-acetylene (3.5 µL, 25 µmol, 250 equiv.) was added to the mixture and the reaction was conducted at 50 °C under argon for 2 h. After reaction, the resulting mixture was concentrated and purified by flash column chromatography (SiO_2) using pentane as eluent to give the desired product ***lf*-NiP6-TMS$_2$** (0.57 mg, 57%).

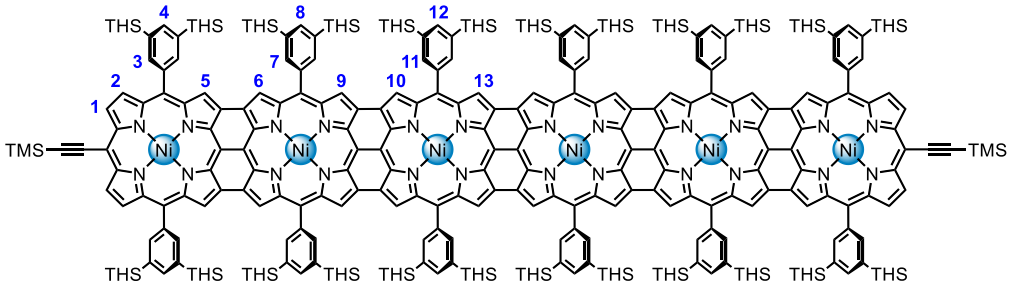

^{1}H NMR (700 MHz, $CDCl_3$, 298 K): δ 8.45 (d, *J* = 4.7 Hz, 4H, **H$_1$**), 7.77 (s, 4H, **H$_4$**), 7.71–7.69 (m, 12H, **H$_{3,8}$**), 7.68 (s, 4H, **H$_{12}$**), 7.55 (d, *J* = 4.7 Hz, 4H, **H$_2$**), 7.53 (s, 8H, **H$_7$**), 7.50 (s, 8H, **H$_{11}$**), 7.23 (s, 4H, **H$_5$**), 6.65 (s, 4H, ***H*$_6$**), 6.62 (s, 4H, **H$_{10/13}$**), 6.61 (s, 4H, **H$_{10/13}$**), 6.59 (s, 4H, **H$_9$**), 1.42 – 0.67 (m, 936H, **H$_{THS}$**), 0.37 (s, 18H, **H$_{TMS}$**).

MALDI-ToF: *m*/*z* = 10060 ($C_{634}H_{1018}N_{24}Ni_6Si_{26}$, $M^{+\bullet}$ requires 10059).

UV–vis–NIR ($CDCl_3$, 298 K) λ_{max} / nm (ε / μM^{-1} cm^{-1}): 413 (0.26), 754 (0.58), 1610 (1.00).

C.4.5 Synthesis of *lf*-NiP8-TMS$_2$

***ls*-ZnP8-Br$_2$:**

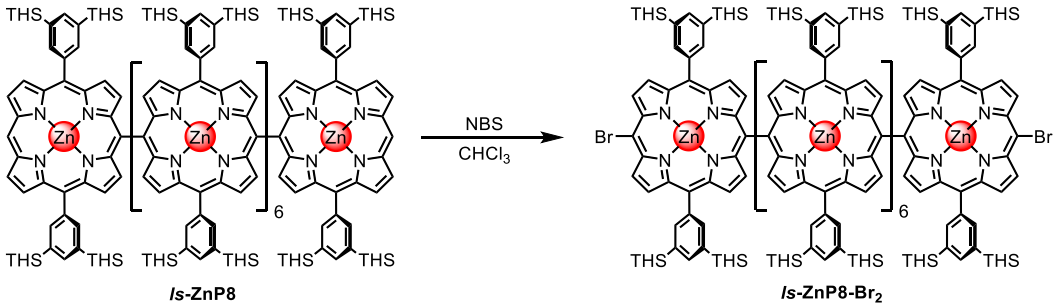

To a solution of ***ls*-ZnP8** (16 mg, 1.2 μmol, 1.0 equiv.) in $CHCl_3$ (5.0 mL) with pyridine (50 μL) in an ice bath (0 ºC), a solution of NBS (0.45 mg, 2.5 μmol, 2.1 equiv.) in $CHCl_3$ (1.0 mL) was added dropwise. The reaction was conducted at 0 ºC for 5 min, and acetone (0.1 mL) was added to quench the excess NBS. The resulting mixture was purified by flash column chromatography (SiO_2) using pentane/CH_2Cl_2 (9:1) as eluent to give the desired product ***ls*-ZnP4-Br$_2$** (13 mg, 82%).

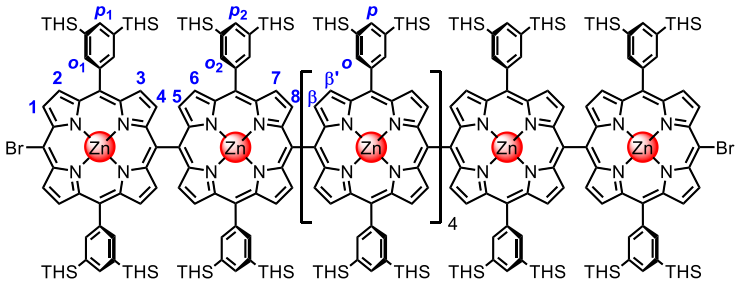

^{1}H NMR (600 MHz, $CDCl_3$, 298 K): δ 9.89 (d, *J* = 4.6 Hz, 4H, **H$_1$**), 9.04 (d, *J* = 4.6 Hz, 4H, **H$_2$**), 8.82 – 8.74 (m, 20H, **H$_{7,\beta'}$**), 8.73 – 8.68 (m, 8H, **H$_{3,6}$**), 8.40 – 8.29 (m, 52H, **H$_{8,\beta,o1,o2,o}$**), 8.24 (d, *J* = 4.6 Hz, 4H, **H$_4$**), 8.18 (d, *J* = 4.6 Hz, 4H, **H$_5$**), 7.94 (s, 4H, **H$_{p1}$**), 7.87 – 7.83 (m, 8H, **H$_p$**), 7.82 (s, 4H, **H$_{p2}$**), 1.46 – 0.41 (m, 1184H).

MALDI-ToF: *m*/*z* = 13394.90 ($C_{832}H_{1360}Br_2N_{32}Si_{32}Zn_8$, $M^{+\bullet}$ requires 13393.28).

UV–vis–NIR ($CDCl_3$, 298 K) λ_{max} / nm (ε / μM^{-1} cm^{-1}): 416 (0.89), 497 (0.89), 576 (0.51) nm.

***ls*-H$_2$P8-Br$_2$:**

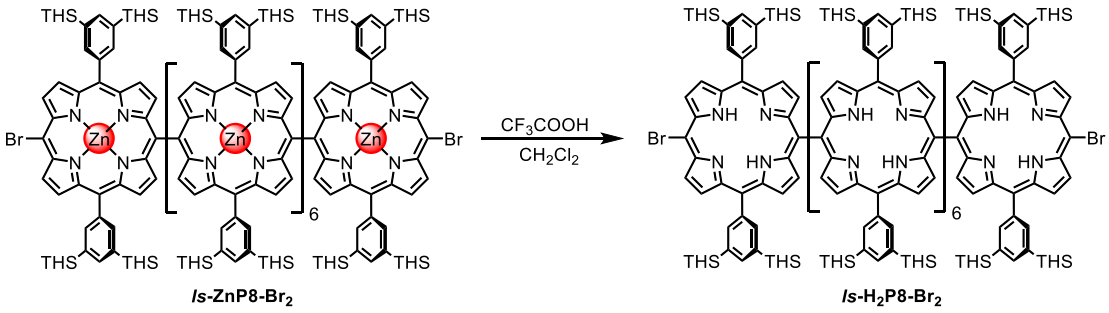

To a solution of ***ls*-ZnP8-Br$_2$** (8.3 mg, 0.62 µmol) in CH_2Cl_2 (2.5 mL) in an ice bath (0 ºC), a solution of CF_3COOH (100 µL) in CH_2Cl_2 (2.5 mL) was added dropwise. The reaction mixture was stirred at 0 ºC for 5 min, followed by addition of triethylamine (1.0 mL) to quench the excess CF_3COOH. After that, the resulting mixture was purified by flash column chromatography on silica gel using pentane/CH_2Cl_2 (9:1) as eluent to give the desired product ***ls*-H$_2$P8-Br$_2$** (7.2 mg, 90%).

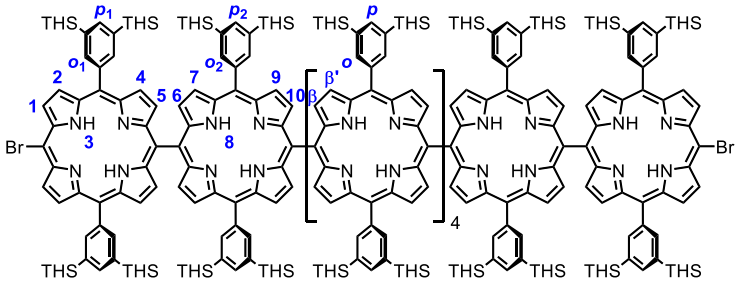

^{1}H NMR (600 MHz, $CDCl_3$, 298 K): δ 9.77 (d, *J* = 4.6 Hz, 4H, **H$_1$**), 8.92 (d, *J* = 4.6 Hz, 4H, **H$_2$**), 8.73 – 8.64 (m, 20H, **H$_{9,\beta'}$**), 8.64 – 8.58 (m, 8H, **H$_{4,7}$**), 8.37 – 8.32 (m, 16H, **H$_o$**), 8.32 – 8.26 (m, 36H, **H$_{10,\beta,o1,o2}$**), 8.18 (d, *J* = 4.7 Hz, 4H, **H$_5$**), 8.14 (d, *J* = 4.7 Hz, 4H, **H$_6$**), 7.94 (s, 4H, **H$_{p1}$**), 7.87 – 7.83 (m, 8H, **H$_p$**), 7.82 (s, 4H, **H$_{p2}$**), 1.48 – 0.35 (m, 1184H, **H$_{THS}$**), –1.36 – – 1.65 (m, 12H, **H$_{8,NH}$**), –2.06 (s, 4H, **H$_3$**).

MALDI-ToF: *m*/*z* = 12889.49 ($C_{832}H_{1376}Br_2N_{32}Si_{32}$, $M^{+\bullet}$ requires 12885.99).

UV–vis–NIR ($CDCl_3$, 298 K) λ_{max} / nm (ε / µM^{-1} cm^{-1}): 415 (0.76), 491 (0.65), 542 (0.45), 602 (0.15), 660 (0.05) nm.

***ls*-NiP8-Br$_2$:**

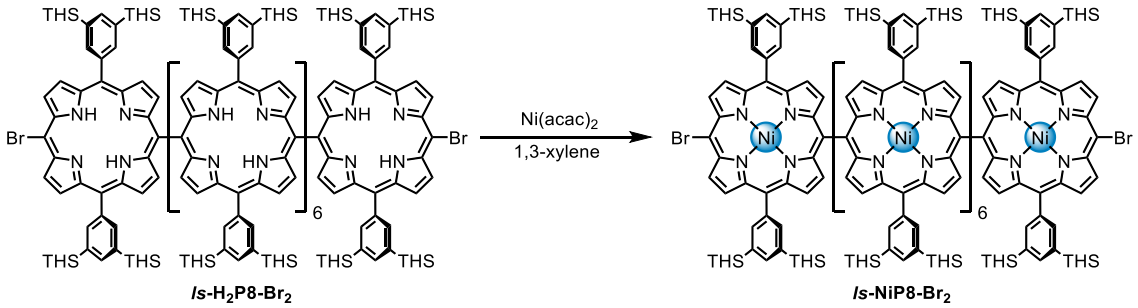

A mixture of ***ls*-H$_2$P8-Br$_2$** (8.0 mg, 0.62 μmol, 1.0 equiv.) and Ni(acac)$_2$ (4.9 mg, 19 μmol, 30 equiv.) in 1,3-xylene (5.0 mL) was evacuated and backfilled with argon for three times, followed by stirring at 120 ºC under argon for 2 h. After reaction, the resulting mixture was concentrated and purified by flash column chromatography (SiO_2) using pentane as eluent to give the desired product ***ls*- NiP8-Br$_2$** (6.5 mg, 78%).

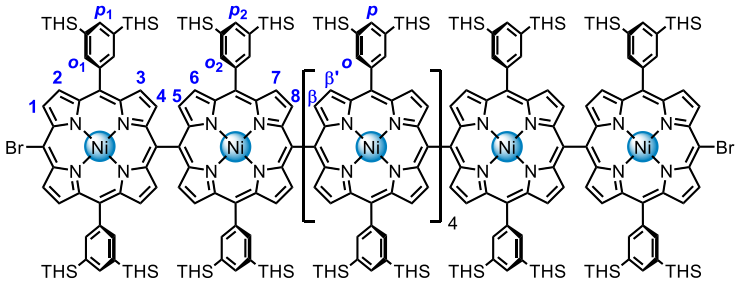

^{1}H NMR (600 MHz, $CDCl_3$, 298 K): δ 9.58 (d, *J* = 4.9 Hz, 4H, **H$_1$**), 8.78 (d, *J* = 4.9 Hz, 4H, ***H*$_2$**), 8.65 – 8.58 (m, 20H, **H$_{7,β'}$**), 8.59 – 8.53 (m, 8H, **H$_{3,6}$**), 8.28–8.20 (m, 20H, **H$_{8,β}$**), 8.16 (d, *J* = 4.9 Hz, 4H, **H$_4$**), 8.15–8.12 (m, 16H, **H$_{*o*}$**), 8.11 (d, *J* = 4.9 Hz, 4H, **H$_5$**), 8.10 – 8.09 (m, 8H, **H$_{*o*2}$**), 8.08–8.07 (m, 8H, **H$_{*o*1}$**), 7.88 – 7.86 (m, 4H, **H$_{*p*1}$**), 7.81 – 7.79 (m, 8H, **H$_{*p*}$**), 7.78 (s, 4H, **H$_{*p*2}$**), 1.45–0.49 (m, 1184H).

MALDI-ToF: *m*/*z* = 13341.61 ($C_{832}H_{1360}Br_2N_{32}Ni_8Si_{32}$, $M^{+\bullet}$ requires 13339.33).

UV–vis–NIR ($CDCl_3$, 298 K) λ_{max} / nm (ε / μM^{-1} cm^{-1}): 413 (0.53), 482 (0.61), 551 (0.31) nm.

***lf*-NiP8-Br$_2$:**

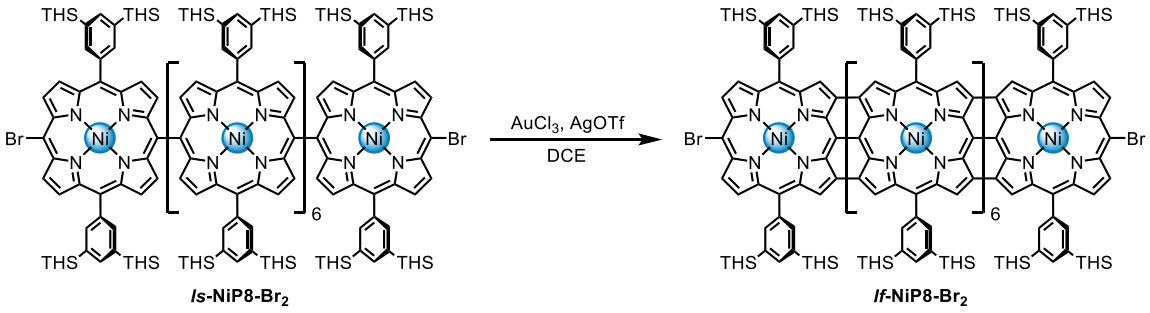

To a solution of ***ls*-NiP8-Br$_2$** (2.0 mg, 0.15 µmol, 1.0 equiv.) in dry DCE (2.5 mL), a suspension of $AuCl_3$ (0.64 mg, 2.1 µmol, 14 equiv.) and AgOTf (2.7 mg, 11 µmol, 70 equiv.) in dry DCE (2.5 mL) was added dropwise and the reaction mixture was stirred at 25 ºC for 15 min. After that, a suspension of $AuCl_3$ (0.13 mg, 0.42 µmol, 2.8 equiv.) and AgOTf (0.54 mg, 2.1 µmol, 14 equiv.) in dry DCE (0.5 mL) was added dropwise to the reaction mixture and the reaction was monitored by UV–vis–NIR spectroscopy with CH_2Cl_2 + 1% triethylamine as solvent. After completion, the resulting mixture was purified by flash column chromatography (SiO_2) using pentane as eluent to give the desired product ***lf*-NiP8-Br$_2$** (1.0 mg, 50%).

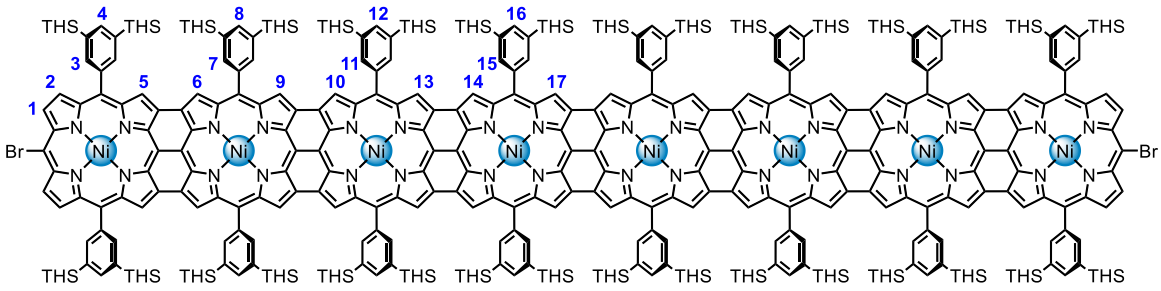

^{1}H NMR (700 MHz, $CDCl_3$, 298 K): δ 8.50 (d, *J* = 4.8 Hz, 4H, ***H*$_1$**), 7.77 (s, 4H, ***H*$_4$**), 7.74 – 7.64 (m, 20H, ***H*$_{3,8,12,16}$**), 7.57 (d, *J* = 4.8 Hz, 4H, ***H*$_2$**), 7.54 (s, 8H, ***H*$_7$**), 7.51 – 7.46 (m, 16H, ***H*$_{11,15}$**), 7.28 (s, 4H, ***H*$_5$**), 6.72 (s, 4H, ***H*$_6$**), 6.66 – 6.53 (m, 20H, ***H*$_{9,10,13,14,17}$**), 1.40 – 0.70 (m, 1184H, ***H*$_{THS}$**).

MALDI-ToF: *m*/*z* = 13335.34 ($C_{842}H_{1350}N_{32}Ni_8Si_{34}$, $M^{+\bullet}$ requires 13345.38).

UV–vis–NIR ($CDCl_3$, 298 K) λ_{max} / nm (ε / μM^{-1} cm^{-1}): 412 (0.29), 776 (0.55), 1788 (0.80) nm.

***lf*-NiP8-TMS$_2$:**

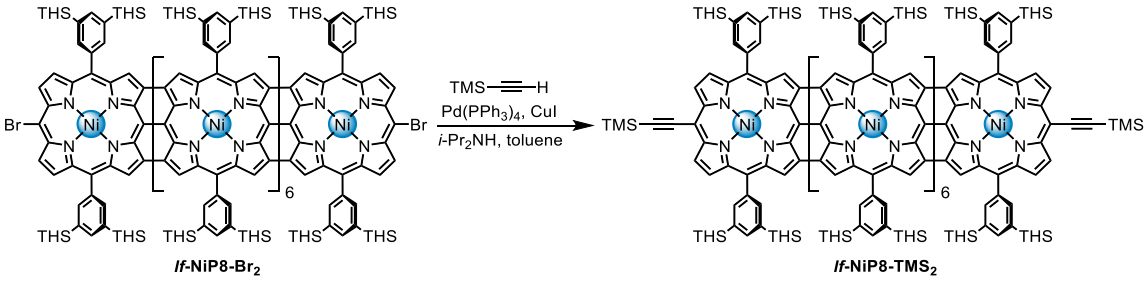

A mixture of ***lf*-NiP4-Br$_2$** (1.0 mg, 0.075 µmol, 1.0 equiv.), $Pd(PPh_3)_4$ (1.1 mg, 1.5 µmol, 20 equiv.), CuI (0.3 mg, 1.5 µmol, 20 equiv.) in dry toluene (1.0 mL) and *i*-Pr_2NH (1.0 mL) was degassed by three freeze-pump-thaw cycles. After that, TMS-acetylene (3.6 µL, 26 µmol, 350 equiv.) was added to the mixture and the reaction was conducted at 50 °C under argon for 2 h. After reaction, the resulting mixture was concentrated and purified by flash column chromatography (SiO_2) using pentane as eluent to give the desired product ***lf*-NiP8-TMS$_2$** (12 mg, 34%).

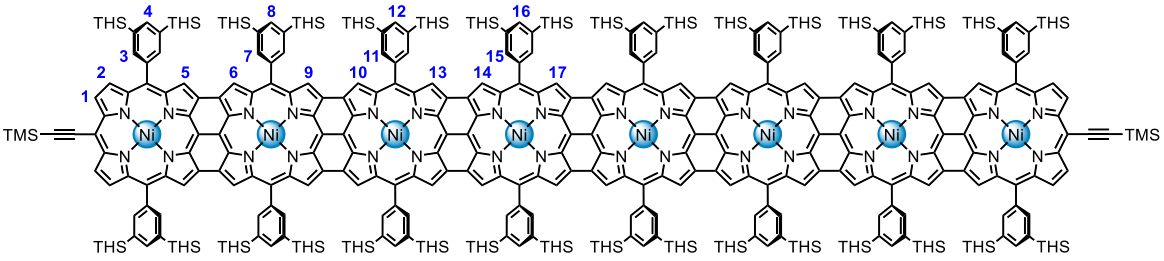

^{1}H NMR (700 MHz, $CDCl_3$, 298 K): δ 8.45 (d, *J* = 4.7 Hz, 4H, **H$_1$**), 7.77 (s, 4H, ***H*$_4$**), 7.71 – 7.68 (m, 12H, **H$_{3,8}$**), 7.68 – 7.65 (m, 8H, **H$_{12,16}$**), 7.55 (d, *J* = 4.7 Hz, 4H, **H$_2$**), 7.52 (s, 8H, **H$_7$**), 7.51 – 7.47 (m, 16H, **H$_{11,15}$**), 7.22 (s, 4H, **H$_5$**), 6.65 (s, 4H, **H$_6$**), 6.62 (s, 4H, **H$_9$**), 6.60–6.56 (m, 16H, **H$_{10,13,14,17}$**), 1.39 – 0.66 (m, 1184H, **H$_{THS}$**), 0.37 (s, 18H, **H$_{TMS}$**).

MALDI-TOF: *m*/*z* = 13348 ($C_{842}H_{1350}N_{32}Ni_8Si_{34}$, $M^{+\bullet}$ requires 13345).

UV–vis–NIR ($CDCl_3$, 298 K) λ_{max} / nm (ε / μM^{-1} cm^{-1}): 413 (0.17), 775 (0.34), 1791 (0.59) nm.

C.5 DFT and TD-DFT Calculations

Molecular models were built in GaussView 6 in which the trihexylsilyl side chains on the porphyrin *meso* aryl groups were replaced with H for all calculations.[377] DFT geometry optimizations of ***lf*-NiP*N*-TMS$_2$** were performed using Gaussian 16/A.03 with the B3LYP/6-31G* functional/basis set.[361,378–381] The minimized structures for short oligomers ($N \leq 6$) were subjected to frequency calculations, revealing no imaginary frequencies.

TD-DFT calculations for ***lf*-NiP*N*-TMS$_2$** were conducted for the first 64 excited states using the the PCM solvent model ($CHCl_3$).[382]

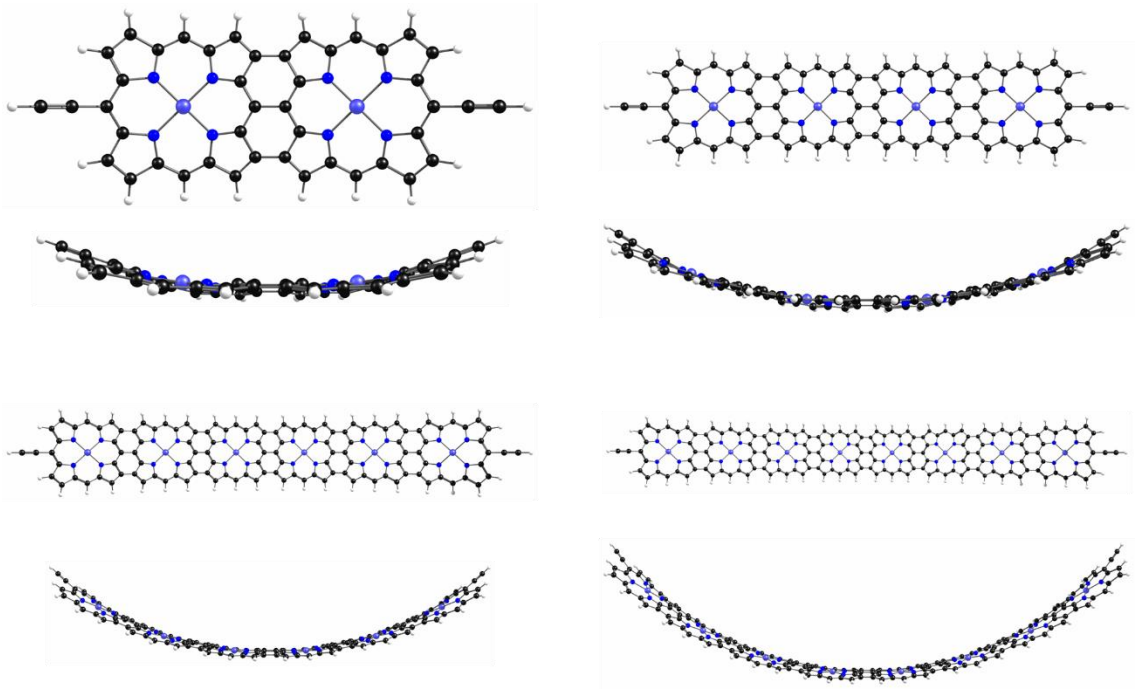

Figure C.1: Optimized geometries (front and side views) of ***lf*-NiP*N*-TMS$_2$** (N = 2, 4, 6 and 8) at B3LYP/6-31G* level of theory.

C.6 NMR and Mass Spectra

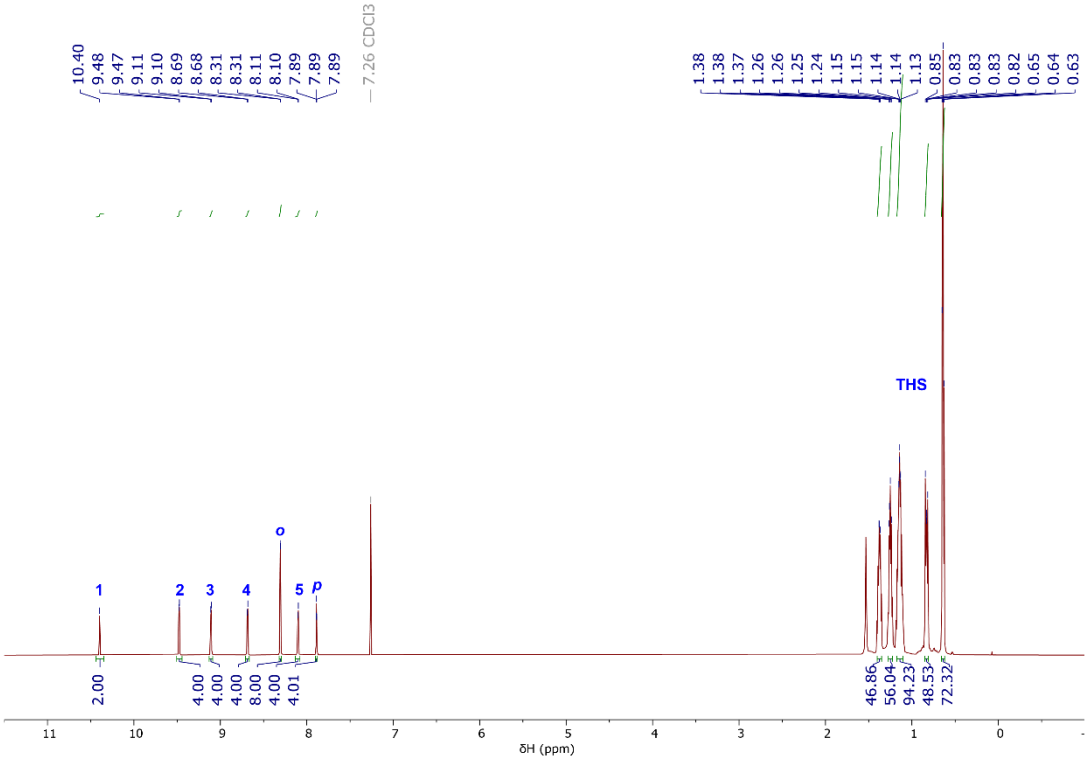

Figure C.2: ^{1}H NMR spectrum of ***ls*-ZnP2-H$_2$** (600 MHz, $CDCl_3$, 298 K).

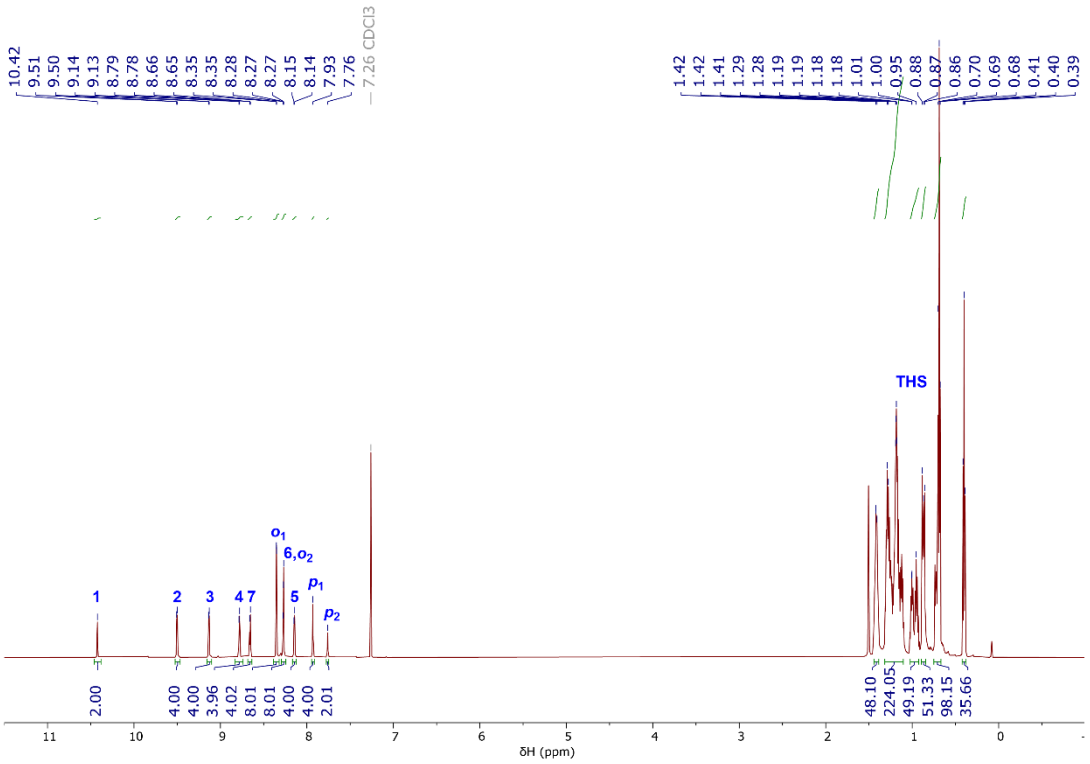

Figure C.3: ^{1}H NMR spectrum of ***ls*-ZnP3-H$_2$** (600 MHz, $CDCl_3$, 298 K).

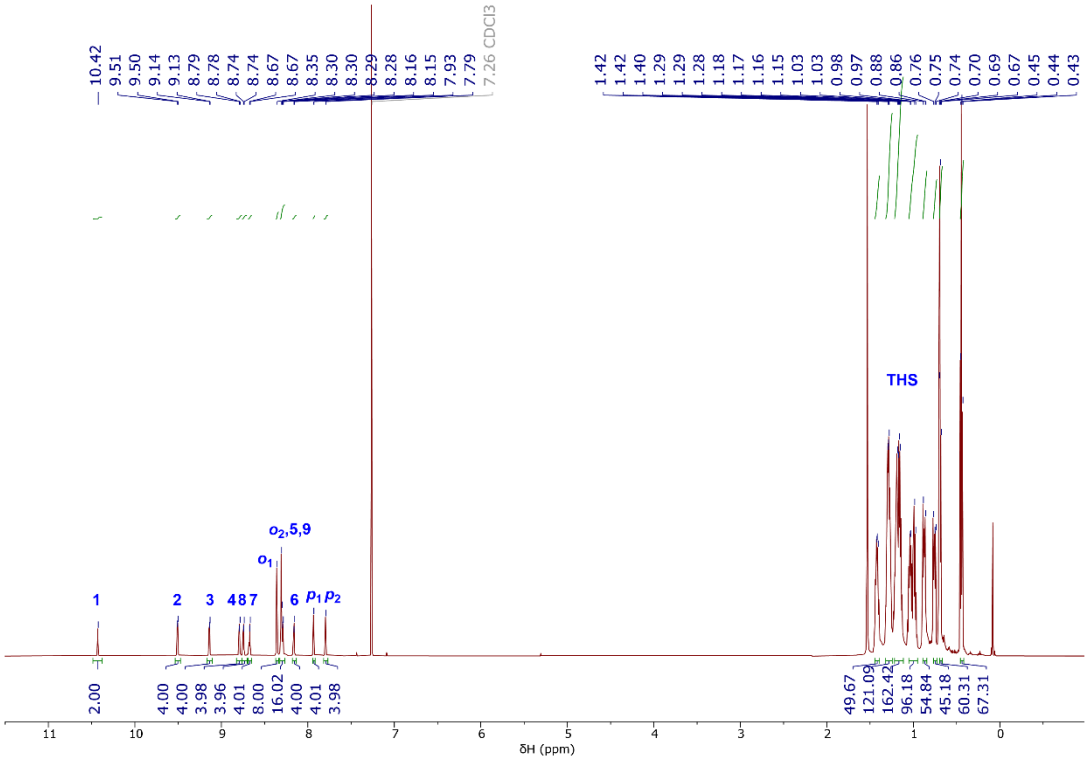

Figure C.4: ^{1}H NMR spectrum of ***ls*-ZnP4-H$_2$** (600 MHz, $CDCl_3$, 298 K).

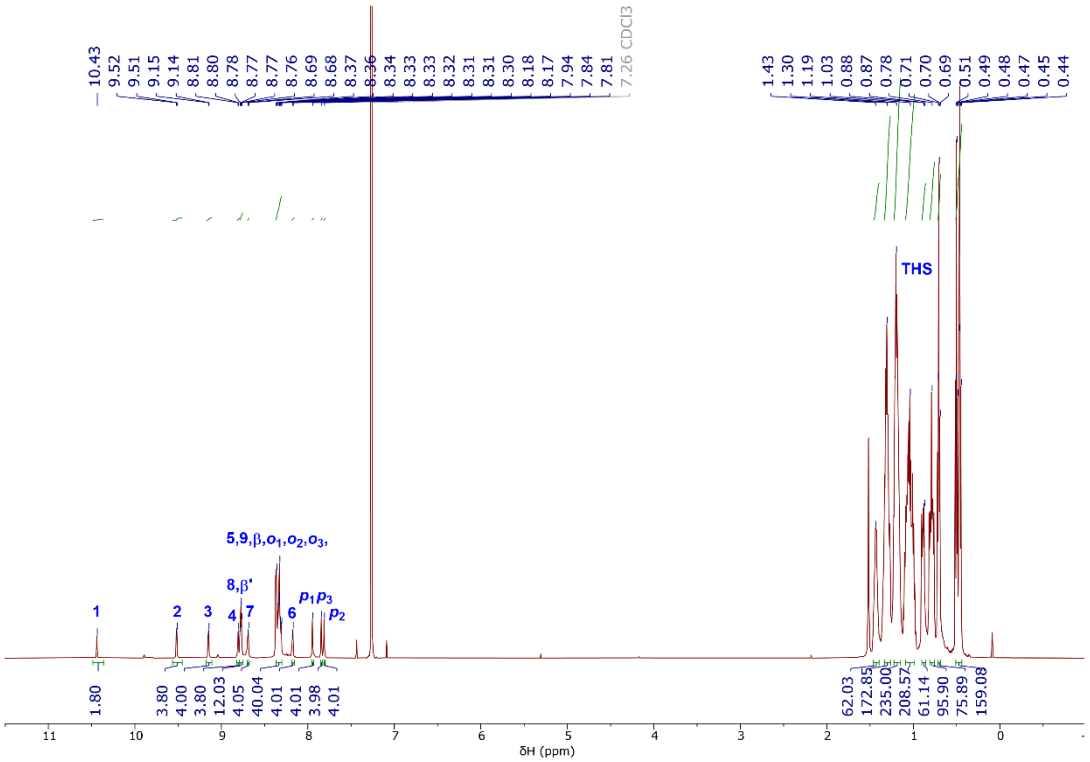

Figure C.5: ^{1}H NMR spectrum of ***ls*-ZnP6-H$_2$** (600 MHz, $CDCl_3$, 298 K).

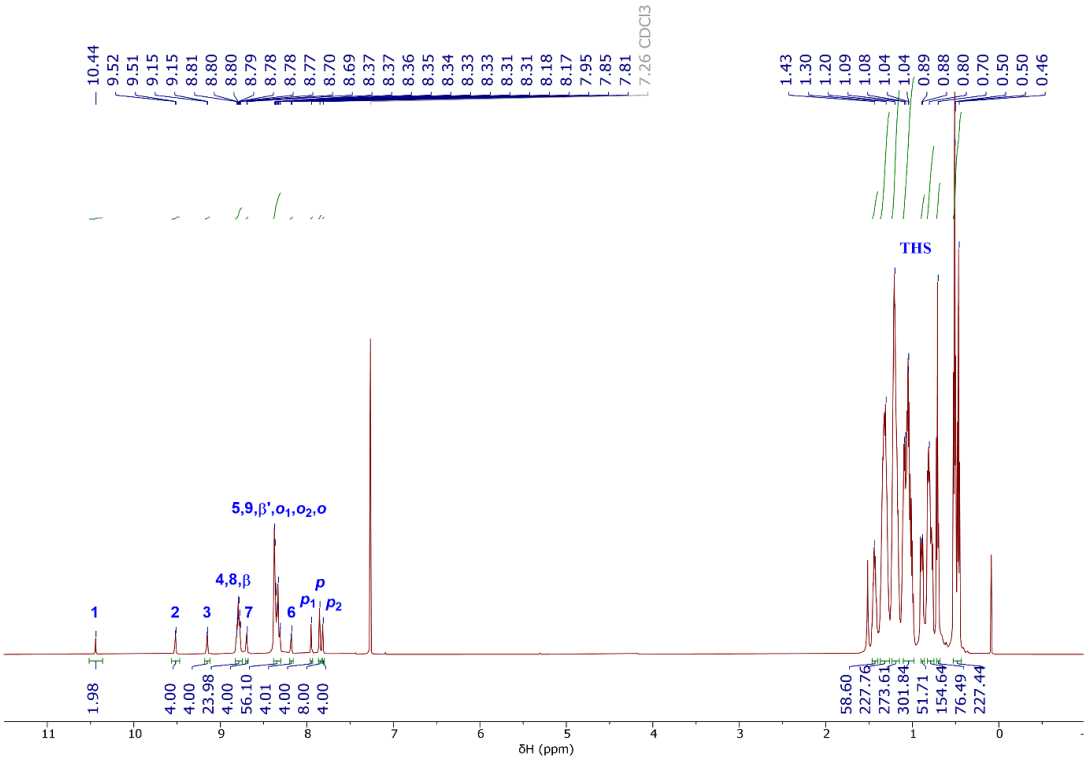

Figure C.6: ^{1}H NMR spectrum of ***ls*-ZnP8-H$_2$** (600 MHz, $CDCl_3$, 298 K).

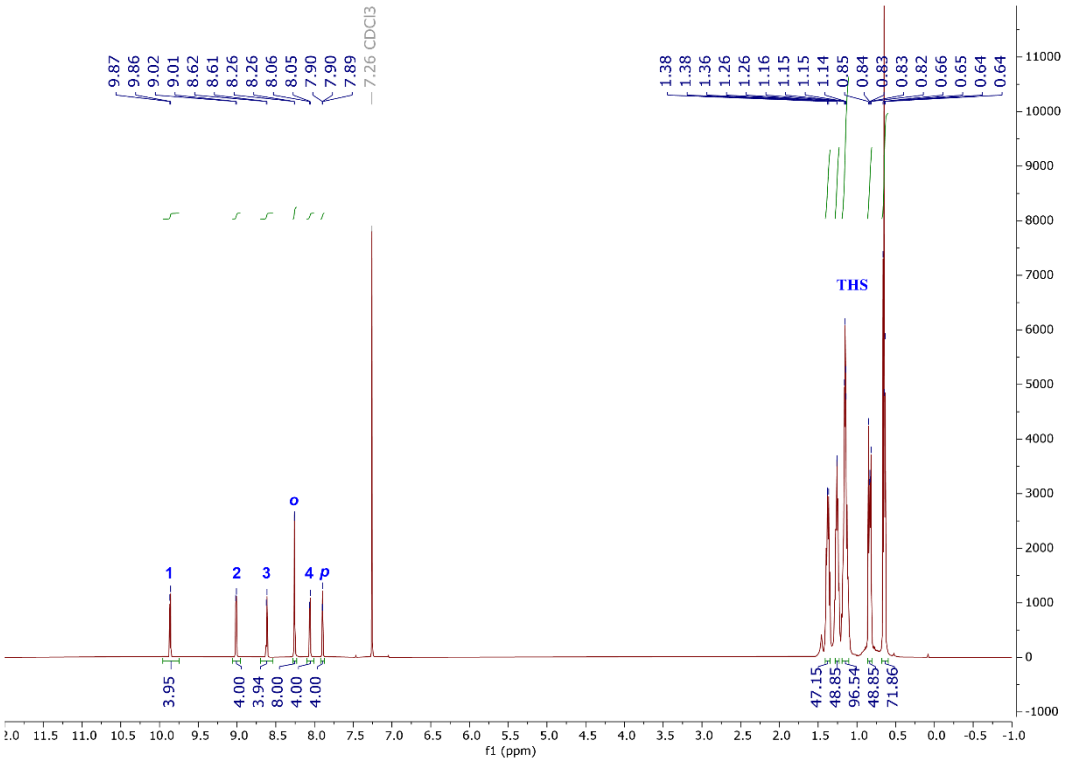

Figure C.7: ^{1}H NMR spectrum of ***ls*-ZnP2-Br$_2$** (600 MHz, $CDCl_3$, 298 K).

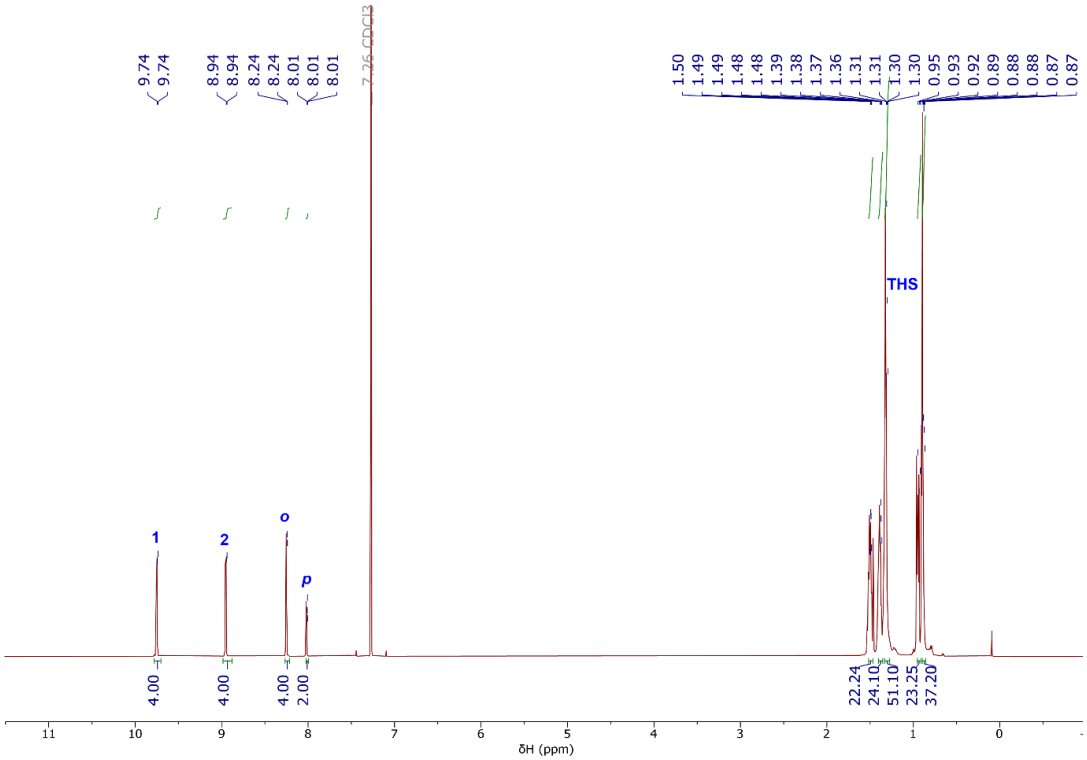

Figure C.8: ^{1}H NMR spectrum of **ZnP1-Br$_2$** (600 MHz, $CDCl_3$, 298 K).

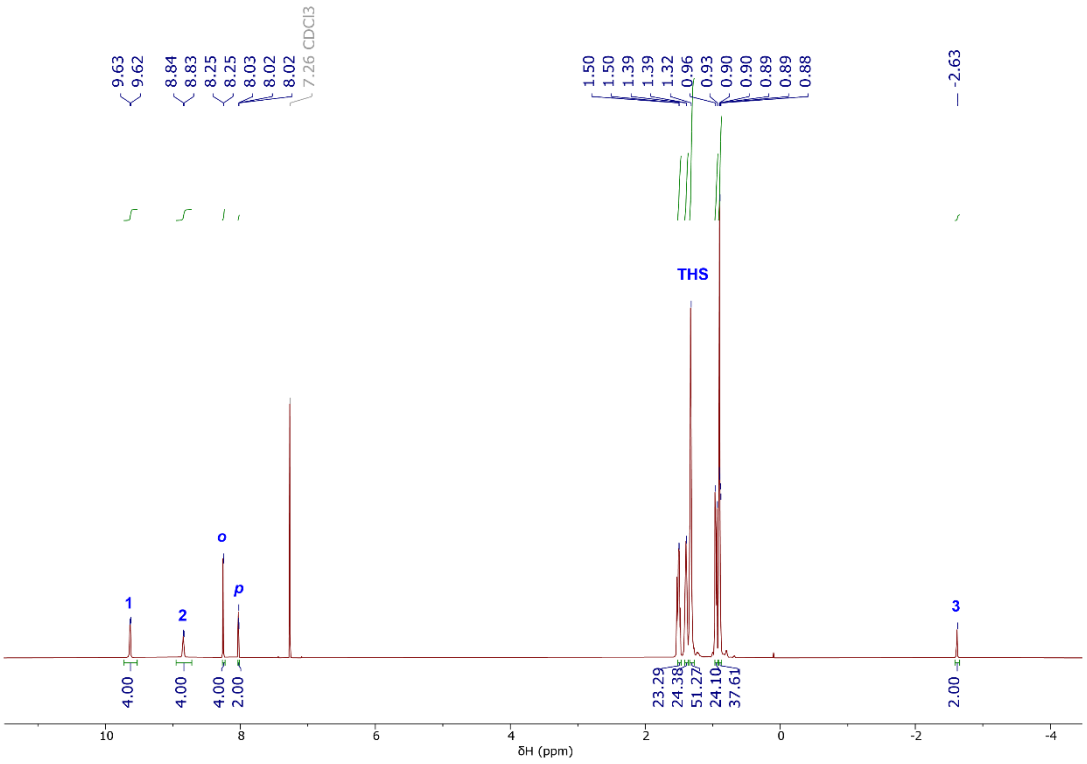

Figure C.9: ^{1}H NMR spectrum of **H$_2$P1-Br$_2$** (600 MHz, $CDCl_3$, 298 K).

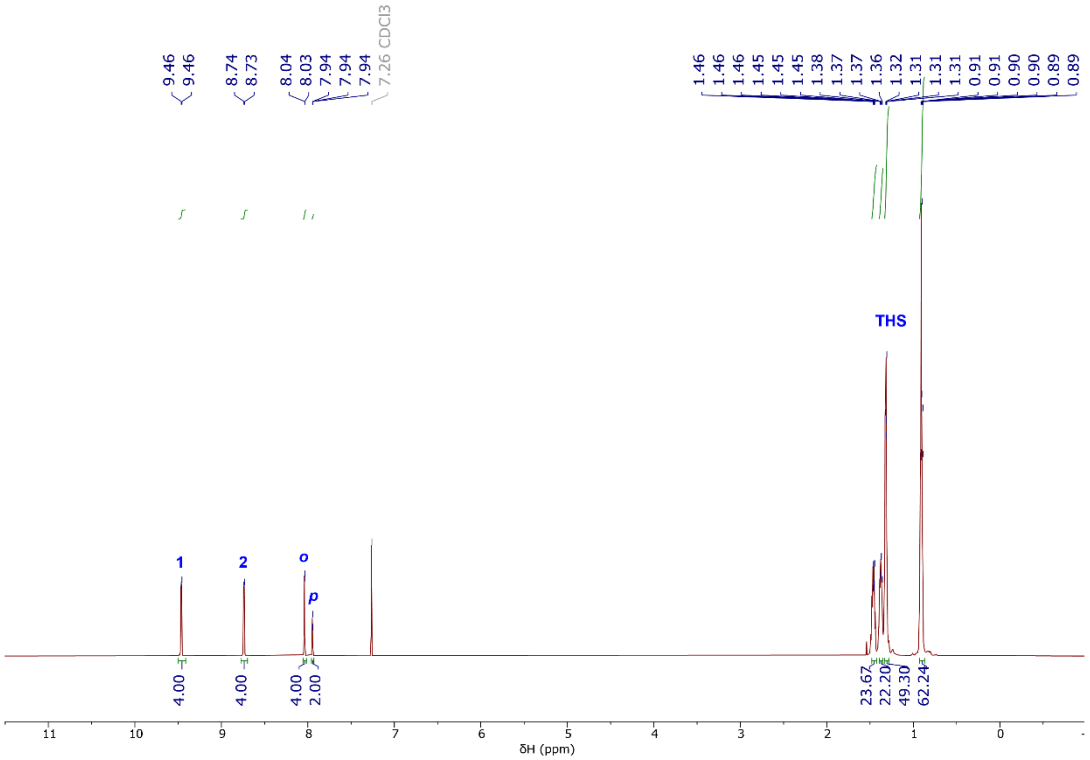

Figure C.10: ^{1}H NMR spectrum of **NiP1-Br$_2$** (600 MHz, $CDCl_3$, 298 K).

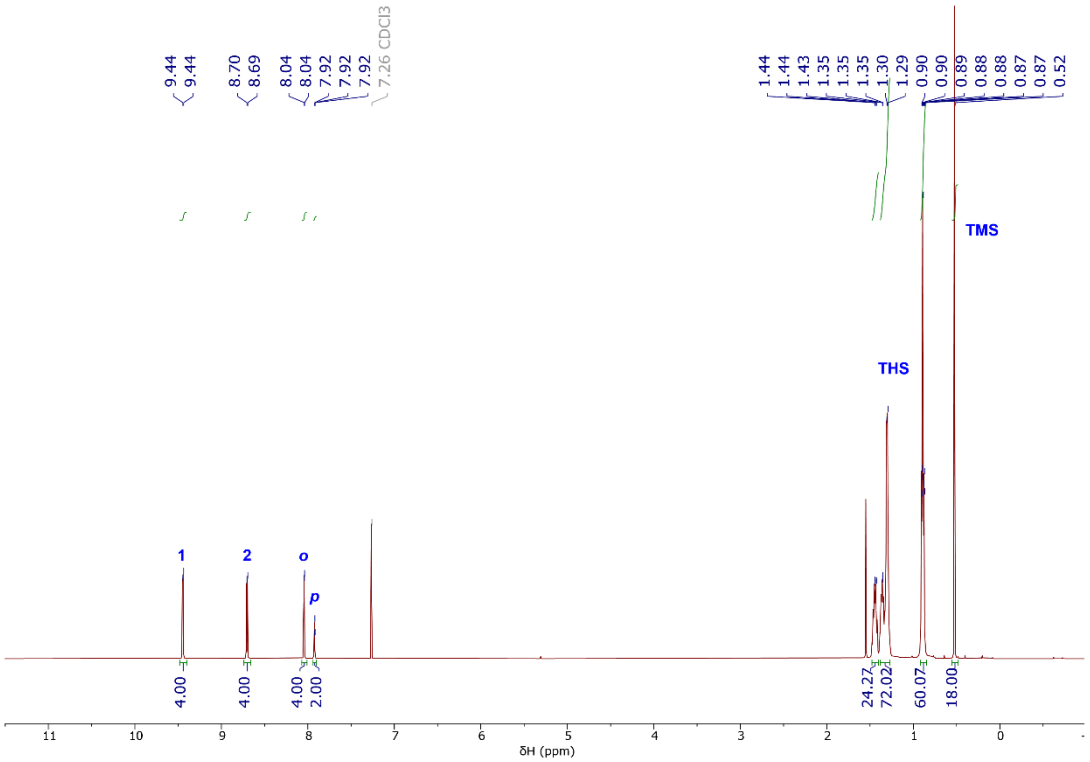

Figure C.11: ^{1}H NMR spectrum of **NiP1-TMS$_2$** (500 MHz, $CDCl_3$, 298 K).

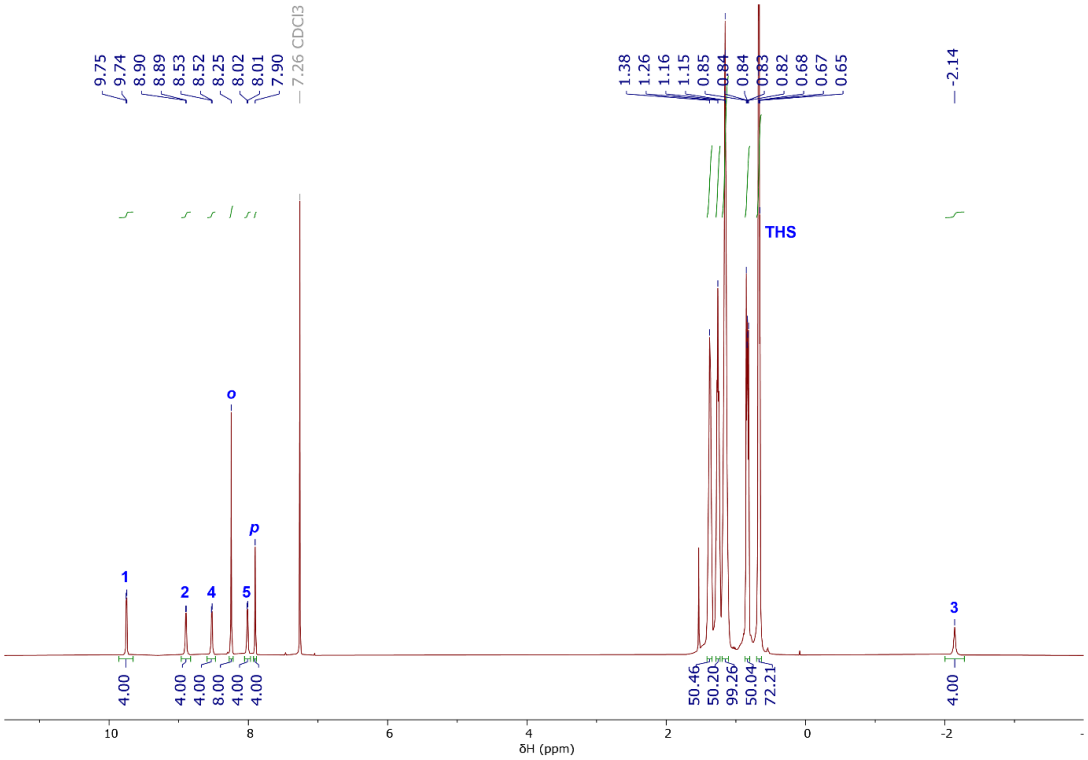

Figure C.12: ^{1}H NMR spectrum of ***ls*-H2P2-Br$_2$** (600 MHz, $CDCl_3$, 298 K).

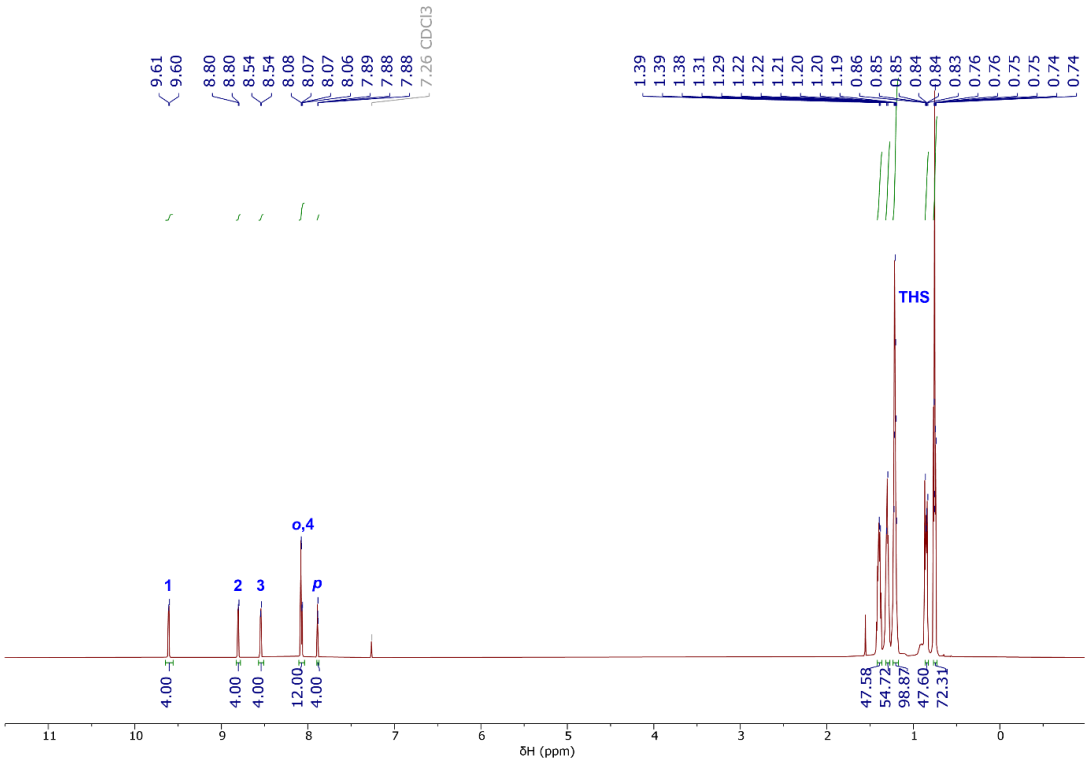

Figure C.13: ^{1}H NMR spectrum of ***ls*-NiP2-Br$_2$** (600 MHz, $CDCl_3$, 298 K).

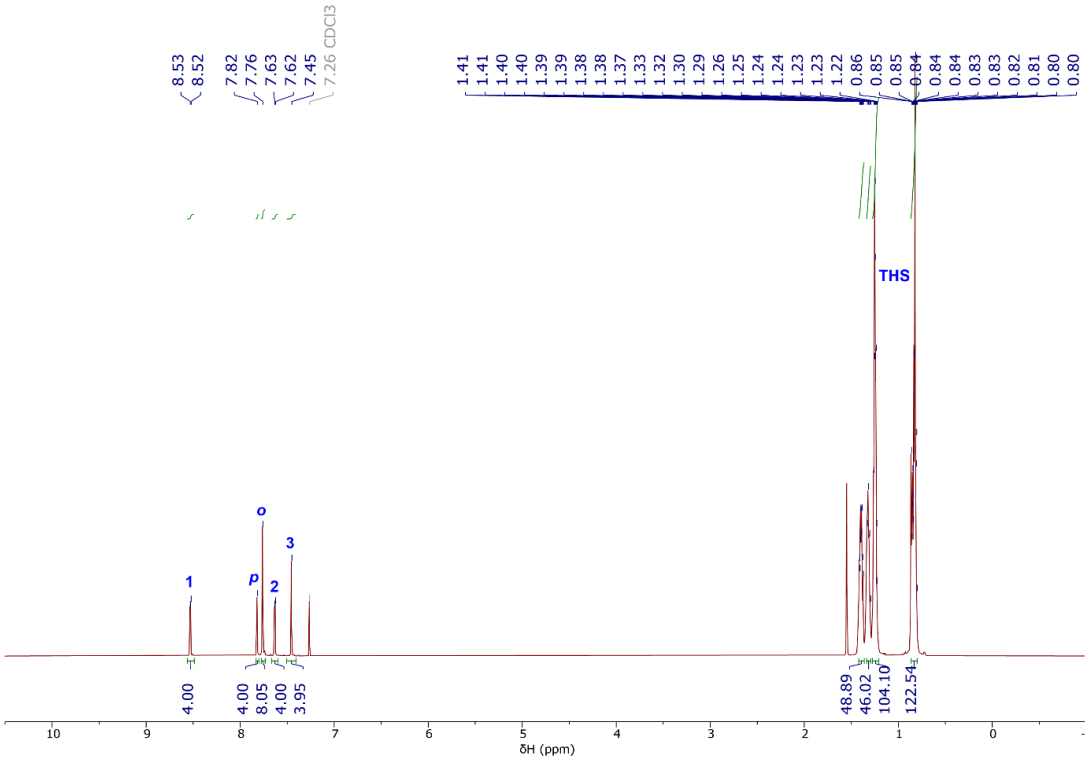

Figure C.14: ^{1}H NMR spectrum of ***lf*-NiP2-Br$_2$** (600 MHz, $CDCl_3$, 298 K).

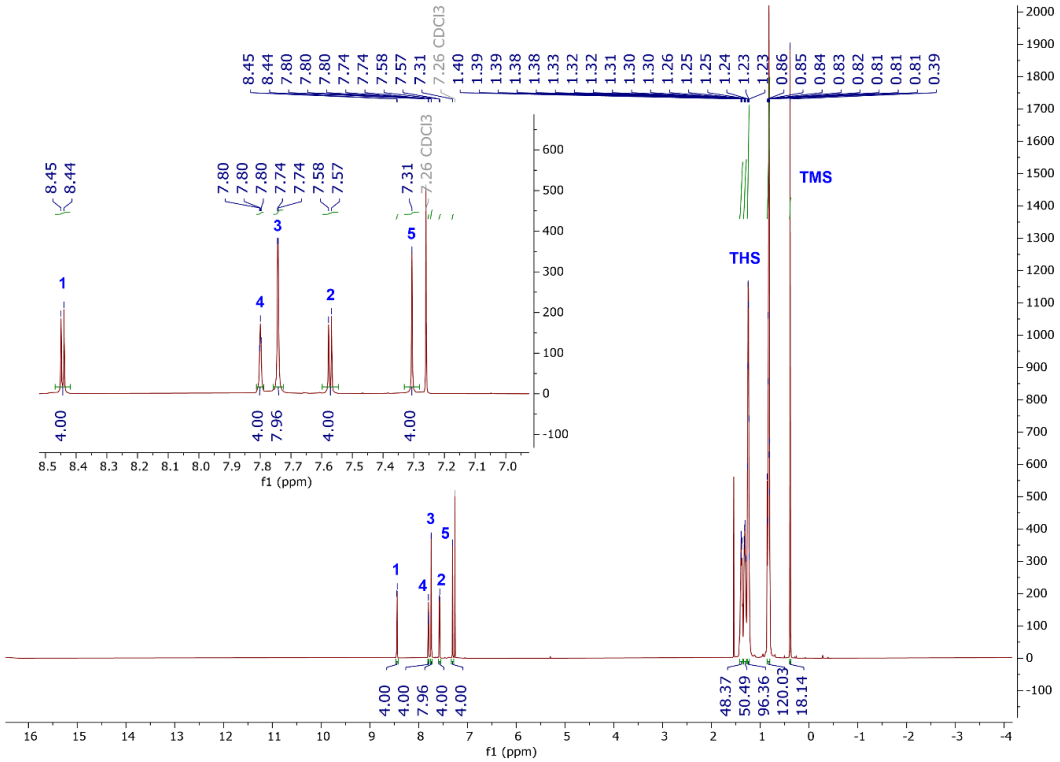

Figure C.15: ^{1}H NMR spectrum of ***lf*-NiP2-TMS$_2$** (500 MHz, $CDCl_3$, 298 K).

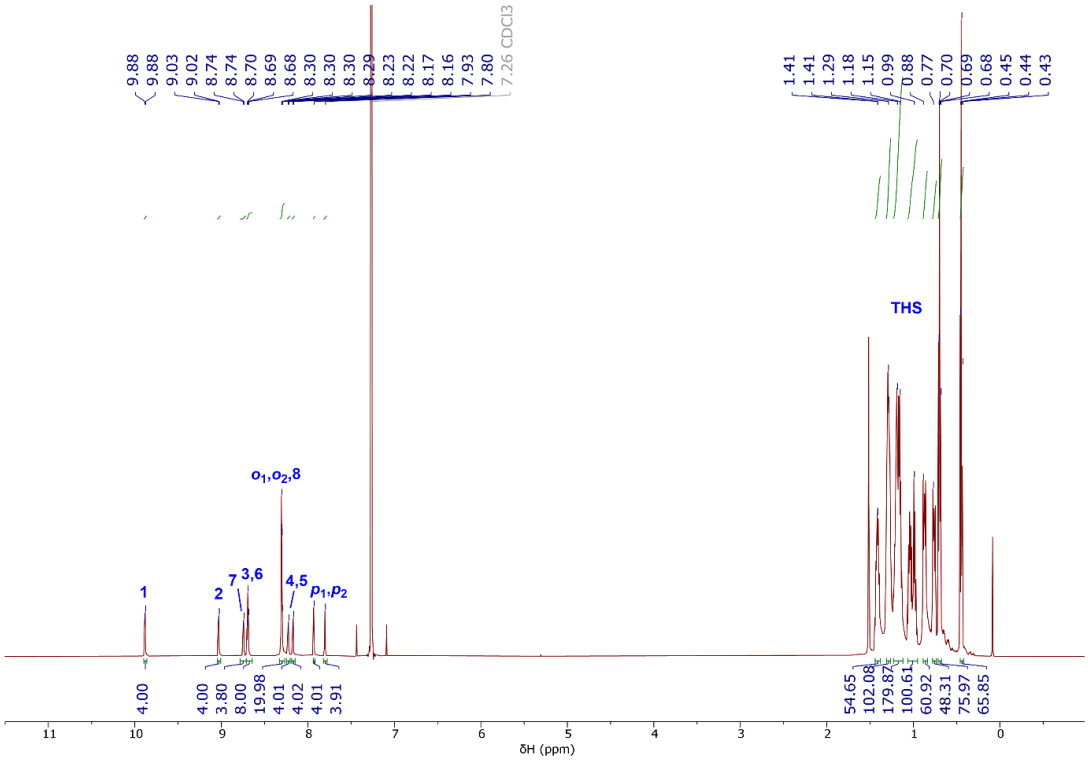

Figure C.16: ^{1}H NMR spectrum of ***ls*-ZnP4-Br$_2$** (600 MHz, $CDCl_3$, 298 K).

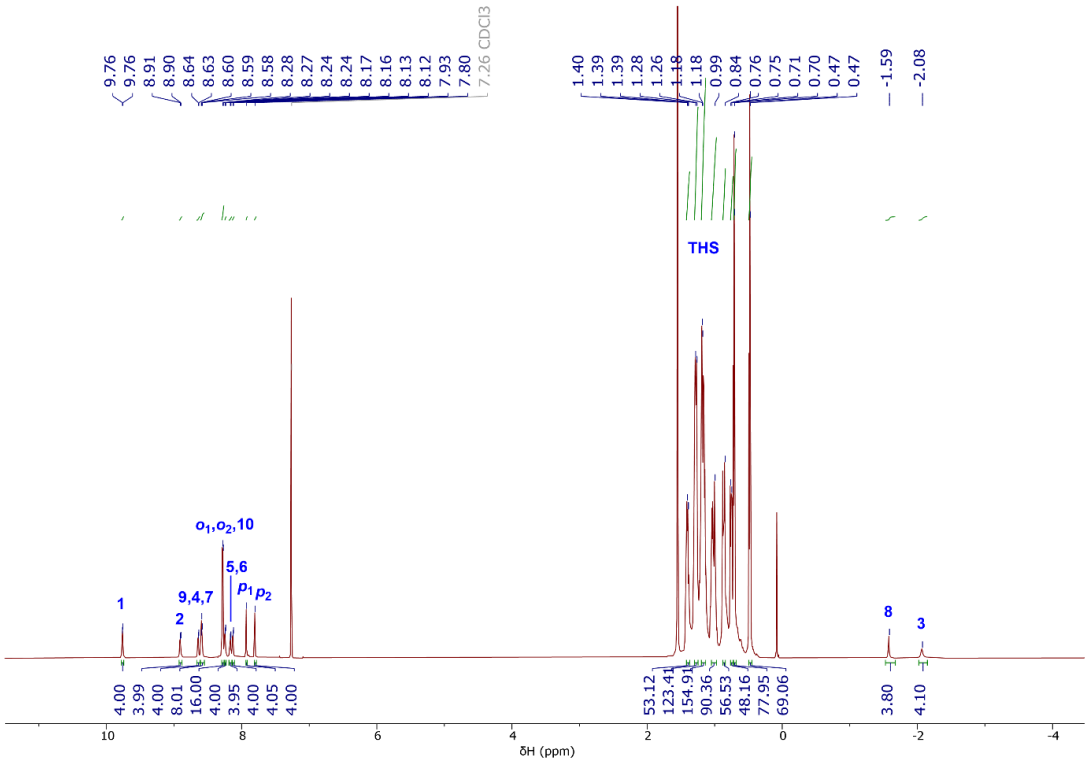

Figure C.17: ^{1}H NMR spectrum of ***ls*-H$_2$P4-Br$_2$** (600 MHz, $CDCl_3$, 298 K).

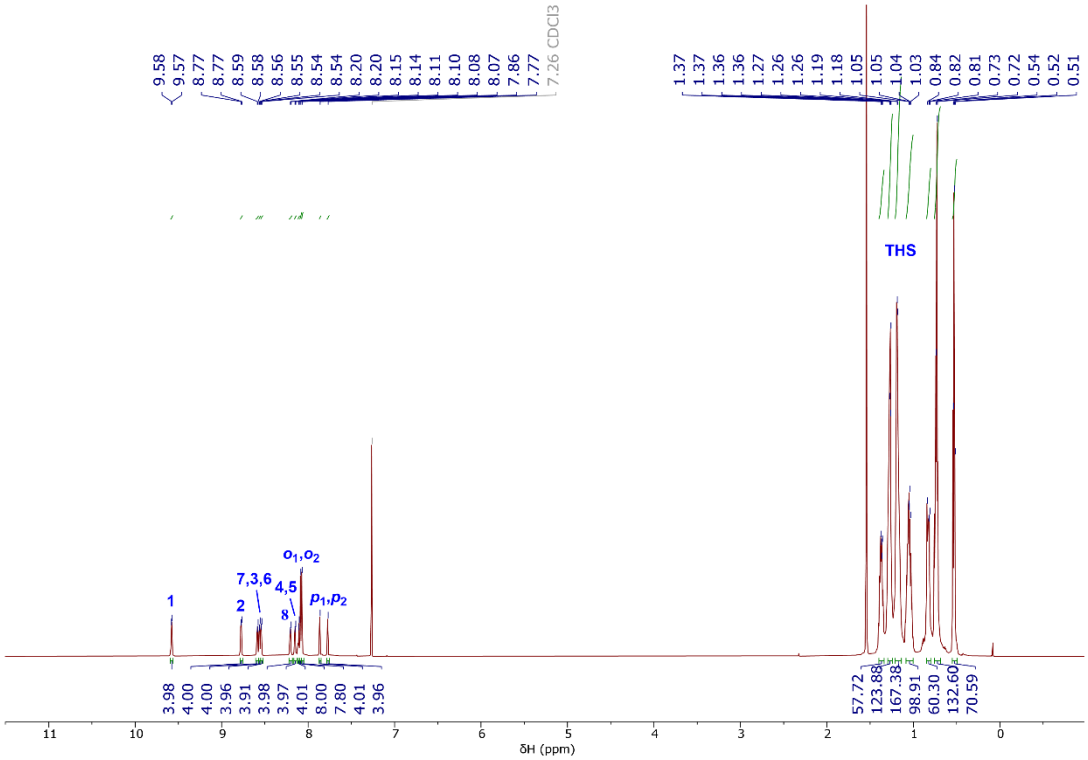

Figure C.18: ^{1}H NMR spectrum of ***ls*-NiP4-Br$_2$** (600 MHz, $CDCl_3$, 298 K).

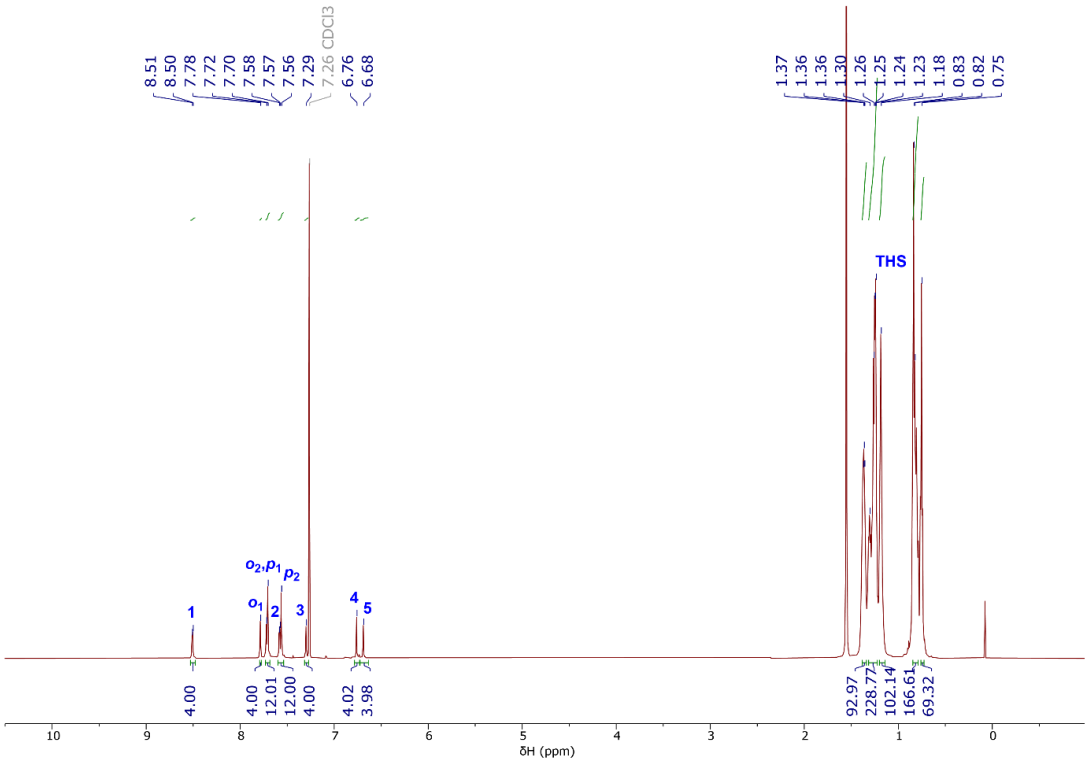

Figure C.19: ^{1}H NMR spectrum of ***lf*-NiP4-Br$_2$** (600 MHz, $CDCl_3$, 298 K).

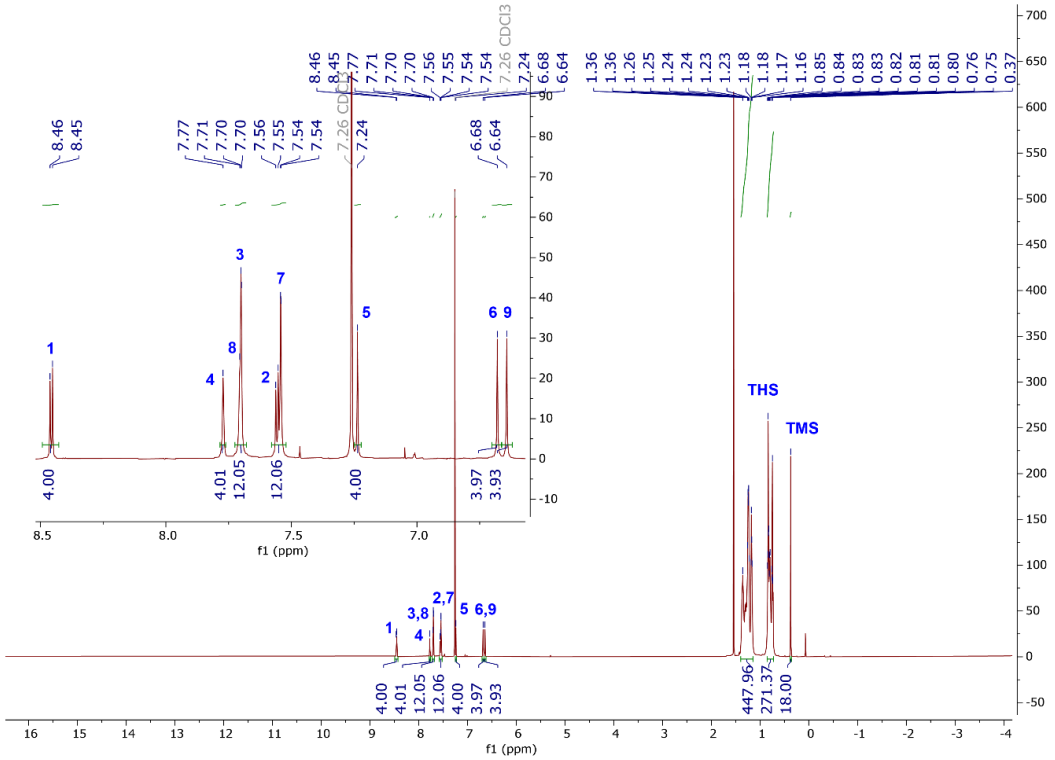

Figure C.20: ^{1}H NMR spectrum of ***lf*-NiP4-TMS$_2$** (500 MHz, $CDCl_3$, 298 K).

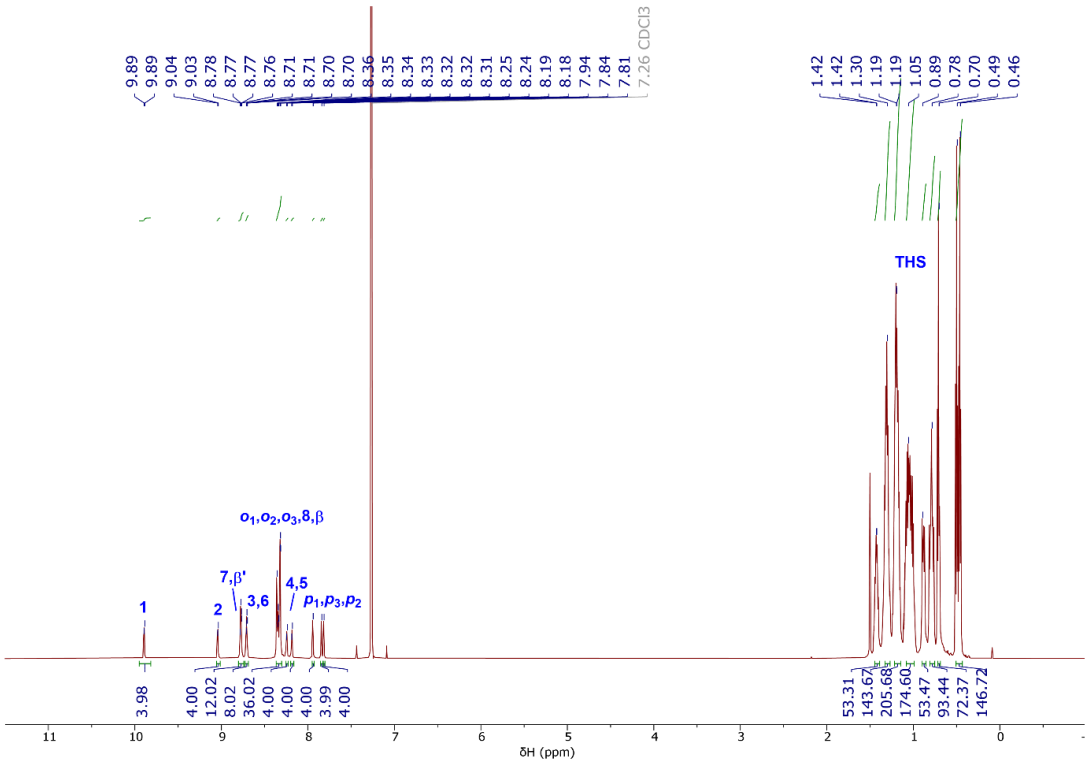

Figure C.21: ^{1}H NMR spectrum of ***ls*-ZnP6-Br$_2$** (600 MHz, $CDCl_3$, 298 K).

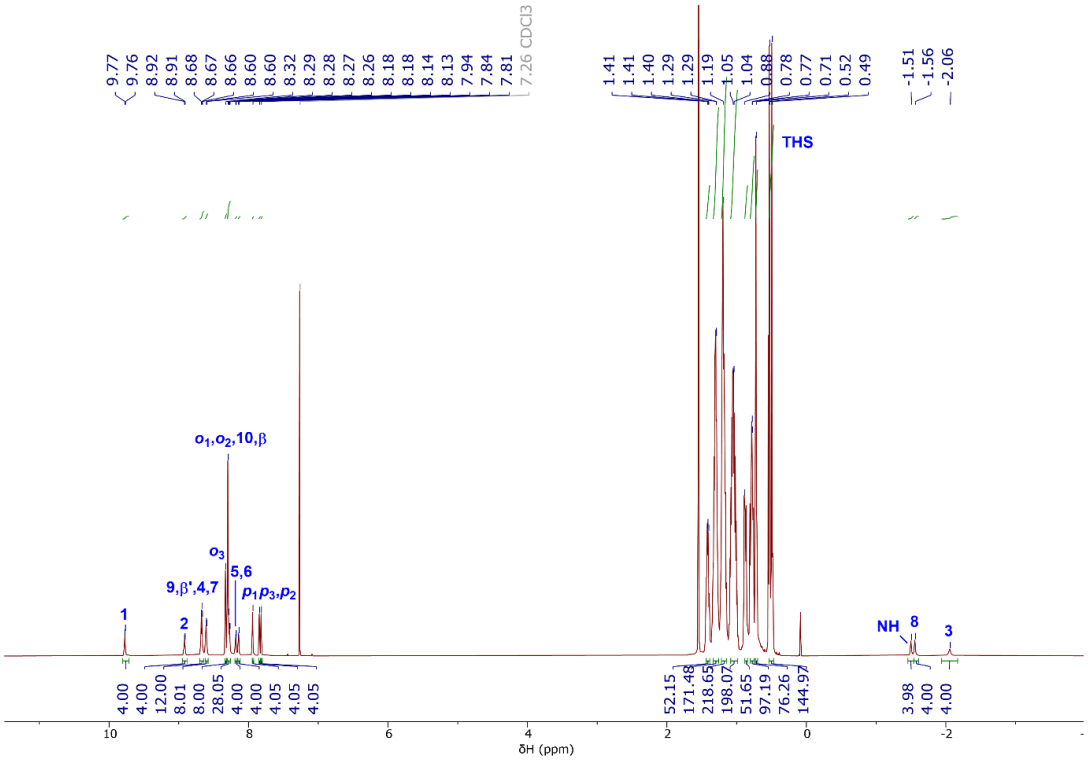

Figure C.22: ^{1}H NMR spectrum of ***ls*-H$_2$P6-Br$_2$** (600 MHz, $CDCl_3$, 298 K).

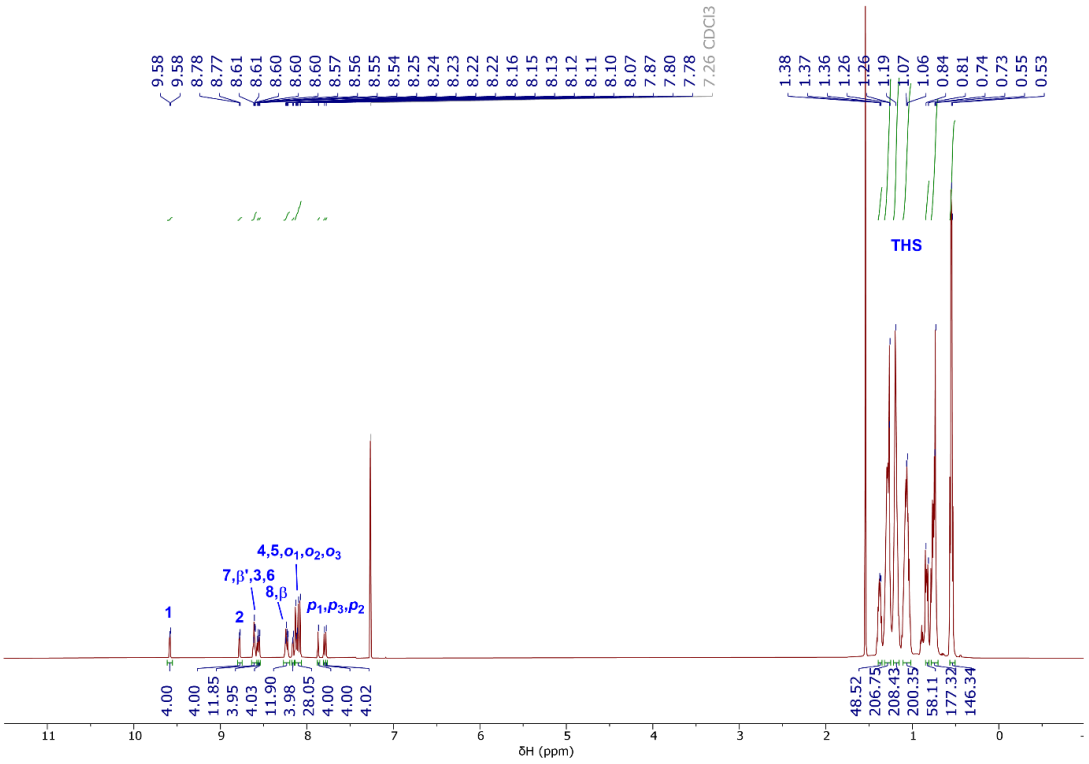

Figure C.23: ^{1}H NMR spectrum of ***ls*-NiP6-Br$_2$** (600 MHz, $CDCl_3$, 298 K).

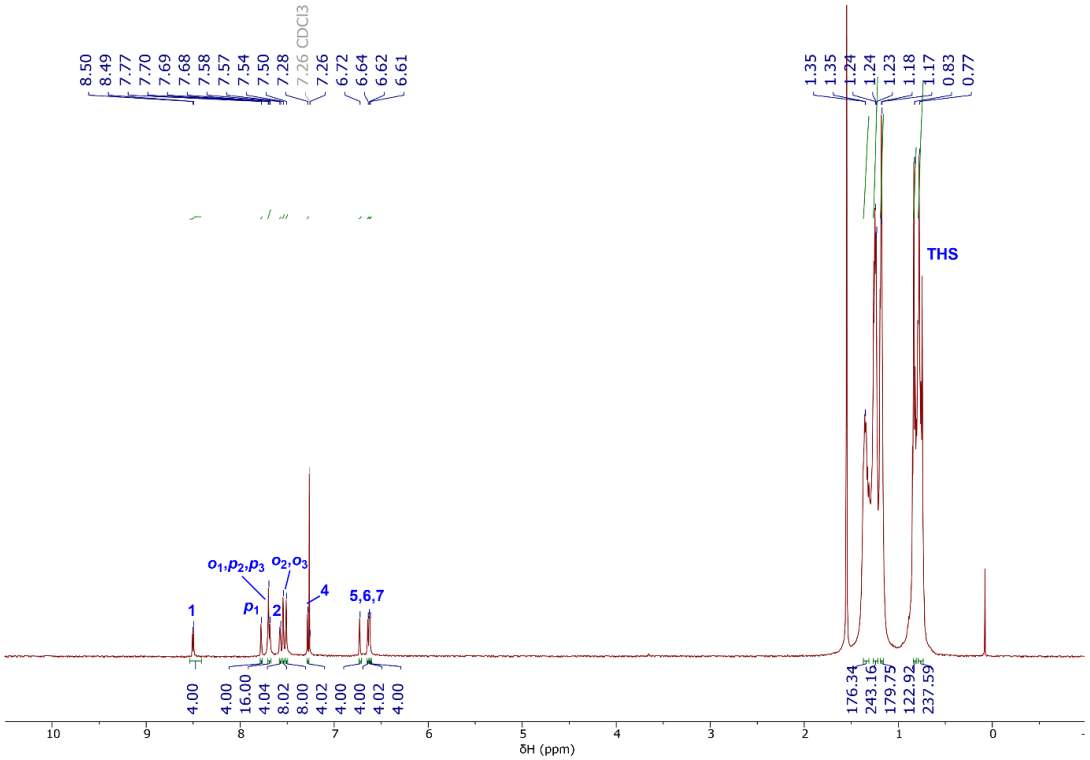

Figure C.24: ^{1}H NMR spectrum of ***lf*-NiP6-Br$_2$** (500 MHz, $CDCl_3$, 298 K).

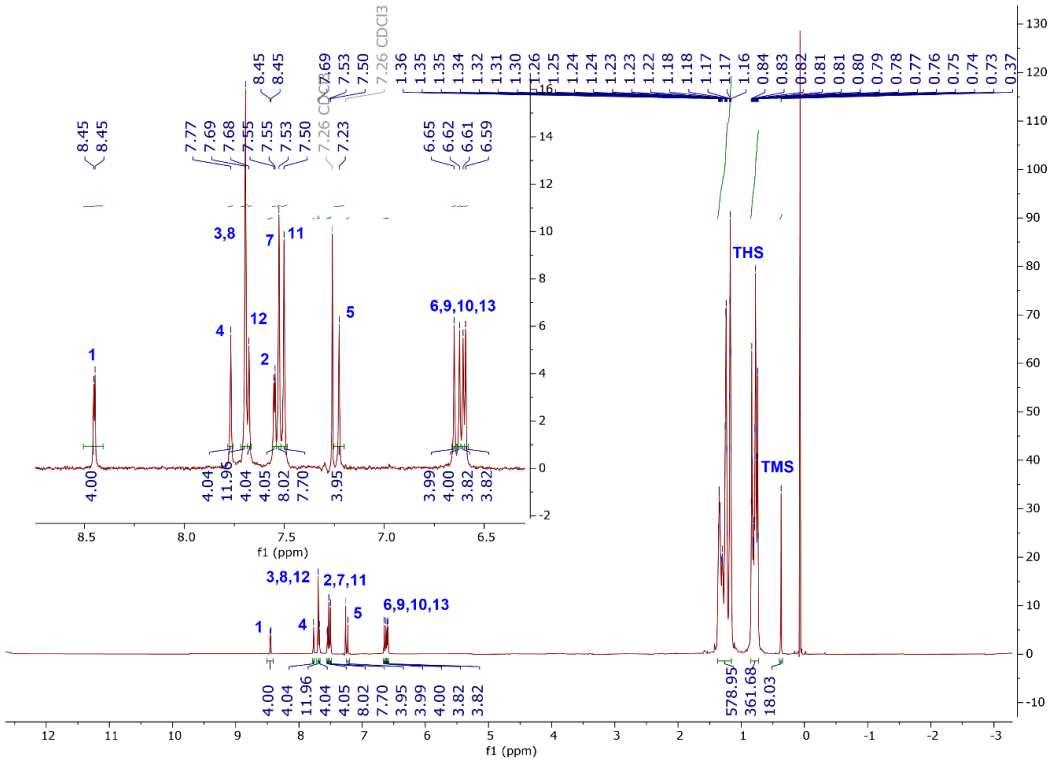

Figure C.25: ^{1}H NMR spectrum of ***lf*-NiP6-TMS$_2$** (700 MHz, $CDCl_3$, 298 K).

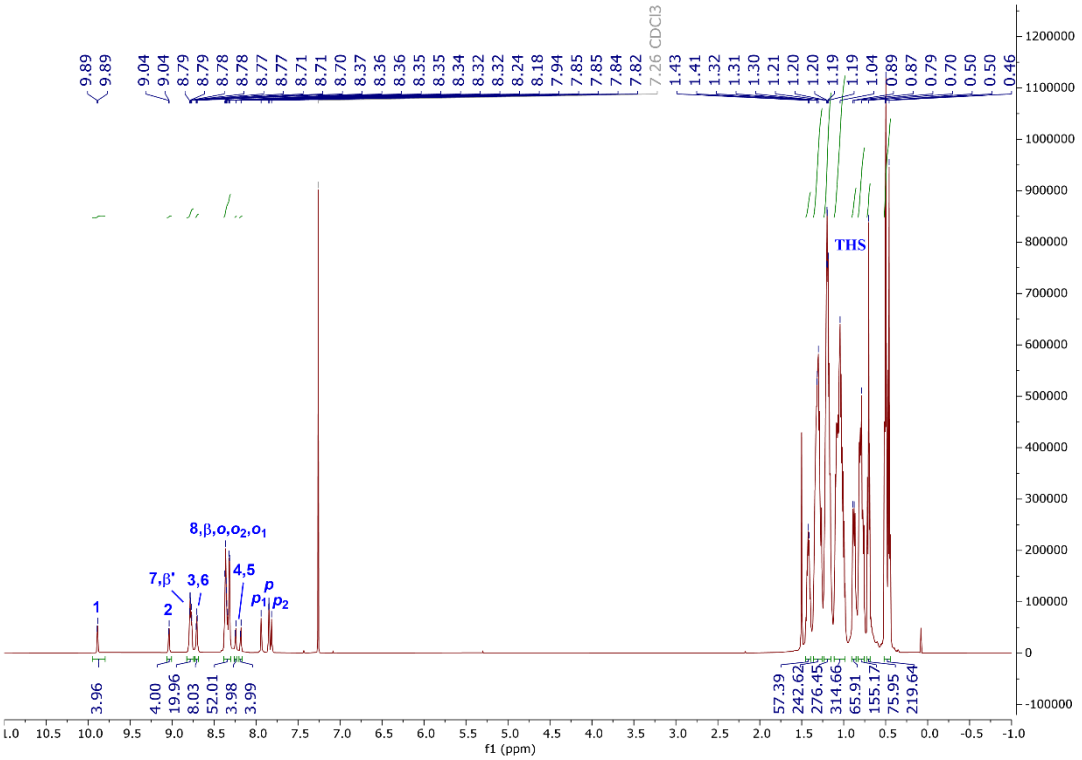

Figure C.26: ^{1}H NMR spectrum of ***ls*-ZnP8-Br$_2$** (600 MHz, $CDCl_3$, 298 K).

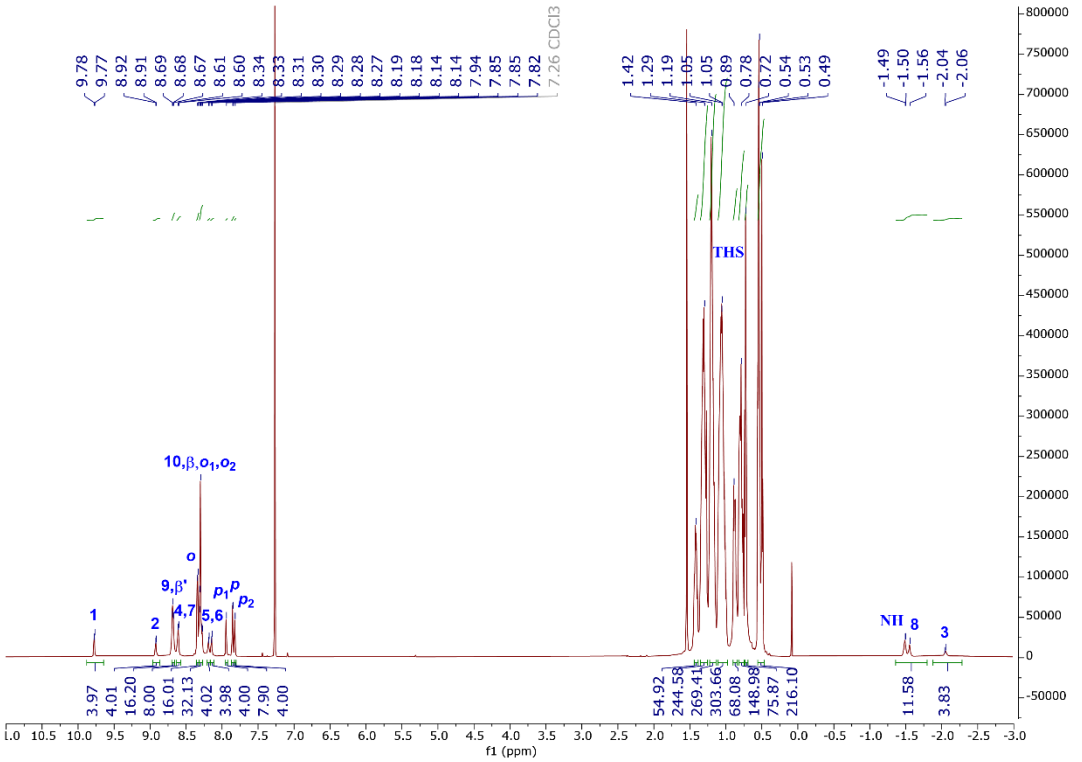

Figure C.27: ^{1}H NMR spectrum of ***ls*-H$_2$P8-Br$_2$** (600 MHz, $CDCl_3$, 298 K).

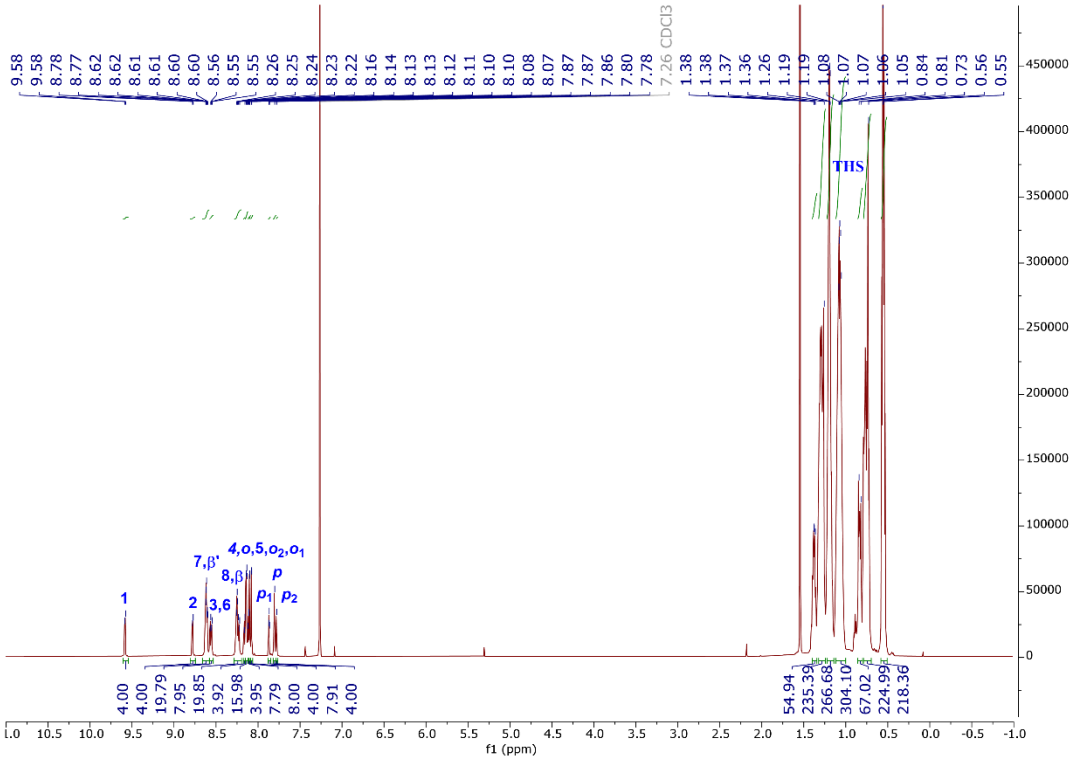

Figure C.28: ^{1}H NMR spectrum of ***ls*-NiP8-Br$_2$** (600 MHz, $CDCl_3$, 298 K).

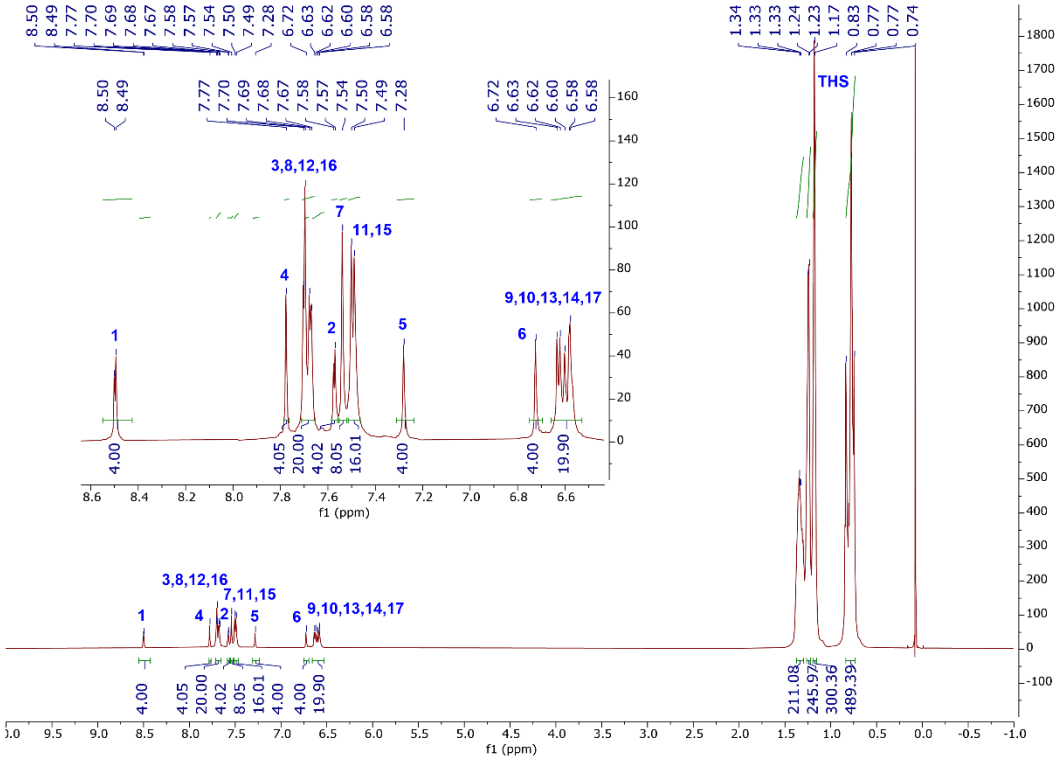

Figure C.29: ^{1}H NMR spectrum of ***lf*-NiP8-Br$_2$** (700 MHz, $CDCl_3$, 298 K).

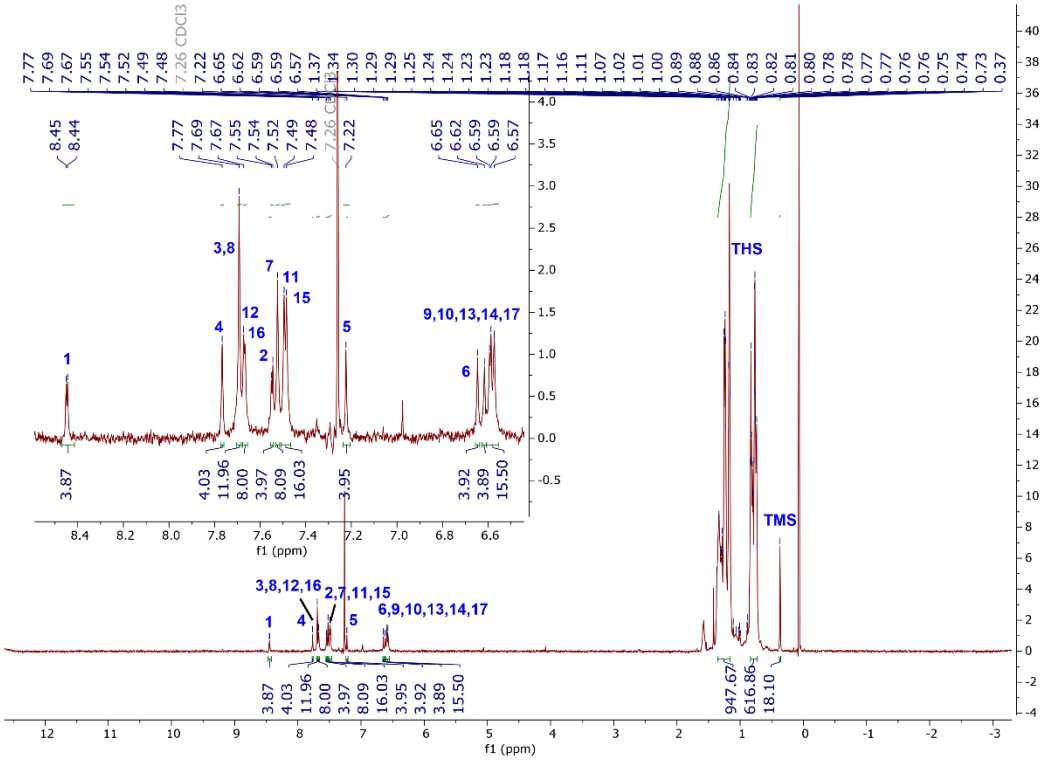

Figure C.30: ^{1}H NMR spectrum of ***lf*-NiP8-Br$_2$** (700 MHz, $CDCl_3$, 298 K).

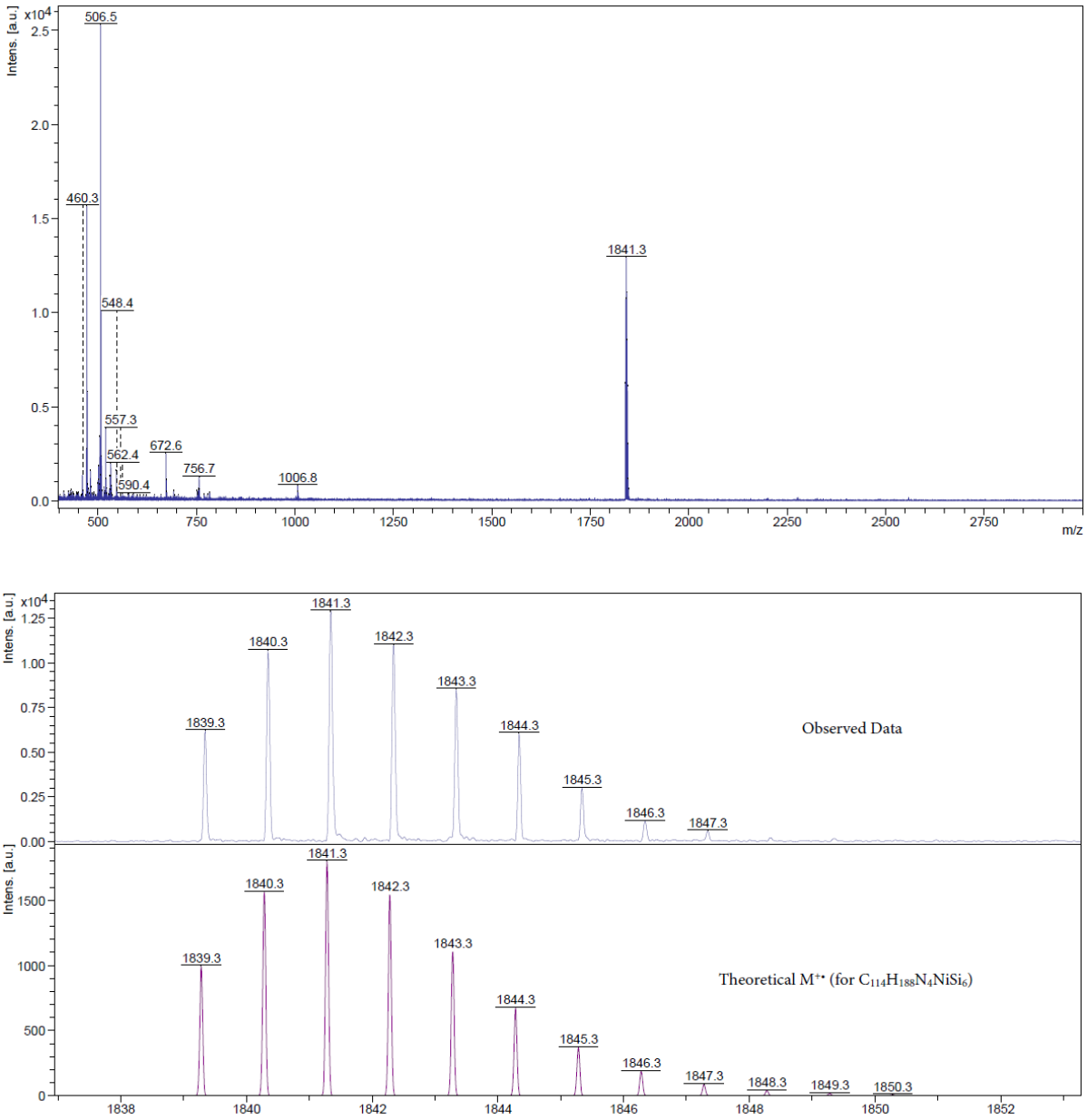

Figure C.31: MALDI-ToF spectrum of **NiP1-TMS$_2$** with DCTB as matrix. Overview (top) and zoomed-view of the $M^{+\bullet}$ region (bottom).

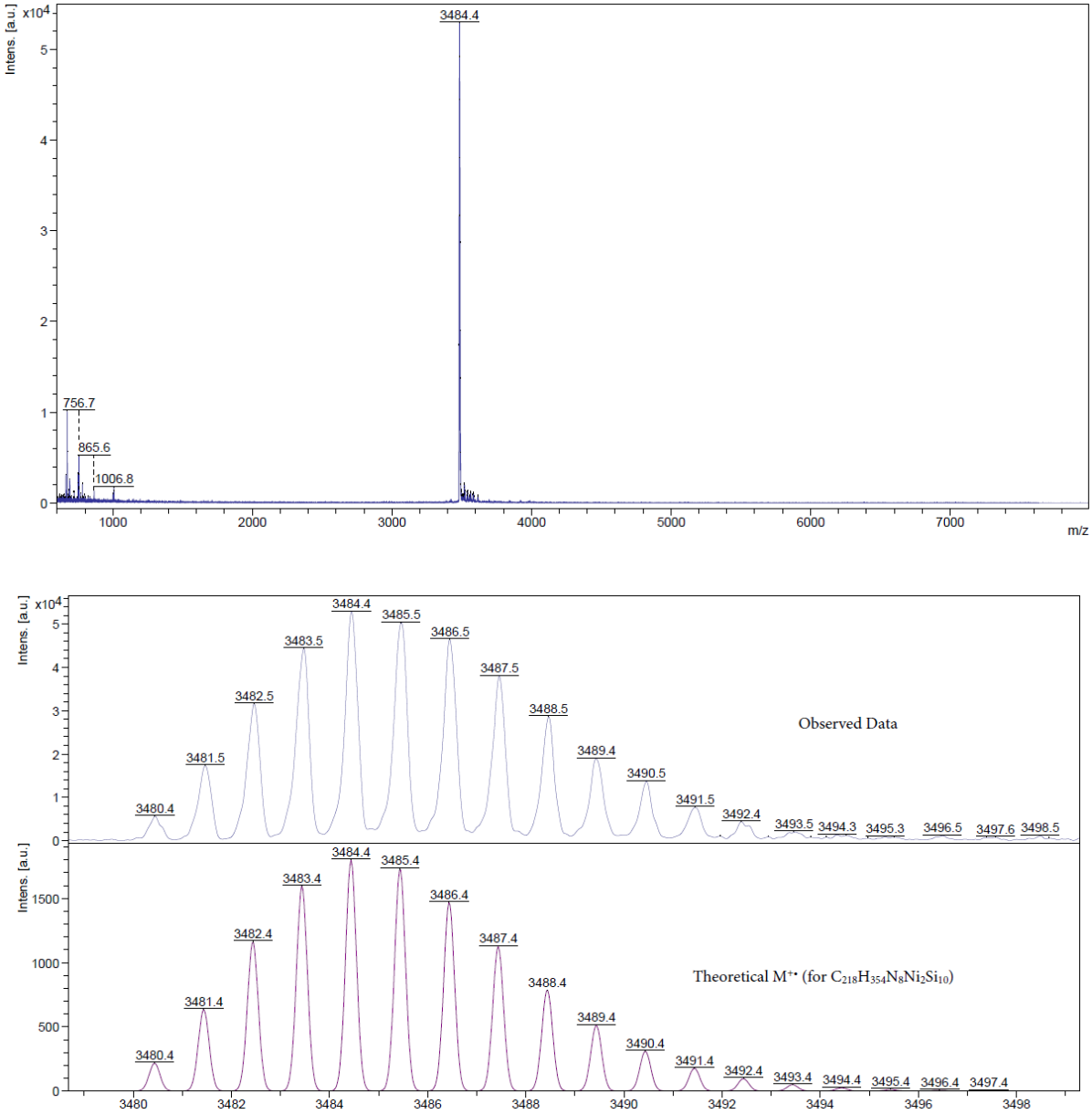

Figure C.32: MALDI-ToF spectrum of ***lf*-NiP2-TMS$_2$** with DCTB as matrix. Overview (top) and zoomed-view of the $M^{+\bullet}$ region (bottom).

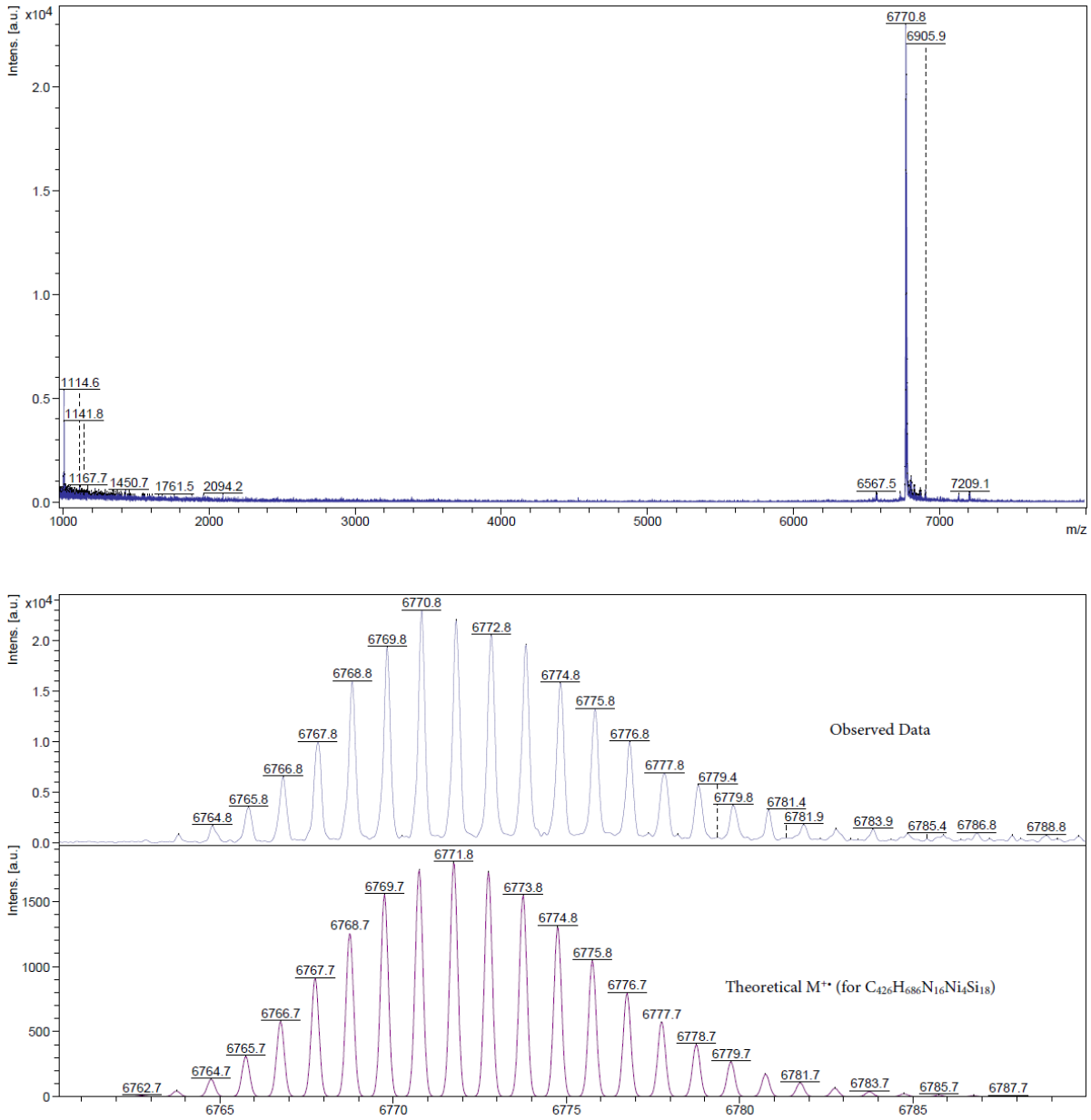

Figure C.33: MALDI-ToF spectrum of ***lf*-NiP4-TMS$_2$** with DCTB as matrix. Overview (top) and zoomed-view of the $M^{+\bullet}$ region (bottom).

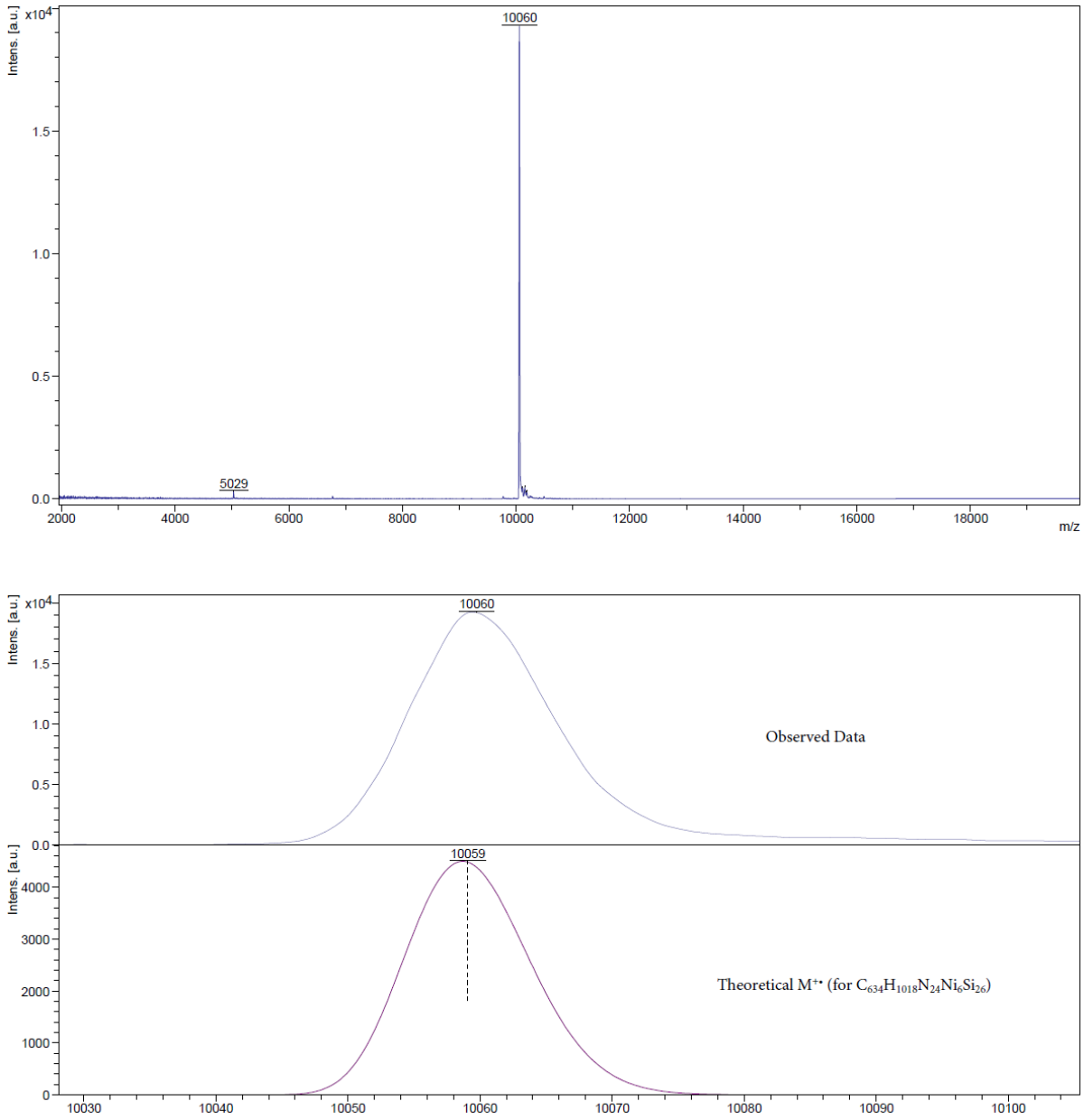

Figure C.34: MALDI-ToF spectrum of ***lf*-NiP6-TMS$_2$** with DCTB as matrix. Overview (top) and zoomed-view of the $M^{+\bullet}$ region (bottom).

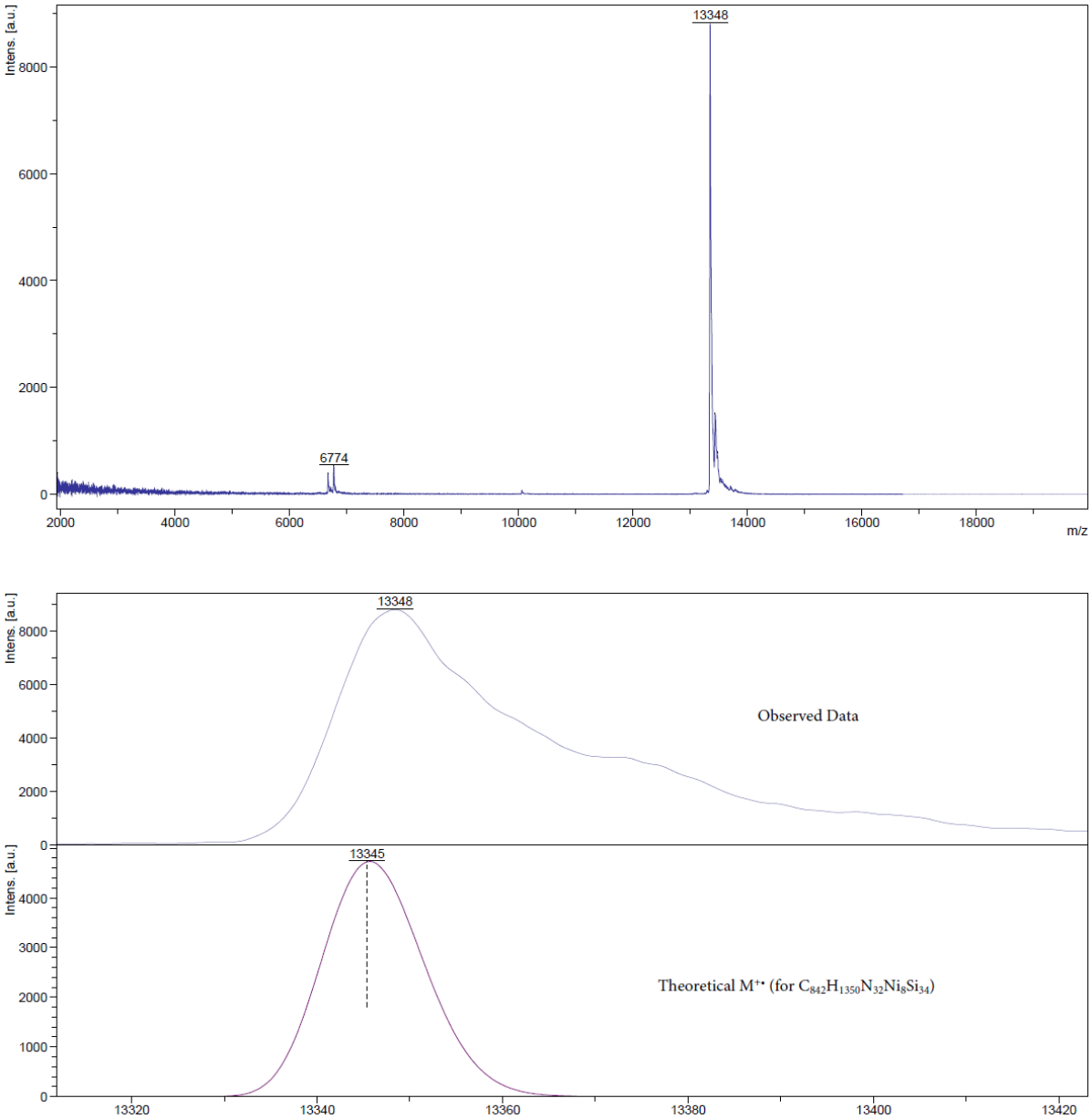

Figure C.35: MALDI-ToF spectrum of ***lf*-NiP8-TMS$_2$** with DCTB as matrix. Overview (top) and zoomed-view of the $M^{+\bullet}$ region (bottom).

Appendix D — Experimental Procedures and Supplementary Details for Chapter 4

D.1 Synthesis of *lf*-NiP8-TAP$_2$

D.1.1 General Methods

All reagents were purchased as reagent grade and used without further purification. Solvents for column chromatography were used in HPLC grade. Dry toluene and diisopropylamine (*i*-Pr_2NH) were obtained from the solvent drying system MBraun MBSPS-5-BenchTop under nitrogen atmosphere (H_2O content < 20 ppm as determined by Karl-Fischer titration). Flash column chromatography was carried out using SiO_2 (60 Å, 230 – 400 mesh) under positive pressure. Analytical thin-layer chromatography was carried out on aluminum-backed silica gel 60 F254 plate. Evaporation in vacuum was performed at 25 – 80 ºC and 900 – 10 mbar. Size exclusion chromatography (SEC) was carried out using Bio-Rad Bio-Beads S-X1 (40 – 80 μm bead size). Semi-preparative gel permeation chromatography (GPC) was carried out on a Shimadzu recycling GPC system equipped with a LC-20 AD pump, SPD-20A UV detector and a set either of JAIGEL 3H (20 × 600 mm) and JAIGEL 4H (20 × 600 mm) columns using toluene/pyridine (99:1) as eluent at a flow rate of 3.5 mL/min.

MALDI-ToF spectrum was measured using a Bruker MALDI Autoflex Speed spectrometer utilizing *trans*-2-[3-(4-*tert*-butylphenyl)-2-methyl-2-propenylidene]-malononitrile (DCTB) as matrix.

UV–vis–NIR absorbance measurement was recorded with a Jasco V770 spectrophotometer using an Infrasil® Quartz 1 cm cuvette. Measurement was carried out at 25 °C under ambient conditions.

Compound ***lf*-NiP8-Br$_2$** was prepared using the methods described in Chapter 3. 1,3,6-tris(dodecyloxy)-8-ethynylpyrene (TAP-acetylene, compound **4.5**) was made following the reported procedures.[9]

D.1.2 Synthesis of *lf*-NiP8-TAP$_2$

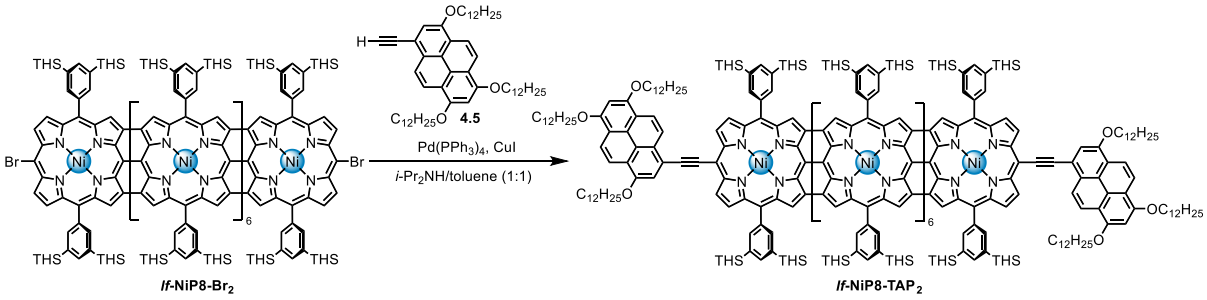

A mixture of ***lf*-NiP8-Br$_2$** (1.0 mg, 0.075 μmol, 1.0 equiv.), Pd(PPh$_3$)$_4$ (1.1 mg, 1.5 μmol, 20 equiv.) and CuI (0.14 mg, 0.75 μmol, 10 equiv.) in dry toluene (0.5 mL) and *i*-Pr$_2$NH (0.5 mL) was degassed by three freeze-pump-thaw cycles. A solution of TAP-acetylene (compound **4.5**, 10 mg, 13 μmol, 170 equiv.) in dry toluene (0.5 mL) and *i*-Pr$_2$NH (0.5 mL) was degassed by three freeze-pump-thaw cycles and transferred to the reaction mixture under argon. After that, the mixture was stirred at 50 ºC under argon for 2 h. Then, a degassed solution of TAP-acetylene (5.0 mg, 6.4 μmol, 85 equiv.) in dry toluene (0.5 mL) and *i*-Pr$_2$NH (0.5 mL) was added to the reaction mixture and the mixture was stirred at 50 ºC for another 20 h. After reaction, the resulting mixture was separated by flash column chromatography (SiO$_2$) using pentane/CH$_2$Cl$_2$ (1:1) as eluent, followed by size-exclusion chromatography (Bio-beads, SX-1) with toluene/pyridine (99:1) as eluent to give a crude mixture. The crude mixture was further subjected to recycling GPC with toluene/pyridine (99:1) as eluent to separate the desired product ***lf*-NiP8-TAP$_2$** (0.11 mg, 11%).

MALDI-TOF: *m*/*z* = 14719.70 ($C_{940}H_{1494}N_{32}Ni_8O_6Si_{32}$, $M^{+\cdot}$ requires 14707.52).

UV–vis–NIR ($CDCl_3$, 298 K) λ_{max} / nm: 414, 770, 1728.

D.2 Device Fabrication

Substrate fabrication

The substrate used for ***lf*-NiP8-TAP$_2$** devices was fabricated using the following procedure. On a degenerately *n*-doped silicon wafer with a layer (300 nm thick) of thermally-grown silicon dioxide (SiO$_2$), a local gate electrode (3 μm wide) was defined by optical lithography with lift-off resist and electron-beam (e-beam) evaporation of titanium (5 nm thick) and platinum (15 nm thick). A layer (10 nm) of hafnium dioxide (HfO$_2$) was then deposited using atomic layer deposition (ALD). Next, source and drain contact electrodes separated by a 7 μm gap (the centre of the gap was aligned to the centre of the gate electrode, which means a 2 μm of horizontal distance between each electrode and gate electrode) were also defined by optical

lithography with lift-off resist and electron-beam (e-beam) evaporation of titanium (5 nm thick) and platinum (45 nm thick).

Graphene nanogaps

A layer (600 nm) of poly(methyl methacrylate) (PMMA) (with a molecular weight of 495 kDa) was spin coated onto chemical vapor deposition (CVD)-grown graphene (purchased from Grolltex) on copper. The copper was then etched in aqueous ammonium persulfate ($(NH_4)_2S_2O_8$) solution (3.6 g in 60 mL water) for 4 h, after which the PMMA protected graphene was transferred 3 times to Milli-Q water and scooped up using the substrate. Air bubbles were further removed by partly submerging the sample in 2-propanol (IPA). The sample was dried overnight and baked at 180 °C for 1 h. The PMMA was then removed in hot acetone (50 °C) for 3 h.

The Z-shaped graphene tape with bowtie shaped structure was patterned by e-beam lithography (EBL) with bi-layer lift-off resist (PMMA495 and PMMA950) and thermal evaporation of aluminum (50 nm thick). The *Z*-shaped graphene pattern was used so the inner graphene leads are coplanar with the bowtie structure (see Figure 4.7 and 4.8), reducing tension on the bowtie-shaped graphene, and maximizing the stability of the junction. PMMA e-beam resist was used as it is positive resist and it can be transformed into smaller molecules after exposure, which make it much easier to be completely removed than negative photoresist. Aluminum was then deposited onto exposed area as oxygen plasma resist, as aluminum can be completely removed by either acidic or basic aqueous solutions. By this method we reduce contamination from residual photoresist on graphene. The flatter configuration and cleaner surface might provide stronger molecule-electrode coupling by better molecule-graphene interfacing. After lift-off, the graphene on unexposed areas (which are not covered by aluminum) was etched with oxygen plasma. The aluminum was subsequently removed by aqueous sodium hydroxide (NaOH) solution (0.5 M; 1.0 g in 50 mL water). The sample was finally immersed in hot acetone (50 °C) overnight to remove any residual PMMA. Example optical image and SEM images are shown in Figure 4.11.

Graphene nanogaps were prepared by feedback-controlled electroburning of the graphene bow-tie shape until the resistance of the tunnel junction exceeds 1.3 GΩ (10^{-7} G_0). The empty nanogaps were characterized by measuring a current map as a function of bias voltage (V_{sd}) and gate voltage (V_g) at room temperature in order to exclude devices containing residual

graphene quantum dots,[9] only clean devices were selected for further measurement. See Figure 4.12 for a typical feedback-controlled electroburning trace and a fit to the Simmons model.

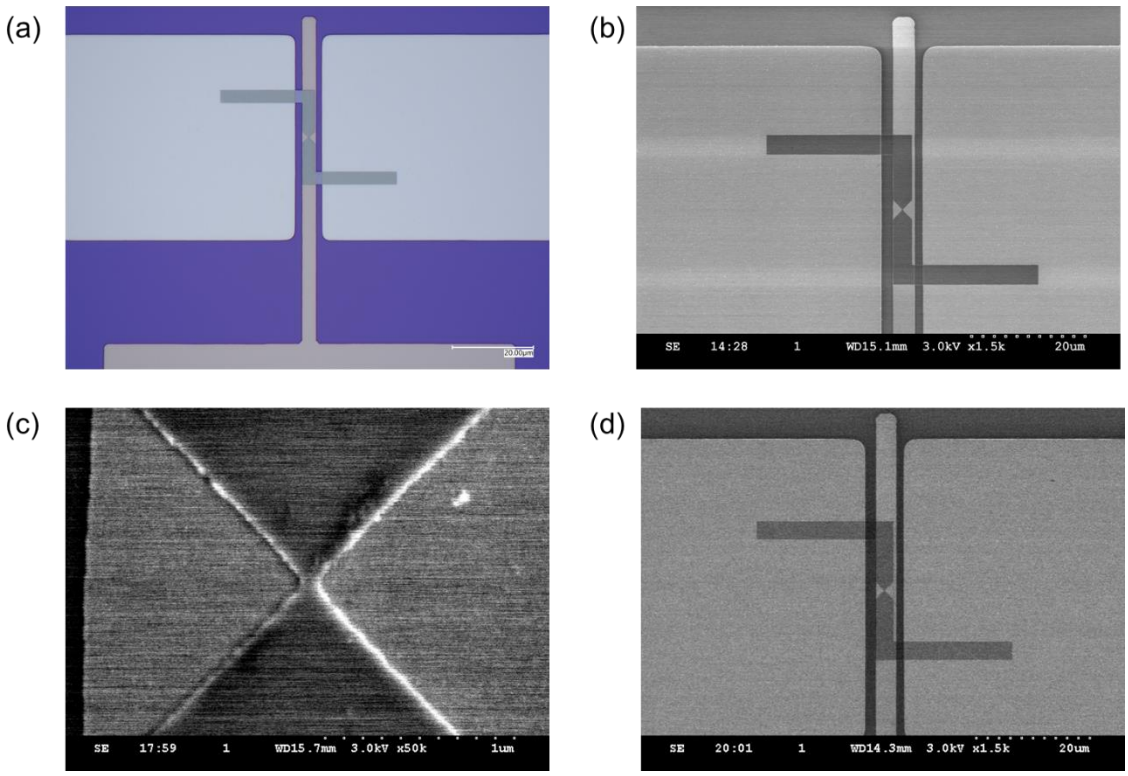

Figure D.1: (a) Example optical image of the Al protected device, fabrication described in the Methods section. The Z-shaped graphene tape with bow-tie center was protected by a 50 nm thick layer of aluminum. (b) Example SEM image of the aluminum-protected device. (c) Example SEM image of the aluminum protected device (zoom-in view of the bowtie-shaped structure). (d) Example SEM image of the device (the aluminum and residual PMMA have been removed). Data were collected and analyzed by Dr. Zhixin Chen and Dr. James O. Thomas.

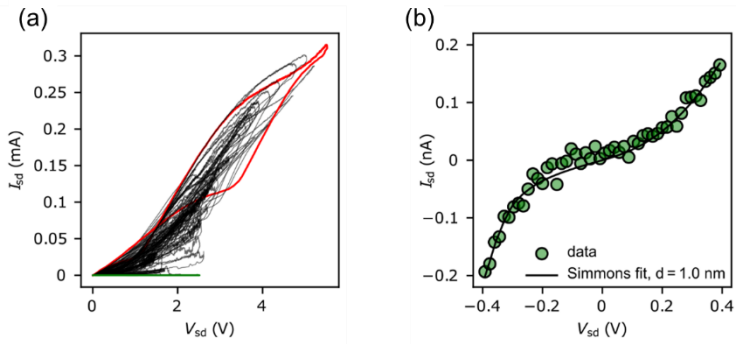

Figure D.2: Typical feedback-controlled electroburning traces to get a graphene nanogap. Data were collected and analyzed by Dr. Zhixin Chen and Dr. James O. Thomas.

D.3 Conductance Measurements

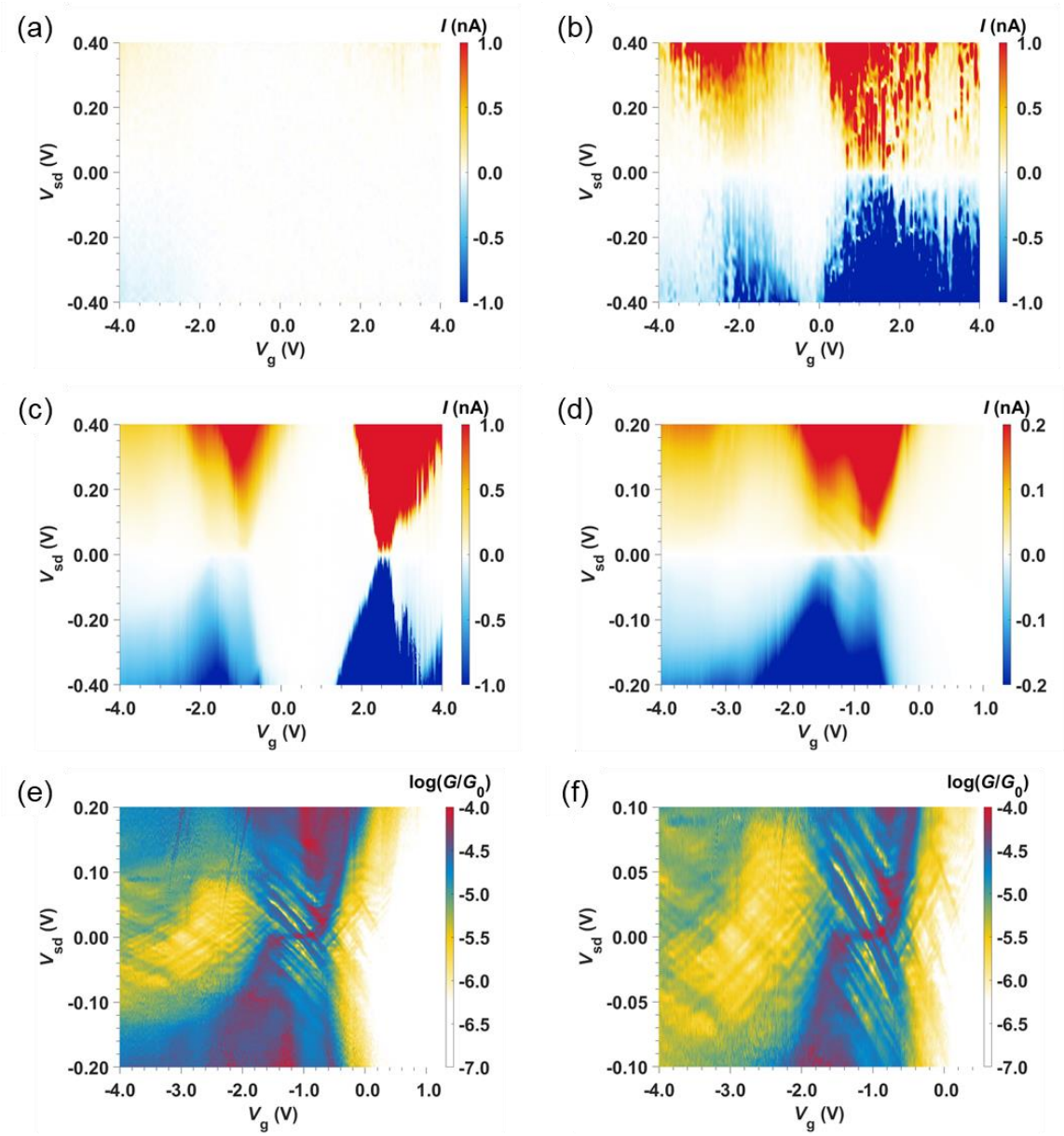

Figure D.3: (a) and (b) Current map as a function of bias voltage (V_{sd}) and gate voltage (V_g) before (a) and after (b) molecule deposition for ***lf*-NiP8-TAP$_2$** measured at room temperature. Full-range (c) and detailed (d) current map as a function of bias voltage (V_{sd}) and gate voltage (V_g) for ***lf*-NiP8-TAP$_2$** single-molecule junction measured at 4.2 K. (e) and (f) Detailed differential conductance map as a function of bias voltage (V_{sd}) and gate voltage (V_g) for ***lf*-NiP8-TAP$_2$** single-molecule junction measured at 4.2 K. Data were collected and analyzed by Dr. Zhixin Chen and Dr. James O. Thomas.

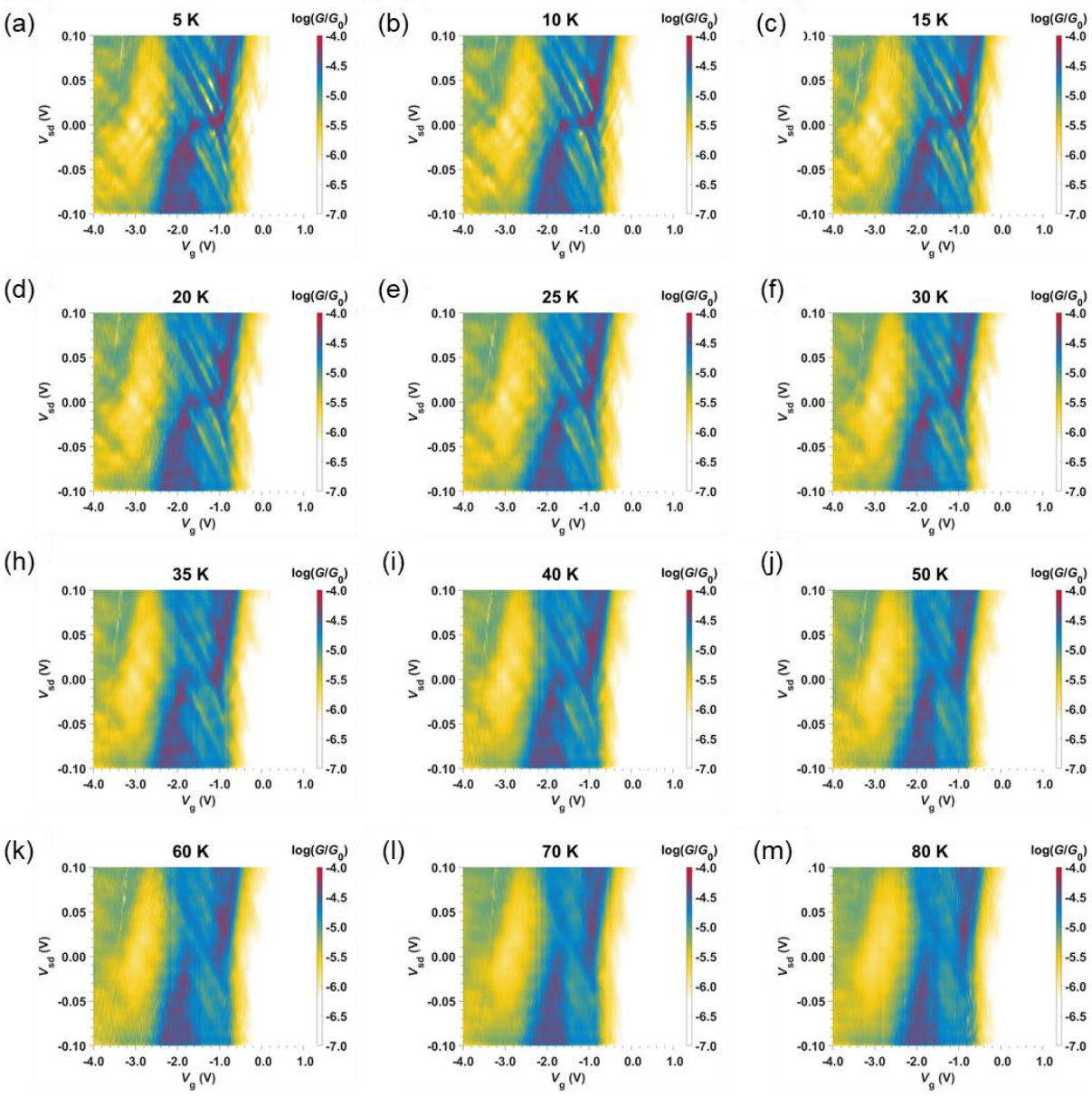

Figure D.4: Differential conductance map as a function of bias voltage (V_{sd}) and gate voltage (V_g) for ***lf*-NiP8-TAP$_2$** single-molecule junction measured at different temperature. Data were collected and analyzed by Dr. Zhixin Chen and Dr. James O. Thomas.

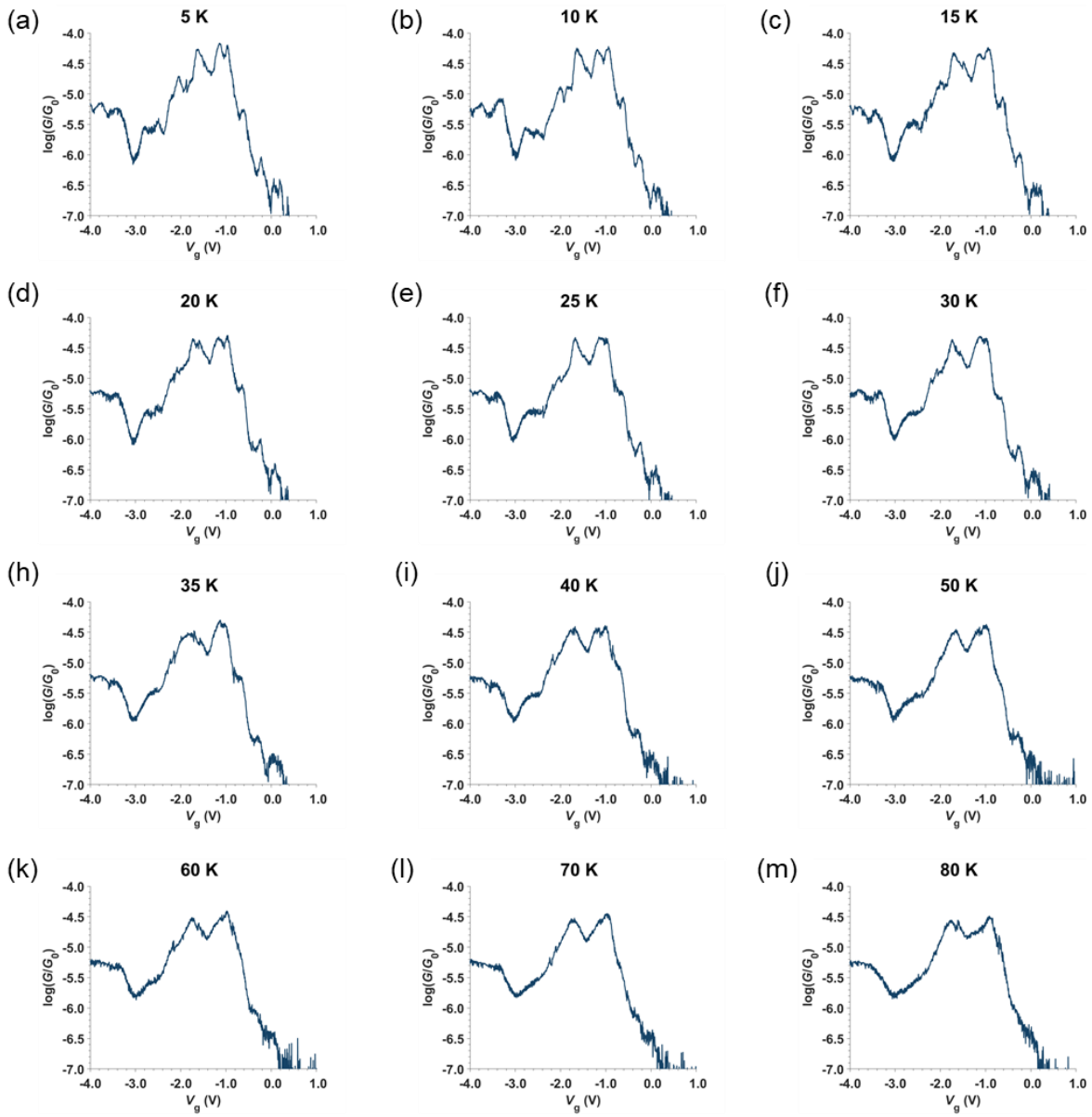

Figure D.5: Differential conductance as a function of gate voltage (V_g) at V_{sd} = 0 V for ***lf*-NiP8-TAP2** single-molecule junction measured at different temperatures. Data were collected and analyzed by Dr. Zhixin Chen and Dr. James O. Thomas.

D.4 Data Analysis

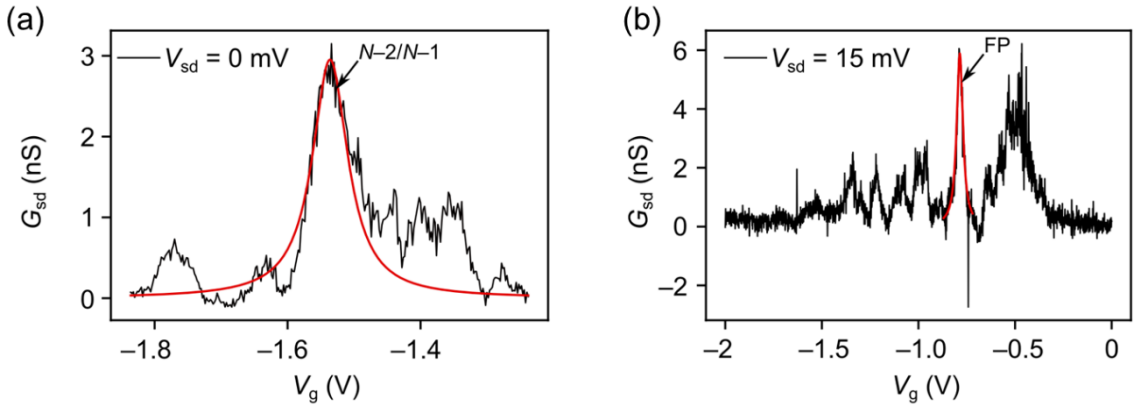

Figure D.6: Fitting Coulomb (a) and FP peaks (b) to Lorentzians with FWHMs of 14.1±0.8 meV (Γ), and 2.1±0.1 meV (Γ_{FP}), respectively (after scaling by their gate coupling). Data were collected and analyzed by Dr. Zhixin Chen and Dr. James O. Thomas.

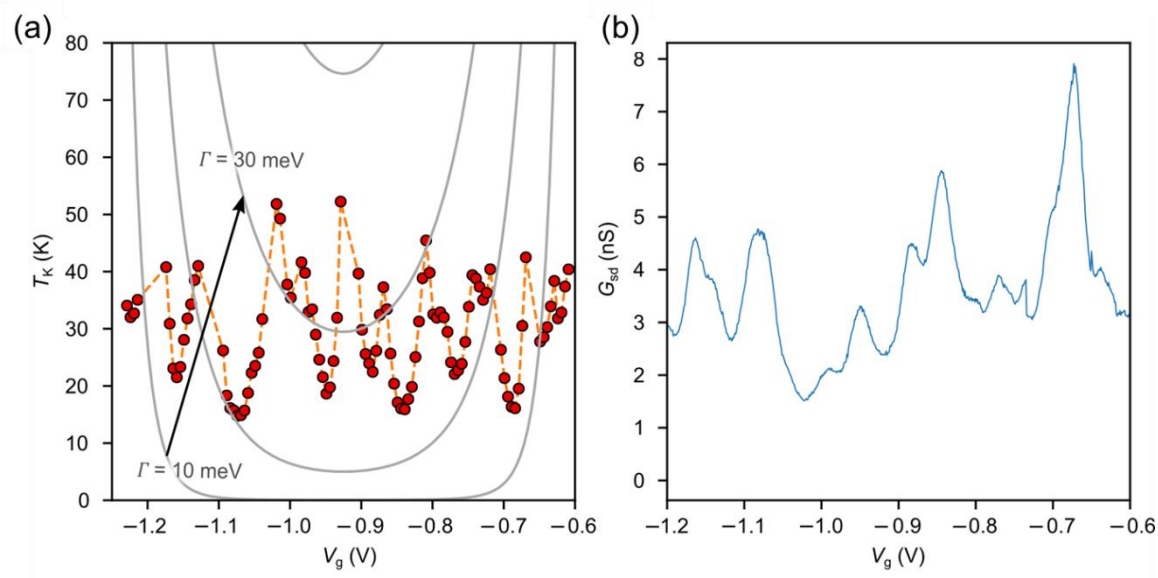

Figure D.7: (a) Kondo temperatures (T_K) extracted from FWHM of G–V_{sd} measurements across N–1 charge state. Grey lines indicate T_K from calculated from the Haldane relation $k_B T_K = \frac{\sqrt{\Gamma U}}{2} e^{-\pi\varepsilon_0(-\varepsilon_0+U)/\Gamma U}$ for different values of Γ, and U = 0.12 eV (the addition energy of the N–1). The gate trace is given in (b) showing the oscillation in conductance due to the coexistence of Kondo and FP channels. Data were collected and analyzed by Dr. Zhixin Chen and Dr. James O. Thomas.

D.5 Magnetic Field Dependence

Further evidence of phase-coherent transmission through the ***lf*-NiP8-TAP$_2$**-graphene device comes from studying the evolution of the conductance with magnetic field strength (Figure 4.18). With increasing field strength applied perpendicular to the graphene plane (Figure 4.18a), there is a slight broadening and reduction in height of the zero-bias peak. However, we do not observe splitting of the Zeeman splitting of the peak, because for a spin-1/2 Kondo resonance this occurs above a critical field, $B_C = 0.5k_BT_K$,[383] which is 6.5 T for our device.

The electrons pick up a field-dependent Aharanov-Bohn phase while traversing the cavity, leading to Fabry-Pérot resonance conditions that depend on field. Due to the multimodal nature of the cavity and its geometry, there is no single periodic evolution of the energy and intensity of the Fabry-Pérot resonances with field. However, we do observe magnetoconductance oscillations, shown in Figure 4.19c, most notably with period of $\Delta B = 0.5$ T. We attribute these oscillations to conductance fluctuations that result from scattering around closed paths within the electroburnt graphene channel.[384,385] The areas enclosed within these paths can be calculated: $A = 2\pi\phi_0/\Delta B$, where $\phi_0 = h/e$. For $\Delta B = 0.5$ T this gives a phase-coherence length at this temperature of $l_\phi = 450$ nm in line with previous reports.[284] The length is approximately half the Fabry-Pérot cavity, indicating that the dominant oscillations are due to coherent transmission pathways around one of the graphene leads. In contrast with the above behavior, a field applied parallel to the graphene plane has no effect on the G–V_{sd} characteristics up to 3 T, which supports our assertion that the chequerboard pattern is dominated by quantum interference within the graphene.

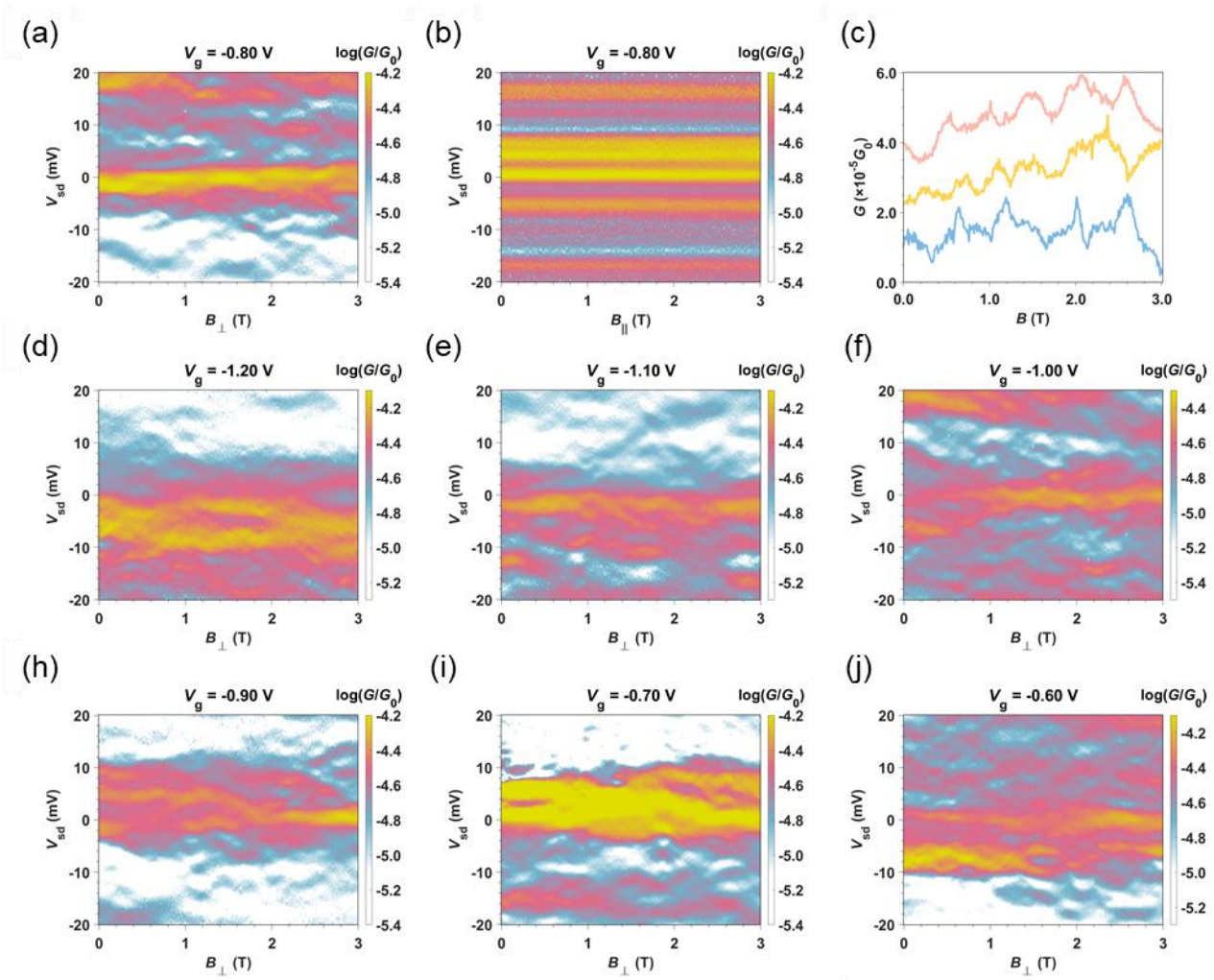

Figure D.8: (a) and (b) Differential conductance map measured as a function of bias voltage (V_{sd}) and magnetic field (B) measured at V_g = –0.80 V. The applied magnetic field is perpendicular (⊥, for (a)) and parallel (∥, for (b)) to transport plane (graphene), respectively. The interference pattern changes significantly as increasing perpendicular magnetic field, but unchanged in parallel magnetic field. (c) Weak magnetoconductance oscillations at V_{sd} = –5 mV (blue), 1 mV (yellow) and 9 mV (red) with a period of ~ 0.5 T (adjacent traces are offset for clarity), the origins of which are discussed in the Supplementary Information. (d)–(i) Differential conductance map measured at different V_g under perpendicular (⊥) magnetic field. The oscillations on interference patterns are significant. Under parallel magnetic no obvious change was observed at all V_g, which are similar with that shown in (b). Data were collected and analyzed by Dr. Zhixin Chen and Dr. James O. Thomas.

D.6 Theoretical Calculations

Geometrical optimizations were carried out using the DFT code SIESTA,[298] with a local density approximation LDA functional, a double-ζ polarized basis, a cut-off energy of 200 Ry and a 0.04 eV/Å force tolerance. From the Hamiltonian and overlap matrices of the DFT calculation of the junction, Gollum[299] calculates the transmission coefficient $T_{nm}(E)$ between scattering channels n, m in the electrodes, from which the transmission coefficient $T_{nm}(E) = \Sigma_{nm}T_{nm}(E)$ is obtained. As discussed in ref. 222, this is equivalent to the expression:

$$T(E) = 4Tr(\Gamma_1 G \Gamma_2 G^{\dagger}) \tag{D.1}$$

Where G is the (retarded) Green's function of the junction and Γ_i is the imaginary part of the self energy of electrode i. The electrical conductance is obtained from

$$G = G_0 \int_{-\infty}^{+\infty} T(E) \left(-\frac{\partial}{\partial E} f(E)\right) dE \tag{D.2}$$

where E_F is the Fermi energy of the device, f(E) is the Fermi distribution function and G_0 is the conductance quantum. At low enough temperatures, this is approximated by $G = G_0T(E_F)$. In the presence of Cl atoms, spin polarized calculations were carried out to obtain the transmission coefficients $T^{\uparrow}$, $T^{\downarrow}$ for the two different spins, from which the total transmission coefficient $T = (T^{\uparrow} + T^{\downarrow})/2$ is obtained.

Figure 4.19 shows the relaxed geometry used to compute the transmission coefficient of single octamer junctions with graphene electrodes (i.e., left and right graphene leads). The octamer is not quite planar, but instead assumes an undulating conformation.

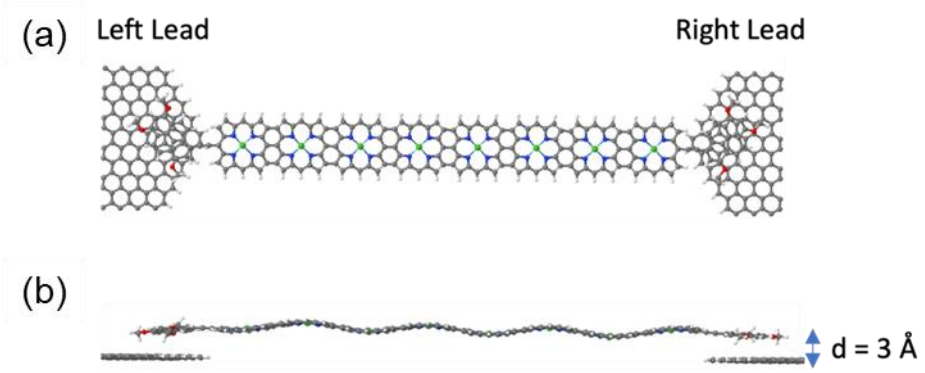

Figure D.9: The top view (a) and side view (b) of the graphene junction used to calculate the transmission coefficients in Figure 4.11f. The distance between the anchors (two pyrene) and graphene is set to 3 Å. Data were collected and analyzed by Prof. Colin J. Lambert et al.

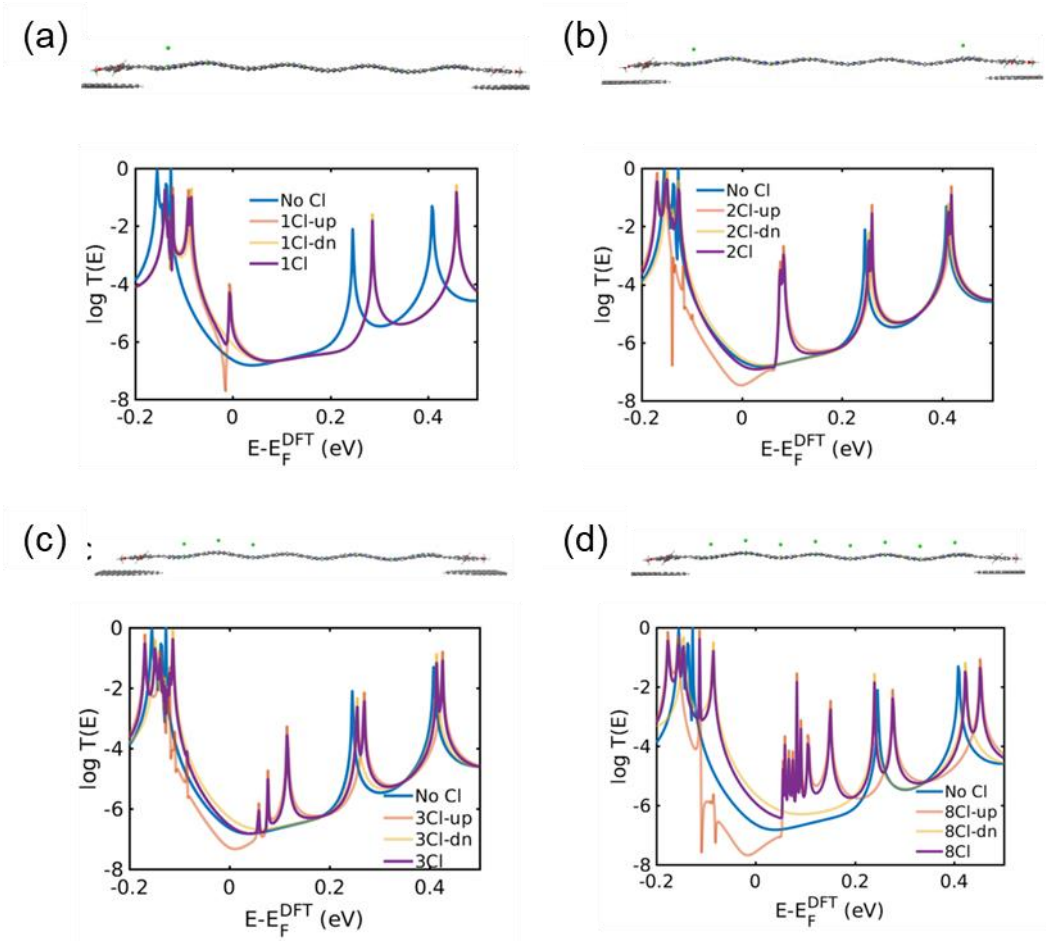

Figure D.10: Transmission against energy for 0, 1, 2, 3 and 8 Cl atoms. In one of the two spin-polarized transmission functions, there are one, two, three and eight extra peaks appearing when one, two, three and eight Cl atoms are present. Data were collected and analyzed by Prof. Colin J. Lambert et al.

As well as mimicking the effect of an electrostatic gate, by oxidizing the octamer, it is interesting to note that the Cl atoms produce additional transport resonances, which are not relevant to our current experiments, (which utilize an electrostatic gate, remote from the junction), but would be relevant in an experiment in which electrochemical gating is employed. To demonstrate this feature, Figure 4.20 shows a comparison between the transmission coefficient of the neutral molecule (blue curve) and the transmission coefficients in the presence of 1, 2, 3 and 8 Cl atoms (purple curves in Figure 4.20a–d, respectively). Also shown are the transmission coefficients $T^{\uparrow}$, $T^{\downarrow}$ for the two different spins. All quantities are plotted against $E - E_{\mathrm{F,DFT}}$, where $E_{\mathrm{F,DFT}}$ is the Fermi energy predicted by density functional theory. Figure 4.20a shows that compared with the neutral case, in the presence of one Cl atom, a new resonance appears near $E - E_{\mathrm{F,DFT}} = 0$ eV whereas in the presence of two Cl atoms, two almost-degenerate resonances appear near $E - E_{\mathrm{F,DFT}} = 0.08$eV. In the presence of three Cl atoms, three

new resonances occur in the range 0.05 to 0.11 eV, while Figure 4.20d shows that the presence of eight Cls leads to eight overlapping resonances in the interval 0.05 to 0.15 eV. As shown in Figure 4.21, these new resonances have a Fano-like characteristic and are associated with the presence of localized states on the Cl atoms.

Table D.1: The Voronoi charge on Cl and octamer, positive value indicates lose electron while negative one indicates gain electron.

Charge(e^-)	1Cl	2Cl	3Cl	8Cl
Octamer	0.26	0.64	0.94	2.46
Cl	-0.33	-0.69	-0.98	-2.54

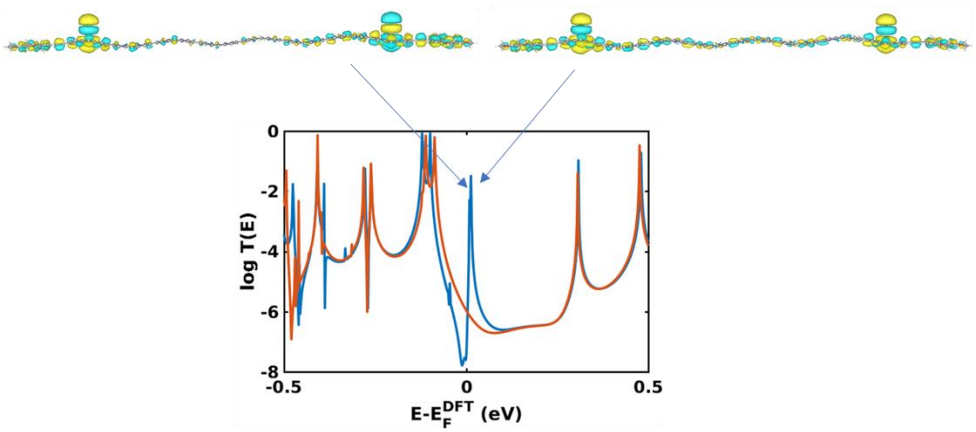

Figure D.11: In the case of 2 Cl atoms, the two new resonances are associated with the two Cl atoms. The corresponding two frontier orbitals of gas phase octamer with two Cl atoms are indicated by the two blue arrows. Data were collected and analyzed by Prof. Colin J. Lambert et al.

Appendix E — Experimental Procedures and Supplementary Details for Chapter 5

E.1 General Methods

All reagents were purchased as reagent grade and used without further purification. Solvents for column chromatography were used in HPLC grade. Dry toluene and diisopropylamine (*i*-Pr_2NH) were obtained from the solvent drying system MBraun MBSPS-5-BenchTop under nitrogen atmosphere (H_2O content < 20 ppm as determined by Karl-Fischer titration). Flash column chromatography was carried out using SiO_2 (60 Å, 230–400 mesh) under positive pressure. Analytical thin-layer chromatography was carried out on aluminum-backed silica gel 60 F254 plate. Evaporation in vacuum was performed at 25–80 ºC and 10–900 mbar. Size exclusion chromatography (SEC) was carried out using Bio-Rad Bio-Beads S-X1 (40–80 μm bead size). Reported yields refer to spectroscopically and chromatographically pure compounds that were dried under high vacuum (0.01–0.005 mbar) before analytical characterization.

NMR spectra were recorded at 298 K using a Bruker AVIII HD 400, a Bruker AVIII HD 500, a Bruker NEO 600 with a broadband helium cryoprobe, or a Bruker AVIII 700 with an inverse TCI $^{1}H/^{13}C/^{15}N$ cryoprobe. ^{1}H NMR spectrum is reported in ppm; coupling constants are given in Hertz, to the nearest 0.1 Hz. The solvent used was $CDCl_3$ which was calibrated to residual $CHCl_3$ at 7.26 ppm. Multiplicity (s = singlet, d = doublet, t = triplet, q = quartet, m = multiplet) and coupling constants were reported whenever possible. ^{1}H NMR signals were assigned based on comparison between compounds, chemical shifts, integrals and coupling constants.

MALDI-ToF spectra were measured using a Bruker MALDI Autoflex Speed spectrometer. *Trans*-2-[3-(4-*tert*-butylphenyl)-2-methyl-2-propenylidene]-malononitrile (DCTB) was employed as matrix.

UV–vis–NIR absorbance measurement was recorded with a Perkin-Elmer Lambda 20 spectrophotometer or a Jasco V770 spectrophotometer using an Infrasil® Quartz 1 cm cuvette. Measurements were carried out at 298 K under ambient conditions.

E.2 Syntheses of *ls*-ZnP*N*-TIPS$_2$

E.2.1 Synthesis of ZnP1-TIPS$_2$

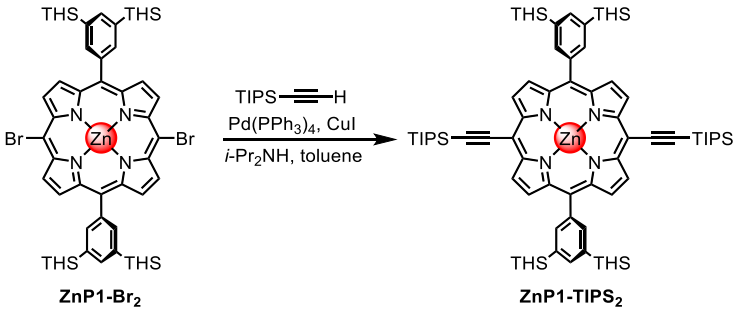

A mixture of **ZnP1-Br$_2$** (50 mg, 28 µmol, 1.0 equiv.), Pd(PPh$_3$)$_4$ (6.4 mg, 5.5 µmol, 20 mol%), CuI (1.0 mg, 5.5 µmol, 20 mol%) in dry toluene (2.0 mL) and *i*-Pr$_2$NH (2.0 mL) was degassed by three freeze-pump-thaw cycles. After that, (triisopropylsilyl)acetylene (TIPS-acetylene, 62 µL, 0.28 mmol, 10 equiv.) was added to the mixture and the reaction was conducted at 50 °C under argon for 2 h. After reaction, the resulting mixture was concentrated and purified by flash column chromatography (SiO_2) using pentane/CH_2Cl_2 (19:1) as eluent to give the desired product **ZnP1-TIPS$_2$** (53 mg, 95%).

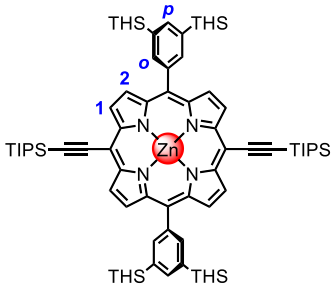

^{1}H NMR (600 MHz, $CDCl_3$, 298 K): δ 9.75 (d, *J* = 4.5 Hz, 4H, **H$_1$**), 8.90 (d, *J* = 4.5 Hz, 4H, **H$_2$**), 8.23 (s, 4H, **H$_o$**), 7.99 (s, 2H, **H$_p$**), 1.53 – 0.70 (m, 198H, **H$_{TIPS,THS}$**).

MALDI-ToF: *m*/*z* = 2015.531 ($C_{126}H_{212}N_4Si_6Zn$, $M^{+\cdot}$ requires 2015.464).

UV–vis–NIR ($CDCl_3$, 298 K) λ_{max} / nm (ε / µM^{-1} cm^{-1}): 436 (0.53), 445 (0.35), 576 (0.02).

E.2.2 Synthesis of *ls*-ZnP2-TIPS$_2$

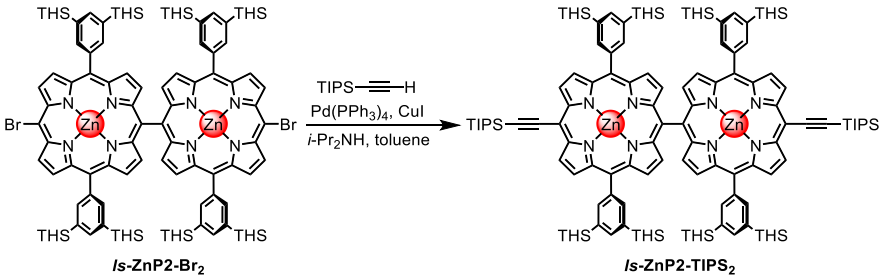

A mixture of ***ls*-ZnP2-Br$_2$** (50 mg, 14 µmol, 1.0 equiv.), Pd(PPh$_3$)$_4$ (3.3 mg, 2.9 µmol, 20 mol%), CuI (0.55 mg, 2.9 µmol, 20 mol%) in dry toluene (1.0 mL) and *i*-Pr$_2$NH (1.0 mL) was degassed by three freeze-pump-thaw cycles. After that, (triisopropylsilyl)acetylene (TIPS-acetylene, 8.1 µL, 36 µmol, 2.5 equiv.) was added to the mixture and the reaction was conducted at 50 °C under argon for 2 h. After reaction, the resulting mixture was concentrated and purified by flash column chromatography (SiO_2) using pentane/CH_2Cl_2 (19:1) as eluent to give the desired product ***ls*-ZnP2-TIPS$_2$** (38 mg, 72%).

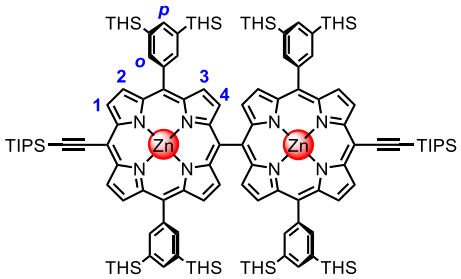

^{1}H NMR (500 MHz, $CDCl_3$, 298 K): δ 9.90 (d, *J* = 4.6 Hz, 4H, **H$_1$**), 9.01 (d, *J* = 4.7 Hz, 4H, **H$_2$**), 8.58 (d, *J* = 4.7 Hz, 4H, **H$_3$**), 8.26 (d, *J* = 1.2 Hz, 8H, **H$_o$**), 8.06 (d, *J* = 4.7 Hz, 4H, **H$_4$**), 7.89 (t, *J* = 1.2 Hz, 4H, **H$_p$**), 1.60 – 0.58 (m, 354H, **H$_{TIPS,THS}$**).

MALDI-ToF: *m*/*z* = 3670.714 ($C_{230}H_{382}N_8Si_{10}Zn_2$, $M^{+\cdot}$ requires 3670.645).

UV–vis–NIR ($CDCl_3$, 298 K) λ_{max} / nm (ε / µM^{-1} cm^{-1}): 430 (0.23), 464 (0.27), 569 (0.05), 615 (0.03).

E.2.3 Synthesis of *ls*-ZnP3-TIPS$_2$

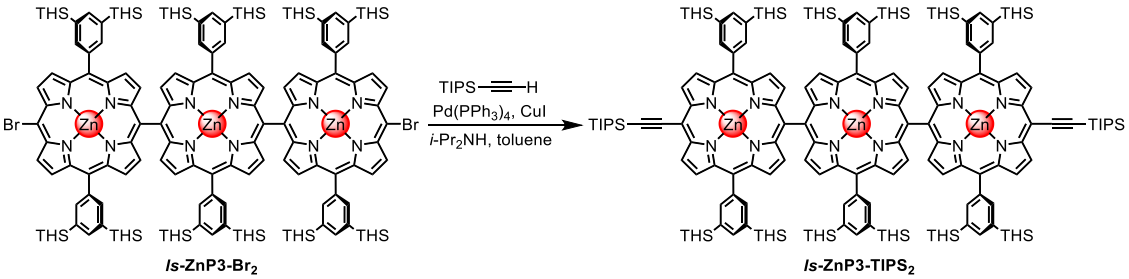

A mixture of ***ls*-ZnP3-Br$_2$** (10 mg, 2.0 µmol, 1.0 equiv.), $Pd(PPh_3)_4$ (0.90 mg, 0.78 µmol, 40 mol%), CuI (0.15 mg, 0.78 µmol, 40 mol%) in dry toluene (1.0 mL) and *i*-Pr_2NH (1.0 mL) was degassed by three freeze-pump-thaw cycles. After that, TIPS-acetylene (4.4 µL, 20 µmol, 10 equiv.) was added to the mixture and the reaction was conducted at 50 °C under argon for 2 h. After reaction, the resulting mixture was concentrated and purified by flash column chromatography (SiO_2) using pentane/CH_2Cl_2 (19:1) as eluent to give the desired product ***ls*-ZnP3-TIPS$_2$** (10 mg, 98%).

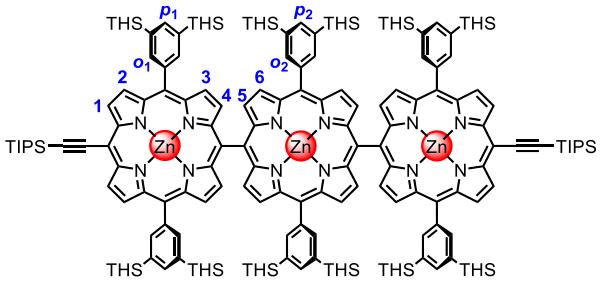

^{1}H NMR (600 MHz, $CDCl_3$, 298 K): δ 9.91 (d, *J* = 4.5 Hz, 4H, **H$_1$**), 9.01 (d, *J* = 4.5 Hz, 4H, **H$_2$**), 8.66 (d, *J* = 4.8 Hz, 4H, **H$_6$**), 8.64 (d, *J* = 4.5 Hz, 4H, **H$_3$**), 8.29 (s, 8H, **H$_{o1}$**), 8.26 (s, 4H, **H$_{o2}$**), 8.18 (d, *J* = 4.8 Hz, 4H, **H$_5$**), 8.16 (d, *J* = 4.5 Hz, 4H, **H$_3$**), 7.91 (s, 4H, **H$_{p1}$**), 7.77 (s, 2H, **H$_{p2}$**), 1.57 – 0.33 (m, 510H, **H$_{TIPS,THS}$**).

MALDI-ToF: *m*/*z* = 5323.781 ($C_{334}H_{552}N_{12}Si_{14}Zn_3$, $M^{+\cdot}$ requires 5324.826).

UV–vis–NIR ($CDCl_3$, 298 K) λ_{max} / nm (ε / μM^{-1} cm^{-1}): 430 (0.34), 479 (0.39), 572 (0.11), 615 (0.04).

E.2.4 Synthesis of *ls*-ZnP4-TIPS$_2$

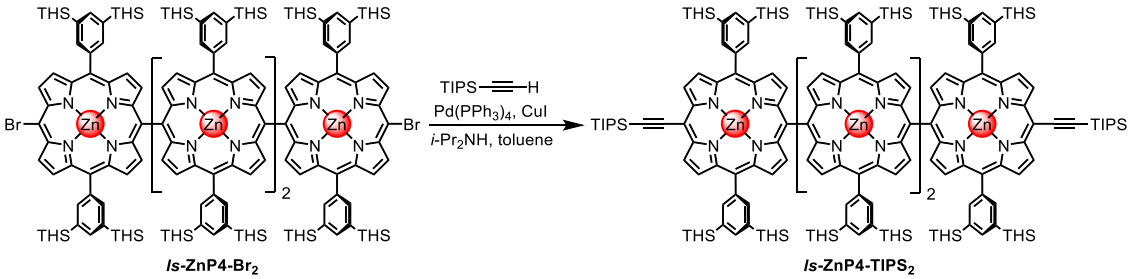

A mixture of ***ls*-ZnP4-Br$_2$** (22 mg, 3.3 µmol, 1.0 equiv.), $Pd(PPh_3)_4$ (1.5 mg, 1.3 µmol, 40 mol%), CuI (0.25 mg, 1.3 µmol, 40 mol%) in dry toluene (2.0 mL) and *i*-Pr_2NH (2.0 mL) was degassed by three freeze-pump-thaw cycles. After that, TIPS-acetylene (7.3 µL, 33 µmol, 10 equiv.) was added to the mixture and the reaction was conducted at 50 °C under argon for 2 h. After reaction, the resulting mixture was concentrated and purified by flash column chromatography (SiO_2) using pentane/CH_2Cl_2 (19:1) as eluent to give the desired product ***ls*-ZnP4-TIPS$_2$** (22 mg, 96%).

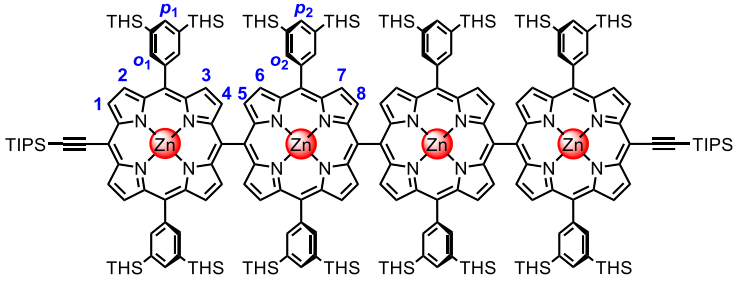

^{1}H NMR (600 MHz, $CDCl_3$, 298 K): δ 9.92 (d, *J* = 4.6 Hz, 4H, **H$_1$**), 9.02 (d, *J* = 4.6 Hz, 4H, **H$_2$**), 8.74 (d, *J* = 4.6 Hz, 4H, **H$_7$**), 8.68 (d, *J* = 4.7 Hz, 4H, **H$_6$**), 8.66 (d, *J* = 4.6 Hz, 4H, **H$_3$**), 8.30 (d, *J* = 6.7 Hz, 20H, **H$_{8,o1,o2}$**), 8.23 – 8.14 (m, 8H, **H$_{4,5}$**), 7.92 (s, 4H, **H$_{p1}$**), 7.80 (s, 4H, **H$_{p2}$**), 1.51 – 0.30 (m, 666H, **H$_{TIPS,THS}$**).

MALDI-ToF: *m*/*z* = 6967.002 ($C_{438}H_{710}N_{16}Si_{18}Zn_4$, $M^{+\cdot}$ requires 6966.913).

UV–vis–NIR ($CDCl_3$, 298 K) λ_{max} / nm (ε / μM^{-1} cm^{-1}): 429 (0.41), 487 (0.49), 573 (0.18), 593 (0.07), 614 (0.05).

E.2.5 Synthesis of *ls*-ZnP6-TIPS$_2$

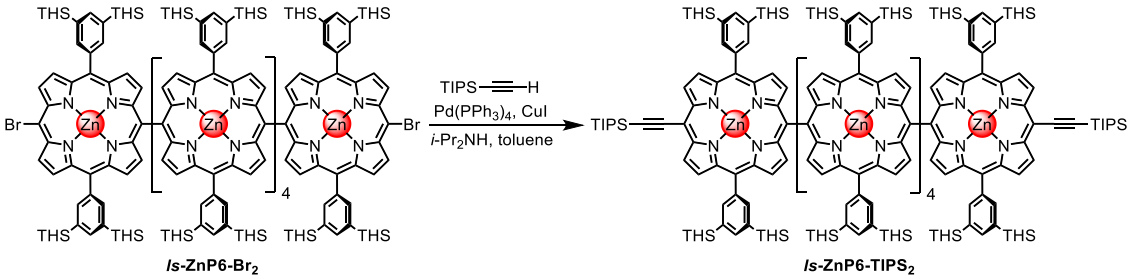

A mixture of ***ls*-ZnP6-Br$_2$** (7.0 mg, 0.69 µmol, 1.0 equiv.), $Pd(PPh_3)_4$ (0.32 mg, 0.28 µmol, 40 mol%), CuI (0.06 mg, 0.28 µmol, 40 mol%) in dry toluene (1.0 mL) and *i*-Pr_2NH (1.0 mL) was degassed by three freeze-pump-thaw cycles. After that, TIPS-acetylene (3.1 µL, 14 µmol, 20 equiv.) was added to the mixture and the reaction was conducted at 50 °C under argon for 2 h. After reaction, the resulting mixture was concentrated and purified by flash column chromatography (SiO_2) using pentane/CH_2Cl_2 (19:1) as eluent to give the desired product ***ls*-ZnP6-TIPS$_2$** (6.9 mg, 96%).

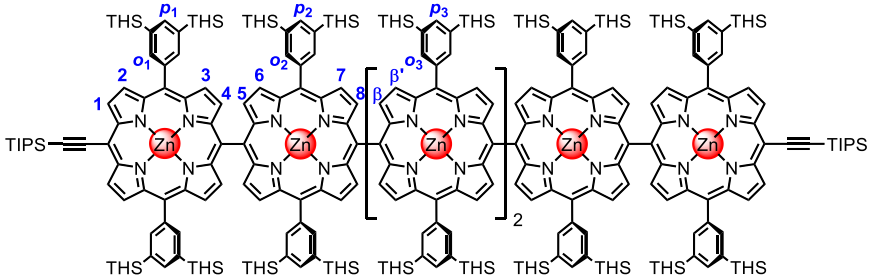

^{1}H NMR (600 MHz, $CDCl_3$, 298 K): δ 9.92 (d, *J* = 4.6 Hz, 4H, **H$_1$**), 9.02 (d, *J* = 4.5 Hz, 4H, **H$_2$**), 8.79 – 8.72 (m, 12H, **H$_{7,\beta'}$**), 8.69 (d, *J* = 4.6 Hz, 4H, **H$_6$**), 8.66 (d, *J* = 4.6 Hz, 4H, **H$_3$**), 8.36 – 8.27 (m, 36H, **H$_{8,\beta,o1,o2,o3}$**), 8.23 – 8.17 (m, 8H, **H$_{4,5}$**), 7.92 (s, 4H, **H$_{p1}$**), 7.83 (s, 4H, **H$_{p3}$**), 7.80 (s, 4H, **H$_{p2}$**), 1.51 – 0.37 (m, 978H, **H$_{TIPS,THS}$**).

MALDI-ToF: *m*/*z* = 10286.473 ($C_{646}H_{1062}N_{24}Si_{26}Zn_6$, $M^{+\cdot}$ requires 10287.369).

UV–vis–NIR ($CDCl_3$, 298 K) λ_{max} / nm (ε / μM^{-1} cm^{-1}): 424 (0.52), 493 (0.59), 575 (0.31).

E.2.6 Synthesis of *ls*-ZnP10-TIPS$_2$

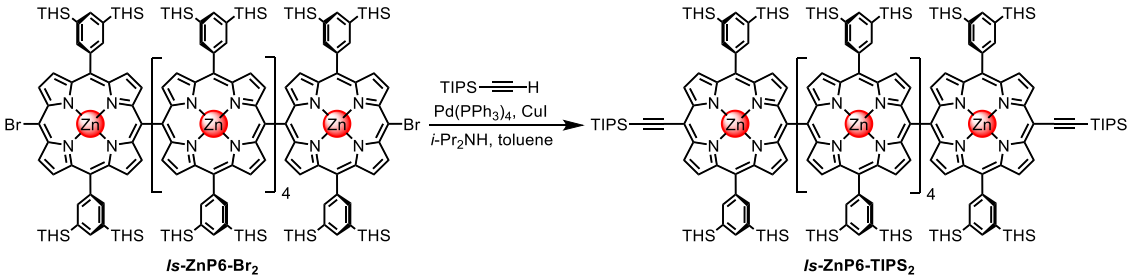

A mixture of ***ls*-ZnP10-Br$_2$** (10 mg, 0.60 µmol, 1.0 equiv.), $Pd(PPh_3)_4$ (1.4 mg, 1.2 µmol, 2.0 equiv.), CuI (0.22 mg, 1.2 µmol, 2.0 equiv.) in dry toluene (1.0 mL) and *i*-Pr_2NH (1.0 mL) was degassed by three freeze-pump-thaw cycles. After that, TIPS-acetylene (2.7 µL, 12 µmol, 20 equiv.) was added to the mixture and the reaction was conducted at 50 °C under argon for 2 h. After reaction, the resulting mixture was concentrated and purified by flash column chromatography (SiO_2) using pentane/CH_2Cl_2 (9:1) as eluent to give the desired product ***ls*-ZnP10-TIPS$_2$** (7.4 mg, 73%).

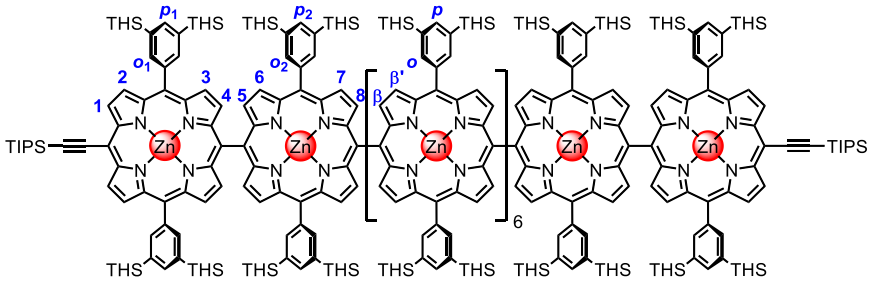

^{1}H NMR (600 MHz, $CDCl_3$, 298 K): δ 9.92 (d, *J* = 4.4 Hz, 4H, **H$_1$**), 9.02 (d, *J* = 4.5 Hz, 4H, **H$_2$**), 8.82 – 8.74 (m, 28H, **H$_{7,\beta'}$**), 8.70 (d, *J* = 4.7 Hz, 4H, **H$_6$**), 8.66 (d, *J* = 4.6 Hz, 4H, **H$_3$**), 8.42 – 8.27 (m, 72H, **H$_{8,\beta,o1,o2,o}$**), 8.21 (d, *J* = 4.7 Hz, 8H, **H$_{4,5}$**), 7.92 (s, 4H, **H$_{p1}$**), 7.86 – 7.82 (m, 12H, **H$_p$**), 7.81 (s, 4H, **H$_{p2}$**), 1.52 – 0.36 (m, 1602H, **H$_{TIPS,THS}$**).

MALDI-ToF: *m*/*z* = 16915.012 ($C_{1062}H_{1742}N_{40}Si_{42}Zn_{10}$, $M^{+\cdot}$ requires 16905.093).

UV–vis–NIR ($CDCl_3$, 298 K) λ_{max} / nm (ε / μM^{-1} cm^{-1}): 412 (0.72), 499 (0.82), 577 (0.52).

E.3 Syntheses of *lf*-ZnP*N*-TIPS$_2$

E.3.1 Synthesis of *lf*-ZnP2-TIPS$_2$

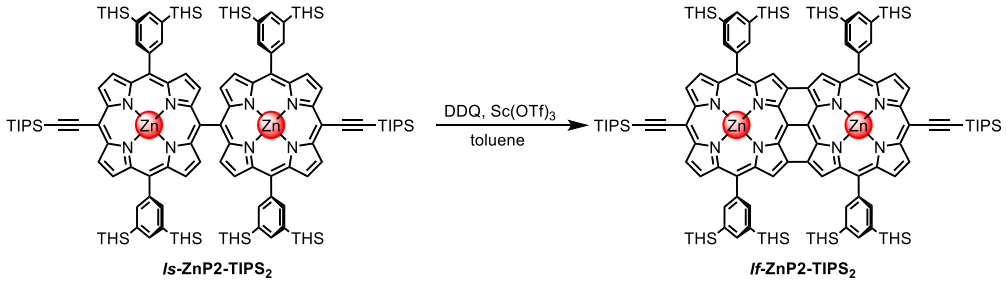

A mixture of ***ls*-ZnP2-TIPS$_2$** (35 mg, 9.5 µmol, 1.0 equiv.), 2,3-dichloro-5,6-dicyano-*p*-benzoquinone (DDQ, 8.7 mg, 38 µmol, 4.0 equiv.), Sc(OTf)$_3$ (24 mg, 50 µmol, 5.2 equiv.) in dry toluene (5.0 mL) was evacuated and refilled with argon five times. After that, the reaction was conducted at 80 °C under argon for 2 h. After completion, the reaction was quenched by addition of triethylamine (Et_3N, 1.0 mL). The resulting mixture was concentrated and purified by flash column chromatography (SiO_2) using pentane/CH_2Cl_2 (19:1) as eluent to give the desired product ***lf*-ZnP2-TIPS$_2$** (34 mg, 97%).

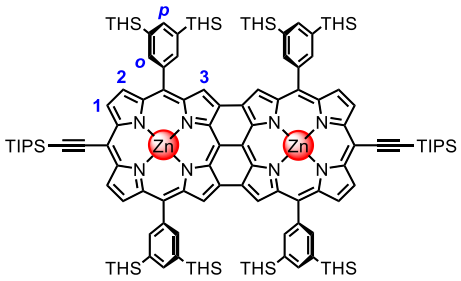

^{1}H NMR (600 MHz, $CDCl_3$, 298 K): δ 8.48 (d, *J* = 4.5 Hz, 4H, **H$_1$**), 7.81 (s, 4H, **H$_p$**), 7.80 (s, 8H, **H$_o$**), 7.46 (d, *J* = 4.5 Hz, 4H, **H$_2$**), 7.08 (s, 4H, **H$_3$**), 1.45 – 0.64 (m, 354H, **H$_{TIPS,THS}$**).

MALDI-ToF: *m*/*z* = 3670.714 ($C_{230}H_{382}N_8Si_{10}Zn_2$, $M^{+\cdot}$ requires 3670.645).

UV–vis–NIR ($CDCl_3$, 298 K) λ_{max} / nm (ε / μM^{-1} cm^{-1}): 434 (0.14), 578 (0.16), 956 (0.03), 1080 (0.05).

E.3.2 Synthesis of *lf*-ZnP3-TIPS$_2$

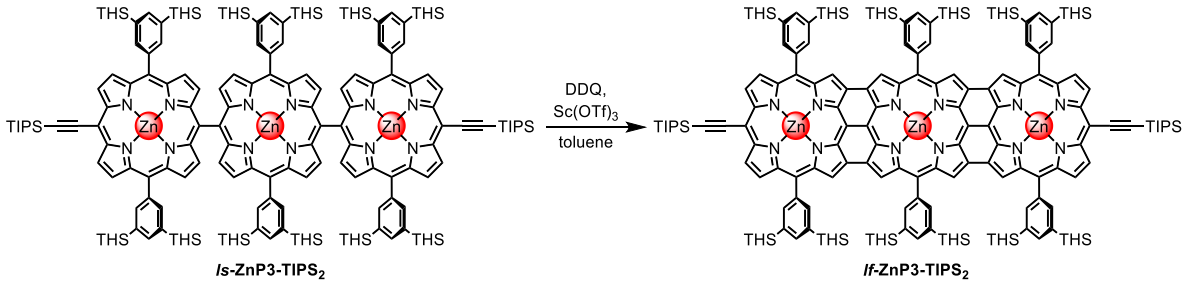

A mixture of ***ls*-ZnP3-TIPS$_2$** (20 mg, 3.8 µmol, 1.0 equiv.), DDQ (6.8 mg, 30 µmol, 8.0 equiv.), Sc(OTf)$_3$ (19 mg, 39 µmol, 10 equiv.) in dry toluene (5.0 mL) was evacuated and refilled with argon five times. After that, the reaction was conducted at 80 °C under argon for 2 h. After completion, the reaction was quenched by addition of Et_3N (1.0 mL). The resulting mixture was concentrated and purified by flash column chromatography (SiO_2) using pentane/CH_2Cl_2 (19:1) as eluent to give the desired product ***lf*-ZnP3-TIPS$_2$** (19 mg, 95%).

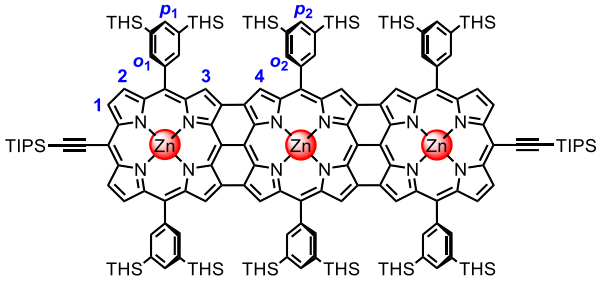

^{1}H NMR (600 MHz, $CDCl_3$, 298 K): δ 8.55 (d, J = 4.5 Hz, 4H, **H$_1$**), 7.79 (s, 4H, **H$_{p1}$**), 7.77 (s, 8H, **H$_{o1}$**), 7.71 (s, 2H, **H$_{p2}$**), 7.57 (s, 4H, **H$_{o2}$**), 7.50 (d, J = 4.5 Hz, 4H, **H$_2$**), 7.08 (s, 4H, **H$_3$**), 6.33 (s, 4H, **H$_4$**), 1.41 – 0.58 (m, 510H, **H$_{TIPS,THS}$**).

MALDI-ToF: m/z = 5316.868 ($C_{334}H_{544}N_{12}Si_{14}Zn_3$, $M^{+\cdot}$ requires 5316.763).

UV–vis–NIR ($CDCl_3$, 298 K) λ_{max} / nm (ε / µM^{-1} cm^{-1}): 433 (0.17), 671 (0.21), 719 (0.10), 1368 (0.18).

E.3.3 Synthesis of *lf*-ZnP4-TIPS$_2$

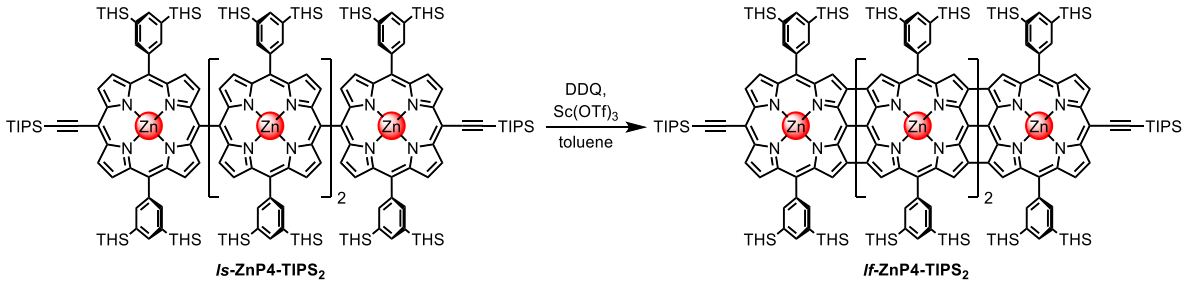

A mixture of ***ls*-ZnP4-TIPS$_2$** (3.5 mg, 0.50 µmol, 1.0 equiv.), DDQ (1.4 mg, 6.0 µmol, 12 equiv.), Sc(OTf)$_3$ (3.8 mg, 7.8 µmol, 16 equiv.) in dry toluene (5.0 mL) was evacuated and refilled with argon five times. After that, the reaction was conducted at 80 °C under argon for 2 h. After completion, the reaction was quenched by addition of Et_3N (1.0 mL). The resulting mixture was concentrated and purified by flash column chromatography (SiO_2) using pentane/CH_2Cl_2 (19:1) as eluent to give the desired product ***lf*-ZnP4-TIPS$_2$** (3.2 mg, 92%).

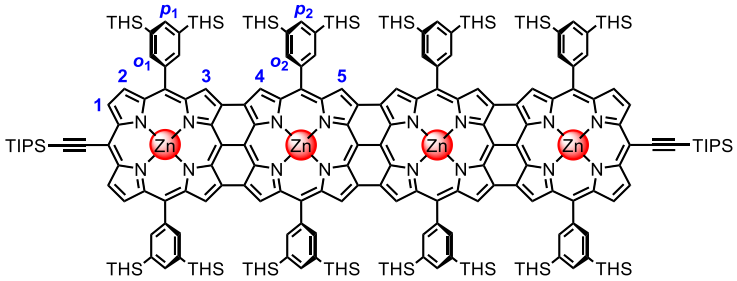

^{1}H NMR (600 MHz, $CDCl_3$, 298 K): δ 8.48 (d, *J* = 4.4 Hz, 4H, **H$_1$**), 7.78 (s, 4H, **H$_{p1}$**), 7.75 (s, 8H, **H$_{o1}$**), 7.69 (s, 4H, **H$_{p2}$**), 7.54 (s, 8H, **H$_{o2}$**), 7.44 (d, *J* = 4.5 Hz, 4H, **H$_2$**), 7.00 (s, 4H, **H$_3$**), 6.37 – 6.30 (m, 8H, **H$_{4,5}$**), 1.45 – 0.57 (m, 666H, **H$_{TIPS,THS}$**).

MALDI-ToF: *m*/*z* = 6967.002 ($C_{438}H_{710}N_{16}Si_{18}Zn_4$, $M^{+\cdot}$ requires 6966.913).

UV–vis–NIR ($CDCl_3$, 298 K) λ_{max} / nm (ε / μM^{-1} cm^{-1}): 431 (0.16), 722 (0.27), 1374 (0.07), 1613 (0.34).

E.3.4 Synthesis of *lf*-ZnP6-TIPS$_2$

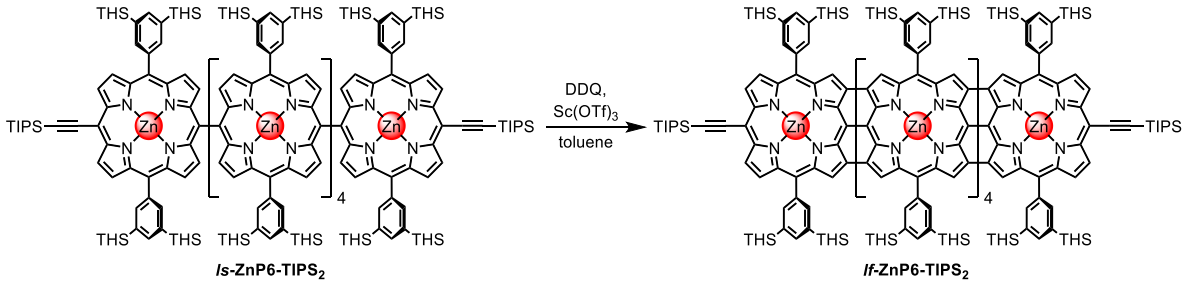

A mixture of ***ls*-ZnP6-TIPS$_2$** (5.0 mg, 0.49 µmol, 1.0 equiv.), DDQ (2.2 mg, 9.7 µmol, 20 equiv.), $Sc(OTf)_3$ (6.2 mg, 13 µmol, 26 equiv.) in dry toluene (5.0 mL) was evacuated and refilled with argon five times. After that, the reaction was conducted at 80 °C under argon for 2 h. After completion, the reaction was quenched by addition of Et_3N (1.0 mL). The resulting mixture was concentrated and purified by flash column chromatography (SiO_2) using pentane/CH_2Cl_2 (19:1) as eluent to give the desired product ***lf*-ZnP6-TIPS$_2$** (4.1 mg, 82%).

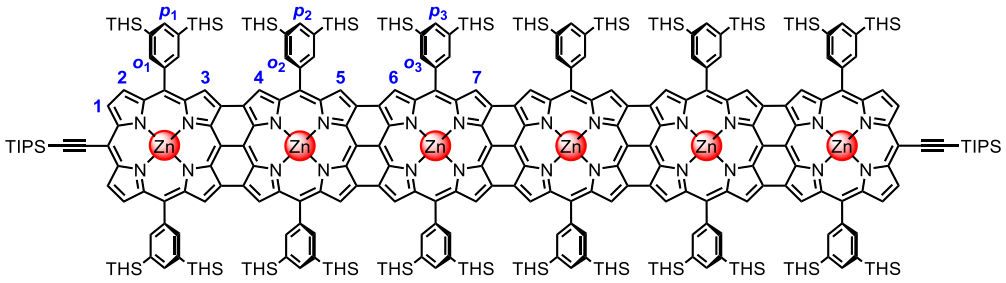

^{1}H NMR (700 MHz, toluene-d_8, 298 K) δ 8.79 (d, J = 4.1 Hz, 4H, **H$_1$**), 8.23 (s, 8H, **H$_{o1}$**), 8.20 (s, 4H, **H$_{p1}$**), 8.11 – 8.07 (m, 8H, **H$_{o2,o3}$**), 8.03 (s, 8H, **H$_{p2}$**), 8.01 (s, 8H, **H$_{p3}$**), 7.78 (d, J = 4.1 Hz, 4H, **H$_2$**), 7.33 (s, 4H), 6.71 – 6.63 (m, 16H, **H$_{4,5,6,7}$**), 1.79 – 0.94 (m, 978H, **H$_{TIPS,THS}$**).

MALDI-ToF: m/z = 10267.571 ($C_{646}H_{1042}N_{24}Si_{26}Zn_6$, $M^{+\cdot}$ requires 10267.212).

UV–vis–NIR ($CDCl_3$, 298 K) λ_{max} / nm (ε / µM^{-1} cm^{-1}): 427 (0.21), 773 (0.36), 1658 (0.11), 2052 (0.65).

E.3.5 Synthesis of *lf*-ZnP10-TIPS$_2$

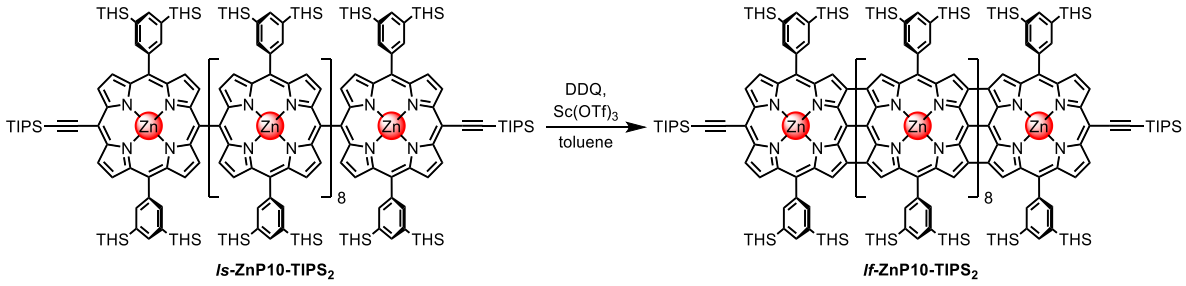

A mixture of ***ls*-ZnP10-TIPS$_2$** (2.5 mg, 0.15 µmol, 1.0 equiv.), DDQ (1.1 mg, 4.7 µmol, 32 equiv.), $Sc(OTf)_3$ (3.0 mg, 6.2 µmol, 42 equiv.) in dry toluene (5.0 mL) was evacuated and refilled with argon five times. After that, the reaction was conducted at 80 °C under argon for 2 h. After completion, the reaction was quenched by addition of Et_3N (1.0 mL). The resulting mixture was concentrated and purified by flash column chromatography (SiO_2) using pentane/CH_2Cl_2 (9:1) as eluent to give the desired product ***lf*-ZnP10-TIPS$_2$** (1.6 mg, 65%).

MALDI-ToF: *m*/*z* = 16877.196 ($C_{1062}H_{1706}N_{40}Si_{42}Zn_{10}$, $M^{+\cdot}$ requires 16868.818).

E.4 UV–vis–NIR–IR Spectroelectrochemistry

Measurements were performed in an optically transparent thin-layer electrochemical cell (OTTLE);[54] path length: ca. 0.2 mm; solvent: dry CH_2Cl_2 containing 0.1 M tetra-*n*-butylammonium hexafluorophosphate (Bu_4NPF_6) as supporting electrolyte. Spectroelectrochemical data were collected during slow cyclic voltammograms (5 mV/s for NIR and IR spectra measurements and 0.5 mV/s for UV–vis spectra measurements), and confirmed that the oxidation is reversible. Sample concentrations were adjusted to a maximum optical density of 0.5–2.5. UV–vis–NIR–IR spectra were acquired using an Agilent Cary 4000 UV–vis Spectrometer and a Bruker Vertex 80 spectrometer. Spectroelectrochemical data were collected during oxidation of oligomers from their neutral to *Q*+ oxidation states (*Q* = 1–3), and the spectra for individual oxidation states were resolved by multivariate curve resolution using the MCR-ALS toolbox in MATLAB.

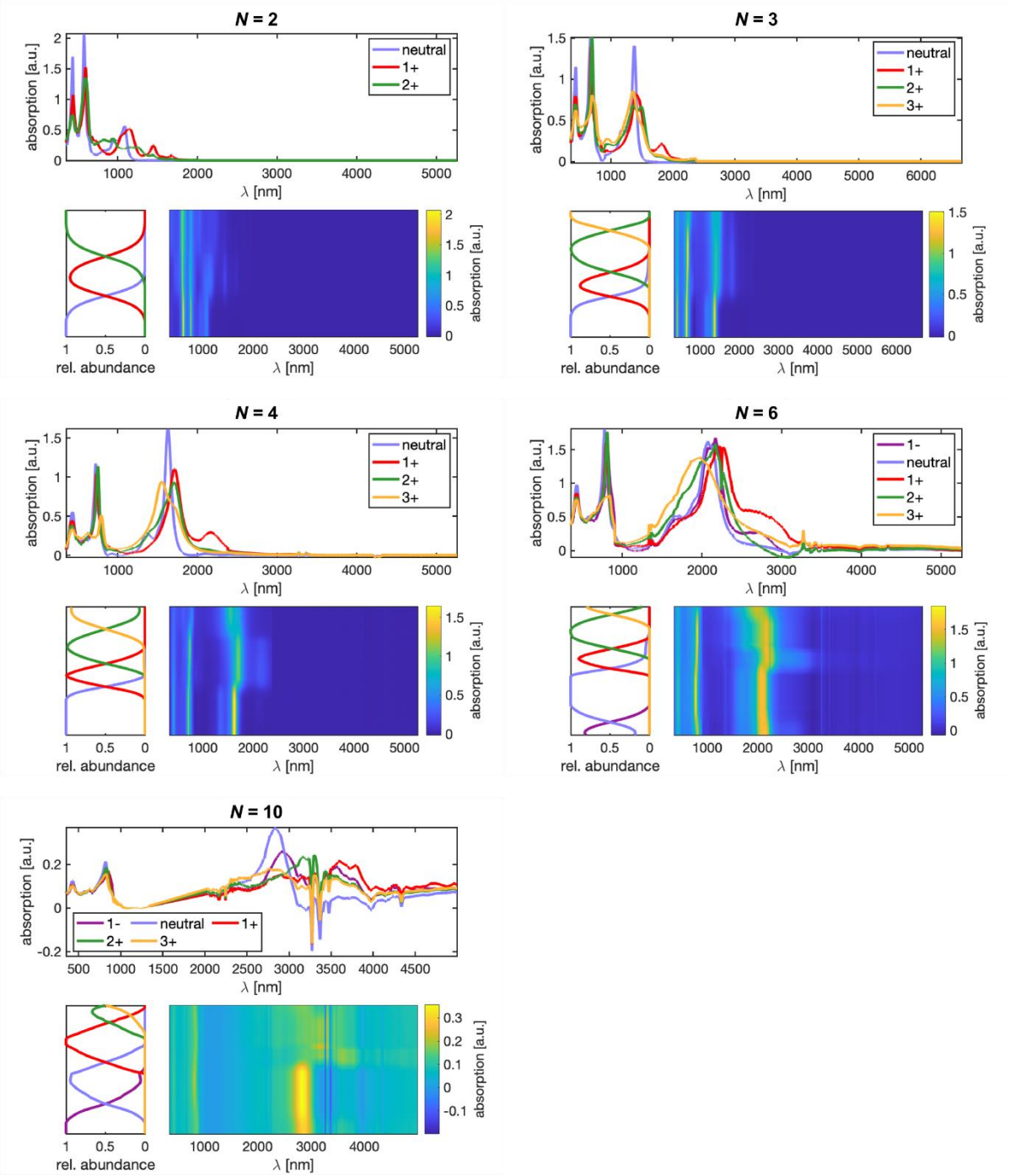

Figure 5.12: Deconvoluted spectroelectrochemical data for oxidation of ***lf*-ZnP*N*-TIPS$_2$** (*N* = 2–4, 6 and 10) in CH_2Cl_2/Bu_4NPF_6. The resolved spectra for individual oxidation states are shown above each contour plot, with the corresponding speciation curves in the left subplots.

E.5 EPR Spectroscopy

E.5.1 cw-EPR measurements

All measurements were performed in CD_2Cl_2/toluene-d_8/THF-d_8 (1:1:1) at room temperature (295 K) at X-band (Bruker EMXmicro spectrometer). In all measurements, radical cations ***lf*-ZnP*N*-TIPS$_2^{+\cdot}$** (*N* = 1–4, 6 and 10; 200 µM) are generated by chemical oxidation with BAHA (0.5 equiv.). The oxidation procedures are analogous to the ones reported in previous studies.[66,102]

Gaussian envelope widths ΔB_N of the experimental and simulated spectra were determined by least-square fitting of the first derivative of a Gaussian normal distribution to each spectrum, where ΔB_N is the full width at half maximum of the fitted Gaussian distribution.

Table E.1: Gaussian envelope widths ΔB_N of the experimental and simulated spectra for cw-EPR measurements of ***lf*-ZnP*N*-TIPS$_2^{+\cdot}$** (*N* = 1–4, 6 and 10).

ΔB_N [mT]	*N* = 1	*N* = 2	*N* = 3	*N* = 4	*N* = 6	*N* = 10
Exp.	0.6332	0.4662	0.4457	0.4295	0.3902	0.3552
Sim.[a]	0.6427	0.4925	0.4472	0.4233	0.3991	0.3904

[a] The isotropic hyperfine couplings for ^{14}N nuclei were calculated based on eqn. 5.10, in which the ^{14}N Mulliken spin densities used were obtained from the geometry optimization of the molecules at B3LYP/6-31G* level of theory.

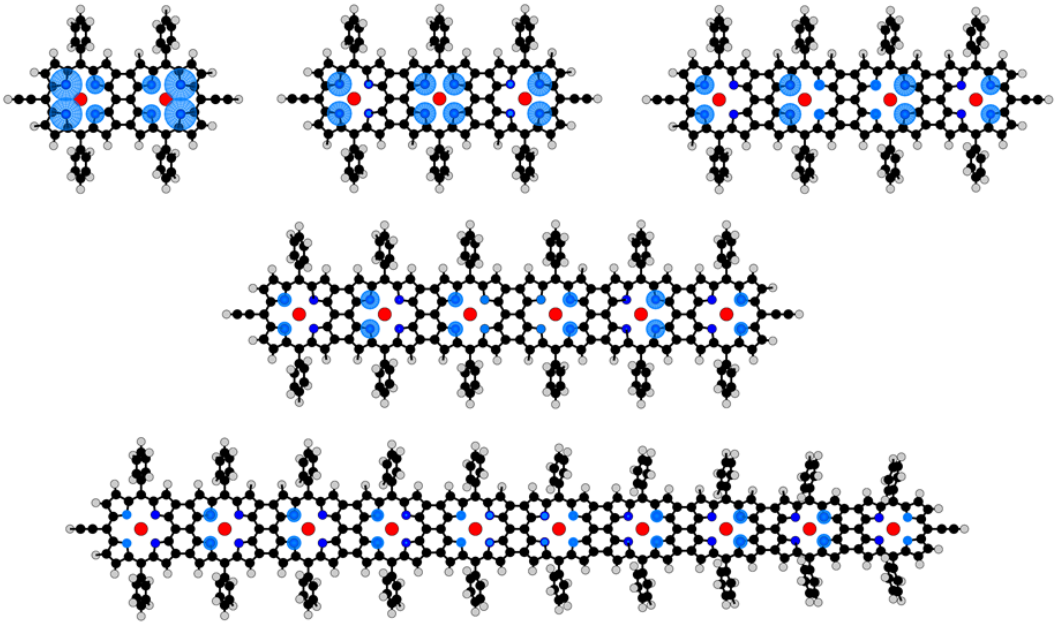

Figure E.1: Schematic visualization of the relative spin densities (blue shades) on the ^{14}N nuclei of ***lf*-ZnP*N*-TIPS$_2^{+\cdot}$** (*N* = 2–4, 6, 10), calculated at B3LYP/6-31G* level of theory. Data were collected and analyzed by Sebastian M. Kopp.

E.5.2 ENDOR measurements

All measurements were performed in frozen glassy solutions of CD_2Cl_2/toluene-d_8/THF-d_8 (1:1:1) at 50 K at W-band (Bruker E680 spectrometer). Porphyrin concentrations between 100–400 μM were used in the experiments with lower sample concentrations typically used in longer systems due to the slightly higher risk of aggregation.

The ^{1}H Mims-ENDOR spectra were measured at the two principal positions of the anisotropic g-tensor ($g_\perp$ and $g_\parallel$) and show a moderate degree of orientation selection for systems with $N \geq 4$. The ^{14}N Mims-ENDOR were only measured at the field position corresponding to the maximum of the spectrum ($g_\perp$).

The simulation of the ENDOR spectra is based on a spin-density distribution that spans the entire length of the molecules for N = 1–10, and is closely guided by DFT calculations at the B3LYP/6-31G* level of theory. The anisotropic hyperfine coupling tensors for all ^{1}H and ^{14}N nuclei used in the ENDOR simulations are calculated from the spin density distribution with a distributed point-dipole model. This results in a global fit of the experimental spectra, where the same spin density distribution is used to calculate the ^{1}H and ^{14}N tensors for each molecule.

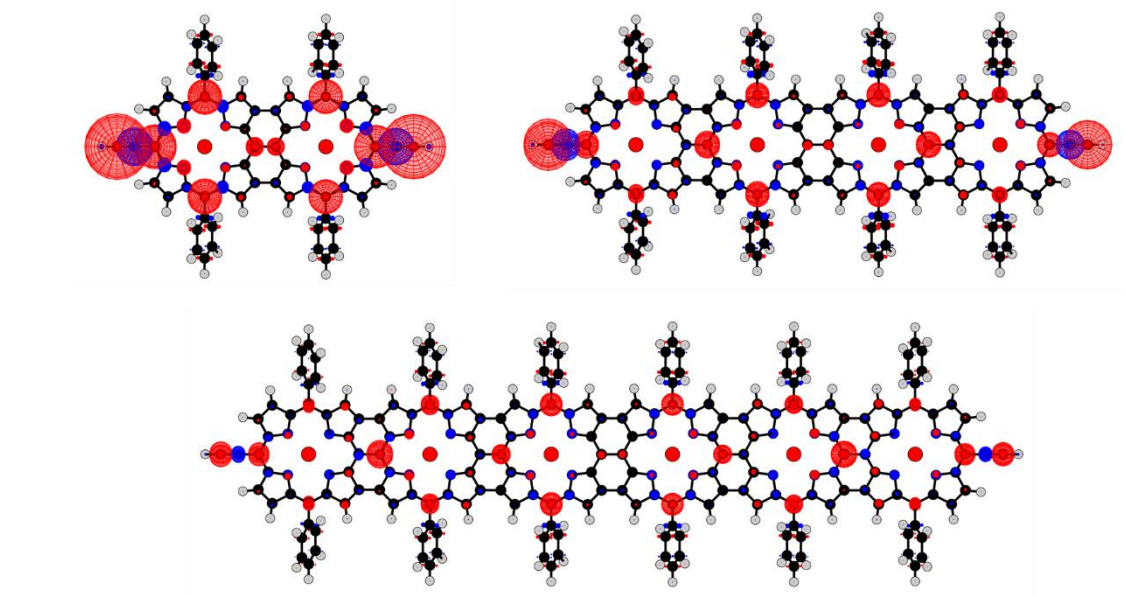

Figure E.2: Schematic visualization of the Mulliken spin density distributions that were used in simulations of the ENDOR spectra for ***lf*-ZnP*N*-TIPS$_2^{+\cdot}$** (N = 2, 4 and 6). Data were collected and analyzed by Sebastian M. Kopp.

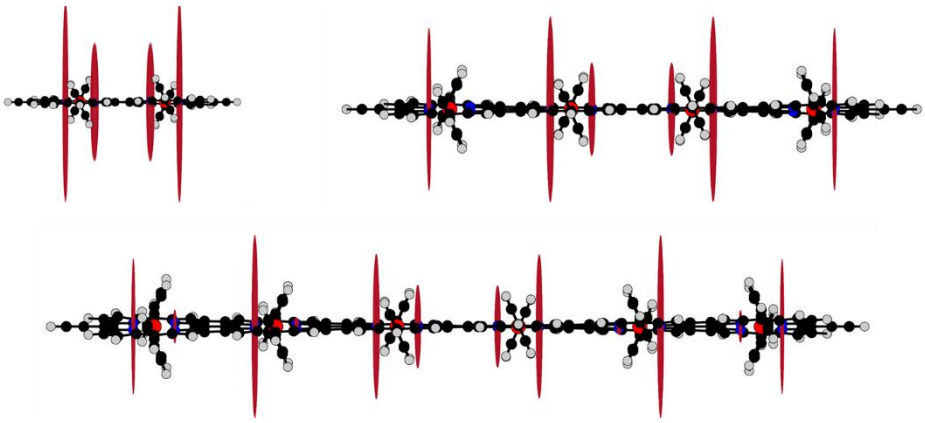

Figure E.3: Schematic visualization of the DFT (B3LYP/EPR-II) calculated anisotropic ^{14}N hyperfine coupling tensors for ***lf*-ZnP*N*-TIPS$_2^{+\cdot}$** (*N* = 2, 4 and 6). Data were collected and analyzed by Sebastian M. Kopp.

E.5.3 Supporting Evidences for Oxidation of *lf*-ZnP*N*-TIPS$_2$ in Air

The echo-detected field sweeps and phase memory time (T_M) measurements further support the presence of radical cations in the isolated samples of ***lf*-ZnP*N*-TIPS$_2$** (*N* = 6 and 10) before addition of a chemical oxidant.

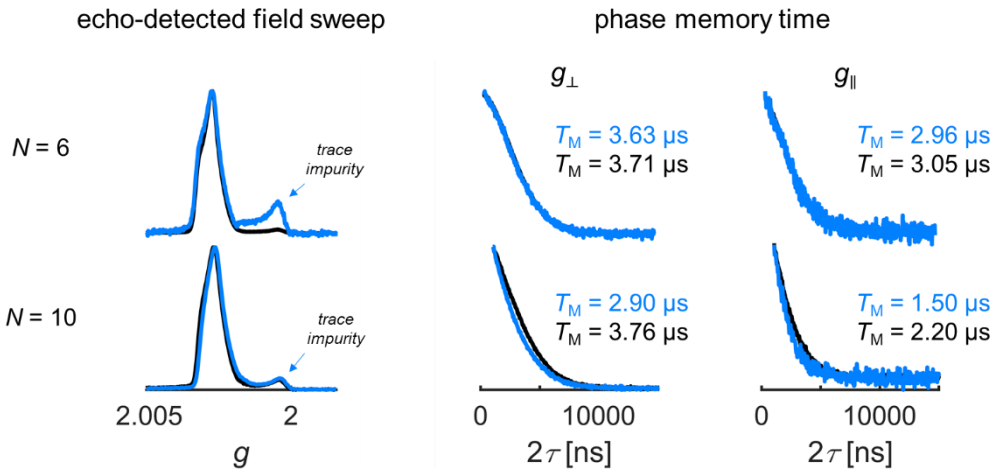

Figure E.4: W-band EPR characterizations of fused porphyrin oligomers before (blue lines) and after (black lines) addition of chemical oxidant BAHA. The phase memory times T_M of the cations formed under aerobic condition and by chemical oxidation were determined at the two principal g-orientations ($g_\perp$ and $g_\parallel$) by Hahn echo experiments. Data were collected and analyzed by Sebastian M. Kopp.

E.6 DFT and TD-DFT Calculations

Molecular models were built in GaussView in which the trihexylsilyl side chains on the porphyrin *meso* aryl groups were replaced with H for all calculations. DFT geometry optimizations of ***lf*-ZnP*N*-TIPS$_2$** and ***lf*-ZnP*N*-TIPS$_2^{+\cdot}$** were performed using Gaussian16/A.03 with the B3LYP/6-31G* functional/basis set. The minimized structures for short oligomers ($N \leq 4$) were subjected to frequency calculations, revealing no imaginary frequencies. TD-DFT calculations for ***lf*-ZnP*N*-TIPS$_2$** and ***lf*-ZnP*N*-TIPS$_2^{+\cdot}$** were conducted for the first 64 excited states using the the PCM solvent model (CH_2Cl_2), with B3LYP, BLYP35 and LC-ωhPBE (ω = 0.1 and 0.2) functionals, together with 6-31G* basis set.

Table E.2: Experimental[a] and TD-DFT calculated[b] UV–vis–NIR–IR absorption properties for ***lf*-ZnP*N*-TIPS$_2^Q$** (Q = 0 and +1).

***lf*-ZnP*N*-TIPS$_2$**	N = 2	N = 3	N = 4	N = 6	N = 10
$\lambda_{abs,III}$ [nm]	1087	1378	1631	2075	2832
($E_{abs,III}$ [eV])	(1.14)	(0.90)	(0.76)	(0.60)	(0.44)
$\lambda_{B3LYP,III}$ [nm]	952	1234	1488	1953	2776
($E_{B3LYP,III}$ [eV])	(1.30)	(1.00)	(0.83)	(0.64)	(0.45)
$\lambda_{BLYP35,III}$ [nm]	911	1223	1433	1883	2664
($E_{BLYP35,III}$ [eV])	(1.36)	(1.01)	(0.86)	(0.66)	(0.47)
$\lambda_{LC\text{-}\omega hPBE_0.1,P2}$ [nm]	979	1245	1474	1860	2423
($E_{LC\text{-}\omega hPBE_0.1,P2}$ [eV])	(1.27)	(1.00)	(0.84)	(0.67)	(0.51)
$\lambda_{LC\text{-}\omega hPBE_0.2,P2}$ [nm]	957	1257	1535	2062	3060
($E_{LC\text{-}\omega hPBE_0.2,P2}$ [eV])	(1.30)	(0.99)	(0.81)	(0.60)	(0.41)
***lf*-ZnP*N*-TIPS$_2^{+\cdot}$**	N = 2	N = 3	N = 4	N = 6	N = 10
$\lambda_{abs,P2}$ [nm]	1674	1822	2161	2785	3600
($E_{abs,P2}$ [eV])	(0.74)	(0.68)	(0.57)	(0.45)	(0.34)
$\lambda_{B3LYP,III}$ [nm]	1087	1378	1631	2075	2832
($E_{B3LYP,III}$ [eV])	(1.14)	(0.90)	(0.76)	(0.60)	(0.44)
$\lambda_{BLYP35,P2}$ [nm]	1593[c]	1759	2129	2785	4359
($E_{BLYP35,P2}$ [eV])	(0.78)	(0.70)	(0.58)	(0.45)	(0.28)
$\lambda_{LC\text{-}\omega hPBE_0.1,P2}$ [nm]	1567[d]	1972	2322	2819	3495
($E_{LC\text{-}\omega hPBE_0.1,P2}$ [eV])	(0.79)	(0.63)	(0.53)	(0.44)	(0.35)
$\lambda_{LC\text{-}\omega hPBE_0.2,P2}$ [nm]	1329	1820	2379	3746	5421
($E_{LC\text{-}\omega hPBE_0.2,P2}$ [eV])	(0.93)	(0.68)	(0.52)	(0.33)	(0.23)

[a] Experimental values of λ_{abs} and E_{abs} were estimated from the absorption peak maximums from the deconvoluted absorption spectra shown in Figure 5.5. [b] Theoretically calculated values were obtained from TD-DFT calculations using B3LYP, BLYP35, LC-ωhPBE (ω = 0.1 and 0.2) functionals, 6-31G* basis set and the PCM solvent model (CH_2Cl_2). [c] It is dipole forbidden from calculation (calculated oscillator strength f = 0). [d] It is dominated by HOMO–1 → SOMO transition.

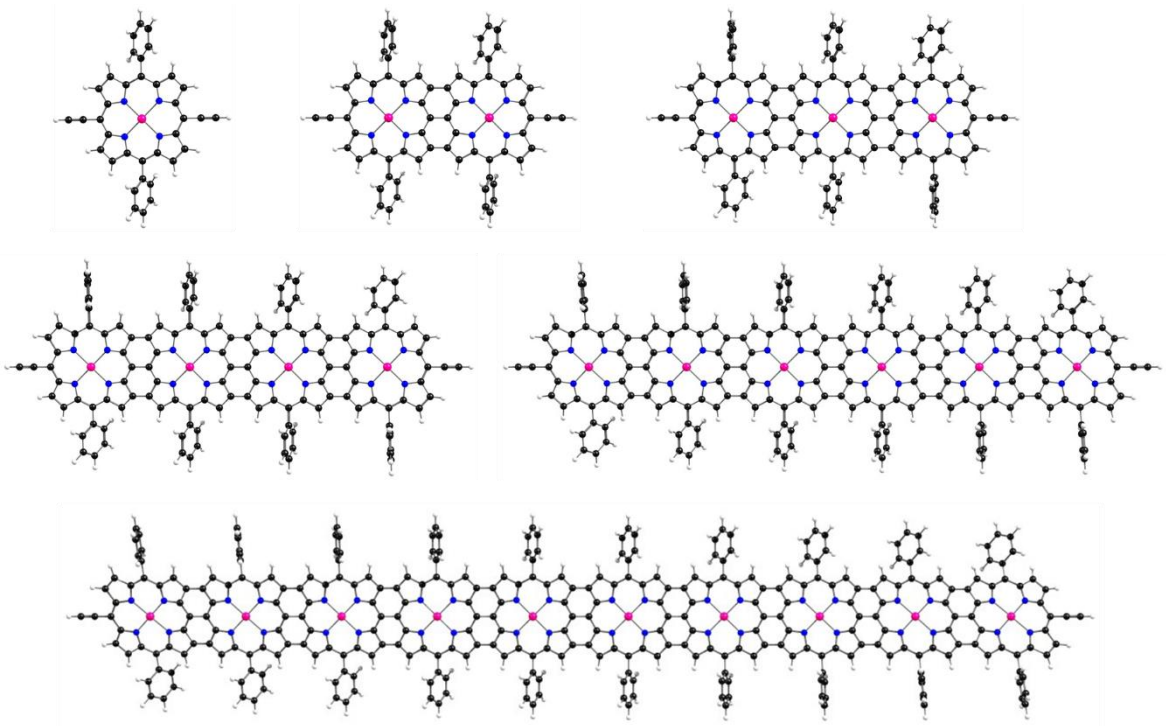

Figure E.5: Optimized geometries of ***lf*-ZnP*N*-TIPS$_2^{+\cdot}$**.

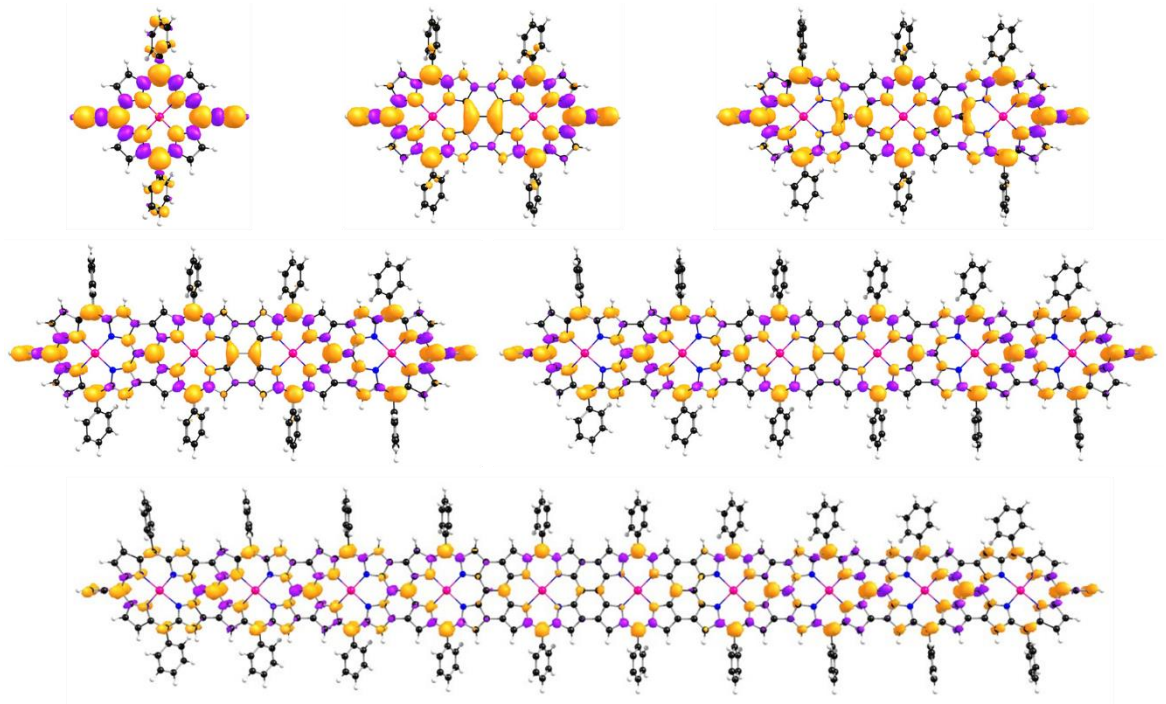

Figure E.6: Spin density isosurfaces at isovalue 0.001 a.u of ***lf*-ZnP*N*-TIPS$_2^{+\cdot}$**.

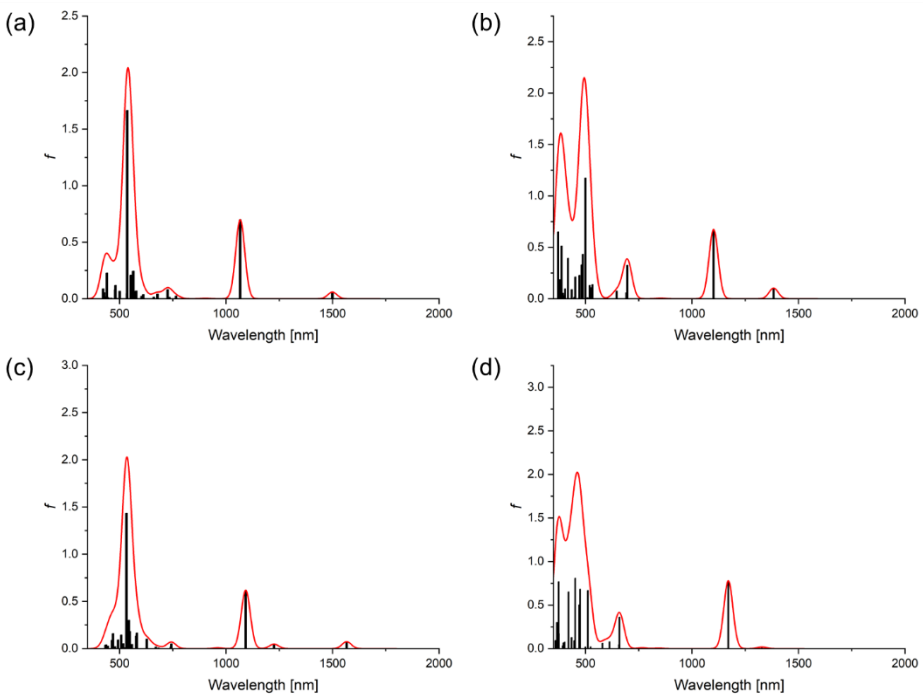

Figure E.7: TD-DFT calculated wavelength vs. oscillator strength *f* of ***lf*-ZnP2-TIPS$_2^{+\cdot}$** (black) and simulated absorption spectra (red). Calculated using B3LYP (a), BLYP35 (b), and LC-ωhPBE (ω = 0.1) (c), and LC-ωhPBE (ω = 0.2) (d) functionals.

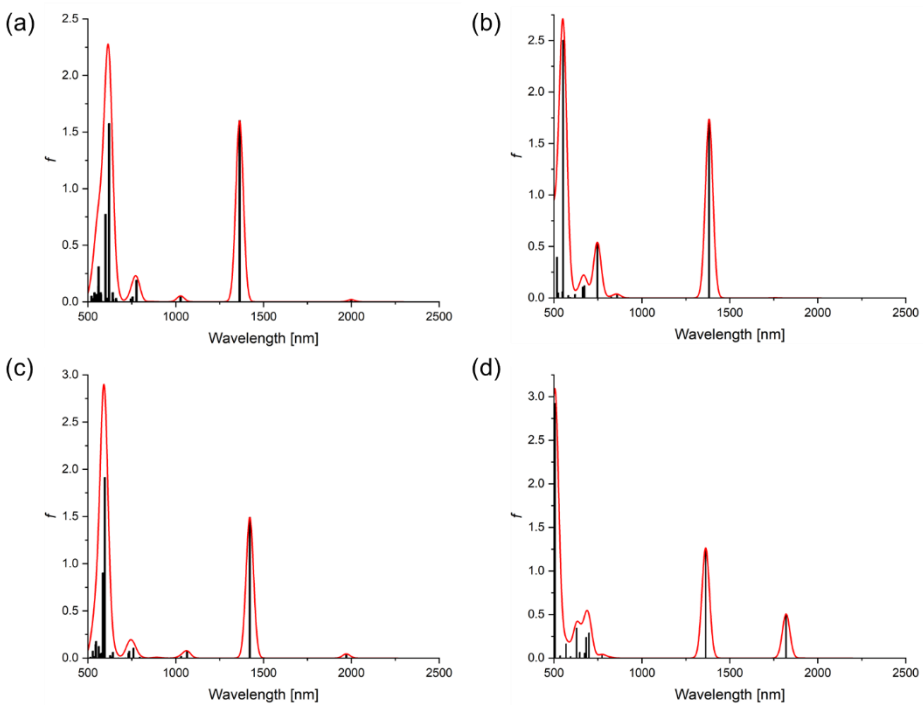

Figure E.8: TD-DFT calculated wavelength vs. oscillator strength *f* of ***lf*-ZnP3-TIPS$_2^{+\cdot}$** (black) and simulated absorption spectra (red). Calculated using B3LYP (a), BLYP35 (b), and LC-ωhPBE (ω = 0.1) (c), and LC-ωhPBE (ω = 0.2) (d) functionals.

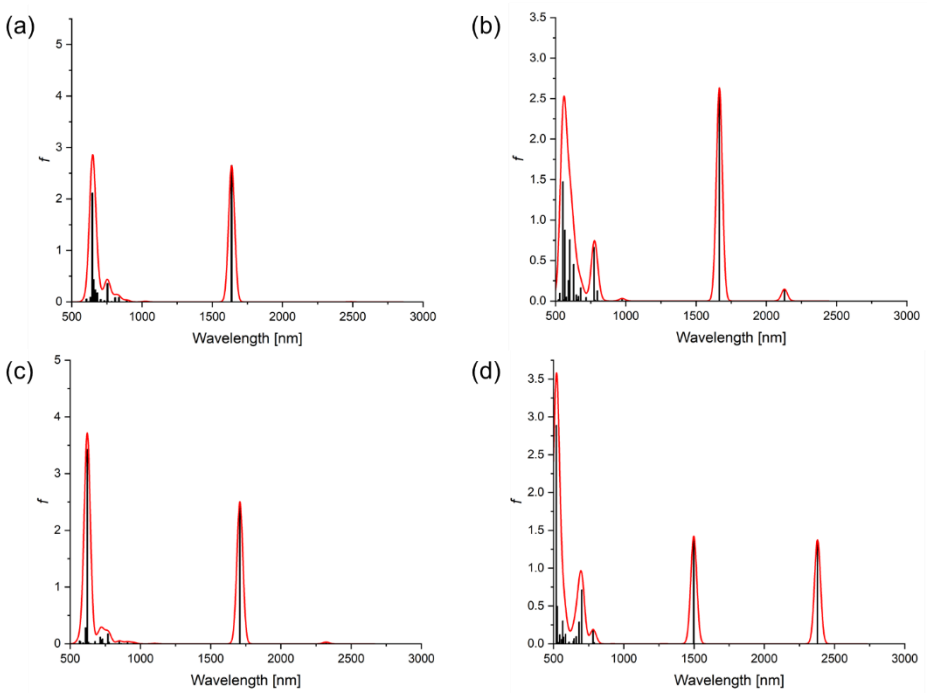

Figure E.9: TD-DFT calculated wavelength vs. oscillator strength *f* of ***lf*-ZnP4-TIPS$_2^{+\cdot}$** (black) and simulated absorption spectra (red). Calculated using B3LYP (a), BLYP35 (b), and LC-ωhPBE (ω = 0.1) (c), and LC-ωhPBE (ω = 0.2) (d) functionals.

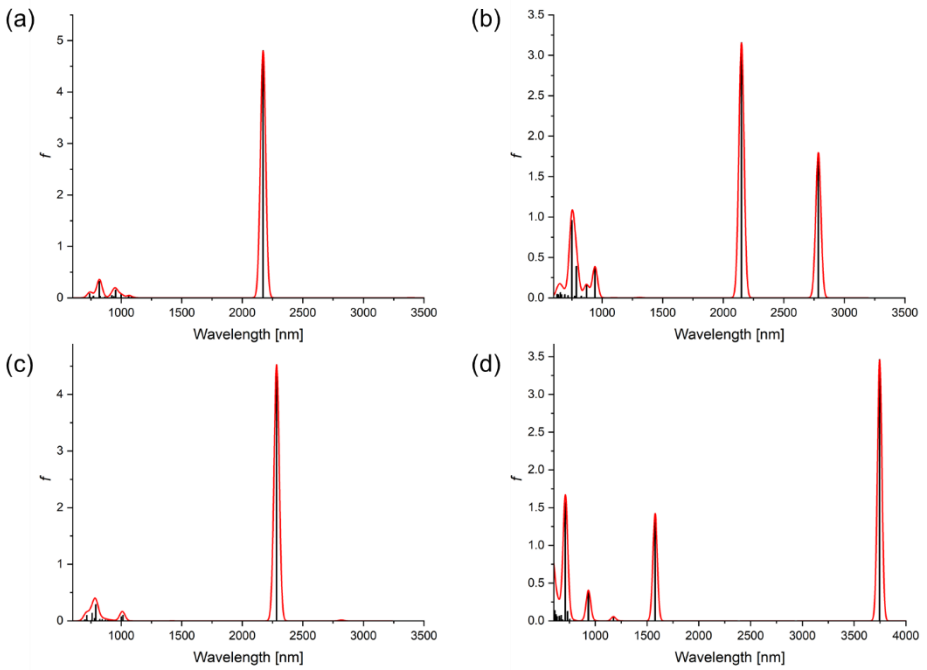

Figure E.10: TD-DFT calculated wavelength vs. oscillator strength *f* of ***lf*-ZnP6-TIPS$_2^{+\cdot}$** (black) and simulated absorption spectra (red). Calculated using B3LYP (a), BLYP35 (b), and LC-ωhPBE (ω = 0.1) (c), and LC-ωhPBE (ω = 0.2) (d) functionals.

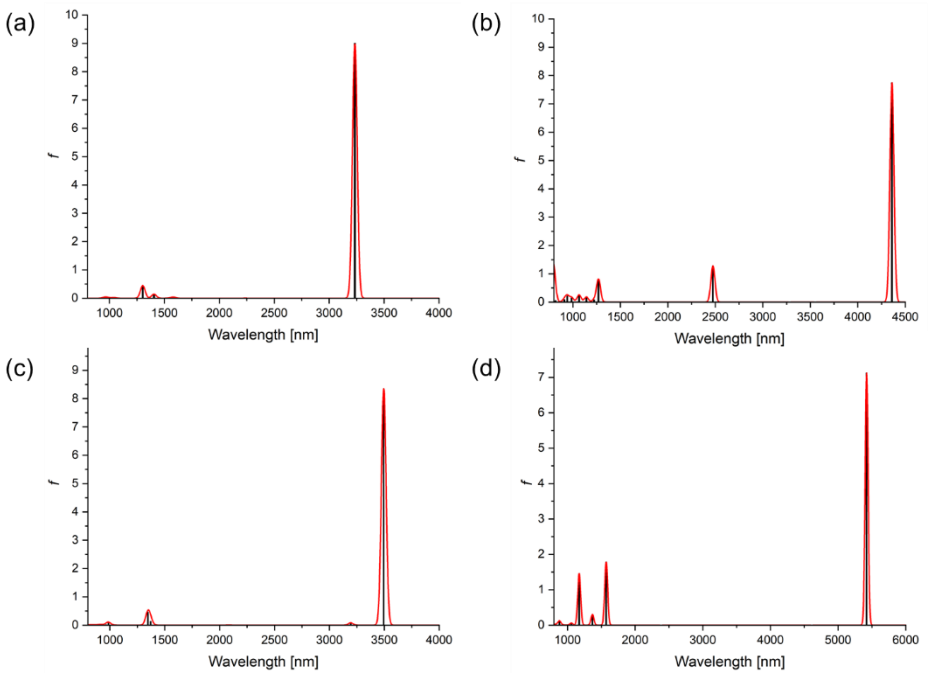

Figure E.11: TD-DFT calculated wavelength vs. oscillator strength *f* of ***lf*-ZnP8-TIPS$_2^{+\cdot}$** (black) and simulated absorption spectra (red). Calculated using B3LYP (a), BLYP35 (b), and LC-ωhPBE (ω = 0.1) (c), and LC-ωhPBE (ω = 0.2) (d) functionals.

E.7 Estimation of the Electronic Coupling Energy

We estimated the electronic coupling energy H for both the butadiyne-linked oligomers and the fused porphyrin oligomers by calculating the splitting of the HOMO levels of a dimer composed of two identical monomers. The four frontier orbitals and the calculated corresponding eigenvalues (energies) E_i for each series of porphyrin dimers are shown Figure 5.24. The HOMO and HOMO–3 for both compounds are derived from the a_{2u} orbital of a D_{4h} metalloporphyrin monomer, whereas the HOMO–1 and HOMO–2 are derived from the a_{1u} orbital (see Chapter 1 for the explanation of a_{2u} and a_{1u} for a porphyrin monomer). We used $2H = E_{HOMO} - E_{HOMO-3}$ to calculate the values of H for both compounds. For the butadiyne-linked dimer, the calculated electronic coupling energy (H = 0.25 eV) is similar to the experimental value (H = 0.24 eV, by the relationship $E_{abs,p1} = 2H$). For the fused porphyrin dimer, the calculated electronic coupling energy is 0.41 eV, about 50% larger than that of a butadiyne-linked dimer. As the H/λ for the fused porphyrin oligomers is about four times greater than that of the butadiyne-linked oligomers, the reorganization energy λ for the fused oligomers is two times smaller than that of the butadiyne-linked oligomers.

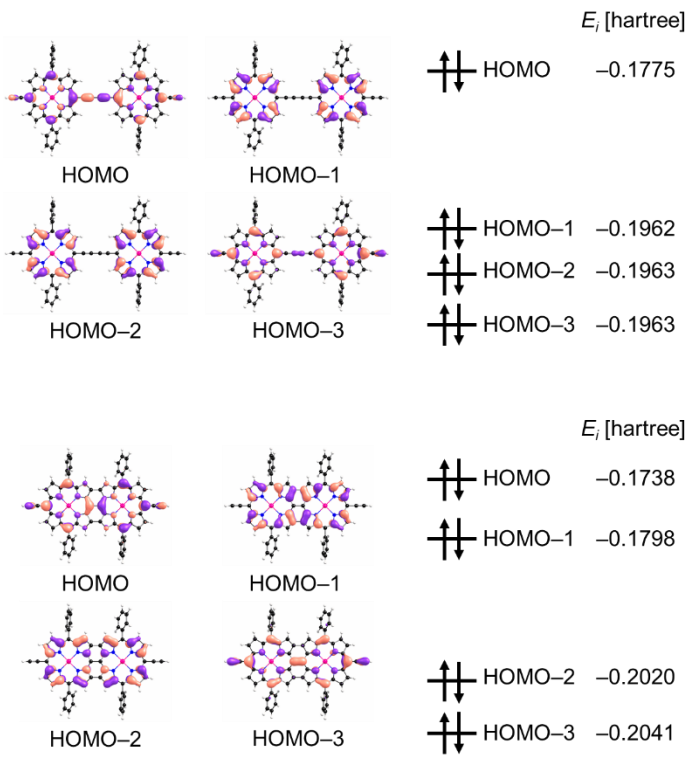

Figure E.12: DFT calculated frontier orbitals of the neutral butadiyne-linked porphyrin dimer and the fused porphyrin dimer. E_i corresponds to the calculated eigenvalue (energy) of the molecular level i. The calculations were performed at B3LYP/6-31G* level of theory in CH_2Cl_2.

E.8 NMR and Mass Spectra

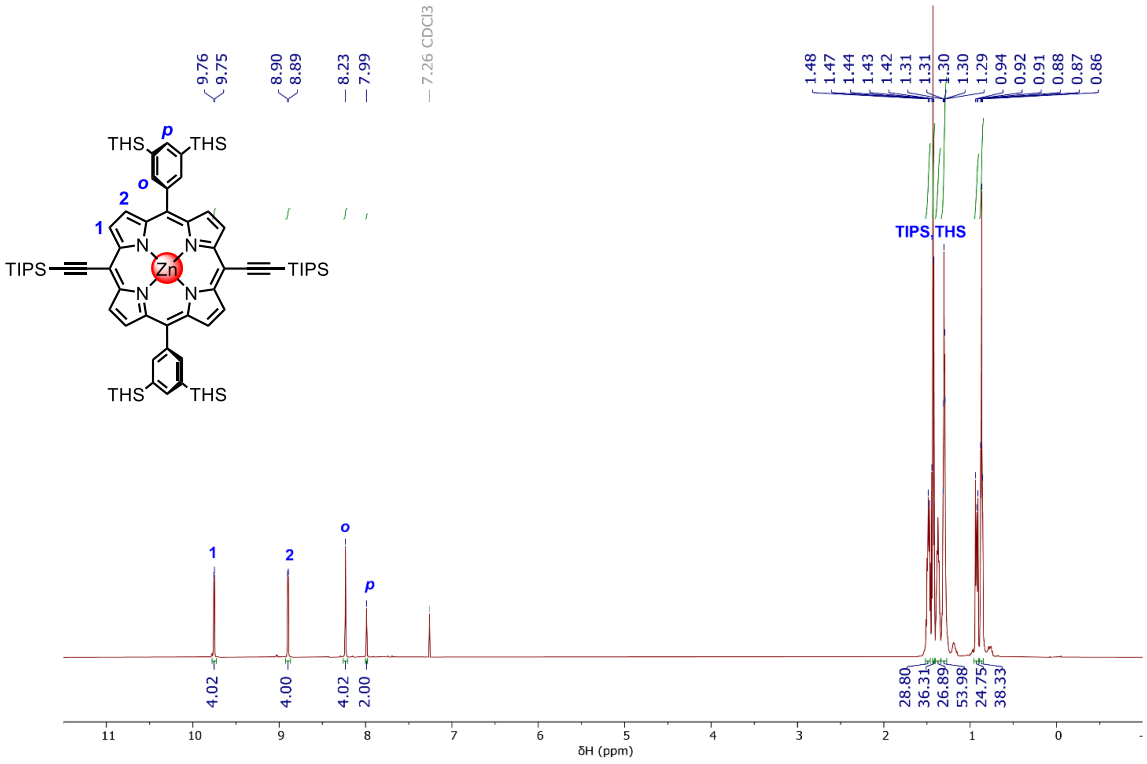

Figure E.13: ^{1}H NMR spectrum of **ZnP1-TIPS$_2$** (600 MHz, $CDCl_3$, 298 K).

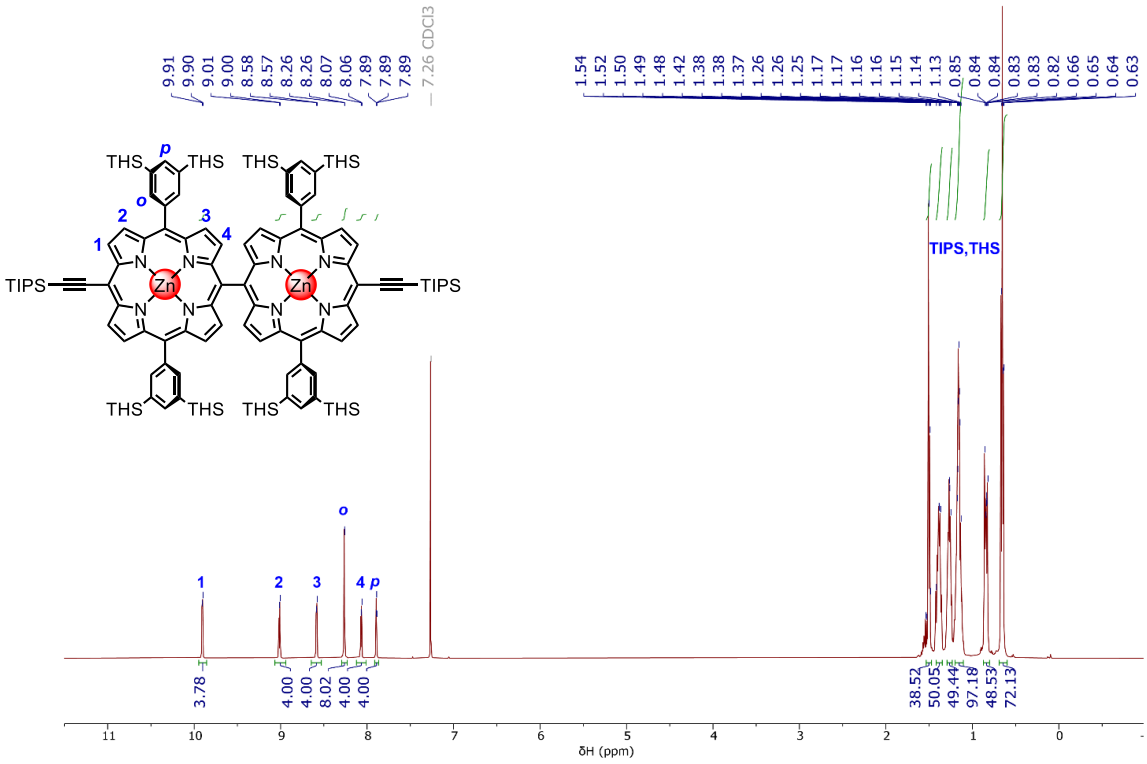

Figure E.14: ^{1}H NMR spectrum of ***ls*-ZnP2-TIPS$_2$** (600 MHz, $CDCl_3$, 298 K).

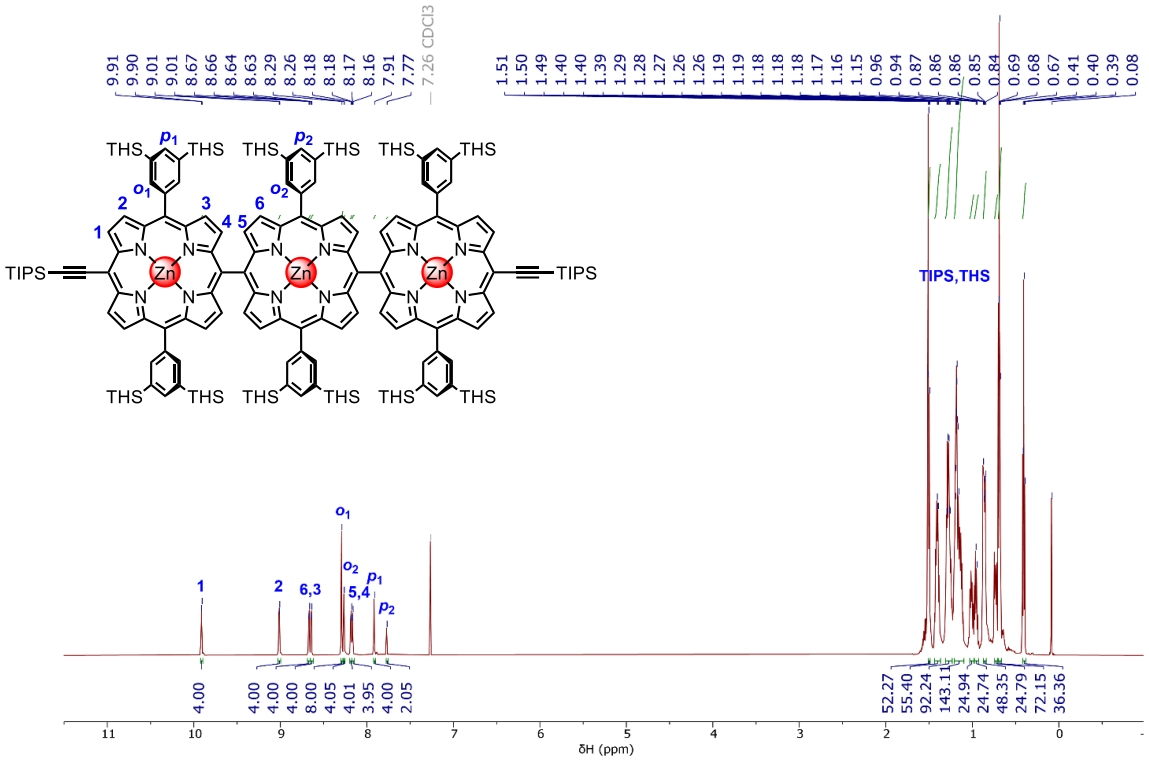

Figure E.15: ^{1}H NMR spectrum of ***ls*-ZnP3-TIPS$_2$** (600 MHz, $CDCl_3$, 298 K).

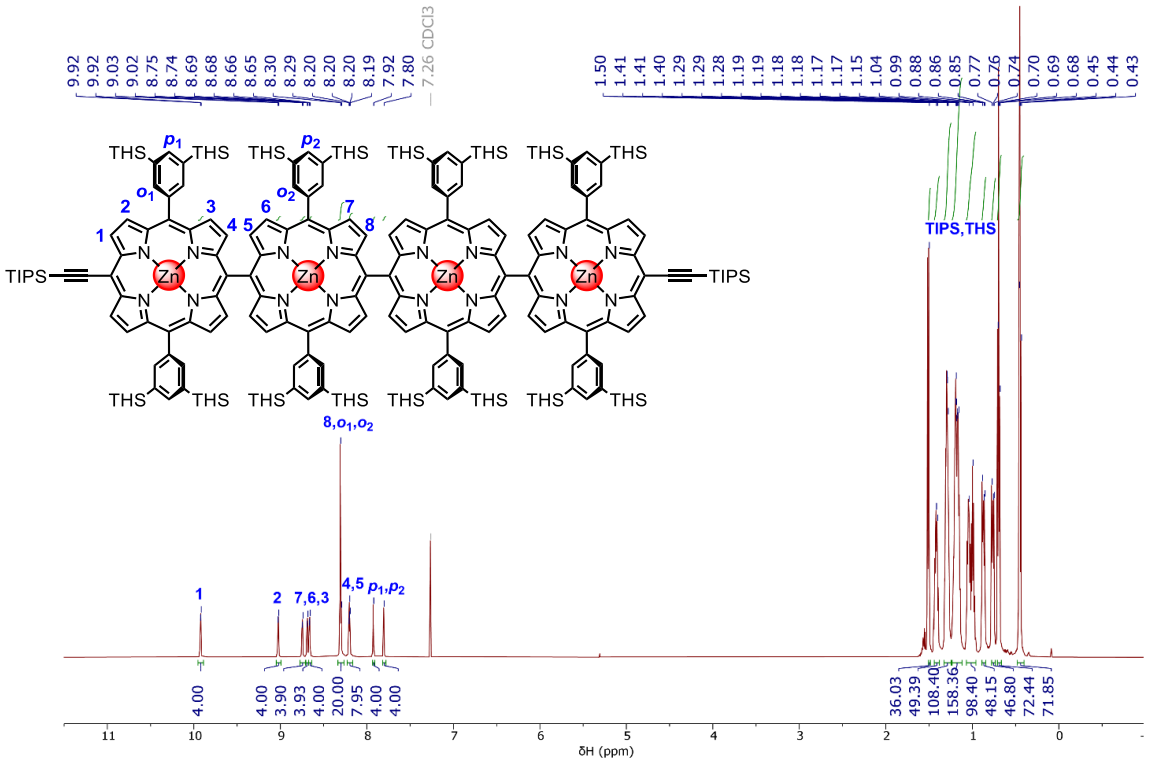

Figure E.16: ^{1}H NMR spectrum of ***ls*-ZnP4-TIPS$_2$** (600 MHz, $CDCl_3$, 298 K).

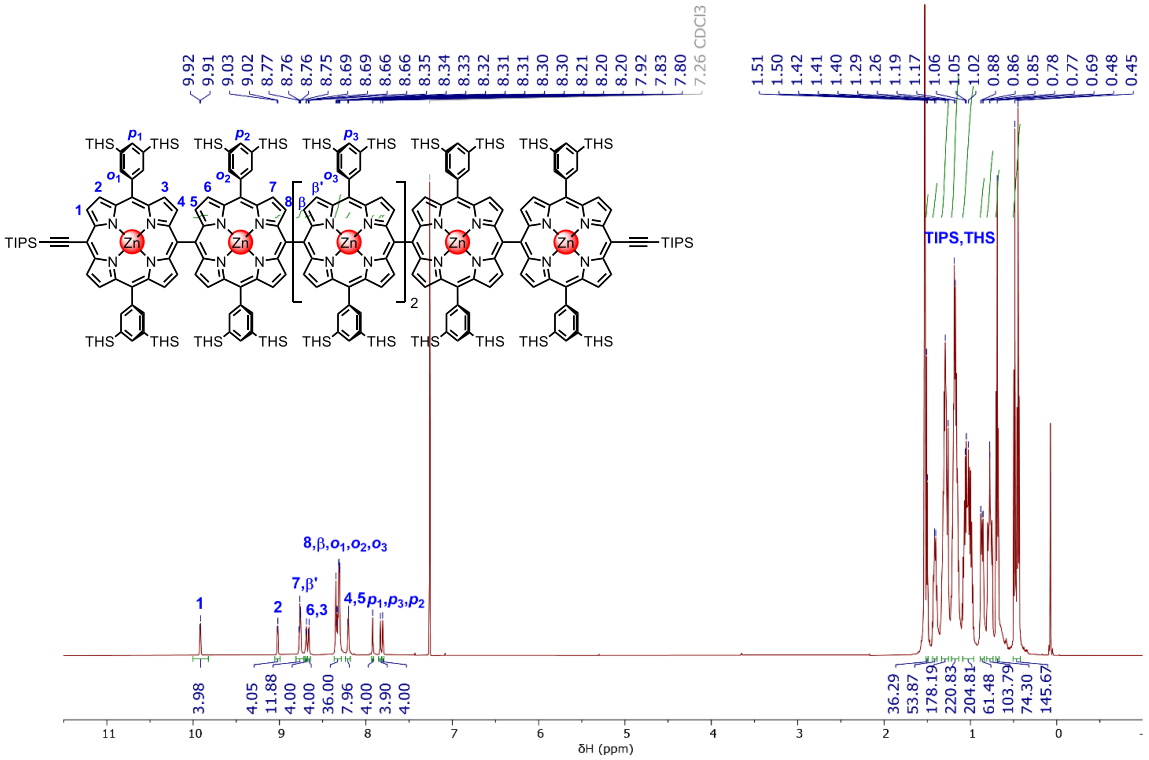

Figure E.17: ^{1}H NMR spectrum of ***ls*-ZnP6-TIPS$_2$** (600 MHz, $CDCl_3$, 298 K).

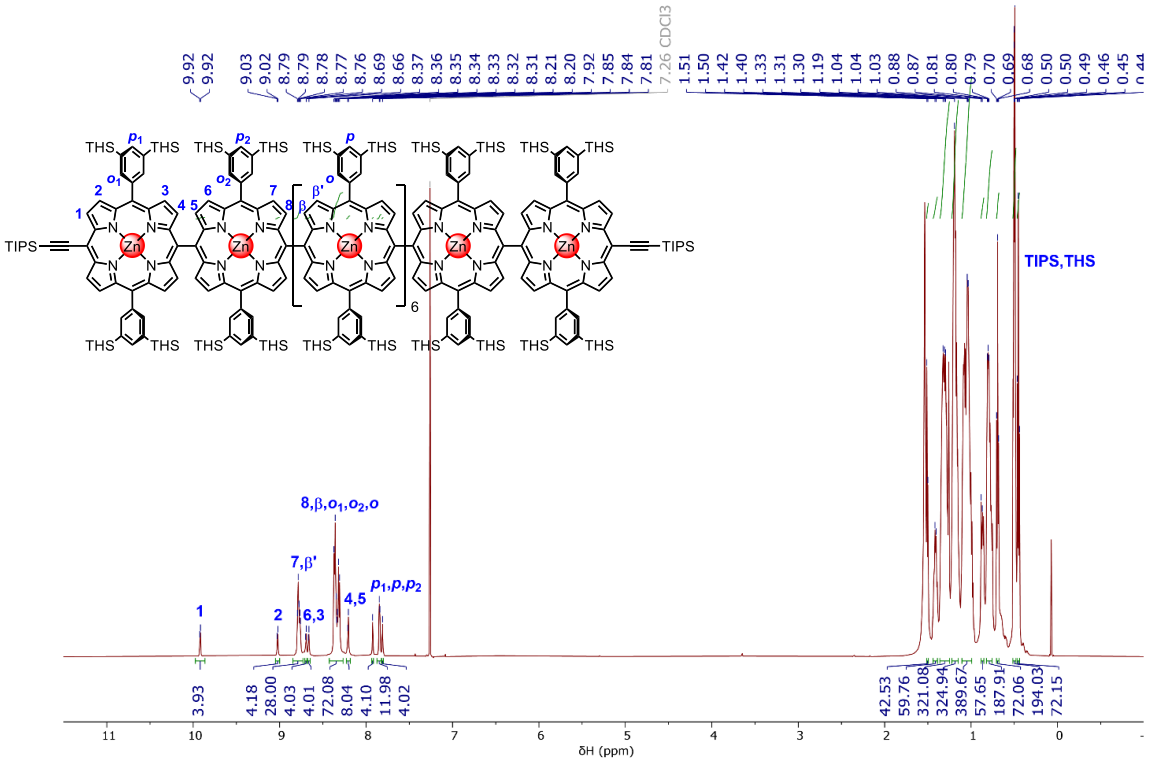

Figure E.18: ^{1}H NMR spectrum of ***ls*-ZnP10-TIPS$_2$** (600 MHz, $CDCl_3$, 298 K).

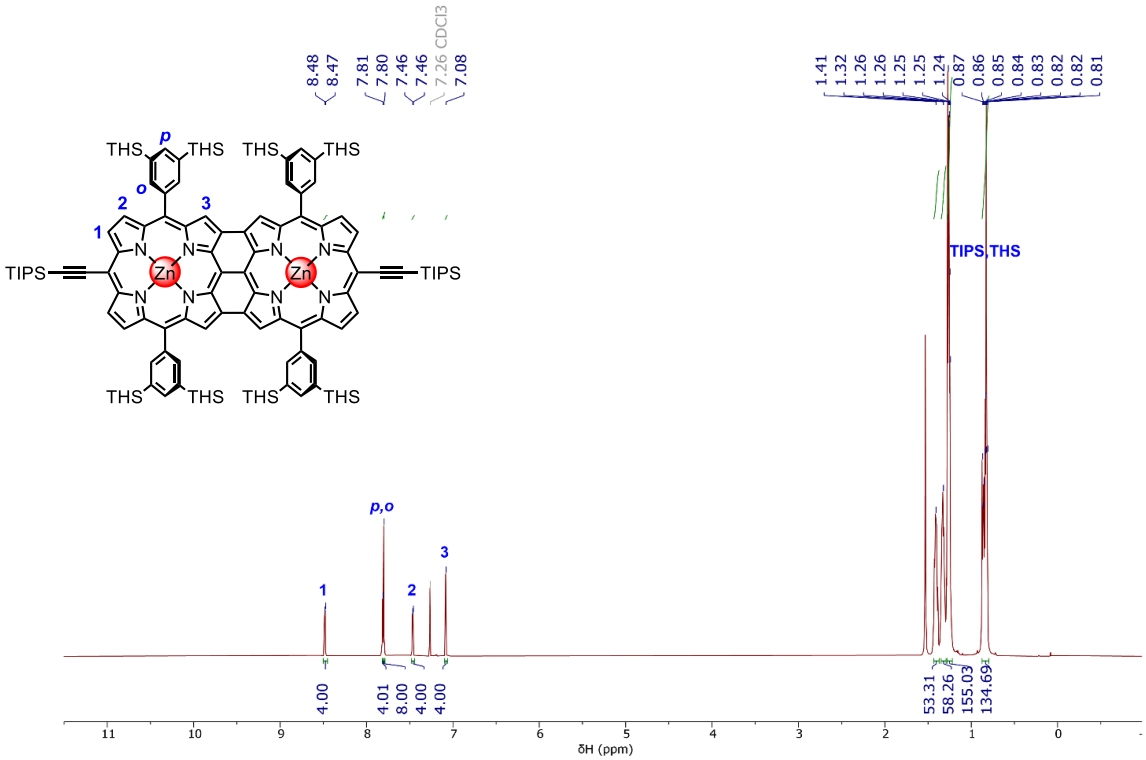

Figure E.19: ^{1}H NMR spectrum of ***lf*-ZnP2-TIPS$_2$** (600 MHz, $CDCl_3$, 298 K).

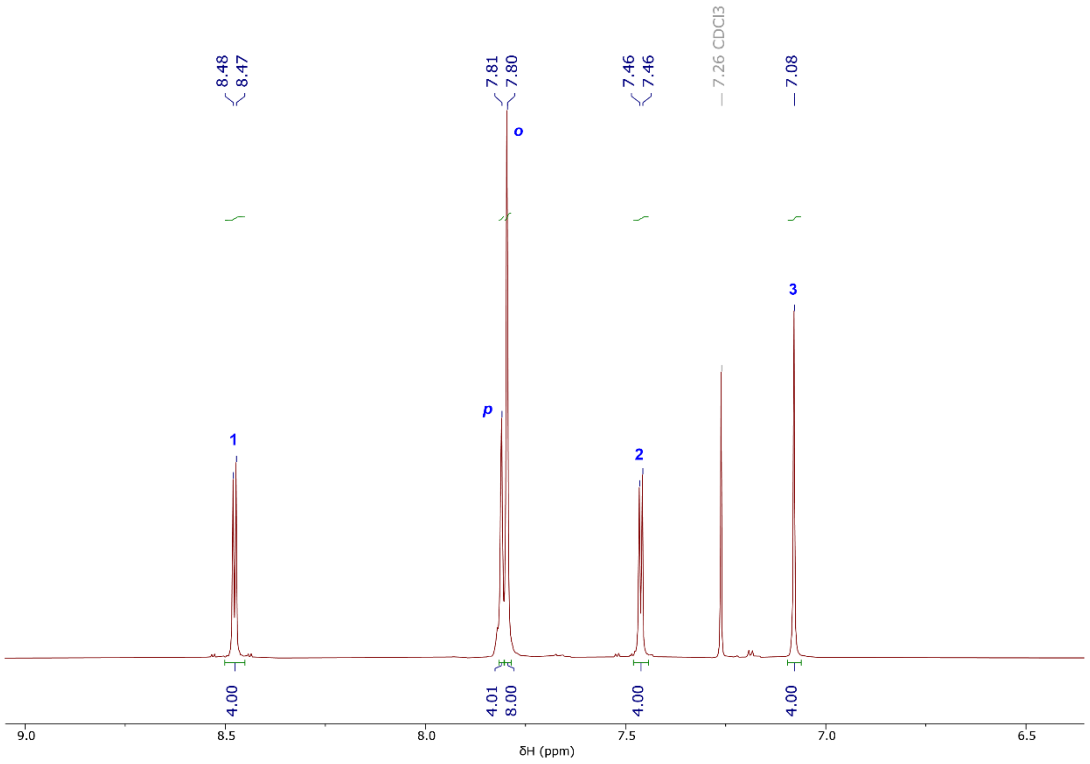

Figure E.20: Selected section of ^{1}H NMR spectrum of ***lf*-ZnP2-TIPS$_2$** (600 MHz, $CDCl_3$, 298 K).

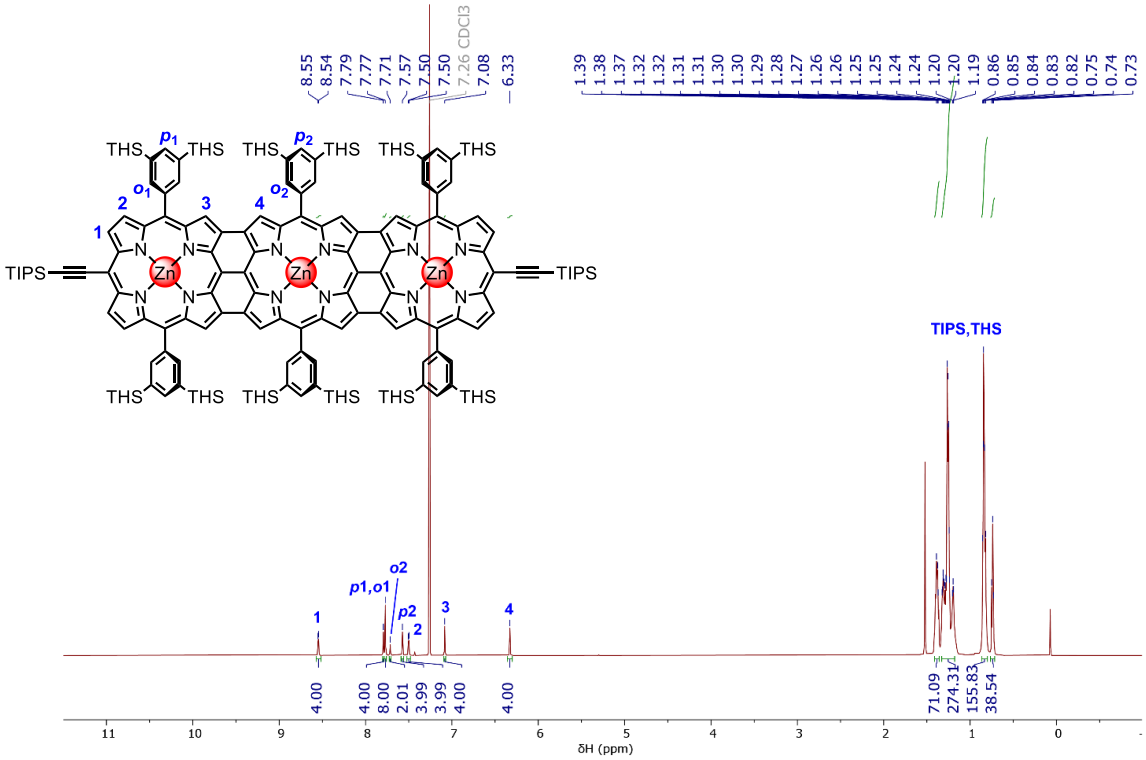

Figure E.11: ^{1}H NMR spectrum of ***lf*-ZnP3-TIPS$_2$** (600 MHz, $CDCl_3$, 298 K).

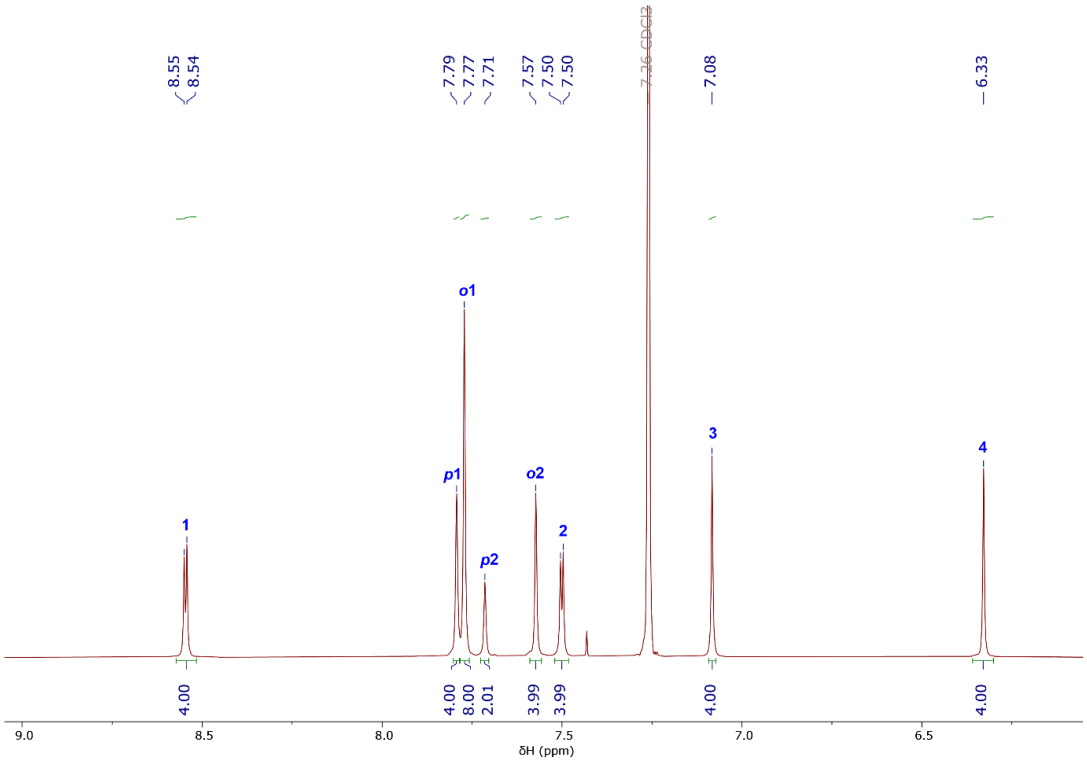

Figure E.12: Selected section of ^{1}H NMR spectrum of ***lf*-ZnP3-TIPS$_2$** (600 MHz, $CDCl_3$, 298 K).

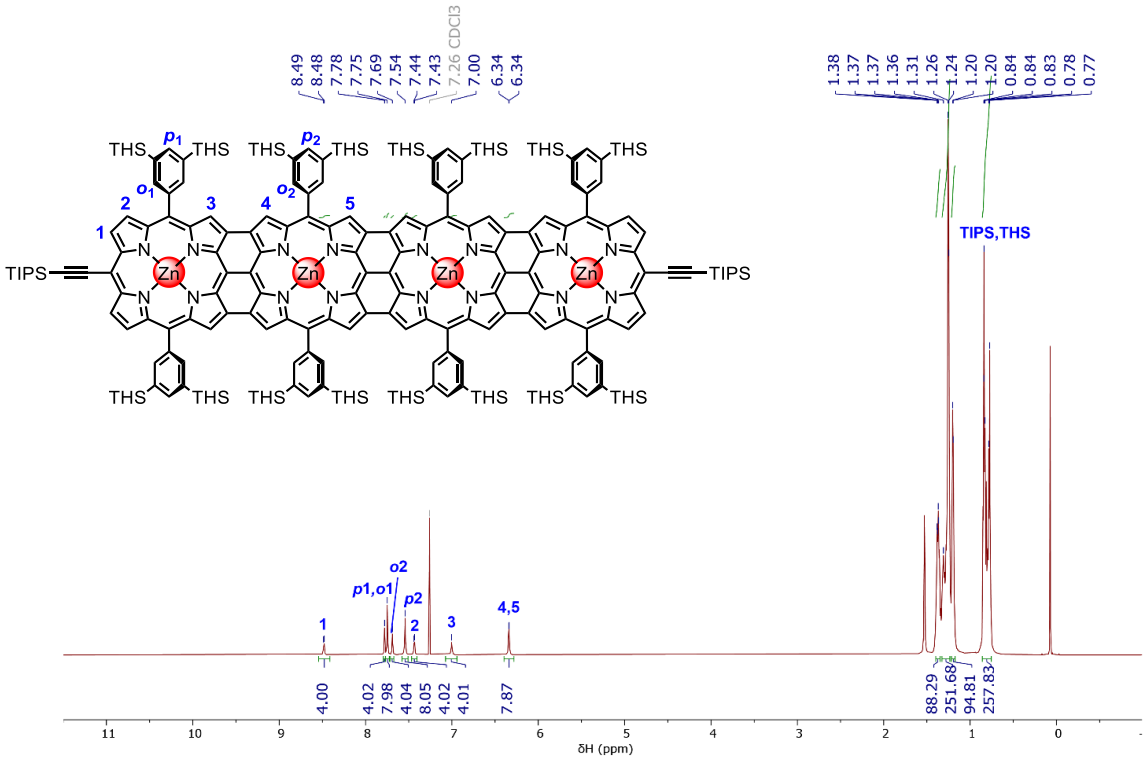

Figure E.13: ^{1}H NMR spectrum of ***lf*-ZnP4-TIPS$_2$** (600 MHz, $CDCl_3$, 298 K).

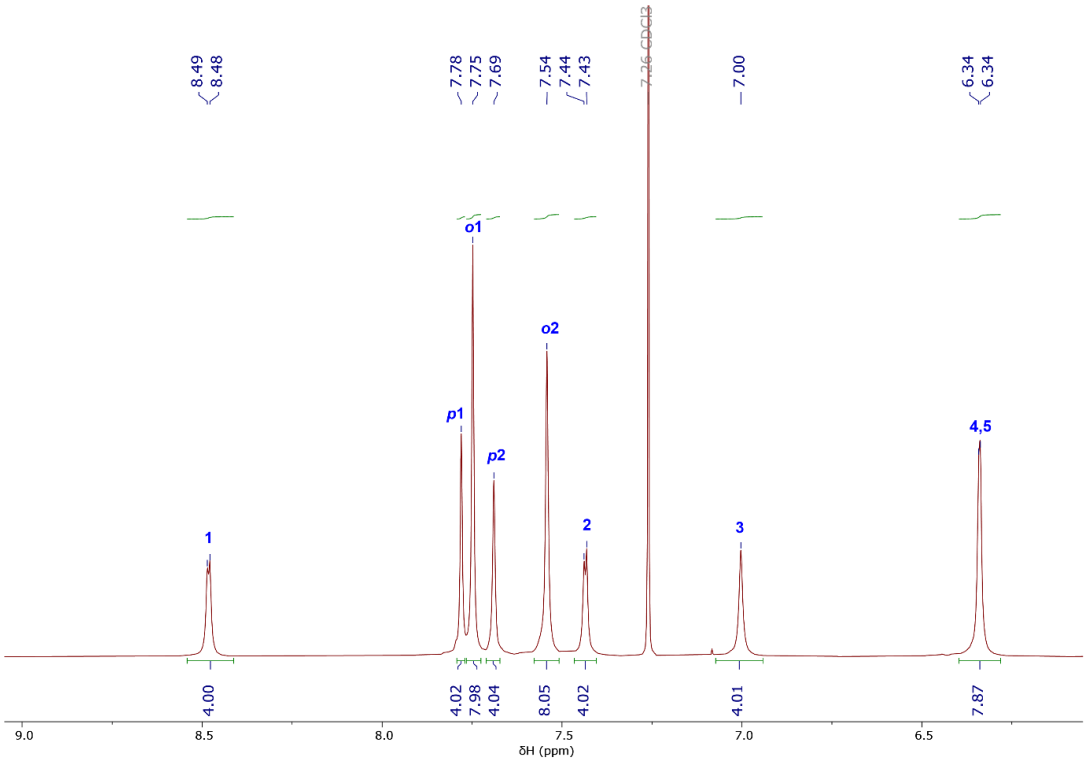

Figure E.14: Selected section of ^{1}H NMR spectrum of ***lf*-ZnP4-TIPS$_2$** (600 MHz, $CDCl_3$, 298 K).

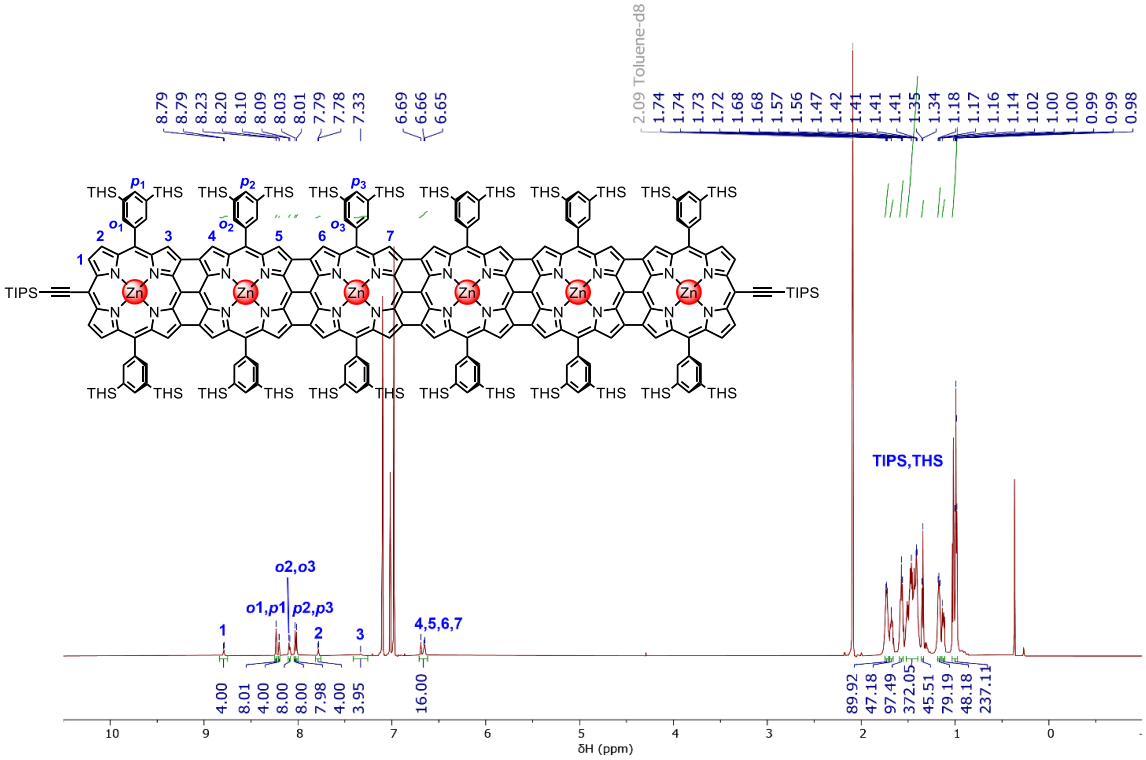

Figure E.15: ^{1}H NMR spectrum of ***lf*-ZnP6-TIPS$_2$** (700 MHz, toluene-d$_8$, 298 K).

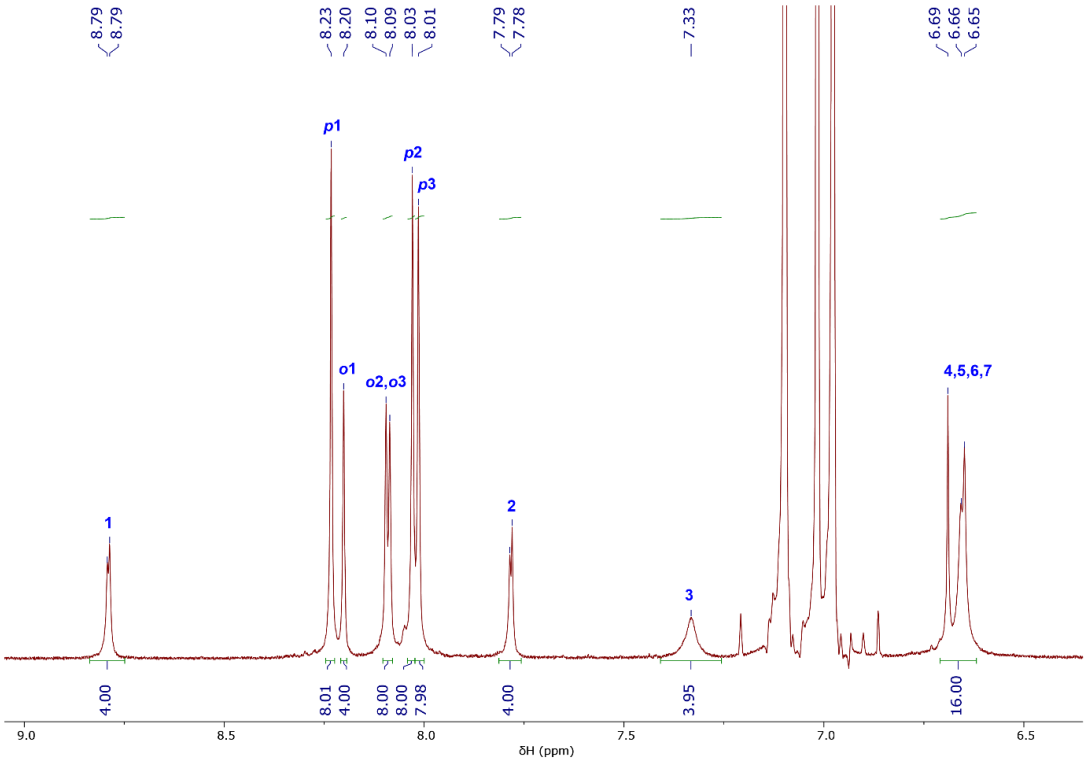

Figure E.16: Selected section of ^{1}H NMR spectrum of ***lf*-ZnP6-TIPS$_2$** (700 MHz, toluene-d$_8$, 298 K).

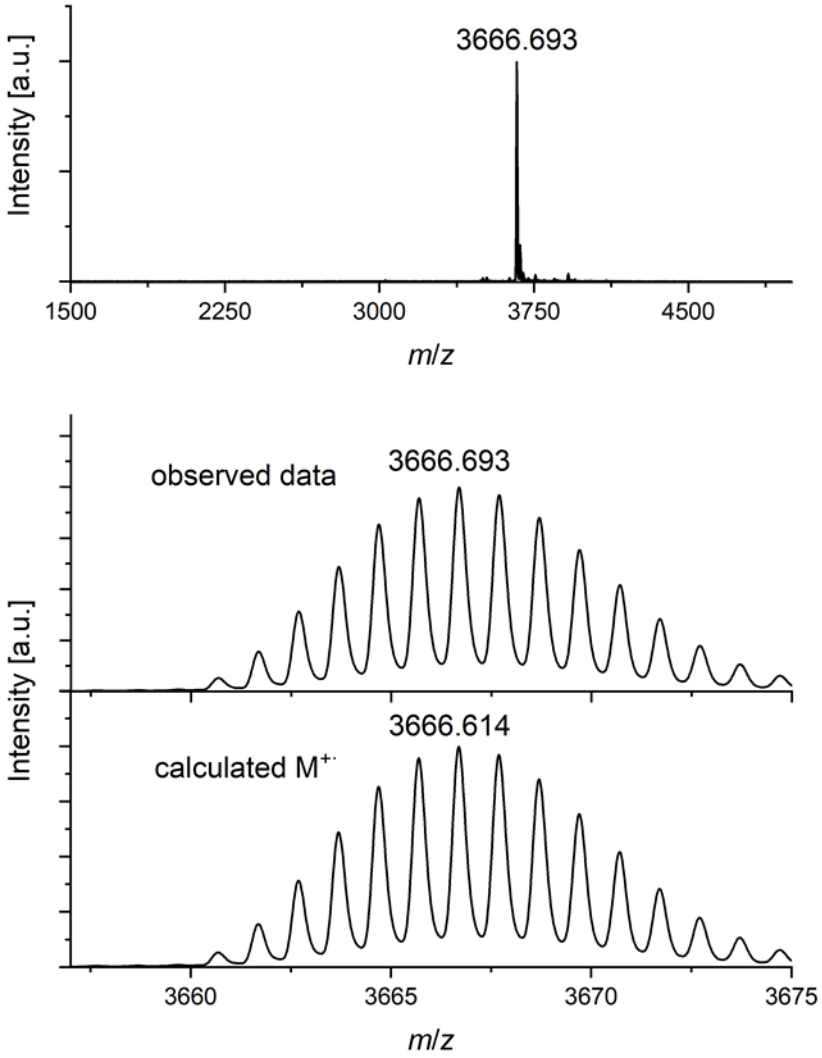

Figure E.17: MALDI-ToF spectrum of ***lf*-ZnP2-TIPS$_2$** with DCTB as matrix. Overview (top) and zoomed-view of the $M^{+\cdot}$ region (bottom).

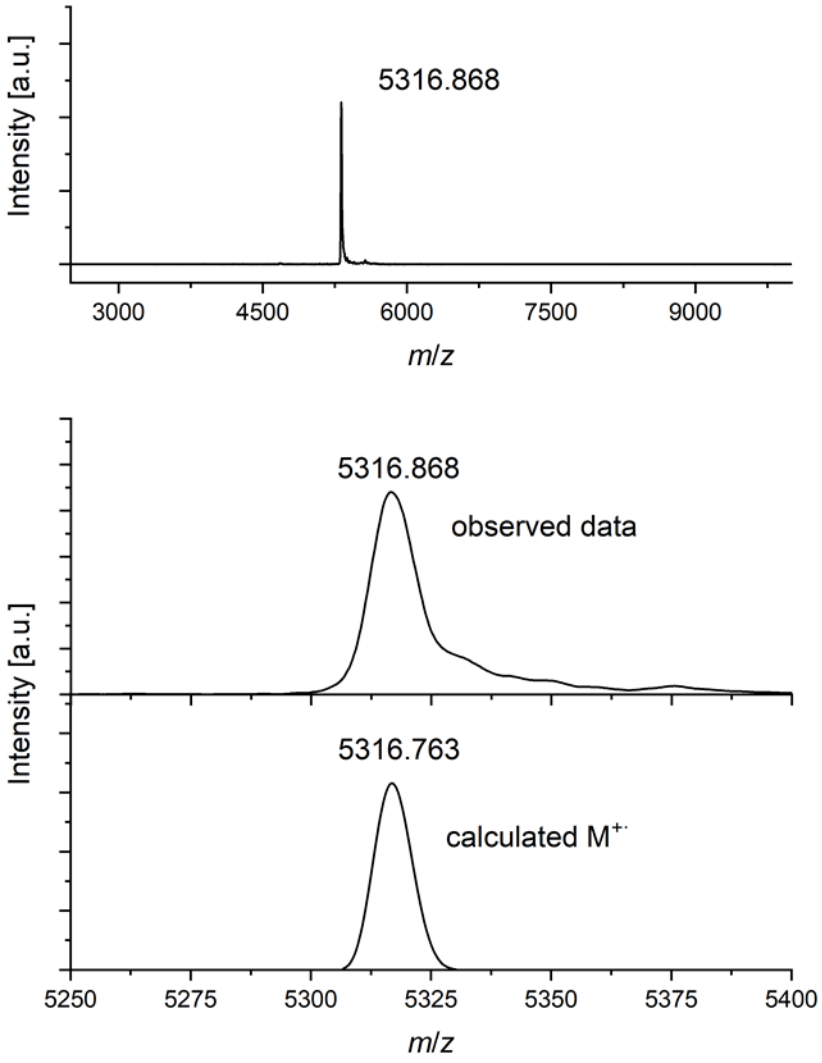

Figure E.18: MALDI-ToF spectrum of ***lf*-ZnP3-TIPS$_2$** with DCTB as matrix. Overview (top) and zoomed-view of the $M^{+\cdot}$ region (bottom).

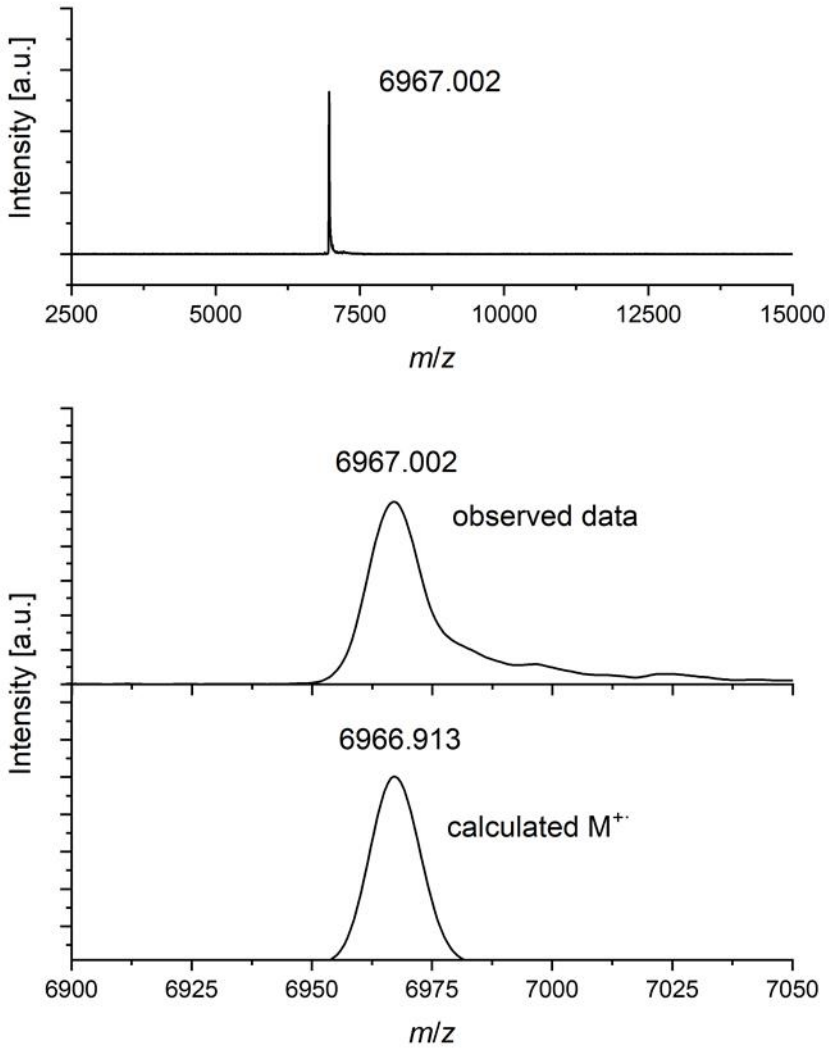

Figure E.19: MALDI-ToF spectrum of ***lf*-ZnP4-TIPS$_2$** with DCTB as matrix. Overview (top) and zoomed-view of the $M^{+\cdot}$ region (bottom).

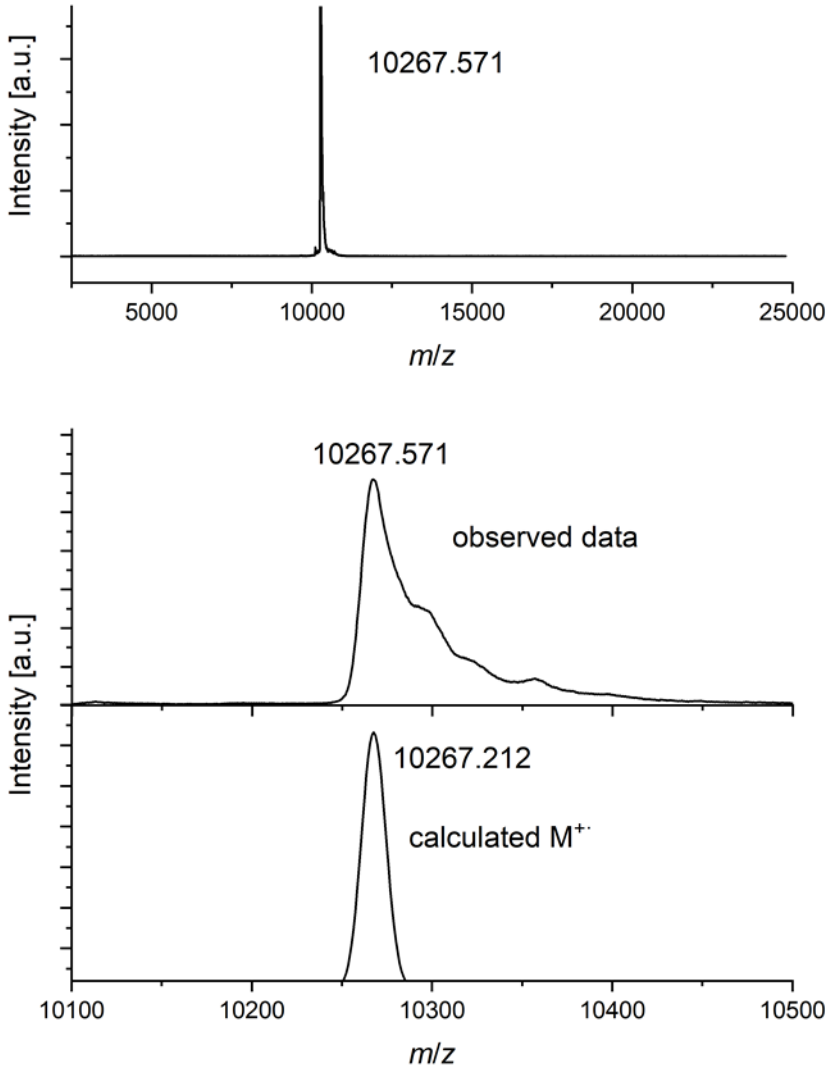

Figure E.20: MALDI-ToF spectrum of ***lf*-ZnP6-TIPS$_2$** with DCTB as matrix. Overview (top) and zoomed-view of the $M^{+\cdot}$ region (bottom).

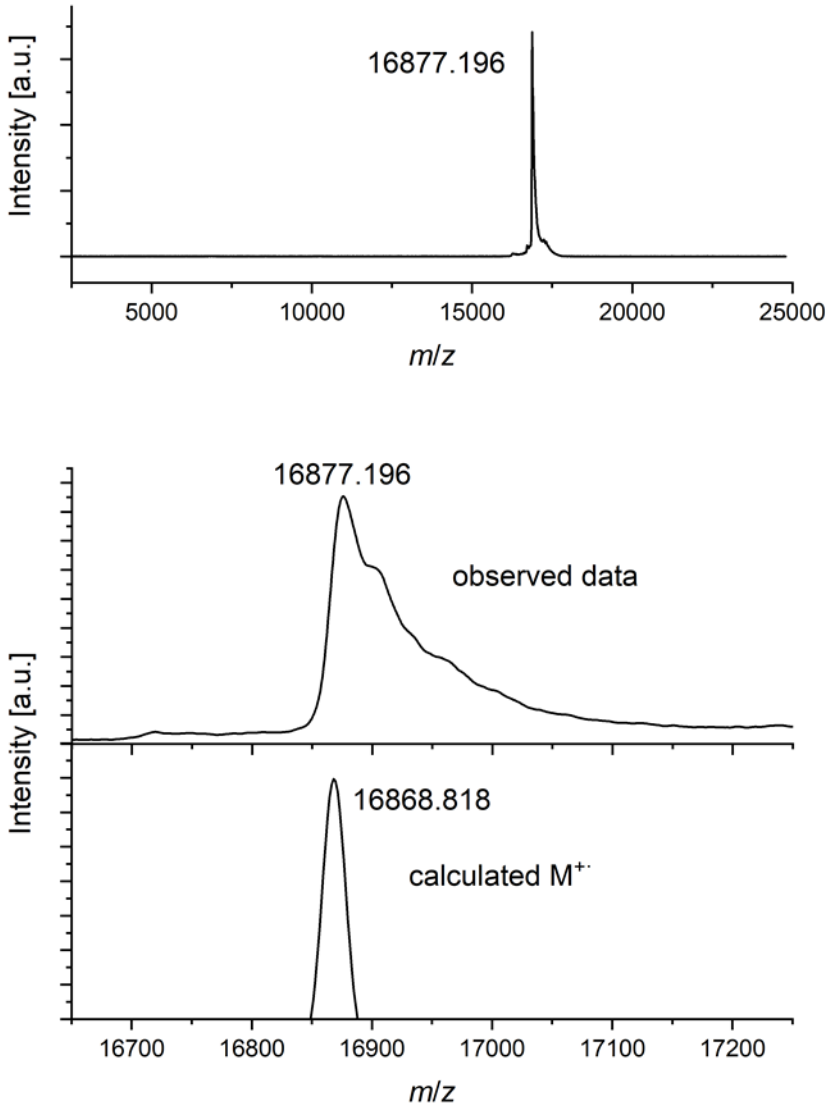

Figure E.21: MALDI-ToF spectrum of ***lf*-ZnP10-TIPS$_2$** with DCTB as matrix. Overview (top) and zoomed-view of the $M^{+\cdot}$ region (bottom).

Reference

1) Milgrom, L. R. *The Colours of Life: An Introduction to the Chemistry of Porphyrins and Related Compounds*; Oxford University Press: Oxford, 1997.
2) Willstätter, R. Chlorophyll. *J. Am. Chem. Soc.* **1915**, *37*, 323–345.
3) Senge, M. O.; Davis, M. Porphyrin (Porphine)—A Neglected Parent Compound with Potential. *J. Porphyrins Phthalocyanines* **2010**, *14*, 557–567.
4) Becker, E. D.; Bradley, R. B. Effects of "Ring Currents" on the NMR Spectra of Porphyrins. *J. Chem. Phys.* **1959**, *31*, 1413.
5) Anderson, H. L. Building Molecular Wires from the Colours of Life: Conjugated Porphyrin Oligomers. *Chem. Commun.* **1999**, 2323–2330.
6) Gouterman, M. Spectra of Porphyrins. *J. Mol. Spec.* **1961**, *6*, 138–163.
7) Gouterman, M.; Wagnière, G. H.; Snyder, L. C. Spectra of Porphyrins: Part II. Four Orbital Model. *J. Mol. Spec.* **1963**, *11*, 108–127.
8) Miller, J. R.; Dorough, G. D. Pyridinate Complexes of Some Metallo-derivatives of Tetraphenylporphine and Tetraphenylchlorin[1]. *J. Am. Chem. Soc.* **1952**, *74*, 3977–3981.
9) Kirksey, C. H.; Hambright, P.; Storm, C. B. Stability Constants and Proton Magnetic Resonance Studies of Zinc *α,β,γ,δ*-Tetraphenylporphin and Substituted Pyridines. *Inorg. Chem.* **1969**, *8*, 2141–2144.
10) Cole, S. J.; Curthoys, G. C.; Magnusson, E. A.; Phillips, J. N. Ligand Binding by Metalloporphyrins. III. Thermodynamic Functions for the Addition of Substituted Pyridines to Nickel(II) and Zinc(II) Porphyrins. *Inorg. Chem.* **1972**, *11*, 1024–1028.
11) Anderson, S.; Anderson, H. L.; Sanders, J. K. M. Expanding Roles for Templates in Synthesis. *Acc. Chem. Res.* **1993**, *26*, 469–475.
12) Bols, P. S.; Anderson, H. L. Template-Directed Synthesis of Molecular Nanorings and Cages. *Acc. Chem. Res.* **2018**, *51*, 2083–2092.
13) Venkataramani, S.; Jana, U.; Dommaschk, M.; Sönnichsen, F. D.; Tuczek, F.; Herges, R. Magnetic Bistability of Molecules in Homogeneous Solution at Room Temperature. *Science* **2011**, *331*, 445–448.
14) Wellm, V.; Groebner, J.; Heitmann, G.; Sönnichsen, F. D.; Herges, R. Toward Photoswitchable Contrast Agents for Absolute 3D Temperature MR Imaging. *Angew. Chem. Int. Ed.* **2021**, *60*, 8220–8226.
15) Huang, X.; Groves, J. T. Oxygen Activation and Radical Transformations in Heme Proteins and Metalloporphyrins. *Chem. Rev.* **2018**, *118*, 2491–2553.

16) Breslow, R.; Gellman, S. H. Intramolecular Nitrene Carbon-Hydrogen Insertions Mediated by Transition-Metal Complexes as Nitrogen Analogs of Cytochrome P-450 Reactions. *J. Am. Chem. Soc.* **1983**, *105*, 6728–6729.

17) McIntosh, J. A.; Coelho, P. S.; Farwell, C. C.; Wang, Z. J.; Lewis, J. C.; Brown, T. R.; Arnold, F. H. Enantioselective Intramolecular C-H Amination Catalyzed by Engineered Cytochrome P450 Enzymes In Vitro and In Vivo. *Angew. Chem. Int. Ed.* **2013**, *52*, 9309–9312.

18) Hyster, T. K.; Farwell, C. C.; Buller, A. R.; McIntosh, J. A.; Arnold, F. H. Enzyme-Controlled Nitrogen-Atom Transfer Enables Regiodivergent C–H Amination. *J. Am. Chem. Soc.* **2014**, *136*, 15505–15508.

19) Costentin, C.; Drouet, S.; Robert, M.; Savéant, J.-M. A Local Proton Source Enhances CO_2 Electroreduction to CO by a Molecular Fe Catalyst. *Science* **2012**, *338*, 90–94.

20) Rao, H.; Schmidt, L. C.; Bonin, J.; Robert, M. A Local Proton Source Enhances CO_2 Electroreduction to CO by a Molecular Fe Catalyst. *Nature* **2017**, *548*, 74–77.

21) Martin, D. J.; Wise, C. F.; Pegis, M. L.; Mayer, J. M. Developing Scaling Relationships for Molecular Electrocatalysis through Studies of Fe-Porphyrin-Catalyzed O_2 Reduction. *Acc. Chem. Res.* **2020**, *53*, 1056–1065.

22) Richert, S.; Cremers, J.; Anderson, H. L.; Timmel, C. R. Exploring Template-Bound Dinuclear Copper Porphyrin Nanorings by EPR Spectroscopy. *Chem. Sci.* **2016**, 7, 6952–6960.

23) Richert, S.; Cremers, J.; Kuprov, I.; Peeks, M. D.; Anderson, H. L.; Timmel, C. R. Constructive Quantum Interference in a Bis-Copper Six-Porphyrin Nanoring. *Nat. Commun.* **2017**, *8*, 14842.

24) Che, C.-M.; Sun, R. W.-Y.; Yu, W.-Y.; Ko, C.-B.; Zhu, N.; Sun, H. Gold(III) porphyrins as a New Class of Anticancer Drugs: Cytotoxicity, DNA binding and Induction of Apoptosis in Human Cervix Epitheloid Cancer Cells. *Chem. Commun.* **2003**, 1718–1719.

25) Zou, T.; Lum, C.-T.; Lok, C.-N.; Zhang, J.-J.; Che, C.-M. Chemical Biology of Anticancer Gold(III) and Gold(I) Complexes. *Chem. Soc. Rev.* **2015**, *44*, 8786–8801.

26) Guldi, D. M.; Nishihara, H.; Venkataraman, L. Molecular Wires. *Chem. Soc. Rev.* **2015**, 44, 842–844.

27) Moore, G. E. Cramming More Components onto Integrated Circuits. *Electronics* **1965**, *38*, 114–116.

28) Tsutsui, M.; Taniguchi, M. Single Molecule Electronics and Devices. *Sensors* **2012**, *12*, 7259–7298.

29) Ratner, M. A Brief History of Molecular Electronics. *Nat. Nanotechnol.* **2013**, *8*, 378–381.
30) Lörtscher, E. Wiring Molecules into Circuits. *Nat. Nanotechnol.* **2013**, *8*, 381–384.
31) Aradhya, S. V.; Venkataraman, L. Single-Molecule Junctions Beyond Electronic Transport. *Nat. Nanotechnol.* **2013**, *8*, 399–410.
32) Sun, L.; Diaz-Fernandez, Y. A.; Gschneidtner, T. A.; Westerlund, F.; Lara-Avila, S.; Moth-Poulsen, K. Single-Molecule Electronics: From Chemical Design to Functional Devices. *Chem. Soc. Rev.* **2014**, *43*, 7378–7411.
33) Xiang, D.; Wang, X.; Jia, C.; Lee, T.; Guo, X. Molecular-Scale Electronics: From Concept to Function. *Chem. Rev.* **2016**, *116*, 4318–4440.
34) Su, T. A.; Neupane, M.; Steigerwald, M. L.; Venkataraman, L.; Nuckolls, C. Chemical Principles of Single-Molecule Electronics. *Nat. Rev. Mater.* **2016**, *1*, 16002.
35) Xin, N.; Guan, J.; Zhou, C.; Chen, X.; Gu, C.; Li, Y.; Ratner, M. A.; Nitzan, A.; Stoddart, J. F.; Guo, X. Concepts in the Design and Engineering of Single-Molecule Electronic Devices. *Nat. Rev. Phys.* **2019**, *1*, 211–230.
36) Li, Y.; Yang, C.; Guo, X. Single-Molecule Electrical Detection: A Promising Route toward the Fundamental Limits of Chemistry and Life Science. *Acc. Chem. Res.* **2020**, *53*, 159–169.
37) Xie, X.; Li, P.; Xu, Y.; Zhou, L.; Yan, Y.; Xie, L.; Jia, C.; Guo, X. Single-Molecule Junction: A Reliable Platform for Monitoring Molecular Physical and Chemical Processes. *ACS Nano* **2022**, *16*, 3476–3505.
38) Gehring, P.; Thijssen, J. M.; van der Zant, H. S. J. Single-Molecule Quantum-Transport Phenomena in Break Junctions. *Nat. Rev. Phys.* **2019**, *1*, 381–396.
39) Gilbert, M.; Albinsson, B. Photoinduced Charge and Energy Transfer in Molecular Wires. *Chem. Soc. Rev.* **2015**, *44*, 845–862.
40) Schubert, C.; Margraf, J. T.; Clark, T.; Guldi, D. M. Molecular Wires – Impact of π-Conjugation and Implementation of Molecular Bottlenecks. *Chem. Soc. Rev.* **2015**, *44*, 988–998.
41) Metzger, R. M. Unimolecular Electronics. *Chem. Rev.* **2015**, *115*, 5056–5115.
42) Cuevas, J. C.; Scheer, E. *Molecular Electronics: An Introduction to Theory and Experiment*, 2nd ed.; World Scientific, 2017.
43) Evers, F.; Korytár, R.; Tewari, S.; van Ruitenbeek, J. M. Advances and Challenges in Single-Molecule Electron Transport. *Rev. Mod. Phys.* **2020**, *92*, 035001.
44) Nitzan, A. Electron Transmission through Molecules and Molecular Interfaces. *Annu. Rev. Phys. Chem.* **2001**, *52*, 681–750.

45) Luo, L.; Choi, S. H.; Frisbie, C. D. Probing Hopping Conduction in Conjugated Molecular Wires Connected to Metal Electrodes. *Chem. Mater.* **2011**, *23*, 631–645.
46) Gamow, G. Zur Quantentheorie des Atomkernes. *Eur. Phys. J. A* **1928**, *51*, 204–212.
47) Tsuji, Y.; Movassagh, R.; Datta, S.; Hoffmann, R. Exponential Attenuation of Through-Bond Transmission in a Polyene: Theory and Potential Realizations. *ACS Nano* **2015**, *9*, 11109–11120.
48) McConnell, H. M. Intramolecular Charge Transfer in Aromatic Free Radicals *J. Chem. Phys.* **1961**, *35*, 508–515.
49) Engelkes, V. B.; Beebe, J. M.; Frisbie, C. D. Length-Dependent Transport in Molecular Junctions Based on SAMs of Alkanethiols and Alkanedithiols: Effect of Metal Work Function and Applied Bias on Tunneling Efficiency and Contact Resistance. *J. Am. Chem. Soc.* **2004**, *126*, 14287–14296.
50) Segal, D.; Nitzan, A.; Ratner, M.; Davis, W. B. Activated Conduction in Microscopic Molecular Junctions. *J. Phys. Chem. B* **2000**, *104*, 2790–2793.
51) Segal, D.; Nitzan, A.; Davis, W. B.; Wasielewski, M. R.; Ratner, M. A. Electron Transfer Rates in Bridged Molecular Systems 2. A Steady-State Analysis of Coherent Tunneling and Thermal Transitions. *J. Phys. Chem. B* **2000**, *104*, 3817–3829.
52) Arnold, D. P.; Johnson, A. W.; Mahendran, M. Some Reactions of *meso*-Formyloctaethylporhyrin. *J. Chem. Soc., Perkin Trans. 1* **1978**, 366–370.
53) Arnold, D. P.; Heath, G. A. Voltammetric and UV to Near-IR Spectroelectrochemical Characterization of the *meso,meso*'-Buta-1,3-diyne-Bridged Octaethylporphyrin Dimers {[M(OEP)](μ-C4)[M(OEP)]} (M_2 = H_4, Co_2, Ni_2, Cu_2, Zn_2, Pd_2, Pt_2, Co/Ni, and Ni/Zn), in Their Neutral, Mononegative, and Dinegative Oxidation States. *J. Am. Chem. Soc.* **1993**, *115*, 12197–12198.
54) Arnold, D. P. Two Rings Are Better Than One: Adventures in Porphyrin Chemistry. *Synlett* **1999**, *3*, 296–305.
55) Anderson, H. L. Conjugated Porphyrin Ladders. *Inorg. Chem.* **1994**, *33*, 972–981.
56) Anderson, H. L.; Martin, S. J.; Bradley, D. D. C. Synthesis and Third-Order Nonlinear Optical Properties of a Conjugated Porphyrin Polymer. *Angew. Chem. Int. Ed. Engl.* **1994**, *33*, 655–657.
57) Parkinson, P.; Kondratuk, D. V.; Menelaou, C.; Gong, J. Q.; Anderson, H. L.; Herz, L. M. Chromophores in Molecular Nanorings: When is a Ring a Ring? *J. Phys. Chem. Lett.* **2014**, *5*, 4356–4361.

58) Posligua, V.; Aziz, A.; Haver, R.; Peeks, M. D.; Anderson, H. L.; Grau-Crespo, R. Band Structures of Periodic Porphyrin Nanostructures. *J. Phys. Chem. C* **2018**, 122, 23790–23798.

59) Winters, M. U.; Dahlstedt, E.; Blades, H. E.; Wilson, C. J.; Frampton, M. J.; Anderson, H. L.; Albinsson, B. Probing the Efficiency of Electron Transfer through Porphyrin-Based Molecular Wires. *J. Am. Chem. Soc.* **2007**, *129*, 4291–4297.

60) Kahnt, A.; Kärnbratt, J.; Esdaile, L. J.; Hutin, M.; Sawada, K.; Anderson, H. L.; Albinsson, B. Temperature Dependence of Charge Separation and Recombination in Porphyrin Oligomer–Fullerene Donor–Acceptor Systems. *J. Am. Chem. Soc.* **2011**, *133*, 9863–9871.

61) Gilbert Gatty, M.; Kahnt, A.; Esdaile, L. J.; Hutin, M.; Anderson, H. L.; Albinsson, B. Hopping versus Tunneling Mechanism for Long-Range Electron Transfer in Porphyrin Oligomer Bridged Donor–Acceptor Systems. *J. Phys. Chem. B* **2015**, *119*, 7598–7611.

62) Sedghi, G.; Sawada, K.; Esdaile, L. J.; Hoffmann, M.; Anderson, H. L.; Bethell, D.; Haiss, W.; Higgins, S. J.; Nichols, R. J. Single Molecule Conductance of Porphyrin Wires with Ultralow Attenuation. *J. Am. Chem. Soc.* **2008**, *130*, 8582–8583.

63) Leary, E.; Limburg, B.; Alanazy, A.; Sangtarash, S.; Grace, I.; Swada, K.; Esdaile, L. J.; Noori, M.; González, M. T.; Rubio-Bollinger, G.; Sadeghi, H.; Hodgson, A.; Agraït, N.; Higgins, S. J.; Lambert, C. J.; Anderson, H. L.; Nichols, R. J. Bias-Driven Conductance Increase with Length in Porphyrin Tapes. *J. Am. Chem. Soc.* **2018**, *140*, 12877–12883.

64) Lin, V. S.-Y.; DiMagno, S. G.; Therien, M. J. Highly Conjugated, Acetylenyl Bridged Porphyrins: New Models for Light-Harvesting Antenna Systems. *Science* **1994**, *264*, 1105–1111.

65) Susumu, K.; Frail, P. R.; Angiolillo, P. J.; Therien, M. J. Conjugated Chromophore Arrays with Unusually Large Hole Polaron Delocalization Lengths. *J. Am. Chem. Soc.* **2006**, *128*, 8380–8381.

66) Moise, G.; Tejerina, L.; Rickhaus, M.; Anderson, H. L.; Timmel, C. R. Spin Delocalization in the Radical Cations of Porphyrin Molecular Wires: A New Perspective on EPR Approaches. *J. Phys. Chem. Lett.* **2019**, *10*, 5708–5712.

67) Li, Z.; Park, T.-H.; Rawson, J.; Therien, M. J.; Borguet, E. Quasi-Ohmic Single Molecule Charge Transport through Highly Conjugated meso-to-meso Ethyne-Bridged Porphyrin Wires. *Nano Lett.* **2012**, *12*, 2722–2727.

68) Bruce, R. C.; Wang, R.; Rawson, J.; Therien, M. J.; You, W. Valence Band Dependent Charge Transport in Bulk Molecular Electronic Devices Incorporating Highly Conjugated Multi-[(Porphinato)Metal] Oligomers. *J. Am. Chem. Soc.* **2016**, *138*, 2078–2081.

69) Tsuda, A.; Furuta, H.; Osuka, A. Completely Fused Diporphyrins and Triporphyrin. *Angew. Chem. Int. Ed.* **2000**, *39*, 2549–2552.

70) Tsuda, A.; Furuta, H.; Osuka, A. Syntheses, Structural Characterizations, and Optical and Electrochemical Properties of Directly Fused Diporphyrins. *J. Am. Chem. Soc.* **2001**, *123*, 10304–10321.

71) Tsuda, A.; Osuka, A. Fully Conjugated Porphyrin Tapes with Electronic Absorption Bands That Reach into Infrared. *Science* **2001**, *293*, 79–82.

72) Sahoo, A. K.; Nakamura, Y.; Aratani, N.; Kim, K. S.; Noh, S. B.; Shinokubo, H.; Kim, D.; Osuka, A. Synthesis of Brominated Directly Fused Diporphyrins through Gold(III)-Mediated Oxidation. *Org. Lett.* **2006**, *8*, 4141–4144.

73) Ouyang, Q.; Zhu, Y.-Z.; Zhang, C.-H.; Yan, K.-Q.; Li, Y.-C.; Zheng, J.-Y. An Efficient PIFA-Mediated Synthesis of Fused Diporphyrin and Triply−Singly Interlacedly Linked Porphyrin Array. *Org. Lett.* **2009**, *11*, 5266–5269.

74) Brennan, B. J.; Kenney, M. J.; Liddell, P. A.; Cherry, B. R.; Li, J.; Moore, A. L.; Moore, T. A.; Gust, D. Oxidative Coupling of Porphyrins Using Copper(II) Salts. *Chem. Commun.* **2011**, *47*, 10034–10036.

75) Sedghi, G.; Esdaile, L. J.; Anderson, H. L.; Martin, S.; Bethell, D.; Higgins, S. J.; Nichols R. J. Comparison of the Conductance of Three Types of Porphyrin-Based Molecular Wires: *β*,*meso*,*β*-Fused Tapes, *meso*-Butadiyne-Linked and Twisted *meso*-*meso* Linked Oligomers. *Adv. Mater.* **2012**, *24*, 653–657.

76) Tanaka, T.; Osuka, A. Triply Linked Porphyrinoids. *Chem. – Eur. J.* **2018**, *24*, 17188–17200.

77) Osuka, A.; Shimidzu, H. *meso*,*meso*-Linked Porphyrin Arrays. *Angew. Chem. Int. Ed. Engl.* **1997**, *36*, 135–137.

78) Aratani, N.; Osuka, A.; Kim, Y. H.; Jeong, D. H.; Kim, D. Extremely Long, Discrete *meso*–*meso*-Coupled Porphyrin Arrays. *Angew. Chem. Int. Ed.* **2000**, *39*, 1458–1462.

79) Aratani, N.; Takagi, A.; Yanagawa, Y.; Matsumoto, T.; Kawai, T.; Yoon, Z. S.; Kim, D.; Osuka, A. Giant *meso*–*meso*-Linked Porphyrin Arrays of Micrometer Molecular Length and Their Fabrication. *Chem. – Eur. J.* **2005**, *11*, 3389–3404.

80) Ikeda, T.; Aratani N.; Osuka, A. Synthesis of Extremely π-Extended Porphyrin Tapes from Hybrid *meso*-*meso* Linked Porphyrin Arrays: An Approach Toward the Conjugation Length. *Chem. – Asian J.* **2009**, *4*, 1248–1256.

81) Cho, H. S.; Jeong, D. H.; Cho, S.; Kim, D.; Matsuzaki, Y.; Tanaka, K.; Tsuda, A.; Osuka, A. Photophysical Properties of Porphyrin Tapes. *J. Am. Chem. Soc.* **2002**, *124*, 14642–14654.

82) Yoon, D. H.; Lee, S. B.; Yoo, K. – H.; Kim, J.; Lim, J. K.; Aratani, N.; Tsuda, A.; Osuka, A.; Kim, D. Electrical Conduction Through Linear Porphyrin Arrays. *J. Am. Chem. Soc.* **2003**, *125*, 11062–11064.

83) Kang, B. K.; Aratani, N.; Lim, J. K.; Kim, D.; Osuka, A.; Yoo, K.-H. Length and Temperature Dependence of Electrical Conduction through Dithiolated Porphyrin Arrays. *Chem. Phys. Lett.* **2005**, *412*, 303–306.

84) Kang, B. K.; Aratani, N.; Lim, J. K.; Kim, D.; Osuka, A.; Yoo, K.-H. Electrical Transport Properties and Their Reproducibility for Linear Porphyrin Arrays. *Mater. Sci. Eng. C* **2006**, *26*, 1023–1027.

85) Algethami, N.; Sadeghi, H.; Sangtarash, S.; Lambert, C. J. The Conductance of Porphyrin-Based Molecular Nanowires Increases with Length. *Nano Lett.* **2018**, *18*, 4482–4486.

86) Leary, E.; Kastlunger, G.; Limburg, B.; Rincón-García, L.; Hurtado-Gallego, J.; González, M. T.; Bollinger, G. R.; Agraït, N.; Higgins, S. J.; Anderson, H. L.; Stadler R.; Nichols, R. J. Long-Lived Charged States of Single Porphyrin-Tape Junctions under Ambient Conditions. *Nanoscale Horiz.* **2021**, *6*, 49–58.

87) Thomas, J. O.; Sowa, J. K.; Limburg, B.; Bian, X.; Evangeli, C.; Swett, J. L.; Tewari, S.; Baugh, J.; Schatz, G. C.; Briggs, G. A. D.; Anderson, H. L.; Mol., J. A. Charge Transport through Extended Molecular Wires with Strongly Correlated Electrons. *Chem. Sci.* **2021**, *12*, 11121–11129.

88) Kaliginedi, V.; Moreno-García, P.; Valkenier, H.; Hong, W.; García-Suárez, V. M.; Buiter, P.; Otten, J. L. H.; Hummelen, J. C.; Lambert, C. J.; Wandlowski, T. Correlations between Molecular Structure and Single-Junction Conductance: A Case Study with Oligo(phenylene-ethynylene)-Type Wires. *J. Am. Chem. Soc.* **2012**, *134*, 5262–5275.

89) Zhao, X.; Huang, C.; Gulcur, M.; Batsanov, A. S.; Baghernejad, M.; Hong, W.; Bryce, M. R.; Wandlowski, T. Oligo(aryleneethynylene)s with Terminal Pyridyl Groups: Synthesis and Length Dependence of the Tunneling-to-Hopping Transition of Single-Molecule Conductances. *Chem. Mater.* **2013**, *25*, 4340–4347.

90) Moreno-García, P.; Gulcur, M.; Manrique, D. Z.; Pope, T.; Hong, W.; Kaliginedi, V.; Huang, C.; Batsanov, A. S.; Bryce, M. R.; Lambert, C.; Wandlowski, T. Single-Molecule Conductance of Functionalized Oligoynes: Length Dependence and Junction Evolution. *J. Am. Chem. Soc.* **2013**, *135*, 12228–12240.

91) Kim, B.; Beebe, J. M.; Jun, Y.; Zhu, X. Y.; Frisbie, G. D. Correlation between HOMO Alignment and Contact Resistance in Molecular Junctions: Aromatic Thiols versus Aromatic Isocyanides. *J. Am. Chem. Soc.* **2006**, *128*, 4970–4971.

92) Sadeghi, H.; Sangtarash, S.; Lambert, C. J. Oligoyne Molecular Junctions for Efficient Room Temperature Thermoelectric Power Generation. *Nano Lett.* **2015**, *15*, 7467–7472.

93) Liu, H.; Wang, N.; Zhao, J.; Guo, Y.; Yin, X.; Boey, F. Y. C.; Zhang, H. Length-Dependent Conductance of Molecular Wires and Contact Resistance in Metal–Molecule–Metal Junctions. *ChemPhysChem* **2008**, *9*, 1416–1424.

94) Xu, W.; Leary, E.; Hou, S.; Sangtarash, S.; González, M. T.; Rubio-Bollinger, G.; Wu, Q.; Sadeghi, H.; Tejerina, L.; Christensen, K. E.; Agraït, N.; Higgins, S. J.; Lambert, C. J.; Nichols, R. J.; Anderson, H. L. Unusual length dependence of the conductance in cumulene molecular wires. *Angew. Chem. Int. Ed.* **2019**, *58*, 8378–8382.

95) Zang, Y.; Fu, T.; Zou, Q.; Ng, F.; Li, H.; Steigerwald, M. L.; Nuckolls, C.; Venkataraman, L. Cumulene Wires Display Increasing Conductance with Increasing Length. *Nano Lett.* **2020**, *20*, 8415–8419.

96) Gunasekaran, S.; Hernangoḿez-Peŕez, D.; Davydenko, I.; Marder, S.; Evers, F.; Venkataraman, L. Near Length-Independent Conductance in Polymethine Molecular Wires. *Nano Lett.* **2018**, *18*, 6387–6391.

97) W. Xu, E. Leary, S. Sangtarash, M. Jirásek, M. T. González, K. E. Christensen, L. Abellán Vicente, N. Agraït, S. J. Higgins, R. J. Nichols, C. J. Lambert, H. L. Anderson. A Peierls Transition in Long Polymethine Molecular Wires: Evolution of Molecular Geometry and Single-Molecule Conductance. *J. Am. Chem. Soc.* **2021**, *143*, 20472–20481.

98) Li, L.; Low, J. Z.; Wilhelm, J.; Liao, G.; Gunasekaran, S.; Prindle, C. R.; Starr, R. L.; Golze, D.; Nuckolls, C.; Steigerwald, M. L.; Evers, F.; Campos, L. M.; Yin, X.; Venkataraman, L. Highly Conducting Single-Molecule Topological Insulators Based on Mono-and Di-Radical Cations. *Nat. Chem.* **2022**, *14*, 1061–1067.

99) Li, L.; Louie, S.; Evans, A. M.; Meirzadeh, E.; Nuckolls, C.; Venkataraman, L. Topological Radical Pairs Produce Ultrahigh Conductance in Long Molecular Wires. *J. Am. Chem. Soc.* **2023**, *145*, 2492–2498.

100) Rawson, J.; Angiolillo, P. J.; Frail, P. R.; Goodenough, I.; Therien, M. J. Electron Spin Relaxation of Hole and Electron Polarons in π-Conjugated Porphyrin Arrays: Spintronic Implications. *J. Phys. Chem. B* **2015**, *119*, 7681–7689.

101) Rawson, J.; Angiolillo, P. J.; Therien, M. J. Extreme Electron Polaron Spatial Delocalization in π-Conjugated Materials. *Proc. Natl. Acad. Sci. U. S. A.* **2015**, *112*, 13779–13783.

102) Peeks, M. D.; Tait, C. E.; Neuhaus, P.; Fischer, G. M.; Hoffmann, M.; Haver, R.; Cnossen, A.; Harmer, J. R.; Timmel, C. R.; Anderson, H. L. Electronic Delocalization in the Radical Cations of Porphyrin Oligomer Molecular Wires. *J. Am. Chem. Soc.* **2017**, *139*, 10461–10471.

103) Chen, L.; Hernandez, Y.; Feng, X.; Müllen, K. From Nanographene and Graphene Nanoribbons to Graphene Sheets: Chemical Synthesis. *Angew. Chem. Int. Ed.* **2012**, *51*, 7640–7654.

104) Van Raden, J. M.; Alexandropoulos, D. I.; Slota, M.; Sopp, S.; Matsuno, T.; Thompson, A. L.; Isobe, H.; Anderson, H. L.; Bogani, L. Singly- and Triply-Linked Magnetic Porphyrin Lanthanide Arrays. *J. Am. Chem. Soc.* **2022**, *144*, 8693–8706.

105) Halliday, D.; Walker, J.; Resnick, R. *Halliday and Resnick's Principles of Physics*, 11th ed.; John Wiley & Sons, Limited, 2020.

106) Bleszynski-Jayich, A. C.; Shanks, W. E.; Peaudecerf, B.; Ginossar, E.; von Oppen, F.; Glazman, L.; Harris, J. G. E. Persistent Currents in Normal Metal Rings. *Science* **2009**, *326*, 272–275.

107) von Schleyer, P. R.; Jiao, H. What is Aromaticity? *Pure Appl. Chem.* **1996**, *68*, 209–218.

108) Krygowski, T. M.; Cyrañski, M. K.; Czarnocki, Z.; Häfelinger, G.; Katritzky, A. R. Aromaticity: A Theoretical Concept of Immense Practical Importance. *Tetrahedron* **2000**, *56*, 1783–1796.

109) Gomes, J. A. N. F.; Mallion, R. B. Aromaticity and Ring Currents. *Chem. Rev.* **2001**, *101*, 1349–1383.

110) Krygowski, T. M.; Cyrañski, M. K. Structural Aspects of Aromaticity. *Chem. Rev.* **2001**, *101*, 1385–1419.

111) Kertesz, M.; Choi, C. H.; Yang, S. Conjugated Polymers and Aromaticity. *Chem. Rev.* **2005**, *105*, 3448–3481.

112) Feixas, F.; Matito, E.; Poater, J.; Solà, M. Quantifying Aromaticity with Electron Delocalisation Measures. *Chem. Soc. Rev.* **2015**, *44*, 6434–6451.

113) Gershoni-Poranne, R.; Stanger, A. Magnetic Criteria of Aromaticity. *Chem. Soc. Rev.* **2015**, *44*, 6597–6615.

114) Jirásek, M.; Anderson, H. L.; Peeks, M. D. From Macrocycles to Quantum Rings: Does Aromaticity Have a Size Limit? *Acc. Chem. Res.* **2021**, *54*, 3241–3251.

115) Sundholm, D.; Fliegl, H.; Berger, R. J. F. Calculations of Magnetically Induced Current Densities: Theory and Applications. *Wiley Interdiscip. Rev.: Comput. Mol. Sci.* **2016**, *6*, 639–678.

116) Hückel, E. Quantentheoretische Beiträge zum Benzolproblem. *Z. Physik* **1931**, *70*, 204–286.

117) Hückel, E. Quanstentheoretische Beiträge zum Benzolproblem. *Z. Physik* **1931**, *72*, 310–337.

118) Hückel, E. Quantentheoretische Beiträge zum Problem der aromatischen und ungesättigten Verbindungen. III. *Z. Physik* **1932**, *76*, 628–648.

119) Atkins, P.; De Paula, J.; Keeler, J. *Atkins' Physical Chemistry*, 11th ed.; Oxford University Press: Oxford, 2018.

120) Anslyn, E. V.; Dougherty, D. A. *Modern Physical Organic Chemistry*; University Science Books: Sausalito, CA, 2006.

121) Peeks, M. D.; Claridge, T. D. W.; Anderson, H. L. Aromatic and Antiaromatic Ring Currents in a Molecular Nanoring. *Nature* **2017**, *541*, 200–203.

122) Peeks, M. D.; Jirasek, M.; Claridge, T. D. W.; Anderson, H. L. Global Aromaticity and Antiaromaticity in Porphyrin Nanoring Anions. *Angew. Chem. Int. Ed.* **2019**, *58*, 15717–15720.

123) Peeks, M. D.; Gong, J. Q.; McLoughlin, K.; Kobatake, T.; Haver, R.; Herz, L. M.; Anderson, H. L. Aromaticity and Antiaromaticity in the Excited States of Porphyrin Nanorings. *J. Phys. Chem. Lett.* **2019**, *10*, 2017–2022.

124) Rickhaus, M.; Jirasek, M.; Tejerina, L.; Gotfredsen, H.; Peeks, M. D.; Haver, R.; Jiang, H.-W.; Claridge, T. D. W.; Anderson, H. L. Global aromaticity at the nanoscale. *Nat. Chem.* **2020**, *12*, 236–241.

125) Kopp, S. M.; Gotfredsen, H.; Deng, J.-R.; Claridge, T. D. W.; Anderson, H. L. Global Aromaticity in a Partially Fused 8-Porphyrin Nanoring. *J. Am. Chem. Soc.* **2020**, *142*, 19393–19401.

126) Jirásek, M.; Rickhaus, M.; Tejerina, L.; Anderson, H. L. Experimental and Theoretical Evidence for Aromatic Stabilization Energy in Large Macrocycles. *J. Am. Chem. Soc.* **2021**, *143*, 2403–2412.

127) Busch, D. H. Structural Definition of Chemical Templates and the Prediction of New and Unusual Materials. *J. Inclusion Phenom. Mol. Recognit. Chem.* **1992**, *12*, 389–395.

128) Anderson, S.; Anderson, H. L.; Sanders, J. K. M. Expanding Roles for Templates in Synthesis. *Acc. Chem. Res.* **1993**, *26*, 469–475.

129) Beves, J. E.; Blight, B. A.; Campbell, C. J.; Leigh, D. A.; McBurney, R. T. Strategies and Tactics for the Metal-Directed Synthesis of Rotaxanes, Knots, Catenanes, and Higher Order Links. *Angew. Chem. Int. Ed.* **2011**, *50*, 9260–9327.

130) Ayme, J.-F.; Beves, J. E.; Campbell, C. J.; Leigh, D. A. Template Synthesis of Molecular Knots. *Chem. Soc. Rev.* **2013**, *42*, 1700–1712.

131) Zhang, D.; Ronson, T. K.; Nitschke, J. R. Functional Capsules via Subcomponent Self-Assembly. Acc. Chem. Res. **2018**, *51*, 2423–2436.

132) Hogben, H. J.; Sprafke, J. K.; Hoffmann, M.; Pawlicki, M.; Anderson, H. L. Stepwise Effective Molarities in Porphyrin Oligomer Complexes: Preorganization Results in Exceptionally Strong Chelate Cooperativity. *J. Am. Chem. Soc.* **2011**, *133*, 20962–20969.

133) Hoffmann, M.; Wilson, C. J.; Odell, B.; Anderson, H. L. Template-Directed Synthesis of a π-Conjugated Porphyrin Nanoring. *Angew. Chem. Int. Ed.* **2007**, *46*, 3122–3125.

134) Hoffmann, M.; Kärnbratt, J.; Chang, M.-H.; Herz, L. M.; Albinsson, B.; Anderson, H. L. Enhanced π-Conjugation around a Porphyrin[6] Nanoring. *Angew. Chem. Int. Ed.* **2008**, *47*, 4993–4996.

135) O'Sullivan, M. C.; Sprafke, J. K.; Kondratuk, D. V.; Rinfray, C.; Claridge, T. D. W.; Saywell, A.; Blunt, M. O.; O'Shea, J. N.; Beton, P. H.; Malfois, M.; Anderson, H. L. Vernier Templating and Synthesis of a 12-Porphyrin Nano-Ring. *Nature* **2011**, *469*, 72–75.

136) Kondratuk, D. V.; Perdigão, L. M. A.; Esmail, A. M. S.; O'Shea, J. N.; Beton, P. H.; Anderson, H. L. Supramolecular Nesting of Cyclic Polymers. *Nat. Chem.* **2015**, *7*, 317–322.

137) Bols, P. S.; Rickhaus, M.; Tejerina, L.; Gotfredsen, H.; Eriksen, K.; Jirásek M.; Anderson, H. L. Allosteric Cooperativity and Template-Directed Synthesis with Stacked Ligands in Porphyrin Nanorings. *J. Am. Chem. Soc.* **2020**, *142*, 13219–13226.

138) Liu, S.; Kondratuk, D. V.; Rousseaux, S. A. L.; Gil-Ramírez, G.; O'Sullivan, M. C.; Cremers, J.; Claridge, T. D. W.; Anderson, H. L. Caterpillar Track Complexes in Template-Directed Synthesis and Correlated Molecular Motion. *Angew. Chem. Int. Ed.* **2015**, *54*, 5355–5359.

139) Rousseaux, S. A. L.; Gong, J. Q.; Haver, R.; Odell, B.; Claridge, T. D. W.; Herz, L. M.; Anderson, H. L. Self-Assembly of Russian Doll Concentric Porphyrin Nanorings. *J. Am. Chem. Soc.* **2015**, *137*, 12713–12718.

140) Bols, P. S.; Anderson, H. L. Shadow Mask Templates for Site Selective Metal Exchange in Magnesium Porphyrin Nanorings. *Angew. Chem. Int. Ed.* **2018**, *57*, 7874–7877.

141) Neuhaus, P.; Cnossen, A.; Gong, J. Q.; Herz, L. M.; Anderson, H. L. A Molecular Nanotube with 3D π-Conjugation. *Angew. Chem. Int. Ed.* **2015**, *54*, 7344–7348.

142) Cremers, J.; Haver, R.; Rickhaus, M.; Gong, J. Q.; Favereau, L.; Peeks, M. D.; Claridge, T. D. W.; Herz, L. M.; Anderson, H. L. Template-Directed Synthesis of a Conjugated Zinc Porphyrin Nanoball. *J. Am. Chem. Soc.* **2018**, *140*, 5352–5355.

143) Deng, J.-R.; Bradley, D.; Jirásek, M.; Anderson, H. L.; Peeks, M. D. Correspondence on "How Aromatic Are Molecular Nanorings? The Case of a Six-Porphyrin Nanoring" *Angew. Chem. Int. Ed.* **2022**, *61*, e202201231.

144) Wolinski, K.; Hinton, J. F.; Pulay, P. Efficient Implementation of the Gauge-Independent Atomic Orbital Method for NMR Chemical Shift Calculations. *J. Am. Chem. Soc.* **1990**, *112*, 8251–8260.

145) Casademont-Reig, I.; Ramos-Cordoba, E.; Torrent-Sucarrat M.; Matito, E. How Aromatic Are Molecular Nanorings? The Case of a Six-Porphyrin Nanoring. *Angew. Chem. Int. Ed.* **2021**, *60*, 24080–24088.

146) Chen, Z.; Wannere, C. S.; Corminboeuf, C.; Puchta, R.; Schleyer, P. v. R. Nucleus-Independent Chemical Shifts (NICS) as an Aromaticity Criterion. *Chem. Rev.* **2005**, *105*, 3842–3888.

147) Cogdell, R. J.; Gall, A.; Köhler, J. The Architecture and Function of the Light-Harvesting Apparatus of Purple Bacteria: From Single Molecules to *in Vivo* Membranes. *Q. Rev. Biophys.* **2006**, *39*, 227–324.

148) Mirkovic, T.; Ostroumov, E. E.; Anna, J. M.; van Grondelle, R.; Govindjee; Scholes, G. D. Light Absorption and Energy Transfer in the Antenna Complexes of Photosynthetic Organisms. *Chem. Rev.* **2017**, *117*, 249–293.

149) McDermott, G.; Prince, S. M.; Freer, A. A.; Hawthornthwaite-Lawless, A. M.; Papiz, M. Z.; Cogdell, R. J.; Isaacs, N. W. Crystal Structure of an Integral Membrane Light-Harvesting Complex from Photosynthetic Bacteria. *Nature* **1995**, *374*, 517–521.

150) van Grondelle, R.; Novoderezhkin, V. I. Energy Transfer in Photosynthesis: Experimental Insights and Quantitative Models *Phys. Chem. Chem. Phys.* **2006**, *8*, 793–807.

151) Pullerits, T.; Chachisvilis, M.; Sundström, V. Exciton Delocalization Length in the B850 Antenna of *Rhodobacter Sphaeroides*. *J. Phys. Chem.* **1996**, *100*, 10787–10792.

152) Novoderezhkin, V.; Monshouwer, R.; van Grondelle, R. Exciton (De)localization in the LH2 Antenna of *Rhodobacter Sphaeroides* as Revealed by Relative Difference Absorption Measurements of the LH2 Antenna and the B820 Subunit. *J. Phys. Chem. B* **1999**, *103*, 10540–10548.

153) Roszak, A. W.; Howard, T.; Southall, J.; Gardiner, A. T.; Law, C. J.; Isaacs, N. W.; Cogdell, R. J. Crystal Structure of the RC-LH1 Core Complex from *Rhodopseudomonas palustris*. *Science* **2003**, *302*, 1969–1972.

154) Yang, J.; Yoon, M.-C.; Yoo, H.; Kim, P.; Kim, D. Excitation Energy Transfer in Multiporphyrin Arrays with Cyclic Architectures: Toward Artificial Light-Harvesting Antenna Complexes. *Chem. Soc. Rev.* **2012**, *41*, 4808–4826.

155) Holm, P. J.; Bhakat, P.; Jegerschold, C.; Gyobu, N.; Mitsuoka, K.; Fujiyoshi, Y.; Morgenstern, R.; Hebert, H. Room to Move: Crystallizing Membrane Proteins in Swollen Lipidic Mesophases. *J. Mol. Biol.* **2006**, *360*, 934–945.

156) Swainsbury, D. J. K.; Qian, P.; Jackson, P. J.; Faries, K. M.; Niedzwiedzki, D. M.; Martin, E. C.; Farmer, D. A.; Malone, L. A.; Thompson, R. F.; Ranson, N. A.; Canniffe, D. P.; Dickman, M. J.; Holten, D.; Kirmaier, C.; Hitchcock, A.; Hunter, C. N. Structures of Rhodopseudomonas Palustris RC-LH1 Complexes with Open or Closed Quinone Channels. *Sci. Adv.* **2021**, *7*, eabe2631.

157) Choi, M.-S.; Yamazaki, T.; Yamazaki, I.; Aida, T. Bioinspired Molecular Design of Light-Harvesting Multiporphyrin Arrays. *Angew. Chem. Int. Ed.* **2004**, *43*, 150–158.

158) Discrete Cyclic Porphyrin Arrays as Artificial Light-Harvesting Antenna. Aratani, N.; Kim, D.; Osuka, A. *Acc. Chem. Res.* **2009**, *42*, 1922–1934.

159) Yong, C.-K.; Parkinson, P.; Kondratuk, D. V.; Chen, W.-H.; Stannard, A.; Summerfield, A.; Sprafke, J. K.; O'Sullivan, M. C.; Beton, P. H.; Anderson, H. L.; Herz, L. M. Ultrafast Delocalization of Excitation in Synthetic Light-Harvesting Nanorings. *Chem. Sci.* **2015**, *6*, 181–189.

160) Otsuki, J. Supramolecular Approach toward Light-Harvesting Materials Based on Porphyrins and Chlorophylls. *J. Mater. Chem. A* **2018**, *6*, 6710–6753.

161) Bressan, G.; Jirásek, M.; Anderson, H. L.; Heisler, I. A.; Meech, S. R. Exciton–Exciton Annihilation as a Probe of Exciton Diffusion in Large Porphyrin Nanorings. *J. Phys. Chem. C* **2020**, *124*, 18416–18425.

162) Nakamura, Y.; Hwang, I.-W.; Aratani, N.; Ahn, T. K.; Ko, D. M.; Takagi, A.; Kawai, T.; Matsumoto, T.; Kim, D.; Osuka, A. Directly *meso–meso* Linked Porphyrin Rings:

Synthesis, Characterization, and Efficient Excitation Energy Hopping. *J. Am. Chem. Soc.* **2005**, *127*, 236–246.

163) Kim, D.; Osuka, A. Photophysical Properties of Directly Linked Linear Porphyrin Arrays. *J. Phys. Chem. A* **2003**, *107*, 8791–8816.

164) Kim, D.; Osuka, A. Directly Linked Porphyrin Arrays with Tunable Excitonic Interactions. *Acc. Chem. Res.* **2004**, *37*, 10, 735–745.

165) Kim, Y. H.; Jeong, D. H.; Kim, D.; Jeoung, S. C.; Cho, H. S.; Kim, S. K.; Aratani, N.; Osuka, A. Photophysical Properties of Long Rodlike *Meso*−*Meso*-Linked Zinc(II) Porphyrins Investigated by Time-Resolved Laser Spectroscopic Methods. *J. Am. Chem. Soc.* **2001**, *123*, 76–86.

166) Aratani, N; Cho, H. S.; Cho, S.; Ahn, T. K.; Kim, D.; Sumi, H.; Osuka, A. Efficient Excitation Energy Transfer in Long *Meso*−*Meso* Linked Zn(II) Porphyrin Arrays Bearing a 5,15-Bisphenylethynylated Zn(II) Porphyrin Acceptor. *J. Am. Chem. Soc.* **2003**, *125*, 9668–9681.

167) Kasha, M.; Rawls, H. R.; El-Bayoumi, M. A. *Pure Appl. Chem.* **1965**, *11*, 371–392.

168) Yang, J.; Yoo, H.; Aratani, N.; Osuka, A.; Kim, D. Determination of the Superradiance Coherence Length of Directly Linked Linear Porphyrin Arrays at the Single-Molecule Level. *Angew. Chem. Int. Ed.* **2009**, *48*, 4323–4327.

169) Ahn, T. K.; Yoon, Z. S.; Hwang, I.-W.; Lim, J. K.; Rhee, H.; Joo, T.; Sim, E.; Kim, S. K.; Aratani, N.; Osuka, A. Effect of Conformational Heterogeneity on Excitation Energy Transfer Efficiency in Directly *meso–meso* Linked Zn(II) Porphyrin Arrays. *J. Phys. Chem. B* **2005**, *109*, 11223–11230.

170) Heilbronner, E. Molecular Orbitals in homologen Reihen mehrkerniger aromatischer Kohlenwasserstoffe: I. Die Eigenwerte yon LCAO-MO's in homologen Reihen. *Helv. Chim. Acta* **1954**, *37*, 921–935.

171) Guo, Q.; Qiu, Y.; Wang, M.; Stoddart, J. F. Aromatic Hydrocarbon Belts. *Nat. Chem.* **2021**, *13*, 402–419.

172) Iijima, S. Helical Microtubules of Graphitic Carbon. *Nature* **1991**, *354*, 56–58.

173) Iijima, S.; Ichihashi, T. Single-Shell Carbon Nanotubes of 1-nm Diameter. *Nature* **1993**, *363*, 603–605.

174) Odom, T. W.; Huang, J.-L.; Kim, P.; Lieber, C. M. Structure and Electronic Properties of Carbon Nanotubes. *J. Phys. Chem. B* **2000**, *104*, 2794–2809.

175) Gupta, N.; Gupta, S. M.; Sharma, S. K. Carbon Nanotubes: Synthesis, Properties and Engineering Applications. *Carbon Letters* **2019**, *29*, 419–447.

176) Li, Y.; Kono, H.; Maekawa, T.; Segawa, Y.; Yagi, A.; Itami, K. Chemical Synthesis of Carbon Nanorings and Nanobelts. *Acc. Mater. Res.* **2021**, *2*, 681–691.

177) Jasti, R.; Bhattacharjee, J.; Neaton, J. B.; Bertozzi, C. R. Synthesis, Characterization, and Theory of [9]-, [12]-, and [18]Cycloparaphenylene: Carbon Nanohoop Structures. *J. Am. Chem. Soc.* **2008**, *130*, 17646–17647.

178) Takaba, H.; Omachi, H.; Yamamoto, Y.; Bouffard, J.; Itami, K. Selective Synthesis of [12]Cycloparaphenylene. *Angew. Chem. Int. Ed.* **2009**, *48*, 6112–6116.

179) Yamago, S.; Watanabe, Y.; Iwamoto, T. Synthesis of [8]Cycloparaphenylene from a Square-Shaped Tetranuclear Platinum Complex. *Angew. Chem. Int. Ed.* **2010**, *49*, 757–759.

180) Povie, G.; Segawa, Y.; Nishihara, T.; Miyauchi, Y.; Itami, K. Synthesis of a Carbon Nanobelt. *Science* **2017**, *356*, 172–175.

181) Povie, G.; Segawa, Y.; Nishihara, T.; Miyauchi, Y.; Itami, K. Synthesis and Size-Dependent Properties of [12], [16], and [24]Carbon Nanobelts. *J. Am. Chem. Soc.* **2018**, *140*, 10054–10059.

182) Cheung, K. Y.; Gui, S.; Deng, C.; Liang, H.; Xia, Z.; Liu, Z.; Chi, L.; Miao, Q. Synthesis of Armchair and Chiral Carbon Nanobelts. *Chem* **2019**, *5*, 838–847.

183) Cheung, K. Y.; Watanabe, K.; Segawa, Y.; Itami, K. Synthesis of a Zigzag Carbon Nanobelt. *Nat. Chem.* **2021**, *13*, 255–259.

184) Han, Y.; Dong, S.; Shao, J.; Fan, W.; Chi, C. Synthesis of a Sidewall Fragment of a (12,0) Carbon Nanotube. *Angew. Chem. Int. Ed.* **2021**, *60*, 2658–2662.

185) Xia, Z.; Pun, S. H.; Chen, H.; Miao, Q. Synthesis of Zigzag Carbon Nanobelts through Scholl Reactions. *Angew. Chem. Int. Ed.* **2021**, *60*, 10311–10318.

186) Haver, R.; Anderson, H. L. Synthesis and Properties of Porphyrin Nanotubes. *Helv. Chim. Acta* **2019**, *102*, e1800211.

187) Martin, D. J.; Wise, C. F.; Pegis, M. L.; Mayer, J. M. Developing Scaling Relationships for Molecular Electrocatalysis through Studies of Fe-Porphyrin-Catalyzed O_2 Reduction. *Acc. Chem. Res.* **2020**, *53*, 1056–1065.

188) Wheeler, S. E.; Houk, K. N.; Schleyer, P. v. R.; Allen, W. D. A Hierarchy of Homodesmotic Reactions for Thermochemistry. *J. Am. Chem. Soc.* **2009**, *131*, 2547– 2560.

189) Haver, R.; Tejerina, L.; Jiang, H.-W.; Rickhaus, M.; Jirasek, M.; Grübner, I.; Eggimann, H. J.; Herz, L. M.; Anderson, H. L. Tuning the Circumference of Six-Porphyrin Nanorings. *J. Am. Chem. Soc.* **2019**, *141*, 7965–7971.

190) Chen, Z.; Wannere, C. S.; Corminboeuf, C.; Puchta, R.; Schleyer, P. v. R. Nucleus-Independent Chemical Shifts (NICS) as an Aromaticity Criterion. *Chem. Rev.* **2005**, *105*, 3842–3888.

191) Jin, L.-M.; Chen, L.; Yin, J.-J.; Guo, C.-C.; Chen, Q.-Y. A Facile and Potent Synthesis of *meso,meso*-Linked Porphyrin Arrays Using Iodine(III) Reagents. *Eur. J. Org. Chem.* **2005**, 3994–4001.

192) Yoshida, N.; Aratani, N.; Osuka, A. Poly(zinc(ii)-5,15-porphyrinylene) from Silver(i)-Promoted Oxidation of Zinc(ii)-5,15-Diarylporphyrins. *Chem. Commun.* **2000**, 197–198.

193) Yoshida, N.; Ishizuka, T.; Osuka, A.; Jeong, D. H.; Cho, H. S.; Kim, D.; Matsuzaki, Y.; Nogami, A.; Tanaka, K. Fine Tuning of Photophysical Properties of *meso–meso*-Linked ZnII–Diporphyrins by Dihedral Angle Control. *Chem. – Eur. J.* **2003**, *9*, 58–75.

194) Fukui, N.; Lee, S.-K.; Kato, K.; Shimizu, D.; Tanaka, T.; Lee, S.; Yorimitsu, H.; Kim, D.; Osuka, A. Regioselective Phenylene-Fusion Reactions of Ni(ii)-Porphyrins Controlled by an Electron-Withdrawing *meso*-Substituent. *Chem. Sci.* **2016**, *7*, 4059–4066.

195) Thordarson, P. Determining Association Constants from Titration Experiments in Supramolecular Chemistry. *Chem. Soc. Rev.* **2011**, *40*, 1305–1323.

196) Hunter, C. A.; Anderson, H. L. What is Cooperativity? *Angew. Chem. Int. Ed.* **2009**, *48*, 7488–7499.

197) Sonoda, M.; Inaba, A.; Itahashi, K.; Tobe, Y. Hexaethynylbenzenes Based on Tandem Sonogashira and Negishi Cross-Coupling Reactions. *Org. Lett.* **2001**, *3*, 2419–2421.

198) Krossing, I. The Facile Preparation of Weakly Coordinating Anions: Structure and Characterisation of Silverpolyfluoroalkoxyaluminates $AgAl(OR_F)_4$, Calculation of the Alkoxide Ion Affinity. *Chem. – Eur. J.* **2001**, *7*, 490–502.

199) Aratani, N.; Osuka, A. Synthesis of *meso-meso* Linked Hybrid Porphyrin Arrays by Pd-Catalyzed Cross-Coupling Reaction. *Org. Lett.* **2001**, *3*, 4213–4216.

200) Fomina, L.; Vazquez, B.; Tkatchouk, E; Fomine, S. The Glaser Reaction Mechanism. A DFT Study. *Tetrahedron* **2002**, *58*, 6741–6747.

201) Judd, C. J.; Nizovtsev, A. S.; Plougmann, R.; Kondratuk, D. V.; Anderson, H. L.; Besley E.; Saywell, A. Molecular Quantum Rings Formed from a π-Conjugated Macrocycle. *Phys. Rev. Lett.* **2020**, *125*, 206803.

202) Hogben, H. J.; Sprafke, J. K.; Hoffmann, M.; Pawlicki, M.; Anderson, H. L. Stepwise Effective Molarities in Porphyrin Oligomer Complexes: Preorganization Results in Exceptionally Strong Chelate Cooperativity. *J. Am. Chem. Soc.* **2011**, *133*, 20962–20969.

203) Hill, A. V. The Combinations of Haemoglobin with Oxygen and with Carbon Monoxide. I. *Biochem. J.* **1913**, *7*, 471–480.

204) Byers, L. D. Probe-Dependent Cooperativity Patterns in Hill-Plots. *J. Chem. Educ.* **1977**, *54*, 352–354.

205) Edelstein, S. J.; Le Novère, N. Cooperativity of Allosteric Receptors. *J. Mol. Biol.* **2013**, *425*, 1424–1432.

206) Abeliovich, H. On Hill Coefficients and Subunit Interaction Energies. *J. Math. Biol.* **2016**, *73*, 1399–1411.

207) Cingil, H. E.; Boz, E. B.; Biondaro, G.; de Vries, R.; Stuart, M. A. C.; Kraft, D. J.; van der Schoot, P.; Sprakel, J. Illuminating the Reaction Pathways of Viromimetic Assembly. *J. Am. Chem. Soc.* **2017**, *139*, 4962–4968.

208) Kikuchi, Y.; Tanaka, Y.; Sutarto, S.; Kobayashi, K.; Toi, H.; Aoyama, Y. Highly Cooperative Binding of Alkyl Glucopyranosides to the Resorcinol Cyclic Tetramer Due to Intracomplex Guest-Guest Hydrogen-Bonding: Solvophobicity/Solvophilicity Control by an Alkyl Group of the Geometry, Stoichiometry, Stereoselectivity, and Cooperativity. *J. Am. Chem. Soc.* **1992**, *114*, 10302–10306.

209) Takeuchi, M.; Imada, T.; Shinkai, S. A Strong Positive Allosteric Effect in the Molecular Recognition of Dicarboxylic Acids by a Cerium(IV) Bis[tetrakis(4-pyridyl)-porphyrinate] Double Decker. *Angew. Chem. Int. Ed.* **1998**, *37*, 2096–2099.

210) Takeuchi, M.; Shioya, T.; Swager, T. M. Allosteric Fluoride Anion Recognition by a Doubly Strapped Porphyrin. *Angew. Chem. Int. Ed.* **2001**, *40*, 3372–3376.

211) Sessler, J. L.; Tomat, E.; Lynch, V. M. Positive Homotropic Allosteric Binding of Silver(I) Cations in a Schiff Base Oligopyrrolic Macrocycle. *J. Am. Chem. Soc.* **2006**, *128*, 4184– 4185.

212) Setsune, J.; Watanabe, K. Cryptand-like Porphyrinoid Assembled with Three Dipyrrylpyridine Chains: Synthesis, Structure, and Homotropic Positive Allosteric Binding of Carboxylic Acids. *J. Am. Chem. Soc.* **2008**, *130*, 2404–2405.

213) Sakai, R.; Okade, S.; Barasa, E. B.; Kakuchi, R.; Ziabka, M.; Umeda, S.; Tsuda, K.; Satoh, T.; Kakuchi, T. Efficient Colorimetric Anion Detection Based on Positive Allosteric System of Urea-Functionalized Poly(phenylacetylene) Receptor. *Macromolecules* **2010**, *43*, 7406–7411.

214) Simon, A. J.; Vallee-Belisle, A.; Ricci, F.; Plaxco, K. W. Intrinsic disorder as a generalizable strategy for the rational design of highly responsive, allosterically cooperative receptors. *Proc. Natl. Acad. Sci. U. S. A.* **2014**, *111*, 15048–15053.

215) Suzuki, Y.; Nakamura, T.; Iida, H.; Ousaka, N.; Yashima, E. Allosteric Regulation of Unidirectional Spring-like Motion of Double-Stranded Helicates. *J. Am. Chem. Soc.* **2016**, *138*, 4852–4859.

216) Berberan-Santos, M. N.; Bodunov, E. N.; Valeur, B. Mathematical Functions for the Analysis of Luminescence Decays with Underlying Distributions 1. Kohlrausch Decay Function (Stretched Exponential). *Chem. Phys.* **2005**, *315*, 171–182.

217) Photophysics of a Butadiyne-Linked Porphyrin Dimer: Influence of Conformational Flexibility in the Ground and First Singlet Excited State. Winters, M. U.; Kärnbratt, J.; Eng, M.; Wilson, C. J.; Anderson, H. L.; Albinsson, B. *J. Phys. Chem. C* **2007**, *111*, 7192–7199.

218) Chang, M.-H.; Hoffmann, M.; Anderson, H. L.; Herz, L. M. Dynamics of Excited-State Conformational Relaxation and Electronic Delocalization in Conjugated Porphyrin Oligomers. *J. Am. Chem. Soc.* **2008**, *130*, 10171–10178.

219) Zhu, B.; Chen, H.; Lin, W.; Ye, Y.; Wu, J.; Li, S. Template-Directed Synthesis of Flexible Porphyrin Nanocage and Nanorings via One-Step Olefin Metathesis. *J. Am. Chem. Soc.* **2014**, *136*, 15126–15129.

220) Yu, G.; Cen, T. Y.; He, Z.; Wang, S. P.; Wang, Z.; Ying, X. W.; Li, S.; Jacobson, O.; Wang, S.; Wang, L.; Lin, L. S.; Tian, R.; Zhou, Z.; Ni, Q.; Li, X.; Chen, X. Porphyrin Nanocage-Embedded Single Molecular Nanoparticle as Cancer Nanotheranostics. *Angew. Chem. Int. Ed.* **2019**, 58, 8799–8803.

221) Kawashima, H.; Ukai, S.; Nozawa, R.; Fukui, N.; Fitzsimmons, G.; Kowalczyk, T.; Fliegl, H.; Shinokubo, H. Determinant Factors of Three-Dimensional Aromaticity in Antiaromatic Cyclophanes. *J. Am. Chem. Soc.* **2021**, *143*, 10676–10685.

222) Lambert, C. J. *Quantum Transport in Nanostructures and Molecules: An Introduction to Molecular Electronics*, IOP Publishing Ltd., 2021.

223) Choi, S. H.; Kim, B.; Frisbie, C. D. Electrical Resistance of Long Conjugated Molecular Wires. *Science* **2008**, *320*, 1482–1486.

224) Sedghi, G.; Sawada, K.; Esdaile, L. J.; Hoffmann, M.; Anderson, H. L.; Bethell, D.; Haiss, W.; Higgins, S. J.; Nichols, R. J. Single Molecule Conductance of Porphyrin Wires with Ultralow Attenuation. *J. Am. Chem. Soc.* **2008**, *130*, 8582–8583.

225) Xu, B.; Tao, N. J. Measurement of Single-Molecule Resistance by Repeated Formation of Molecular Junctions. *Science* **2003**, *301*, 1221–1223.

226) Hybertsen, M. S.; Venkataraman, L. Structure–Property Relationships in Atomic-Scale Junctions: Histograms and Beyond. *Acc. Chem. Res.* **2016**, *49*, 452–460.

227) van Ruitenbeek, J. M.; Alvarez, A.; PinÄeyro, I.; Grahmannet, C.; Joyez, P.; Devoret, M. H.; Esteve, D.; Urbina, C. Adjustable Nanofabricated Atomic Size Contacts. *Rev. Sci. Instrum.* **1996**, *67*, 108–111.

228) Wang, L.; Wang, L.; Zhang, L.; Xiang, D. Advance of Mechanically Controllable Break Junction for Molecular Electronics. *Top. Curr. Chem.* **2017**, *375*, 61.

229) Park, H.; Lim, A. K. L.; Alivisatos, A. P.; Park, J.; McEuen, P. L. Fabrication of Metallic Electrodes with Nanometer Separation by Electromigration. *Appl. Phys. Lett.* **1999**, *75*, 301–303.

230) Lau, C. S.; Mol, J. A.; Warner, J. H; Briggs, G. A. D. Nanoscale Control of Graphene Electrodes. *Phys. Chem. Chem. Phys.* **2014**, *16*, 20398–20401.

231) Leary, E.; La Rosa, A.; Gonzalez, M. T.; Rubio-Bollinger, G.; Agrait, N.; Martin, N. Incorporating Single Molecules into Electrical Circuits. The Role of the Chemical Anchoring Group. *Chem. Soc. Rev.* **2015**, *44*, 920–942.

232) Huang, C.; Rudnev, A. V.; Hong, W.; Wandlowski, T. Break Junction Under Electrochemical Gating: Testbed for Single-Molecule Electronics. *Chem. Soc. Rev.* **2015**, *44*, 889–901.

233) Moth-Poulsen, K.; Bjornholm, T. Molecular Electronics with Single Molecules in Solid-State Devices. *Nat. Nanotechnol.* **2009**, *4*, 551–556.

234) Perrin, M. L.; Burzuri, E.; van der Zant, H. S. Single-Molecule Transistors. *Chem. Soc. Rev.* **2015**, *44*, 902–919.

235) Lambert, C. J. Basic Concepts of Quantum Interference and Electron Transport in Single-Molecule Electronics. *Chem. Soc. Rev.* **2015**, *44*, 875–888.

236) Zwick, P.; Dulić, D.; van der Zant, H. S. J.; Mayor, M. Porphyrins as Building Blocks for Single-Molecule Devices. *Nanoscale* **2021**, *13*, 15500–15525.

237) Chen, F.; Li, X.; Hihath, J.; Huang Z.; Tao, N. Effect of Anchoring Groups on Single-Molecule Conductance: Comparative Study of Thiol-, Amine-, and Carboxylic-Acid-Terminated Molecules. *J. Am. Chem. Soc.* **2006**, *128*, 15874–15881.

238) Park, Y. S.; Whalley, A. C.; Kamenetska, M.; Steigerwald, M. L.; Hybertsen, M. S.; Nuckolls, C.; Venkataraman, L. Contact Chemistry and Single-Molecule Conductance: A Comparison of Phosphines, Methyl Sulfides, and Amines. *J. Am. Chem. Soc.* **2007**, *129*, 15768–15769.

239) Cheng, Z. L.; Skouta, R.; Vazquez, H.; Widawsky, J. R.; Schneebeli, S.; Chen, W.; Hybertsen, M. S.; Breslow, R.; Venkataraman, L. *In Situ* Formation of Highly Conducting

Covalent Au–C Contacts for Single-Molecule Junctions. *Nat. Nanotechnol.* **2011**, *6*, 353 –357.

240) Hong, W.; Manrique, D. Z.; Moreno-García, P.; Gulcur, M.; Mishchenko, A.; Lambert, C. J.; Bryce, M. R.; Wandlowski, T. Single Molecular Conductance of Tolanes: Experimental and Theoretical Study on The Junction Evolution Dependent on The Anchoring Group. *J. Am. Chem. Soc.* **2012**, *134*, 2292–2304.

241) Kamenetska, M.; Quek, S. Y.; Whalley, A. C.; Steigerwald, M. L.; Choi, H. J.; Louie, S. G.; Nuckolls, C.; Hybertsen, M. S.; Neaton, J. B.; Venkataraman, L. Conductance and Geometry of Pyridine-Linked Single-Molecule Junctions. *J. Am. Chem. Soc.* **2010**, *132*, 6817–6821.

242) Venkataraman, L.; Klare, J. E.; Nuckolls, C.; Hybertsen, M. S.; Steigerwald, M. L. Dependence of Single-Molecule Junction Conductance on Molecular Conformation. *Nature* **2006**, *442*, 904–907.

243) Leary, E.; Gonzalez, M. T.; van der Pol, C.; Bryce, M. R.; Filippone, S.; Martín, N.; Rubio-Bollinger, G.; Agraït, N. Unambiguous One-Molecule Conductance Measurements under Ambient Conditions. *Nano Lett.* **2011**, *11*, 2236–2241.

244) Hong, W.; Li, H.; Liu, S.-X.; Fu, Y.; Li, J.; Kaliginedi, V.; Decurtins, S.; Wandlowski, T. Trimethylsilyl-Terminated Oligo(phenylene ethynylene)s: An Approach to Single-Molecule Junctions with Covalent Au–C σ-Bonds. *J. Am. Chem. Soc.* **2012**, *134*, 19425–19431.

245) Millar, D.; Venkataraman, L.; Doerrer, L. H. Efficacy of Au−Au Contacts for Scanning Tunneling Microscopy Molecular Conductance Measurements. *J. Phys. Chem. C* **2007**, *111*, 47, 17635–17639.

246) Chen, W.; Widawsky, J. R.; Vázquez, H.; Schneebeli, S. T.; Hybertsen, M. S.; Breslow, R.; Venkataraman, L. Highly Conducting π-Conjugated Molecular Junctions Covalently Bonded to Gold Electrodes. *J. Am. Chem. Soc.* **2011**, *133*, 17160–17163.

247) Tanaka, Y.; Kato, Y.; Tada, T.; Fujii, S.; Kiguchi, M.; Akita, M. "Doping" of Polyyne with an Organometallic Fragment Leads to Highly Conductive Metallapolyyne Molecular Wire. *J. Am. Chem. Soc.* **2018**, *140*, 10080–10084.

248) Tanaka, Y.; Kato, Y.; Sugimoto, K.; Kawano, R.; Tada, T.; Fujii, S.; Kiguchi, M.; Akita, M. Single-Molecule Junctions of Multinuclear Organometallic Wires: Long-Range Carrier Transport Brought About by Metal–Metal Interaction. *Chem. Sci.* **2021**, *12*, 4338–4344.

249) Ikeda, T.; Lintuluoto, J. M.; Aratani, N.; Yoon, Z. S.; Kim, D.; Osuka, A. Synthesis of Doubly Strapped *meso–meso*-Linked Porphyrin Arrays and Triply Linked Conjugated Porphyrin Tapes. *Eur. J. Org. Chem.* **2006**, *14*, 3193–3204.

250) Blake, I. M.; Krivokapic, A.; Katterle, M.; Anderson, H. L. Fusion and Planarization of a Quinoidal Porphyrin Dimer. *Chem. Commun.* **2002**, 1662–1663.

251) Richert, S.; Limburg, B.; Anderson, H. L.; Timmel, C. R. On the Influence of the Bridge on Triplet State Delocalization in Linear Porphyrin Oligomers. *J. Am. Chem. Soc.* **2017**, *139*, 12003–12008.

252) Kamo, M.; Tsuda, A.; Nakamura, Y.; Aratani, N.; Furukawa, K.; Kato, T.; Osuka, A. Metal-Dependent Regioselective Oxidative Coupling of 5,10,15-Triarylporphyrins with DDQ-$Sc(OTf)_3$ and Formation of an Oxo-quinoidal Porphyrin. *Org. Lett.* **2003**, *5*, 2079–2082.

253) Nakamura, Y.; Aratani, N.; Furukawa, K.; Osuka, A. Synthesis and Characterizations of Free Base and Cu(II) Complex of a Porphyrin Sheet. *Tetrahedron* **2008**, *64*, 11433–11439.

254) Fendt, L.-A.; Fang, H.; Plonska-Brzezinska, M. E.; Zhang, S.; Cheng, F.; Braun, C.; Echegoyen, L.; Diederich, F. *meso,meso*-Linked and Triply Fused Diporphyrins with Mixed-Metal Ions: Synthesis and Electrochemical Investigations. *Eur. J. Org. Chem.* **2007**, 4659–4673.

255) Tanaka, T.; Lee, B. S.; Aratani, N.; Yoon, M.-C.; Kim, D.; Osuka, A. Synthesis and Properties of Hybrid Porphyrin Tapes. *Chem. – Eur. J.* **2011**, *17*, 14400–14412.

256) Cho, S.; Yoon, M.-C.; Kim, K. S.; Kim, P.; Kim, D. Electron Delocalization in Various Triply Linked Zinc(II) Porphyrin Arrays: Role of Antiaromatic Junctions Between Aromatic Porphyrins. *Phys. Chem. Chem. Phys.* **2011**, *13*, 16175–16181.

257) Makino, M.; Aihara, J.-i. Macrocyclic Aromaticity of Porphyrin Units in Fully Conjugated Oligoporphyrins. *J. Phys. Chem. A* **2012**, *116*, 8074–8084.

258) Valiev, R. R.; Baryshnikov, G. V.; Nasibullin, R. T.; Sundholm, D.; Ågren, H. When are Antiaromatic Molecules Paramagnetic? *J. Phys. Chem. C* **2020**, *124*, 21027–21035.

259) Kopp, S. M.; Gotfredsen, H.; Deng, J.-R.; Claridge, T. D. W.; Anderson, H. L. Global Aromaticity in a Partially Fused 8-Porphyrin Nanoring. *J. Am. Chem. Soc.* **2020**, *142*, 19393–19401.

260) Torras, J.; Casanovas, J.; Alemán, C. Reviewing Extrapolation Procedures of the Electronic Properties on the π-Conjugated Polymer Limit. *J. Phys. Chem. A* **2012**, *116*, 7571–7583.

261) González, M. T.; Leary, E.; García, R.; Verma, P.; Herranz, M. Á.; Rubio-Bollinger, G.; Martín, N.; Agraït, N. Break-Junction Experiments on Acetyl-Protected Conjugated Dithiols under Different Environmental Conditions. *J. Phys. Chem. C* **2011**, *115*, 17973–17978.

262) Luo, L.; Choi, S. H.; Frisbie, C. D. Probing Hopping Conduction in Conjugated Molecular Wires Connected to Metal Electrodes. *Chem. Mater.* **2011**, *23*, 631−645.

263) Yamada, R.; Kumazawa, H.; Tanaka, S.; Tada, H. Electrical Resistance of Long Oligothiophene Molecules. *Appl. Phys. Express* **2009**, *2*, 025002.

264) Lafferentz, L.; Ample, F.; Yu, H.; Hecht, S.; Joachim, C.; Grill, L. Conductance of a Single Conjugated Polymer as a Continuous Function of Its Length. *Science* **2009**, *323*, 1193–1197.

265) Greenwald, J. E.; Cameron, J.; Findlay, N. J.; Fu, T.; Gunasekaran, S.; Skabara, P. J.; Venkataraman, L. Highly Non-Linear Transport Across Single-Molecule Junctions via Destructive Quantum Interference. *Nat. Nanotechnol.* **2021**, *16*, 313–317.

266) Liu, J.; Huang, X.; Wang, F.; Hong, W. Quantum Interference Effects in Charge Transport through Single-Molecule Junctions: Detection, Manipulation, and Application. *Acc. Chem. Res.* **2019**, *52*, 151–160.

267) Prins, F.; Barreiro, A.; Ruitenberg, J. W.; Seldenthuis, J. S.; Aliaga-Alcalde, N.; Vandersypen, L. M.; van der Zant, H. S. Room-Temperature Gating of Molecular Junctions Using Few-Layer Graphene Nanogap Electrodes. *Nano Lett.* **2011**, *11*, 4607–4611.

268) Mol, J. A.; Lau, C. S.; Lewis, W. J.; Sadeghi, H.; Roche, C.; Cnossen, A.; Warner, J. H.; Lambert, C. J.; Anderson, H. L.; Briggs, G. A. Recent Progress in Single-Molecule Transistors: Their Designs, Mechanisms and Applications. *Nanoscale* **2015**, *7*, 13181–13185.

269) Jia, C. C.; Ma, B. J.; Xin, N.; Guo, X. F. Carbon Electrode-Molecule Junctions: A Reliable Platform for Molecular Electronics. *Acc. Chem. Res.* **2015**, *48*, 2565–2575.

270) Limburg, B.; Thomas, J. O.; Holloway, G.; Sadeghi, H.; Sangtarash, S.; Hou, I. C.; Cremers, J.; Narita, A.; Müllen, K.; Lambert, C. J.; Briggs, G. A. D.; Mol, J. A.; Anderson, H. L. Anchor Groups for Graphene-Porphyrin Single-Molecule Transistors. *Adv. Funct. Mater.* **2018**, *28*, 1803629.

271) Cao, Y.; Dong, S.; Liu, S.; He, L.; Gan, L.; Yu, X.; Steigerwald, M. L.; Wu, X.; Liu, Z.; Guo, X. Building High-Throughput Molecular Junctions Using Indented Graphene Point Contacts. *Angew. Chem. Int. Ed.* **2012**, *51*, 12228–12232.

272) Thomas, J. O.; Limburg, B.; Sowa, J. K.; Willick, K.; Baugh, J.; Briggs, G. A. D.; Gauger, E. M.; Anderson, H. L.; Mol, J. A. Understanding Resonant Charge Transport Through Weakly Coupled Single-Molecule Junctions. *Nat. Commun.* **2019**, *10*, 4628.

273) Braun, S.; Salaneck, W. R.; Fahlman, M. Energy-Level Alignment at Organic/Metal and Organic/Organic Interfaces. *Adv. Mater.* **2009**, *21*, 1450–1472.

274) Scott, G. D.; Natelson, D. Kondo Resonances in Molecular Devices. *ACS Nano* **2010**, *4*, 3560–3579.

275) Kouwenhoven, L.; Glazman, L. Revival of the Kondo Effect. *Physics World* **2001**, 14, 33–38.

276) Park, J.; Pasupathy, A. N.; Goldsmith, J. I.; Chang, C.; Yaish, Y.; Petta, J. R.; Rinkoski, M.; Sethna, J. P.; Abruña, H. D.; McEuen, P. L.; Ralph, D. C. Coulomb Blockade and the Kondo Effect in Single-Atom Transistors. *Nature* **2002**, *417*, 722–725.

277) Liang, W.; Shores, M. P.; Bockrath, M.; Long, J. R.; Park, H. Kondo Resonance in a Single-Molecule Transistor. *Nature* **2002**, *417*, 725–729.

278) Parks, J. J.; Champagne, A. R.; Hutchison, G. R.; Flores-Torres, S.; Abruna, H. D.; Ralph, D. C. Tuning the Kondo Effect with a Mechanically Controllable Break Junction. *Phys. Rev. Lett.* **2007**, *99*, 026601.

279) Frisenda, R.; Gaudenzi, R.; Franco, C.; Mas-Torrent, M.; Rovira, C.; Veciana, J.; Alcon, I.; Bromley, S. T.; Burzuri, E.; van der Zant, H. S. Kondo Effect in a Neutral and Stable All Organic Radical Single Molecule Break Junction. *Nano Lett.* **2015**, *15*, 3109–3114.

280) Goldhaber-Gordon, D.; Göres, J.; Kastner, M. A.; Shtrikman, H.; Mahalu, D.; Meirav, U. From the Kondo Regime to the Mixed-Valence Regime in a Single-Electron Transistor. *Phys. Rev. Lett.* **1998**, *81*, 5225–5228.

281) Nagaoka, K.; Jamneala, T.; Grobis, M.; Crommie, M. F. Temperature Dependence of a Single Kondo Impurity. *Phys. Rev. Lett.* **2002**, *88*, 077205.

282) Oksanen, M.; Uppstu, A.; Laitinen, A.; Cox, D. J.; Craciun, M. F.; Russo, S.; Harju, A.; Hakonen, P. Single-Mode and Multimode Fabry-Pérot Interference in Suspended Graphene. *Phys. Rev. B* **2014**, *89*, 121414.

283) Rickhaus, P.; Maurand, R.; Liu, M. H.; Weiss, M.; Richter, K.; Schonenberger, C. Ballistic Interferences in Suspended Graphene. *Nat. Commun.* **2013**, *4*, 2342.

284) Gehring, P.; Sadeghi, H.; Sangtarash, S.; Lau, C. S.; Liu, J.; Ardavan, A.; Warner, J. H.; Lambert, C. J.; Briggs, G. A. D.; Mol, J. A. Quantum Interference in Graphene Nanoconstrictions. *Nano Lett.* **2016**, 16, 4210–4216.

285) Hwang, C.; Siegel, D. A.; Mo, S. K.; Regan, W.; Ismach, A.; Zhang, Y. G.; Zettl, A.; Lanzara, A. Fermi Velocity Engineering in Graphene by Substrate Modification. *Sci. Rep.* **2012**, *2*, 590.

286) Liang, W. J.; Bockrath, M.; Bozovic, D.; Hafner, J. H.; Tinkham, M.; Park, H. Fabry–Perot Interference in a Nanotube Electron Waveguide. *Nature* **2001**, *411*, 665–669.

287) Bian, X.; Chen, Z.; Sowa, J. K.; Evangeli, C.; Limburg, B.; Swett, J. L.; Baugh, J.; Briggs, G. A. D.; Anderson, H. L.; Mol, J. A.; Thomas, J. O. Charge-State Dependent Vibrational Relaxation in a Single-Molecule Junction. *Phys. Rev. Lett.* **2022**, 129, 207702.

288) Moth-Poulsen, K.; Bjornholm, T. Molecular Electronics with Single Molecules in Solid-State Devices. *Nat. Nanotechnol.* **2009**, *4*, 551–556.

289) Osorio, E. A.; Bjørnholm, T.; Lehn, J. M.; Ruben, M.; van der Zant, H. S. J. Single-Molecule Transport in Three-Terminal Devices. *J. Phys.: Condens. Matter* **2008**, *20*, 374121.

290) Déprez, C.; Veyrat, L.; Vignaud, H.; Nayak, G.; Watanabe, K.; Taniguchi, T.; Gay, F.; Sellier, H.; Sacépé, B. A Tunable Fabry-Perot Quantum Hall Interferometer in Graphene. *Nat. Nanotechnol.* **2021**, *16*, 555–562.

291) Ronen, Y.; Werkmeister, T.; Najafabadi, D. H.; Pierce, A. T.; Anderson, L. E.; Shin, Y. J.; Lee, S. Y.; Lee, Y. H.; Johnson, B.; Watanabe, K.; Taniguchi, T.; Yacoby, A.; Kim, P. Aharonov-Bohm Effect in Graphene-Based Fabry-Pérot Quantum Hall Interferometers. *Nat. Nanotechnol.* **2021**, *16*, 563–569.

292) Song, S. M.; Cho, B. J. Investigation of Interaction Between Graphene and Dielectrics. *Nanotechnology* **2010**, *21*, 335706.

293) Tikhonenko, F. V.; Horsell, D. W.; Gorbachev, R. V.; Savchenko, A. K. Weak Localization in Graphene Flakes. *Phys. Rev. Lett.* **2008**, *100*, 056802

294) Hewson, A. C. *The Kondo Problem to Heavy Fermions*; Cambridge University Press: Cambridge, 2009.

295) Liu, J. Y.; Zhao, X. T.; Al-Galiby, Q.; Huang, X. Y.; Zheng, J. T.; Li, R. H.; Huang, C. C.; Yang, Y.; Shi, J.; Manrique, D. Z.; Lambert, C. J.; Bryce, M. R.; Hong, W. Radical-Enhanced Charge Transport in Single-Molecule Phenothiazine Electrical Junctions. *Angew. Chem. Int. Ed.* **2017**, *56*, 13061–13065.

296) Koole, M.; Thijssen, J. M.; Valkenier, H.; Hummelen, J. C.; van der Zant, H. S. Electric-Field Control of Interfering Transport Pathways in a Single-Molecule Anthraquinone Transistor. *Nano Lett.* **2015**, *15*, 5569–5573.

297) O'Driscoll, L. J.; Hamill, J. M.; Grace, I.; Nielsen, B. W.; Almutib, E.; Fu, Y.; Hong, W.; Lambert, C. J.; Jeppesen, J. O. Electrochemical Control of the Single Molecule Conductance of a Conjugated Bis(pyrrolo)tetrathiafulvalene Based Molecular Switch. *Chem. Sci.* **2017**, *8*, 6123–6130.

298) Soler, J. M.; Artacho, E.; Gale, J. D.; García, A.; Junquera1, J.; Ordejón, P.; Sánchez-Portal, D. The SIESTA Method for *Ab Initio* Order-*N* Materials Simulation. *J. Phys.: Condens. Matter* **2002**, *14*, 2745.

299) Ferrer, J.; Lambert, C. J.; García-Suárez, V. M.; Manrique, D. Z.; Visontai, D.; Oroszlany, L.; Rodríguez-Ferradás, R.; Grace, I.; Bailey, S. W. D.; Gillemot, K.; Sadeghi, H.; Algharagholy, L. A. GOLLUM: A Next-Generation Simulation Tool for Electron, Thermal and Spin Transport. *New J. Phys.* **2014**, *16*, 093029.

300) Gröning, O.; Wang, S.; Yao, X.; Pignedoli, C. A.; Barin, G. B.; Daniels, C.; Cupo, A.; Meunier, V.; Feng, X.; Narita, A.; Müllen, K.; Ruffieux, P.; Fasel, R. Engineering of Robust Topological Quantum Phases in Graphene Nanoribbons. *Nature* **2018**, *560*, 209–213.

301) Brédas, J. L.; Street, G. B. Polarons, Bipolarons, and Solitons in Conducting Polymers. *Acc. Chem. Res.* **1985**, *18*, 309–315.

302) Coropceanu, V.; Cornil, J.; da Silva Filho, D. A.; Olivier, Y.; Silbey, R.; Brédas, J.-L. Charge Transport in Organic Semiconductors. *Chem. Rev.* **2007**, *107*, 926–952.

303) Sakanoue, T.; Sirringhaus, H. Band-Like Temperature Dependence of Mobility in a Solution-Processed Organic Semiconductor. *Nat. Mater.* **2010**, *9*, 736–740.

304) Bässler, H.; Köhler, A. Charge Transport in Organic Semiconductors. *Top. Curr. Chem.* **2011**, *312*, 1–65.

305) Bakulin, A. A.; Rao, A.; Pavelyev, V. G.; van Loosdrecht, P. H. M.; Pshenichnikov, M. S.; Niedzialek, D.; Cornil, J.; Beljonne, D.; Friend, R. H. The Role of Driving Energy and Delocalized States for Charge Separation in Organic Semiconductors. *Science* **2012**, *335*, 1340–1344.

306) Tamura, H.; Burghardt, I. Ultrafast Charge Separation in Organic Photovoltaics Enhanced by Charge Delocalization and Vibronically Hot Exciton Dissociation. *J. Am. Chem. Soc.* **2013**, *135*, 16364–16367.

307) Hush, N. S. Distance Dependence of Electron Transfer Rates. *Coord. Chem. Rev.* **1985**, *64*, 135–157.

308) Brunschwig, B. S.; Creutz, C.; Sutin, N. Optical Transitions of Symmetrical Mixed-Valence Systems in the Class II–III Transition Regime. *Chem. Soc. Rev.* **2002**, *31*, 168–184.

309) Hankache, J.; Wenger, O. S. Organic Mixed Valence. *Chem. Rev.* **2011**, *111*, 5138–5178.

310) Heckmann, A.; Lambert, C. Organic Mixed-Valence Compounds: A Playground for Electrons and Holes. *Angew. Chem. Int. Ed.* **2012**, *51*, 326–392.

311) Talipov, M. R.; Boddeda, A.; Timerghazin, Q. K.; Rathore, R. Key Role of End-Capping Groups in Optoelectronic Properties of Poly-*p*-phenylene Cation Radicals. *J. Phys. Chem. C* **2014**, *118*, 21400–21408.

312) Robin, M. B.; Day, P. Mixed Valence Chemistry-A Survey and Classification. *Adv. Inorg. Chem. Radiochem.* **1967**, *9*, 247–422.

313) Nelsen, S. F.; Chang, H.; Wolff, J. J.; Adamus, J. Polycyclic Bis(hydrazine) and Bis(hydrazyl) Radical Cations: High and Low Inner-Sphere Reorganization Energy Organic Intervalence Compounds. *J. Am. Chem. Soc.* **1993**, *115*, 12276–12289.

314) Bonvoisin, J.; Launay, J.-P.; Van der Auweraer, M.; De Schryver, F. C. Organic Mixed-Valence Systems: Electrochemical and Optical Studies of Intervalence Transition in Partly Oxidized Aromatic Polyamines. *J. Phys. Chem.* **1994**, *98*, 5052–5057.

315) Talipov, M. R.; Jasti, R.; Rathore, R. A Circle Has No End: Role of Cyclic Topology and Accompanying Structural Reorganization on the Hole Distribution in Cyclic and Linear Poly-*p*-phenylene Molecular Wires. *J. Am. Chem. Soc.* **2015**, *137*, 14999–15006.

316) Talipov, M. R.; Ivanov, M. V.; Rathore, R. Inclusion of Asymptotic Dependence of Reorganization Energy in the Modified Marcus-Based Multistate Model Accurately Predicts Hole Distribution in Poly-p-phenylene Wires. *J. Phys. Chem. C* **2016**, *120*, 6402–6408.

317) Lane, P. A.; Wei, X.; Vardeny, Z. V. Studies of Charged Excitations in π-Conjugated Oligomers and Polymers by Optical Modulation. *Phys. Rev. Lett.* **1996**, *77*, 1544–1547.

318) Österbacka, R.; An, C. P.; Jiang, X. M.; Vardeny, Z. V. Two-Dimensional Electronic Excitations in Self-Assembled Conjugated Polymer Nanocrystals. *Science* **2000**, *287*, 839–842.

319) Heimel, G. The Optical Signature of Charges in Conjugated Polymers. *ACS Cent. Sci.* **2016**, *2*, 309–315.

320) Meier, H.; Stalmach, U.; Kolshorn, H. Effective Conjugation Length and UV/vis Spectra of Oligomers. *Acta Polym.* **1997**, *48*, 379–384.

321) Ivanov, M. V.; Talipov, M. R.; Boddeda, A.; Abdelwahed, S. H.; Rathore, R. Hückel Theory + Reorganization Energy = Marcus–Hush Theory: Breakdown of the 1/*n* Trend in π-Conjugated Poly-*p*-phenylene Cation Radicals Is Explained. *J. Phys. Chem. C* **2017**, *121*, 1552–1561.

322) Norris, J. R.; Uphaus, R. A.; Crespi, H. L.; Katz, J. J. Electron Spin Resonance of Chlorophyll and the Origin of Signal I in Photosynthesis. *Proc. Natl. Acad. Sci. U. S. A.* **1971**, *68*, 625–628.

323) Seth, J.; Palaniappan, V.; Johnson, T. E.; Prathapan, S.; Lindsey, J. S.; Bocian, D. F. Investigation of Electronic Communication in Multi-Porphyrin Light-Harvesting Arrays. *J. Am. Chem. Soc.* **1994**, *116*, 10578–10592.

324) Wilson, T. M.; Hori, T.; Yoon, M.-C.; Aratani, N.; Osuka, A.; Kim, D.; Wasielewski, M. R. Rapid Intramolecular Hole Hopping in *meso*−*meso* and *meta*-Phenylene Linked Linear and Cyclic Multiporphyrin Arrays. *J. Am. Chem. Soc.* **2010**, *132*, 1383–1388.

325) Richert, S.; Limburg, B.; Anderson, H. L.; Timmel, C. R. On the Influence of the Bridge on Triplet State Delocalization in Linear Porphyrin Oligomers. *J. Am. Chem. Soc.* **2017**, *139*, 12003–12008.

326) Chen, Z.; Deng, J.-R.; Hou, S.; Bian, X.; Swett, J. L.; Wu, Q.; Baugh, J.; Briggs, G. A. D.; Mol, J. A.; Lambert, C. J.; Anderson, H. L.; Thomas, J. O. Phase-Coherent Charge Transport Through a Porphyrin Nanoribbon-Graphene Junction. *arXiv* **2022**, DOI: 10.48550/arXiv.2205.08499.

327) Krejčik, M.; Daněk, M.; Hartl, F. J. Simple Construction of an Infrared Optically Transparent Thin-Layer Electrochemical Cell: Applications to the Redox Reactions of Ferrocene, $Mn_2(CO)_{10}$ and $Mn(CO)_3$(3,5-di-t-butyl-catecholate)$^-$ *Electroanal. Chem. Interfacial Electrochem.* **1991**, *317*, 179–187.

328) Arnold, D. P.; Hartnell, R. D.; Heath, G. A.; Newby, L.; Webster, R. D. Remarkable Homology in the Electronic Spectra of the Mixed-Valence Cation and Anion Radicals of a Conjugated Bis(porphyrinyl)butadiyne. *Chem. Commun.* **2002**, 754–755.

329) Wilson, G. J.; Arnold, D. P. Time-Dependent Density Functional Molecular Orbital and Excited State Calculations on Bis(porphyrinyl)butadiynes in the Monocationic, Neutral, Monoanionic, and Dianionic Oxidation States. *J. Phys. Chem. A* **2005**, *109*, 6104–6113.

330) Renz, M.; Theilacker, K.; Lambert, C.; Kaupp, M. A Reliable Quantum-Chemical Protocol for the Characterization of Organic Mixed-Valence Compounds. *J. Am. Chem. Soc.* **2009**, *131*, 16292–16302.

331) Kaupp, M.; Renz, M. Parthey, M.; Stolte, M.; Würthner, F.; Lambert, C. Computational and Spectroscopic Studies of Organic Mixed-Valence Compounds: Where Is the Charge? *Phys. Chem. Chem. Phys.* **2011**, *13*, 16973–16986.

332) McConnell, H. M. Indirect Hyperfine Interactions in the Paramagnetic Resonance Spectra of Aromatic Free Radicals. *J. Chem. Phys.* **1956**, *24*, 764.

333) Takeda, N.; Miller, J. R. Poly(3-decylthiophene) Radical Anions and Cations in Solution: Single and Multiple Polarons and Their Delocalization Lengths in Conjugated Polymers. *J. Phys. Chem. B* **2012**, *116*, 14715–14723.

334) Ghosh, R.; Pochas, C. M.; Spano, F. C. Polaron Delocalization in Conjugated Polymer Films. *J. Phys. Chem. C* **2016**, *120*, 11394–11406.

335) Brédas, J.-L.; Beljonne, D.; Coropceanu, V.; Cornil, J. Charge-Transfer and Energy-Transfer Processes in π-Conjugated Oligomers and Polymers: A Molecular Picture. *Chem. Rev.* **2004**, *104*, 4971–5004.

336) Sirringhaus, H.; Sakanoue, T.; Chang, J. F. Charge-Transport Physics of High-Mobility Molecular Semiconductors. *Phys. Status Solidi B* **2012**, *249*, 1655–1676.

337) Tanaka, T.; Lee, B. S.; Aratani, N.; Yoon, M.-C.; Kim, D.; Osuka, A. Synthesis and Properties of Hybrid Porphyrin Tapes. *Chem. – Eur. J.* **2011**, *17*, 14400–14412.

338) Mori, H.; Tanaka, T.; Aratani, N.; Lee, B. S.; Kim, P.; Kim, D.; Osuka, A. An Electron-Deficient Porphyrin Tape. *Chem. – Asian J.* **2012**, *7*, 1811–1816.

339) Mori, H.; Kim, T.; Kim, D.; Osuka, A. Trimeric and Tetrameric Electron-Deficient Porphyrin Tapes. *Chem. – Asian J.* **2016**, *11*, 1454–1463.

340) Jerschow, A.; Müller, N. Suppression of Convection Artifacts in Stimulated-Echo Diffusion Experiments. Double-Stimulated-Echo Experiments. *J. Magn. Reson.* **1997**, *125*, 372–375.

341) Wang, L.; Fan, K.; Daniel, Q.; Duan, L.; Li, F.; Philippe, B.; Rensmo, H.; Chen, H.; Sun, J.; Sun, L. Electrochemical Driven Water Oxidation by Molecular Catalysts *in situ* Polymerized on the Surface of Graphite Carbon Electrode. *Chem. Commun.* **2015**, *51*, 7883–7886.

342) Hsu, T.-W.; Kim, C.; Michaudel, Q. Stereoretentive Ring-Opening Metathesis Polymerization to Access All-*cis* Poly(*p*-phenylenevinylene)s with Living Characteristics. *J. Am. Chem. Soc.* **2020**, *142*, 11983–11987.

343) Yokoyama, S.; Hirose, T.; Matsuda, K. Photoinduced Four-State Three-Step Ordering Transformation of Photochromic Terthiophene at a Liquid/Solid Interface Based on Two Principles: Photochromism and Polymorphism. *Langmuir* **2015**, *31*, 6404–6414.

344) Gaefke, G.; Höger, S. [(3-Cyanopropyl)diisopropylsilyl]acetylene, a More Stable Analogue of [(3-Cyanopropyl)dimethylsilyl]acetylene. *Synthesis* **2008**, *14*, 2155–2157.

345) Lehnherr, D.; Gao, J.; Hegmann, F. A.; Tykwinski, R. R. Synthesis and Electronic Properties of Conjugated Pentacene Dimers. *Org. Lett.* **2008**, *10*, 4779–4782.

346) Sonoda, M.; Inaba, A.; Itahashi, K.; Tobe, Y. Synthesis of Differentially Substituted Hexaethynylbenzenes Based on Tandem Sonogashira and Negishi Cross-Coupling Reactions. *Org. Lett.* **2001**, *3*, 2419–2421.

347) Rathore, R.; Burns, C. L.; Deselnicu, M. I. Multiple-Electron Transfer in a Single Step. Design and Synthesis of Highly Charged Cation-Radical Salts. *Org. Lett.* **2001**, *3*, 2887–2890.

348) Benson, S.W. Statistical Factors in the Correlation of Rate Constants and Equilibrium Constants. *J. Am. Chem. Soc.* **1958**, *80*, 5151–5154.

349) Bailey, W. F.; Monahan, A. S. Statistical Effects and the Evaluation of Entropy Differences in Equilibrium Processes. *J. Chem. Ed.* **1978**, *55*, 489–493.

350) Ercolani, G.; Piguet, C.; Borkovec, M.; Hamacek, J. Symmetry Numbers and Statistical Factors in Self-Assembly and Multivalency. *J. Phys. Chem. B* **2007**, *111*, 12195–12203.

351) Würth, C.; Grabolle, M.; Pauli, J.; Spieles, M.; Resch-Genger, U. Relative and Absolute Determination of Fluorescence Quantum Yields of Transparent Samples. *Nat. Protoc.* **2013**, *8*, 1535–1550.

352) Taniguchi, M.; Lindsey, J. S.; Bocian, D. F.; Holten, D. Comprehensive Review of Photophysical Parameters (ε, Φ_f, τ_s) of Tetraphenylporphyrin (H_2TPP) and Zinc Tetraphenylporphyrin (ZnTPP) – Critical Benchmark Molecules in Photochemistry and Photosynthesis. *J. Photochem. Photobiol. C* **2021**, *46*, 100401.

353) Camargo, F. V. A.; Hall, C. R.; Anderson, H. L.; Meech, S. R.; Heisler, I. A. Time Resolved Structural Dynamics of Butadiyne-Linked Porphyrin Dimers. *Struct. Dynamics* **2016**, *3*, 023608.

354) Stevens, A. L.; Kaeser, A.; Schenning, A. P. H. J.; Herz, L. M. Morphology-Dependent Energy Transfer Dynamics in Fluorene-Based Amphiphile Nanoparticles. *ACS Nano* **2012**, *6*, 4777–4787.

355) Mollay, B.; Lemmer, U.; Kersting, R.; Mahrt, R. F.; Kurz, H.; Kauffmann, H. F.; Bässler, H. Dynamics of Singlet Excitations in Conjugated Polymers: Poly(phenylenevinylene) and Poly(phenylphenylenevinylene). *Phys. Rev. B* **1994**, *50*, 10769–10779.

356) Powell, R. C.; Soos, Z. G. Singlet Exciton Energy Transfer in Organic Solids. *J. Luminescence* **1975**, *11*, 1–45.

357) Herz, L. M.; Silva, C.; Grimsdale, A. C.; Müllen, K.; Phillips, R. T. Time-Dependent Energy Transfer Rates in a Conjugated Polymer Guest-Host System. *Phys. Rev. B* **2004**, *70*, 165207.

358) Chenu, A.; Scholes, G. D. Coherence in Energy Transfer and Photosynthesis. *Annu. Rev. Phys. Chem.* **2015**, *66*, 69–96.

359) Monshouwer, R.; Abrahamsson, M.; van Mourik, F.; van Grondelle, R. Superradiance and Exciton Delocalization in Bacterial Photosynthetic Light-Harvesting Systems. *J. Phys. Chem. B* **1997**, *101*, 7241–7248.

360) Ha, J.-H.; Cho, H. S.; Song, J. K.; Kim, D.; Aratani, N.; Osuka, A. Excitonic Coupling Strength and Coherence Length in the Singlet and Triplet Excited States of *meso–meso* Directly Linked Zn(II)porphyrin Arrays. *ChemPhysChem* **2004**, *5*, 57–67.

361) Frisch, M. J.; Trucks, G. W.; Schlegel H. B.; Scuseria, G. E.; Robb M. A.; Cheeseman J. R.; Scalmani, G.; Barone, V.; Petersson, G. A.; Nakatsuji, H.; Li, X.; Caricato, M.; Marenich, A. V.; Bloino, J.; Janesko, B. G.; Gomperts, R.; Mennucci B.; Hratchian, H. P.; Ortiz, J. V.; Izmaylov, A. F.; Sonnenberg, J. L.; WilliamsYoung, D.; Ding, F.; Lipparini, F.; Egidi, F.; Rega, N.; Zheng, G.; Liang, W.; Hada, M.; Ehara, M.; Toyota, K.; Fukuda, R.; Hasegawa, J.; Ishida, M.; Nakajima, T.; Honda, Y.; Kitao, O.; Nakai, H.; Vreven, T.; Throssell, K.; Montgomery Jr., J. A.; Peralta, J. E.; Ogliaro, F.; Bearpark, M. J.; Heyd, J. J.; Brothers, E. N.; Kudin, K. N.; Staroverov, V. N.; Keith, T. A.; Kobayashi, R.; Normand, J.; Raghavachari, K.; Rendell, A. P.; Burant, J. C.; Iyengar, S. S.; Tomasi, J.; Cossi, M.; Millam, J. M.; Klene, M.; Adamo, C.; Cammi, R.; Ochterski, J. W.; Martin, R. L.; Morokuma, K.; Farkas, O.; Foresman, J. B.; Fox, D. J. Gaussian 16, Revision A.03. Gaussian Inc.: Wallingford CT 2016.

362) Cieplak, P.; Caldwell, J.; Kollman, P. Molecular Mechanical Models for Organic and Biological Systems Going Beyond the Atom Centered Two Body Additive Approximation: Aqueous Solution Free Energies of Methanol and *N*-Methyl Acetamide, Nucleic Acid Base, and Amide Hydrogen Bonding and Chloroform/Water Partition Coefficients of the Nucleic Acid Bases. *J. Comput. Chem.* **2001**, *22*, 1048–1057.

363) Essmann, U.; Perera, L.; Berkowitz, M. L.; Darden, T.; Lee, H.; Pedersen, L. G. A Smooth Particle Mesh Ewald Method. *J. Chem. Phys.* **1995**, *103*, 8577–8593.

364) Shang, C.; Philpott, J. M.; Bampos, N.; Barker, P. D.; Wales, D. J. How to Make a Porphyrin Flip: Dynamics of Asymmetric Porphyrin Oligomers. *Phys. Chem. Chem. Phys.* **2015**, *17*, 27094–27102.

365) Skopec, C. E.; Cukrowski, I.; Marques, H. M. Using Artificial Neural Networks to Develop Molecular Mechanics Parameters for the Modelling of Metalloporphyrins: Part IV. Five-, Six-Coordinate Metalloporphyrins of Mn, Co, Ni and Cu. *J. Mol. Struct.* **2006**, *783*, 21–33.

366) Case, D. A.; Belfon, K.; Ben-Shalom, I. Y.; Brozell, S. R.; Cerutti, D. S.; Cheatham, III, T. E.; Cruzeiro, V. W. D.; Darden, T. A.; Duke, R. E.; Giambasu, G.; Gilson, M. K.; Gohlke, H.; Goetz, A. W.; Harris, R.; Izadi, S.; Izmailov, S. A.; Kasavajhala, K.; Kovalenko, A.; Krasny, R.; Kurtzman, T.; Lee, T. S.; LeGrand, S.; Li P.; Lin, C.; Liu, J.; Luchko, T.; Luo, R.; Man, V.; Merz, K. M.; Miao, Y. Mikhailovskii, O.; Monard, G.; Nguyen, H.; Onufriev, A.; Pan, F.; Pantano, S.; Qi, R.; Roe, D. R.; Roitberg, A.; Sagui, C.; Schott-Verdugo, S.; Shen J.; Simmerling, C. L.; Skrynnikov, N. R.; Smith, J.; Swails, J.; Walker, R. C.; Wang, J.; Wilson, L.; Wolf, R. M.; Wu, X.; Xiong, Y.; Xue, Y.; York D. M.; Kollman P. A. AMBER 2020, University of California, San Francisco, 2020.

367) Li, P. F.; Merz, K. M. MCPB.py: A Python Based Metal Center Parameter Builder. *J. Chem. Inf. Model.* **2016**, *56*, 599–604.

368) Seminario, J. M. Calculation of Intramolecular Force Fields from Second-Derivative Tensors. *Int. J. Quantum. Chem.* **1996**, *60*, 1271–1277.

369) Frisch, M. J.; Trucks, G. W.; Schlegel, H. B.; Scuseria, G. E.; Robb, M. A.; Cheeseman, J. R.; Scalmani, G.; Barone, V.; Mennucci, B.; Petersson, G. A.; Nakatsuji, H.; Caricato, M.; Li, X.; Hratchian, H. P.; Izmaylov, A. F.; Bloino, J.; Zheng, G.; Sonnenberg, J. L.; Hada, M.; Ehara, M.; Toyota, K.; Fukuda, R.; Hasegawa, J.; Ishida, M.; Nakajima, T.; Honda, Y.; Kitao, O.; Nakai, H.; Vreven, T.; Montgomery Jr., J. A.; Peralta, J. E.; Ogliaro, F.; Bearpark, M.; Heyd, J. J.; Brothers, E.; Kudin, K. N.; Staroverov, V. N.; Keith, T; Kobayashi, R.; Normand, J.; Raghavachari, K.; Rendell, A.; Burant, J. C.; Iyengar, S. S.; Tomasi, J.; Cossi, M.; Rega, N.; Millam, J. M.; Klene, M.; Knox, J. E.; Cross, J. B.; Bakken, V.; Adamo, C.; Jaramillo, J.; Gomperts, R.; Stratmann, R. E.; Yazyev, O.; Austin, A. J.; Cammi, R.; Pomelli, C.; Ochterski, J. W.; Martin, R. L.; Morokuma, K.; Zakrzewski, V. G.; Voth, G. A.; Salvador, P.; Dannenberg, J. J.; Dapprich, S.; Daniels, A. D.; Farkas, Ö.; Foresman, J. B.; Ortiz, J. V.; Cioslowski, J.; Fox, D. J. Gaussian 09, Revision A.03. Gaussian Inc.: Wallingford CT 2009.

370) Gotfredsen, H.; Deng, J.-R.; Van Raden, J. M.; Righetto, M.; Hergenhahn, J.; Clarke, M.; Bellamy-Carter, A.; Hart, J.; O'Shea, J.; Claridge, T. D. W.; Duarte, F.; Saywell, A.; Herz, L. M.; Anderson, H. L. Bending a Photonic Wire into a Ring. *Nat. Chem.* **2022**, *14*, 1436–1442.

371) Abraham, M. J.; Murtola, T.; Schulz, R.; Páll, S.; Smith, J. C.; Hess, B.; Lindahl, E. GROMACS: High Performance Molecular Simulations Through Multi-Level Parallelism from Laptops to Supercomputers. *SoftwareX* **2015**, *1–2*, 19–25.

372) Wang, J. M.; Wolf, R. M.; Caldwell, J. W.; Kollman, P. A.; Case, D. A. Development and Testing of a General Amber Force Field. *J. Comput. Chem.* **2004**, *25*, 1157–1174.

373) Bussi, G.; Donadio, D.; Parrinello, M. Canonical Sampling Through Velocity Rescaling. *J. Chem. Phys.* **2007**, *126*, 014101.

374) Parrinello, M.; Rahman, A. Polymorphic Transitions in Single Crystals: A New Molecular Dynamics Method. *J. Appl. Phys.* **1981**, *52*, 7182–7190.

375) Cieplak, P.; Caldwell, J.; Kollman, P. Molecular Mechanical Models for Organic and Biological Systems Going Beyond the Atom Centered Two Body Additive Approximation: Aqueous Solution Free Energies of Methanol and *N*-Methyl Acetamide, Nucleic Acid Base, and Amide Hydrogen Bonding and Chloroform/Water Partition Coefficients of the Nucleic Acid Bases. *J. Comput. Chem.* **2001**, *22*, 1048–1057.

376) Essmann, U.; Perera, L.; Berkowitz, M. L.; Darden, T.; Lee, H.; Pedersen, L. G. A Smooth Particle Mesh Ewald Method. *J. Chem. Phys.* **1995**, *103*, 8577–8593.

377) Dennington, R.; Keith, T. A.; Millam, J. M. GaussView, Version 6. Semichem Inc., Shawnee Mission, KS, 2016.

378) Ditchfield, R.; Hehre, W. J.; Pople, J. A. Self-Consistent Molecular-Orbital Methods. IX. An Extended GaussianType Basis for Molecular-Orbital Studies of Organic Molecules. *J. Chem. Phys.* **1971**, *54*, 724–728.

379) Hehre, W. J.; Ditchfield, R.; Pople, J. A. Self-Consistent Molecular Orbital Methods. XII. Further Extensions of Gaussian-Type Basis Sets for Use in Molecular Orbital Studies of Organic Molecules. *J. Chem. Phys.* **1972**, *56*, 2257–2261.

380) Hariharan, P. C.; Pople, J. A. The Influence of Polarization Functions on Molecular Orbital Hydrogenation Energies. *Theor. Chim. Acta* **1973**, *28*, 213–222.

381) Rassolov, V. A.; Pople, J. A.; Ratner, M. A.; Windus, T. L. 6-31G* Basis Set for Atoms K through Zn. *J. Chem. Phys.* **1998**, *109*, 1223–1229.

382) Tomasi, J.; Mennucci, B.; Cammi, R. Quantum Mechanical Continuum Solvation Models. *Chem. Rev.* **2005**, *105*, 2999–3094.

383) Houck, A. A.; Labaziewicz, J.; Chan, E. K.; Folk, J. A.; Chuang, I. L. Kondo Effect in Electromigrated Gold Break Junctions. *Nano Lett.* **2005**, *5*, 1685–1688.

384) Lee, P. A.; Stone, A. D.; Fukuyama, H. Universal Conductance Fluctuations in Metals: Effects of Finite Temperature, Interactions, and Magnetic Field. *Phys. Rev. B* **1987**, *35*, 1039–1070.

385) Staley, N. E.; Puls, C. P.; Liu, Y. Suppression of Conductance Fluctuation in Weakly Disordered Mesoscopic Graphene Samples Near the Charge Neutral Point. *Phys. Rev. B* **2008**, *77*, 155429.